A Framework for Regional Scale Quantitative Landslide Risk Analysis

William Pollock

A dissertation

submitted in partial fulfillment of the

requirements for the degree of

Doctor of Philosophy

University of Washington

2020

Reading Committee:

Joseph Wartman, Chair

Alison Duvall

Chris Massey

Program Authorized to Offer Degree:

Civil and Environmental Engineering

University of Washington

Abstract

A Framework for Regional Scale Quantitative Landslide Risk Analysis

William Pollock

Chair of the Supervisory Committee:

Professor Joseph Wartman

Department of Civil and Environmental Engineering

Landslides are among the most common and damaging natural hazards on earth. Policy makers, land use planners, and community members need to know not only when and where landslides are likely to occur (hazard) but also the consequences on the human-built environment (risk). Existing methods for quantitative landslide hazard analysis contain several critical limitations, including oversimplification of the diverse range of landslide phenomena, computationally expensive models which prohibit application on local or regional scales, dependence on costly and rare landslide inventories, and deterministic methods which do not account for uncertainty in environmental and human inputs. Landslide hazard is rarely translated into landslide risk due to a lack of quantitative data necessary to model landslide runout and estimate the vulnerability of people, buildings, and infrastructure.

I address these challenges through the development and validation of a multimodal, regional scale framework for coseismic and precipitation-induced landslide risk analysis which implements physically-based models in a probabilistic system. I develop new tools to characterize landslide runout and the vulnerability of elements at risk.

By applying the multimodal landslide risk analysis framework at two study regions, I explore questions at the intersection of natural hazards, human ecology, and policy-making. In the country of Lebanon, geologic risk has soared due to the influx of 1.5 million refugees fleeing the civil war in neighboring Syria. I examine the temporal and spatial patterns of landslide risk within Lebanon, noting the impact of refugee resettlement policies and illustrating the utility of real-time risk analyses for immediate refugee crisis response.

Seattle, Washington, is one of the most landslide-prone urban areas in the United States. However, up until now, no estimates of landslide risk have been available for land use decision-making in the region. I perform a probabilistic landslide hazard and risk analysis for the city of Seattle, providing quantitative, spatially explicit estimates of landslide-related losses in future precipitation and earthquake events. By disaggregating the unique consequences of Seattle's various types of landslides, this work informs targeted risk mitigation strategies to protect individuals and the built environment from preventable landslide losses.

TABLE OF CONTENTS

LIST OF FIGURES

LIST OF TABLES

DEDICATION

For my grandparents, Ed, Nan, David, and Ann

who have left a legacy of faith, compassion, and education.

Introduction

I. Global consequences of landslides

Damaging landslides are a common occurrence worldwide. Multi-decade inventories show an increasing incidence of fatal landslides as well as growing landslide-related damages (Cascini et al., 2005; Petley, 2012). Landslides are responsible for over 4000 annual deaths worldwide and over $16 billion in damages among only a handful of developed countries (Bowman, 2015; Froude and Petley, 2018; Haque et al., 2015). In the United States alone, 25 – 50 people are killed annually with ~ $3.5 – 4 billion in damages (Bowman, 2015; Schuster and Highland, 2001). Catastrophic landslides make headlines every year. The 2008 M7.9 Wenchuan Earthquake in China triggered ~ 200,000 landslides which killed almost 30,000 people and left over five million homeless (Wang et al., 2014; Xu et al., 2014). On 28 September 2018, a M7.5 earthquake near the Indonesian city of Palu triggered massive flowslides which enveloped part of the city, burying up to 5,000 people (Petley, 2018). The deadliest precipitation-induced landslide disaster to date in the 21st century occurred 16 – 17 June 2013 when monsoon rainfall triggered landslides across the state of Uttarakhand, India, killing 6000. The majority of the casualties occurred when two successive debris flows devastated the village of Kedarnath and two smaller settlements downstream (Allen et al., 2016). In May 2014, a loess flowslide engulfed part of the town of Abe Barek in Badakhshan Province of Afghanistan in a highly mobile, two-stage failure, killing an estimated 2700 (Zhang et al., 2015).

Although landslide fatalities are concentrated in economically developing regions, large-fatality disasters have occurred in the United States as well (Anderson and Holcombe, 2013). A month prior to the Abe Barek flowslide, a highly mobile flowslide destroyed the community of

Steelhead Haven near the town of Oso in Washington State. With 43 fatalities and direct damages in excess of $50 million, the so-called "SR 530" or "Oso" Flowslide was the worst landslide disaster in U.S. history since the 1985 Mameyes landslide killed 129 in Ponce, Puerto Rico (Jibson, 1992; Keaton et al., 2014). Prior to the Oso flowslide, the deadliest single landslide in the conterminous U.S. was a 2005 debris flow which inundated part of the coastal California community of La Conchita, killing 10 individuals and damaging 36 homes (Jibson, 2005). However, the cumulative consequences of smaller, lower profile landslides is often as great or greater than these large, catastrophic events (Dowling and Santi, 2014; Bowman, 2015, Alexander, 2015). For instance California frequently experiences widespread, fatal debris flows during the winter season, especially after major wildfires. Such events killed 20 in 1969, 25 in 1982, 16 in 2003, and 21 in 2018 (Campbell, 1975; Ellen and Wieczorek, 1988; Cannon and DeGraff; Niehaus, 2018).

II. The utility of risk analysis

In recent years, there have been attempts to systematically catalogue damaging landslides in "one-stop" global inventories for the purpose of estimating losses (EM-DAT, 2018; Kirschbaum, 2010; Marc et al., 2018; Petley, 2012; Tanyas et al., 2017). However, whether from explicit or implicit methodological constraints, smaller, low-fatality events often go unrecorded (Froude and Petley, 2018). In additional to under-recording, landslide damages are significantly underestimated due to complex, cascading disasters which attribute damages to a triggering (e.g. hurricane, earthquake) event (Anderson and Holcombe, 2013) and inventory-based loss estimation is unable to account for future conditions of our dynamic natural-human environment

brought on by population growth, urban expansion, and climate change (van Westen et al., 2006). The field of risk analysis bridges the past and the future, allowing for the estimation of present and future losses due to landslides.

Landslides are an inevitable part of the Earth's evolving landscape, but the devastating human consequences which often accompany them are not. The human consequences of landslides can be mitigated through a suite of strategies, including reducing hazard through physical engineering works, reducing exposure through land use zoning and early warning systems, and reducing vulnerability through education and insurance. Quantitative landslide risk analysis forms the basis for assessing risk, analyzing the costs and benefits of risk mitigation strategies, and evaluating the effectiveness of risk management.

III. Outline

Chapter 1 presents a brief background of landslide risk analysis, including the current state of practice and its limitations. While the steps of quantitatively analyzing landslide risk have been well-established in the past thirty years of scholarship, doing so in practice remains challenging, especially at the regional scale, and few real-world examples exist. Modern risk analyses typically focus only on landslide initiation and rely on general assumptions about post-failure movement (runout) and the vulnerability of the elements at risk. Furthermore, they rarely consider more than one mode of landslide or one type of triggering event, providing an incomplete assessment of landslide losses.

In **Chapter 2**, I develop a framework for multimodal landslide risk analysis which includes both precipitation-induced and earthquake-triggered (coseismic) landslides. Terrain is assessed for susceptibility to different modes of landslides. Within each susceptible zone, mode-specific geotechnical models are utilized to assess landslide initiation under a suite of triggering scenarios. An empirical-statistical runout module is used to define the hazard from each mode, including the inundation envelope and process intensity. Vulnerability curves and element-at-risk data is coupled with the computed hazard to produce trigger- and mode-specific risk scenarios. Finally, risk data is aggregated to create a comprehensive landslide risk profile. Uncertainty in input parameters is explicitly modeled through a Monte Carlo process.

Chapter 3 focuses on predicting the runout of highly mobile, un-channelized flowslides, which are among the deadliest types of landslides. While much work has been done to model the initiation and runout of flowslides, communities still lack practical policy instruments to effectively regulate land use and protect citizens. This chapter presents a novel database of flowslide runout data and develops a probabilistic hazard evaluation tool for use by urban planners. I illustrate the use of this tool in a flowslide-prone region of northwestern Washington State.

Understanding of human vulnerability to landslides is essential for predicting and preventing human loss of life. While much recent scholarship has been devoted to quantifying the physical vulnerability of buildings to landslides, no comparable work has been done to quantify human vulnerability. I address this void in **Chapter 4** by creating a new landslide fatality database, developing an empirical human vulnerability relationship to estimate an individual's probability

of death, and detailing the human characteristics, behaviors, and settings which contribute to landslide mortality. A suite of evidence-based, actionable strategies are proposed by which to minimize personal landslide risk.

In **Chapter 5**, I use a preliminary version of the multimodal framework to explore the landslide risk of vulnerable populations in the country of Lebanon. The forced migration of those displaced by a decade of civil war in Syria has highlighted the need for studies to guide humanitarian aid and resettlement policies. In 2011, armed conflict in the region precipitated the largest refugee crisis in a generation, with over 1.5 million Syrians displaced to neighboring Lebanon. This dramatic influx of Syrian refugees has rapidly changed the population distribution in geomorphically-active areas of Lebanon, increasing the already significant landslide risk faced by the Lebanese population. I utilize the multimodal framework to develop a landslide risk profile for Syrian refugees and the Lebanese population and recommend actionable strategies to reduce risk using targeted aid.

Chapter 6 details the full application of the multimodal framework to perform a probabilistic landslide risk analyses of the city of Seattle, Washington. Uncertainty in material parameters is combined with regional groundwater and runout data to predict the probabilities of landslide impact throughout the city. New vulnerability curves are applied to Seattle's building stock inventory to produce spatially explicit estimates of human and structural landslide risk in twelve precipitation and seismic triggering scenarios. I disaggregate landslide hazard and risk to explore the diverging consequences of Seattle's frequent winter storms and probable ground-shaking intensities. This chapter highlights the utility of risk maps for regulating hillslope

development and explores the challenges of landslide risk analysis in a heavily urbanized environment.

References

Alexander, D. (2015). Vulnerability to landslides. In *Landslide Hazard and Risk*. Glade, T., Anderson, M., Crozier, M. (*Eds*.) Chichester, England: John Wiley & Sons Ltd.

Allen, S., Rastner, P., Arora, M., Huggel, C., Stoffel, M. (2016). Lake outburst and debris flow disaster at Kedarnath, June 2013: hydrometeorological triggering and topographic predisposition. *Landslides*, 13, 1479-1491. https://doi.org/10.1007/s10346-015-0584-3

Anderson, M., Holcombe, E. (2013). *Community-based landslide risk reduction: Managing disasters in small steps*. Washington: The World Bank. Available at: http://documents.worldbank.org/curated/en/698831468320378989/Community-based-landslide-risk-reduction-managing-disasters-in-small-steps

Bowman, E. (2015). Small landslides—frequent, costly, and manageable. In *Landslides Hazards, Risks, and Disasters*. Davies, T. (*Ed*.) Amsterdam: Elsevier. http://dx.doi.org/10.1016/B978-0-12-396452-6.00012-4

Campbell, R. (1975). Soil slips, debris flows, and rainstorms in the Santa Monica Mountains and vicinity, Southern California. *U.S. Geological Survey Professional Paper 851*. Washington: United States Government Printing Office

Cannon, S., DeGraff, J. (2009). The increasing wildfire and post-fire debris-flow threat in Western USA, and implications for consequences of climate change. In: K. Sassa, P. Canuti, (*Eds*.) *Landslides – Disaster Risk Reduction*. Berlin: Springer-Verlag

Cascini, L., Bonnard, C., Corominas, J., Jibson, R., Montero-Olarte, J. (2005). Landslide hazard and risk zoning for urban planning and development. In: *Landslide Risk Management*. Hungr, O., Fell, R., Couture, R., Eberhardt, E. (*Eds*.) Leiden: Balkema

Dowling, C., Santi, P. (2014). Debris flows and their toll on human life: a global analysis of debris-flow fatalities from 1950 to 2011. *Nat. Hazards*, 71, 203-227. https://doi.org/10.1007/s11069-013-0907-4

Ellen, S., Wieczorek, G. (1988). Landslides, floods, and marine effects of the storm of January 3-5, 1982, in the San Francisco Bay region, California. *U.S. Geological Survey Professional Paper 1434*. Washington: United States Government Printing Office.

EM-DAT. (2018). "Home." https://www.emdat.be/. Accessed: Nov. 2018.

Froude, M., Petley, D. (2018a). Global fatal landslide occurrence from 2004 to 2016. *Nat. Hazards Earth Syst. Sci.*, 18, 2161-2181. https://doi.org/10.5194/nhess-18-2161-2018

Haque, U., Blum, P., da Silva, P., Anderson, P., Pilz, J., Chalov, S., Malet, J-P., Auflic, M., Andres, N., Pyoiadji, E., Lamas, P., Zhang, W., Peshevski, I., Petursson, H., Kurt, T., Dobrev, N., Garia-Davalillo, J., Halkia, M., Ferri, S., Gaprindashvili, G., Engstrom, J., Keellings, D. (2016). Fatal landslides in Europe. *Landslides*, 13, 1545-1554, https://doi.org/10.1007/s10346-016-0689-3

Jibson, R. (1992). The Mameyes, Puerto Rico, landslide disaster of October 7, 1985. In *Landslides/Landslide Mitigation; GSA Reviews in Engineering Geology, 9th*. Slosson, J., Keene, A., Johnson J. (*Eds*.) Geological Society of America.

Jibson, R. (2005). Landslide hazards at La Conchita, California. *Open-File Report 2005-1067*. Reston, VA: United States Geological Survey

Keaton, J., Wartman, J., Anderson, S., Benoit, J., daLaChapelle, J., Gilbert, R., Montgomery, D. (2014). The 22 March 2014 Oso landslide, Snohomish County, Washington. *Geotechnical Extreme Events Reconnaissance Report*, GEER Association. Available at: http://www.geerassociation.org/index.php/component/geer_reports/?view=geerreports&id=30

Kirschbaum, D., Adler, R., Hong, Y., Hill, S., Lerner-Lam, A. (2010). A global landslide catalog for hazard applications: method, results, and limitations. *Nat. Hazards*, 52, 561-575. https://doi.org/10.1007/s11069-009-9401-4

Marc, O., Stumpf, A., Malet, J-P., Gosset, M., Uchida, T., Chiang, S-H. (2018). Initial insights from a global database of rainfall-induced landslide inventories: The week influence of slope and strong influence of total storm rainfall. *Earth Surf. Dynam*., 6, 903-922. https://doi.org/10.5194/esurf-6-903-2018

Niehaus, R. (2018). The economic impacts of the Montecito mudslides: a preliminary assessment. Santa Barbara: Robert D. Niehaus, Inc. Available at: https://www.rdniehaus.com/app/uploads/2019/08/RDN_Montecito_Mudslides_Impacts-1.pdf

Petley, D. (2012). Global patterns of loss of life from landslides. *Geology*, 40, 927-930. https://doi.org/10.1130/G33217.1

Petley, D. (2018). "The Palu landslides – the worst landslide disaster in five years?" *The Landslide Blog*. https://blogs.agu.org/landslideblog. Accessed: Nov. 2018

Schuster, R., Highland, L. (2001). Socioeconomic and environmental impacts of landslides in the western hemisphere. *Open-File Report 01-276*, Denver: United States Geological Survey

Tanyas, H., van Westen, C., Allstadt, K., Nowicki Jessee, M., Gorum, T., Jibson, R., Godt, J., Sato, H., Schmitt, R., Marc, O., and Hovius, N. (2017). Presentation and analysis of a worldwide database of earthquake-induced landslide inventories. *J. Geophys. Res. Earth Surf.*, 122, 1991-2015, https://doi.org/10.1002/2017JF004236

van Westen, C., van Asch, T., Soeters, R. (2006). Landslide hazard and risk zonation—Why is it still so difficult? *Bull. Eng. Geol. Environ.*, 65, 167-184. https://doi.org/10.1007/s10064-005-0023-0

Wang, F., Sun, P., Highland, L., Cheng, Q. (2014). Key factors influencing the mechanism of rapid and long runout landslides triggered by the 2008 Wenchuan earthquake, China. *Geoenviron. Disasters*, 1. https://doi.org/10.1186/s40677-014-0001-6

Xu, C., Xu, X., Yao, X., Dai, F. (2014). Three (nearly) complete inventories of landslides triggered by the May 12, 2008 Wenchuan Mw 7.9 earthquake of China and their spatial distribution statistical analysis. *Landslides*, 11, 441-461. https://doi.org/10.1007/s10346-013-0404-6

Zhang, J., Gurung, D., Liu, R., Murthy, M., Su, F. (2015). Abe Barek landslide and landslide susceptibility assessment in Badakhshan province, Afghanistan. *Landslides*, 12, 597-609. https://doi.org/10.1007/s10346-015-0558-5

Chapter 1 – Background of landslide risk analysis

1.1 Definitions

The terminology of landslide risk analysis is seldom standardized between countries or even within any one country. In this work I will utilize the following definitions, drawn largely from the work of the JTC-1 Joint Technical Committee on Landslides and Engineered Slopes (Fell et al., 2008) and the Australian Geomechanics Society (AGS, 2007).

Susceptibility is a qualitative or quantitative description of the type, volume, and spatial distribution of landslides which have or may potentially occur in an area. Although landslides often occur more frequently in highly susceptible areas, the temporal probability of occurrence is not evaluated.

Hazard is a situation that could potentially harm an element of value. In regard to landslides, hazard is a description of the type, volume, location, and frequency of landslide occurrence. Landslide susceptibility can be transformed into landslide hazard through assigning an explicit probability of failure to a discrete landslide susceptibility zone within a time period of interest.

Exposure links hazard, describing the occurrence of a landslide, with the elements at risk from that hazard; colloquially it is the probability of being in "the wrong place at the wrong time." Some elements at risk, such as people and vehicles, move in and out of area which may be impacted by landslides. If they are not present when a landslide occurs, then they experience no adverse effects from that event. Other elements, such as buildings and transportation networks, are fixed in place and have an exposure equal to one.

Vulnerability is the potential for something to suffer harm from a human perspective, be it from a natural hazard, anthropogenic crisis, or even intangible or perceived threats (Lee and Jones, 2014). When applied to natural hazards, human vulnerability can be classified into physical and social vulnerability. *Physical vulnerability* describes the potential for damage to infrastructure or lives given an encounter with a discrete hazard—such as a landslide or earthquake—in time and space. *Social vulnerability* describes a host of complex and interrelated socio-economic factors, such as poverty, gender, class, and age, which affect the magnitude of adverse physical and non-physical consequences during and after an event (Wisner and Luce, 1993; Wisner et al., 2004). Social vulnerability is only quantifiable on relative scales and is problematic to implement in natural hazard risk assessment (Lee and Jones, 2014).

Resilience is a related concept to vulnerability, albeit emphasizing the positive ability of individuals and communities to recover from shock rather than the negative consequences they suffer (Smith, 2013). Resilience is necessarily time-integrated, measuring how long it takes a system to return to full capacity.

Risk is a measure of the combined likelihood and magnitude of loss due to an adverse event. It is generally described as the product of hazard and vulnerability (**Figure 1.1**). Elements at risk include infrastructure, populations, environmental features, and economic activities, and risk is correspondingly quantified in dollars lost, deaths caused, and economic downtime forced by a disaster (Fell et al., 2008). Risk may be assessed as direct losses from a discrete event or integrated over time to include all losses from secondary effects until the return of the affected

system to its pre-event status (Leroi, 2017). Risk can be evaluated for an individual or a society, be that a subset demographic, community, or country defined by culturo-linguistic, socio-economic, spatial, or geo-political factors. It is often beneficial to quantify the burden (in deaths, financial or environmental losses, etc.) of landslide disasters to a society without any differentiation between members of the society (e.g. **Chapters 5** and **6**). This allows for useful comparison of landslide risk between large entities of interest (e.g. states, countries) as well as standards of acceptable risk across varied sectors. However, rarely does everyone in a society share equal risk, the spatial distribution, status, or life patterns of a subset of members subjecting them to greater hazard or consequences. Thus it is also beneficial to refine risk assessment toward individual risk (e.g. **Chapter 5**). In the extreme case, individual risk is the risk to a single (nameable) person, accounting for their specific patterns of life and typically expressed as an annual probability of being killed from a given hazard (AGS, 2007, Leroi et al., 2005).

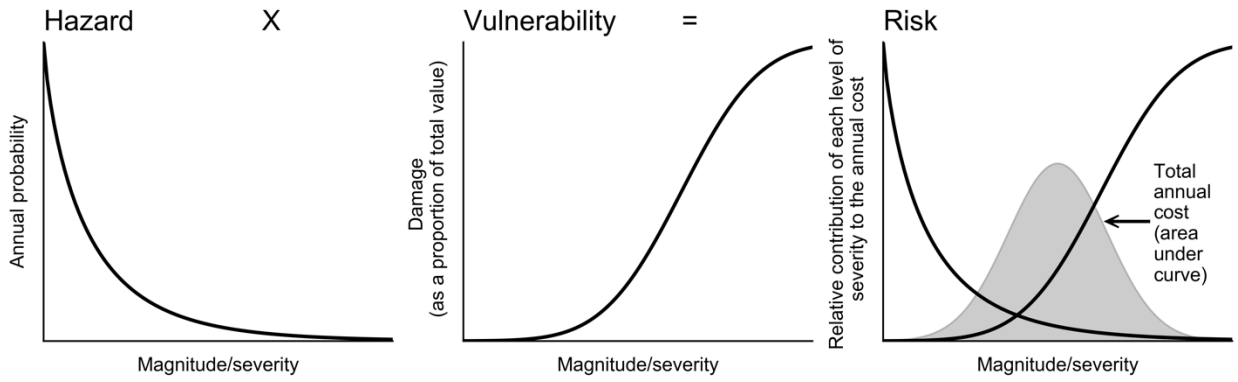

Figure 1.1. Visual representation of risk. Risk is the product of hazard, vulnerability and exposure. In the case of fixed elements, exposure is unity, such as in the case shown. Modified after Lee and Jones (2004)

1.2 What is landslide risk analysis?

Landslide risk analysis involves estimating the consequences of landslides in time and space to elements at risk within an area of interest. Risk can be quantified through the combination of a series of statistical probabilities describing independent landslide events and the element(s) of interest which they might impact:

$$R_{(Loss\ of\ Life)} = \sum_{1}^{n} \left(P_{l(S:T)}\ x\ P_{r(S)}\ x\ P_{e(S:T)}\ x\ V_p \right) \quad \textbf{(1.1)}$$

and

$$R_{(Infrastructure)} = \sum_{1}^{n} \left(P_{l(S:T)}\ x\ P_{r(S)}\ x\ (1)\ x\ V_i\ x\ E \right) \quad \textbf{(1.2)}$$

where $R_{(Loss\ of\ Life)}$ is the annual probability that an individual will be killed or the annual monetary loss due to landslide damage ($R_{(Infrastructure)}$), $P_{l(S:T)}$ is the probability in space and time of a landslide occurring (*initiation hazard*), $P_{r(S)}$ is the spatial probability of a landslide reaching the element at risk (*runout*), $P_{e(S:T)}$ is the spatial-temporal probability of the element at risk being in the area affected by the landslide at the time of occurrence (*exposure*), $V_{(p\ or\ i)}$ is the probability of death or degree of damage if present and impacted by a landslide (*vulnerability*), and E is the monetary value of the element at risk (Fell et al., 2005; van Westen et al., 2006). In the case of static infrastructure the exposure, $P_{e(S:T)}$, is equal to one. The elements of the risk equation are shown in **Figure 1.2**. In the case of an indoor population, the vulnerability, V_p, in **Equation 1.1** may include the vulnerability of the occupied building, V_i, as well as conditional, behavioral factors such as the ability to take evasive action. Risk to environmental features and economic activity may also be included in risk analyses, although it is less common. Quantifying losses to

these elements is more challenging, as it may involve making subjective estimates of value and considering the post-event time until the system returns to pre-event capacity.

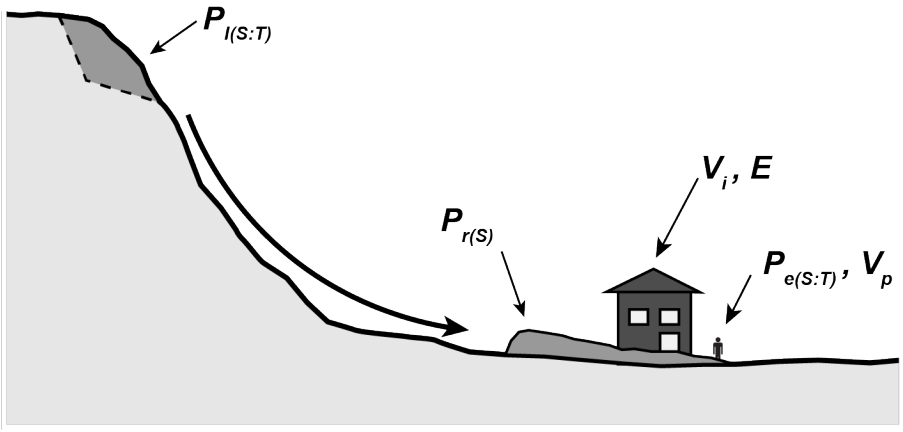

Figure 1.2. Elements of the risk equation. Modified after van Westen et al. (2006)

1.3 Why do landslide risk analysis?

No standardized landslide risk management framework exists in the United States. Most landslide-related maps used for land use planning focus on susceptibility, rather than hazard or risk (Hungr et al., 2016). This can lead to significant and tragic consequences; two illustrations are provided below:

Figure 1.3 shows a geologic "critical area" map of the Stillaguamish River Valley in Snohomish County, Washington, produced under the Washington Growth Management Act, which serves as the basis for land use zoning and development regulation (Copsey, 2002). The map only identifies zones susceptible to landslide failures; it does not show their possible runout zones,

estimated frequencies of occurrence, or the consequences of failure. The 2014 Oso Flowslide (see **Chapter 3**), which killed 43 people, inundated the community of Steelhead Haven which was located in the mapped flood hazard zone, but outside of the landslide hazard zone (Keaton et al., 2014).

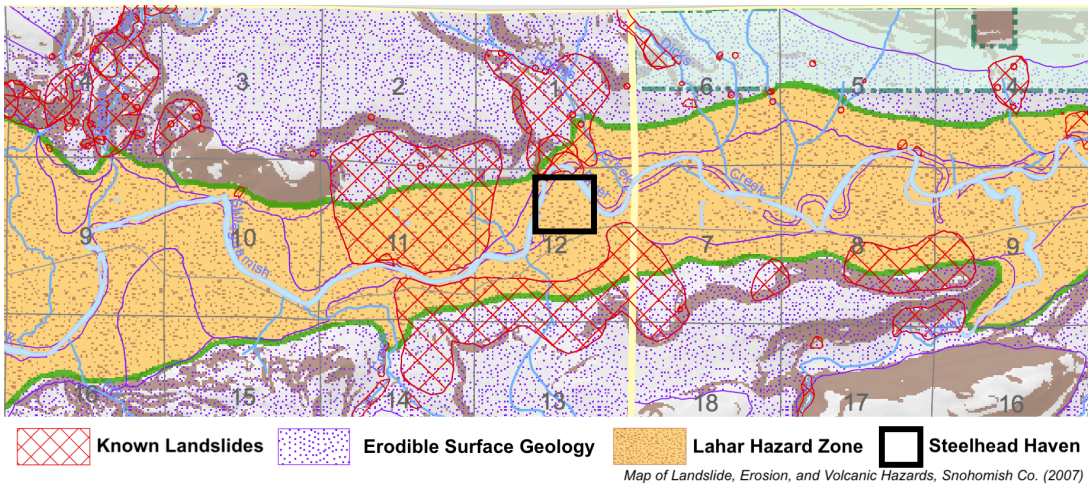

Figure 1.3. The Snohomish County, WA, landslide zoning map for the North Fork of the Stillaguamish River Valley (Snohomish County, 2007).

Figure 1.4 shows zones of coseismic landslide susceptibility above the community of La Conchita, California. This map serves as the basis for where landslide investigations must be carried out as part of the development permitting process. Again, the map delineates only landslide source zones, with no indication of potential runout, magnitude, or frequency of failures. In January 2005, a previously active landslide zone remobilized into a rapid debris flow, destroying 36 houses and killing 10 people (Jibson, 2005).

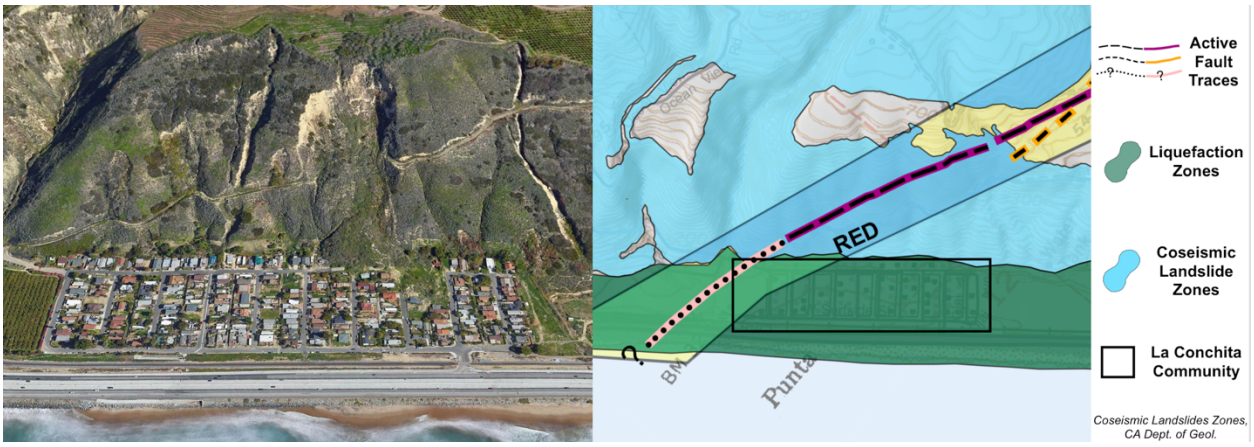

Figure 1.4. The La Conchita, CA, landslide complex (*left*) and the California Department of Geology landslide zoning map of the area (*right*; California Geological Survey, 2002). Base image from Google Earth™.

In both cases, the existing maps used for land use planning failed to capture the risk posed to people living near but outside of landslide susceptible zones.

Risk analyses (and the maps they produce) are a useful end product, as they inform a spectrum of end-users, from policy makers to individual citizens, of the concrete consequences of landslides. However, risk analysis is only the first step of holistic risk management (Fell et al., 2008). Once risk maps are produced, experts and end-users must undertake risk evaluation, determining what risk is acceptable individually and societally. If risk is deemed unacceptable, options to mitigate that risk must be considered in order to reduce it to an acceptable level.

1.4 Current state of practice and remaining challenges

Public awareness of landslide hazard and risk has increased dramatically over the past fifty years thanks to their increased impact on the human environment due to burgeoning human development and social vulnerability, concerns about a changing climate and more frequent

landslide-triggering weather events, greater reporting and recording of disasters in the digital era, and high-level risk reduction campaigns such as the United Nations' International Decade for Natural Disaster Reduction from 1990 – 2000 and the Hyogo and Sendai frameworks for action (UN, 2005; 2015). Within the United States, landslides have received increased attention in the last two decades due to high profile disasters such as the Oso Flowslide, La Conchita debris flow, and the 2018 Montecito debris flows. However, state, county, and municipal land use policies have been slow to follow suit, increasingly including landslide susceptibility, but not hazard or risk, their zoning regulations (Hungr et al., 2016). In part, this is due to a limited and non-standardized body of "best available science" regarding landslide risk (Copsey, 2002).

Academic interest in landslide hazards has exponentially increased over the past three decades as measured by annual publications (**Figure 1.5**). However, few of these provide a practical framework through which to perform landslide risk analysis. In any given year, the relative number of annual published works generally decreases with the increasing complexity of the analysis. For instance, in a Scopus search of academic publications in 2017, there were 136 articles related to landslide susceptibility, 87 related to landslide hazard, and 71 related landslide risk. Of the articles about landslide risk, only 27 relate to risk analysis, and only 5 to quantitative risk analysis (QRA).

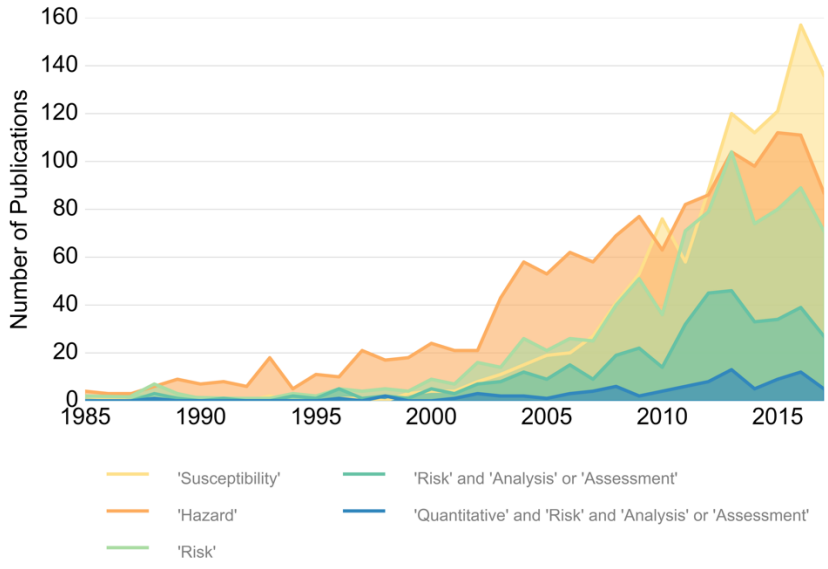

Figure 1.5. Publications relating to landslide hazards based a Scopus search of title, keywords, and abstracts.

Performing a full QRA remains a challenging task, and very few published works actually calculate total risk. While the hazard component of the risk equation is often the most technically intensive to establish, modeling landslide runout and estimating the vulnerability of elements at risk remain two of the greatest barriers to risk analysis for more than a very small (site- or community-scale) area (van Westen et al., 2006; Corominas et al., 2014). The complexity of modeling runout and vulnerability stems from their position at the nexus of the natural and human environments. Landslides that initiate in similar materials and under similar conditions may behave very differently post-failure due to downslope morphology and material composition. Runout modeling must capture the effects of confinement, obstruction, and compositional changes on the inundation extent and intensity of landslide debris. Little data exists to support modeling runout, and the computational expense of doing so in a three-dimensional GIS environment remains high, especially on regional scales.

Once landslide debris is delivered to the human-built environment, vulnerability describes the response of an elements at risk, conditioned on the composition, speed, location, and intensity of the hazard as well as the state of the element itself. The sheer number of factors which influence vulnerability mean that most risk assessments use data-driven approaches based on a limited body of published empirical datasets. All existing methods of estimating human vulnerability rely on expert judgement, due the large uncertainties in modeling human behavior (Corominas et al., 2014).

In addition to these limitations of existing landslide QRA methodology, I have identified five core characteristics needed to expand the usefulness, practicability, and transferability of QRA practice. These characteristics are individually present in a small handful of published studies but have yet to be combined in a single risk assessment framework.

1.) *They need to be generated at a regional scale*. Regional scale hazard and risk maps provide the basic data for land use planning at the scale of a local government, as wells as guiding detailed local and site-specific studies and future mapping priorities (Highland and Bobrowsky, 2008). Methodologies for land risk analysis have been well developed on site-specific (<1:5,000) and local (1:5,000 – 1:25,000) scales or for linear features such as transportation corridors and oil pipelines (van Westen et al., 2006). However, due to detailed parameterization and the computational expense of expanding sophisticated, high-resolution methods, risk analysis at a regional (1:25,000 – 1:250,000) scale is considered, at best, possible only qualitatively or semi-quantitively using existing methods (van Westen et al., 2006). However, land use zoning, warning systems, and

disaster emergency planning often occur at regional scales, extending from 100 – 10,000 km^2 (Corominas et al., 2014). At the same time, other end-users such as citizens, city planners, and developers often need to compare and evaluate the risk of small parcels (home – neighborhood scale) across a region, but site-specific investigations at every parcel are not economically feasible.

2.) *They should be underpinned by a physical basis*. Physically-based models are not dependent on the present situation, as are statistical models (van Westen et al., 2006). In this way they are able to predict future events in a fluctuating natural and human environment and are insensitive to past changes which could bias the landslide record. Furthermore, because they capture the physical processes which lead to landslide failures, physical models are not limited to the area in which there were developed but are transmissible across geologic and climatic regions. Physically-based models also do not require detailed landslide inventories, which are rare, costly to develop, often incomplete, and too short to capture large, infrequent events (Guzzetti, 2000). Finally, statistical models are inherently dynamic; as more events are added to the landslide record, the models change. While this may not reflect a lesser degree of accuracy than physically-based models, the dynamic nature of statistical models may be an obstacle in communicating and creating public trust in the model results.

3.) *They need to account for mechanistically distinct modes of landsliding*. Diverse modes of landsliding effect unique consequences on the human-built environment (Corominas et al., 2014; Fell et al., 2008; Grant, 2017). For instance, rapid flow-type landslides pose

the greatest threat to human life, while slow moving landslides may cause as great or greater damage to infrastructure (Dowling and Santi, 2014; Fell et al., 2008; McDougall, 2017; **Chapter 3**) The majority of existing deterministic hazard models consider only shallow, planar landslides represented by the infinite slope equation (van Westen et al., 2006). A complete risk assessment must include the unique consequences of every potential mode of landsliding, requiring mode-specific hazard modules (Fell et al., 2008).

4.) *They need to be probabilistic*. A single valued risk analysis, based on mean values of input parameters may be appropriate where these parameters are well characterized. However, at a regional scale the only parameters which are well characterized are those of fixed, observable features such as terrain and static infrastructure. Large uncertainties in soil strength, pore water pressure, soil thickness, etc. will create large, potentially unconservative uncertainties in slope stability results. **Figure 1.6** shows a simplified case in which the mean factor of safety of two slopes is identical, but one has a significantly higher probability of failure due to uncertainty. A single-valued analysis would consider both of these cases "safe." Neglecting or underestimating uncertainty in geotechnical designs has led to the many catastrophic failures (e.g. Seed et al., 2008; Morgenstern et al., 2015). A second related problem with single-valued analyses is that they belie the complex and uncertain nature of natural hazards when communicating risk to the public.

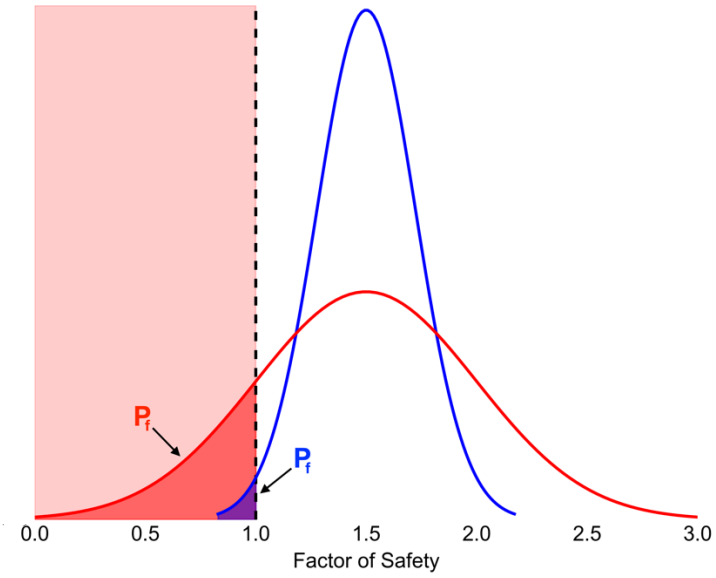

Figure 1.6. In the idealized case above, the factor of safety probability density functions for two slopes (*red* and *blue*) have the same mean. However, the slope represented in red has a far greater probability of failure (P_f) due to uncertainty. Modified after Lacasse (2017).

5.) *The underlying data, models, and results should be open-source*. Simply *more* technical information does not lead to better land use outcomes. Scientific products that are not readily understandable, practicable, and locally relevant are often ignored by land use planners in the decision-making process (Michaels, 2005; Mills et al., 2008; DeGraff, 2012). Landslide risk analysis methods must be transparent, repeatable, and flexible. Transparency serve to establish credibility and trust among the communities which must accept and act on the results, a critical step in risk mitigation (Covello and Allen, 1988). Repeatability and flexibility allow the QRA process to be adapted as updated data becomes available, new methods are developed, and in response to the needs of different stakeholders and evaluation by the engineering community. The open-source movement of the last two decades has given rise to a plethora of freely-available datasets and computational tools. Utilizing open-source resources for landslide risk analysis supports

transparently-produced scientific products that are accessible to a wide range of end-users.

This work represents an advancement in the quantitative analysis of landslide risk via the development of a novel framework and computational platform for regional scale landslide risk analysis that 1) accounts for mechanistically distinct types of failure through mode-specific physically-based models , 2) explicitly addresses the variability of input data, 3) incorporates new tools for characterizing landslide runout and vulnerability, and 4) provides insight into the drivers of landslide risk by allowing disaggregation by landslide mode, triggering scenario, and element at risk to determine what factors most contribute to the consequences. I utilize open-source tools to promote the transparency and flexibility of the framework. The landslide risk analysis methods and products developed in this work facilitate risk reduction strategies to reduce preventable landslide losses.

References

AGS. (2007). Guideline for landslide susceptibility, hazard and risk zoning for land use management. Australian Geomechanics Society Landslide Taskforce Landslide Zoning Working Group. *Australian Geomechanics*, 42(1), 13-36.

California Geological Survey. (2002). Earthquake zones of required investigation: Pitas Point Quadrangle. California Geological Survey Geologic Information and Publications.

Copsey, A. (2002). *The designation and protection of critical areas under the Growth Management Act*. Office of the Attorney General. Olympia: State of Washington

Corominas, J., van Westen, C., Frattini, P., Cascini, L., Malet, J.-P., Fotopoulou, S., et al. (2014). Recommendations for the quantitative analysis of landslide risk. *Bull. Eng. Geol. Environ.*, 73, 209-263. https://doi.org/10.1007/s10064-013-0538-8

Covello, V., Allen, F. (1988). Seven cardinal rules of risk communication. Washington: Environmental Protection Agency. Available at: https://archive.epa.gov/care/web/pdf/7_cardinal_rules.pdf

DeGraff, J. (2012). Solving the dilemma of transforming landslide hazard maps into effective policy and regulations. Nat. Hazards Earth Syst. Sci., 12, 53-60. www.nat-hazards-earth-syst-sci.net/12/53/2012/

Dowling, C., Santi, P. (2014). Debris flows and their toll on human life: a global analysis of debris-flow fatalities from 1950 to 2011. *Nat. Hazards*, 71, 203-227. https://doi.org/10.1007/s11069-013-0907-4

Fell, R., Corominas, J., Bonnard, C., Cascini, L., Leroi, E., Savage, W. (2008). Guidelines for landslide susceptibility, hazard, and risk zoning for land use planning. *Eng. Geol.*, 102, 85-98. https://doi.org/10.1016/j.enggeo.2008.03.022

Grant, A. (2017). Regional-scale coseismic landslide hazard modeling and consequence analysis. (*doctoral dissertation*). Seattle: University of Washington

Guzzetti, F. (2000). Landslide fatalities and the evaluation of landslide risk in Italy. *Engineering Geology*, 58, 89-107. https://doi.org/10.1016/S0013-7952(00)00047-8

Highland, L., Bobrowsky, P. (2008). The landslide handbook—A guide to understanding landslides. *Circular 1325*. Reston, VA: U.S. Geological Survey

Hungr, O. (2016). A review of landslide hazard and risk assessment methodology. In *Landslides and Engineered Slopes: Experience, Theory and Practice*. Aversa et al. (*Eds*.) Rome: Associazione Geotecnica Italiana

Jibson, R. (2005). Landslide hazards at La Conchita, California. *Open-File Report 2005-1067*. Reston, VA: United States Geological Survey

Keaton, J., Wartman, J., Anderson, S., Benoit, J., daLaChapelle, J., Gilbert, R., Montgomery, D. (2014). The 22 March 2014 Oso landslide, Snohomish County, Washington. *Geotechnical Extreme Events Reconnaissance Report*, GEER Association. Available at: http://www.geerassociation.org/index.php/component/geer_reports/?view=geerreports&id=30

Lacasse, S. (2017). "Landslide risk management and risk governance, with examples from practice." Presentation at the LARAM School for Landslide Risk Assessment and Mitigation 2017, Salerno, Italy.

Lee, E., Jones, D. (2014). *Landslide Risk Assessment*. London: ICE Publishing

Leroi, E. (2017). "Landslide risk management." Presentation at the LARAM School for Landslide Risk Assessment and Mitigation 2017, Salerno, Italy.

Leroi, E., Bonnard, C., Fell, R., McInnes, R. (2005). Risk assessment and management. In Landslide Risk Management. Hungr, O., Fell, R., Couture, R., Eberhardt, E. (*Eds*.) Leiden: Balkema.

McDougall, S. (2017). 2014 Canadian geotechnical colloquium: landslide runout analysis—current practice and challenges. *Can. Geotech*., 54, 605-620. https://doi.org/10.1139/cgj-2016-0104

Michaels, S. (2005). Addressing landslide hazards: Towards a knowledge management perspective. In: T. Glade, M. Anderson, M. Crozier, (*Eds*.) *Landslide Hazard and Risk*. West Sussex: John Wiley & Sons

Mills, A., Francis, T., Shandas, V., Whittaker, K, Graybill, J. (2008). Using best available science to protect critical areas in Washington state: Challenges and barriers to planners. *Urban Ecosyst*., https://doi.org/10.1007/s11252-008-0071-x

Morgenstern, N., Vick, S., Van Zyl, D. (2015). Report on Mount Polley tailings storage facility breach. Independent Expert Engineering Investigation and Review Panel, Victoria: Province of British Columbia. Available at: https://www.mountpolleyreviewpanel.ca/sites/default/files/report/ReportonMountPolleyTailingsStorageFacilityBreach.pdf

Seed, R., Bea, R., Athanasopoulos-Zekkos, A., Boutwell, G., Bray, J., Cheung, C., et al. (2008). New Orleans and Hurricane Katrina. IV: Orleans East Bank (metro) protected basin. *Geotch. Geoenviron. Eng.*, 134(5), 762-779. https://doi.org/10.1061/(ASCE)1090-0241(2008)134:5(762)

Smith, K. (2013). *Environmental hazards: Assessing risk and reducing disaster*. London: Routledge.

Snohomish County. (2007). Landslide, erosion, and volcanic hazards. Snohomish County Planning and Development Services. Available at: https://snohomishcountywa.gov/DocumentCenter/View/8247/Landslide-Erosion-and-Volcanis-Hazards-Countrywide?bidId=

UN. (2005). Hyogo framework for action 2005-2015: Building the resilience of nations and communities to disasters. Geneva: United Nations

UN. (2015). Sendai framework for disaster risk reduction. Geneva: United Nations

van Westen, C., van Asch, T., Soeters, R. (2006). Landslide hazard and risk zonation—Why is it still so difficult? *Bull. Eng. Geol. Environ.*, 65, 167-184. https://doi.org/10.1007/s10064-005-0023-0

Wisner, B., Blaikie, P., Cannon, T., Davis, I. (2004). *At risk: Natural hazards, people's vulnerability and disasters*. London: Routledge.

Wisner, B., Luce, H. (1993). Disaster vulnerability: Scale, power and daily life. *GeoJournal*, 30(2), 127-140. https://doi.org/10.1007/BF00808129

Chapter 2 – Framework for multimodal landslide risk analysis

Portions of this chapter were published as:

Pollock, W., Grant, A., Wartman, J., Abou-Jaoude, G. (2019). Multimodal method for landslide risk analysis. *MethodsX*, 6, 827-836. https://doi.org/10.1016/j.mex.2019.04.012.

2.1 Multimodal method for landslide risk analysis

Landslide hazard may be quantitatively analyzed through either statistical or physically-based approaches (Corominas et al., 2014). Physically-based models may be data intensive on regional scales and significantly simplify landslide geometry and processes; however, they provide key advantages over statistical models in quantitative risk assessment. Physically-based models are not dependent on the stasis of present environmental conditions, as are statistical models (van Westen et al., 2006). Furthermore, because they capture the underlying physical processes which lead to landslide failures, physically-based models are not limited to the area in which there were developed, but are transmissible across geologic, physiographic, and climatic regions. As a key goal of risk assessment is to disaggregate the risk contribution of different triggering scenarios, such as storm precipitation or earthquake shaking, statistical models are less useful for risk assessment when triggering data is not linked to the landslide record. Finally, unlike statistical models, physically-based models do not require detailed landslide inventories, which are rare, costly to develop, often incomplete, and too short to capture large, infrequent events (Guzzetti, 2000; Malamud et al., 2004).

In this work, I follow the pixel-based, multimodal coseismic landslide hazard method of Grant et al. (2016). I update the method of Grant et al. (2016), develop a parallel set of mode-specific models for rainfall-induced landslides, and extend the method to include runout, exposure, and vulnerability modules to produce quantitative landslide risk. The process and governing equations of the multimodal method are described in the following sections and visualized in

Figure 2.1. They have been coded into a modular, python-based computational platform, the application of which is demonstrated in **Chapters 5** and **6**.

Figure 2.1. *(following page).* Flowchart of the multimodal framework for landslide risk analysis, including the pre-processing, hazard initiation, and runout modelling steps.

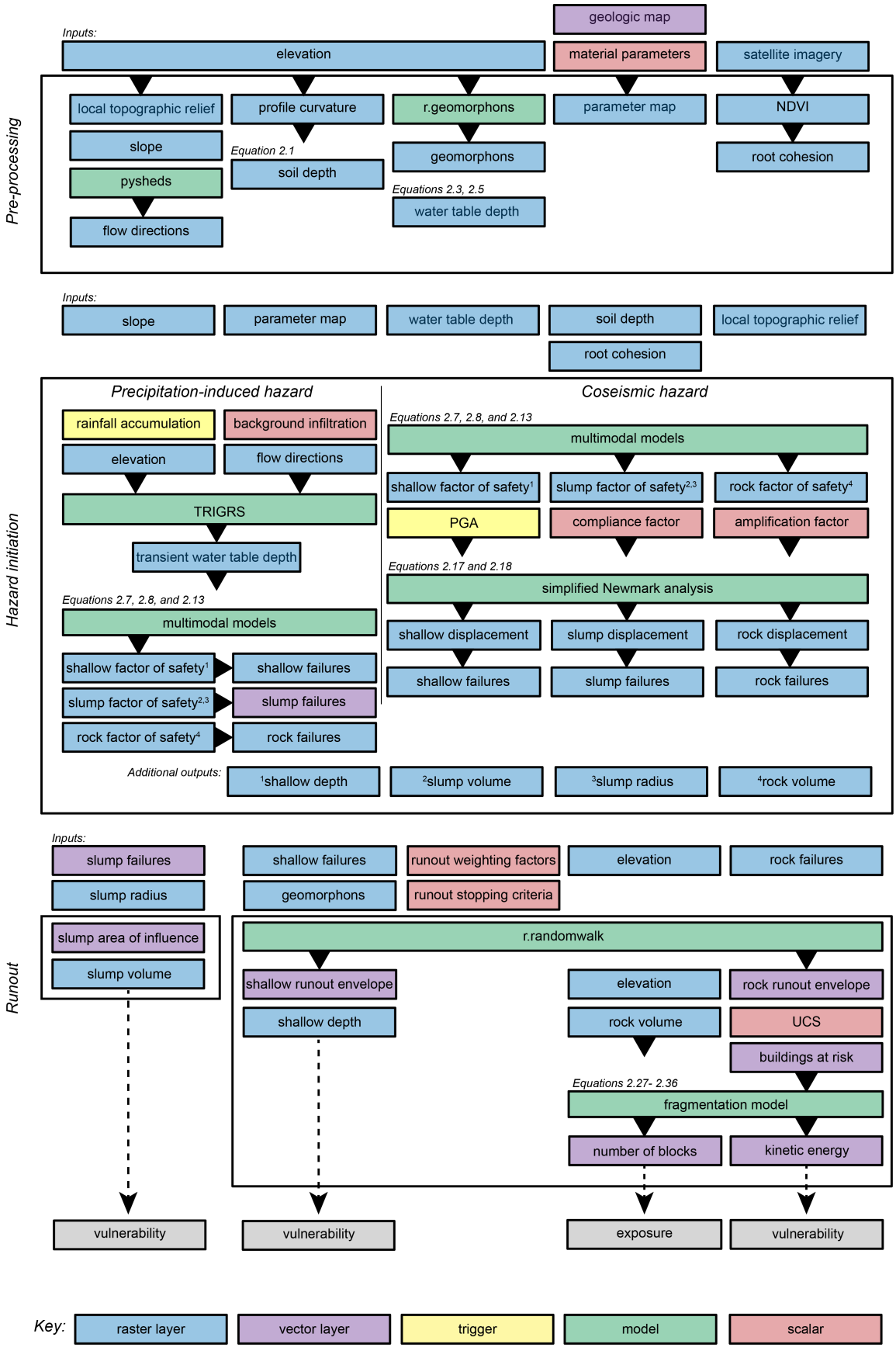
Pre-processing
Inputs:
elevation
geologic map
material parameters
satellite imagery
local topographic relief
profile curvature
r.geomorphons
parameter map
NDVI
slope
Equation 2.1
geomorphons
root cohesion
pysheds
soil depth
Equations 2.3, 2.5
water table depth
flow directions
Hazard initiation
Inputs:
slope
parameter map
water table depth
soil depth
local topographic relief
root cohesion
Precipitation-induced hazard
Coseismic hazard
rainfall accumulation
background infiltration
Equations 2.7, 2.8, and 2.13
multimodal models
elevation
flow directions
shallow factor of safety1
slump factor of safety2,3
rock factor of safety4
TRIGRS
PGA
compliance factor
amplification factor
transient water table depth
Equations 2.17 and 2.18
simplified Newmark analysis
Equations 2.7, 2.8, and 2.13
shallow displacement
slump displacement
rock displacement
multimodal models
shallow factor of safety1
shallow failures
shallow failures
slump failures
rock failures
slump factor of safety2,3
slump failures
rock factor of safety4
rock failures
Additional outputs:
1shallow depth
2slump volume
3slump radius
4rock volume
Runout
Inputs:
slump failures
shallow failures
runout weighting factors
elevation
rock failures
slump radius
geomorphons
runout stopping criteria
slump area of influence
r.randomwalk
slump volume
shallow runout envelope
elevation
rock runout envelope
shallow depth
rock volume
UCS
buildings at risk
Equations 2.27- 2.36
fragmentation model
number of blocks
kinetic energy
vulnerability
vulnerability
exposure
vulnerability
Key:
raster layer
vector layer
trigger
model
scalar

2.2 Modes of failure

Traditional large-scale landslide hazard and risk analyses rely on the simplistic infinite slope method to capture all modes of landsliding. However, unique modes of landsliding cause unique consequences to the human environment (Fell et al., 2008; van Westen et al., 2006). Slow-moving landslides most dramatically affect static infrastructure, especially linear transportation networks, while rapid, localized flows pose greater risk to human lives (Dowling and Santi, 2014; McDougall, 2017). General infinite slope assumptions miss nuanced consequences of unique modes of movement. Hungr et al. (2014) revised the traditional Varnes' classification describe 32 unique modes of landsliding. After Grant et al. (2016), I simplify this classification to three basic landslide modes corresponding to the initial failure process – 1) rock falls and slides; 2) shallow, planar soil slides; and 3) deep-seated, rotational slumps in soil and rock. All three modes may be produced by seismic- or precipitation-triggering, and in some cases, they may be collocated, as shown in **Figure 2.2** in which a shallow slide occurred on the margin of a rotational slump.

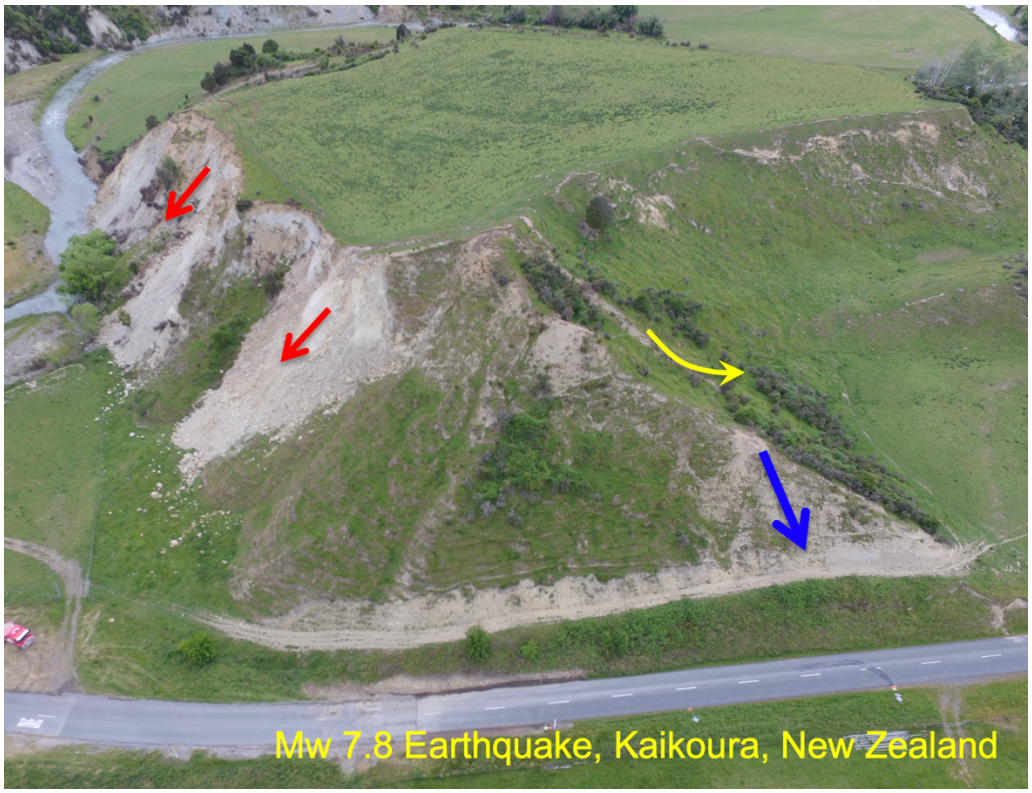

Figure 2.2. Coseismic rock avalanches (*red*), a shallow disrupted slide (*blue*) and a deep-seated rotational slump (*yellow*) triggered by the 2016 Kaikoura earthquake in New Zealand. Image: J. Wartman.

I further differentiate between landslide modes on the basis of post-failure movement. Rock falls and slides may disintegrate into rock avalanches, and in the presence of abundant water, shallow soil slides will mobilize into debris flows (channelized) or debris avalanches (un-channelized). The landslide typology used in this work is given in **Table 2.1**. **Figures 2.3 – 2.6** provide examples of the landslide modes corresponding to the definitions provided in **Table 2.2**.

Table 2.1. Landslide typology used in this work. Velocity classes after Cruden and Varnes (1996)

Trigger	*Mode number, material, and initial failure type*	*Movement*	*Velocity class*
seismic	(1) rock fall/slide	(1a) rock avalanche	very rapid – extremely rapid
	(2) shallow disrupted soil slide		very rapid – extremely rapid
	(3) soil/rock rotational slump		slow – very rapid
precipitation	(1) rock fall/slide	(1a) rock avalanche	very rapid – extremely rapid
	(2) shallow soil slide	(2a) confined debris flow	very rapid – extremely rapid
		(2b) unconfined debris avalanche	very rapid – extremely rapid
	(3) soil/rock rotational slump		very slow – very rapid

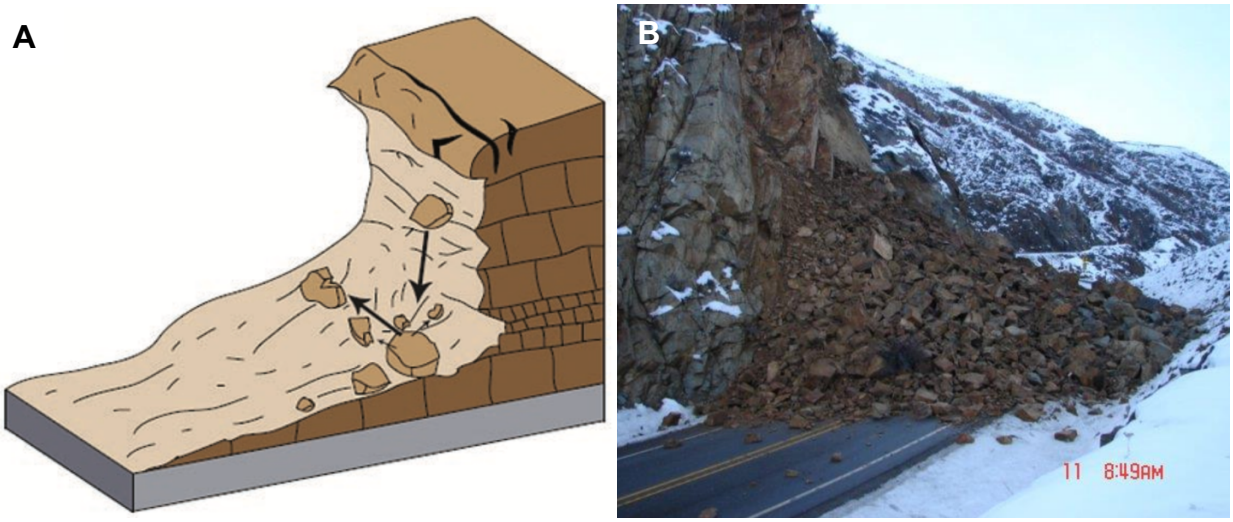

Figure 2.3. Rock fall and rock avalanche. (*A*) Simplified diagram and (*B*) rock avalanche near Waterville, Washington, 2016. Figure from Highland and Bobrowsky (2008), based on Cruden and Varnes (1996). Image: Washington State Department of Transportation.

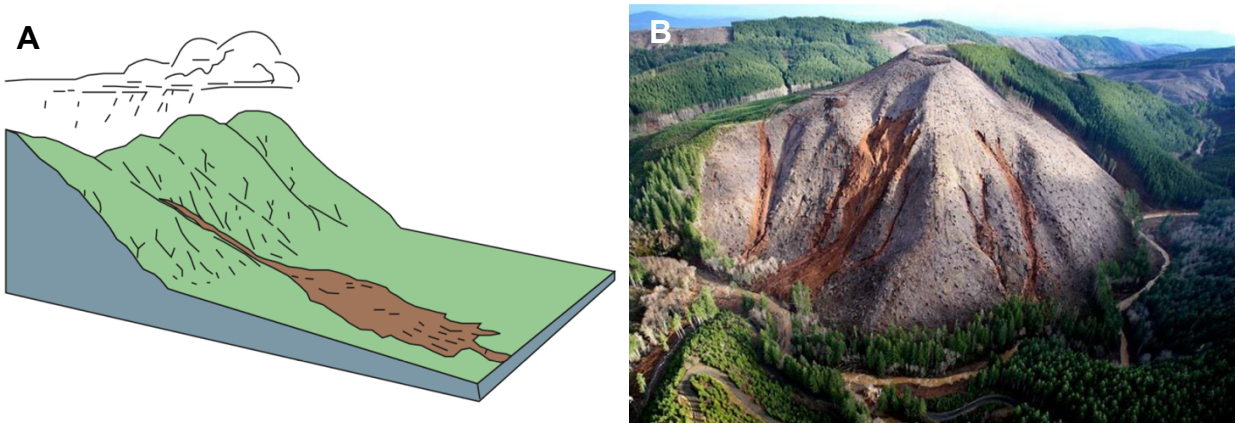

Figure 2.4. Soil slide transitioning into a debris flow. (*A*) Simplified diagram and (*B*) debris flows at Stillman Creek, Washington, 2008. Figure from Highland and Bobrowsky (2008), based on Cruden and Varnes (1996). Image: Washington State Department of Natural Resources.

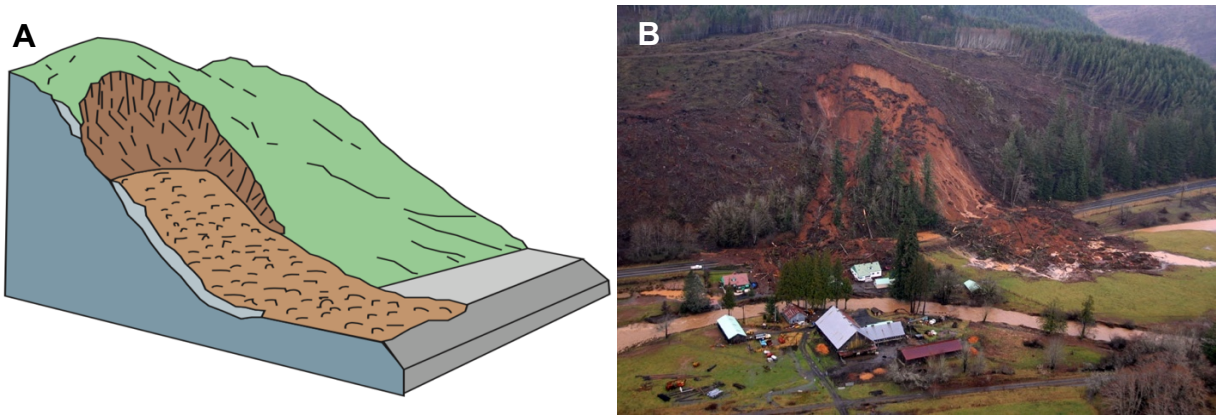

Figure 2.5. Soil slide transitioning into a debris avalanche. (*A*) Simplified diagram and (*B*) debris avalanche in Pe Ell, Washington, 2007. Figure from Highland and Bobrowsky (2008), based on Cruden and Varnes (1996). Image: Washington State Department of Natural Resources.

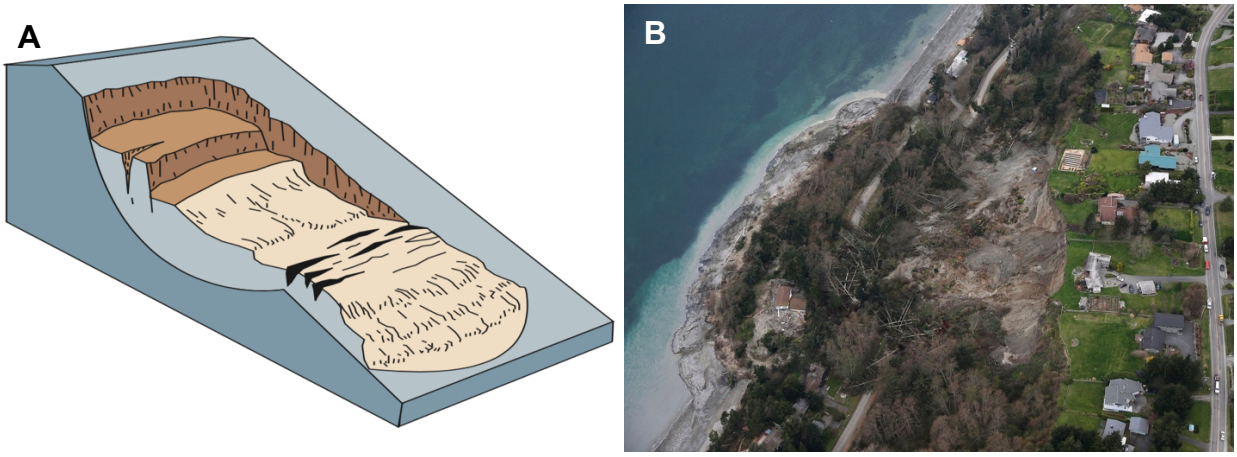

Figure 2.6. Rotational slump. (*A*) Simplified diagram and (*B*) deep-seated, rotational slump in Coupeville, Washington, 2013. Figure from Highland and Bobrowsky (2008), based on Cruden and Varnes (1996) Image: T. Warren.

Table 2.2. Definitions for the landslide modes used in the multimodal model and introduced in **Table 2.1**. Definitions and terminology adopted from Hungr et al. (2014) and Keefer (1984).

Mode	*description*
(1) rock fall/slide	Small failures occur as the detachment, fall, rolling, and bouncing of rock fragments. May occur singly or in clusters, but there is little dynamic interaction between the most mobile moving fragments, which interact mainly with the substrate (path). Fragments can break during impacts. Larger, structurally-controlled rock slides occur as a sliding mass of rock on a planar rupture surface.
(1a) rock avalanche	Extremely rapid, massive, flow-like motion of fragmented rock from a large rock slide or rock fall
(2) disrupted soil slide	Sliding of a mass of granular material on a shallow, planar surface parallel with the ground. Usually, the sliding mass is a veneer of colluvium, weathered soil, or pyroclastic deposits sliding over a stronger substrate.
(2a) debris flow	Very rapid to extremely rapid surging flow of saturated debris in a steep channel. Strong entrainment of material and water from the flow path.
(2b) debris avalanche	Very rapid to extremely rapid shallow flow of partially or fully saturated debris on a steep slope, without confinement in an established channel. Sometimes called a "flowslide."
(3) rotational slump	Sliding of a mass of homogeneous and usually cohesive soil or weak, non-structurally controlled rock on a semi-spherical or ellipsoidal rupture surface. Prominent main scarp and back-tilted landslide head. Normally slow to rapid.

2.3 Terrain-based susceptibility

Statistical studies have found a correlation between slope and landslide mode (e.g. Keefer, 2013; Wartman et al., 2013). In order to limit excess computation, I divide the terrain into slope-based zones susceptible to each failure mode in which mode-specific physical models are applied (**Table 2.3**). Slopes from 15 – 50° are zoned as prone to shallow, planar slides, and slopes from 10 – 35° are considered susceptible to rotational slumps (Zezere, 2005). Rock falls are limited to slopes steeper than 35° (Grant et al., 2016). Slopes shallower than 15° are not considered likely to fail in any landslide mode (Tanyas et al., 2017).

Table 2.3. Slope ranges for mode-specific susceptible zones.

Mode	*Slope range (degrees)*
(1) rock fall	35 – 90
(2) shallow soil slides	15 – 50
(3) soil / rock slumps	10 – 35

2.4 Input data

2.4.1 Elevation

The most basic input for the multimodal method is a digital elevation model (DEM). In the computational platform, the resolution and coordinate reference system of the DEM define the project; all other input and output layers are re-projected to match. Landslides are scale dependent, and thus care must be taken to choose a resolution of analysis that is appropriate to the process being modeled (Medwedeff et al., 2020). To complicate matters, analyses of geomorphometric factors, slope hydrological response, and limit-equilibrium-based stability also exhibit scale-dependence, specific to the model used (Sirbu et al., 2019; Chang et al., 2019; Penna et al., 2014). Finally landslide hazard analyses are limited by the resolution of available data and the computational power necessary to process it. The advent of LiDAR has resulted in elevation data available at very high resolutions (< 1 m). However, the highest resolution supported by the elevation data may be too fine to accurate represent landslide processes, create "landslides" too small to functionally be of human concern, may violate model assumptions, or be too computationally expensive to process. I examine the sensitivity of the multimodal method to DEM resolution in **Appendix 2.1** and **2.2**, and I find that resolutions of ~5 m provide a good balance between accuracy and efficiency. This figure is in line with previous studies which found that higher DEM resolution does not necessarily produce better results when predicting landslide initiation (Tarolli and Tarboton, 2006; Penna et al., 2014).

The DEM forms the basis of five secondary inputs. 1.) Local relief is measured within a moving circular window of a user-defined size based on the scale of major topographic features within the area of interest. Topographic waveform or stream channel analyses can be used to automate the selection of window size. However, the multimodal method is not sensitive to local relief window size, and user-judgement is usually sufficient (**Appendix 2.1**). 2.) Slope is calculated at individual cells and as an average within a moving window one quarter the size of the window for local relief. This average slope, representing a "smoothed" topographic surface is used in the rock and rotational slump models to prevent over-prediction from local oversteepening. 3.) Topographic profile curvature is used to estimate soil depth. 4.) As a preprocessing step for the precipitation-induced failure models, the DEM is pit-filled and used to extract flow directions with the python-based module pysheds (Bartos, 2020). Finally, 5.) the DEM is used to perform a basic morphometric analysis with the GRASS GIS module r.geomorphons (Jasiewicz and Stepinski, 2013) which is used to determine channelization for runout analyses.

2.4.2 Soil depth

Depth of mobile regolith (hereafter called "soil depth") is an important input parameter to process-based landslide models. It is often assumed to be uniform across a landscape owing to the expense of soil depth surveys (e.g. Montgomery and Dietrich, 1994). However, soil depth varies significantly, a function of inter-related factors such as topography, parent material, climate, and vegetation, and the assumption of uniformity may lead to significant under- or over-prediction of landsliding (Lanni et al., 2012; Ho et al., 2012). Dietrich et al. (1995) proposed a process-based model for soil depth estimation. Numerous statistical approaches have been

developed relating mobile regolith depth to easily-measured topographic variables such as slope, curvature, wetness index, contributing area, and distance from hilltop (Patton et al., 2018; Lanni et al., 2012; Ho et al., 2012). Patton et al. (2018) demonstrate that a profile curvature-based prediction relationship performed reasonably well across multiple catchments with a variety of underlying lithologies, climatic regimes, and topographic characteristics:

$$d = \left(\frac{\Delta d}{\Delta C}\right) + d_{C=0} \quad \textbf{(2.1)}$$

where d is the soil depth, $d_{C=0}$ is the average soil depth measured at locations of zero curvature, and $\Delta d/\Delta C$ can be calculated from the regression:

$$\frac{\Delta d}{\Delta C} = -446.3 * \sigma_C + 30.3 \quad \textbf{(2.2)}$$

where σ_C is the standard deviation of curvature [m^{-1}].

2.4.3 Water table depth

The water table is typically a repressed imitation of the land surface (Snyder, 2008). Peck and Payne (2003) propose a regression between the land surface elevation (LSE) and water table elevation (WTE) for determining the elevation of the water table over regional scales:

$$WTE = 0.9505 * LSE - 1.9955 \quad \textbf{(2.3)}$$

where both WTE and LSE are in meters. Where site-specific water table elevation is available, a site-specific regression can be produced following the method of Peck and Payne (2003), with the added constraint of the water table being coincident with the land surface at sea level (if present):

$$WTE = a * LSE \quad \textbf{(2.4)}$$

Water table depth (WTD) is calculated as the difference between the land and water surface elevations:

$$WTD = LSE - WTE \quad \textbf{(2.5)}$$

2.4.4 Satellite imagery

The presence and type of vegetation influences the location of shallow precipitation-induced landslides, primarily through its contribution to effective soil cohesion through a root network (Montgomery et al., 1998). The presence and relative health of vegetation can be rapidly assessed through multispectral satellite imagery. Grant et al. (2016) observed a clear relationship between shallow coseismic landslide occurrence and the relative normalized difference vegetation index (NDVI). NDVI can be calculated from the red and near infrared (NIR) bands:

$$NDVI = \frac{NIR - red}{NIR + red} \quad \textbf{(2.6)}$$

where low values correspond to bare soil and values approaching one correspond to dense, healthy vegetation (Brown, 2020; Weiss et al., 2004). By examining the distribution of NDVI values in areas of observable vegetation classes (e.g. mature forest, grasslands, etc.) and combining it with knowledge of the local vegetation, discrete classes of root cohesion can be assigned across the landscape (Schmidt et al., 2001; Cislaghi et al., 2016). In this work I adopt three classes of root cohesion—none, moderate, and high—although any number of classes could be used. Examples are given in **Chapters 5** and **6**.

2.4.5 Geologic map and soil strength parameters

Soil and rock units are identified on the basis of geologic mapping. Material strength and hydrologic parameters are assigned to each geologic unit. Vertical heterogeneity is not explicitly taken into account, although unique input parameters are be assigned to mobile regolith and the underlying material. The maps may be consolidated into a smaller number of similar units depending on the detail of published parameter values (e.g. Burns et al., 2018). Required parameters include cohesion, friction angle, unit weight, hydraulic diffusivity, vertical conductivity, and parameters of soil-water characteristic curves (Gardner, 1958).

Surficial geology maps necessarily simplify complex, transitional, and ambiguous geologic realities into discrete two-dimensional boundaries. Uncertainty in geologic maps comes from at least three sources (Lark et al., 2015). *Conceptual* uncertainty describes the artificiality of representing a spatially continuous or irregular transition between different units by a line. Such divisions will often vary between surveyors. *Interpretation* uncertainty exists because evidence

of a geologic contact is not observable everywhere due to surficial cover, land-access permissions, or the practical resource limitations of a field campaign. Thus, the location of geologic boundaries is also subject to the interpretation of the surveyor. The final type of uncertainty is *scale-dependent* uncertainty. A map line drawn at 1:24,000 scale with a 0.5 mm pen will represent a 12 m band on the ground, within which the location of the geologic boundary it represents is uncertain.

These three sources of uncertainty are especially relevant for landslide risk analysis when key parameters, such as soil strength, are assigned on the basis of mapped geologic units. Twelve (or more) meters of uncertainty may not matter in open land but will be very important to a homeowner whose property is on the boundary of a particularly weak geologic unit.

In the multimodal method, I only address scale-dependent uncertainty. Conceptual and interpretation uncertainty will vary by map, location, and surveyor and are beyond the scope of this work, although an assumption of some conceptual uncertainty is implicit in our approach. The United States Geological Survey (USGS) standard for its map products is that 90% of all points must fall within $1/50^{th}$ of a map inch (USGS, 1999). At a 1:24,000 scale this translates to 12.2 m. In the multimodal model, the accuracy and scale of the adopted geologic map is a required input. This produces an accuracy window size (12.2 m in the example above) which is converted to the closest higher odd number of cells based on the DEM resolution. Values of friction angle and cohesion throughout the domain are then averaged within a circular moving window based on the number of cells to "smear" the parameters across geologic boundaries,

preventing adjacent cells from having an artificially discrete transition between weak and strong materials (**Figure 2.7**).

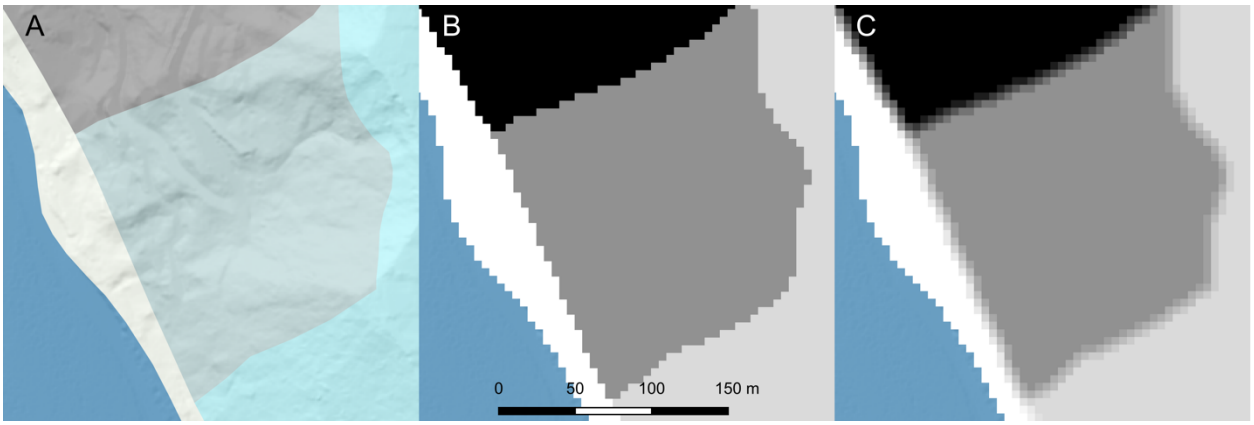

Figure 2.7. Starting with a surficial geologic map (*A*), material parameters are assigned to mapped units at the pixel size of the underlying elevation model (*B*). The borders between units are then smoothed using a circular moving window based on the horizontal map accuracy and resolution (*C*).

2.4.6 Distributions of material parameters

Where empirical distributions of parameters do not exist in a given area, distributions are assigned based on data from other regions. For instance, mean and standard deviations of friction angle and cohesion may not be known. In such cases, mean values are adopted from best-estimate values in published studies of similar geologic units and then increased to meet the limiting criteria of static stability. Standard deviations are estimated based on a coefficient of variation (COV) of 0.1 and 0.3 for friction angle and cohesion, respectively (Jones et al., 2002; Grant, 2017; Wang, 2014; Wang and Rathje, 2015; Phoon and Kulhawy, 1999). This method falls between a purely data-driven (empirical testing) approach and a logic tree approach in which the weights of medium, upper, and lower-bound strengths are fixed subjectively (Wang

and Rathje, 2015). Friction angle is assumed to be normally distributed while cohesion, and saturated hydraulic conductivity are assumed to be log-normally distributed (Jones et al., 2002; Bicocchi et al., 2019)

2.4.7 Triggering factors.

Both seismic and precipitation landslide triggers are considered in this framework. Potential earthquake and storm triggering scenarios must be converted into the actual factors which trigger landslides (e.g. peak ground acceleration (PGA) or rainfall accumulations). These factors may be produced from observed earthquake or rainfall scenarios taken from the historical record or developed in probabilistic hazard analyses. In the latter case, PGA or time-dependent rainfall intensities are assigned a probability of exceedance within a time period or associated with a return period. A full risk curve considers every plausible event on a magnitude-frequency plot for a region; however, it is only practicable to consider select discrete events. For instance, one might consider 10% probability of exceedance ground shaking intensities in 50, 100, and 500 years or 5, 10, 50, and 100-year return period storms (see Corominas et al., 2014). The user must decide the appropriate number of events to balance computational expense with a complete analysis appropriate to the study area in question and the data available.

2.4.8 Elements at risk.

Only physical elements at risk are included in this framework, including populations, commercial or residential structures, critical facilities, transportation networks, communication

lines and utilities (**Figure 2.8**). Risk to economic activities may be derived from direct landslide damages to some or all of the elements above but are not directly considered in this framework. The nature of available data will determine the format. Population may be rasterized at the resolution of the study, denoting the number of people within a pixel (e.g. **Chapter 5**) or as a vector layer attribute (e.g. **Chapter 6**). Discrete elements such as buildings may be polygonised for analyses at an individual element-scale (e.g. **Chapter 6**) or rasterized in a "built-up grid" (e.g. **Chapter 5**; Ehrlich and Tenerelli, 2013; Pesaresi et al., 2015) for cumulative regional risk analysis. Common sources of publicly available element-at-risk GIS data include city building databases (e.g. Seattle Geodata, 2015; Portland Maps, 2018), crowed-sourced infrastructure repositories (e.g. OpenStreetMap: www.openstreetmap.org), national census data (e.g. U.S. Census Bureau: www.census.gov), satellite-derived infrastructure maps (e.g. Microsoft, 2018), global population density estimates (e.g. Pesaresi et al., 2013), and global mapping of human built-up presence (e.g. Pesaresi et al., 2015). Included as either separate raster data or as vector feature attributes should be sufficient information for determining vulnerability and value, such as number of individuals, number of building stories, material type, cost per area for repairs, total building value, etc.

Figure 2.8. Examples of elements are risk in West Seattle, Washington State. (*A*) Building inventory (Seattle Geodata, 2015), (*B*) road inventory (OpenStreetMap, 2018), and (*C*) population by census block represented as points (U.S. Census Bureau, 2018).

2.5 Precipitation-induced landslide models

2.5.1 Transient water table depth.

I use the open-source Fortran code, TRIGRS, to compute transient changes in the water table in response to precipitation represented as intensity-duration pairs (Baum et al., 2008). TRIGRS uses the one-dimensional Richards equation to describe vertical rainfall infiltration through a two-layer, unsaturated-saturated soil profile divided by a capillary fringe (**Figure 2.9**). A simple runoff routing procedure diverts excess water from less permeable grid cells to more permeable cells downslope. One of the optional outputs of TRIGRS is a three-dimensional grid of pore pressure at user-specified depth intervals (Baum et al., 2008; Reid et al., 2015). I use this output to calculate changes in water table depth as the driver of precipitation-induced landslides.

2.5.2. Debris flows/avalanches

The static factor of safety of against shallow, planar slides is calculated with the classic infinite slope equation, modified to include the effects of root cohesion (Duncan et al., 2014):

$$FS = \frac{(c + c_r) + (\gamma z \cos^2 \beta - u) \tan \varphi}{\gamma z \cos \beta \sin \beta} \quad (2.7)$$

where FS is the factor of safety, c is cohesion, c_r is root cohesion [kPa], γ is unit weight of the soil [kN/m^3], β is the slope angle [rad], φ is the friction angle [rad], and u is the pore pressure acting on the failure plane, $u = \gamma_w(z - z_w)$. γ_w is the unit weight of water [kN/m^3].

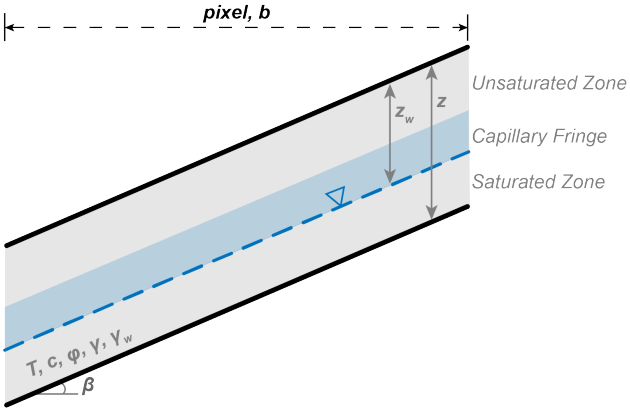

Figure 2.9. Geometry of the shallow landslide initiation model. Modified after Baum et al. (2008).

The volume of a single failing cell is the product of its plan area and the failure depth, z. Adjacent failing cells are combined in a GIS environment to identify the spatial extent and volume of individual shallow landslide sources.

2.5.3 Rock falls

Rainfall-induced rock falls are modeled as Culmann wedge-like masses with a tension crack in the slope face (Wyllie and Mah, 2004), including the effects of pore-pressure acting in the tension crack and on the failure plane (**Figure 2.10**):

$$FS = \frac{cA + (W\cos\alpha - U - V\sin\alpha)\tan\varphi}{W\sin\alpha + V\cos\alpha} \quad \textbf{(2.8)}$$

where *W* is the weight of the sliding block:

$$W = \frac{1}{2}\gamma H^2\left[\left(1 - \frac{z_c}{h}\right)^2 \cot\alpha * (\cot\alpha\tan\beta - 1)\right] \quad \textbf{(2.9)}$$

U is the pore pressure acting on the sliding plane:

$$U = \frac{1}{2}\gamma_w z_w (h + b\tan\beta - z_c)\csc\alpha \quad \textbf{(2.10)}$$

and *V* is the pore pressure acting in the tension crack

$$V = \frac{1}{2}\gamma_w {z_w}^2 \quad \textbf{(2.11)}$$

FS is the factor of safety of the rock wedge, γ is the unit weight of rock [kN/m^3], h is the height of rock face [m], β is the slope angle [rad], φ is the friction angle [rad], γ_w is the unit weight of water [kN/m^3], z_w is the depth of the water table [m], c is the cohesion [kPa], z_c is the critical tension crack depth [m], and α is the critical failure plane angle [rad]. The height of the failing wedge is constrained to 35% of the local relief based on observation from past earthquakes and calibration on a coseismic landslide inventory from New Zealand (Meunier et al., 2008; **Appendix 2.1**). I assume that the critical tension crack will develop under dry conditions, in which case, depth z_c is:

$$z_c = \frac{1}{h}\left(1 - \sqrt{\cot\beta \tan\alpha}\right) \quad (\mathbf{2.12})$$

after Wyllie and Mah (2004). The critical failure plane is typically given as $\alpha = \left(\frac{\beta+\varphi}{2}\right)$ (Collins and Sitar, 2011; Wyllie and Mah, 2004). However, this assumes the absence of water and is inexact for low slopes, especially when there is cohesion (e.g. due to mineral bonding; Taylor, 1948; Collins and Sitar, 2011). The critical angle occurs when the factor of safety is at a minimum or $\delta_{FS}/\delta_\alpha = 0$. I solve this graphically for the range of susceptible slope values and create a regression relationship between α and β for each unit, described by a unique set of material and topographic parameters and each ground water configuration.

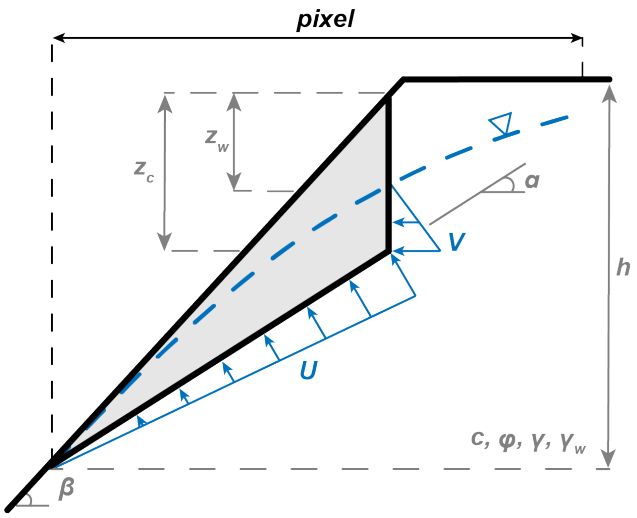

Figure 2.10. Geometry of precipitation-induced rock fall model.

The rock wedge model in **Equation 2.8** represents idealized failure geometry and combines individual pixel properties with larger hillslope conditions. As such the volume associated with **Equation 2.9** encompasses a slope parallel slice of the larger hillslope at each cell. After adjacent failing cells are aggregated, the total rock fall volume is estimated by the product of the average wedge volume and the width of the hillside involved.

2.5.4 Rotational slumps

Although slope stability methods for non-planar failure surfaces have been well-established in the geotechnical profession over the last century (Duncan et al., 2014), their implementation in a grid-based GIS framework is challenging due to the computational expense of iteratively testing multiple failure surfaces in each pixel. Both commercial and open-source three-dimensional slope stability programs have been produced (e.g. Slide[3], Rocscience Inc.; Scoops3D, Reid et al., 2015), but these can only be coarsely implemented at greater than watershed scale (e.g. Reid et

al., 2000, 2015). I develop an efficient, three-dimensional, pixel-based rotational failure model that computes the limit-equilibrium FS for a uniform, idealized failure surface that combines larger hillslope conditions with individual pixel properties, such as cohesion and friction angle (**Figure 2.11**). The efficiency of the model comes from the limiting assumption of a single prescribed failure surface. The location of this failure surface, defined by a depth parameter, *p*, is determined through a simple regression process, analogous to that used to determine α for the rock fall model, that isolates the least stable failing mass.

To account for wet conditions, the water pore pressure is added to the factor of safety equation, based on a slope-parallel ground water table. I project the radius of failure, *R* [m], perpendicular to the slope to create three-dimensional geometry:

$$FS = \frac{2\pi Rbc + (W\cos\alpha - F_w)\tan\varphi}{W\sin\alpha} \quad \textbf{(2.13)}$$

where *c* and φ are the cohesion [kPa] and friction angle [rad] of the soil mass, and α is the basal angle [rad] given by $\alpha = \sin^{-1}\frac{(4(\sin\delta)^3\sin\theta)}{3(2\delta-\sin 2\delta)}$. The weight of the sliding block, W, is

$$W = \frac{\pi\gamma b^2}{3}(3R - b) \quad \textbf{(2.14)}$$

and the resultant force of the pore water pressure, F_w, is:

$$F_w = \frac{1}{3}\pi\gamma_w q^2(3R - q) \tag{2.15}$$

where b and q are defined as $b = R(1 - \cos\ \delta\ )$ and $q = R(1 - \cos\ \theta\ )$. The radius of failure is a function of local relief:

$$R = \frac{H}{4}\left(\frac{\cos\beta}{p\,(\sin\beta)^2} + \frac{p}{\cos\beta}\right) \tag{2.16}$$

where H is local hillslope relief [m] and p is the depth parameter. The internal angle, δ, is computed as $\delta = \sin^{-1}\frac{H}{2R\sin\beta}$ [rad] for slopes $10° \leq \beta \leq 35°$, and θ is determined by the water table depth. The volume of overlapping failures is averaged.

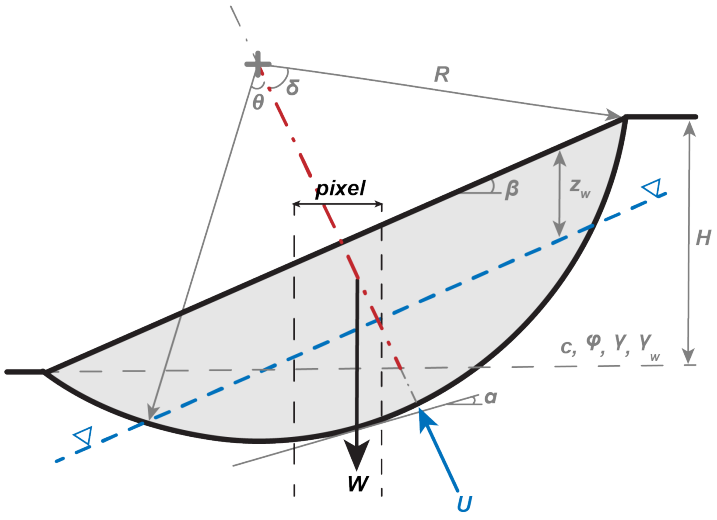

Figure 2.11. Geometry of rotational slump model. The depth of failure is determined as a percentage, p, of the perpendicular hillslope bisector segment in red. p may be greater than 100% (as shown).

Each model is applied on a pixel-by-pixel basis, producing raster maps of FS against each mode of failure. Factors of safety below one are assumed to be failing. Due to the overlapping susceptibility zones, individual cells may be modeled as simultaneously failing in two modes under the same input conditions.

2.6 Coseismic landslide models

For coseismic landslides I utilize the same equations as for precipitation-induced landslides (**Equations 2.7**, **2.8**, and **2.13**). Dry season conditions are modelled either with a deeper ground water table or by omitting the pore pressure terms altogether.

2.6.1 Coseismic displacements

Static factors of safety for all modes are converted to critical accelerations using the adapted Newmark (1965) equation of Chen and Tsai (2017):

$$k_y = \frac{FoS - 1}{\frac{1}{\tan\varphi} + \tan\alpha} \qquad (\mathbf{2.17})$$

where α is the inclination of the failure plane (equal to β for shallow failures) and φ is the material friction angle. **Equation 2.17** is valid for planar and wedge type failures as well as for deep, rotational failures in which the failure plane intersect the slope crest and toe, as in **Figure 2.11** (Chien and Tsai, 2017).

Coseismic displacements, D_N [cm], are estimated based on the PGA after Saygili and Rathje (2008):

$$\ln D_N = 5.52 - 4.43\left(\frac{k_y}{PGA}\right) - 20.93\left(\frac{k_y}{PGA}\right)^2 + 42.61\left(\frac{k_y}{PGA}\right)^3 - 28.74\left(\frac{k_y}{PGA}\right)^4 + 0.72\ln PGA \quad \textbf{(2.18)}$$

Other displacement relationship can be used (e.g. Meehan and Vahedifard, 2013), including multivariable equations if additional data is available (Saygili and Rathje, 2008; Jibson et al., 2007). For rotational slumps, coseismic displacements are estimated using **Equation 2.18**, with a 70% reduction factor applied to the PGA to account for the compliant (non-rigid) nature of deep failure masses (Grant et al., 2016).

2.6.2 Topographic amplification

Peak ground acceleration has been recognized to exert a dominant control on the location of coseismic landslides (Meunier et al., 2007). Compilations of coseismic landslide inventories show that landslides tend to cluster at ridge crests and near breaks in slope, such as at the crest of a steeper "inner gorge," within a broader valley. This spatial "preference" of coseismic mass-wasting has been attributed to topographic amplification earthquake ground motion, which produces more intense shaking at topographic irregularities (Densmore and Hovius, 2000; Meunier et al., 2007, 2008; Burbank and Anderson, 2012).

Observationally, a suite of ground motions from five earthquakes in Japan showed that ridgelines experienced a 2.5-fold increase in the intensity of shaking when compared to the shaking at their base (Jibson, 1987; Kramer 1996). Similar studies in Italy and New Zealand recorded base to crest amplification factors are commonly in the range of 2 – 7 (Massa et al., 2013). I adopt a fixed topographic amplification term of 1.6 for rock slope failures based on literature and calibration using a detailed coseismic landslide inventory in New Zealand (Ashford and Sitar, 2002; **Appendix 2.1**)

2.6.3 Coseismic displacement thresholds

The threshold level of displacement which will trigger catastrophic failure varies by slope material and thickness of the shear zone and is not easily determined (Picarelli and Olivares, 2011). In the multimodal method failure is anticipated at coseismic displacements of 5 cm, 5 cm, and 15 cm for shallow slides, rock fall, and rotational slumps, respectively, after Grant et al. (2016).

2.7 Runout modeling

2.7.1 Runout routing using r.randomwalk

The runout envelope of shallow soil failures and rock fall is determined using the open-source landslide runout code r.randomwalk, (Mergili et al., 2015). A random walk is a Monte Carlo approach to routing an object through space (Pearson, 1905; Gamma, 1999). In the case of

landslide runout, flow paths start at user-defined source cells and are built pixel-by-pixel using quasi-random selection from among the adjacent cells (**Figure 2.12**). The selection of cells is constrained by weighted terrain factors including the steepest downhill descent (f_β) and the perpetuation of flow direction (f_d). Routing continues until a break criterion is reached such as a reach angle or a horizontal travel distance, L_{max}.

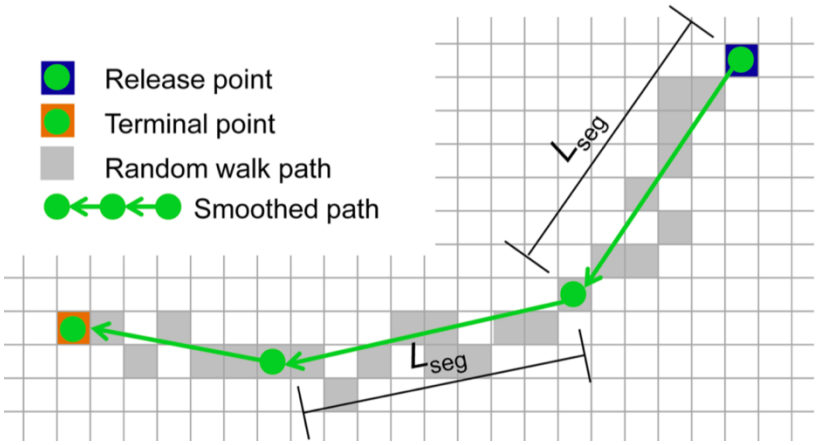

Figure 2.12. Runout routing in r.randomwalk. The total runout length L_{max} is calculated along a smoothed path by summing increments of the user-defined length L_{seg}. Figure: Mergili et al. (2015).

The r.randomwalk aggregates the random walks from each source cell into a map of impact frequency, describing the number of times a downslope cell was crossed by a flow path (**Figure 2.13**). The runout envelope is defined by all cells crossed by a least one randomwalk. Uncertainty in the weighting factors f_β and f_d which control the lateral spreading of individual random walks is accounted for by random uniform sampling between the ranges of 7 – 10 and 1 – 3, respectively, after Mergili et al. (2015).

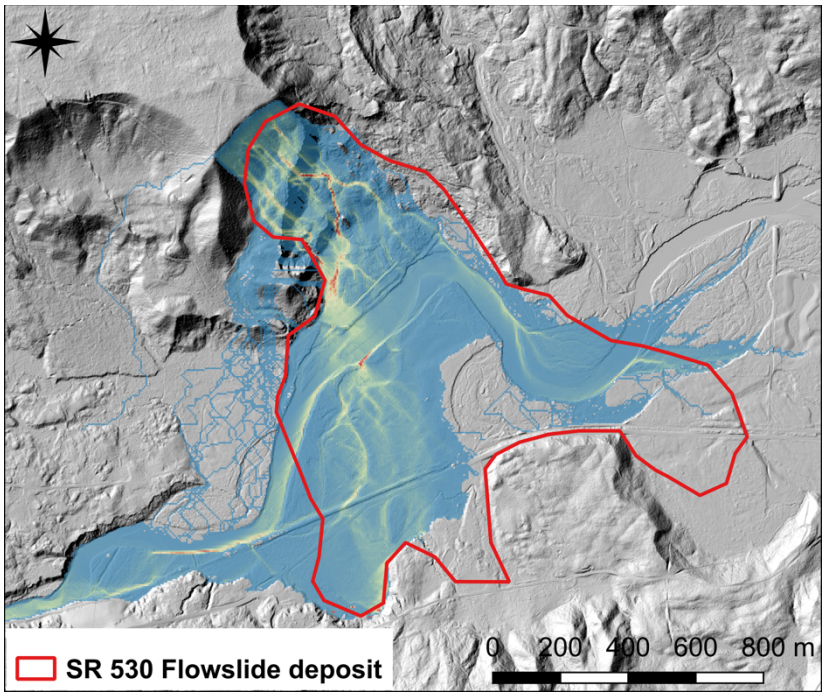

Figure 2.13. The output of r.randomwalk compared the observed runout of the 2014 "SR 530" or "Oso" Flowslide in Washington State.

2.7.2 Runout stopping criteria

Attempts to quantify and predict the runout length of landslides date at least as far back as Albert Heim's seminal 1932 work, *Bergsturz and Menschenleben* ("Landslides and Human Lives"). Heim was the first to develop and popularize the theory that landslide runout is fundamentally driven by its volume. Since then, numerous empirical runout relationship have been proposed, the majority of which take one of two forms: 1.) relating volume (V) to a *fahrboschung* ("driving slope") angle, equivalent to the ratio between the vertical and horizontal distances from landslide headscarp to toe, H_{max} and L_{max} respectively:

$$\log\left(\frac{H_{max}}{L_{max}}\right) = a * \log V + b \tag{2.19}$$

or 2.) relating volume solely to the total length:

$$\log(L_{max}) = a * \log V + b \tag{2.20}$$

An extended discussion of these runout relationships is given in **Chapter 3**. **Equations 2.19** and **2.20** are produced via ordinary least-squares (OLS) regression on log-transformed pairs of volume and length (or *fahrboschung*). For runout prediction, engineers are interested in producing length values in arithmetic, not logarithmic space. **Equations 2.19** and **2.20** can be anti-logged to take the power law form:

$$L_{max} = V^a * 10^b \tag{2.21}$$

However, performing OLS regression on log-transformed data produces a biased equation when the dependent variable is anti-logged (Finney, 1941; Ferguson, 1986). **Equation 2.21** will underestimate L_{max}, with the degree of underestimation increasing with greater scatter (Corominas 1996; Hansen 1996). Of particular import for landslide runout prediction, this bias is non-conservative and often significantly so due to a high degree of scatter in the empirical data.

Finney (1941) proposed a correction factor (FCF) for least-squares regression on log-transformed data. **Equation**s **2.19** and **2.20** implicitly assume the statistical model:

$$\log(L_{max}) = a * \log V + b \pm \varepsilon \quad \textbf{(2.22)}$$

where ε is independent, additive, normally-distributed error with mean zero and variance of σ^2. Thus the anti-logged form is:

$$L = V^a * 10^b * \eta \quad \textbf{(2.23)}$$

where the multiplicative errors, η, are lognormally distributed, of the expectation:

$$\eta = e^{\left\{\frac{\sigma^2 * (\ln 10)^2}{2}\right\}} \quad \textbf{(2.24)}$$

which simplifies to:

$$FCF = \eta = e^{\{2.65 * \sigma^2\}} \quad \textbf{(2.25)}$$

for base ten-transformed data, where σ is the standard error of the estimate (SEE) in log units (Hansen, 1996; Ferguson, 1986). Thus, η is greater than one unless there is no scatter around the regression line ($\sigma^2 = 0$).

Thus, the bias-corrected, predictive form of **Equation 2.21** is:

$$L = V^a * 10^b * FCF \quad (\mathbf{2.26})$$

2.7.3 Global empirical runout relationships

In many locations, sufficiently detailed inventories of the locally-applicable modes of landsliding are not available from which to produce predictive runout relationships that supply the stopping criteria for r.randomwalk. I have compiled global datasets of three modes of long-runout landslides to provide preliminary estimates of runout lengths in such cases, including coseismic rock avalanches and disrupted soil slides, confined debris flows, and unconfined debris avalanches (sometimes called flowslides). A description of the datasets and the methods used to compile them are given in **Chapter 3** and **Appendices 2.3** and **3.1**. Following the form of **Equation 2.20**, the regression coefficients for each mode are given in **Table 2.4**. These relationships are visualized in **Figure 2.14**.

Table 2.4. Length-volume relationship parameters.

Mode	*a*	*b*	σ	r^2	*n*
coseismic disrupted slides and rock avalanches	0.3931	0.3269	0.1479	0.83	3999
flowslides (unconfined)	0.3476	0.9578	0.3174	0.92	577
debris flows (confined)	0.2369	1.7472	0.5334	0.30	400

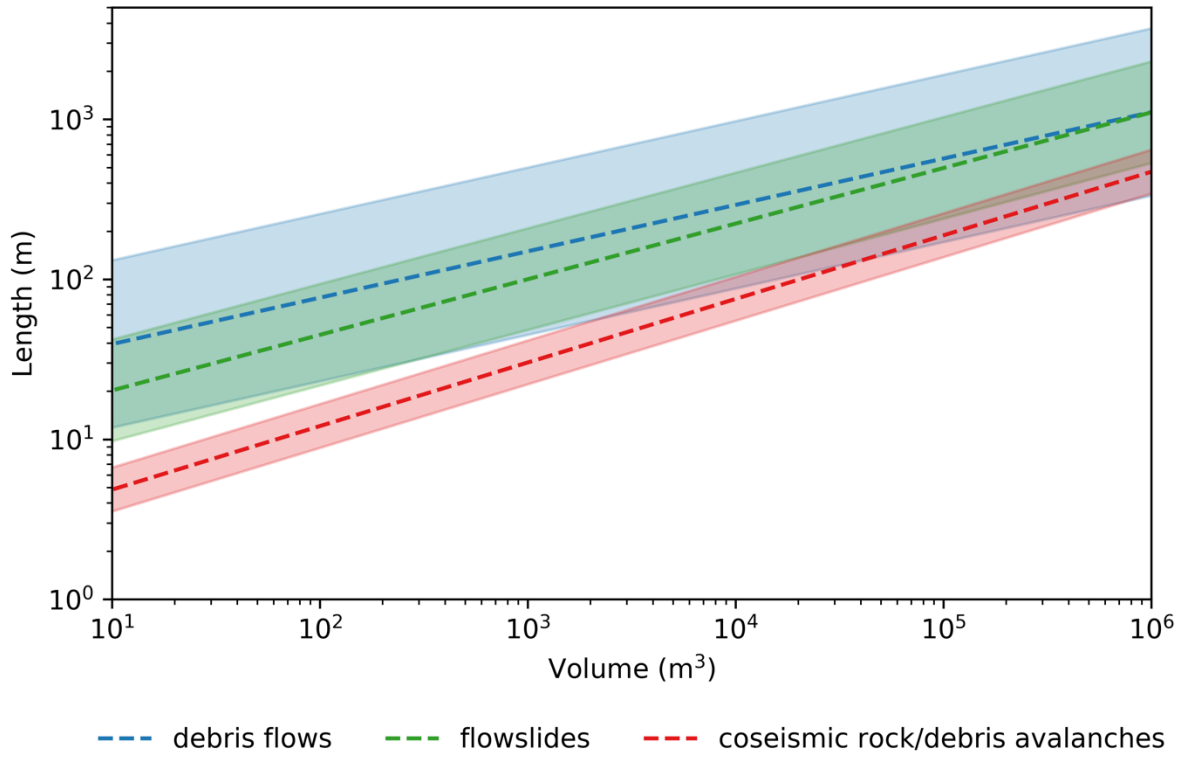

Figure 2.14. Selected length-volume runout relationships. Shaded area shows one standard deviation around the mean.

2.7.4 Channelized and un-channelized terrain

I differentiate debris flows and debris avalanches by the terrain morphology of individual sources. Ten landform elements are identified from the base DEM using r.geomorphons (Jasiewicz and Stepinski, 2013). Landslide source areas which fall in confined landforms such as pits, valleys, and hollows are categorized as debris flows (**Figure 2.15**).

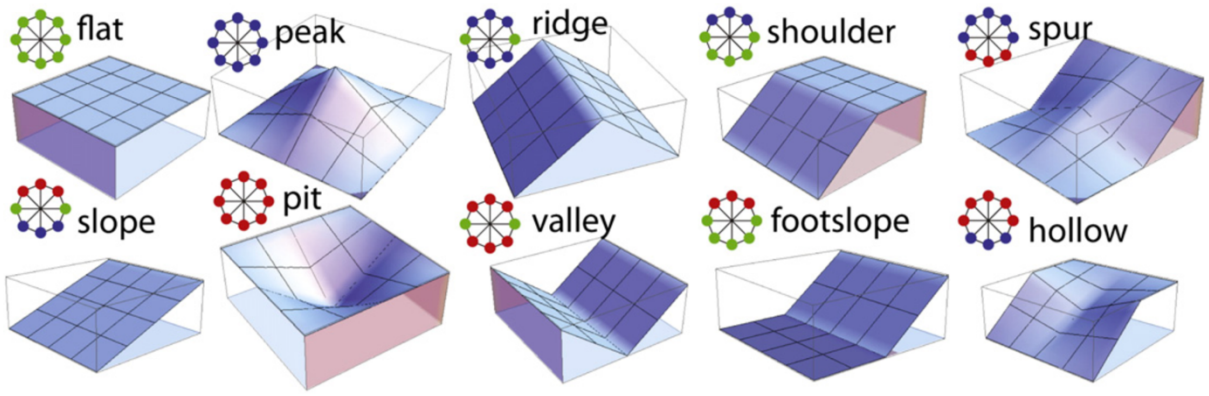

Figure 2.15. Simplified morphologies for the ten landforms recognized in r.geomorphons. Radial diagrams illustrate the elevation difference between the cell being analyzed and its eight neighbors in a GIS environment: green: same; blue: lower; red: higher. Figure from Jasiewicz and Stepinski (2013).

2.7.5 Rotational slumps

Rotational slumps are not considered to have significant runout in the multimodal framework. The area of influence of each rotational slump is delineated by a spatial buffer equal to the radius of failure, R (**Equation 2.16**). By creating a buffer of R rather than the oblique projection of the failing ground surface in **Figure 2.11**, slight conservativism is introduced by overpredicting the head and toe of the landslide. It is possible for rotational slumps to transition into long runout flowslides (e.g. Wartman et al., 2016). Such cases could be modeled in a future version of the multimodal framework by including a module for evaluating flow liquefaction triggering criteria (see **Chapter 3**).

2.8 Process intensity

2.8.1 Shallow slides and rotational slumps

The vulnerability of elements at risk is a function of intensity of the hazard. For rotational slumps I adopt volume for the process intensity (Fell, 1994), which can be calculated from **Equation 2.14**, omitting the term for unit weight. The process intensity of shallow landslides is commonly reported as the flow height (Ciurean et al., 2017; Fuchs et al., 2007). As r.randomwalk is a statistical rather than process-based model, it only provides information about the areal extent of landslide inundation. I make the basic assumption that the maximum flow height can be approximated by the depth of failure in **Equation 2.7**. For both rotational and shallow failures, I use the mean intensity values (volume and failure depth, respectively) of all cells aggregated into a single source zone.

2.8.2 Rock avalanches

As noted in **Section 2.2**, large rock falls and slides may disintegrate into rock avalanches. The post-failure motion of a rock avalanche is rapid and highly destructive, making predictive modeling of the mobility, areal extent, and intensity of rock avalanche runout a key element in risk analysis (Locat et al., 2003). Falling blocks move downslope on individual trajectories governed by the gradient, topographic confinement, slope material, and collisions with other blocks. Individual blocks may explode or fragment into multiple sub-blocks, with dispersive trajectories, dramatically influencing mobility and degree of spreading of the rock avalanche

(Ruiz-Carulla, 2018; Locat et al., 2006). Fragmentation is a function of initial block size, velocity, rock strength and elasticity, discontinuities, and the properties of the surrounding terrain or colliding rock fragments (Crosta et al., 2015). The complexity of the process makes fragmentation extremely difficult to model (Locat et al., 2006; Corominas et al., 2017) and few hazard analyses even attempt to include it (Crosta et al., 2015; Ruiz-Carulla, 2018; Giacomini et al., 2009).

Excluding the effects of fragmentation can have significant consequences for hazard and risk analysis. Ignoring fragmentation in rock fall propagation models overestimates the kinetic energy and mobility of rock avalanche runout. Simultaneously, however, the probability of impact and spreading of the avalanche may be underestimated since fragmentation creates multiple, diverging trajectories (Matas et al., 2017; Corominas et al., 2019). I have made an initial, rudimentary effort to incorporate the effects of fragmentation by implementing the model of Locat et al. (2006).

As movement progresses downslope, initial potential energy is converted to kinetic energy, which is progressively dissipated by friction and damping in impacts with the surrounding terrain as wells as internal friction and fragmentation. Locat et al. (2003, 2006) describe the energy balance of an entire rock avalanche system at any time during post-failure mass movement:

$$\Delta E_T = \Delta E_P + \Delta E_K + \Delta E_F + \Delta E_D = 0 \qquad (\mathbf{2.27})$$

where ΔE_T is the change in total energy, ΔE_P is the change in potential energy, ΔE_K is the change in kinetic energy, ΔE_F is the energy lost to basal friction, and ΔE_D is the energy lost in internal fragmentation. From **Equation 2.27**, energy consumed by friction and disintegration reduce the kinetic energy available to perpetuate motion. Based on nine large rock avalanches, Locat et al. (2006) find that approximately 20% of the potential energy of large rock avalanches is spent in internal fragmentation:

$$\Delta E_D \approx 0.2 * \Delta E_P \quad \textbf{(2.28)}$$

Equations 2.27 and **2.28** imply that approximately 80% of the initial potential energy is lost to friction over the duration of the avalanche, or $E_F = 0.8E_P$. This replicates the effect of the initial failing mass falling from 80% of actual height with the implicit (unrealistic) simplification that the fragmentation energy is lost at the moment of release.

Using the frictional "sled" model proposed by Heim (1932), the velocity of the failing material represented by a rigid block (i.e. ignoring internal deformation) can be estimated at any point along the runout path by

$$v = \sqrt{2g\Delta z} \quad \textbf{(2.29)}$$

where g is the acceleration due to gravity and Δz is the height difference between the center of gravity (CoG) "energy line," defined by $\frac{H_{CoG}}{L_{CoG}}$, and a point along the runout path. Without an a priori assumption of the deposit geometry permitting a calculation the center of gravity, I

conservatively approximate energy line with the *fahrboschung* line, $\frac{H_{CoG}}{L_{CoG}} \approx \frac{H_{max}}{L_{max}}$ (Erismann and Abele, 2001). Thus, accounting for the artificially lowered fall height due to fragmentation, the calculation of Δz for point i becomes:

$$\Delta z = 0.8H_{max}\left(1 - \frac{L_i}{L_{max}}\right) - H_i \tag{2.30}$$

Where H_{max} is the total fall height, L_{max} is the total runout length, and H_i and L_i describe the elevation and distance from the release point to the point of interest (**Figure 2.16**).

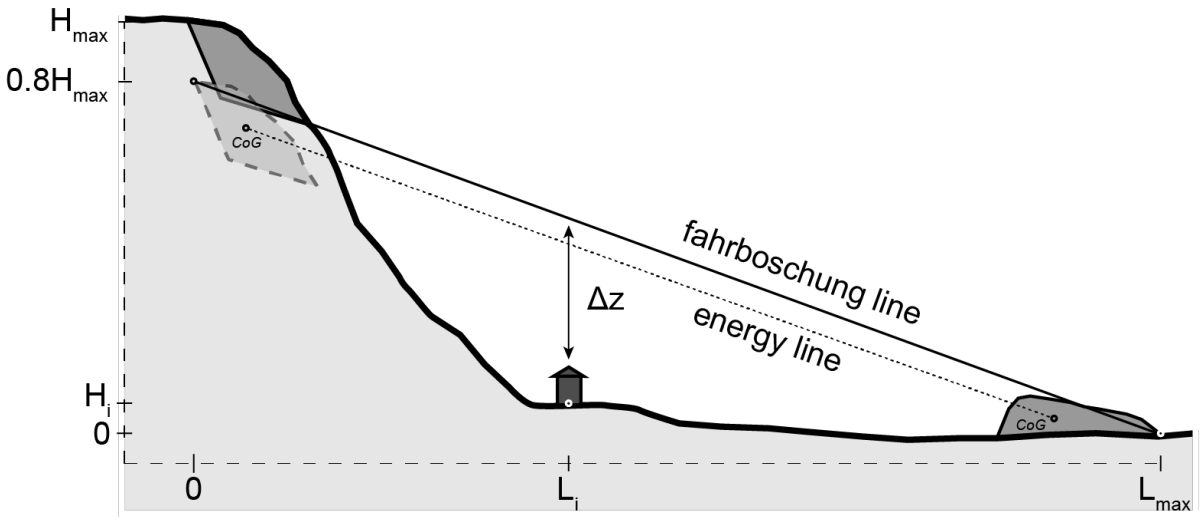

Figure 2.16. Assuming only 80% of the original potential energy is available for conversion to kinetic energy and subsequently lost in basal friction, the height difference Δz, and thus velocity, can be computed from an artificial *fahrboschung* line. Note that this introduces the generally conservative error of using the *fahrboschung* line instead of the energy line (Erismann and Abele, 2001).

By measuring grain size distributions along a the transects of nine rock avalanches, Locat et al. (2006) empirically derive a relationship between the potential energy per unit volume and the degree of fragmentation in a rock avalanche ($R^2 = 0.94$):

$$\gamma H_G = \sigma_c \left[0.006 + 0.012\left(\frac{D_{50}}{d_{50}}\right)\right] \quad \textbf{(2.31)}$$

where γ is the rock unit weight [kN/m^3], D_{50} is the average initial block diameter, d_{50} is the average debris block diameter, σ_c is the uniaxial compressive strength derived from a point load test, and $H_G = H_{max} - H_i$. **Equation 2.31** can be rearranged to solve for the diameter reduction ratio:

$$R_r = \frac{D_{50}}{d_{50}} = \frac{1}{0.012}\left[\frac{\gamma H_G}{\sigma_c} - 0.006\right] \quad \textbf{(2.32)}$$

Equation 2.32 is used to calculate the block diameter, d_{50}, at any point along the runout path as $d_{50} = \frac{D_{50}}{R_r}$. Diameter is related to the spherical block volume, V_b:

$$V_b = \frac{3}{4}\pi\left(\frac{d_{50}}{2}\right)^3 \quad \textbf{(2.33)}$$

Since slope-scale discontinuity spacing is not accounted for in the multimodal method, the original block diameter, D_{50}, is assumed to equal to the pixel resolution.

For both rock falls and debris avalanches, the volume of material passing points downslope can be described by a power law (Massey et al., 2012a). Based on four coseismic rock avalanches in New Zealand (Massey et al., 2012b), I define a power law relationship between the proportion of the initial volume, V_L, passing a proportion of the total runout distance, P_L (**Figure 2.17**; $R^2 = 0.79$):

$$P_V = 10^{-4.19} * {P_L}^{-10.17} \quad \textbf{(2.34)}$$

This relationship implies that deposition will begin at approximately 38% of the total runout distance.

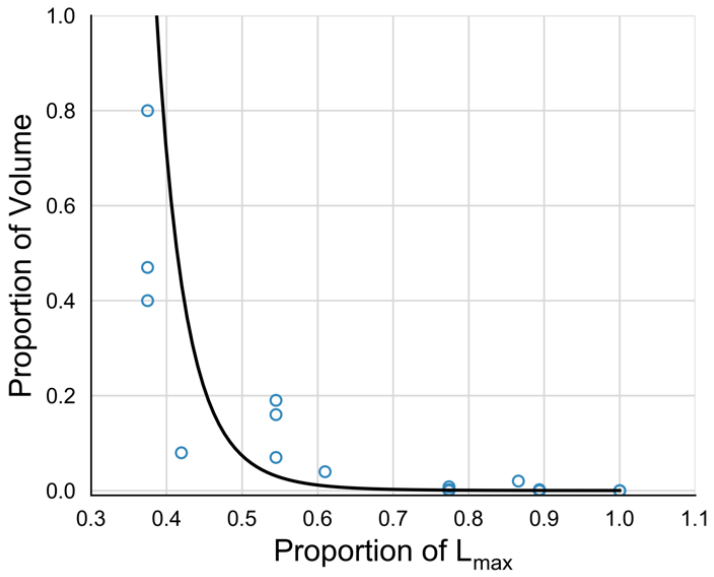

Figure 2.17. Power law relationship between the proportion of the initial rock avalanche volume passing a proportion of the total runout distance, L_{max} base on four coseismic rock avalanches in New Zealand.

From **Equation 2.34** and assuming an initial cubic block size determined by the pixel resolution, the equivalent number of blocks of mean diameter passing any point along the rock avalanche runout path can be calculated as:

$$N_b = \frac{V * P_V}{V_b} * \frac{\pi}{6} \quad \textbf{(2.35)}$$

The last term, $\pi / 6$, accounts for a "packing" scale factor that assumes blocks are initially cubic but end spherical due to mechanical rounding. I consider only the "design" boulder of mean diameter, d_{50}, but future versions of the model could use probabilistic block sizes drawn from real rock avalanche particle-size distributions (e.g. Locat et al., 2006).

Finally, the kinetic energy of each block is calculated as:

$$KE_{b_i} = \frac{1}{2} * \frac{\gamma}{g} V_b v^2 \quad \textbf{(2.36)}$$

Where γ is the rock unit weight, g is gravity, V_b is the block volume, and v is the velocity. The **Equations 2.27** – **2.36** represent a rudimentary attempt to approximate the complex dynamics of fragmenting rock fall in a computationally efficient manner. Despite the significant assumptions about the energy loss and geometry of rock avalanche deposits, the kinetic energy model above showed acceptable agreement with an existing GIS-based rock avalanche model and an observed rock fall/avalanche in les Cretaux, Switzerland, (Jaboyedoff and Labiouse, 2011; **Appendix 2.4)**.

2.9 Exposure

The exposure of non-stationary elements at risk is typically estimated based on temporal patterns of daily life or traffic volumes (e.g. Lee and Jones, 2014; Budetta et al., 2004). The temporal exposure of stationary elements at risk is one. However, depending on the resolution of the study and the magnitude of landslide events, both stationary and non-stationary elements at risk may have a spatial component to their exposure (e.g. Corominas et al., 2005). For example, in the case of a single rock-block fall, the area impacted by the rock and the area occupied by a person may both be only a fraction of the occupied pixel size in a GIS framework. Despite both occupying the same pixel at the same time, the rock and the person may have a low probability of impact, determined as a function of their individual sizes and the pixel resolution (Ruiz-Carulla, 2018; Nicolet et al., 2016). In this framework, exposure values are provided as an attribute of the element at risk layer or assumed constant for the area of interest.

Unlike materially continuous rotational slumps or shallow landslides, rock avalanches are composed of discrete boulders which each pose a unique hazard to elements at risk. It is possible to be within the runout apron of a rock fall without being impacted by debris, as many fortunate survivor stories attest (e.g. Massey et al., 2017; Taig et al., 2015). The probability of impact (*exposure*) is a function of the movement of both the hazard and the element at risk.

For a spatially discrete threat, such as that of being hit by a single falling boulder, the probability of impact on an object within a portion of the slope is:

$$P_{1(S:H)} = \frac{D + d}{L} \quad \textbf{(2.37)}$$

where D is the diameter of the design boulder which travels along a path on either side of an object of diameter, d, and L is the length of the slope perpendicular to the runout path (Massey et al., 2017; Montgomery and Ward, 1995). The probability of no impact for a single boulder is the complement:

$$1 - P_{1(S:H)} \quad \textbf{(2.38)}$$

The probability of N boulders passing through L but all missing the object is:

$$\left(1 - P_{1(S:H)}\right)^N \quad \textbf{(2.39)}$$

so the probability of at least one impact out of N boulders is:

$$P_{N(S:H)} = 1 - \left(1 - P_{1(S:H)}\right)^N \quad \textbf{(2.40)}$$

In the multimodal framework, **Equation 2.40** is used to calculate the exposure for each building at risk, with d equal to the slope-perpendicular axis of the building (Massey et al., 2014b). Only indoor populations are considered in the current version of the multimodal framework; the exposure of resident people is lumped into vulnerability due to the resolution of empirical data, as described below and in **Chapter 4**.

2.10 Vulnerability

Vulnerability is the means by which physical hazard can create disparate losses among different populations while impacting them, by all appearances, equally. In quantitative landslide risk assessment, the inclusion of vulnerability is limited to the physical damage (as a probability of death or a proportion of initial value lost) as correlated to a measurable intensity metric of the landslide hazard such as flow height, velocity, kinetic energy, or momentum (Lee and Jones, 2014).

The vulnerability of infrastructure is evaluated economically, expressed through a damage ratio, D_r, between the cost to repair and the cost to replace the structure (Massey et al., 2019; Quan Luna et al., 2011; Papathoma-Kohle et al., 2015; Fuchs et al., 2007; Totschnig et al., 2013):

$$D_r = \frac{cost\ to\ repair}{cost\ to\ replace} \tag{2.41}$$

Vulnerability curves mathematically express the relationship between the damage ratio and the process intensity (Ciurean et al., 2017). Due to the detailed input data requirements and complex nature of landslide-structure interaction, vulnerability curves are usually created using data-driven rather than analytical methods (Corominas et al., 2014). Numerous curves have been proposed by fitting a chosen mathematical distribution to intensity-damage pairs from observed landslide events (e.g. Ciurean et al., 2017; Fuchs et al, 2012; Papathoma-Kohle et al., 2012, 2015; Rheinberger et al., 2013; Totschnig and Fuchs, 2013; see review in Massey et al., 2019).

However, vulnerability is a function not only of the hazard intensity but also of building typology, such as the construction material, foundation type, number of stories, orientation of windows and doors, and maintenance state (Safeland, 2011; Du et al., 2013), creating the need for unique vulnerability curves for each class of structure.

2.10.1 Structural vulnerability to shallow landslides and rock falls

I create new structural vulnerability curves for use in the multimodal method by compiling published data and developing a novel database of damage-intensity pairs for the 2018 Montecito, California debris flows. Data sources as well as the Montecito vulnerability dataset and a discussion of its development are given in **Appendix 2.5**. Because observed landslide damage data is limited, I create vulnerability curves for two landslide modes and two building types: 1.) debris flows/avalanches impacting masonry/concrete structures, 2.) debris flows/avalanches impacting timber-frame structures, 3.) rock falls impacting masonry/concrete structures, and 4.) rock falls impacting timber-frame structures. An implicit limitation of the underlying data is that almost all observed damage-intensity pairs are for residential structures. Applying vulnerability curves developed on smaller, lighter residential structures to dense industrial and urban architecture may overpredict vulnerability.

Following Totschnig et al. (2011) and Papathoma-Kohle et al. (2012), a modified Weibull damage function was fitted to the debris flow/avalanche damage-intensity data, of the form:

$$V = 1 - e^{-a * I^b} \quad \textbf{(2.42)}$$

where I is the debris flow intensity measured in flow depth [m]. **Figures 2.18** and **2.19** show the vulnerability curves for masonry/concrete and timber-frame structures, respectively. The fitting parameters for all of the vulnerability curves are provided in **Table 2.5**.

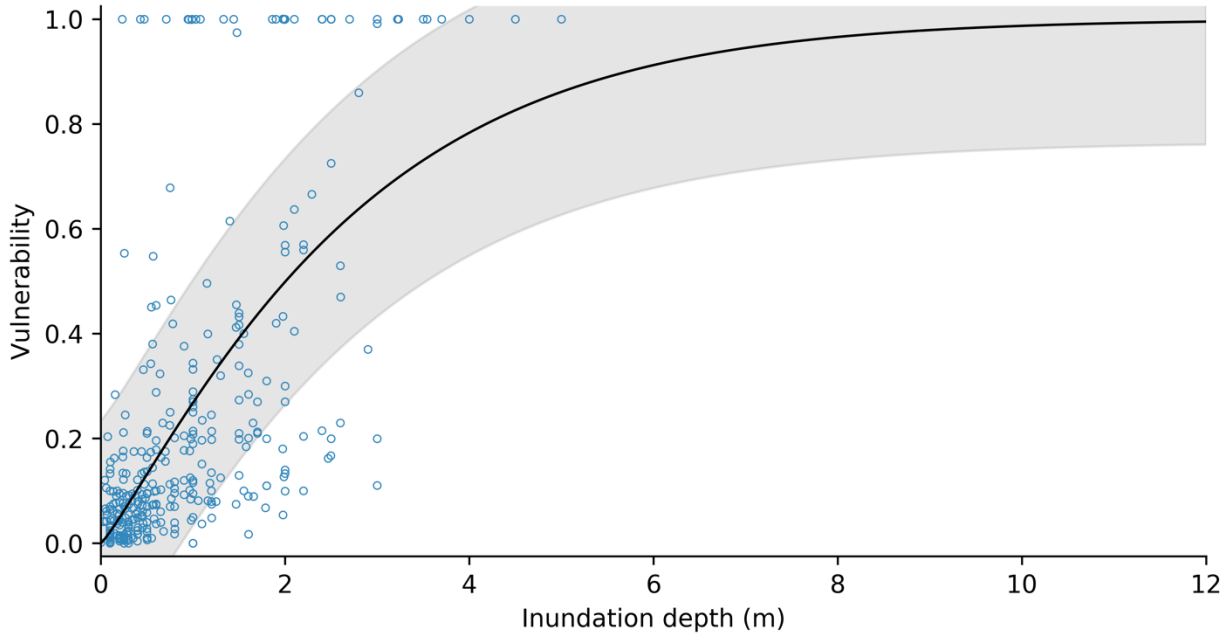

Figure 2.18. Structural vulnerability curve for masonry and concrete buildings impacted by debris flows/avalanches.

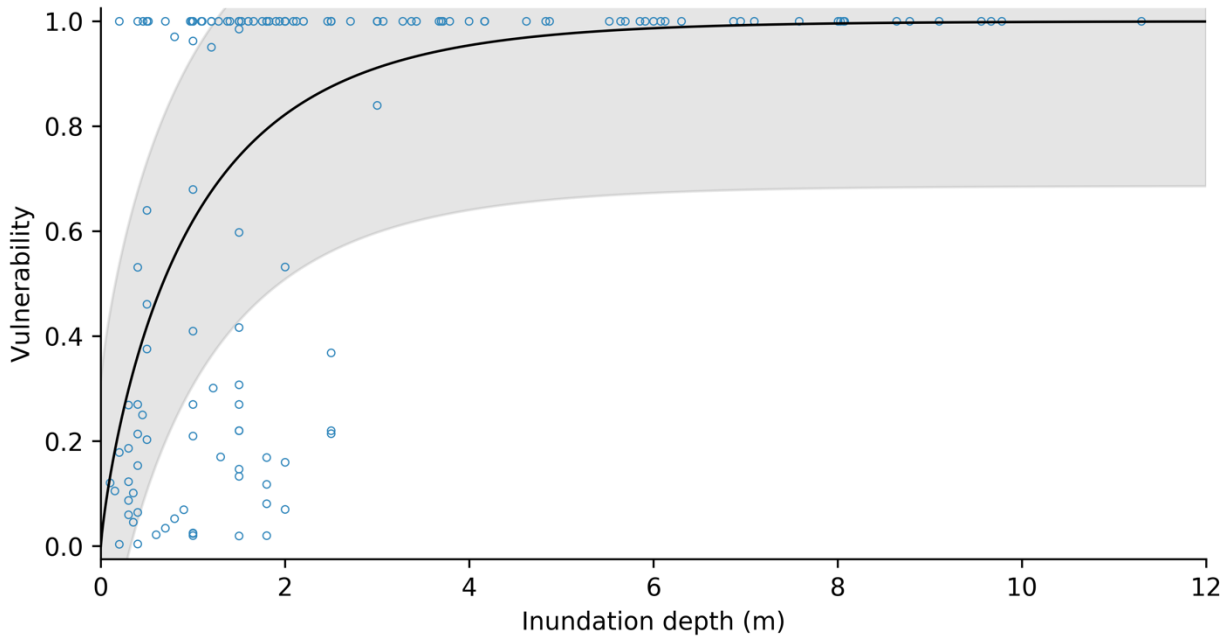

Figure 2.19. Structural vulnerability curve for timber-frame buildings impacted by debris flows/avalanches.

After Massey et al. (2019), a modified Frechet damage function was fitted to the rock fall intensity-vulnerability data, of the form:

$$V = e^{-\left(\frac{I+b}{b}-1\right)^{-a}} \quad \textbf{(2.43)}$$

where I is the rock fall intensity measured in kinetic energy [kJ]. **Figures 2.20** and **2.21** show the vulnerability curves for masonry/concrete and timber-frame structures, respectively.

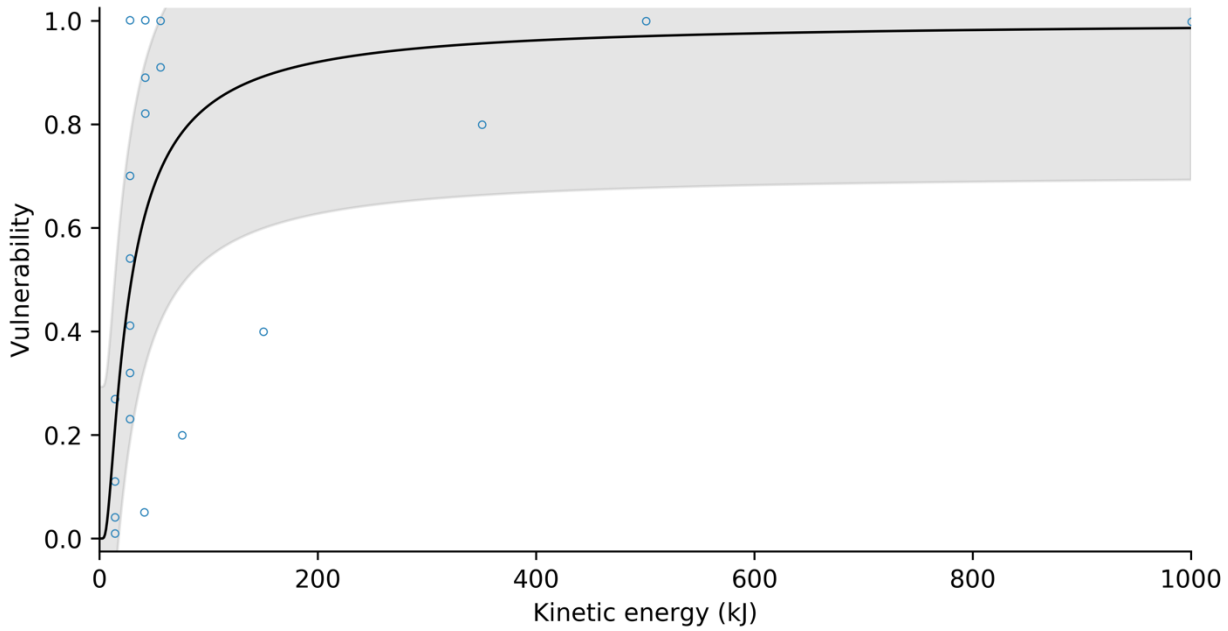

Figure 2.20. Structural vulnerability curve for masonry and concrete buildings impacted by rock fall.

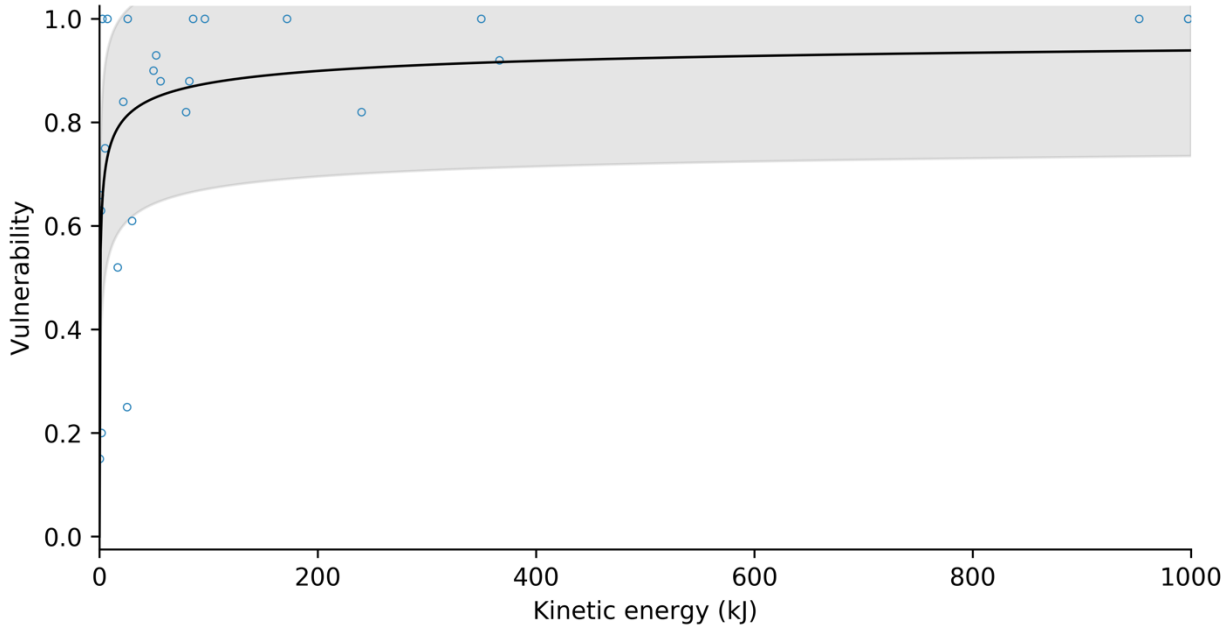

Figure 2.21. Structural vulnerability curve for timber-frame buildings impacted by rock fall.

Table 2.5. Fitting parameters for structural vulnerability functions. *Standard deviation of the residuals.

Building material	*a*	*b*	σ*	*pseudo* R^2	*n*
Debris flow					
masonry / concrete	0.3119	1.1470	0.2347	0.40	350
timber	0.9677	0.8359	0.3140	0.33	170
Rock fall					
masonry / concrete	1.1073	21.0732	0.2932	0.36	21
timber	0.3239	0.1959	0.2040	0.37	26

2.10.2 Structural vulnerability to rotational slumps

Many large rotational slumps are slow-moving and are subject to periods of higher (and lower) activity based on seasonal ground-water fluctuations. Structures wholly within the moving mass may experience little damage, while those on the boundaries are subject to differential displacement (AGS, 2007). Damages to structures on slow moving slumps have been linked to intensity metrics such as landslide area (Galli and Guzzetti, 2007), volume (Fell, 1994; Catani et al., 2005), rate of movement (Mansour et al., 2011), and differential settlement at specific sites on the landslide body (Peduto et al., 2018). However, the latter two intensity metrics require detailed, longitudinal monitoring of existing landslides and are difficult to incorporate into predictive modeling of new or dormant slumps. I adopt the volume-based vulnerability values of Catani et al. (2005) which is an update of work by Fell (1994; **Table 2.6** and **Figure 2.21**).

Table 2.6. Structural vulnerability to rotational slumps (Catani et al., 2005)

Volume (m^3)	Vulnerability
< 1×10^3	0.05
1×10^3 - 5×10^4	0.10
5×10^4 - 1×10^6	0.30
> 1×10^6	0.60

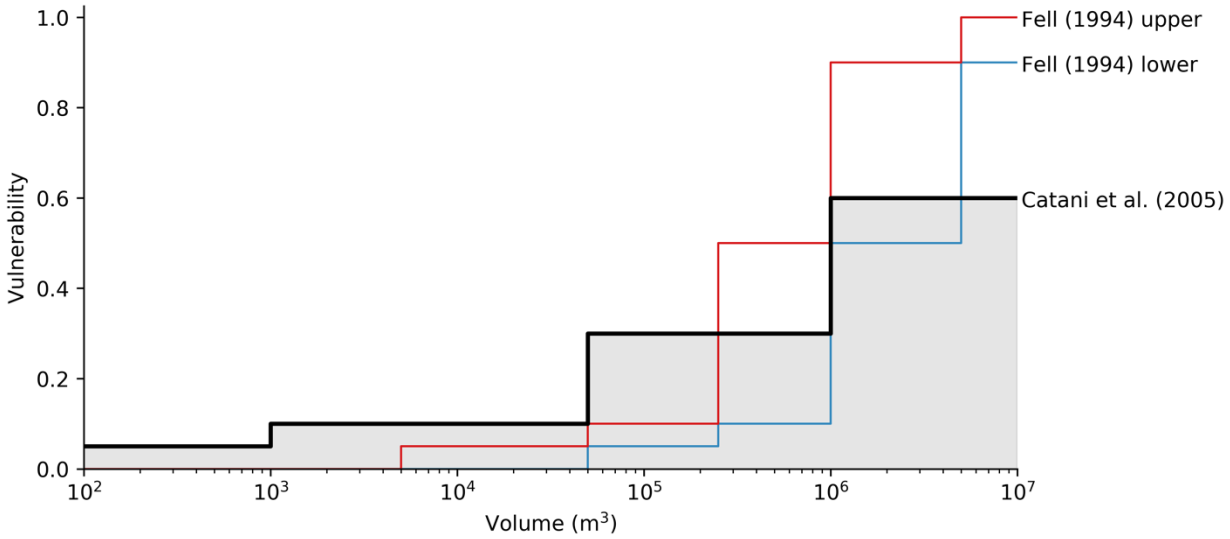

Figure 2.22. Structural vulnerability to rotational slumps. The heuristic values of Catani et al. (2005) are used as an upper bound. For slumps of a given volume, vulnerability values are randomly sampled from the shaded area.

2.10.3 Human vulnerability

Rather than a damage ratio, human vulnerability is often evaluated as the probability of death given direct impact by a landslide or occupancy in an impacted structure (Corominas et al., 2014). Structural damage is of secondary importance to human loss of life, yet little has been done to quantify human physical vulnerability. Almost all existing methods rely heavily on subjective, expert-based estimates. In **Chapter 4** I address this void by presenting an empirical human vulnerability curve for rapid landslides, including debris and rock avalanches and debris

flows. Deep-seated rotational slumps often develop slowly, allowing residents to evacuate (Lee and Jones, 2014); thus, a nominal human vulnerability of 0.0001 is adopted in the multimodal method. Based on post event interviews after the 2011 Christchurch, New Zealand, earthquake, Taig et al. (2015) estimate the vulnerability of individuals in homes struck by rock falls to be between 0.5 – 0.9 depending on the time of day. Taig et al. (2015) observed that because the earthquake occurred in daytime hours, individuals were able to see and evade oncoming boulders, preventing multiple fatalities. Although the ability of humans to take evasive action plays an important role in the estimation of physical vulnerability, it is difficult to predict, as it depends on the specific individual's prior knowledge, awareness, physical ability, and decision-making (see **Chapter 4**). In the multimodal method I adopt values for human vulnerability to rock falls/avalanches on a per-building basis by random, uniform sampling within the range 0.5 – 0.9, as I do not attempt to predict ex ante human awareness or evasion of hazards based on time of day.

2.11 Risk

The risk equations (**1.1** and **1.2**) are applied on a per-pixel basis to calculate the loss within every building or occupied pixel associated with each triggering scenario and landslide mode. Since each scenario is associated with an annual frequency, the loss values can be summed spatially to plot total risk curves (**Figure 2.23**) or societal ("F-N") risk curves (e.g. **Figure 5.7**) or be temporally aggregated into maps of annualized risk (e.g. **Figures 5.5** and **6.19**).

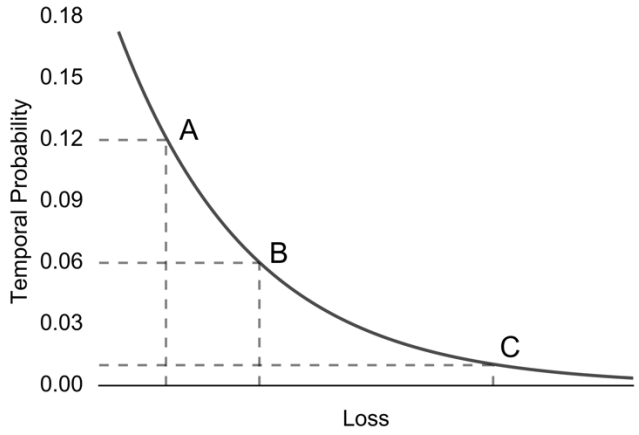

Figure 2.23. Example of a total risk curve. The three landslide scenarios shown, *A*, *B*, and *C* are associated with a unique frequency and level of loss. Modified after Corominas et al. (2014)

2.11.1 Annualizing risk

The first element of the risk equation (**Equations 1.1** and **1.2**) is the temporal probability of the hazard within a given time period. In landslide risk assessment this is often equated to the temporal probability of a triggering event, such as a rainstorm or earthquake that associated with an estimated average time between occurrence or "return period." The temporal probability of an event of frequency, f, during a given time period, t, is:

$$P_{(T)} = 1 - (1 - f)^t \quad \textbf{(2.44)}$$

where f is equal to $1 \,/\, return\ period$ (Lee and Jones, 2014). When annualizing risk, the time period of interest is $t = 1$ year and **Equation 2.44** reduces to:

$$P_{(T)} = f \tag{2.45}$$

2.12 Probabilistic implementation of the multimodal method

Uncertainty can be explicitly included in landslide risk analyses through simplified procedures such as the method of moments or comprehensively considered through a Monte Carlo process (Hungr, 2016). Due to the computational simplicity of the model, I have adapted the multimodal method to run in a Monte Carlo simulation. A deterministic application of the landslide risk analysis model in the country of Lebanon is given in **Chapter 5**, while **Chapter 6** incorporates uncertainty in a probabilistic landslide risk analysis of Seattle, Washington.

2.12.1 Combining scenarios

As mentioned in **Section 2.5**, individual cells are allowed to "fail" in multiple modes simultaneously. Similarly, elements at risk may be "impacted" and damaged with the GIS environment of the multimodal framework multiple times by the same or different modes of landslides across different triggering scenarios and individual Monte Carlo runs. However, neglecting reconstruction, each structure is able to be totally destroyed only once and each individual killed only once. This leads to the questions of which mode, triggering scenario, and run is associated with the damage, how damage accumulates, and how to prevent overpredicting risk through cumulative losses greater than the total value (or resident population) of a building. There is no single "correct" way to combine hazard or risk scenarios. Due to the focus on risk of this work, I have adopted a method that aggregates different scenarios *after* the final risk

calculation for each building in each Monte Carlo run. Other approaches could involve aggregating during the calculation of hazard (e.g. Grant et al., 2016).

Within each return period, for each run in the Monte Carlo simulation, the three landslide modes are processed separately and then iteratively aggregated into a running mean and variance of risk on a per building basis, according to the method of Welford (1962). For scenario *k* of scenarios *1 – n*:

$$M_k = M_{k-1} + \frac{(x_k - M_{k-1})}{k} \quad \textbf{(2.46)}$$

and:

$$S_k = S_{k-1} + (x_k - M_{k-1}) * (x_k - M_k) \quad \textbf{(2.47)}$$

where M is the mean, x_k is the value in scenario k, and variance is:

$$\sigma^2 = \frac{S_k}{k-1} \quad \textbf{(2.48)}$$

for $2 \leq k \leq n$.

Different modes of failure are combined at the return period (i.e. triggering scenario) level. The risk (human and monetary) is summed across modes at each building and then capped at the

maximum value or occupancy of that building. This process is illustrated in **Figure 2.24**. In *panel A*, representing a single Monte Carlo run associated with one mode of landslide, building *X* is struck by shallow landslide runout. The module r.randomwalk produces only the total runout envelope which may be associated with more than one source zone, each with a unique intensity (i.e. failure depth), I_1 and I_2. For that scenario, the risk to building *X*, R_X, is a function of the maximum intensity, I_1. Panel *B* represents one run of the Monte Carlo simulation, now showing risk to building *X* from all three modes, which is calculated separately. The different modes cannot properly be combined at this level, because the strength parameters used in the factor of safety calculation for each mode are chosen separately, even though they share an initial groundwater condition. Within a single return period of *n* Monte Carlo runs, **Equations 2.46 – 2.48** are used to calculate the mean and standard deviation or risk separately for each mode. A single run contributes *1/n* of the total for each mode. For a given return period, the mean risks (+/- one standard deviation, etc.) are summed for each building and capped at the total value (or occupancy) of the building (**Figure 2.24,** *panel C*). Note that this is more realistic than the option of selecting only the maximum risk of the three modes because it reflects the possibility that in a single triggering event a building could be impacted by multiple modes of landsliding whose individual consequences accumulate to complete loss. Finally, in *panel D*, the annual contributions of each return period event are summed.

Figure 2.24. *(following page)*. Process for combining risk scenarios. (*A*) in single Monte Carlo run, a runout zone may be associated with more than one source zone. The risk to building X (R_X) is a function of the source zone with the highest intensity. (*B*) In a single Monte Carlo run, hazard from multiple modes is calculated simultaneously, but not combined, and thus treated as separate scenarios. (*C*) For each building the mean risk from each mode is summed and capped at the total value (or occupancy) of that building. (*D*) The total annual risk for each building is the sum of the annual contributions from each return period (rp).

A
Same return period
Same mode
Multiple sources

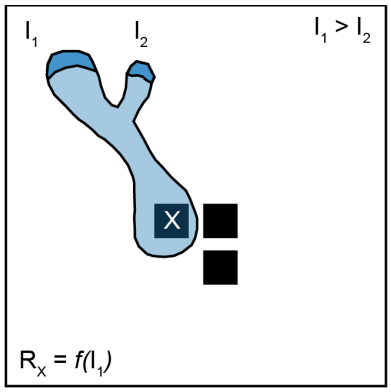

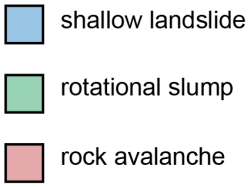

B
Same return period
Different modes

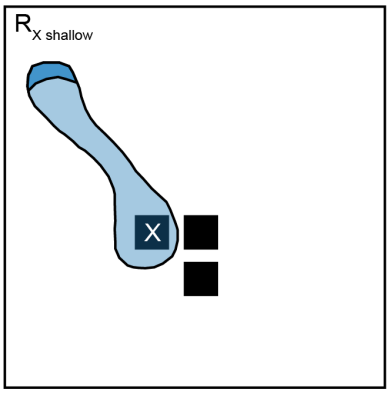

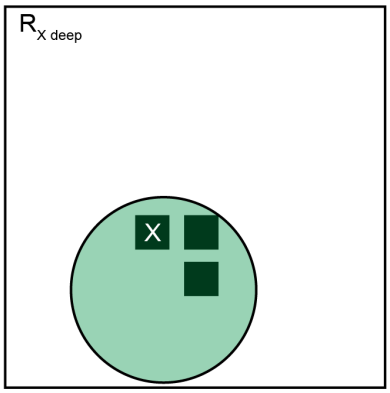

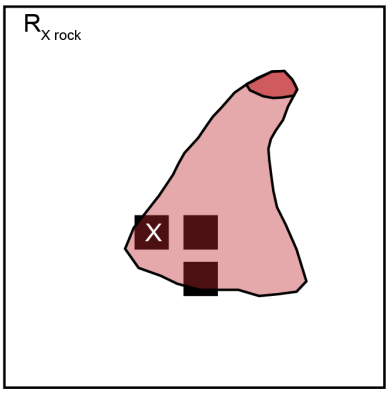

C
Same return period

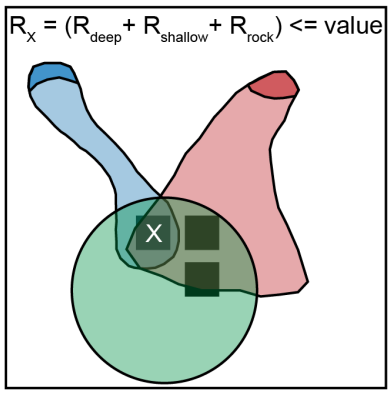

D
Different return periods

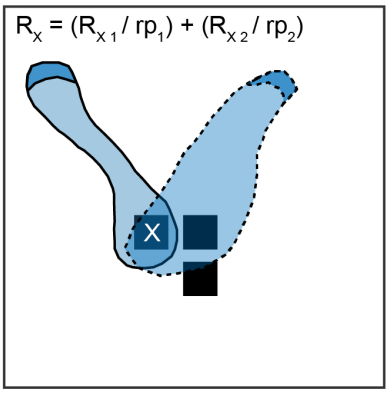

This approach implies that, in any given run, the element at risk could be destroyed by all three different modes, so long as total risk to that building aggregated across all Monte Carlo runs and modes does not exceed the total value or occupancy of that building. The reasons for aggregating modes at the return period rather than scenario level are both practical and theoretical. Aggregating at the scenario level would be both memory intensive and prevent an accurate disaggregation of the risk contributions by mode. Additionally, sampling of the soil and rock material parameters occurs independently in each scenario. For instance, within a surficial geologic unit, rock strength may be sampled two standard deviations below its mean while the colluvial soil weathered from the same rock unit may be sampled two standard deviations above its mean strength, a physically unlikely case.

References

AGS. (2007). Commentary on practice note guidelines for landslide risk management 2007. *Aust. Geomech*. 42, 115-158.

Alvioli, M., Baum, R. (2016). Parallelization of the TRIGRS model for rainfall-induced landslides using the message passing interface. *Environ. Modelling Software*, 81, 122-135

Ashford, S., Sitar, N. (2002). Simplified method for evaluating seismic stability of steep slopes. *J. Geotech. Geoenviron. Eng*., 128, 119-128. https://doi.org/10.1061/(ASCE)1090-0241(2002)128:2(119)

Asteriou, P., Tsiambaos, G. (2016). Empirical model for predicting rockfall trajectory direction. *Rock Mech. Rock Eng.*, 49, 927-941, https://doi.org/10.1007/s00603-015-0798-7

Bartos, M. (2020). Pysheds. Available at: https://github.com/mdbartos/pysheds. Accessed: May 2020.

Baum, R., Savage, W., Godt, J. (2002). TRIGRS—a Fortran program for transient rainfall infiltration and grid-based regional slope stability analysis. *Open-File Report 02-0424*. Reston, VA: United States Geological Survey.

Baum, R., Savage, W., Godt, J. (2008). TRIGRS—A Fortran program for transient rainfall infiltration and grid-based regional slope-stability analysis, version 2.0. *Open-File Report 2008-1159*. Reston, VA: United States Geological Survey

Beven, K., Kirkby, M. (1979). A physically based, variable contributing area model of basin hydrology. *Hydrological Sci. Bull.*, 24, 43-69. https://doi.org/10.1080/02626667909491834

Bicocchi, G., Tofani, V., D'Abrosio, M., Tacconi-Stefanelli, C., Vannocci, P., Casagli, N., Lavorini, G., Trevisani, M., Catani, F. (2019). Geotechnical and hydrological characterization of hillslope deposits for regional landslide prediction modeling. *Bull. Eng. Geol. Environ.*, 78, 4875-4891. https://doi.org/10.1007/s10064-018-01449-z

Brown, J. (2020). "NDVI, the foundation for remote sensing Phenology." United States Geological Survey. Available at: https://www.usgs.gov/land-resources/eros/phenology/science/ndvi-foundation-remote-sensing-phenology?qt-science_center_objects=0#qt-science_center_objects. Accessed June 2020.

Brown, J. (2020). NDVI, the foundation for remote sensing phenology. Available at: https://www.usgs.gov/land-resources/eros/phenology/science/ndvi-foundation-remote-sensing-phenology?qt-science_center_objects=0#qt-science_center_objects. Accessed: May 2020.

Budetta, P. (2004). Assessment of rockfall risk along roads. *Nat. Hazards Earth Syst. Sci.*, 4, 71-81. https://doi.org/10.5194/nhess-4-71-2004

Burbank, D., Anderson, R. (2012). *Tectonic Geomorphology, 2nd Ed*. West Sussex: John Wiley & Sons.

Burns, W., Calhoun, N., Franczyk, J., Lindsey, K., Ma, L. (2018). Landslide hazard and risk study: Central and Western Multnomah County, Oregon. *Oregon Department of Geology and Mineral Industries Interpretive Map 57*. Portland: Oregon Department of Geology and Mineral Industries. Available at: https://www.oregongeology.org/pubs/ims/p-ims-057.htm

Cascini, L., Bonnard, C., Corominas, J., Jibson, R., Montero-Olarte, J. (2005). Landslide hazard and risk zoning for urban planning and development. In: O. Hungr, R. Fell, R. Couture, E. Eberhardt (*Eds*.) *Landslide Risk Management*. Leiden: Balkema

Catani, F., Casagli, N., Ermini, L., Righini, G., Menduni, G. (2005). Landslide hazard and risk mapping at catchment scale in the Arno River basin. *Landslides*, 2, 329-342. https://doi.org/10.1007/s10346-005-0021-0

Chang, K-T., Merghadi, A., Yunus, A., Pham, B., Dou, J. (2019). Evaluating scale effects of topographic variables in landslide susceptibility models using GIS-based machine learning techniques. *Sci. Rep.*, 9. https://doi.org/10.1038/s41598-019-48773-2

Chien, Y.-C., Tsai, C.-C. (2017). Immediate estimation of yield acceleration for shallow and deep failures in slope-stability analyses. *Int. J. Geomech*., 17. https://doi.org/10.1061/(ASCE)GM.1943-5622.0000884

Cislaghi, A., Chiaradia, E., Bischetti, G. (2017). Including root reinforcement variability in a probabilistic 3D stability model. *Earth Surf. Process. Landforms*, 42, 1789-1806. https://doi.org/10.1002/esp.4127

Ciurean, R., Hussin, H., van Westen, C., Jaboyedoff, M., Nicolet, P., Chen, L., Frigerio, S., and Glade, T. (2017). Multi-scale debris flow vulnerability assessment and direct loss estimation of buildings in the Eastern Italian Alps. *Nat. Hazards*, 85, 929-957. https://doi.org/10.1007/s11069-016-2612-6

Collins, B., Sitar, N. (2011). Stability of steep slopes in cemented sands. *J. Geotech. Geoenviron. Eng*., 137, 43-51.

Copsey, A. (2002). *The designation and protection of critical areas under the Growth Management Act*. Office of the Attorney General. Olympia: State of Washington

Corominas, J. (1996). The angle of reach as a mobility index for small and large landslides. *Can. Geotech. J.*, 33, 260-271. https://doi.org/10.1139/t96-005

Corominas, J., Copons, R., Moya, J., Vilaplana, J., Altimir, J., Amigo, J. (2005). Quantitative assessment of the residual risk in a rockfall protected area. *Landslides*, 2, 343-357. https://doi.org/10.1007/s10346-005-0022-z

Corominas, J., Copons, R., Vilaplana, J., Altimir, J., Amigo, J. (2003). Integrated landslide susceptibility analysis and hazard assessment in the principality of Andorra. *Nat. Hazards.*, 30, 421-435, https://doi.org/10.1023/B:NHAZ.0000007094.74878.d3

Corominas, J., Matas, G., Ruiz-Carulla, R. (2019). Quantitative analysis of risk from fragmental rockfalls. *Landslides*, 16, 5-21. https://doi.org/10.1007/s10346-018-1087-9

Corominas, J., Mavrouli, O., Ruiz-Carulla, R. (2017). Rockfall occurrence and fragmentation. In: K. Sassa, M. Mikos, Y. Yin (*Eds*.) *Advancing Culture of Living with Landslides*. WLF 2017. Springer, Cham.

Corominas, J., van Westen, C., Frattini, P., Cascini, L., Malet, J.-P., Fotopoulou, S., Catani, F., Van Den Eeckhaut, M., Mavourli, O., Agliardi, F., Pitilakis, K., Winter, M., Pastor, M., Ferlisi, S., Tofani, V., Hervas, J., Smith, J. (2014). Recommendations for the quantitative analysis of landslide risk. *Bull. Eng. Geol. Environ.*, 73, 209-263. https://doi.org/10.1007/s10064-013-0538-8

Covello, V., Allen, F. (1988). Seven cardinal rule of risk communication. Washington: Environmental Protection Agency.

Crosta, G., Agliardi, F. (2004). Parametric evaluation of 3D dispersion of rockfall trajectories. *Nat. Hazards Earth Syst. Sci.*, 4, 583-598, https://doi.org/10.5194/nhess-4-583-2004

Crosta, G., Agliardi, F., Frattini, P., Lari, S. (2015). Key issues in rock fall modelling, hazard and risk assessment for rockfall protection. In: G. Lollino et al. (*Eds*.) *Engineering Geology for Society and Territory – Volume 2*. Springer, Cham.

Cruden, D., Varnes, D. (1996). Landslide types and processes. In: K. Turner, R. Schuster (*Eds*.) *Landslides: Investigation and Mitigation*. Washington: Transportation Research Board

Deitrich, W., Reiss, R., Hsu, M-L., Montgomery, D. (1995). A process-based model for colluvial soil depth and shallow landsliding using digital elevation data. *Hydrol. Processes*, 9, 383-400. https://doi.org/10.1002/hyp.3360090311

Densmore, A., Hovius, A. (2000). Topographic fingerprints of bedrock landslides. *Geology*, 28, 371-374. https://doi.org/10.1130/0091-7613(2000)28<371:TFOBL>2.0.CO;2

Dowling, C., Santi, P. (2014). Debris flows and their toll on human life: A global analysis of debris-flow fatalities from 1950 to 2011. *Nat. Hazards*, 71, 203-227. https://doi.org/10.1007/s11069-013-0907-4

Du, J., Yin, K., Nadim, F., Lacasse, S. (2013). Quantitative vulnerability estimation for individual landslides. Paris: Proceedings of the 18th International Conference on Soil Mechanics and Geotechnical Engineering.

Duncan, J., Wright, S., Brandon, T. (2014). *Soil Strength and Slope Stability*. Hoboken: John Wiley & Sons.

Ehrlich, D., Tenerelli, P. (2013). Optical satellite imagery for quantifying spatio-temporal dimension of physical exposure in disaster risk assessments. *Nat. Hazards*, 68, 1271-1289, https://doi.org/10.1007/s11069-012-0372-5

Erismann, T., Abele, G. (2001). *Dynamics of Rockslides and Rockfalls*. Berlin: Springer.

Fell, R. (1994). Landslide risk assessment and acceptable risk. *Can. Geotech. J.*, 31, 261-272. https://doi.org/10.1139/t94-031

Fell, R., Corominas, J., Bonnard, C., Cascini, L., Leroi, E., Savage, W. (2008). Guidelines for landslide susceptibility, hazard, and risk zoning for land use planning. *Eng. Geol.*, 102, 85-98. https://doi.org/10.1016/j.enggeo.2008.03.022

Ferguson, R. (1986). River loads underestimated by rating curves. *Water Resources Research*, 22, 74-76.

Finney, D. (1941). On the distribution of a variate whose logarithm is normally distributed. *J. R. Stat. Soc. London.*, Ser. B, 7, 155-161.

Fuchs, S., Heiss, K., and Hubl, J. (2007). Toward an empirical vulnerability function for use in debris flow risk assessment. *Nat. Hazards Earth Syst. Sci.*, 7, 495-506. https://doi.org/10.5194/nhess-7-495-2007

Fuchs, S., Tsao, T-C., Keiler, M. (2012). Quantitative vulnerability functions for use in mountain hazard risk management. Grenoble: Proceedings of the 12th Congress Interpraevent.

Galli, M., Guzzetti, F. (2007). Landslide vulnerability criteria: A case study from Umbria, Central Italy. *Environ. Manage.*, 40, 649-664. https://doi.org/10.1007/s00267-006-0325-4

Gamma, P. (1999). dfwalk—Ein murgang-simulationsprogramm zur gefahrenzonierung. (*doctoral dissertation*). Bern: University of Bern

Gardner, W. (1958). Some steady-state solutions of the unsaturated moisture flow equation with application to evaporation from a water table. *Soil Sci.*, 85, 228-232.

Giacomini, A., Buzzi, O., Renard, B., Giani, G. (2009). Experimental studies on fragmentation of rock falls on impact with rock surfaces. *Int. J. Rock Mech. Mining Sci*., 46, 708-715. https://doi.org/10.1016/j.ijrmms.2008.09.007

Grant, A. (2017). Regional-scale coseismic landslide hazard modeling and consequence analysis. (*doctoral dissertation*). Seattle: University of Washington

Grant, A., Wartman, J., Abou-Jaoude, G. (2016). Multimodal method for coseismic landslide hazard assessment. *Eng. Geol.*, 212, 146-160. https://doi.org/10.1016/j.enggeo.2016.08.005

Guzzetti, F. (2000). Landslide fatalities and the evaluation of landslide risk in Italy. *Engineering Geology*, 58, 89-107. https://doi.org/10.1016/S0013-7952(00)00047-8

Hansen, D. (1996). The angle of reach as a mobility index for small and large landslides: Discussion. *Can. Geotech. J.*, 33, 1027-1029.

Heim, A. (1932). *Landslides and Human Lives (Bergsturz und Menschenleben)*. Trans. N. Skermer. BiTech Pub, Vancouver, B.C.

Highland, L., Bobrowsky, P. (2008). The landslide handbook—A guide to understanding landslides. *Circular 1325*. Reston, VA: U.S. Geological Survey

Ho, J.-Y., Lee, K., Chang, T.-C., Wang, Z.-Y., Liao, Y.H. (2012). Influences of spatial distribution of soil thickness on shallow landslide prediction. *Eng. Geol.*, 124, 38-46. https://doi.org/10.1016/j.enggeo.2011.09.013

Hungr, O. (2016). A review of landslide hazard and risk assessment methodology. In: Aversa et al. (*Eds*.) *Landslides and Engineered Slopes: Experience, Theory and Practice*. Rome: Associazione Geotecnica Italiana

Hungr, O., Clague, J., Morgenstern, N., VanDine, D., Stadel, D. (2016). A review of landslide risk acceptability practices in various countries. In: Aversa et al. (*Eds*.) *Landslides and Engineered Slopes: Experience, Theory and Practice*. Rome: Associazione Geotecnica Italiana

Hungr, O., Leroueil, S., Picarelli, L. (2014). The Varnes classification of landslide types, an update. *Landslides*, 11, 167-194. https://doi.org/10.1007/s10346-013-0436-y

Jaboyedoff, M., Labiouse, V. (2011). Technical note: preliminary estimation of rockfall runout zones. *Nat. Hazards Earth Syst. Sci.*, 11, 819-828. https://doi.org/10.5194/nhess-11-819-2011

Jasiewicz, J., Stepinski, T. (2013). Geomorphons—a pattern recognition approach to classification and mapping of landforms. *Geomorphology*, 182, 147-156. https://doi.org/10.1016/j.geomorph.2012.11.005

Jibson, R. (1987). Summary of research on the effects of topographic amplification of earthquake shaking on slope stability. *Open-File Report 87-268*. Reston, VA: U.S. Geological Survey.

Jibson, R. (2005). Landslide hazards at La Conchita, California. *Open-File Report 2005-1067*. Reston, VA: United States Geological Survey

Jibson, R. (2007). Regression models for estimating coseismic landslide displacement. *Eng. Geol.*, 91, 209-218. https://doi.org/10.1016/j.enggeo.2007.01.013

Jibson, R., Harp, E., Michael, J. (1998). A method for producing digital probabilistic seismic landslide hazard maps: An example from the Los Angeles, California, area. *Open-File Report 98-113*. Denver: United States Geological Survey

Jibson, R., Harp, E., Michael, J. (2000). A method for producing digital probabilistic seismic landslide hazard maps. *Eng. Geol.*, 58, 271-289.

Jones, A., Kramer, S., Arduino, P. (2002). *Estimation of Uncertainty in Geotechnical Properties for Performance-based Earthquake Engineering*. PEER Report 2002/16. Berkeley, CA: Pacific Earthquake Engineering Research Center, University of California, Berkeley

Keaton, J., Wartman, J., Anderson, S., Benoit, J., dela Chapelle, J., Gilbert, R., Montgomery, D. (2014). The 22 March 2014 Oso landslide, Snohomish County, Washington. *Geotechnical Extreme Events Reconnaissance Report*, GEER Association

Keefer, D. (1984). Landslides caused by earthquakes. *GSA Bull.*, 95, 406-421. https://doi.org/10.1130/0016-7606(1984)95<406:LCBE>2.0.CO;2

Keefer, D. (2013). Landslides generated by earthquakes: immediate and long-term effects. In: J. Shroder, L. Owen, (*Eds*.) *Treatise on Geomorphology*. Vol 5, Tectonic Geomorphology, 250-266. San Diego, CA: Academic Press.

Kramer, S. (1996). *Geotechnical Earthquake Engineering*. Upper Saddle River, New Jersey: Prentice Hall.

Lacasse, S. (2017). "Landslide risk management and risk governance, with examples from practice." Presentation at the LARAM School for Landslide Risk Assessment and Mitigation 2017, Salerno, Italy.

Lan, H., Martin, C., Zhou, C., Lim, C. (2010). Rockfall hazard analysis using LiDAR and spatial modeling. *Geomorphology*, 118, 213-223, https://doi.org/10.1016/j.geomorph.2010.01.002

Lanni, C., Borga, M., Rigon, R., Tarolli, P. (2012). Modelling shallow landslide susceptibility by means of a subsurface flow path connectivity index and estimates of soil depth spatial distribution. *Hydrol. Earth Syst. Sci*., 16, 3959-3971. https://doi.org/10.5194/hess-16-3959-2012

Lark, R., Lawley, R., Barron, A., Aldiss, D., Ambrose, K., Cooper, A., Lee, J., Waters, C. (2015). Uncertainty in mapped geological boundaries held by a national geological survey: Eliciting the geologist' tacit error model. *Solid Earth*, 6, 727-745. https://doi.org/10.5194/se-6-727-2015

Lee, E., Jones, D. (2014). *Landslide Risk Assessment*. London: ICE Publishing

Leroi, E. (2017). "Landslide risk management." Presentation at the LARAM School for Landslide Risk Assessment and Mitigation 2017, Salerno, Italy.

Leroi, E., Bonnard, C., Fell, R., McInnes, R. (2005). Risk assessment and management. In: Hungr, O., Fell, R., Couture, R., Eberhardt, E. (*Eds*.) *Landslide Risk Management*. Leiden: Balkema.

Locat, P., Couture, R., Leroueil, S., Locat, J., Jaboyedoff, M. (2006). Fragmentation energy in rock avalanches. *Can. Geotech. J.*, 43, 830-851. https://doi.org/10.1139/t06-045

Locat, P., Couture, R., Locat, J., Leroueil, S. (2003). Assessment of the fragmentation energy in rock avalanches. 3rd Canadian Conf. on Geotechnique and Natural Hazards. Edmonton, 2003.

Malamud, B., Turcotte, D., Guzzetti, F., Reichenbach, P. (2004). Landslide inventories and their statistical properties. *Earth Surf. Process. Landforms*, 29, 687-711. https://doi.org/10.1002/esp.1064

Mansour, M., Morgenstern, N., Martin, C. (2011). Expected damage from displacement of slow-moving slides. *Landslides*, 8, 117-131. https://doi.org/10.1007/s10346-010-0227-7

Marc, O., Stumpf, A., Malet, J., Gosset, M., Uchida, T., Chiang, S. (2018). Toward a global database of rainfall-induced landslide inventories: first insights from past and new events. *Earth Surf. Dyn. Discuss*. https://doi.org/10.5194/esurf-2018-20, *in review*

Massa, M., Barani, S., Lovati, S. (2014). Overview of topographic effects based on experimental observations: Meaning, causes and possible interpretations. *Geophys. J. Int*., 197, 1537-1550. https://doi.org/10.1093/gji/ggt341

Massey, C., McSaveney, M., Heron, D., Lukovic, B. (2012a). Canterbury Earthquakes 2010/11 Port Hills slope stability: Pilot study for assessing life-safety risk from rockfalls (boulder rolls). *GNS Science Consultancy Report 2011/311*. GNS Science.

Massey, C., McSaveney, M., Taig, T., Richards, L., Litchfield, N., Rhoades, D., et al. (2014a). Determining rockfall risk in Christchurch using rockfalls triggered by the 2010-2011 Canterbury earthquake sequence. *Earthquake Spectra*, 30, 155-181.

Massey, C., McSaveney, M., Yetton, M., Heron, D. Lukovic, B, Bruce, Z. (2012b). Canterbury Earthquakes 2010/11 Port Hills slope stability: Pilot study for assessing life-safety risk from cliff collapse. *GNS Science Consultancy Report 2012/57*. GNS Science.

Massey, C., Taig, T., Della Pasqua, F., Lukovic, B., Ries, W., Archibald, G. (2014b). Canterbury Earthquakes 2010/11 Port Hills slope stability: Debris avalanche risk assessment for Richmond Hill. *GNS Science Consultancy Report 2014/34*. GNS Science.

Massey, C., Taig, T., Howarth, J., Ries, W., Lukovic, B., Archibald, G., McSaveney, M., Ashraf, S., Hancox, G. (2017). Franz Josef guiding area landslide risk assessment. *GNS Science Consultancy Report 2017/56*. GNS Science.

Massey, C., Thomas, K-L., King, A., Singeisen, C., Taig, T., Horspool, N. (2019). SLIDE (Wellington): Vulnerability of dwellings to landslides (Project No. 16/SP740). *GNS Science report; 2018/17*. GNS Science.

Matas, G., Lantada, N., Corominas, J., Gili, J., Ruiz-Carulla, R., Prades, A. (2017). RockGIS: A GIS-based model for the analysis of fragmentation in rockfalls. *Landslides*, 14, 1565-1578. https://doi.org/10.1007/s10346-017-0818-7

McDougall, S. (2017). 2014 Canadian geotechnical colloquium: landslide runout analysis—current practice and challenges. *Can. Geotech. J.*, 54, 605-620. https://doi.org/10.1139/cgj-2016-0104

Medwedeff, W., Clark, M., Zekkos, D., West, J. (2020). Characteristic landslide distributions: An investigation of landscape controls on landslide size. Earth Planetary Science Letters, 539. https://doi.org/10.1016/j.epsl.2020.116203

Meehan, C., Vahedifard, F. (2013). Evaluation of simplified methods for predicting earthquake-induced slope displacements in earth dams and embankments. *Eng. Geol.*, 152, 180-193. https://doi.org/10.1016/j.enggeo.2012.10.016

Mergili, M., Krenn, J., Chu, H.-J. (2015). r.randomwalk v1, a multi-functional conceptual tool for mass movement routing. *Geosci. Model. Dev.*, 8, 4027-4043.

Meunier, P., Hovius, N., Haines, A. (2007). Regional patterns of earthquake-triggered landslides and their relation to ground motion. *Geophysical Research Letters*, 34. https://doi.org/10.1029/2007GL031337

Meunier, P., Hovius, N., Haines, J. (2008). Topographic site effects and the location of earthquake induced landslide. *Earth Planet. Sci. Let.*, 272, 221-232. https://doi.org/10.1016/j.epsl.2008.07.020

Microsoft. (2018). "U.S. building footprints." [Dataset]: https://github.com/Microsoft/USBuildingFootprints. Accessed: November 2018.

Montgomery, D., Dietrich, W. (1994). A physically based model for the topographic control on shallow landsliding. *Water Resources Research*, 30, 1153-1171. https://doi.org/10.1029/93WR02979

Montgomery, D., Sullivan, K., Greenberg, H. (1998). Regional test of a model for shallow landsliding. *Hydrol. Process.*, 12, 943-955. https://doi.org/10.1002/(SICI)1099-1085(199805)12:6<943::AID-HYP664>3.0.CO;2-Z

Montgomery, R., Ward, J. (1995). Casualty areas from impacting inert debris for people in the open. *RTI Report No. RTI/5180/60-31F*. Cocoa Beach, Florida: Research Triangle Institute.

Morgenstern, N., Vick, S., Van Zyl, D. (2015). Report on Mount Polley tailings storage facility breach. Independent Expert Engineering Investigation and Review Panel, Victoria: Province of British Columbia

Newmark, N. (1965). Effects of earthquakes on dams and embankments. *Geotechnique*, 15, 139-160. https://doi.org/10.1680/geot.1965.15.2.139

Nicolet, P., Jaboyedoff, M., Cloutier, C., Crosta, G., Levy, S. (2016). Brief communication: On direct impact probability of landslides on vehicles. *Nat. Hazards Earth Syst. Sci.*, 16, 995-1004. https://doi.org/10.5194/nhess-16-995-2016

OpenStreetMap. (2018). "Home." https://www.openstreetmap.org. Accessed: Nov. 2018

Pack, R., Tarboton, D., Goodwin, C. (1998). The SINMAP approach to terrain stability mapping. In *International Congress of the International Association of Engineering Geology and the Environment Proceedings, 8th, September 21-25, 1998. Vancouver*, 2, 1157-1165, Rotterdam: Balkema

Papathoma-Kohle, M., Keiler, M., Totschnig, R., Glade, T. (2012). Improvement of vulnerability curves using data from extreme events: Debris flow event in South Tyrol. *Nat. Hazards*, 64, 2083-2105. https://doi.org/10.1007/s11069-012-0105-9

Papathoma-Kohle, M., Zischg, A., Fuchs, S., Glade, T., Keiler, M. (2015). Loss estimation for landslides in mountain areas – An integrated toolbox for vulnerability assessment and damage documentation. *Environ. Modell. Software*, 63, 156-169. https://doi.org/10.1016/j.envsoft.2014.10.003

Patton, N., Lohse, K., Godsey, S., Crosby, B., Seyfried, M. (2018). Predicting soil thickness on soil mantled hillslopes. *Nat. Commun*., 9. https://doi.org/10.1038/s41467-018-05743-y

Pearson, K. (1905). The problem of the random walk. *Nature*, 72, 294.

Peck, M., Payne, D. (2003). Development of an estimated water-table map for coastal Georgia and adjacent parts of Florida and South Carolina. In: K. Hatcher (*Ed*.) *Proceedings of the 2003 Georgia Water Resources Conference*. Athens Georgia: University of Georgia. 23-24 April 2003.

Peduto, D., Nicodemo, G., Caraffa, M., Gulla, G. (2018). Quantitative analysis of consequences to masonry buildings interacting with slow-moving landslide mechanisms: A case study. *Landslides*, 15, 2017-2030. https://doi.org/10.1007/s10346-018-1014-0

Penna, D., Borga, M., Aronica, G., Brigandi, G., Tarolli, P. (2014). The influence of grid resolution on the prediction of natural and road-related shallow landslides. *Hydrol. Earth Syst. Sci.*, 18, 2127-2139. https://doi.org/10.5194/hess-18-2127-2014

Pesaresi, M., Ehrlich, D., Florczyk, A., Freire, S., Julea, A., Kemper, T., Soille, P., Syrris, V. (2015). GHS built-up grid, derived from Landsat, multitemporal (1975, 1990, 2000, 2014). European Commission, Joint Research Centre (JRC) [Dataset] PID: http://data.europa.eu/89h/jrc-ghsl-ghs_built_ldsmt_globe_r2015b

Pesaresi, M., Huadong, G., Blaes, X., Erlich, D., Ferri, S., Gueguen, L., Halkia, M., Kauffmann, M., Kemper, T., Lu, L., Marin-Herrera, M., Ouzounis, G., Scavazzon, M., Soille, P., Syrris, V., Zanchetta, L. (2013). A global human settlement layer from optical HR/VHR RS data: concept and first results. *IEEE J. Sel. Top. Appl. Earth Obs. Remote Sens.*, 6(5), 2102-2131, https://doi.org/10.1109/JSTARS.2013.2271445

Phoon, K-K., Kulhawy, F. (1999). Characterization of geotechnical variability. *Can. Geotech. J.*, 36, 612-624. https://doi.org/10.1139/t99-038
Picarelli, L., Olivares, L. (2011). Guidelines: recommended models of landslide triggering processes and run-out to be used in QRA. *Safeland Deliverable 1.8*. Available at: https://www.ngi.no/eng/Projects/SafeLand
Portland Maps (2018). "Building footprints." [Dataset]: http://gis-pdx.opendata.arcgis.com/datasets/16cf185db38f41deaec0bd66f1ddd8d3_48. Accessed: Nov. 2018.
PortlandMaps. (2020). "Building Footprints." [Dataset]: https://gis-pdx.opendata.arcgis.com/datasets/1078959662ce49cca059fe2f8930c194_48. Accessed: June 2020.
Quan Luna, B., Blahut, J., van Westen, C., Sterlacchini, S., van Asch, T., Akbas, O. (2011). The application of numerical debris flow modelling for the generation of physical vulnerability curves. *Nat. Hazards Earth Syst. Sci.*, 11, 2047-2060. https://doi.org/10.5194/nhess-11-2047-2011
Reid, M., Christian, S., Brien, D. (2000). Gravitational stability of three-dimensional stratovolcano edifices. *Geophysical Research*, 105, 6043-6056. https://doi.org/10.1029/1999JB900310
Reid, M., Christian, S., Brien, D., Henderson, S. (2015). Scoops3D—Software to analyze three-dimensional slope stability throughout a digital landscape. Techniques and Methods 14-A1; Section A, Modeling Methods; *Book 14, Landslide and Debris-Flow Assessment*. Reston, VA: United States Geological Survey
Rheinberger, C., Romang, H., Brundl, M. (2013). Proportional loss functions for debris flow events. *Nat. Hazards Earth Syst. Sci*., 13, 2147-2156. https://doi.org/10.5194/nhess-13-2147-2013
Ruiz-Carulla, R. (2018). Rockfall analysis: Failure, fragmentation and propagation characterization. (*doctoral dissertation*). Barcelona: Polytechnic University of Catalonia
Safeland. (2011). Physical vulnerability of elements at risk to landslides: Methodology for evaluation, fragility curves and damage states for buildings and lifelines. *Safeland Deliverable 2.5*. Available at: https://cordis.europa.eu/project/id/226479/reporting
Saygili, G., Rathje, E. (2008). Empirical predictive models for earthquake-induced sliding displacements of slopes. *Geotech. Geoenviron. Eng.*, 134(6), 790-803. https://doi.org/10.1061/(ASCE)1090-0241(2008)134:6(790)
Schmidt, K., Roerring, J., Stock, J., Deitrich, W., Montgomery, D., Schaub, T. (2001). The variability of root cohesion as an influence on shallow landslide susceptibility in the Oregon Coast Range. *Can. Geotech. J.*, 38, 995-1024, https://doi.org/10.1139/t01-031
Seattle Geodata. (2015). "2009 Building Outlines." [Dataset]: https://data.seattle.gov/dataset/2009-Building-Outlines/y7u8-vad7. Accessed: November 2018.
Seattle Geodata. (2018). "Environmentally critical areas." [Dataset]: https://data.seattle.gov/dataset/City-Of-Seattle-Environmentally-Critical-Areas/zwze-9nv3. Accessed: November 2018.
Seed, R., Bea, R., Athanasopoulos-Zekkos, A., Boutwell, G., Bray, J., Cheung, C., Cobos-Roa, D., Cohen-Waeber, J., Collins, B., Harder, L., Kayen, R., Pestana, J., Riemer, M., Rogers, J., Storesund, R., Vera-Grunauer, X., Wartman, J. (2008). New Orleans and Hurricane

Katrina. IV: Orleans East Bank (metro) protected basin. *Geotch. Geoenviron. Eng.*, 134, 762-779. https://doi.org/10.1061/(ASCE)1090-0241(2008)134:5(762)

Sirbu, F., Dragut, L., Oguchi, T., Hayakawa, Y., Micu, M. (2019). Scaling land-surface variables for landslide detection. *Progress in Earth and Planetary Sci.*, 6. https://doi.org/10.1186/s40645-019-0290-1

Smith, K. (2013). *Environmental hazards: Assessing risk and reducing disaster*. London: Routledge.

Snyder, D. (2008). Estimated depth to ground water and configuration of the water table in the Portland, Oregon area. *Scientific Investigations Report 2008-5059*. Reston, VA: United States Geological Survey. Available at: https://pubs.usgs.gov/sir/2008/5059/

Taig, T., Massey, C., Taig, M., Becker, J., Heron, D. (2015). Survey of Port Hills red zone residents' experience following the 22 February 2011 earthquake. *GNS Science Report 2015/09*. GNS Science.

Tanyas, H., van Westen, C., Allstadt, K., Nowicki Jessee, M., Gorum, T., Jibson, R., Godt, J., Sato, H., Schmitt, R., Marc, O., and Hovius, N. (2017). Presentation and analysis of a worldwide database of earthquake-induced landslide inventories. *J. Geophys. Res. Earth Surf.*, 122, 1991-2015, https://doi.org/10.1002/2017JF004236

Tarolli, P., Tarboton, D. (2006). A new method for determination of most likely landslide initiation points and the evaluation of digital terrain model scale in terrain stability mapping. *Hydrol. Earth Syst. Sci*., 10, 663-677. https://doi.org/10.5194/hess-10-663-2006

Taylor, D. (1948). *Fundamentals of Soil Mechanics*. New York: Wiley.

Totschnig, R., Fuchs, S. (2013). Mountain torrents: Quantifying vulnerability and assessing uncertainties. *Eng. Geol.*, 155, 31-44. https://doi.org/10.1016/j.enggeo.2012.12.019

Totschnig, R., Sedlacek, W., and Fuchs, S. (2011). A quantitative vulnerability function for fluvial sediment transport. *Nat. Hazards*, 58, 681-703. https://doi.org/10.1007/s11069-010-9623-5

Tran, T., Alvioli, M., Lee, G., An, H. (2017). Three-dimensional, time-dependent modeling of rainfall-induced landslides over a digital landscape: a case study. *Landslides*, 15, 1071-1084. https://doi.org/10.1007/s10346-017-0931-7

U.S. Census Bureau. (2018). "American fact finder." https://factfinder.census.gov. Accessed: Nov. 2018.

UN. (2005). Hyogo framework for action 2005-2015: Building the resilience of nations and communities to disasters. Geneva: United Nations. Available at: https://www.undrr.org/publication/hyogo-framework-action-2005-2015-building-resilience-nations-and-communities-disasters#:~:text=The%20WCDR%20was%20held%20from,Nations%20and%20Communities%20to%20Disasters.&text=It%20underscored%20the%20need%20for,nations%20and%20communities%20to%20disasters.

UN. (2015). Sendai framework for disaster risk reduction. Geneva: United Nations. Available at: https://www.undrr.org/publication/sendai-framework-disaster-risk-reduction-2015-2030

United States Geological Survey (USGS). (1999). Map accuracy standards. *USGS Fact Sheet 171-99*. Reston, VA: U.S. Geological Survey.

van Westen, C., van Asch, T., Soeters, R. (2006). Landslide hazard and risk zonation—Why is it still so difficult? *Bull. Eng. Geol. Environ.*, 65, 167-184. https://doi.org/10.1007/s10064-005-0023-0

Wang, Y. (2014). Probabilistic assessments of the seismic stability of slopes: Improvements to site-specific and regional analyses. (*doctoral dissertation*). Austin, Texas: University of Texas at Austin.

Wang, Y., Rathje, E. (2015). Probabilistic seismic landslide hazard maps including epistemic uncertainty. *Eng. Geol*., 196, 313-324. https://doi.org/10.1016/j.enggeo.2015.08.001

Wartman, J., Dunham, L., Tiwari, B., Pradel, D. (2013). Landslides in eastern Honshu induced by the 2011 Tohoku earthquake. *Bull. Seismol. Soc. Am.*, 103(2B), 1503-1521, https://doi.org/10.1785/0120120128

Weiss, J., Gutzler, D., Coonrod, J., Dahm, C. (2004). Long-term vegetation monitoring with NDVI in a diverse semi-arid setting central New Mexico, USA. *J. Arid Environ*., 58, 249-272. https://doi.org/10.1016/j.jaridenv.2003.07.001

Welford, B. (1962). Note on a method for calculating corrected sums of squares and products. *Technometrics*, 4, 419-420.

Wisner, B., Blaikie, P., Cannon, T., Davis, I. (2004). *At risk: Natural hazards, people's vulnerability and disasters*. London: Routledge.

Wisner, B., Luce, H. (1993). Disaster vulnerability: Scale, power and daily life. *GeoJournal*, 30, 127-140. https://doi.org/10.1007/BF00808129

Wyllie, D., Mah, C. (2004). *Rock Slope Engineering: Civil and Mining 4th Ed*. London: Spon Press.

Zezere, J., Trigo, R., Trigo, I. (2005). Shallow and deep landslides induced by rainfall in the Lisbon region (Portugal): Assessment of relationships with the North Atlantic Oscillation. *Nat. Hazards Earth Syst. Sci.*, 5, 331-344. https://doi.org/10.5194/nhess-5-331-2005

Chapter 3—Re-examination of runout probability for flowslides

3.1 Introduction

Flow-type landslides often travel at high velocities and are capable of inundating large areas well beyond their point of initiation, making them one of the deadliest modes of mass-wasting (Jakob and Hungr, 2005; Hurlimann et al., 2019). Between 1950 and 2011, rapid flow-type landslides conservatively caused over 77,000 fatalities (Dowling and Santi, 2014), and in the western United States, widespread debris flows caused by winter storms frequently tally direct damages to property and infrastructure in the hundreds of millions of dollars (Schuster and Highland, 2001; Harp et al., 1996). Many catastrophic flow-type landslide events have occurred in the last two decades, both in the United States and globally (**Table 3.1**). All of these events were very rapid and highly mobile, with almost all of the damage occurring in populated, flat runout zones away from the source of the failures.

Table 3.1. A selection of notable flow-type landslide disasters 2000 – 2020.

Location		Year	Fatalities / Damage	Source
United States				
	San Bernardino, CA	Dec. 2003	16 / >$1B	Cannon and DeGraff (2009)
	La Conchita, CA	Jan. 2005	10 / n/a	Jibson (2005)
	Oso, WA	Mar. 2014	43 / $80M	Washington DNR (2014)
	Montecito, CA	Jan. 2018	21 / $200M	Niehaus (2018)
World				
	Zhouqu, China	Aug. 2010	1765	Tang et al. (2011)
	Kedernath, India	June 2013	6074	Martha et al. (2014)
	Badakhshan, Afghanistan	May 2014	2700	Zhang et al. (2015)
	Guangdong, China	Dec. 2015	77	Yin et al. (2016)
	Mocoa, Columbia	Mar. 2017	409	Garcia-Delgado et al. (2019)
	Freetown, Sierra Leone	Aug. 2017	500	Cui et al. (2019)
	Hiroshima, Japan	July 2018	104	Petley (2019)

While water-infused, flow-type landslides, including the events in **Table 3.1**, are inconsistently labeled in landslide literature and common usage as “mudslides,” “debris flows,” “earth flows,” or simply “landslides,” they share the characteristic process of a rapid flow of saturated material involving excess pore-pressure. I use the labels “debris flow” and “flowslide” to refer to

channelized and unconfined flow-type landslides, respectively (Hungr et al., 2014). Flowslides are particularly dangerous to humans because of their ability to spread laterally from the point of initiation.

While much work has been done to model the initiation and runout of flowslides and debris flows, communities still lack practical policy instruments to effectively regulate land use and protect citizens. In this chapter I aim to fill this void by presenting a practical tool for delineating areas and populations at risk from flowslide events. I illustrate the use of this tool by applying it to a flowslide-prone region in northwestern Washington State, U.S.

3.1.1 Current landslide zoning practices

Despite the severe human consequences of flow-type landslides, landslide management policies worldwide are piecemeal or non-existent, even in the regions with the greatest exposure to landslides. Where landslide management policies do exist, they are typically limited to delineating areas of potential instability and contain no information about landslide frequency, downslope inundation areas, or consequences on the human and built environment (Hungr et al., 2016).

Landslide land use policies have historically been based on landslide inventory maps or landslide susceptibility maps (Hungr et al., 2016). Landslide inventory maps are useful for delineating areas of past landslide activity or cataloguing the damages from a particular event. However, landslide inventories are limited to the observable features at the time of the mapping, and they

often miss extreme, infrequent events whose topographic signature has been diminished by erosion, human activity, or subsequent events. Landslide susceptibility maps indicate areas which are vulnerable to future landslides based on shared environmental characteristics with past landslides such as topography, geologic unit, or distance to a stream channel. Neither type of map explicitly provides information about the timing, runout, or consequences of future failures, and thus they are insufficient for land use decisions targeted at reducing landslide *losses* (Lombardo et al., 2014; Shipman, 2011; Hungr et al., 2016).

In fact, the two deadliest single landslides in the United States occurred in communities with pre-existing development policies regarding landslide hazards, extensive landslide susceptibility maps, and a recent history of landslide activity.

3.1.1.1 La Conchita, California

Prior to 2014, the deadliest single landslide disaster in the conterminous United States was a 2005 debris flow in the narrow coastal community of La Conchita, California, which destroyed a dozen homes and killed ten residents. Despite episodic damaging debris flows, including a similar but less mobile slump/earth flow which severely damaged nine houses in 1995, land use restrictions in the community were limited to a mapped landslide susceptibility zone on the overshadowing coastal bluff. The susceptibility map did not consider the potential runout areas (**Figure 3.1**; California Geological Survey, 2002).

After the 2005 disaster, landslide risk reduction proposals foundered amid conflicting concerns of legal responsibility and personal freedoms, and La Conchita remains in much the same

situation as it was in prior to 2005 (Goldberg, 2006). A lack of technical information is partly responsible. The post-disaster report by the United States Geological Survey concluded that "no part of the community can be considered safe from landslides. Unfortunately, we currently lack the understanding to accurately forecast what might happen in each possible rainfall scenario" (Jibson, 2005).

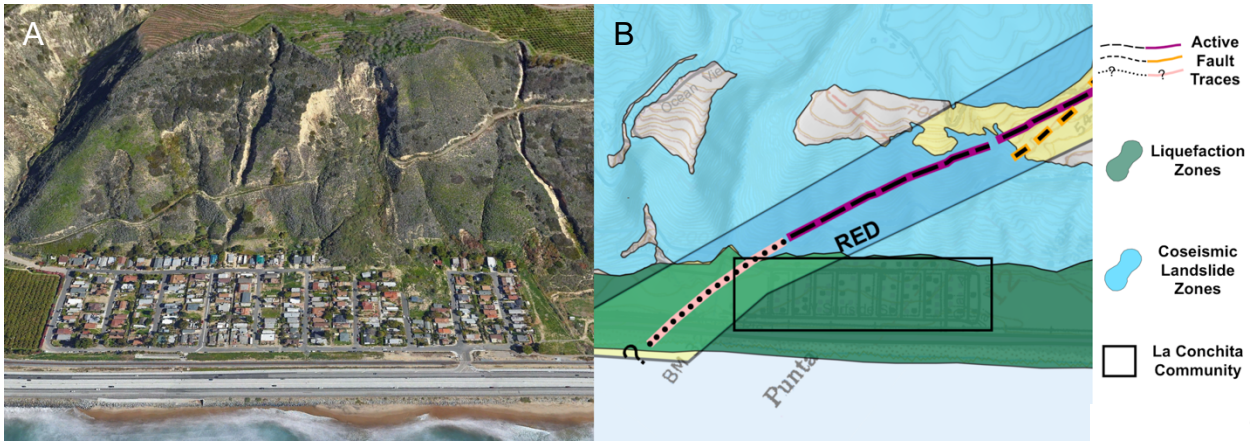

Figure 3.1. (A) The La Conchita, CA, landslide complex in 2016 (Google Earth). The large scar in the center of the image is from the 1995 landslide. The 2005 debris flow mobilized along the right side of the 1995 scar and spread into the community. (B) the 2002 California Department of Geology landslide zoning map of the area (California Geological Survey, 2002).

3.1.1.2 Steelhead Haven, Washington

On the morning of Saturday, 22 March 2014, following an abnormally wet month, a 200 m high bluff of unconsolidated glacial and colluvial deposits collapsed and flowed over two kilometers in 1 – 2 minutes, overwhelming the 35-home neighborhood of Steelhead Haven in northwestern Washington State. Forty-three people were killed in the event, making it the worst landslide event in the conterminous United States. Direct damages from the event exceeded $80 million in addition to a two-month closure of State Route 530 and over $50 million in two out-of-court settlements between the State of Washington and victim's families (Washington DNR, 2014;

Keaton et al., 2014). The State officially named the flowslide for the state route it destroyed, but literature and media have adopted the label "Oso Flowslide" for the nearby town of Oso, Washington, (Iverson et al., 2015). In this work, I use the more commonly recognized name, "Oso Flowslide."

The Oso Flowslide was not without precedent. Episodic landslide activity had been observed on the slope north of Steelhead Haven since at least 1937 (Miller and Miller, 1999), and in 2006, a large flowslide at the site sent ~ 2 million m^3 of debris flowing into the North Fork of the Stillaguamish River (NFSR), pushing the river several hundred feet to the south (Keaton et al., 2014). A study in 1999 noted the site had potential for "a large catastrophic failure," although the runout from such an event was anticipated to be on the order of a 1967 debris flow which had displaced the river over 200 m southward (Miller and Miller, 1999). Development in Steelhead Haven was guided by a geologic hazards map that identified zones of historic landslide activity (**Figure 3.2**; Snohomish County, 2007). However, the map did not include areas of potential downslope inundation.

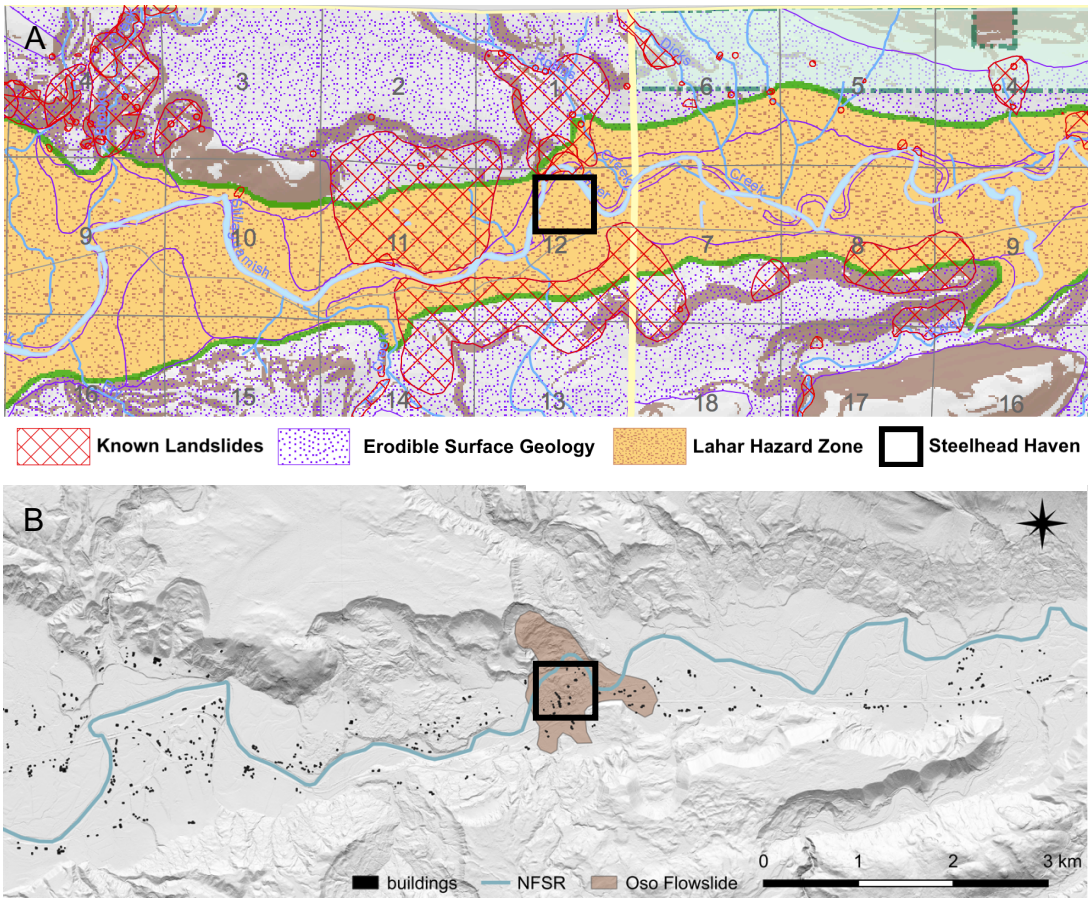

Figure 3.2. (*A*) the 2007 geologic hazards map used to regulate development in the NFSR valley (Snohomish County, 2007). The community of Steelhead Haven (box) is outside of the mapped landslide zone (red hatching). (*B*) a bare-earth elevation model showing the inundation areas of the 2014 Oso Flowslide (data: Washington Dept. Natural Resources,).

Following the Oso Flowslide, Snohomish County took immediate action to examine and update their landslide zoning policies. On 23 April 2014, the Snohomish County Council proposed a six-month moratorium on new residential development within one half-mile of identified landslide zones, an area encompassing 88% of the unincorporated, non-National Forest land in the county (Snohomish County, 2014; **Figure 3.3**). The proposal failed to pass over economic concerns. Instead, the 2015 update of the Snohomish County Hazard Mitigation Plan includes the explicit provision that the hazard mapping does not include areas of landslide runout, citing a lack of established scientific understanding (Snohomish County, 2015).

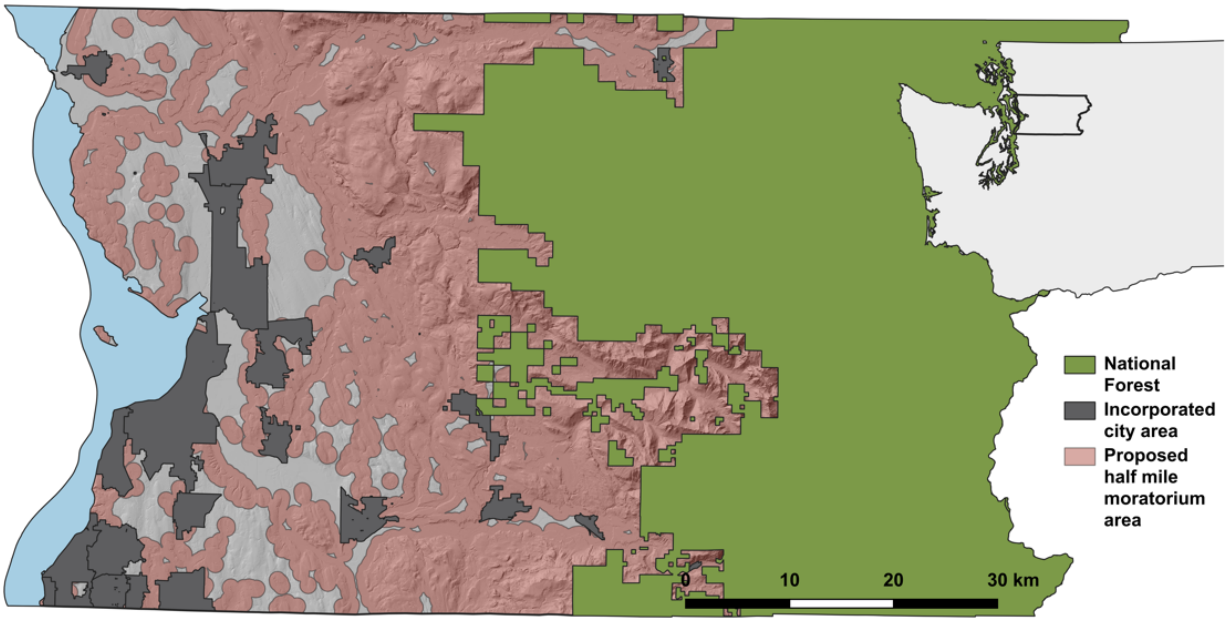

Figure 3.3. Extent of the 2014 proposed half mile "no development" buffer for landslide susceptibility zones in Snohomish County.

The cases of La Conchita and Oso are striking in their similarity. Both landslides occurred in mapped landslide susceptibility zones and impacted communities with established geologic hazards land use regulations. However, the damage and fatalities from the events occurred in runout zones which fell outside the mapped areas of landslide susceptibility. After each event, community members and the local government sought to change the land use practices relating to landslide hazards, but these efforts were hampered by a lack of available and applicable scientific products.

3.1.2 Challenges of incorporating landslide runout in land use policies

Runout analyses predict the post-failure movement of landslides and are a key component of landslide hazard and risk assessments. They may include estimates of intensity (velocity, volume, depth), extent (travel path, depositional area) and temporal progression (pore pressure development, bulking, deposition), but at a minimum they must predict the maximum flow-parallel distance landslide debris will travel from the point of initial failure. Runout analyses may not be included in landslide zoning for a number of reasons. Although numerous competent numerical models for predicting landslide propagation have been produced in recent years (McDougall, 2017), they remain computationally expensive, highly dependent on detailed input parameterization, and best suited for backward – rather than forward – analysis. Due to a low number of required parameters, empirical models are ideal for large-scale land use zoning, and dozens of flexible empirical models have been proposed (McDougall, 2017). However, these inventory-based predictive relationships have been developed using an amalgamation of mobility index definitions, event-classification schemes, and heterogeneous landslide catalogues, resulting in differing conclusions from very similar datasets (Corominas, 1996; Guo et al., 2016; Hunter and Fell, 2003; Legros, 2002). Additionally, few models are explicitly probabilistic, instead implying a false dichotomy of "safe" and "unsafe" areas. Finally, minimal guidance is available to practitioners preforming runout analyses (McDougall, 2017) and it is often not broadly applicable, limited to a specific site, subset of landslide classes, or geo-climatic setting.

3.1.3 Objectives of this work

As urban planners grapple with protecting communities through informed landslide hazard zoning and communication of landslide hazards to the public, reliable, practical tools for landslide runout prediction at the regional scale are needed from the scientific community (Cascini et al., 2005). Landslide-hazard informed land use zoning is a complex and challenging task which must balance not only public safety, but also issues of personal property rights, economic and technical practicality, housing availability, aesthetics, environmental protection, and viability in a given socio-political environment (Hungr, 2016; Miscolta-Cameron, 2016; Copsey, 1999; Olshansky, 1998). However, the process of developing geologic hazard-informed development regulations begins with the production of robust, practical recommendations from the scientific community (Olshansky and Rodgers, 1987; Copsey, 2002; Lombardo et al., 2014). These recommendations must help land use planners perform three critical analyses related to mobile, flow-type landslide hazards:

1.) *Stability analysis*: Where (and when) will a potentially mobile landslide initiate?
2.) *Liquefaction analysis*: Will the failing mass develop into a rapid, mobile flow?
3.) *Runout analysis*: How far will a flow-type landslide travel post failure?

In this chapter, I briefly review the existing body of research which addresses the first two questions and focus on the third question of landslide runout, which remains one of the most challenging issues in landslide risk analysis (van Westen et al., 2006; Fell et al., 2008). To this end, I carefully define the mechanism of flowsliding; collect, synthesize, and curate published and unpublished flowslide data; develop a new predictive relationship for unobstructed flowslide runout, and provide a probabilistic hazard evaluation tool for use by urban planners. I show that

unobstructed flowslide runout behavior is highly predictable based on the volume of the event alone and that the empirical predictive relationship applies over the full range of terrestrial landslide volumes.

3.2. Background

3.2.1 Terminology

Landslides occur in innumerable forms. Materials, degrees of confinement, topographic obstruction, and failure mechanisms occur in natural gradations, frustrating attempts at rigorous categorization. In addition, even a simple landslide varies in time and space. For example, a coherent block rafting on a liquefied basal layer may disintegrate into a uniformly liquefied flow. Entrainment of debris and water may alter the makeup of the failing mass. Downslope topography may confine an initially open-slope failure. Thus, the process of grouping landslide events using quantitative and qualitative thresholds is a complicated but necessary task for creating useful inventories for the forward prediction of landslide runout.

Although the term "flowslide" has existed in geotechnical engineering literature for many decades (e.g. Koppejan et al., 1948), a precise and widely-accepted definition has not existed until recent efforts to consolidate and unify the various landslide classification schemes in geotechnical practice. I adopt a definition of "flowslide" based on the Hungr et al. (2014) update to the Varnes classification:

> "Very rapid to extremely rapid flow of sorted or unsorted saturated granular material on moderate slopes, involving excess pore-pressure or liquefaction of material originating from the landslide source. The material may range from loose sand to loose debris (fill or mine waste), loess and silt. Usually originates as a multiple retrogressive failure. May occur subaerially, or under water."

"Very rapid" and "extremely rapid" velocity classes are defined as 3 m/min – 5 m/sec and > 5 m/sec, respectively (Cruden and Varnes, 1996). However, failure velocity is better viewed as a characteristic of flowsliding than as a criterion due to its difficulty to accurately measure without instrumentation and because other failure modes are capable of producing extreme failure velocities (e.g. rock falls, debris flows, and debris avalanches). Hungr et al. (2014) distinguish "flowslides" from "debris flows" by degree of confinement, with the latter events governed by steep channelization which concentrates the energy of the failure and often results in much longer runouts. I deviate from the definition of Hungr et al. (2014) by including rock, silts, and sensitive clays as flowsliding materials rather than giving them separate classifications. This reflects a focus on the liquefaction mechanism rather than geotechnical material, since entrainment can significantly alter the content of a landslide (e.g. Hungr and Evans, 2004) complicating classification.

Finally, flowslides occur both subaerially and subaqueously, and they are especially common in the marine environment (Hungr et al., 2014; Hampton et al., 1996). Due to the vast, remote nature of the marine environment and the limitations of bathymetry, only very large subaqueous

events are typically documented. However, these events are of special importance in understanding flowslide runout due to their near-perfectly unobstructed nature.

3.2.2 Stability analysis

Landslide hazard analyses must delineate locations where landslides may initiate (susceptibility) as well as the potential volume and temporal probability of failure (Fell et al., 2008). While numerous empirical methods have been employed for landslide hazard mapping, they are often limited by the incompleteness of landslide inventories, dependence on climatic and environmental stasis, and non-transmissibility from their region of origin. Thus, physically-based slope stability models are generally preferable for qualitative hazard and risk assessment (van Westen et al., 2006). Numerous deterministic slope stability programs are freely available to model shallow (< 3 m) or deep (> 3 m) landslide initiation in a GIS environment at local or regional scales (**Table 3.2**).

Table 3.2. Selected open-source slope-stability scripts or stand-alone software.

shallow	*Reference*
LISA	Hammond et al. (1992)
SHALSTAB	Montgomery et al. (1994)
SINMAP	Pack et al. (1998)
PISA-M	Haneberg (2006)
TRIGRS	Baum et al. (2008)
deep	
r.slope.stability	Mergili et al. (2014)
Scoops3D	Reid et al. (2015)
this work	**Chapter 2** and Pollock et al. (2019)

The typical output of these programs is a grid-based map of the limit equilibrium factor of safety based on a triggering scenario such as an input rain storm, ground water conditions, or

earthquake ground shaking intensity. The failure volume may be calculated as a program output (e.g. Scoops3D) or inferred from the initial model assumptions (e.g. SHALSTAB). Temporal probability of occurrence is assumed to be that of the triggering event. These programs can be used on regional scales to assess the location, size, and timing of landslides as an input to a flowslide susceptibility and runout analyses.

3.2.3 Liquefaction analysis

When sheared, particulate matter will tend to change volume, and thus void ratio. Dense material will dilate, and loose material will contract until it reaches steady state. In the undrained loading of saturated, contractive material, when no volume change can occur, the load will be transferred to the pore fluid resulting in a loss of shear strength, or strain-softening. When the residual shear strength of a soil drops below the shear stress required for static equilibrium, flow liquefaction occurs. Liquefaction potential is commonly evaluated through undrained triaxial or direct shear tests and field testing. However, test-based liquefaction susceptibility is only practical on a site-specific basis rather than the larger regional scales of land use planning. Furthermore, both laboratory experiments and field studies have demonstrated that flowslides often develop in initially dilative soil, undermining traditional methods as the sole screening technique (Fleming et al., 1989; Iverson et al., 1997; Davies et al., 2002; Gabet and Mudd, 2006; Cascini et al., 2013). Test-based methods also may not capture the effects of downslope topography, water sources, or substrate material, all of which influence the evolution from initial failure to flow (Dufresne, 2014; Hutchinson, 2002; Hungr and Evans, 2004) and may be invalidated by sample disturbance (Hunter and Fell, 2001). For these reasons, flowslide

susceptibility analyses based on remote sensing, geological maps, or basic geotechnical information available from existing boreholes is necessary for zoning purposes. Although no definitive evaluation procedure yet exists which can capture the complex and varied environmental conditions under which flowslides can develop, laboratory and field observations support basic screening criteria such as grain size distribution, topographic form, previous movement, proximity to water, and water content.

3.2.3.1 Grain Size

Although most common in loose, granular material, laboratory and field data has since evinced flow liquefaction in silts (Ishihara 1984; Ishihara et al., 1990; Fletcher et al., 2002), gravels (Yegian et al., 1994; Evans and Seed, 1987; Bezerra et al., 2005; Calhoun, 2007), sensitive clays (Meyerhof, 1957; Aas, 1981; Geertsema et al., 2006), and some types of rock (Hutchinson, 2002; Bowman and Take, 2015).

Hunter and Fell (2001) and Isihara et al. (1980) developed empirical ranges of particle size distribution, indicating liquefaction potential in an assortment of materials. However, these ranges are merely those observed in a limited database of case histories and are not prescriptive. In analyzing a small set of slumps and flows in central California, Gabet and Mudd (2006) found that soils with > 45% sand content transformed into flows, agreeing that, while not prescriptive, greater sand content increases the likelihood of liquefaction. However, some fine-grained content is likely necessary to prohibit drained conditions. Ellen and Fleming (1987) observed that after the intense storm of 3 – 5 January 1982 in the San Francisco Bay Region, debris flows were primarily restricted to soils with a clay content between 8 and 25%. In a series of

experiments testing soil failure mode and mobility, McKenna et al. (2012) observed that the maximum runout, associated with a flowing rather than sliding mode of failure, occurred at approximately 10% fine-grained content. McKenna et al. (2012) also developed a threshold dry density below which soils are likely to flow:

$$\rho_t = 8.48\,x\,10^{-6}f^3 - 1.33\,x\,10^{-3}f^2 + 5.27\,x\,10^{-2}f + 1.04 \qquad \textbf{(3.1)}$$

Where *f* is the fines content of the soil. **Equation 3.1** was used to predict the failure mode of 96 shallow landslides in Oregon and Colorado with 79% accuracy (McKenna, et al., 2012).

3.2.3.2 Topographic form

Topographic morphology is a proxy for ground water levels, with hollows and concavities exhibiting greater wetness (Lockyear, 2018; Beven and Kirkby, 1979; Grabs et al., 2009). Intuitively, elevated pore water pressures associated with topographic concavities should promote the development of flowslides. Lockyear (2018) found that concave topography and confinement both contributed to high mobility. McKenna et al. (2012) found geomorphic setting (concavities versus open slopes) predicted failure mode with 77% accuracy.

Initial slope angle has also been proposed as a contributing factor in the development of flowslides due to its influence, along with pore-water pressure, on the effective stress conditions within a slope. Sandy embankments greater than 18.4 degrees over a 5 m drop have been traditionally considered susceptible to flowslides in the Netherlands, while event inventories commonly show flows developing on slopes greater than 20 degrees (Silvis and de Groot, 1995;

Iverson et al., 1997, 2015; Ellen and Fleming, 1987; McKenna et al., 2012). However, many flowslides have developed at shallower angles, especially in anthropogenically modified slopes (e.g. Hunter and Fell, 2001).

3.2.3.3 Previous movement

Remobilization of previously failed material may be accompanied by an increased likelihood of flowslide development. Loss of vegetation cover can increase the effective rainfall intensity and reduction in macropores can decrease hillslope drainage, both effects enhancing soil wetness (Mirus et al., 2017). Additionally, initially dense soil may dilate in shear and travel only a short distance before the concomitant decrease in pore pressure increases the shear strength. Subsequent saturation of the failed mass, now in a loose, contractive state, can trigger catastrophic collapse and liquefaction (Gabet and Mudd, 2006). Similar behavior has been witnessed in natural flow failures (Ellen et al., 1989; Harp et al., 2004) and reproduced in field experiments (Harp et al., 1990). Lockyear (2018) found that previous movement was positively correlated with high landslide mobility.

3.2.3.4 Proximity to water

Flowslides may also develop as water is entrained along the downslope travel path. Entrainment of the North Fork of the Stillaguamish River and the saturated sediments surrounding it is, in part, credited for the extreme mobility of the Oso Flowslide (Iverson et al., 2015; Wartman et al., 2016). Basal liquefaction of a saturated substrate is the likely cause of the excessive mobility of otherwise dry rock avalanches. (Dufresne, 2014; Dufresne and Davies, 2008).

3.2.3.5 Water content

Ellen and Fleming (1987) defined an approximate mobility index (AMI) as the ratio of in situ water content to the water content at the liquid limit. AMI > 1 indicates the ability for soil to hold more water than its liquid limit and is correlated to the ability of a soil to flow, while soils with AMI < 0.45 are unlikely to (Ellen and Fleming, 1987; McKenna et al., 2012).

Other criterion have been proposed to test liquefaction susceptibility, many of which combine critical state theory with laboratory testing. While these methods are theoretically more rigorous and may be effective for the majority of cases, they are only practical on site-specific scales and with considerable time and expense. Furthermore, flowslides have developed in material deemed unsusceptible to liquefaction by common testing criterion, and I conclude that no liquefaction susceptibility testing procedure yet exists which can account for all of the variability of geologic, compositional, hydrologic, and state conditions which are found in soil slopes. Thus, there is no substitute for a thorough review of local landslide records, expert judgement, and careful application of safety factors in evaluating the potential for flow liquefaction.

3.2.4 Runout analysis

The most commonly used index of landslide mobility is the "fahrboschung," or "angle of reach," defined as the inclination of the line connecting the crest of a landslide headscarp to the terminus of its deposit along the centerline of motion (Heim, 1932). It is commonly expressed as the ratio of maximum vertical fall height to maximum horizontal travel distance, *H/L* (**Figure 3.4**). Scheidegger (1973) showed that the angle of reach represented the average coefficient of friction

in a friction-governed landslide model. Reach angle has remained the primary index of landslide mobility due its ease of calculation, intuitive association to friction and potential energy, and historical precedent. Heim (1932), Scheidegger (1973), Hsu (1975), Li (1983), Hutchinson (1988) and many subsequent studies observed a trend among mass-wasting events of decreasing angle of reach (signifying increasing mobility) with increasing volume. This led to inventory-based ordinary least squares (OLS) regression relationships relating reach angle to volume of the form $log(H/L) = a\ log(V) + b$. However, small inventories including diverse failure types led to highly scattered data and poorly fitting regression equations (Davies, 1982; Legros, 2002; Melosh, 1987; Shaller, 1991; e.g. Edgers and Karlsrud, 1982; Guo et al., 2014; Hampton et al., 1996). Subsequent work improved predictive empirical relationships by parsing data sets by material type (Finlay et al., 1999; Golder Associates Limited, 1995; Hunter and Fell, 2003), travel classification (Corominas, 1996; Hunter and Fell, 2003; Hutchinson, 1988), and degree of obstruction (Corominas, 1996; Golder Associates Limited, 1995; Nicoletti and Sorriso-Valvo, 1991; Shaller, 1991). However poor correlations between the angle of reach and volume persisted (Hunter and Fell, 2003). Other mobility inputs have been proposed, such as downslope angle (Hunter and Fell, 2003) and potential energy (Howard, 1973; McSaveney, 1975); however, they have proven difficult to transfer beyond their inventories of origin (Guo et al., 2014; Whittall et al., 2017).

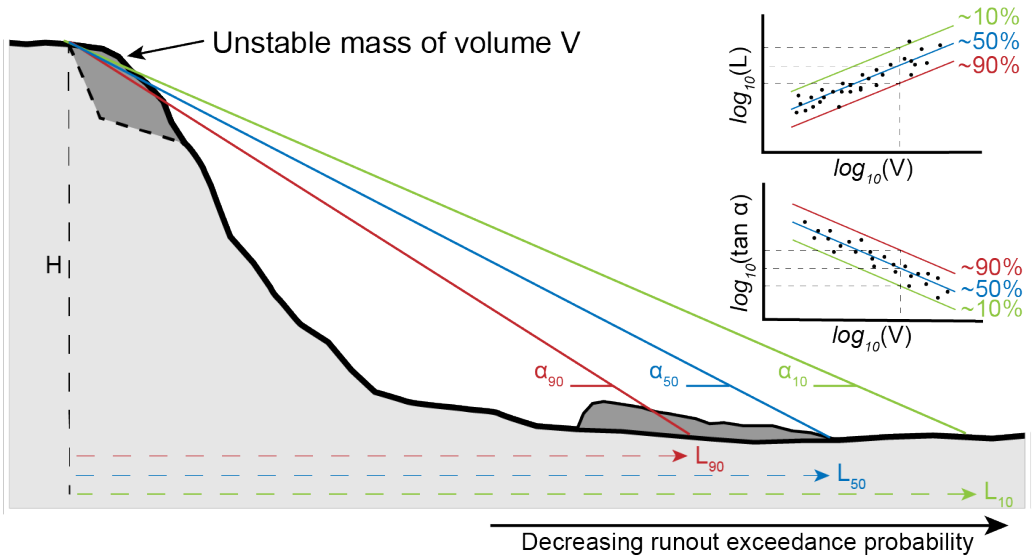

Figure 3.4. Probabilistic runout prediction based on a volume-reach angle, α, relationship (*bottom inset*) and volume-length relationship (*top inset*). In the case shown, the blue line corresponds to both the observed reach angle and the 50% runout exceedance probability.

Hsu (1975) was the first to depart from the traditional direct association of the angle of reach to landslide mobility, noting that Heim's initial observations of the Elm landslide described it as a "flow" and were full of language ascribing the rock debris fluid-like characteristics. He argued that, as a flow event, large rock avalanches such as those examined by Scheidegger (1973), should not be modeled as frictional, sliding blocks, but as fluids. Based on scale modeling of the Elm rockslide event using a bentonite suspension, Hsu suggested that flow behavior of landslides is kinematically similar to that of a thixotropic fluid, decreasing in viscosity with increasing shear rate. He also found that fall height had little influence on the runout of scaled, bentonite flows. The sole governing parameter appeared to be spreading, thus derivatively, volume (Hsu 1975). Subsequently, Davies (1982) and Legros (2002) concluded that the inclusion of the fall height only added scatter to runout data of large landslides and avalanches, reducing the regression statistics in almost every case. However, Legros (2002) only examined the mobility

of “long-runout” landslides (i.e. those which run out further than a frictional model would predict), and he grouped his database by environment (volcanic, non-volcanic, Martian, submarine, debris low) without regard for mechanism of failure, obstruction, and confinement, all of which have been shown to influence the mobility of an event (Corominas, 1996).

3.3 Flowslide database

3.3.1 Inclusion criteria

An extensive literature search returned 557 unconfined, low-obstruction flowslides. The inherent temporal and spatial variability of the flowsliding process makes events of this style particularly difficult to classify and compare. Dozens of mass-wasting classification schemes exist throughout literature (Hungr et al., 2014), with the most commonly adopted (Hutchinson, 1988; Skempton and Hutchinson, 1969; Varnes, 1958, 1978) differing mainly in their respective delineation of flow-type events (Crozier, 1986). Therefore, the database includes events based primarily on description of key flowslide characteristics rather than the classification assigned by the authors. Descriptions of the surrounding topography and failure progression; pre- and post-event photography; plan and profile diagrams; etc. were used to evaluate the events. Events were included in the database if they were “unconfined,” that is, exhibiting freedom to spread laterally and without a clear topographic control of runout path for the majority of the failing mass and the majority of the motion. Events which were obstructed by an opposing topographic rise were not included in the database. The degree of confinement and obstruction were often apparent in plan-view diagrams of landslide deposits (**Figure 3.5**).

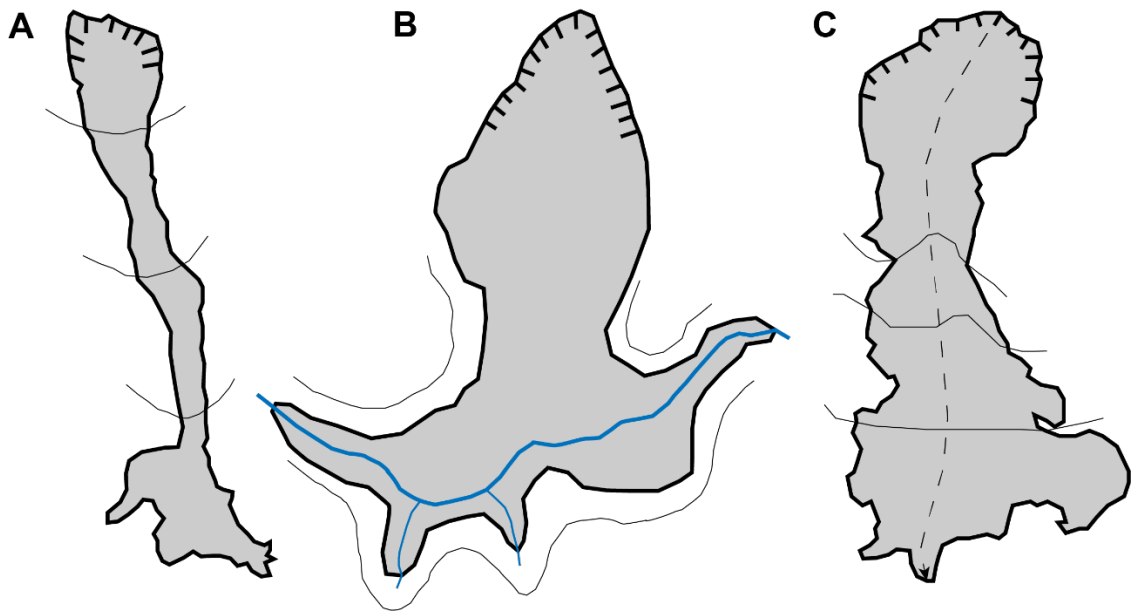

Figure 3.5. Topographic constraint classes: (*A*) confined (Johnson's Landing debris flow, British Columbia, Canada, 2012); (*B*) obstructed (Abe Barek flowslide, Badakhshan, Afghanistan, 2014); and (*C*) open slope (Shenzhen flowslide, Guangdong, China, 2015). Modified after Golder Associates Limited (1995) and Nicoletti and Sorriso-Valvo (1991).

Lively debate still exists as to the mechanism of flow-type events (Davies, 1982; Golder Associates, 1995; Hungr, 1990; Shaller, 1991) although flow liquefaction has been recognized as the most probable dominant mechanism of flowsliding, with other more exotic mechanisms possibly playing a secondary role (Hungr, 1990; Golder Associates, 1995). Therefore, I only included events of which the authors described flow-type movement and evidence of at least partial saturation suggestive of flow liquefaction.

In compiling the flowslide database, I looked for sources which included estimates of volume, length of runout, and height of fall (or diagrams from which they could be reliably estimated), as well as descriptions of the travel path sufficiently detailed to evaluate the degree of obstruction

and confinement. Unless overwhelming contrary evidence existed from event descriptions, the author's judgement of obstruction and confinement (when given) was assumed.

3.3.2 Description

22% of the database comes from small open-slope flows in Switzerland (Hurlimann et al., 2015). This data set includes volume and runout length, but not fall height. Ninety-five small open-slope flow events (16%) are derived from the landslide inventory of the Geotechnical Engineering Office of Hong Kong (GEO). Fourteen percent of the database comes from the inventory of Hunter and Fell (2001) and references therein, including failures of cut, fill, and natural slopes in Hong Kong; stockpiles of granular waste from mining operations; fill embankments; and sensitive clays. Detailed information about each subclass of failure is provided in Hunter and Fell (2001). **Figure 3.6** shows the distribution of different subclasses of failures. Eighteen percent of the database consists of subaqueous events, primarily in the extreme volume range of $1 \times 10^8 – 1 \times 10^{13}$ m^3. Most of these events are poorly documented. Low resolution bathymetry makes the slide source area, travel path, and deposit difficult to distinguish, leading to significant uncertainty in volume, length, and height estimates (Edgers and Karlsrud, 1982). Twenty-eight events (4.9%) which occurred in the glacially deposited materials of North America are of particular interest because of their similar geologic setting to the Oso Flowslide. These events encompass a narrow volume range of $1 \times 10^4 – 4 \times 10^7$ m^3 with runout ranging from 90 – 2000 m. The remainder of the database consists of subaerial flowslides, primarily natural slope failures in Europe and Asia.

The database contains subaerial landslides with volumes from 1 x 10^1 – 2 x 10^{10} m^3 and horizontal runouts of 12 m to 19 km. The inclusion of subaqueous events extends the upper limit of these ranges to 5 x 10^{12} m^3 and to 700 km, respectively. The database is dominated by small volume (10^1 – 10^3 m^3) events from two publicly available inventories (Hunter and Fell, 2001; Hurlimann et al., 2015). The database contains fewer than expected low-mid volume (10^3 – 10^5 m^3) events. I attribute this to a recording bias: generally only very large, catastrophic events have been well-documented in the past. On the other hand, small-volume, open-source inventories tend to be both recent and large, recording the local mass-wasting response to a discrete trigger, typically a precipitation event. Finally, due to the vast, remote nature of the marine environment and the limitations of bathymetry, only very large sub-aqueous events are typically documented, leading to high-volume bias of subaqueous events. The database is provided in **Appendix 3.1.**

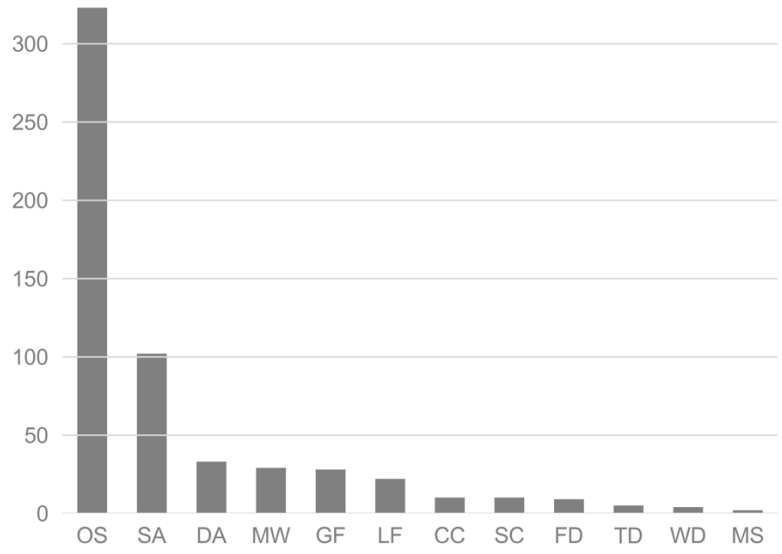

Figure 3.6. Distribution of failure subclasses. Abbreviations are OS: open slope debris flows; SA: subaqueous; DA: rock debris; MW: mine waste; GF: glacial soils; LF: loess; CC: chalk; SC: sensitive clay; FD: hydraulic fill dams; TD: tailings dams; WD: municipal and construction waste; MS: mining.

3.4. Results

3.4.1 Analysis of the flowslide database

For the 287 subaerial events for which height, length, and volume data was available, I performed a traditional OLS regression analysis of reach angle versus volume (**Figure 3.7**). The coefficient of determination (R^2) was 0.42, indicating minor correlation. The events generally cluster by material type, with quick clays and fill dams producing the most mobile failures. Natural slope failures in Hong Kong show no statistical trend, and failures in mine waste actually exhibit a *decrease* in mobility with increasing volume. For the same 287 events, I performed a regression analysis of length versus volume. The results showed a strong correlation ($R^2 = 0.83$). I also performed a regression on the total 475 subaerial events for which there was volume and length data (**Figure 3.8**). Subclassess remained roughly clustered, but each subset showed a stronger trend of increasing mobility with increasing volume using length instead of reach angle as the mobility index. Most notably, the scatter in mobility of large volume events ($> 10^5$ m^3) is dramatically reduced when fall height is ignored. Finally, the entire database of 577 events was analyzed, including submarine flowslides (**Figure 3.9**). The results showed a very strong correlation between runout length and volume ($R^2 = 0.91$). Inclusion of the submarine events shifted the regression equation to show a slightly greater degree of mobility than that of only the subaerial events (a = 0.34 vs 0.30). The final regression relationship for all 577 subaerial and subaqueous events is:

$$\log L = 0.348 \log V + 0.958 \qquad \textbf{(3.2)}$$

where L is the total runout length [m] and V is the landslide volume [m^3]. The standard deviation of the residuals is 0.317. The regression constants and statistics for all of the relationships are summarized in **Table 3.3**. Although the correlation between flowslide volume and runout length is strong, the variability around the predicted runout length encompasses over an order of magnitude, as others have noted in similar analyses (Guo et al., 2016). However, since the variability can be statistically quantified, landslide runout can be framed probabilistically, much as is done for other natural hazards (McDougall et al., 2012). **Figure 3.9** shows the lengths of runout associated with different runout exceedance probabilities, as calculated from the flowslide database. This relationship can be used both for landslide zoning and for evaluating the probability of runout impact on an existing structure where the distance away from the landslide source zone is already known. In a GIS environment, distances associated with unique runout exceedance probabilities can define a series of geometric buffers – or runout "contours" – around potential landslide sources. This process can be repeated for representative landslide volumes corresponding to the range of plausible events.

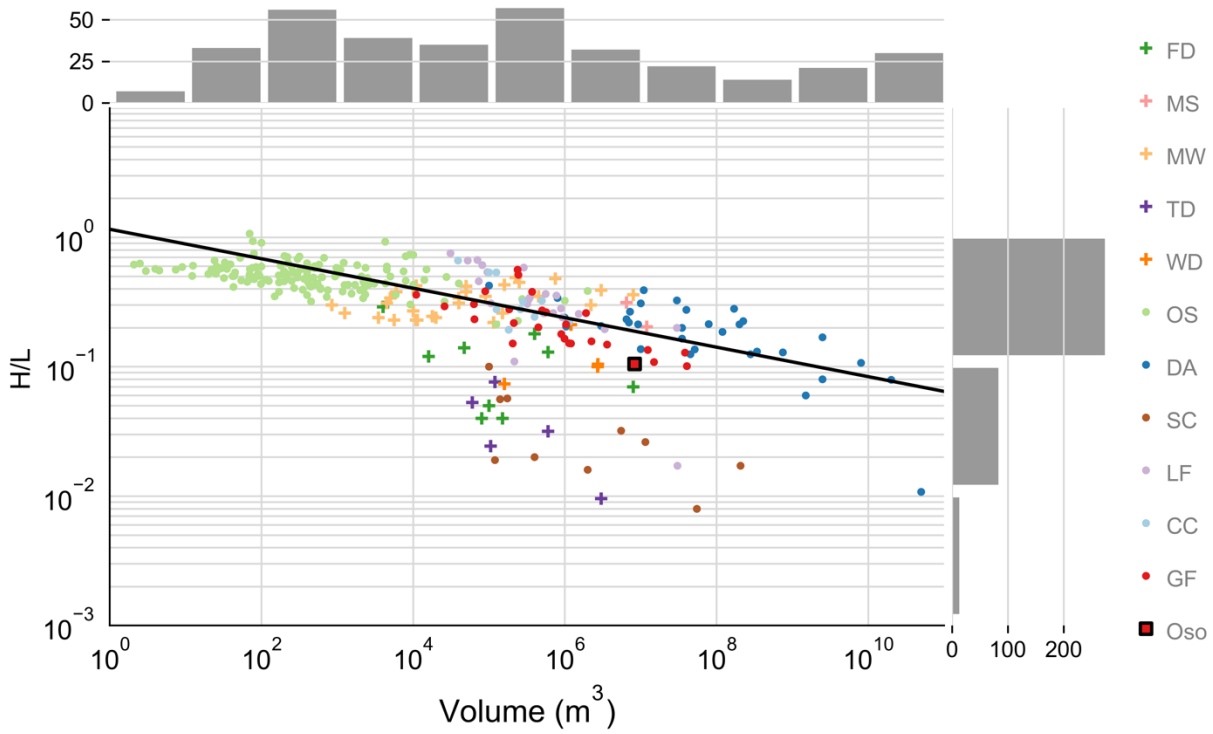

Figure 3.7. Reach angle-volume relationship for subaerial flowslides. See **Figure 3.6** for abbreviation key. The Oso Flowslide (red square) is not included in the regression.

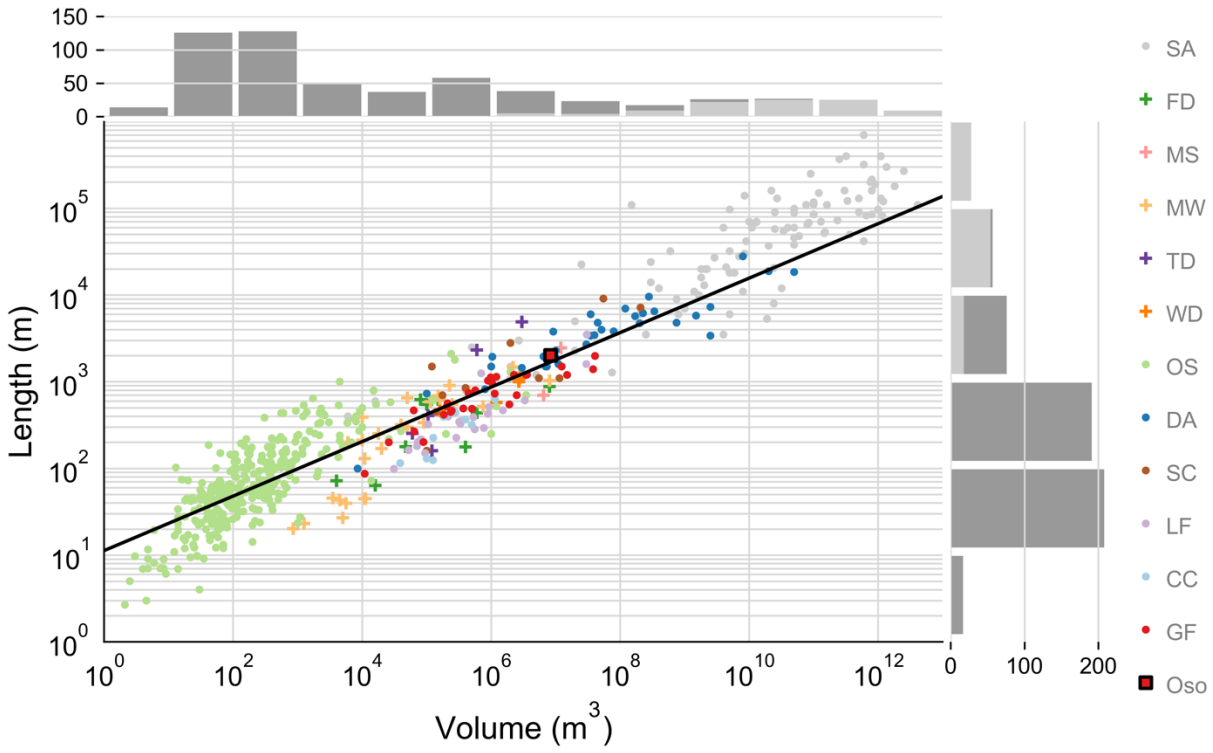

Figure 3.8. Length-volume relationship for subaerial flowslides. The Oso Flowslide (red square) and the submarine flowslides (grey circles) are not included in the regression. See **Figure 3.6** for abbreviation key.

Table 3.3. Regression parameters for subsets of the flowslide database.

Set	*Relationship*	*a*	*b*	R^2	*n*
Subaerial, *with height data*	reach angle-volume	-0.114	-0.029	0.419	287
Subaerial, *with height data*	length-volume	0.331	0.940	0.832	287
Subaerial, *excluding FD, TD, and SC*	reach angle-volume	-0.092	-0.061	0.574	263
Subaerial, *glacial*	length-volume	0.312	0.984	0.804	28
Subaerial, *all*	length-volume	0.314	1.052	0.821	475
Subaerial and subaqueous	length-volume	0.348	0.958	0.923	577

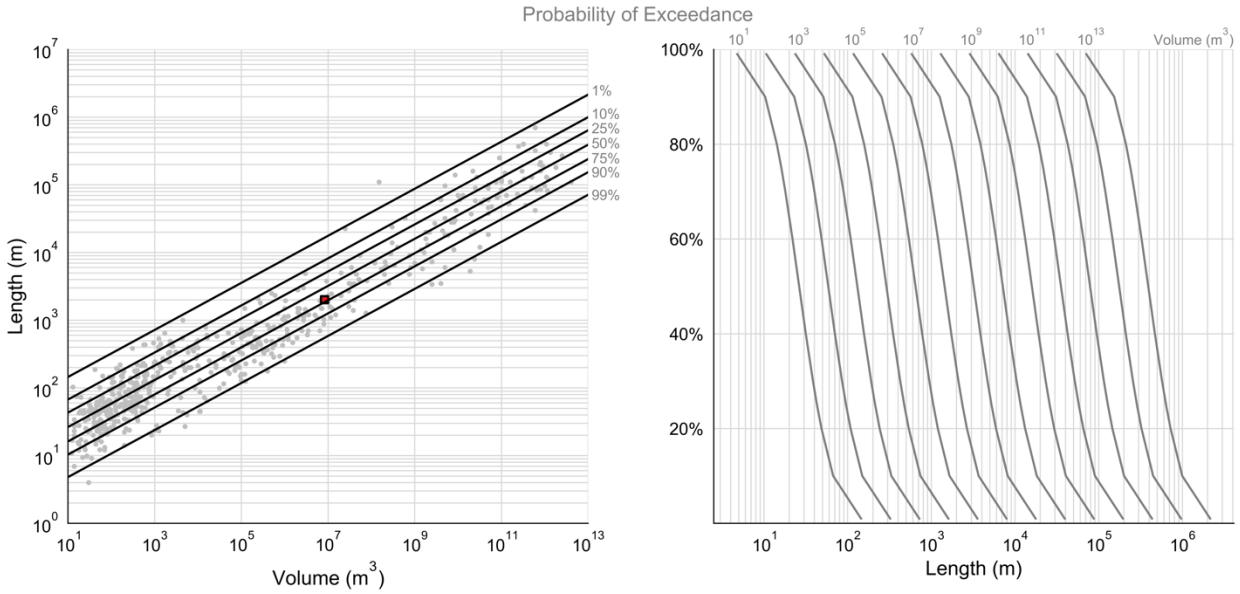

Figure 3.9. Length-volume relationship for the full flowslide database, excluding the Oso Flowslide (*red square*), for zoning purposes (*left*). A more intuitive view of the data for the purpose of evaluating the probability of runout impact on an existing structure (*right*).

3.4.2 Application for landslide susceptibility zoning in northwestern Washington State

I demonstrate how the empirical runout relationship in **Equation 3.2** can be applied for landslide runout analyses through a simple worked example in the flowslide-prone central reach of the North Fork of the Stillaguamish River (NFSR) valley between the cities of Oso and Darrington, Washington.

3.4.2.1 North Fork of the Stillaguamish River Valley

When the Cordilleran Ice Sheet advanced into the Puget lowlands ~17,500 years ago it blocked the west-trending valleys of the Cascade Range, creating ice marginal lakes (LaHusen et al, 2016; Porter and Swanson, 1998). One such lake formed in the NFSR valley, between the

present-day cities of Arlington and Darrington, filling the valley with a sequence of glaciolacustrine clay, silt and fine sand; coarser advance outwash; and till, capped by recessional outwash sand and gravel. When the ice retreated ~16,400 years ago, the NFSR quickly incised ~200 m through the weaker glacial deposits leaving broad terraces such as the Whitman Bench (~275 a.s.l) just northwest of Oso (Porter and Swanson, 1998; Booth et al., 2017). During the Holocene, lateral channel migration of the NFSR widened the valley, impinging on the valley walls and leading to episodic deep-seated landslides initiating from the terrace crest.

Booth et al. (2017) mapped over 200 deep-seated landslides in the NFSR valley occurring over the past 6000 years. The combination of loose, highly permeable coarse-grained outwash over lower permeability till and glaciolacustrine deposits and the wet climate of the last 6000 years caused many of these landslides to liquefy and runout long distances, lapping the valley floor in landslide deposits. However, most of the deposits have been overprinted by fluvial channel migration and subsequent landslides. One of the youngest of these landslides, the "Rowan" flowslide, was exceptionally large (3.6×10^7 m^3) and crossed most of the valley floor to pin the NFSR against the southern side of the valley ~ 500 ^{14}C yr B.P. It has similar scarp and deposit morphologies to the Oso Flowslide, suggesting similar dynamics (LaHusen et al., 2016). The 2014 Oso Flowslide was only the most recent in a series of massive flowslides which will continue to inundate the NFSR valley until the mechanically weak glacial sediments have been removed from the valley walls (LaHusen et al., 2016).

3.4.2.2. Runout analysis in the NFSR valley

Local sedimentary architecture makes the terraces of the NFSR valley prone to 1 x 10^6 – 1 x 10^7 m^3 slope-clearing landslides and smaller landslides of ~1 x 10^5 m^3 that involve only the recessional outwash at the upper portion of the terrace (Perkins et al., 2017). I use the ends of this proposed range and **Equation 3.2** corrected for bias when anti-logged (**Chapter 2**, **Section 2.7.2**) to produce three scenarios of runout exceedance probability over a 9 km stretch of the central NFSR valley (**Figure 3.10**).

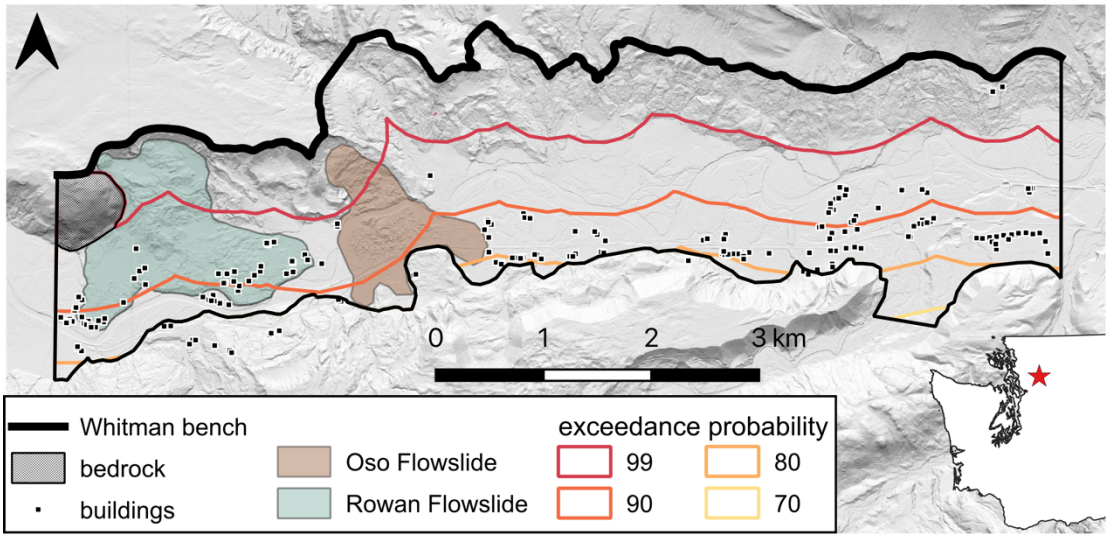

Figure 3.10. Runout exceedance probability contours in the NFSR valley for a 1 x 10^7 m^3 flowslide originating from the Whitman bench. The Rowan flowslide (3.6 x 10^7 m^3) was not exceptionally mobile for a failure of its volume, while the much smaller Oso flowslide (8.3 x 10^6 m^3) traveled approximately the same distance.

The Rowan and Oso flowslides are similarly mobile despite the former having over four times greater volume. The Rowan flowslide's apparent low mobility may be in part due the erosion of thin distal deposits since prehistoric times, reducing the preserved runout length. Both flowslides are less mobile than approximately 80% of global flowlides of 1 x 10^7 m^3, near the upper volume range of the most probable failures in the NFSR valley.

Moderately large flowslides 1 – 2 orders of magnitude smaller than the Oso or Rowan flowslides are likely capable of inundating the full width of the NFSR valley (**Figure 3.11**). When considering the runout potential of flowslides from both the north and south terrace margins, only a small strip of land and the center of the valley has less than a 30% probability of inundation from failures of 1 x 10^5 m^3 and less than a 70% probability for failures of 1 x 10^6 m^3. Relatively few of the remaining buildings in the NFSR valley occupy the lower susceptibility center of the valley. Fifty-eight percent of buildings lie beyond the 50% runout exceedance contour for 1 x 10^5 m^3 flowslides, while no buildings are beyond the 60% runout exceedance contour for 1 x 10^6 m^3 failures.

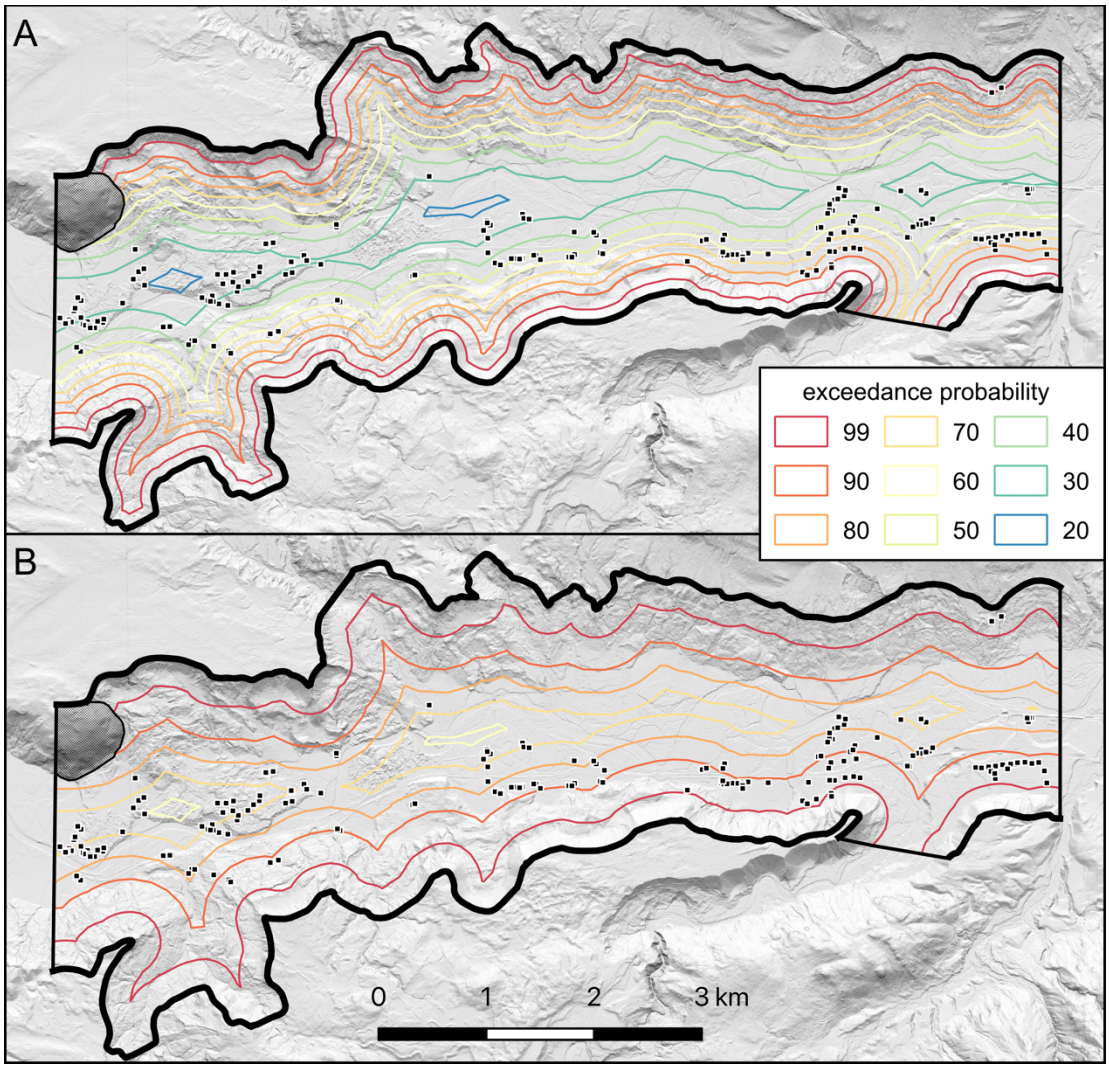

Figure 3.11. Runout exceedance probability contours for (*A*) small-moderate failures of 1 x 10^5 m^3 and (*B*) large failures of 1 x 10^6 m^3 initiating from the north or south benches. The locations of existing buildings are shown as black squares.

3.4.2.3 Extending landslide susceptibility to risk for land use zoning

Modeling landslide hazard requires not only predicting landslide runout, but also the magnitude and timing of potential landslides. Although landslide risk assessment would ideally include all credible landslide scenarios, in practice, only the most likely and the most extreme (worst) cases are often considered. Landslide inventories can provide information on the timing and size of

future landslides, but the time scale of large landslides often far exceeds historical records. Although landslide volume is a necessary input to runout relationships, it is rarely apparent except in the case of pre-existing failure that might remobilize (e.g. Machan et al., 2018). Multiple physically-based models exist which can be used to identify failure surfaces associated with the lowest mechanical stability (Reid et al., 2015; **Chapter 2**, **Section 2.5.4**). Additionally, local geology may constrain landslide size. Perkins et al. (2017) couple generalized sedimentary architecture and a physical stability model to identify the characteristic landslide volumes of three glacially altered valleys in Washington, including the NFSR valley. The calibration of surface roughness to known landslide ages has allowed local historical inventories to be extended (LaHusen, 2019). In the NFSR valley, Booth et al. (2017) use this technique to date 218 landslides and constrain landslide activity in this valley. These methods could be coupled with the runout modeling presented here to create preliminary hazard and risk maps for the NFSR valley. These maps could be correlated to local thresholds of risk tolerance to create tiered landslide-hazard development regulations with more stringent requirements closer to the valley margins.

3.5 Discussion and conclusion

3.5.1 Oso Flowslide mobility

When viewed in the context of minimally obstructed, unconfined flowslides, the Oso Flowslide was not abnormally mobile as some have claimed (Iverson and George, 2016; Iverson et al., 2015; White et al., 2015). While the Oso flowslide is more mobile than 70 – 75% of similarly

sized flowslides when considering reach angle, its mobility is less remarkable using the metric of runout length alone. Considering only subaerial events, the Oso Flowslide runout is only slightly more mobile than global, similarly-sized events. However, in the context of subaerial and subaqueous events, the Oso Flowslide is ~8% below the mean runout for global flowslides.

3.5.2 Reach angle versus length as a mobility metric

Fall height is a poor indicator of the reach of flow-types landslides, adding significant scatter to regressions of flowslide runout (Baum et al., 1998; Legros, 2002). Hsu's (1975) comparison of flow-type landslides to the movement of thixotropic fluids suggests that the initial fall height, which generally makes up most of the total vertical fall height, is effectively "forgotten" by the failing mass as the initial kinetic energy is quickly dissipated (Legros, 2002). This may reflect the progression of a failing coherent block breaking apart and fluidizing as adjacent material undergoes undrained loading and liquefies. I suggest three additional explanations for the weak correlation between reach angle and volume.

1. Although runout length is simple to measure accurately, fall height can be difficult to estimate especially when using old contour maps or photography. As fall height is typically an order of magnitude less than runout length, it is especially sensitive to resolution-based uncertainties on the order of meters to tens of meters.

2. A simple measure of reach angle treats a failure as a single, instantaneous event. However, flowslides can progress as multistage failures. For instance, the Oso Flowslide

occurred as a two-stage failure, the first stage being a reactivation of previous landslide deposits which originated partway up the slope face and created the catastrophic flood of debris which reached the opposing valley wall, and a second stage of primarily large, coherent blocks failing and back-rotating from the top of the Whitman bench (Keaton et al., 2014; Stark et al., 2017; Wartman et al., 2016). Although almost all of the recorded length came from the stage one failure, a significant portion of the recorded height came from the stage two failure. Combining the events by a simple measurement of post-failure *H* and *L* would only minimally overestimate the true horizontal runout of the debris but would significantly overestimate the true vertical drop of the runout material. Therefore, in multistage events, *H* and *L* may have little direct relation.

3. The progression of failure in some materials may lead to flow developing after the initial fall. For instance, in the case of the chalk cliff failures described by Hutchinson (2002) and Bowman and Take (2015), a simple measurement of *H* and *L* assumes a mechanistically continuous event. However, in some cases, the failure is bimodal: a semi-coherent collapse of a portion of the cliff face, including large vertical drop, leads to undrained loading upon impact and a liquefaction flow which can runout hundreds of meters with little decrease in elevation. Thus, even though a failure is temporally continuous, liquefaction flowsliding may not occur until after the initial fall.

3.5.3 Submarine flowslides

Use of the reach angle as a mobility index in comparisons of subaerial and subaqueous landslides has led to conclusions that subaqueous events are much more mobile (Locat and Lee, 2002), although that trend is ambiguous (Edgers and Karlsrud, 1982). The effects of the submarine environment on the mechanism of travel are unquantified. Drag forces on the exposed surfaces of a subaqueous landslide create suspension flows which deplete the mass of the main, dense flow and could work to decrease mobility (Locat and Lee, 2002). The frontal portion of the flow may hydroplane at speeds in excess of 5 – 6 m/s adding mobility to the debris (Laval et al., 1988; Mohrig et al., 1999). However, the effect these processes have on apparent mobility relative to subaerial flowslides is likely minor. Volume depletion due to suspension flow is likely insignificant relative to the (considerable) margin of error in estimating the total failed volume. Basal liquefaction in subaerial flowslides reduces shearing resistance along the failure plane, mimicking the suggested hydroplaning of submarine slides.

When runout length is viewed as a solely volume-dependent process, submarine flowslides are only slightly more mobile than subaerial flowslides. This slight increase in mobility is likely a result of the complete unobstruction of many of these events, whereas smaller subaerial events even on an open-slope path are more effected by rougher small-scale topography and vegetation. In addition, submarine flowslides are completely saturated from initiation and therefore more likely to undergo complete, rapid liquefaction than subaerial flowslides.

Marine landsides give important insight into the runout patterns of flowslides. Submarine landslides can be multiple orders of magnitude larger than their largest subaerial counterparts. The prehistoric Saymareh rock avalanche in Iran involved 44 Gm^3 of material and ran out 19 km (Roberts and Evans, 2013). In comparison, submarine slides can easily involve 1000 – 5000 Gm^3 of material (Robert and Evans, 2013) and runouts in excess of 700 km have been documented (Embley, 1976). The consistency of large and small magnitude events suggests that flowsliding is a largely scale-independent process. Although flowslide runout appears random within any small volume range, it is predictable and probabilistic when compared across eleven orders of magnitude. Additionally, the marine environment provides an important source of new data. There are vast swaths of flowslide-prone, open slopes such as on continental margins, fjordal valleys, and volcanic island slopes, subject to frequent environmental triggers such as wave action and seismic activity. Additionally, the depositional setting of the marine environment often leaves loose, contractive soils, and the saturation criterion for liquefaction is met by default. Finally, gentle marine topography leaves most submarine slides unequivocally unobstructed, which is rarely, if ever, the case in subaerial flowslides.

3.5.4 Sources of uncertainty

Although probabilistic, empirical runout relationships such as the one presented here are easy to integrate into landslide hazard and risk assessments (e.g. Whittall, 2015) and demonstrate that the recent Oso Flowslide runout was not extreme, caution must be taken in adopting this and similar models in practice. I note the following weaknesses of regression-based runout relationships and this work in particular:

1.) Inherent in using empirical landslide runout relationships for forward prediction is the necessity of estimating the input parameter—typically volume—pre-failure. However, failing volume is rarely constrained except in the case of slow-developing failures which provide surficial expressions of failure planes, such as tension cracks and flank shear zones.

2.) Similarly, predictive use of the relationship presented in **Equation 3.2** requires a reliable evaluation of flow liquefaction susceptibility. Some material- and setting-based criteria exist (Davies et al., 2002; Hunter and Fell, 2001; McKenna et al., 2012; 2014), but this remains an active field of study.

3.) Although effort was made to collect data from a wide range of settings, the inventory presented here is dominated by small-volume, localized events, particularly those in the Swiss Alps and Hong Kong. The site-specific influence of these events is unquantified. This bias is a function of the data currently available but will decrease as more inventories are created and published.

4.) Although the relationship presented here has a strong coefficient of determination (over 90% of the variation in runout length is explained by volume alone), it is notable that over one order of magnitude in runout length exists between the 10th and 90th percentiles of runout exceedance. Conservative assumptions of acceptable

runout exceedance using this relationship may produce overconservative hillslope-toe setbacks depending on local conditions.

Recognizing these limitations, I suggest that empirical runout relationships, such as that presented here, are most useful for regional scale or first-pass runout assessments.

3.5.5 Utility for developing landslide management policies

As human development spreads into mountainous, geologically-hazardous regions, policy makers are confronted with the need to regulate land use to protect both the natural environments and humans. However, the scientific tools necessary to create robust and enforceable policies are often not available, actionable, politically and economically feasible, or sufficiently compelling to unite different stakeholders (Mills et al., 2008; Copsey, 2002; Schuster and Kockleman, 1996). This has been the case for landslide-related land use regulation, which commonly omits the consideration of landslide runout due to a lack of clear scientific guidance for scale-appropriate landslide runout analyses. The empirical tool presented in this chapter provides a transferrable, rapid method of preliminary landslide runout hazard zoning that does not require extensive local calibration or prohibitively intensive computation. Additionally, it may be easily coupled with existing methods of assessing potential landslide stability, size, and frequency for rapid, regional scale risk assessment.

In an ideal world, scientists could provide policy makers with perfect information about landslide hazards, precisely delineating dangerous areas and regulating anthropogenic activity. However,

nature is not so clear, and geologic hazards are stochastic. Simultaneously, individual freedom, human expansion, and economic growth require that some level of geologic risk is accepted in new development. Limitations notwithstanding, I believe that empirical runout relationships such as that presented in this chapter can fill a critical gap in the resources available to practitioners responsible for land use decisions. Empirically-based runout relationships can be rapidly applied across large regions in a GIS framework. Additionally, inherent scatter allows for uncertainty to be quantified probabilistically.

References

Aas, G. (1981). The stability of natural slopes in quick clays. *Proc. Int. Conf. Soil Mechanics and Foundation Engineering*. 3, 333-38.

Baum, R., Chleborad, A., Schuster, R. (1998). Landslides triggered by the winter 1996-97 storms in the Puget lowland, Washington. *USGS Open-File Report 98-239*. Reston, VA: U.S. Geological Survey.

Baum, R., Savage, W., Godt, J. (2008). TRIGRS—A Fortran program for transient rainfall infiltration and grid-based regional slope-stability analysis, version 2.0. *Open-File Report 2008-1159*. Reston, VA: United States Geological Survey

Beven, K., Kirkby, M. (1979). A physically based, variable contributing area model of basin hydrology. *Hydrological Sci. Bull.*, 24, 43-69. https://doi.org/10.1080/02626667909491834

Bezerra, F., da Fonseca, V., Vita-Finzi, C., Lima-Filho, F., Saadi, A. (2005). Liquefaction-induced structures in quaternary alluvial gravels and gravelly sediments, NE Brazil. *Eng. Geol.*, 76, 191-208. https://doi.org/10.1016/j.enggeo.2004.07.007

Booth, A., LaHusen, S., Duvall, A., Montgomery, D. (2017). Holocene history of deep-seated landsliding in the North Fork Stillaguamish River valley from surface roughness analysis, radiocarbon dating, and numerical landscape evolution modeling. *J. Geophys. Res. Earth Surf.*, 122, 456-472. https://doi.org/10.1002/2016JF003934

Bowman, E., and Take, W. (2015). The runout of chalk cliff collapses in England and France—case studies and physical model experiments. *Landslides*. 12, 225-239. https://doi.org/10.1007/s10346-014-0472-2

Calhoun, N. (2015). LiDAR and geomorphic characteristics of landslide-induced liquefaction deposits in the eastern Swiss Alps. (*masters thesis*). Burnaby, BC: Simon Fraser University.

California Geological Survey. (2002). Earthquake zones of required investigation: Pitas Point Quadrangle. *California Geological Survey Geologic Information and Publications*. Sacramento: California Geological Survey.

Cannon, S., DeGraff, J. (2009). The increasing wildfire and post-fire debris-flow threat in Western USA, and implications for consequences of climate change. In: K. Sassa, P. Canuti (*Eds*.) *Landslides—Disaster Risk Reduction*. Berlin: Springer-Verlag.

Cascini, L., Bonnard, C., Corominas, J., Jibson, R., Montero-Olarte, J. (2005). Landslide hazard and risk zoning for urban planning and development. In: O. Hungr, R. Fell, R. Couture, E. Eberhardt (*Eds*.) *Landslide Risk Management, Proc. Int. Conf. Landslide Risk Management, Vancouver, Canada*. London: A.A. Balkema Publishers.

Cascini, L., Cuomo, S., Pastor, M., Sacco, C. (2013). Modelling the post-failure stage of rainfall-induced landslides of the flow type. *Can. Geotech. J.,* 50, 924-34. https://doi.org/10.1139/cgj-2012-0375

Copsey, A. (1999). Including best available science in the designation and protection of critical areas under the growth management act. *Seattle U. L. Review*, 23, 97-143.

Copsey, A. (2002). *The designation and protection of critical areas under the Growth Management Act*. Office of the Attorney General. Olympia: State of Washington

Corominas, J. (1996). The angle of reach as a mobility index for small and large landslides. *Can. Geotech. J.*, 33, 260-71. https://doi.org/10.1139/t96-005

Crozier, M. (1986). *Landslides: Causes, consequences, and environments*. London: Croom Helm.
Cruden, D., Varnes, D. (1996). Landslide types and processes. In: K. Turner and R. Schuster (*Eds*.) *Landslides: Investigation and Mitigation*. Washington: Transportation Research Board.
Cui, Y., Cheng, D., Choi, C., Jin, W., Lei, Y., Kargel, J. (2019). The cost of rapid and haphazard urbanization: Lessons learned from the Freetown landslide disaster. *Landslides*, 16, 1167-1176. https://doi.org/10.1007/s10346-019-01167-x
Davies, M. McRoberts, E., Martin, T. (2002). Static liquefaction of tailings—fundamentals and case histories. *Proc. Tailings Dams 2002*. ASDSO/USCOLD, Las Vegas.
Davies, T. (1982). Spreading of rock avalanche debris by mechanical fluidization. *Rock Mech*., 15, 9-24. https://doi.org/10.1007/BF01239474
Dowling, C., Santi, P. (2014). Debris flows and their toll on human life: a global analysis of debris-flow fatalities from 1950 to 2011. *Nat. Hazards*, 71, 203-227. https://doi.org/10.1007/s11069-013-0907-4
Dufresne, A. (2014). An overview of rock avalanche-substrate interactions. *Proc. World Landslide Forum 3*, Beijing, 2-6 June 2014.
Dufresne, A., Davis, T. (2009). Longitudinal ridges in mass movement deposits. *Geomorphology*, 105, 171-181. https://doi.org/10.1016/j.geomorph.2008.09.009
Edgers, L. and Karlsrud, K. (1982). Soil flows generated by submarine slides—case studies and consequences. In: J. Connor, C. Chryssostomidis (*Eds*.) *Proceedings of the 3rd International Conference on the Behavior of Offshore Structures, Massachusetts Institute of Technology, Cambridge, Mass*. New York: Hemisphere Publishing Corporation.
Ellen, S., Cannon, S., Reneau, S. (1988). Distribution of debris flows in Marin County. In: S. Ellen, G. Wieczorek (*Eds*.) *Landslides, floods, and marine effects of the storm of January 3-5, 1982, in the San Francisco Bay region, California*. U.S. Geological Survey Professional Paper 1434. Washington: United States Government Printing Office.
Ellen, S., Fleming, R. (1987). Mobilization of debris flows from soil slips, San Francisco Bay region, California. *Rev. Eng. Geol.*, 7, 31-40.
Embley, R. (1976). New evidence for occurrence of debris flow deposits in the deep sea. *Geology*, 4, 371-374. https://doi.org/10.1130/0091-7613(1976)4<371:NEFOOD>2.0.CO;2
Evans, M., Seed, H. (1987). Undrained cyclic triaxial testing of gravels—the effect of membrane compliance. *Earthquake Engineering Research Center Report No. UCB/EERC-87/08*. Berkeley, CA: University of California.
Fell, R., Corominas, J., Bonnard, C., Cascini, L., Leroi, E., Savage, W. (2008). Guidelines for landslide susceptibility, hazard and risk zoning for land use planning. *Eng. Geol.*, 102, 85-98. https://doi.org/10.1016/j.enggeo.2008.03.022
Finlay, P., Mostyn, G., Fell, R. (1999). Landslide risk assessment: Prediction of travel distance. *Can. Geotech. J*., 36, 556-562. https://doi.org/10.1139/t99-012
Fleming, R., Ellen, S., Algus, M. (1989). Transformation of dilative and contractive landslide debris into debris flows—an example from Marin County, California. *Eng. Geol*., 27, 201-223. https://doi.org/10.1016/0013-7952(89)90034-3
Fletcher, L., Hungr, O., and Evans, S. (2002). Contrasting failure behavior of two large landslides in clay and silt. *Can. Geotech. J*., 39, 46-62. https://doi.org/10.1139/t01-079

Gabet, E., Mudd, S. (2006). The mobilization of debris flows from shallow landslides. *Geomorphology*, 74, 207-218. https://doi.org/10.1016/j.geomorph.2005.08.013

Garcia-Delgado, H., Machuca, S., Medina, E. (2019). Dynamic and geomorphic characterizations of the Mocoa debris flow (March 31, 2017, Putumayo Department, southern Colombia). *Landslides*, 16, 597-609. https://doi.org/10.1007/s10346-018-01121-3

Geertsema, M., Clague, J., Schwab, J., Evans, S. (2006). An overview of recent large catastrophic landslides in northern British Columbia, Canada. *Eng. Geol*., 83, 120-143. https://doi.org/10.1016/j.enggeo.2005.06.028

Goldberg, S. (2006). Falling into the Pacific: California landslides and land use controls. *S. Cal. Rev. L. & Social Justice*, 16, 95-161.

Golder Associates Limited. (1995). Mined rock and overburden piles: runout characteristics of debris from dump failures in mountainous terrain: Stage 2: analysis, modelling and prediction. *Interim Report, Report No. 932-1493*. Prepared in association with O. Hungr Geotechnical Research Ltd. British Columbia Mine Waste Rock Pile Research Committee and CANMET. Contract No. 23440-0-9198-X86.

Grabs, T., Seibert, J., Bishop, K., Laudon, H. (2009). Modeling spatial patterns of saturated areas: A comparison of the topographic wetness index and a dynamic distributed model. *J. Hydrology*, 373, 15-23. https://doi.org/10.1016/j.jhydrol.2009.03.031

Guo, C., Zhang, Y., Montgomery, D., Du, Y., Zhang, G., Wang, S. (2016). How unusual is the long-runout of the earthquake-triggered giant Luanshibao landslide, Tibetan Plateau, China? *Geomorphology*, 259, 145-54. https://doi.org/10.1016/j.geomorph.2016.02.013

Guo, D., Hamada, M., He, C., Wang, Y., Zou, Y. (2014). An empirical model for landslide travel distance prediction in Wenchuan earthquake area. *Landslides*. 11. 281-91. https://doi.org/10.1007/s10346-013-0444-y

Hammond, C., Hall, D., Miller, S., Swetik, P. (1992). Level I stability analysis (LISA) documentation for version 2.0. *General Technical Report INT-285*. Intermountain Research Station, United States Department of Agriculture.

Hampton, M., Lee, H., Locat, J. (1996). Submarine landslides. *Rev. of Geophy*., 34, 33-59. https://doi.org/10.1029/95RG03287

Haneberg, W. (2007). PISA-m: Map-based probabilistic infinite slope analysis. *Version 1.0.1 User Manual*. Seattle: Haneberg GeoScience.

Harp, E., Chleborad, A., Schuster, R., Cannon, S., Reid, M., Wilson, R. (1996). Landslides and landslide hazards in Washington State due to February 5-9, 1996 storm. *U.S. Geological Survey Administrative Report to the Federal Emergency Management Agency*. Reston, VA: U.S. Geological Survey.

Harp, E., Reid, M., Michael, J. (2004). Hazard analysis of landslides triggered by Typhoon Chata'an on July 2, 2002, in Chuuk State, Federated States of Micronesia. *USGS Open-File Report 2004-1348*. Reston, VA: U.S. Geological Survey.

Harp, E., Wells, W., Sarmiento, J. (1990). Pore pressure response during failure in soils. *GSA Bull.*, 102, 428-438. https://doi.org/10.1130/0016-7606(1990)102<0428:PPRDFI>2.3.CO;2

Heim, A. (1932). *Landslides and human lives (Bergsturz und menschenleben)*. Trans. N. Skermer. BiTech Pub, Vancouver, B.C.

Howard, K. (1973). Avalanche mode of motion: Implications from lunar examples. *Science*, 180, 1052-1055. https://doi.org/10.1126/science.180.4090.1052

Hsu, K. (1975). Catastrophic debris streams (sturzstroms) generated by rockfalls. GSA Bull., 86. 129-140. https://doi.org/10.1130/0016-7606(1975)86<129:CDSSGB>2.0.CO;2

Hungr, O. (1990). Mobility of rock avalanches. *Report of the National Research Institute for Earth Science and Disaster Prevention*. 46, 11-20.

Hungr, O. (2016). A review of landslide hazard and risk assessment methodology. In: Aversa et al. (*Eds*.) *Landslides and Engineered Slopes: Experience, Theory and Practice*. Rome: Associazione Geotecnica Italiana

Hungr, O., Clague, J., Morgenstern, N., VanDine, D., Stadel, D. (2016). A review of landslide risk acceptability practices in various countries. In: Aversa et al. (*Eds*.) *Landslides and Engineered Slopes: Experience, Theory and Practice*. Rome: Associazione Geotecnica Italiana

Hungr, O., Evans, S. (2004). Entrainment of debris in rock avalanches: An analysis of a long run-out mechanism. *GSA Bull.*, 116, 1240-1252. https://doi.org/10.1130/B25362.1

Hungr, O., Leroueil, S., and Picarelli, L. (2014). The Varnes classification of landslide types, an update. *Landslides*, 11, 167-94. https://doi.org/10.1007/s10346-013-0436-y

Hunter, G., Fell, R. (2001). "Rapid" failure of soil slopes. *UNICIV Report R-400*. The University of New South Wales, School of Civil and Environmental Engineering, Sydney, Australia.

Hunter, G., Fell, R. (2003). Travel distance angle for "rapid" landslides in constructed and natural soil slopes. *Can. Geotech. J*., 40, 1123-1141.

Hurlimann, M., Coviello, V., Bel, C., Guo, X., Berti, M., Graf, C., Hubl, J., Miyata, S., Smith, J., Yin, H-Y. (2019). Debris-flow monitoring and warning: Review and examples. *Earth-Science Rev.*, 199, https://doi.org/10.1016/j.earscirev.2019.102981

Hutchinson, J. (1988). General report: morphological and geotechnical parameters of landslides in relation to geology and hydrogeology. In: C. Bonnard (*Ed*.) *Proceedings of the 5th International Symposium on Landslides, Vol. 1*. Lausanne, Switzerland. Rotterdam: A.A. Balkema.

Hutchinson, J. (2002). Chalk flows from the coastal cliffs of northwest England. *Rev. in Eng. Geol.*, 25, 257-302.

Ishihara, K. (1984). Post-earthquake failure of a tailings dam due to liquefaction of the pond deposit. *Int. Conf. Case Histories in Geotechnical Engineering*, 3, 1129-1143.

Ishihara, K., Okusa, S., Oyagi, N., Ischuk, A. (1990). Liquefaction-induced flow slide in the collapsible loess deposit in Soviet Tajik. *Soils and Foundations*, 30, 73-89. https://doi.org/10.3208/sandf1972.30.4_73

Ishihara, K., Troncoso, J., Kawase, Y., Takahashi, Y. (1980). Cyclic strength characteristics of tailings materials. *Soils and Foundations*, 20, 127-142. https://doi.org/10.3208/sandf1972.20.4_127

Iverson, R., George, D. (2016). Modelling landslide liquefaction, mobility bifurcation and the dynamics of the 2014 Oso disaster. *Geotechnique*, 66, 175-187. https://doi.org/10.1680/jgeot.15.LM.004

Iverson, R., George, D., Allstadt, K., Reid, M., Collins, B., Vallance, J., Schilling, S., Godt, J., Cannon, C., Magirl, C., Baum, R., Coe, J., Schulz, W., Bower, J. (2015). Landslide mobility and hazards: implications of the 2014 Oso disaster. *Earth and Planetary Science Letters,* 412, 197-208. https://doi.org/10.1016/j.epsl.2014.12.020

Iverson, R., Reid, M., LaHusen, R. (1997). Debris-flow mobilization from landslides. *Annual Rev. Earth Planet. Sci*., 25, 85-138.

Jakob, M. Hungr, O. (2005) Introduction. In: M. Jakob, O. Hungr (*Eds*.) *Debris Flow Hazards and Related Phenomena*. Chichester, UK: Praxis Publishing.

Jibson, R. (2005). Landslide hazards at La Conchita, California. *Open-File Report 2005-1067*. Reston, VA: United States Geological Survey. Available at: https://pubs.usgs.gov/of/2005/1067/

Keaton, J., Wartman, J., Anderson, S., Benoit, J., daLaChapelle, J., Gilbert, R., Montgomery, D. (2014). The 22 March 2014 Oso landslide, Snohomish County, Washington. *Geotechnical Extreme Events Reconnaissance Report*, GEER Association. Available at: http://www.geerassociation.org/index.php/component/geer_reports/?view=geerreports&id=30

Koppejan, A., Wamelen, B., Weinberg, L. (1948). Coastal flow slides in the Dutch province of Zeeland. *Proc. 2nd Int. Conf. Soil Mech*., Rotterdam.

LaHusen, S. (2019). Landslides in Cascadia: Using geochronometry and spatial analysis to understand the timing, triggering and spatial distribution of slope failures in the Pacific Northwest United States. (*doctoral dissertation*). Seattle: University of Washington.

LaHusen, S., Duvall, A., Booth, A., Montgomery, D. (2016). Surface roughness dating of long-runout landslides near Oso, Washington (USA), reveals persistent postglacial hillslope instability. *Geology*, 44, 111-114. https://doi.org/10.1130/G37267.1

Laval, A., Cremer, M., Beghin, P., Ravenne, C. (1988). Density surges: Two-dimensional experiments. *Sedimentology*, 35, 73-84. https://doi.org/10.1111/j.1365-3091.1988.tb00905.x

Legros, F. (2002). The mobility of long-runout landslides. *Eng. Geol*., 63, 301-31. https://doi.org/10.1016/S0013-7952(01)00090-4

Li, T. (1983). A mathematical model for predicting the extent of a major rockfall. *Zeitschrift fur Geomorphologie*. 27, 473-482.

Locat, J., Lee, H. (2002). Submarine landslides: Advances and challenges. *Can. Geotech. J*., 39, 193-212. https://doi.org/10.1139/t01-089

Lockyear, R. (2018). Identification of parameters for predicting long-runout landslides in the western United States. (*masters thesis*). Golden, CO: Colorado School of Mines.

Lombardo, K., Boggs, J., Boudreau, J. , Chiles, P., Erickson, J., Gerstel, W., Montgomery, D., Shipman, L., Radcliff-Sinclair, R., Strachan, S., Sugimura, D., Trimm, B. (2014). SR 530 Landslide commission: Final Report. SR 530 Landslide Commission, Report submitted to Washington State Governor Jay Inslee, 15 December 2014.

Machan, G., Hammond, C., Westover, T. (2018). Rattlesnake Hills landslide: Overview and monitoring. *Proceedings of the 69th Highway Geology Symposium*. Portland Maine, 10-13 September 2018.

Martha, T., Roy, P., Govindharaj, K., Kumar, K., Diwakar, P., Dadhwal, V. (2015). Landslides triggered by the June 2013 extreme rainfall event in parts of Uttarakhand state, India. *Landslides*, 12, 135-146. https://doi.org/10.1007/s10346-014-0540-7

McDougall, S. (2017). 2014 Canadian geotechnical colloquium: Landslide runout analysis – current practice and challenges. *Can. Geotech. J*., 54, 605-620. https://doi.org/10.1139/cgj-2016-0104

McDougall, S., McKinnon, M., and Hungr, O. (2012). Developments in landslide runout prediction. In: J. Clague, D. Stead (*Eds*.) *Landslides: Types, Mechanisms and Modelling*. Cambridge: Cambridge University Press.

McKenna, J., Santi, P., Amblard, X., Negri, J. (2012). Effects of soil-engineering properties on the failure mode of shallow landslides. *Landslides*, 9, 215-228. https://doi.org/10.1007/s10346-011-0295-3

McKenna, J., Santi, P., Baum, R. (2014). An experimental method for testing soil mobility of landslides. *GSA Bull*., 126, 271-288. https://doi.org/10.1130/B30870.1

McSaveney, M. (1975). The Sherman Glacier rock avalanche of 1964: Its emplacement and subsequent effects on the glacier beneath it. (*doctoral dissertation*). Columbus, OH: Ohio State University.

Melosh, H. (1979). Acoustic fluidization: a new geologic process? *J. of Geophys. Res*., 84, 7513-7520. https://doi.org/10.1029/JB084iB13p07513

Mergili, M., Marchesini, I., Alvioli, M., Metz, M., Schneider-Muntau, B., Rossi, M., Guzzetti, F. (2014). A strategy for GIS-based 3-D slope stability modelling over large areas. *Geosci. Model Dev*., 7, 2969-2982. https://doi.org/10.5194/gmd-7-2969-2014

Meyerhof, G. (1957). The mechanism of flow slides in cohesive soils. *Geotechnique*. 7, 41-49. https://doi.org/10.1680/geot.1957.7.1.41

Miller, L., Miller, D. (1999). Hazel/Gold Basin landslides: Geomorphic review draft report. Seattle: M2 Environmental Services. Available at: http://www.netmaptools.org/Pages/Hazel/Hazel_GoldBasin.pdf

Mills, A., Francis, T., Shandas, V., Whittaker, K, Graybill, J. (2008). Using best available science to protect critical areas in Washington state: Challenges and barriers to planners. *Urban Ecosyst*., https://doi.org/10.1007/s11252-008-0071-x

Mirus, B., Smith, J., Baum, R. (2017). Hydrologic impacts of landslide disturbances: Implications for remobilization and hazard persistence. *Water Resources Research*, 53, 8250-8265. https://doi.org/10.1002/2017WR020842

Miscolta-Cameron, A. (2016). Science and strategy: How scientific and technical information are used in disputes over landslide regulations in Seattle, WA. (*masters thesis*). Bellingham, WA: Western Washington University

Mohrig, D., Elverhoi, A., Parker, G. (1999). Experiments on the relative mobility of muddy subaqueous and subaerial debris flows, and their capacity to remobilize antecedent deposits. *Marine Geol*., 154, 117-129. https://doi.org/10.1016/S0025-3227(98)00107-8

Montgomery, D., Dietrich, W. (1994). A physically based model for the topographic control on shallow landsliding. *Water Resources Research*, 30, 1153-1171. https://doi.org/10.1029/93WR02979

Nicoletti, P. and Sorriso-Valvo, M. (1991). Geomorphic controls of the shape and mobility of rock avalanches. *GSA Bull*., 103, 1365-1373. https://doi.org/10.1130/0016-7606(1991)103<1365:GCOTSA>2.3.CO;2

Niehaus, R. (2018). The economic impacts of the Montecito mudslides: A preliminary assessment. Santa Barbara: Robert D. Niehaus, Inc. Available at: https://www.rdniehaus.com/app/uploads/2019/08/RDN_Montecito_Mudslides_Impacts-1.pdf

Olschansky, R. (1998). Regulation of hillside development in the United States. *Environ. Management*, 22, 383-392. https://doi.org/10.1007/s002679900113

Olschansky, R., Rogers, J. (1987). Unstable ground: Landslide policy in the United States. *Ecology Law Quarterly*, 13, 939-1006.

Pack, R., Tarboton, D., Goodwin, C. (1998). The SINMAP approach to terrain stability mapping. *8th Congress Int. Assn. Engineering Geology*, Vancouver, BC, Canada, 21-25 September 1998.

Perkins, J., Reid, M., Schmidt, K. (2017). Control of landslide volume and hazard by glacial stratigraphic architecture, northwest Washington State, USA. *Geology*, 45, 1139-1142. https://doi.org/10.1130/G39691.1

Petley, D. (2019). "The ten most important landslide events of 2018." The Landslide Blog. Available at: https://blogs.agu.org/landslideblog/2019/01/04/important-landslide-events-of-2018/. Accessed June 2020.

Pollock, W., Grant, A., Wartman, J., Abou-Jaoude, G. (2019). Multimodal method for landslide risk analysis. *MethodsX*, 6, 827-836. https://doi.org/10.1016/j.mex.2019.04.012

Porter, S., Swanson, T. (1998). Radiocarbon age constraints on rates of advance and retreat of the Puget Lobe of the Cordilleran ice sheet during the last glaciation. *Quaternary Res*., 50, 205-213. https://doi.org/10.1006/qres.1998.2004

Reid, M., Christian, S., Brien, D., Henderson, S. (2015). Scoops3D—Software to analyze three-dimensional slope stability throughout a digital landscape. Techniques and Methods 14-A1; Section A, Modeling Methods; Book 14, Landslide and Debris-Flow Assessment. Reston, VA: United States Geological Survey

Roberts, N., Evans, S. (2013). The gigantic Seymareh (Saidmarreh) rock avalanche, Zagros Fold—Thrust Belt, Iran. *J. Geological Soc. London*, 170, 685-700.

Scheidegger, A. (1973). On the prediction of the reach and velocity of catastrophic landslides. *Rock Mech.*, 5, 231-236. https://doi.org/10.1007/BF01301796

Schuster, R., Highland, L. (2001). Socioeconomic and environmental impacts of landslides in the western hemisphere. U.S. Geological Survey Open-File Report 01-276.

Schuster, R., Kockelman, W. (1996). Principles of landslide hazard reduction. In: K. Turner, R. Schuster (*Eds*.) *Landslides: Investigation and Mitigation*. Washington: Transportation Research Board.

Shaller, P., (1991). Analysis of a large moist landslide, Lost River Range, Idaho, U.S.A. *Can. Geotech. J*., 28, 584-600. https://doi.org/10.1139/t91-073

Shipman, H. (2001). Coastal landsliding on Puget Sound: A review of landslides occurring between 1996 and 1999. *Report #01-06-019*. Washington State Department of Ecology. Available at: https://fortress.wa.gov/ecy/publications/SummaryPages/0106019.html

Silvis, F., de Groot, M. (1995). Flow slides in the Netherlands: Experience and engineering practice. *Can. Geotech. J*., 32, 1086-1092. https://doi.org/10.1139/t95-107

Skempton, A., Hutchinson, J. (1969). Stability of natural slopes and embankment foundations. *Proc. 7th Int. Conf. Soil Mechanics and Foundation Engineering*, Sociedad Mexicana de Mecana de Suelos, Mexico City.

Snohomish County (2014). REVISED Options for landslide regulations: Setbacks and slope height. *Memorandum, May 2, 2014*. Everett, WA: Snohomish County Council Office.

Snohomish County. (2007). Landslide, erosion, and volcanic hazards. Snohomish County Planning and Development Services. Available at: https://snohomishcountywa.gov/DocumentCenter/View/8247/Landslide-Erosion-and-Volcanis-Hazards-Countrywide?bidId=

Snohomish County. (2015). Hazard mitigation plan: September 2015 update. Snohomish County Emergency Management. Available at: https://snohomishcountywa.gov/2429/Hazard-Mitigation-Plan

Stark, T., Baghdady, A., Hungr, O., Aaron, J. (2017). Case study: Oso, Washington, landslide of March 22, 2014—Material properties and failure mechanism. *J. Geotech. Geoenviron. Eng*., 143. https://doi.org/10.1061/(ASCE)GT.1943-5606.0001615

Tang, C., Zhu, J., Chang, M., Ding, J., Qi, X. (2012). An empirical-statistical model for predicting debris-flow runout zones in the Wenchuan earthquake area. *Quat. Int*., 250, 63-73.

van Westen, C., van Asch, T., Soeters, R. (2006). Landslide hazard and risk zonation—why is it still so difficult? *Bulletin of Engineering Geology and the Environment*, 65, 167-184. https://doi.org/10.1007/s10064-005-0023-0

Varnes, D. (1958). Landslide types and processes. In: E. Eckel (*Ed*.) *Special Report 29: Landslides and Engineering Practice*. Washington: Highway Research Board, National Research Council.

Varnes, D. (1978). Slope movement types and processes. In: R. Schuster, R. Krizek (*Eds*.) *Special Report 176: Landslides: Analysis and Control.* Washington: Transportation Research Board, National Research Council.

Wartman, J., Montgomery, D., Anderson, S., Keaton, J., Benoit, J., dela Chapelle, J., Gilbert, R. (2016). The 22 March 2014 Oso landslide, Washington, USA. *Geomorphology*, 253, 275-288. http://dx.doi.org/10.1016/j.geomorph.2015.10.022

Washington Department of Natural Resources (DNR). (2014). Significant deep-seated landslides in Washington State—1984 to 2014. Olympia: Washington Department of Natural Resources. Available at: https://www.dnr.wa.gov/publications/ger_list_large_landslides.pdf?yy063v

White, J., Morgan, M., Berry, K. (2015). The West Salt Creek Landslide: A Catastrophic Rockslide and Rock/Debris Avalanche in Mesa County, Colorado. *Colorado Geological Survey Bulletin 55*. Golden, CO: Colorado Geological Survey.

Whittall, J. (2015). Runout exceedance prediction for open pit slope failures. (*masters thesis*). Vancouver: University of British Columbia.

Whittall, J., Eberhardt, E., McDougall, S. (2017). Runout analysis and mobility observations for large open pit slope failures. *Can. Geotech. J*., 54, 373-391. https://doi.org/10.1139/cgj-2016-0255

Yegian, M., Ghahraman, V., and Harutiunyan, R. (1994). Liquefaction and Embankment Failure Case Histories, 1988 Armenia Earthquake. *J. Geotech. Eng*., 120, 581-96. https://doi.org/10.1061/(ASCE)0733-9410(1994)120:3(581)

Yin, Y., Li, B., Wang, W., Zhan, L., Xue, Q., Gao, Y., Zhang, N., Chen, H., Liu, T., Li, A. (2016). Mechanism of the December 2015 catastrophic landslide at the Shenzhen landfill and controlling geotechnical risks of urbanization. *Engineering*, 2, 230-49. https://doi.org/10.1016/J.ENG.2016.02.005

Zhang, J., Gurung, D., Liu, R., Murthy, M., Su, F. (2015). Abe Barek landslide and landslide susceptibility assessment in Badakhshan Province, Afghanistan. *Landslides*. 12. 597-609. https://doi.org/10.1007/s10346-015-0558-5

Chapter 4 – Human vulnerability to landslides

The content of this chapter is submitted for publication as:

Pollock, W. and Wartman, J. Human vulnerability to landslides.

4.1 Introduction

Due to their high velocity, large impact pressures, and ability to run out long distances over flat terrain, rapid landslides are a particularly devastating threat to human health. From 2004 – 2016 landslides have caused an annual average of over 4000 deaths worldwide, and in the United States alone, they are estimated to kill 25 – 50 people each year (Froude and Petley, 2018; Schuster and Highland, 2001). Understanding human vulnerability to landslides is essential for predicting and preventing human loss of life. While much scholarship has been devoted to quantifying the physical vulnerability of buildings to landslides, no comparable work has been done to quantify human vulnerability for use in risk assessment. The few methods that exist rely on expert judgment and are not easily transferable (AGS, 2007; Corominas et al., 2014; Lee and Jones, 2014). Furthermore, these methods only inform the potential for human loss and do not explore the underlying causes of human mortality, leaving scientists, decision-makers, emergency responders, and the public without evidence-based strategies for maximizing survival rates in landslides (Kennedy et al., 2015). In this paper, we address this void by (1) presenting a new landslide fatality database; (2) creating an empirical human vulnerability relationship to estimate an individual's probability of death; (3) detailing the human characteristics, behaviors, and settings that contribute to landslide mortality; and (4) proposing a suite of evidence-based, actionable strategies to minimize personal landslide risk.

4.2 Background

4.2.1 Landslide modes

The term “landslide” has many meanings in academic and colloquial usage. In this work, we focus on rapid landslides, having velocities of > 5 m/s (Cruden and Varnes, 1996), as these pose the greatest threat to human life (Petley, 2010b). We do not explicitly filter by material or mode of landslide as media sources rarely contain sufficient description to do so, but all the events considered here fall within the categories of debris flow, flowslide, rock/debris avalanche, and debris slide (Hungr et al., 2014), with the majority being highly fluidized, channelized debris flows spreading onto populated depositional fans.

4.2.2 Vulnerability

Vulnerability is the potential to suffer harm from a human perspective. The natural sciences focus on physical vulnerability, which quantitatively describes the degree or probability of tangible damage, injuries, or deaths on a scale from 0 (none) to 1 (complete). Physical vulnerability is a fundamental component of risk analysis (Fell et al., 2005; Papathoma-Kohle et al., 2016). A recent emphasis on vulnerability—rather than hazard—as the primary driver in environmental disasters has prompted numerous efforts to quantify human and infrastructural vulnerability to different natural hazards such as snow avalanches (Wilhelm, 1998; Jonasson et al, 1999; Keylock and Barbolini, 2001; Barbolini et al., 2004a, b), tsunamis (Reese et al., 2007; Omira et al., 2009; Papathoma et al., 2003; Domney-Howes and Papathoma, 2006), floods

(Steinfuhrer et al., 2009; Wallingford et al., 2009), hurricanes (Pita et al., 2011; Davidson et al., 2003), and earthquakes (Menoni et al., 2002; Rashed and Weeks, 2003; Spence et al., 2008).

Landslide vulnerability may be quantified through heuristic, analytical, or data-driven methods (Corominas et al., 2014). Heuristic methods typically provide discrete vulnerability values for a range of process intensities, based on expert judgment (e.g. Glade, 2004; Finlay 1996; Jaiswal et al., 2011). Analytical methods use physical or conceptual models to link process intensity and vulnerability without requiring ex post data (e.g. Mavrouli and Corominas, 2010; Fotopoulou and Pitilakis, 2016; Uzielli et al., 2008). Data-driven methods typically involve back-analyzing empirical loss data to develop a mathematical relationship ("vulnerability curve") between process-intensity and vulnerability (e.g. Fuchs et al., 2019a; Peduto et al., 2017). While early risk analyses relied on heuristic vulnerability matrices, vulnerability curves have become popular among practitioners as they provide a direct, mathematical means through which to translate hazard to loss, and explicit model uncertainty may be incorporated into probabilistic analyses (Papathoma-Kohle et al., 2017).

4.2.3 Human vulnerability to landslides

The physical vulnerability of infrastructure to landslides has been the subject of an emerging body of data-driven studies and practical tools for practitioners (Papathoma-Kohle, 2015; Fuchs et al., 2019a; Massey et al., 2019). Although infrastructural losses are of secondary importance to the risk to humans themselves, research investigating the vulnerability of people to landslides is rare (Lin et al., 2017; Massey et al., 2019; Glade, 2003). The reasons for this are manifold.

Human casualties in landslides are often related to the collapse of occupied buildings and thus are indirect, a function of structural vulnerability (Jakob et al., 2012; Uzielli et al., 2008; Li et al., 2010). Human vulnerability also depends on human behavior, including factors that are difficult to measure, such as prior knowledge of hazards, situational awareness, and decision-making capability (Eidsvig et al., 2014). Human data is ephemeral and challenging to collect in the chaotic aftermath of a disaster. While damaged buildings are measurable weeks or months after an event, the people involved will often have relocated, been dispersed to hospitals, or be dead. Finally, ethical approval is required for human subjects research, presenting a further challenge to studies of human vulnerability. As a consequence, almost all existing methods of estimating human vulnerability rely on elements of expert judgement (AGS, 2007; Safeland, 2001; Corominas et al., 2014; Lee and Jones, 2014).

Many modern risk analyses utilize the semi-empirical estimates of human vulnerability from two place-based studies. Finlay (1996) compiled a database of 27 fatal or near-fatal landslides, primarily in Hong Kong. The database does not include the number of people exposed to each landslide, and thus, the probability of death or injury of an exposed individual cannot be directly estimated. Semi-empirical values of human vulnerability have been estimated from the Hong Kong data in an event tree and as a function of landslide volume (Finlay 1996; Moore et al., 2001; **Table 4.1**). Michael-Leiba et al. (2005) computed human vulnerability as the ratio of fatalities to building occupants in 24 landslides in the Australian landslide database, three of which involved fatalities. Based on these events, they produced an average human vulnerability of 0.1 for all landslides and recommend heuristically reducing this value to 0.05 to account for intrinsic under-representation of non-fatal landslides in the database (Michael-Leiba et al., 2005).

Most modern landslide risk assessments utilize the findings of these pioneering studies; however, the results may not be particularly transferable, as they are constrained by the limited types of landslides, process intensities, building stock, and socio-behavioral idiosyncrasies of the original study locations (Lee and Jones, 2014; AGS, 2007d). Furthermore, vulnerability estimates such as these only inform the potential for loss rather than strategies to reduce such losses (Papathoma-Kohle et al., 2015).

Table 4.1. Human vulnerability values for an indoor population derived from fatal landslide occurrences in Hong Kong (Finlay, 1996; Moore et al., 2001).

Case	**Recommended value**	**Range**	**Comments**
Building collapses	1.0	0.9 – 1.0	Death is almost certain
Building inundated with debris and person buried	1.0	0.8 – 1.0	Death is highly likely
Debris strikes building only	0.05	0 – 0.1	Very high chance of survival
Volume (m^3)	**Recommended value**		
50	0.0002		
100	0.006		
500	0.011		
1000	0.026		
2500	0.04		
5000	0.17		

4.2.4 Landslide mortality

Mortality, as defined by the medical profession, refers to the rate of death within a population. Here we adopt the term, using landslide mortality to refer not only to the rate of death in landslide incidents but also more generally to the contributing human factors and actions. Although landslide vulnerability is widely under-studied, the underlying causes of landslide mortality have rarely even been discussed in academic literature (Kennedy et al., 2015). A handful of studies describe the patterns of injury and death in landslides (Sheeju et al., 2019;

Langdon et al., 2019; Gueri and Perez, 1986; Homma et al., 2016; Pereira et al., 2013; Memchoubi et al., 2012). However, we are aware of only two studies that analyze the situations and behavior that contribute to these outcomes (Sanchez et al., 2009; Argrawal et al., 2013). In practical terms, this represents a critical gap in our understanding of the human consequences in landslides, leaving decision-makers, first responders, and at-risk citizens with little scientific guidance for reducing human losses.

4.2.5 The role of human behavior in landslide mortality

Ex post evidence shows that landslide damage to structures scales with the process intensity, measured as flow velocity, impact pressure, inundation depth or area, or failure volume (Papathoma-Kohle et al., 2015; Totschnig and Fuchs, 2013; Fuchs et al., 2007; Galli and Guzzetti, 2007). While the vulnerability of structures and the vulnerability of the people inside them are conceptually linked (Finlay, 1996; Du et al., 2013), the relationship between the two is unclear, and they may be dramatically different in similar processes (Fell, 1994). Uzielli et al. (2008) and Li et al. (2010) proposed smooth exponential relationships between structural and human vulnerability. Other researchers have suggested there is a process intensity threshold at which the probability of death of indoor populations dramatically increases due to common structural design elements. Debris intrusion through windows is credited with the exponential increase in building damage at debris heights of 1.0 – 1.7 m (Totschnig et al., 2011; Papathoma-Kohle et al., 2012, 2016), and Massey et al. (2019) noted that fatalities become more likely when inundation depths exceed the bottom window height (typically 1.0 – 1.4 m), evinced by three fatal landslides in New Zealand.

Finlay (1996) notes that indoor populations have high vulnerability (> 0.8) if they buried by intruding debris or if the building collapses. Functional destruction of masonry structures is estimated to occur at debris heights greater than 2.5 m (Akbas et al., 2009; Fuchs et al., 2019a; Quan Luna et al., 2011), while the lateral load-bearing capacity of a typical timber-frame wall is exceeded by debris heights of 1.4 – 1.6 m (Massey et al., 2019). In the 2018 Montecito, CA, debris flows, flow heights of > 1 m were associated with extensive to complete damage of structures (Kean et al., 2019).

Based on structural vulnerability, we would expect mortality approaching 100% once the structural resistance is exceeded. However, there are numerous cases of humans surviving large landslides even when inundation depths exceed 1 – 2 meters (e.g. Diver, 1999; Metivier-Hart, 2017). A direct relationship between structural and human vulnerability ignores the inherent differences in coping potential between individuals and the ability of humans to act to dynamically change their own vulnerability (Crozier and Glade, 2005). In this work, we test the idea that human behavior—rather than process intensity—governs landslide mortality over a range of process intensities.

4.3 Methods

4.3.1 Construction of the fatality database

We reviewed academic literature, government reports, news stories, survivor accounts, coroner reports, and legal filings to compile a database of landslide events that impacted occupied structures. The basic information required for inclusion in the database was the flow depth of debris at the structure, the number of occupants, and the outcome for the exposed individuals (survived or deceased). We recorded basic information about the landslide (date, time of day, mode of failure), structure (construction material, location), and individuals (age, gender). When available, we also used first or second-hand accounts to reconstruct individuals' prior knowledge of the threat, location in the structure, and behavior around the time of the impact, using proxies for deceased individuals (Sanchez et al., 2009; Staes et al., 1994; Yale et al., 2003). Proxies were survivors who were in or around the same residence as decedents at the time of impact. For deceased victims we compiled the cause of death when coroner reports were available. For survivors we recorded if they escaped on their own or were rescued by others and if rescued, the time of rescue and relation to the rescuer. We were unable to reconstruct complete information in all fields for all individuals. No direct human subjects research was performed as part of this work, and all sources are public record. Identifying information, even when publicly available, was anonymized to protect individuals' privacy. The database is provided in **Appendix 4.1**.

The influence of landslide inundation depth on the probability of death was examined through non-linear regression. Binary logistic regression was used to assess the impact of demographic,

situational, and behavioral factors on human mortality. The inclusion criteria introduce a non-random sampling bias, although it is not systematic for most variables. News reports that include inundation depth are infrequent unless the event is particularly noteworthy, such as cases of partial burial or dramatic rescues, or contains other human-interest elements. Thus we anticipate that extreme low- and high-intensity events are underrepresented. We do not believe the reporting bias systematically affects the results based on other factors such as age, time of day, structural material, etc.

4.3.2 Uncertainties related to post-event reconstruction

Reconstructing technical details of rapid, traumatic events, sometimes many years after they occurred, has many sources of uncertainty. We assigned qualitative levels of confidence (low, medium, high) to flow depth estimates based on the method through which they were produced.

Without photographic evidence during a landslide, flow depths are most reliably estimated from measuring mudlines. Such data is highly ephemeral and rarely collected in the chaos immediately following a large-scale disaster (Kean et al., 2019). In lieu of such data, post-event debris deposition depth can be used as a proxy for the flow depth (Fuchs et al., 2007; Akbas et al., 2009; Fuchs et al., 2019b). Although also altered by erosion, rescue operations, or recovery and rebuilding, landslide deposits may last months to years after an event and be measured in ground surveys or elevation differencing (e.g. Wartman et al., 2016). Where either of these methods was used, we categorized flow depth measurements as high quality. Estimates of flow depths based on witness recollections, especially when they were gauged using objects of known

height, were regarded as medium quality. We categorized as low quality the minority of cases in which flow height was approximated non-numerically, e.g., "chest high" or "waist high". In such cases, we must ask, "whose chest?" We used average biological measurements for the country of origin and gender of the victim to estimate the likely range of flow heights. This included cases in which victims were reported as being buried up to their chest (waist, neck, etc.), with the assumption that such approximations are only relevant to a standing (rather than prone) human.

Issues of scale limit the back-analysis of past events. At the scale of a community, a single flow depth may be associated with an entire structure (e.g., Kean et al., 2019). However, at the scale of a building, it is unlikely that all rooms will be inundated equally (Quan Luna et al., 2011). The disparity between the scale of reported flow depths (often for an entire structure) and the scale of exposed individuals (who may be anywhere within the structure, including on upper floors), adds further uncertainty to post-event analysis (Totschnig and Fuchs, 2013).

There is considerable variation between the reference objects from which inundation depth is measured in descriptive accounts. It may refer to the initial impact to the outside or inside of a structure, the maximum flow height on or above a person, the final burial depth of a victim or structure, or the debris deposition height within a destroyed building's footprint. The current variety and scarcity of data regarding landslide morbidity do not allow for these cases to be analyzed separately. We record how the inundation depth (flow or deposit) relative to a reference object (building or person) was estimated, but do not use this information any further

in the analysis. When referring to the landslide intensity, we use the generic term "inundation depth."

Finally, landslide events occur over a period of time. In many cases, the entire event may be over in a handful of seconds, while in others, such as extensive debris flows, the event may transition between multiple modes of mass-wasting over the course of hours (Hungr et al., 2014). In such cases, it is often impossible to attribute damage or fatalities to a single moment with singular, describable flow characteristics.

4.3.3 Vulnerability curves

Landslide vulnerability curves mathematically link relative damage from none (zero) to complete (one) to the process intensity for each element at risk (Ciurean et al., 2017). The production of robust landslide vulnerability curves is data-intensive, requiring extensive datasets of damage-intensity pairs for individual elements at risk (e.g., per building), making vulnerability curves rare and typically tied to a specific event and region (Papathoma-Kohle et al., 2015; Totschnig and Fuchs, 2013). Numerous proxies for process intensity have been used in vulnerability curves for physical infrastructure, such as landslide area (Galli and Guzzetti, 2007), momentum flux (Prieto et al., 2018), impact force or pressure (Zhang et al., 2018; Kang and Kim, 2016; Rheinberger et al., 2013), velocity (Kang and Kim, 2016; Quan Luna et al., 2011), volume (Winter et al., 2013), and deposit or flow height (Fuchs et al., 2007; Totschnig et al., 2011; Quan Luna et al., 2011; Totschnig and Fuchs, 2013; Ciurean et al., 2017). We adopted flow height, as

it is one of the most easily reconstructable landslide characteristic ex post facto and is relevant to a primary cause of death in landslides (suffocation due to burial).

In landslide risk analysis, human vulnerability may be expressed as the probability that an individual will be killed in a landslide (Corominas et al., 2014). The probability of death for an individual in a given structure can be calculated as the ratio of fatalities to occupants (Michael-Leiba et al., 2004):

$$P_D = \frac{number\ of\ fatalities}{number\ of\ occupants} \quad \textbf{(4.1)}$$

The basic mathematical requirements for a vulnerability curve are that it (1) must define vulnerability within the confined interval [0, 1], passing through the origin and (2) be monotonically increasing within the interval [0, + ∞) of the independent variable (Papathoma-Kohle et al., 2012; Ciurean et al., 2017). In light of these criteria, we chose a modified Weibull cumulative distribution as the underlying model to represent human vulnerability to landslides, of the form:

$$V = 1 - e^{-a * I^b} \quad \textbf{(4.2)}$$

where I is the landslide intensity measured as inundation depth (Totschnig et al., 2011; Fuchs et al., 2019b). We evaluate the goodness-of-fit of the proposed model based on the root mean squared error (RMSE). Some structural vulnerability studies provide a coefficient of determination (R^2) values to demonstrate the robustness of their vulnerability curve. We note that R^2 is an inadequate goodness-of-fit metric for nonlinear regression (Spiess et al., 2010), yet

we report pseudo R^2 values as a widely accepted point of comparison to prior vulnerability studies (Fuchs et al., 2019a).

4.4 Database

4.4.1 General statistics

Our database consists of 334 exposed individuals in 95 impacted buildings and 38 unique landslide events between 1887 – 2019. The gender distribution of exposed individuals is 44% male, 36% female, with the remainder unknown. Victim ages range from 4 months – 91 years with a mean of 36.4 ± 24.2 years. Inundation depths range from 0.2 – 11.3 m (8 in – 37 ft) with a mean of 2.8 ± 2.3 m. Fifty-seven percent of the inundation depths were deemed of "high" quality, 28% of "medium" quality, and 15% of "low" quality, reflecting the high proportion of cases which came from two well-studied landslide events in Washington and California. These two events, the 2014 SR 530 "Oso," Washington, flowslide, and the 2018 Montecito, California, debris flows, collectively comprise 39% of the individuals and 52% of the structures in our database. Forty-nine percent of all exposed individuals were killed, while 20% were rescued by others, and 28% escaped or self-rescued. In the remaining cases, all we know is that the individual survived.

4.4.2 Landslide location

Due to the specific inclusion criteria, the database is not representative of global landslide-human interactions and is subject to reporting bias based on the existence of English-language media accounts and academic studies. Most of our data comes from the United States, with 36% of total landslides events, 73% of impacted structures, and 75% of affected individuals, reflecting the limitations of an English-language search and the intense scrutiny of fatal landslides in the U.S. (Kirschbaum et al., 2010). Reporting bias is especially pronounced when considering countries by the United Nations threshold of economic development (United Nations, 2020). Economically developing countries represent 42% of events, 17% of structures, and 15% of individuals, although global databases indicate that these nations experience greater numbers of fatal landslides and overall fatalities than economically developed countries (Dowling and Santi, 2014; UNISDR, 2009, Kirschbaum et al., 2010; Petley, 2012; Froude and Petley, 2018).

4.4.3 Cause of death

Of the 157 decedents, the primary cause of death is known for 77 (49%). Traumatic injury was the immediate cause of death in 66 cases, while 8 individuals died by mechanical asphyxiation and 3 by drowning. Traumatic injury is a common cause of death in other landslides (**Table 4.2**). In a single landslide event in July 2011 in India, blunt force trauma to the head and vital organs was the cause of death in five out of the six fatalities (Memchoubi et al., 2012). In a 2019 landslide in Kerala, India, blunt force trauma was the primary cause of death in 18 out of 19 fatalities (Sheeju et al., 2019). In both cases, asphyxia played a secondary role, as the primary

cause of death in only one fatality in each landslide. A 2013 landslide in Oshima, Japan, resulted in a high proportion of non-fatal, severe chest and pelvic trauma, which the authors extrapolated as the presumed cause of death among decedents, although no post-death analysis was performed (Homma et al., 2016).

In contrast, a study of landslide fatalities after a series of storm-triggered landslides in Chuuk, Micronesia, in 2002 found that suffocation by burial was the primary cause of death in approximately 90% of decedents, regardless of their location inside or outside of a home (Sanchez et al., 2009). In January 2011, a tropical storm triggered flooding and mudslides around Rio de Janeiro, Brazil, killing 845. The primary causes of death were mechanical and simple asphyxia, respectively. One-third of the deceased experienced a traumatic injury, but it was not determined to be the primary cause of death in any case (Pereira et al., 2013). Out of five landslide fatalities in New Zealand 1998 – 2013, asphyxia (unspecified) was the primary cause of death in three cases (Massey et al., 2019). In one of these cases, the debris flow entered the dwelling but did not cause its complete collapse (Beetham, 2011).

Table 4.2. Primary cause of death in selected landslide disasters (percent). [1]asphyxia was a contributing cause in ten cases, [2]asphyxia was a contributing cause in two cases, [3]type of asphyxia not specified in two cases

Location	*Mechanical asphyxia*	*Simple asphyxia*	*Traumatic injury*	*Reference*
India (2011)	-	1 (17)	5 (83)	Memchoubi et al. (2012)
India (2019)	-	1 (5)	18 (95)[1]	Sheeju et al. (2019)
Micronesia (2002)	39 (91)	-	4 (9)	Sanchez et al. (2001)
Brazil (2011)	(75)	(25)	-	Pereira et al. (2013)
California (2018)	-	-	18 (100)	SBCSO (2018)
Washington (2014)	-	-	43 (100)	Snohomish Co. MEO (2014)
Australia (1995)	8 (44)	1 (6)	9 (50)[2]	Hand (2000)
Australia (2011)	-	2 (100)	-	Barnes (2012)
New Zealand (1998-2013)	3 (60)[3]	-	2 (40)	Massey et al. (2019)

The patterns of types of fatal and non-fatal injuries appear to be a function of the landslide type and the location of the victim. Both the 2014 Washington and 2018 California events were highly fluid but contained large amounts of boulders, trees, and large debris, such as cars and disintegrated structures (Keaton et al., 2014; Kean et al., 2019). Most of the decedents in these events were indoors at the time of inundation, and their homes were partially or completely destroyed. This may have temporarily protected the victims from burial and suffocation but also increased their chances of receiving a fatal traumatic injury from moving furniture or structural elements.

While the 2002 Micronesia and 2011 Brazil events were also characterized by highly fluidized landslides, the construction and contents of residences in these areas likely contributed to the lower percentage of deaths caused by traumatic injury. Sanchez et al. (2009) found that of 22 indoor decedents, 68% sheltered in structures with concrete walls, which are less likely to collapse in small or mid-sized debris flows.

4.4.4 Extreme cases

The extreme cases of total mortality (36%) or total survival (26%) make up the majority of the dataset; in only 33 impacted structures (38%) were there both survivors and fatalities. It is unlikely that this dataset accurately represents the entire population of occupied, landslide-impacted structures; numerous other examples of much larger landslides overwhelming structures and killing all occupants exist, as do examples of very shallow inundation depths which posed a negligible risk to human life.

The scale of large events leads to an under-sampling bias. Large events with deep inundation depths are capable of overwhelming many structures at once. In these large scale disasters, structure-by-structure inundation depths and fatality statistics are rare; rather, average depths and aggregate fatalities are commonly reported in the media. This has been the case for numerous high-profile landslides such as the 2014 Abe Barek, Afghanistan, flowslide (50 – 70 m; 2000+ fatalities); the 2015 Shenzhen, China, flowslide (6 – 15 m; 77 fatalities); and the 2015 El Cambray, Columbia, landslide (12 – 15 m, 220+ fatalities).

Similarly, we expect that the extremely low magnitude events are also substantially under-sampled in our database. Inundation depths below 0.9 m appear to rarely pose a significant risk to an indoor population, often because such low depths are less likely to penetrate into homes (Eidsvig et al., 2014; Papathoma-Kohle et al., 2012). Thus the knowledge of threat (or lack thereof) or mitigative (in)action of potential victims has little relation to their probability of death for shallow events which impact but do not enter a structure. We suspect that, while common, these events are of little media interest and go mostly unreported. For these reasons, only buildings with inundation depths between 0.9 – 5.9 – the range in which both survivors and decedents are commonly observed – are included in the analysis of landslide mortality (**Section 4.5.3** and following).

4.5 Results

4.5.1 Probability of death and critical depth

The likelihood of dying in a landslide generally increases with increasing process intensity. The regression statistics indicate a mild correlation between human vulnerability and inundation depth. The probability of death rapidly increases between 0 – 2 m, although no fatalities are recorded below inundation depths of 0.8 m. Based on experience in New Zealand and Europe, we believe this is due to the intrusion of debris into buildings through structural weak points such as windows, commonly set at heights of ~1 m, after which debris may overwhelm and bury occupants (Massey et al., 2019; Totschnig and Fuchs, 2013; Fuchs et al., 2007; Totschnig et al., 2011).

Between inundation depths of 0.9 – 5.9 m, the mortality rate varies widely, encompassing 82% of exposed individuals and 76% of structures. Only one fatality occurred at depths shallower than 0.9 m, while the maximum inundation depth survived by an individual recorded in our database is 9.6 m. Approximately 90% of individuals were in a structure impacted by less than 6 meters of debris, including 99% of survivors. Within the zone of 0.9 – 5.9 m, the probability of death has no correlation with inundation depth through nonlinear regression or binary logistic regression (depth binned in 1 m increments), suggesting that this is a critical zone for human mortality (**Figure 4.1**).

Fifty-three percent of structures only had 1 – 2 occupants, reflecting the prevalence of adults living singly or with a partner. Since the probability of death is a function of the number of people exposed, values of 0, 0.5, and 1 are over-represented in our database. This led to additional uncertainty, particularly at the extreme ends of the range of inundation depths. For instance, in the case of the second-highest inundation depth that was survived (9.1 m), the victim was the only person home, resulting in a probability of death of zero. However, the victim survived with severe injuries in very favorable circumstances, while all four occupants of an adjacent home were killed, indicating that the actual probability of death in this home was closer to one. Similarly, a child was killed when a debris flow inundated a squatter hut in Hong Kong with only 0.8 m of debris. Since only one other individual—an adult—was home, the calculated probability of death was 50%, almost certainly an overprediction for landslides of this mild intensity. Considering only buildings in which more than two people are exposed mildly improved the fit of the vulnerability function (**Table 4.3**), similar to the improvement of infrastructural vulnerability functions when using damage ratios instead of damage states (Massey et al., 2019). However, excluding data with fewer exposed individuals has little rationale beyond pursuing better regression statistics and only minimally alters the form of the final vulnerability function (**Figure 4.1**).

We also tested the influence of cases in which the debris depth was estimated with low confidence. The regression results indicated a slightly weaker fit when using only the cases of medium or high confidence rather than using all cases (**Table 4.3**), indicating the data quality was insignificant relative to the other factors contributing to human vulnerability.

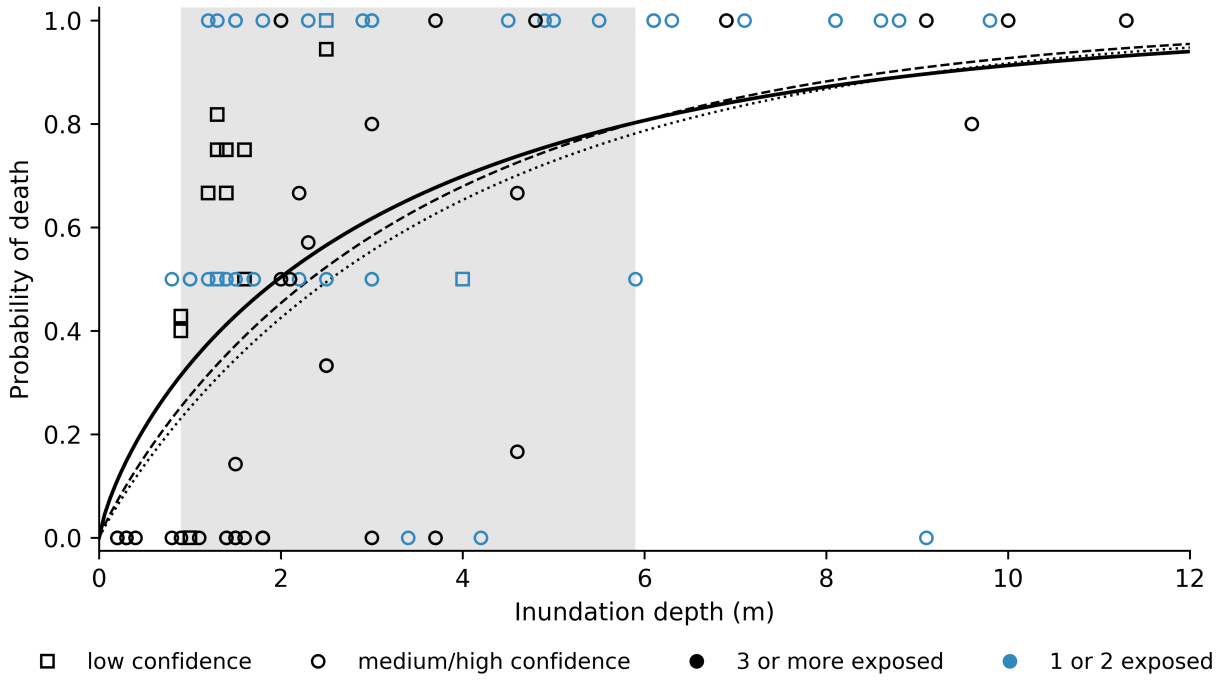

Figure 4.1. Human vulnerability curved based on the entire database (solid line). Considering only cases in which more than two people are exposed (dotted line) or only medium/high confidence cases (dashed line) has little effect on the relationship. One additional total fatality case (30 m inundation depth) is not shown but included in all regressions. Between inundation depths of 0.9 – 5.9 m (grey shading) there is no statistical relationship between probability of death and process intensity, suggesting that there is a critical zone in which other factors dominate landslide mortality.

Table 4.3. Regression parameters for the vulnerability functions shown in **Figures 4.1**, **4.2**, and **4.3**.

Subset	*a*	*b*	*Pseudo R^2*	*RMSE*	*n*
More than two individuals exposed	0.2899	0.9343	0.415	0.302	46
Inundation depths 0.9 – 5.9 m	0.4917	0.5164	0.053	0.376	72
Medium/High confidence cases	0.3216	0.9115	0.320	0.354	82
Economically developing nations	0.8782	1.6095	0.480	0.139	17
Economically developed nations	0.2752	0.9520	0.344	0.341	79
Final (*all points*)	0.4096	0.7758	0.277	0.348	96

Disaggregating by the economic development of the host nation suggests a strong socioeconomic component to human vulnerability (**Figure 4.2**). Human vulnerability in economically developing nations shows less scatter than in developed nations (**Table 4.3**), although due to the low number of data points (17) and the lack of zero-fatality cases, there is potential for

overfitting. Even so, economically developing nations have significantly greater human vulnerability than developed nations at almost all inundation depths. Although vulnerability curves for both economically developing and developed nations show the highest increase in vulnerability in the 0 – 2 m range, the increase is almost twice as rapid for developing nations. In developing nations, the probability of death reaches ~100% at 2.5 m, while the corresponding probability in developed nations is only 50%. Considering only cases of inundation depth 0.9 – 5.9 m, individuals in developing nations had six times the likelihood of death of those in developed nations (p-value < 0.001).

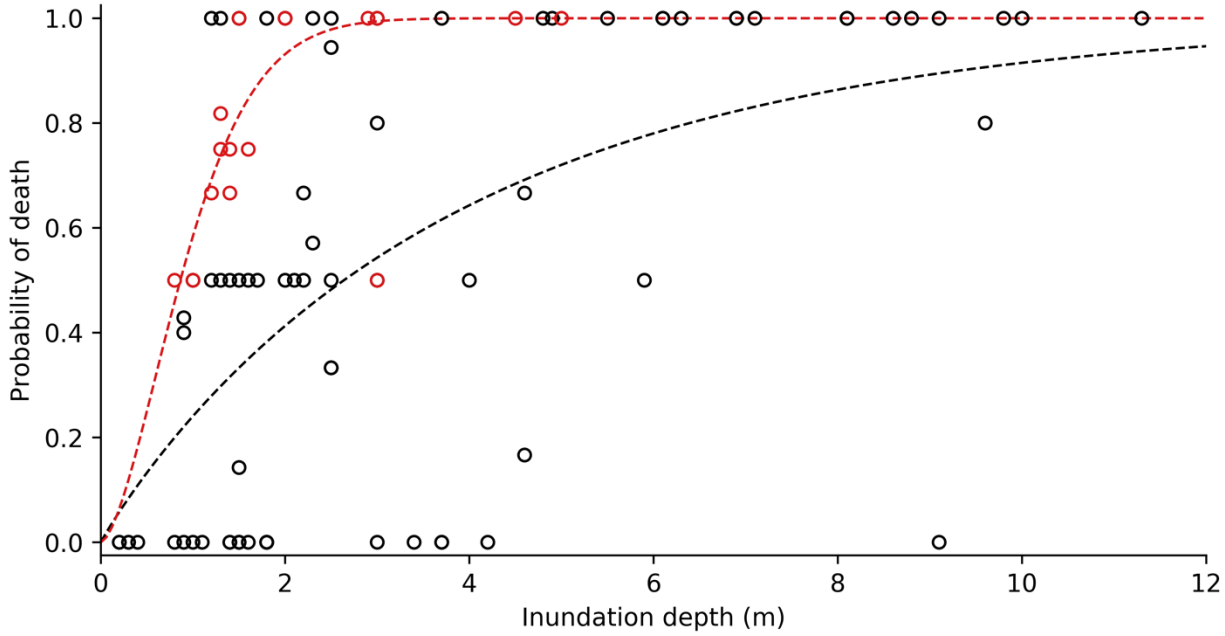

Figure 4.2. At inundation depths of approximately 2 m, predicted human vulnerability in economically developing nations (red dashes) is over 50% higher than in economically developed nations (black dashes). One additional total fatality case (30 m inundation depth) is not shown but included in the regression for developing nations.

Figure 4.3 shows the final vulnerability curve for the entire range of inundation depths represented in the database. Regression parameters are given in **Table 4.3**. The poor fit of the

regression model indicates that caution must be used for any predictive application and highlights the need for more human vulnerability data to disentangle the influence of additional complicating factors. Nevertheless, the explicit data scatter has the advantage of being statistically quantifiable for use in probabilistic analyses, as has been done for vulnerability curves for other types elements at risk (Massey et al., 2019), as well as in other aspects of landslide risk assessment (McDougall et al., 2012; Schilling, 2014).

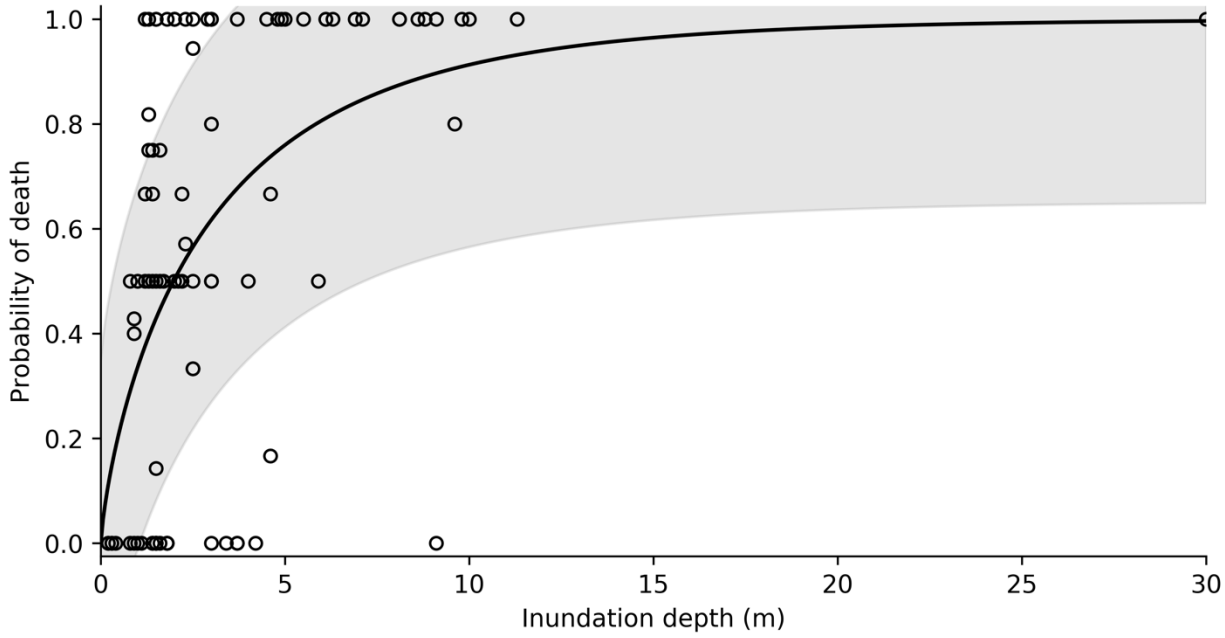

Figure 4.3. Human vulnerability to landslides over the range of common landslide inundation depths (n = 96). Grey shading represents ± one standard deviation.

4.5.2 Rescue and time to rescue

The first minutes after a landslide are critical. Of victims who survived due to being rescued, 77% were first located by neighbors and 11% by emergency response personnel. Due to their

proximity, neighbors located and began to rescue landslide victims more rapidly than emergency personnel who often had to travel miles to reach the landslide site. Of those located by neighbors, the majority (68%) were found in the first minutes after the event with only five victims (10%) being located more than an hour after the event. Although the time at which emergency personnel located and began the rescue of landslide victims is known in only four cases, the minimum time is one hour with a maximum time of 12 hours. Rescues begun by neighbors were often completed by emergency personnel as specialized equipment was needed to extract buried victims.

4.5.3 Demographic and situational risk factors

4.5.3.1 Gender and age.

Our data shows an over-representation of men, with a male to female ratio of 1.24 compared to 1.02 globally and 0.98 in the United States, from which the majority of our data comes (United Nations, 2019). The reasons for this are unclear. Since almost all cases are from residential structures, occupational or recreational over-exposure to hazard are unlikely causes (Wallingford, 2006), although the difference may be explained by the relatively high proportion of individuals for which gender is not known (19%). Women are slightly more likely to be killed than men, although the correlation is not statistically significant (**Table 4.4**).

Individuals between 40 – 59 years of age were 3.25 times more likely to be killed in a landslide than those from 0 – 19 years (**Table 4.4**). Children (0 – 19 yrs.) and the elderly (80 – 99 yrs.) have the highest survival rates of all age groups, both 57%. We suspect sampling bias is

partially responsible for the high relative survival rate among children and the elderly. Children's ages were almost always included in news reports, whereas mid-range adult ages were often only available from obituaries. Additionally, among the 115 individuals for which we could identify the occupied floor at the time of the landslide, 82% of individuals on the second or third floors were under the age of 40. Eleven percent of children were on upper floors, a far safer location in a landslide impacted structure, as is discussed in **Section 4.5.4.2**.

4.5.3.2 Construction material.

The physical vulnerability of structures, and thus also their occupants, is a function of the construction material, with timber-frame structures having less resistance to landslides and rock falls than masonry or concrete structures (Massey et al., 2019). We differentiate between rigid construction materials, including masonry, stone, and reinforced concrete, and more flexible materials such as wood, bamboo, and plastic. The latter category dominates the dataset at 76% of the structures, while rigid materials were used in only 9% of structures. Surprisingly, individuals in rigid structures were 3.1 times more likely to be killed than those in the flexible structures (**Table 4.4**). Considering only those structures impacted by 0.9 – 5.9 m of debris, the median inundation depth was 2.7 m for rigid structure and 1.8 m for flexible structures, suggesting that the over-representation of large events impacting rigid structures helps to explain this difference. The structural resilience of rigid materials may be both a blessing and a curse. Although debris may exert less damage on rigid structures at low and moderate inundation depths, if it intrudes into the building through structurally weak areas such as windows and doors, debris may fill the building rather than exiting, thus trapping and burying the occupants. At inundation depths capable of collapsing buildings regardless of construction material, falling

masonry or concrete slabs may be more deadly than the landslide itself (e.g. Hand, 2000; Hudson, 1982)

4.5.3.3 Distance from slope.

While the exact duration of warning prior to inundation is not known in most cases, the distance of an impacted structure to the slope where the landslide initiated can serve as a proxy for time. The odds of death increase with decreasing distance, with individuals less than 100 m from the slope 1.6 times more likely to be killed, although the results are not statistically significant (**Table 4.4**). We suspect that this is due to decreased time to identify and react to approaching landslide debris, although the people closest to the slope may also be more likely to notice warning signs of an impending landslide such trees cracking, sudden changes in surficial water flow, or outrunner rocks and soil. No statistically significant relationship exists between awareness and distance from slope for individuals in our database.

4.5.3.4 Time of day.

Time of day has no clear influence on landslide mortality (**Table 4.4**). However, individuals were 15 – 20 times more likely to be aware of an imminent threat in the morning (4 am – 12 pm) than in the night (8 pm – 4 am) or evening (12 pm – 8 pm; p-values < 0.05). Twice as many people were killed during the night than during the rest of the day, reflecting the high proportion of people in their homes at this time. People killed by landslides while outside – more likely during daytime hours – are not included in our results.

Table 4.4. Crude odds ratio (OR) for demographic and situational factors potentially associated with mortality in landslides of inundation depths 0.9 – 5.9 m. P-values associated with statistical significance (< 0.05) are in bold.

Factor	*Deaths*	*Survival Rate (%)*	*OR*	*95% CI*	*p-value*
Economic development					
Developed	92	59.6	*ref*		
Developing	37	19.6	6.077	2.800 – 13.192	**< 0.001**
Gender					
Female	46	49.5	1.356	0.785 – 2.342	0.274
Male	52	57.0	*ref*		
Age					
0 – 19 (children)	24	57.1	*ref*		
20 – 39	22	37.1	2.256	0.949 – 5.365	0.066
40 – 59	22	29.0	3.259	1.275 – 8.335	**0.014**
60 – 79	13	38.1	2.167	0.775 – 6.054	0.140
80 – 99 (elderly)	3	57.1	1.000	0.204 – 4.893	1.000
Construction material					
Rigid	23	37.8	3.119	1.495 – 6.506	**0.002**
Flexible	59	65.5	*ref*		
Distance from slope (m)					
0 – 99	53	50.0	1.622	0.927 – 2.837	0.090
100 – 499	6	0	*n/a*	*n/a*	*n/a*
500 – 999	10	54.5	1.351	0.531 – 3.438	0.527
> 1000	37	61.9	*ref*		
Time of day					
12 pm – 8 pm	7	53.3	1.157	0.379 – 3.534	0.798
8 pm – 4 am	84	53.1	1.169	0.674 – 2.029	0.578
4 am – 12 pm	31	56.9	*ref*		

4.5.4 Behavioral risk factors

4.5.4.1 Awareness and mitigative action.

Based on firsthand accounts of landslide survivors, we were able to coarsely identify their awareness of an imminent threat and their subsequent actions. This information cannot be precisely known for those who were killed, so we relied on the survivor accounts as proxies for the deceased. We were not able to reconstruct the extent of forewarning; in some cases, it may have been as long as tens of minutes. However, in all cases, the individuals exposed to landslide inundation did not have sufficient time, will, or means to evacuate.

Awareness of an approaching threat, even if its location and nature were unknown, sharply decreased the odds of death, with those who were not aware eight times more likely to be killed (p-value < 0.001; **Table 4.5**). Three-quarters of individuals who recognized a threat took some form of protective action, such as moving away from the perceived direction of the threat, escaping vertically to a higher floor or the top of furniture, or sheltering in a prepared refuge area in their home. However, a significant minority of individuals either took no action or moved closer to the oncoming landslide out of curiosity. Those who took no protective action were five times more likely to be killed (p-value < 0.001). The survival rate among those who were aware of a threat was 82%, while among those who took protective action, it increased to 84%.

4.5.4.2 Floor occupied.

The exact location of individuals in a home was rarely available, but in 77% of cases we could identify the floor occupied at the time of the landslide. The survival rate of individuals on the second or third floors, including attics and roofs, was 95%, with those on the ground floor twelve times more likely to be killed (p-value < 0.001; **Table 4.5**). The only known case of a second floor fatality involved the violent destruction of the entire home.

Table 4.5. Crude odds ratio for behavioral factors potentially associated with mortality in landslides of inundation depths 0.9 – 5.9 m.

Factor	***Deaths***	***Survival Rate (%)***	***OR***	***95% CI***	***p-value***
Awareness					
Not Aware	32	36.0	8.081	3.858 – 16.924	**< 0.001**
Aware	22	82.0	*ref*		
Protective action					
No	39	51.9	5.014	2.484 – 10.123	**< 0.001**
Yes	15	84.4	*ref*		
Floor occupied					
ground	77	60.1	11.948	1.563 – 91.356	**0.017**
upper	1	94.7	*ref*		

4.5.5 Key actions

In the 1970s, health professionals pioneered the concept of "positive deviance," or the uncommon, beneficial practices of a few members of an at-risk community which lead to better outcomes than those of their neighbors (Wray, 1972; Wishik and Van der Vynckt, 1976). Such practices are typically affordable, acceptable, and sustainable in a community because they are already practiced by at-risk peers (Marsh and Schroeder, 2002). The concept of positive deviance can be adopted for disaster risk reduction. Engineering, political, or societal solutions to reduce risk may be unaffordable, unpalatable, or infeasible; however, behavioral change is a potent means for individuals to reduce their own risk. As we examined survivor stories, we identified six key, "positively deviant" actions that lead to beneficial outcomes.

Before a landslide event:

Be informed about potential hazards and talk to people who have experienced them: Prior experience with natural hazards is associated with greater preparation, more realistic perception of risk to future hazards, and enhanced ability to cope during hazardous events (Sattler et al., 2000; Becker et al., 2017; Hoffmann and Muttarak, 2017; Dunn et al., 2016). In two cases, individuals with prior first-hand experience of landslides recognized the signs of oncoming debris before seeing it and dashed to safer areas, narrowly escaping death.

Move areas of high occupancy, such as bedrooms, upstairs or to the downhill side of a home: Bedrooms are often on the uphill side of residential dwellings, placing occupants

closest to potential landslide hazards during the night, when they are least likely to be aware of an imminent threat (Taig et al., 2015). One family survived a debris flow by sheltering in a downhill bedroom while the two uphill bedrooms were completely inundated (McPhee, 1989). If moving bedrooms is unfeasible, moving beds away from exterior walls may also reduce risk (Faber, 2016)

During a landslide event:

Escape vertically: Mortality rate dramatically decreases for those above the ground floor of a landslide-impacted structure, even when the entire home is destroyed. Two survivors of the 2014 Oso landslide in Washington State credited this with saving their lives: "Being upstairs [in our home], I think that gave us a chance" (Keaton et al., 2014). For those in one-story homes without roof access, moving higher onto countertops and furniture protected them from suffocation or being swept away (McPhee, 1989; Cobery et al., 2012).

Identify and relocate to interior, unfurnished areas: Areas such as closets, bathrooms, and interior hallways can offer additional protection in landslides disasters. These small spaces are less likely to collapse due to the density of structural elements and are generally free from unsecured furniture, which could pin or crush a person. In an exceptional case of survival, a victim of the 2005 La Conchita, California, landslide dove into a closet which had been prepared as a refuge area and survived being buried by over 9 m of debris (Metivier-Hart, 2017).

Open downhill doors and windows: Doors commonly open inward, making it easier for landslide debris to enter structures than exit. In the case of fluid landslides, this may lead to a buildup of debris than can bury and suffocate occupants, or in extreme cases, develop enough pressure to rip apart the structure. We were surprised by the number of quick-thinking individuals who opened downhill doors or kicked out windows in order to allow debris to flow through their home. However, we also note that individuals who did so after debris had begun to accumulate risked being swept out of their homes (McPhee, 1989).

If caught in landslide debris:

Continue to make noise and motion: It is rare for a landslide to engulf the entire community, meaning that the family and neighbors of victims usually begin rescue activities within minutes after the event. In most cases, victims are found quickly, even if they cannot be fully rescued without professional aid. Buried survivors who were successfully rescued often made noise through calling, whistling, or tapping on debris. Those partially buried attracted rescuers through waiving, and in at least one case, a fully buried man was able to poke a stick to the surface and use it to flag down rescuers.

Conversely, we also identified key actions which put individuals at greater risk:

Opening a door out of curiosity: It is a typical human response to move toward unknown or unfamiliar phenomena, whether to identify a potential threat or out of curiosity (Wallingford, 2006). In at least four cases, as a result of hearing unfamiliar sounds or

seeing mud flowing in the streets, residents opened their front door only to be swept away by a surge of debris.

Sheltering behind or beside large furniture: The high percentage of landslides deaths that occur due to blunt force trauma, even among victims who are indoors at the time, suggests that unsecured furniture is a significant contributor to landslide mortality. In the Crescenta Valley flood a man was crushed by a piano propelled by debris (Cobery et al., 2012). When a debris flow in Los Angeles inundated the home of a family of four, the two teenage children almost drowned from being pinned between a bed and a wall by the force of the flow, while the parents, buoyed on the top of the bed, survived unscathed (McPhee, 1989).

4.6 Discussion

4.6.1 Physical vulnerability.

Human vulnerability to landslides increases with increasing process intensity, although the relationship is neither as clear nor as robust as for buildings (Fuchs et al., 2019b). The data scatter around the best-fit regression is the product of compounding the inherent variability in structural vulnerability with additional human situational and behavioral factors. Case-based structural vulnerability curves represent the characteristics of the underlying landslide event and region. Differences in building construction and material quality, size, orientation, and flow characteristics result in very different vulnerability curves, even when the same methodology is

used (Fuchs et al., 2019b; Ciurean et al., 2017). Thus, efforts to produce a "global" building vulnerability function from compiled datasets have produced large uncertainties in the final relationship (Massey et al., 2019). Human vulnerability couples structural vulnerability, with its already significant degree of variability, with a diverse range of demographic, situational, and behavioral human factors that produce further scatter in the data. However, many human factors are not readily predictable ex ante for use in quantitative risk assessment. As such, human vulnerability curves such as **Figure 4.3** provide a practical improvement on single-valued, heuristic estimates by coupling vulnerability and process intensity while quantifying model uncertainty.

Differences in the vulnerability curves for humans and for buildings demonstrate the difficulty in mathematically linking structural and human vulnerability (Uzielli et al., 2008; Li et al., 2010). While the vulnerability of buildings is most varied between inundation depths of 0.25 – 2.5 (**Figure 4.4**), human vulnerability is most varied at greater inundation depths, between 0.9 – 5.9 m. The lower bound may be function of anthropometric measures. Based on average leg to height ratios, Du et al. (2013) suggest a critical landslide depth of 0.8 m, although structures will shelter an indoor population until the debris intrudes through openings or exceeds the load capacity of a wall. Inundation depths of 2.5 m or greater result in the functional destruction, and often collapse, of almost all buildings regardless of construction material (Akbas et al., 2009; Tsao et al., 2010). However, 23% of the survivors in our database occupied buildings inundated by at least this much debris, indicating that human vulnerability is not a simple function of either the vulnerability of the occupied structure or the process intensity; rather, within this zone, human behavior is the primary factor in landslide mortality.

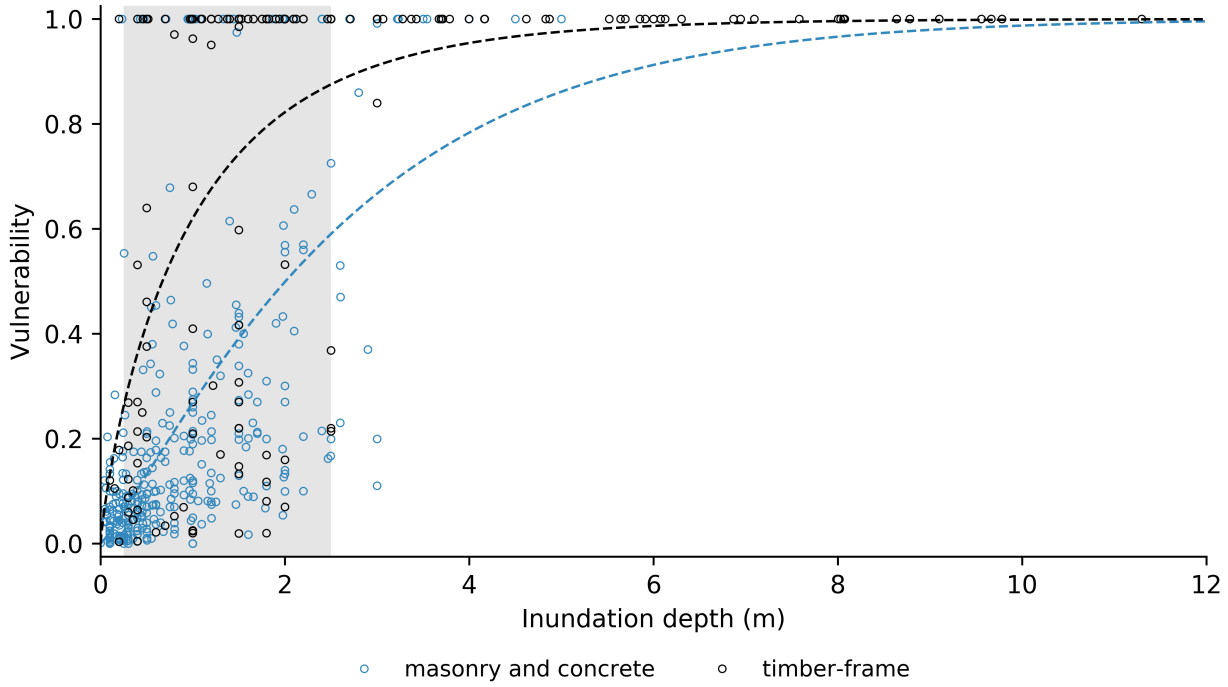

Figure 4.4. Compilation of published datasets of structural vulnerability to landslides. Structural vulnerability varies widely for inundation depths 0.25 – 2.5 m (grey shading), but above this range, almost all buildings are destroyed. Data sources are provided in **Appendix 2.5**

Within the critical inundation depths of 0.9 – 5.9 m, the overall mortality rate is 47%. While this is lower than global landslide mortality rates produced by other methods (Kennedy et al., 2016), it is high relative to other environmental hazards, reflecting the violent nature of landslide processes (Alexander and Magni, 2013; Dresser et al., 2016; Alderman et al., 2012, Kennedy et al., 2015). While the language colloquially used regarding landslide victims such as "buried alive" (e.g. Metivier-Hart, 2017) implies death by suffocation, traumatic injury is at least as common a cause of death. For indoor populations, unsecured furniture and collapsing structural elements may be more dangerous than the landslide itself, as is the case for earthquakes (Doocy et al., 2013; Glass et al., 1977).

4.6.2 Socioeconomic pressures.

Politically and economically disadvantaged populations suffer greater human losses in environmental disasters of all types, including landslides (Dowling and Santi, 2014; Santi et al., 2011; Kennedy et al., 2016). Our results suggest that a socioeconomic component to physical vulnerability is a dominant reason, with individuals in economically developing nations up to twice as vulnerable to landslides as those in developed nations. The rate at which landslide victims were rescued was lower in economically developing nations (15%) than in developed nations (20%), suggesting that fewer resources and personnel available for emergency response are contributing to greater landslide mortality. However, no individuals in developing nations were reported as self-rescuing compared to 32% of landslide victims in developed nations, leading us to believe that there is a substantial reporting bias in the English-language media, which omits landslide events that do not include fatalities or dramatic rescues.

4.6.3 Gender.

Men are overrepresented in our database, but this is likely a byproduct of uneven sampling rather than systemic overexposure to landslide hazards. Landslide fatality databases from Italy, Switzerland, and Portugal show that in these countries far more men die in landslides than do women, a difference attributed to increased occupational exposure and more risk-taking behavior (Salvati et al., 2018; Badoux et al., 2016; Pereira et al., 2016; Wallingford, 2006). However, since most of the individuals in our database were at home at the time of the landslide, the first explanation is unsatisfactory. In our database, women had a slightly higher mortality rate than

men, indicating that behavioral vulnerability associated with risk-taking is also an insufficient explanation.

As in this work, Sanchez et al. (2009) found that women had a higher mortality rate than men during the 2002 Micronesia landslides, although it was not associated with a statistically significant increase in the probability of death. However, in the 2010 Uganda landslides, men were almost 2.5 times more likely to be killed (Agrawal et al., 2016), leading us to believe that the location of the victim plays an important role in the gender distribution of different landslide mortality datasets. In the Uganda event, more landslide injuries occurred outdoors, whereas in Micronesia more landslide fatalities occurred indoors, where the mortality rate between males and females tends to equalize (Pereira et al., 2016).

4.6.4 Age.

Environmental disasters do not impact populations uniformly or at random (Hewitt, 1997; Wisner et al., 2004). A "saddle" shaped distribution of mortality rate by age, in which children and the elderly are disproportionately likely to suffer injury or death, has been observed in other natural hazards (Li et al., 2010; Glass et al. 1977; Zahran et al., 2008). Many explanations have been proposed, including that children and the elderly are less physically able to escape from hazardous areas or resist the physical trauma of a violent landslide or that children have lesser understanding of the hazard and fewer life experiences to draw on for rapid decision-making (Wallingford, 2006; Zahran et al., 2008). Indicator-based frameworks for landslide vulnerability

have adopted these results, assigning greater vulnerability to the young and aged (Eidsvig et al., 2014; Park et al., 2016; Uzielli et al., 2008; Li et al., 2010).

However, our results indicated that landslides might not "discriminate" by age in the same manner as other natural hazards. Middle-age adults (40 – 59) were statistically more likely to be killed in a landslide than any other age group, contrary to the generally accepted view of age-based vulnerability. In part, this is because landslides are a rapid-onset, localized hazard which stratifies mortality by building, room, and floor, meaning that social norms which organize residential spaces by generation strongly control who will be injured or killed in a landslide. In U.S. homes, master bedrooms—more likely occupied by a middle-aged adult(s) than by children or elderly parents—are often located on the ground floor (Vollmer et al., 2005), where landslide impacts are the most severe. Since social norms vary by culture, region-specific mortality-age distributions may take different forms. In the 1995 Kobe, Japan, earthquake, the elderly experienced higher mortality because they customarily slept on the ground floor of wooden homes with heavy tiled roofs (Kunii et al., 1995).

4.6.5 Construction material.

More durable construction material does not necessarily commute landslide risk. While buildings constructed out of masonry or concrete may be able to resist greater inundation depths than timber frame buildings prior to catastrophic failure, when they do collapse, it is often fatal for the occupants (Massey et al., 2019; Sanchez et al., 2009). Additionally, when masonry buildings collapse, they leave fewer cavities in which individuals can be sheltered (Coburn and

Spence, 2002). Du et al. (2013) estimate that the vulnerability of humans during the total collapse of masonry and reinforced concrete structures is 1.9 and 1.3 times greater than for timber frame structures.

4.6.6. Hazard awareness.

Education and awareness of potential landslide threats is a common risk reduction strategy (Davis et al., 2020; WGS, 2017; Highland and Brobrowsky, 2008). In a study of residents' experiences during rock falls triggered by the 22 February 2011 earthquake in Port Hills, New Zealand, Taig et al. (2015) found that the ability to recognize approaching boulders and take evasive action likely saved the lives of multiple individuals. In particular, residents who have familiarized themselves with the local landslide history, the direction from which landslides will come, and landslide precursors such as extra surficial water, falling and bouncing rocks, ground tremors, and rumbling noises are more likely to take early and appropriate mitigative action such as evacuating, moving to the interior or downhill side of a home, or relocating to a higher floor, attic, or roof.

Furthermore, knowledge of the local landslide hazards increases the likelihood of an individual making advanced preparations, such as identifying or creating a structurally reinforced refuge space, relocating bedrooms to the downhill side of a home, and moving beds away from windows and doors (Metivier-Hart, 2017; Taig et al., 2015; Faber, 2016). This indicates that outreach products which inform citizens of local landslide hazard and risk, landslide triggers and precursors, and protective actions during a landslide event are a critical component of landslide

risk reduction (e.g. WGS, 2017; Davis et al., 2020; WGS and DOGAMI, 2015). However, public outreach and advisories must be unambiguous for their intended audience. In the days leading up to the 2018 Montecito debris flow disaster, different risk perceptions between scientists, emergency managers, and the public led to a false sense of security among residents of a designated "voluntary evacuation zone" (Hayden, 2018a), and during the debris flow event, an ambiguous emergency SMS message instructing residents to "go to high ground" led some individuals to evacuate their homes only to be swept away (Hayden, 2018b).

4.6.7 Emergency response.

Few people simply walk away from being caught in a landslide. The significant percentage of survivors who were rescued suggests that an immediate emergency response may save up to 20% of potential fatalities. Such a response is often launched immediately by the surviving family and neighbors of the victims, as is the case in other environmental disasters (Merchant et al., 2010; Clukey, 2010). The presence of volunteer rescuers may increase the initial effectiveness of emergency response due to the rapidity in which they can locate trapped victims (Cobern and Spence, 2002). However, they may lack the specialized knowledge, training, and equipment necessary to perform triage, complete a rescue, and avoid becoming secondary victims themselves (Pereira et al., 2013; Zhang et al., 2015; Hand, 2000).

4.6.8 Landslide morbidity.

Finally, fatalities are not the whole story. Direct experience of a landslide, or membership in a community affected by one—including first responders—may have repercussions that far outlast the emergency response and are not limited to those who were physically injured by the landslide. After the 1998 Sarno, Italy, debris flows, surviving community members reported financial, occupational, psychological, and domestic problems resulting from the event. Symptoms of post-traumatic stress disorder (PTSD) were almost universal among survivors (Catapano et al., 2001). Studies suggest that levels of PTSD, material damage, social conflict, and the likelihood of bereavement are higher among landslide victims than those of other natural hazards, while their loss of social support is greater (Yang et al., 2011; Norris et al., 2004). This may be due to the relatively high mortality rate in landslide disasters, as well as the complete material destruction which often accompanies landslides, requiring survivors to relocate away from built-in social support structures. Regardless of the reasons, landslides can have severe, persistent consequences that may not be apparent from immediate post-disaster assessments. The long-term personal and community recovery necessary after a landslide disaster emphasizes the need for pre-disaster preparedness planning and post-disaster interventions that focus on more than only survival actions (Gowan et al., 2015).

4.7 Conclusions

At intermediate inundation depths, human behavior is the most significant factor in landslide mortality. Hazard preparation, situational awareness, and informed protective action such as

moving to a higher floor or a prepared refuge space are potent and readily accessible means of lowering personal landslide risk. However, such strategies are predicated on scientific products such as landslide hazard and risk maps that are understandable, accessible, and communicable to the general public. The development of such products and education campaigns to put them in the hands of at-risk populations are the first steps to landslide risk reduction. Rapid rescue operations after a landslide disaster save up to 20% of landslide victims but may be hindered by the long distances emergency personnel must travel to a disaster site. Thus community programs to train citizen first-responders could be a crucial step to saving lives. Finally, this work highlights the need for more human vulnerability data to be preserved in the aftermath of landslide disasters to inform landslide risk assessments, understand the complex situational and behavioral factors which contribute to landslide mortality, and design evidence-based emergency-response plans and outreach products to maximize survival rates in landslides.

References

Agliardi, F., Crosta, G., Frattini, P. (2009). Integrating rockfall risk assessment and countermeasure design by 3D modelling techniques. *Nat. Hazards Earth Syst. Sci.*, 9, 1059-1073. https://doi.org/10.5194/nhess-9-1059-2009

Agrawal, S., Gopalakrishnan, T., Gorokhovich, Y., Doocy, S. (2013). *Prehosp. Disaster Med.*, 28, 314-321. https://doi.org/10.1017/S1049023X13000356

AGS. (2007). Commentary on practice note guidelines for landslide risk management 2007. *Aust. Geomech*. 42, 115-158.

Akbas, S., Blahut, J., Sterlacchini, S. (2009). Critical assessment of existing physical vulnerability estimation approaches for debris flows. Proceedings of Landslide Processes: From Geomorphologic Mapping to Dynamic Modelling, Strasbourg.

Alderman, K., Turner, L., Tong, S. (2012). Floods and human health: A systematic review. *Environment Int*., 47, 37-47. https://doi.org/10.1016/j.envint.2012.06.003

Alexander, D., Magni, M. (2013). Mortality in the L'Aquila (Central Italy) earthquake of 6 April 2009. *PLoS Curr*., 5. https://doi.org/10.1371/50585b8e6efd1

Badoux, A., Andrex, N., Techel, F., Hegg, C. (2016). Natural hazard fatalities in Switzerland from 1946 to 2015. *Nat. Hazards Earth Syst. Sci*., 16, 2747-2768. https://doi.org/10.5194/nhess-16-2747-2016

Barbolini, M., Cappabianca, F., Sailer, R. (2004). Empirical estimate of vulnerability relations for use in snow avalanche risk assessment. In: C. Brebbia (*Ed*.) *Risk Analysis IV*. WIT Press. DOI: 10.2495/RISK040481

Barbolini, M., Cappabianca, F., Savi, F. (2004). Risk assessment in avalanche-prone areas. *Ann. Glaciol*., 38, 115-122. https://doi.org/10.3189/172756404781815103

Barnes, M., (2012). Inquest into the deaths caused by the south-east Queensland floods of January 2011. Brisbane: Office of the State Coroner.

Becker, J., Paton, D., Johnston, D., Ronan, K., McClure, J. (2017). The role of prior experience in informing and motivating earthquake preparedness. *Int. J. Disaster Risk Reduct*., 179-193. https://doi.org/10.1016/j.ijdrr.2017.03.006

Beetham, D. (2012). Ohope Beach landslide of 18 June 2011. *GNS Science Report 2011/46*. GNS Science.

Catapano, F., Malafronte, R., Lepre, F., Cozzolino, P., Arnone, R., Lorenzo, E., Tartaglia, G., Starace, F., Magliano, L., Maj, M. (2001). Psychological consequences of the 1998 landslide in Sarno, Italy: A community study. *Acta. Psychiatr. Scand*., 104, 438-442. https://doi.org/10.1034/j.1600-0447.2001.00512.x

Ciurean, R., Hussin, H., van Westen, C., Jaboyedoff, M., Nicolet, P., Chen, L., Frigerio, S., and Glade, T. (2017). Multi-scale debris flow vulnerability assessment and direct loss estimation of buildings in the Eastern Italian Alps. *Nat. Hazards*, 85, 929-957. https://doi.org/10.1007/s11069-016-2612-6

Clukey, L. (2010). Transformative experiences for hurricanes Katrina and Rita disaster volunteers. *Disasters*, 34, 644-656. https://doi.org/10.1111/j.1467-7717.2010.01162.x

Cobery, A., Lawler, M., Lawler, P. (2012). *The Great Crescenta Valley Flood*. Charleston, South Carolina: History Press.

Coburn, A., Spence, R. (2002). *Earthquake Protection*. West Sussex: John Wiley & Sons.

Corominas, J., van Westen, C., Frattini, P., et al. (2014). Recommendations for the quantitative analysis of landslide risk. *Bull. Eng. Geol. Environ*., 73, 209-263. https://doi.org/10.1007/s10064-013-0538-8

Crozier, M., Glade, T. (2005). Landslide hazard and risk: Issues, concepts and approach. In: T. Glade, M. Anderson, M. Crozier (*Eds*.) *Landslide Hazard and Risk*. West Sussex: John Wiley & Sons

Cruden, D., Varnes, D. (1996). Landslide types and processes. In: K. Turner and R. Schuster (*Eds*.) *Landslides: Investigation and Mitigation*. Washington: Transportation Research Board.

Davidson, R., Zhao, H., Kumar, V. (2003). Quantitative model to forecast changes in hurricane vulnerability of regional building inventory. *J. Infrastruct. Syst.*, 9, 55-64. https://doi.org/10.1061/(ASCE)1076-0342(2003)9:2(55)

Davis, L., West, J., Peek, L., Hughes, K., Godt, S., et al. (2020). Landslide Guide for Residents of Puerto Rico. United States Geologic Survey Guidebook. https://www.usgs.gov/news/new-landslide-guidebook-puerto-rico-residents

Diver, S. (1999). *Survival*. Sydney: Pan Macmillan Australia.

Dominey-Howes, D., Papathoma, M. (2007). Validating a tsunami vulnerability assessment model (the PTVA Model) using field data from the 2004 Indian Ocean tsunami. *Nat. Hazards*, 40, 113-136. https://doi.org/10.1007/s11069-006-0007-9

Doocy, S., Cherewick, M., Kirsch, T. (2013). Mortality following the Haitian earthquake of 2010: A stratified cluster survey. Population Health Metrics, 11. https://doi.org/10.1186/1478-7954-11-5

Dowling, C., Santi, P. (2014). Debris flows and their toll on human life: a global analysis of debris-flow fatalities from 1950 to 2011. *Nat. Hazards*, 71, 203-227. https://doi.org/10.1007/s11069-013-0907-4

Dresser, C., Allison, J., Broach, J., Smith, M-E., Milsten, A. (2016). High-amplitude Atlantic hurricanes produce disparate mortality in small, low-income countries. *Disaster Medicine Public Health Preparedness*, 10, 832-837. https://doi.org/10.1017/dmp.2016.62

Du, J., Yin, K., Nadim, F., Lacasse, S. (2013). Quantitative vulnerability estimation for individual landslides. Paris: Proceedings of the 18th International Conference on Soil Mechanics and Geotechnical Engineering.

Dunn, P., Ahn, A., Bostrom, A., Vidale, J. (2016). Perceptions of earthquake early warning on the U.S. West Coast. *Int. J. Disaster Risk Reduct*., 20, 112-122. http://dx.doi.org/10.1016/j.ijdrr.2016.10.019

Eidsvig, U., Papathoma-Kohle, M., Du, J., Glade, T., Vangelsten, B. (2014). Quantification of model uncertainty in debris flow vulnerability assessment. *Eng. Geol.*, 181, 15-26. https://doi.org/10.1016/j.enggeo.2014.08.006

Faber, E. (2016). Development of a landslide risk rating system for small-scale landslides affecting settlements in Guatemala City. (*masters thesis*). Golden, Colorado: Colorado School of Mines.

Fell, R. (1994). Landslide risk assessment and acceptable risk. *Can. Geotech. J.*, 31, 261-272. https://doi.org/10.1139/t94-031

Fell, R., Corominas, J., Bonnard, C., Cascini, L., Leroi, E., Savage, W. (2008). Guidelines for landslide susceptibility, hazard and risk zoning for land use planning. *Eng. Geol.*, 102, 85-98. https://doi.org/10.1016/j.enggeo.2008.03.022

Fell, R., Ho, K., Lacasse, S., Leroi, E. (2005). A framework for landslide risk assessment and management. In: O. Hungr, R. Fell, R. Couture, E. Eberhardt (*Eds*.) Landslide Risk Management. London: Taylor & Francis.

FEMA. (2017). Hazus tsunami model technical guidance. Washington, D.C.: Federal Emergency Management Agency, 171 p. https://www.fema.gov/media-library/assets/documents/24609. (accessed May 2020).

Finlay, P. (1996). The risk assessment of slopes. (*doctoral dissertation*). Sydney: University of New South Wales

Fotopoulou, S., Pitilakis, K. (2017). Vulnerability assessment of reinforced concrete buildings at precarious slopes subjected to combined ground shaking and earthquake induced landslide. *Soil Dyn. Earthquake Eng*., 93, 84-98. http://dx.doi.org/10.1016/j.soildyn.2016.12.007

Froude, M., Petley, D. (2018). Global fatal landslide occurrence from 2004 to 2016. *Nat. Hazards Earth Syst. Sci.*, 18, 2161-2181. https://doi.org/10.5194/nhess-18-2161-2018

Fuchs, S., Heiser, M., Schlogl, M., Zischg, A., Papathoma-Kohle, M., Keiler, M. (2019a). Short communication: A model to predict flood loss in mountain areas. *Environ. Modell. Software*, 117, 176-180. https://doi.org/10.1016/j.envsoft.2019.03.026

Fuchs, S., Heiss, K., and Hubl, J. (2007). Toward an empirical vulnerability function for use in debris flow risk assessment. *Nat. Hazards Earth Syst. Sci.*, 7, 495-506. https://doi.org/10.5194/nhess-7-495-2007

Fuchs, S., Keiler, M., Ortlepp, R., Schinke, R., Papathoma-Kohle, M. (2019b). Recent advances in vulnerability assessment for the built environment exposed to torrential hazards: Challenges and the way forward. *J. Hydrol.*, 575, 587-595. https://doi.org/10.1016/j.jhydrol.2019.05.067

Fuchs, S., Tsao, T-C., Keiler, M. (2012). Quantitative vulnerability functions for use in mountain hazard risk management. Grenoble: Proceedings of the 12th Congress Interpraevent.

Galli, M., Guzzetti, F. (2007). Landslide vulnerability criteria: A case study from Umbria, Central Italy. *Environ. Manage.*, 40, 649-664. https://doi.org/10.1007/s00267-006-0325-4

Glade, T. (2003). Vulnerability assessment in landslide risk analysis. *Die Erde*, 134, 123-146.

Glass, R., Urrutia, J., Sibony, S., Smith, H., Garcia, B., Rizzo, L. (1977). Earthquake injuries related to housing in a Guatemalan village. *Science*, 197. https://doi.org/10.1126/science.197.4304.638

Gowan, M., Sloan, J., Kirk, R. (2015). Prepared for what? Addressing the disaster readiness gap beyond preparedness for survival. *BMC Public Health*, 15. https://doi.org/10.1186/s12889-015-2440-8

Grant, A. (2017). Regional-scale coseismic landslide hazard modelling and consequence analysis. *(doctoral dissertation)*. Seattle: University of Washington.

Gueri, M., Perez, L. (1986). Medical aspects of the "El Ruiz" avalanche disaster, Columbia. *Disasters*, 10, 150-157. https://doi.org/10.1111/j.1467-7717.1986.tb00580.x

Hand, D. (2000). Report of the inquest into the deaths arising from the Thredbo landslide. New South Wales: State Coroner.

Hayden, T. (2018a). "Internal records reveal mixed messages, missed opportunities before 1/9 debris flow." Santa Barbara Independent. Available at: https://www.independent.com/2018/05/24/internal-records-reveal-mixed-messages-missed-opportunities-before-1-9-debris-flow/. Accessed May 2020.

Hayden, T. (2018b). "Public survey exposes Montecito debris flow communication failures." Santa Barbara Independent. Available at: https://www.independent.com/2018/06/14/public-survey-exposes-montecito-debris-flow-communication-failures/. Accessed: May 2020.

Hewitt, K. (1997). *Regions of Risk: A Geographical Introduction to Disasters*. Essex: Addison Wesley Longman.

Highland, L., Bobrowsky, P. (2008). The landslide handbook—A guide to understanding landslides. *Circular 1325*. Reston, VA: U.S. Geological Survey

Hoffmann, R., Muttarak, R. (2017). Learn from the past, prepare for the future: Impacts of education and experience on disaster preparedness in the Philippines and Thailand. *World Development*, 96, 32-51. http://dx.doi.org/10.1016/j.worlddev.2017.02.016

Homma, Y., Watari, T., Baba, T., Suzuki, M., Shimizu, T., Fujii, Y., Takazawa, Y., Maruyama, Y., Kaneko, K. (2016). *Disaster Medicine Public Health Preparedness*, 10, 248-252. https://doi.org/10.1017/dmp.2015.167

Hudson, R. (1982). Report on the rainstorm of August 1982. *GCO Report No. 7/82*. Hong Kong Geotechnical Engineering Office.

Hungr, O., Leroueil, S., Picarelli, L. (2014). The Varnes classification of landslide types, an update. *Landslides*, 11, 167-194. https://doi.org/10.1007/s10346-013-0436-y

Iverson, R. (1997). The physics of debris flows. *Rev. Geophys.*, 35, 245-296. https://doi.org/10.1029/97RG00426

Jaiswal, P., van Westen, C., Jetten, V. (2011). Quantitative estimation of landslide risk from rapid debris slides on natural slopes in the Nilgiri hills, India. *Nat. Hazards Earth Syst. Sci.*, 11, 1723-1743. www.nat-hazards-earth-syst-sci.net/11/1723/2011/

Jakob, M., Stein, D., Ulmi, M. (2012). Vulnerability of buildings to debris flow impact. *Nat. Hazards*, 60, 241-261. https://doi.org/10.1007/s11069-011-0007-2

Jonasson, K., Siguroson, S., Arnalds, P. (1999). Estimation of avalanche risk. Rit Veourstofu Islands VI-R99001-UR01.

Kang, H-s., Kim, Y-t. (2016). The physical vulnerability of different types of building structure to debris flow events. *Nat. Hazards*, 80, 1475-1493. https://doi.org/10.1007/s11069-015-2032-z

Kean, J., Staley, D., Lancaster, J., Rengers, F., Swanson, B., Coe, J., Hernandez, J., Sigman, A., Allstadt, K., Lindsay, D. (2019a). Inundation, flow dynamics, and damage in the 9 January 2018 Montecito debris-flow event, California, USA: Opportunities and challenges for post-wildfire risk assessment. *Geosphere*, 15. https://doi.org/10.1130/GES02048.1

Kean, J., Staley, D., Lancaster, J., Rengers, F., Swanson, B., Coe, J., Hernandez, J., Sigman, A., Allstadt, K., Lindsay, D. (2019b). Debris-flow inundation and damage data from the 9 January 2018 Montecito debris-flow event, U.S. Geological Survey data release, http://doi.org/10.5066/P9JQJU0E

Keaton J., Wartman J., Anderson S., Benoit, J., dela Chapelle, J., Gilbert, R. (2014). The 22 March 2014 Oso Landslide, Snohomish County, Washington. Geotechnical Extreme Events Reconnaissance Report.

Kennedy, I., Petley, D., Murray, V. (2016). Landslides. In: K. Koenig, C. Schultz (*eds*). Koenig and Schultz's Disaster Medicine: Comprehensive Principles and Practices. Cambridge: Cambridge University Press. https://doi.org/10.1017/CBO9781139629317.045

Kennedy, I., Petley, D., Williams, R., Murray, V. (2015). A systematic review of the health impacts of mass earth movements (landslides). *PLoS Curr*., 7. https://doi.org/10.1371/currents.dis.1d49e84c8bbe678b0e70cf7fc35d0b77

Keylock, C., Barbolini, M. (2001). Snow avalanche impact pressure – vulnerability relations for use in risk assessment. *Can. Geotech. J*., 38, 227-238. https://doi.org/10.1139/t00-100

King, A., Bell, R., Heron, D., Matcham, I., Schmidt, J., Cousins, W., Reese, S., Wilson, T., Johnston, D., Henderson, R., et al. (2009). RiskScape Project: 2004 – 2008. *GNS Science Consultancy Report 2009/247*. GNS Science.

Kirschbaum, D., Adler, R., Hong, Y., Hill, S., Lerner-Lan, A. (2010). A global landslide catalog for hazard applications: Method, results, and limitations. *Nat. Hazards*, 52, 561-575. https://doi.org/10.1007/s11069-009-9401-4

Kunii, O., Akagi, M., Kita, E. (1995). The medical and public health response to the great Hanshin-Awaji earthquake in Japan: A case study in disaster planning. *Medicine Global Survival*, 2, 214-226.

Langdon, S., Johnson, A., Sharma, R. (2019). Debris flow syndrome: Injuries and outcomes after the Montecito debris flow. *Am. Surg*. 85, 1094-1098.

Lee, M., Jones, D. (2014). *Landslide Risk Assessment*. London: Institution of Civil Engineers. 2nd Ed.

Li, Z., Nadim, F., Huang, H., Uzielli, M., Lacasse, S. (2010). Quantitative vulnerability estimation for scenario-based landslide hazards. *Landslides*, 7, 125-134. https://doi.org/10.1007/s10346-009-0190-3

Lin, Q., Wang, Y., Liu, T., Zhu, Y., Sui, Q. (2017). The vulnerability of people to landslides: A case study on the relationship between casualties and volume of landslides in China. *Int. J. Environ. Res. Public Health*, 14, 212. https://doi.org/10.3390/ijerph14020212

Lo, W-C., Tsao, T-C., Hsu, C-H. (2012). Building vulnerability to debris flows in Taiwan: A preliminary study. *Nat. Hazards*, 64, 2107-2128. https://doi.org/10.1007/s11069-012-0124-6

Marsh, D., Schroeder, D. (2002). The positive deviance approach to improve health outcomes: Experience and evidence from the field—Preface. *Food and Nutrition Bull.*, 23, 3-6. https://doi.org/10.1177/15648265020234S201

Massey, C., Thomas, K-L., King, A., Singeisen, C., Taig, T., Horspool, N. (2019). SLIDE (Wellington): Vulnerability of dwellings to landslides (Project No. 16/SP740). *GNS Science report; 2018/17*. GNS Science.

Mavrouli, O., Corominas, J. (2010). Rockfall vulnerability assessment for reinforced concrete buildings. *Nat. Hazards Earth Syst. Sci.*, 10, 2055-2066. https://doi.org/10.5194/nhess-10-2055-2010

McDougall, S., McKinnon, M., Hungr, O. (2012) Developments in landslide runout prediction. In: J. Clague, D. Stead (*Eds*.) *Landslides: Types, Mechanisms and Modelling*. Cambridge: Cambridge University Press.

McPhee, J. (1989). *The Control of Nature*. New York: Farrar, Straus and Giroux

Memchoubi, P., Loyi, M., Nabachandra, H. (2012). Landslide fatalities: A study of six cases. *J. Indian Acad. Forensic Med.*, 34, 182-184

Menoni, S., Pergalani, F., Boni, M., Petrini, V. (2002). Lifelines earthquake vulnerability assessment: A systemic approach. *Soil Dyn. Earthquake Eng.*, 22, 1199-1208. https://doi.org/10.1016/S0267-7261(02)00148-3

Merchant, R., Leigh, J., Lurie, N. (2010). Health care volunteers and disaster response—First, be prepared. *N. Engl. J. Med.*, 362, 872-873. https://doi.org/10.1056/NEJMp1001737

Metivier-Hart, D. (2017). *A Silent Stillness—Buried Alive: One Woman's Remarkable Story of Survival, Hope and Rescue; the Last Survivor of the La Conchita Landslide*. Xlibris.

Michael-Leiba, M., Baynes, F., Scott, G., Granger, K. (2005). Quantitative landslide risk assessment of Cairns, Australia. In: T. Glade, M. Anderson, M. Crozier. *Landslide Hazard and Risk*. West Sussex: John Wiley & Sons.

Moore, R., Hencher, S., Evans, N. (2001). An approach for area and site-specific natural terrain hazard and risk assessment. In: K. Ho, K. Li (*Eds*.) *Geotechnical Engineering: Meeting Society's Needs*, Hong Kong: Proceedings of the 14th South East Asian Geotechnical Conference.

Norris, F., Murphy, A., Baker, C., Perilla, J. (2004). Postdisaster PTSD over four waves of a panel study of Mexico's 1999 flood. *J. of Traumatic Stress*, 17, 283-292. https://doi.org/10.1023/B:JOTS.0000038476.87634.9b

Oakley, N., Cannon, F., Munroe, R., Lancaster, J., Gomberg, D., Ralph, F. (2018). Brief communication: Meteorological and climatological conditions associated with the 9 January 2018 post-fire debris flows in Montecito and Carpinteria, California, USA. *Nat. Hazards Earth Syst. Sci*., 18, 3037-3043. https://doi.org/10.5194/nhess-18-3037-2018.

Omira, R., Baptista, M., Miranda, J., Toto, E., Catita, C, Catalao, J. (2010). Tsunami vulnerability assessment of Casablanca-Morocco using numerical modelling and GIS tools. *Nat. Hazards,* 54, 75-95. https://doi.org/10.1007/s11069-009-9454-4

Papathoma-Kohle, M. (2016). Vulnerability curves vs. vulnerability indicators: Application of an indicator-based methodology for debris-flow hazards. *Nat. Hazards Earth Syst. Sci*., 16, 1771-1790. www.nat-hazards-earth-syst-sci.net/16/1771/2016/

Papathoma-Kohle, M. (2016). Vulnerability curves vs. vulnerability indicators: Application of an indicator-based methodology for debris-flow hazards. *Nat. Hazards Earth Syst. Sci.*, 16, 1771-1790. www.nat-hazards-earth-syst-sci.net/16/1771/2016/

Papathoma-Kohle, M., Gems, B., Sturm, M., Fuchs, S. (2017). Matrices, curves and indicators: A review of approaches to assess physical vulnerability to debris flows. *Earth Sci. Rev*., 171, 272-288. http://dx.doi.org/10.1016/j.earscirev.2017.06.007

Papathoma-Kohle, M., Keiler, M., Totschnig, R., Glade, T. (2012). Improvement of vulnerability curves using data from extreme events: Debris flow event in South Tyrol. *Nat. Hazards*, 64, 2083-2105. https://doi.org/10.1007/s11069-012-0105-9

Papathoma-Kohle, M., Zischg, A., Fuchs, S., Glade, T., Keiler, M. (2015). Loss estimation for landslides in mountain areas – An integrated toolbox for vulnerability assessment and damage documentation. *Environ. Modell. Software*, 63, 156-169. https://doi.org/10.1016/j.envsoft.2014.10.003

Papathoma, M., Dominey-Howes, D., Zong, Y., Smith, D. (2003). Assessing tsunami vulnerability, an example from Herakleio, Crete. *Nat. Hazards Earth Syst. Sci.*, 3, 377-389. https://doi.org/10.5194/nhess-3-377-2003

Park, Y., Pradhan, A., Kim. U., Kim, Y-T., Kim, S. (2016). Development and application of urban landslide vulnerability assessment methodology reflecting social and economic variables. *Advances in Meteorology*, 2016. http://dx.doi.org/10.1155/2016/4572498

Pereira, B., Morales, W., Cardoso, R., Fiorelli, R., Fraga, G., Briggs, S. (2013). Lessons learned from a landslide catastrophe in Rio de Janeiro, Brazil. *Am. J. Disaster Med.*, 8, 253-258. https://doi.org/10.5055/ajdm.2013.0131

Pereira, S., Zezere, J., Quaresma, I., Santos, P., Santos, M. (2016). Mortality patterns of hydro-geomorphologic disasters. *Risk Analysis*, 36, 1188-1210. https://doi.org/10.1111/risa.12516

Petley, D. (2010). Landslide hazards. In: I. Alcantara-Ayala and A. Goudie (*Eds*.) *Geomorphological Hazards and Disaster Prevention*. Cambridge: Cambridge U. Press.

Petley, D. (2012). Global patterns of loss of life from landslides. *Geology*. 40, 927-930. https://doi.org/10.1130/G33217.1

Pita, G., Pinelli, J-P., Gurley, K., Weekes, J., Mitrain-Reiser, J. (2011). Wind vulnerability curves for low-rise commercial-residential buildings in the Florida public hurricane loss model. First International Symposium on Uncertainty Modelling and Analysis and Management and Fifth International Symposium on Uncertainty Modelling and Analysis. https://doi.org/10.1061/41170(400)75

Prieto, J., Journeay, M., Acevedo, A., Arbalaez, J., Ulmi, M. (2018). Development of structural debris flow fragility curves (debris flow buildings resistance) using momentum flux rate as a hazard parameter. *Eng. Geol.*, 239, 144-157. https://doi.org/10.1016/j.enggeo.2018.03.014

Quan Luna, B., Blahut, J., van Westen, C., Sterlacchini, S., van Asch, T., Akbas, O. (2011). The application of numerical debris flow modelling for the generation of physical vulnerability curves. *Nat. Hazards Earth Syst. Sci.*, 11, 2047-2060. https://doi.org/10.5194/nhess-11-2047-2011

Rashed, T., Weeks, J. (2003). Assessing vulnerability to earthquake hazards through spatial multicriteria analysis of urban areas. *Int. J. Geographical Information Sci*., 17, 547-576. https://doi.org/10.1080/1365881031000114071

Reese, S., Cousins, W., Power, W., Palmer, N., Tejakusuma, I., Nugrahadi, S. (2007). Tsunami vulnerability of buildings and people in South Java—Field observations after the July 2006 Java tsunami. *Nat. Hazards Earth Syst. Sci.*, 7, 573-589. https://doi.org/10.5194/nhess-7-573-2007

Rheinberger, C., Romang, H., Brundl, M. (2013). Proportional loss functions for debris flow events. *Nat. Hazards Earth Syst. Sci.*, 13, 2147-2156. https://doi.org/10.5194/nhess-13-2147-2013

Safeland. (2011). Physical vulnerability of elements at risk to landslides: Methodology for evaluation, fragility curves and damage states for buildings and lifelines. *Safeland Deliverable 2.5*. Available at: https://www.ngi.no/eng/Projects/SafeLand

Salvati, P., Petrucci, O., Rossi, M., Bianchi, C., Pasqua, A., Guzzetti, F. (2018). Gender, age and circumstances analysis of flood and landslide fatalities in Italy. *Science of the Total Environment*, 610-611, 867-879. http://dx.doi.org/10.1016/j.scitotenv.2017.08.064

Sanchez, C., Lee, T-S., Young, S., Batts, D., Benjamin, J., Malilay, J. (2009). Risk factors for mortality during the 2002 landslides in Chuuk, Federated States of Micronesia. *Disasters*, 33, 705-720. https://doi.org/10.1111/j.1467-7717.2009.01105.x

Santa Barbara County Sheriff's Office (SBCSO). (2018). "Names released of Montecito residents fatally injured during flood incident." Available at: https://www.sbsheriff.org/names-released-montecito-residents-fatally-injured-flood-incident/

Santi, P., Hewitt, K., VanDine, D., Cruz, E. (2011). Debris-flow impact, vulnerability, and response. *Nat. Hazards*, 56, 371-402. https://doi.org/10.1007/s11069-010-9576-8

Sattler, D., Kaiser, C., Hittner, J. (2000). Disaster preparedness: Relationships among prior experience, personal characteristics, and distress. *J. Applied Social Psychology*, 30, 1396-1420. https://doi.org/10.1111/j.1559-1816.2000.tb02527.x

Schilling, S. (2014). Laharz_py: GIS tools for automated mapping of lahar inundation hazard zones. *USGS Open-File Report 2014-1073*. Reston, VA: U.S. Geological Survey.

Schuster, R., Highland, L. (2001). Socioeconomic and environmental impacts of landslides in the western hemisphere. *USGS Open-File Report 01-276*. Reston, VA: U.S. Geological Survey.

Sheeju, P., Hussain, S., Balaram, N. (2019). Patterns of injuries in victims of landslide. *J. Medical Sci. Clinical Research*, 7, 123-127. https://dx.doi.org/10.18535/jmscr/v7i10.24

Snohomish County Medical Examiner's Office. (2014). "Media update as of July 23, 2014 at 9:00 AM." https://snohomishcountywa.gov/ArchiveCenter/ViewFile/Item/3913

Spence, R., So, E., Jenny, S., Castella, H., Ewald, M., Booth, E. (2008). The Global Earthquake Vulnerability Estimation System (GEVES): An approach for earthquake risk assessment for insurance applications. *Bull. Earthquake Eng.*, 6, 463-483. https://doi.org/10.1007/s10518-008-9072-7

Spiess, A-N., Neumeyer, N. (2010). An evaluation of R^2 as an inadequate measure for nonlinear models in pharmacological and biochemical research: A Monte Carlo approach. *BMC Pharmacology*, 10. https://doi.org/10.1186/1471-2210-10-6

Staes, C., Orengo, J., Malilay, J., Rullan, J., Noji, E. (1994). Deaths due to flash floods in Puerto Rico, January 1992: Implications for prevention. *Int. J. Epidemiology*, 23, 968-975. https://doi.org/10.1093/ije/23.5.968

Steinfuhrer, A., De Marchi, B., Kuhlicke, C., Scolobig, A., Tapsell, S., Tunstall, S. (2009). Vulnerability, resilience and social constructions of flood risks in exposed communities: A cross-country comparison of case studies in Germany, Italy, and the UK. *FLOODsite Report Number T11-07-12*.

Taig, T., Massey, C., Taig, M., Becker, J., Heron, D. (2015). Survey of Port Hills red zone residents' experience following the 22 February 2011 earthquake. *GNS Science Report 2015/09*. GNS Science.

Totschnig, R., Fuchs, S. (2013). Mountain torrents: Quantifying vulnerability and assessing uncertainties. *Eng. Geol.*, 155, 31-44. https://doi.org/10.1016/j.enggeo.2012.12.019

Totschnig, R., Sedlacek, W., and Fuchs, S. (2011). A quantitative vulnerability function for fluvial sediment transport. *Nat. Hazards*, 58, 681-703. https://doi.org/10.1007/s11069-010-9623-5

Tsao, T-C., Hsu, W-K., Cheng, C-T., Lo, W-C., Chen, C-Y., Chang, Y-L., Ju, J-P. (2010). A preliminary study of debris flow risk estimation and management in Taiwan. In: S-C. Chen (*Ed*.) Internationales Symposion Interpraevent in the Pacific Rim: Taipei.

UNISDR (2009). Chapter 2: Global disaster risk: Patterns, trends and drivers. In: *Global Assessment Report on Disaster Risk Reduction*. Available at: https://www.preventionweb.net/english/hyogo/gar/report/index.php?id=9413

United Nations. (2019). World Population Prospects 2019. United Nations, Department of Economic and Social Affairs, Population Division. Online Edition: https://population.un.org/wpp/

United Nations. (2020). World economic situation and prospects. New York: United Nations. Available at: https://www.un.org/development/desa/dpad/publication/world-economic-situation-and-prospects-2020/

Uzielli, M., Nadim, F., Lacasse, S., Kaynia, A. (2008). A conceptual framework for quantitative estimation of physical vulnerability to landslides. *Eng. Geol*., 102, 251-256. https://doi.org/10.1016/j.enggeo.2008.03.011

Vollmer, J., Schulze, P., Chebra, J. (2005). The American master bedroom: Its changing location and significance to the family. *J. Interior Design*, 31, 1-13. https://doi.org/10.1111/j.1939-1668.2006.tb00413.x

Wallingford, H. (2006). Flood risks to people. Defra/Environment Agency Flood and Coastal Defense R&D Programme FD2321/PR.

Wartman, J., Montgomery, D., Anderson, S., Keaton, J., Benoit, J., dela Chapelle, J., Gilbert, R. (2016). The 22 March 2014 Oso landslide, Washington, USA. *Geomorphology*, 253, 275-288. http://dx.doi.org/10.1016/j.geomorph.2015.10.022

Washington Geological Survey (WGS) and Oregon Department of Geology and Mineral Industries (DOGAMI). (2015). A homeowner's guide to landslides for Washington and Oregon. https://www.dnr.wa.gov/publications/ger_homeowners_guide_landslides.pdf

Washington Geological Survey (WGS). (2017). Landslide hazards in Washington State. *Washington Geological Survey Fact Sheet*. Olympia: Washington State Department of Natural Resources. Available at: https://www.dnr.wa.gov/publications/ger_fs_landslide_hazards.pdf

Wilhelm, C. (1998). Quantitative risk analysis for evaluation of avalanche protection projects. Oslo: Proceedings of the 25 Years of Snow Avalanche Research.

Winter, M., Smith, J., Fotopoulou, S., Pitilakis, K., Mavrouli, O., Corominas, J., Agyroudis, S. (2013). The physical vulnerability of roads to debris flow. 18th International Conference on Soil Mechanics and Geotechnical Engineering: Challenges and Innovations in Geotechnics, Paris.

Wishik, S., Van der Vynckt, S. (1976). The use of nutritional 'positive deviants' to identify approaches for modification of dietary practices. *Am. J. Public Health*, 66, 38-42. https://doi.org/10.2105/ajph.66.1.38

Wisner, B., Blaikie, P., Cannon, T., Davis, I. (2004). *At Risk: Natural Hazards, People's Vulnerability and Disasters*. New York: Routledge.

Wray, J. (1972). Can we learn from successful mothers? *J. Trop. Pediatr. Environ. Child Health*, 18, 279. https://doi.org/10.1093/tropej/18.4.279

Yale, J., Cole, T., Garrison, H., Runyan, C., Ruback, J. (2003). Motor vehicle-related drowning deaths associated with inland flooding after Hurricane Floyd: A field investigation. *Traffic Injury Prevention*, 4, 279-284. https://doi.org/10.1080/714040485

Yang, P., Yen, C-F., Tang, T-C., Chen, C-S., Yang, R-C., Huang, M-S., Jong, Y-J., Yu, H-S. (2011). Posttraumatic stress disorder in adolescents after Typhoon Morakot-associated mudslides. *J. Anxiety Disord.*, 25, 362-368. https://doi.org/10.1016/j.janxdis.2010.10.010

Zahran, S., Peek, L., Brody, S. (2008). Youth mortality by forces of nature. *Children, Youth, and Environments*, 18, 371-388.

Zhang, J., Gurung D., Liu, R., Murthy, M., Su, F. (2015). Abe Barek landslide and landslide susceptibility assessment in Badakhshan Province, Afghanistan. *Landslides*, 12, 597-609. https://doi.org/10.1007/s10346-015-0558-5

Zhang, S., Zhang, L., Li, X., Xu, Q. (2018). Physical vulnerability models or assessing building damage by debris flows. *Eng. Geol.*, 247, 145-158. https://doi.org/10.1016/j.enggeo.2018.10.017

Chapter 5—Multimodal quantitative landslide risk assessment for the country of Lebanon

The contents of this chapter are published as:

Pollock, W., Wartman, J., Abou-Jaoude, G., Grant, A. (2019). Risk at the margins: A natural hazards perspective on the Syrian refugee crisis in Lebanon. *Int. J. Disaster Risk Reduct*., 36. https://doi.org/10.1016/j.ijdrr.2018.11.026

and

Pollock, W., Wartman, J., Abou-Jaoude, G., Grant, A. (2019). Quantitative coseismic and precipitation-induced landslide risk mapping for the country of Lebanon. GeoCongress. Philadelphia: ASCE; 2019. https://doi.org/10.1061/9780784482155.013

5.1 Introduction

The 2010 – 2011 "Arab Spring" swept into Syria with a populist revolt in March 2011, since devolving into a devastating, internal war which has become one of the largest humanitarian catastrophes of our time. To present, over 400,000 Syrians have been killed, with a million injured and over 12.2 million displaced (UNHCR, 2018a). The crisis has had a devastating spillover effect on Syria's neighbors, especially the country of Lebanon, where Syrian refugees have swelled its population by 40%, almost twenty years ahead of pre-crisis growth projections (DAR-IAURIF, 2005). The influx of 1.5 million refugees coupled with a refugee non-encampment policy has strained Lebanon's already weakened infrastructure and environment (Yassin et al., 2015), pushing vulnerable populations into high-hazard areas and creating a potent incubator for a secondary disaster within a disaster.

In this work, we examine how regional crises, humanitarian disasters, and political policy-making affect a country's geologic risk profile. While a vast body of literature takes a hazard-dominant view of disaster, we adopt a human ecology perspective, emphasizing the role of civil crisis and response. We offer a novel, transferrable model framework for rapid landslide risk assessment at the scale and pace of humanitarian crises. We analyze the landslide risk to Syrian refugees in Lebanon on a quarterly basis over five years of the Syrian Crisis, illustrating the need for real-time risk analyses in immediate refugee crisis response. Specific to Lebanon, we present a comprehensive landslide (i.e., mass-wasting) risk profile including a suite of triggering scenarios and landslide modes, identify the unique spatial risk-signatures of different

demographic groups, and study the impacts of Lebanon's evolving no-camp policy on environmental risk.

5.2 The Syrian Crisis

In the context of populist "Arab Spring" uprisings in the beginning of 2011, a pro-democracy uprising against the Syrian regime joined the country in civil war. The following seven years of conflict have displaced over 12 million—half of Syria's prewar population—making it the most significant refugee crisis in a generation (UNHCR, 2018a). Out of the 5.6 million refugees who have fled Syria, 1.5 million have settled in Lebanon, which with a pre-crisis population of only 4.5 million, hosts the highest number of refugees per capita worldwide. The influx of refugees from the Syrian crisis has put a heavy burden on Lebanon, a country already suffering from a fragile sectarian governmental structure, sub-standard infrastructure, chronic socio-economic weakness, and destabilization from regional wars (Salloukh, 2017; Yassin et al., 2015). These factors play an essential role in the Government of Lebanon's (GoL) evolving policies regarding Syrian refugees.

5.2.1 Lebanese refugee response

Throughout the first three years of the Syrian crisis, the GoL pursued a refugee "policy of no policy," maintaining de facto open borders and little regulation of Syrian refugees (Mourad, 2017; Yassin et al., 2015). Disassociation from the Syrian crisis was symptomatic of gridlock between pro- and anti-Syrian-regime political factions and fears that Syrian instability would

exacerbate Lebanon's own sectarian strife (Mourad, 2017). The United Nations High Commissioner for Refugees (UNHCR) began aiding small numbers of Syrians fleeing to the northern Lebanese district of Akkar in April 2011. By the end of 2011, 4,840 Syrians were registered with the UNHCR mostly in north Lebanon. As fighting in Syria intensified, the influx of Syrians into Lebanon increased dramatically, with 175,000 registered with the UNHCR by the end of 2012 and 860,000 by the end of 2013. Shortly after exceeding 1 million registered refugees in mid-2014, the GoL took decisive action to decrease the Syrian population in Lebanon, closing its borders to Syrian refugees and ordering a stay on the registration of refugees with the UNHCR (Janmyr, 2018). Although the number of registered refugees subsequently declined, the actual number of Syrians in Lebanon remains much higher **(Figure 5.1)** due to unregistered births, fear of registration, and lack of access (LHIF, 2014; UNHCR, 2017a). The number of unregistered Syrians in Lebanon has grown from ~500,000 in 2013 to ~1.5 million at present (GoL and UN, 2017; ICG, 2013).

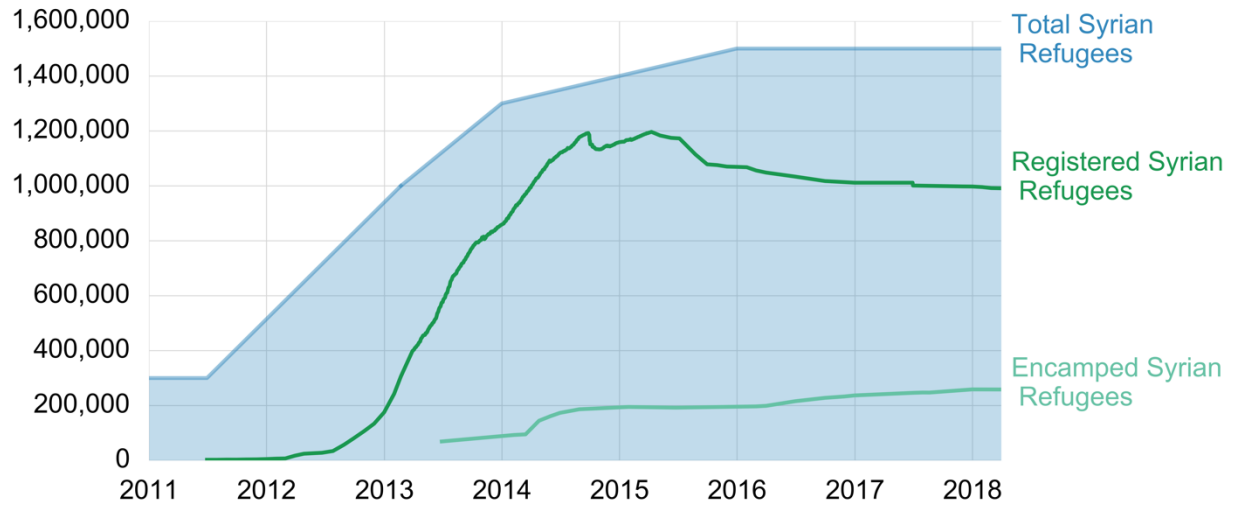

Figure 5.1. Population of Syrians in Lebanon throughout the crisis. The total number is currently ~1.5 million, with 300,000 of these working in Lebanon prior to 2011 but now considered refugees by the Lebanese government and NGOs.

Syrians in Lebanon face housing, economic, socio-cultural, and legal marginalization. The 2017 Vulnerability Assessment of Syrian Refugees in Lebanon (UNHCR, 2017a) found that only 74% of Syrians 15 and older had legal residency, facilitating exploitive labor practices (Janmyr and Mourad, 2018). A saturated job market, dwindling savings, and demand-driven increases in the cost of living mean that 58% of Syrian refugee households do not spend enough to meet basic survival needs (UNHCR, 2017a). Additionally, Lebanon's already strained housing sector, public services, and education system have deteriorated, escalating tensions among Syrians and the communities that host them and, in extreme cases, prompting municipal policies which target Syrian freedoms (Janmyr, 2016; Yassin et al., 2015). These forces conspire to create a high degree of marginalization in economy, shelter, place, and power.

5.2.2 Settlement patterns

Fearing that the establishment of Syrian refugee camps could promote long term settlement—repeating the 65-year "temporary" asylum of Palestinian refugees—the GoL has strictly prohibited formal refugee camps (Janmyr, 2016). Thus, Syrian refugees have dispersed throughout Lebanon, integrating into local communities and finding shelter where it is available. The majority (73%) live in residential structures, while 9% live in non-residential units such as garages, barns, and workshops. However, a significant minority (17%) have bridged the gap between urban and encamped settlement, self-establishing informal tented settlements (ITS). The majority of these refugees do not have legal residency, available through registration with the UNHCR (Janmyr, 2018; UNHCR, 2017a). Some ITS are effectively small refugee camps,

with administration, security staff, medical and sanitation services, and established support of NGOs. while many others are merely clusters of families living in timber and plastic tents on informally rented land (**Figure 5.2**; Sanyal, 2017). Syrian refugees from the socioeconomic upper classes have migrated to the coastal cities, attracted by employment opportunities, while the poorest Syrians have stayed near the Syrian border (Thorleifsson, 2016). This has led to numerous ITS in the Bekaa valley and northern districts where Syrians have been unable to find affordable housing (**Figure 5.3**). The divergent settlement patterns of Syrians in Lebanon led us to distinguish between three demographic groups in our consideration of landslide risk: urban Lebanese, urban Syrian refugees, and encamped Syrian refugees, each subject to a unique combination of spatial distribution, settlement style, exposure characteristics, and physical vulnerability. Syrian refugees are bureaucratically categorized as "registered," "unregistered," and "recorded," while their spaces of refuge reflect a spectrum between urban integration and informal encampment (Janmyr and Mourad, 2018; Sanyal, 2017). Quantitative data about the delineation and overlap of these categories is scarce. Based on annual survey trends of Syrian refugees in Lebanon, we adopt the simplifying generalization that urban refugees are registered with the UNHCR while encamped refugees are unregistered (UNHCR, 2017a).

Figure 5.2. An informal refugee camp in the Bekaa Valley, Lebanon. Image: R. Watkins /Department for International Development, CC BY 2.0

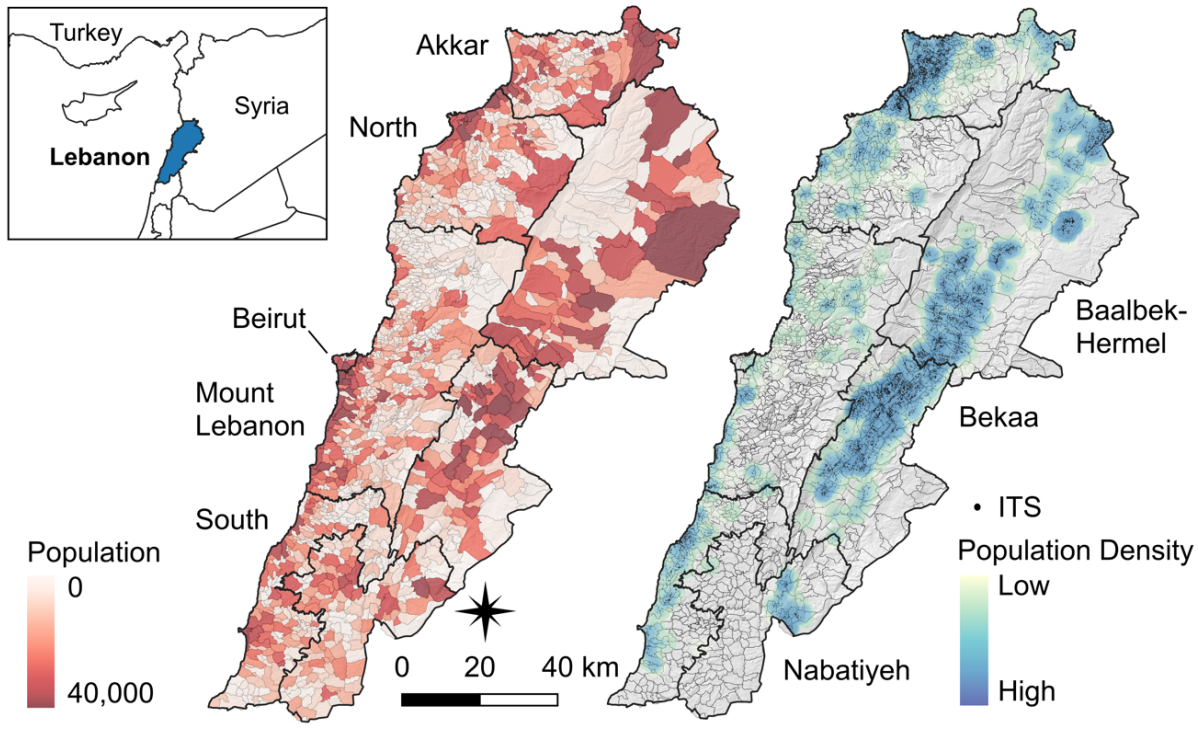

Figure 5.3. Spatial distribution of registered Syrian refugees by cadastre as of January 2018 (left) and the location and population density of informal tented settlements (ITS) established by Syrian refugees as of December 2017 (right). Data from the UNHCR (2018b).

5.3 Camp policies

5.3.1 UNHCR policy on refugee camps

Within the humanitarian aid community, Lebanon has become the focal point of debate among stakeholders regarding the merits of establishing refugee camps (ICG, 2013; Sanyal, 2017; Turner, 2015; Yassin et al., 2015). The GoL's "no camp" policy aligns with the UNHCR's most recent settlement policy, albeit for different reasons. The UNHCR has historically held a strong preference for managing refugees through encampment (Turner, 2015). Localizing refugees

streamlines aid distribution, monitoring, and administration as well as making refugees "visible" for the purpose of fundraising (ICG, 2013; Turner, 2015). In addition, the isolation and self-containment of refugee camps provide a measure of protection for both refugees and host communities (UNHCR, 2014). Criticized by human rights organizations for "warehousing" refugees in camps, the UNHCR underwent an internal review process, producing major policy updates to its treatment of urban (non-encamped) refugees in 2009 and 2014 (Verdirame and Pobjoy, 2013; Yassin et al., 2015). The 2014 Policy on Alternatives to Camps represents a 180-degree shift in the UNHCR policy toward camps, stating, "UNHCR's policy is to pursue alternatives to camps, whenever possible." The policy's rationale reflects both the current reality of forced displacement, with 60% of refugees living outside of camps, and the negative effects engendered by encampment, such as fostering dependency and restricting freedom of movement (UNHCR, 2014; UNHCR, 2017b).

5.3.2 Environmental hazard community

Largely absent from the ongoing controversy about refugee management through encampment is the voice of the environmental hazards scientific community. Increasing recognition has been given within technical fields to "disasters of social vulnerability" in which indiscriminate natural hazards become discriminating "unnatural" disasters, incurring greater losses among the socially marginalized (Hewitt, 1997, 2012). The environmental hazards community has diagnosed the trend of impoverished and powerless populations settling in regions of high hazard, interacting destructively with their environment, and having limited access to protections (Santi et al., 2011; Wisner and Luce, 1993). Marginalized populations have also been observed to suffer a

disproportionately greater loss in disasters (e.g. Dowling and Santi, 2014; Hewitt, 1997; Morris et al., 2002), although the processes through which this occurs have not been quantified. Application of this knowledge to resettlement aid has been inconsistent and problematic (Felix, et al., 2015). UNHCR internal surveys suggest that refugees in camps face a higher risk of secondary displacement from natural disasters than those integrated into host communities, due to the anthropogenic increases in exposure and vulnerability produced by encampment. Limited undeveloped land may force refugee camps into marginal areas. Additionally, rapidly-produced, inexpensive shelter solutions often provide little protection from extreme events, and high population density serves as a consequence multiplier, as recent disasters in Rwandan, Kenyan, and Thai refugee camps have demonstrated (UNHCR, 2018c). During the 2018 monsoon season, 150,000 – 200,000 Rohingya refugees were identified by the UNHCR and its partners as "at risk" to landslides and flash flooding in a hilly encampment around Cox Bazaar, Bangladesh, due to space constraints and environmental degradation (UNEP, 2018; UNHCR, 2018d). Although risk-informed settlement is a minimum standard of humanitarian response, literature is devoid of the quantitative comparison of natural hazard risk experienced by encamped and urban refugee communities (Sphere, 2011). Long-term trends show an increase in extreme climate events and forced human resettlement, especially in climate change hotspots, highlighting the urgent need for increased data and research in the area of disaster risk reduction among displaced peoples (NRC, 2015; UN, 2015; UNHCR, 2017b).

5.4 Definitions

5.4.1 Vulnerability

We define vulnerability as *the potential for something to suffer harm from a human perspective*, be it from a natural hazard, anthropogenic crisis, or intangible or perceived threats (Lee and Jones, 2014). In this work, we focus on limited, but standardized, *physical human vulnerability*—the potential for loss of life in a discrete hazard—while acknowledging that the complex socio-economic factors of social vulnerability may play a dominant role in post-disaster loss, suffering, and recovery (Lee and Jones, 2014; Wisner et al., 2004).

5.4.2 Risk

We define risk as *the combined likelihood and magnitude of loss due to an adverse event*. Elements at risk include infrastructure, populations, environmental features, and economic activities. Risk is correspondingly quantified in fatalities, dollars lost, and economic downtime caused by a disaster (Fell et al., 2008). It is often beneficial to quantify the burden (in deaths, financial or environmental losses, etc.) of landslide disasters to a society without any differentiation between members. This allows for useful comparison of landslide risk between large entities of interest (e.g. regions, countries) as well as standards of acceptable risk across varied sectors. However, rarely does everyone in a society share equal risk, the spatial distribution, status, or life patterns of member subsets subjecting them to greater hazard,

vulnerability, or exposure. Thus it may also be beneficial to individualize risk as *the annual probability of death of a single person experiencing a given hazard* (AGS, 2007a).

5.5 Natural environment of Lebanon

5.5.1 Topography and geology

Lebanon is a small (10,452 km^2), mountainous country on the eastern Mediterranean. The primary city centers lie on a narrow (5 – 15 km) coastal shelf (**Figure 5.4**). Forested, inland hills rise steeply to the crest of the Mount Lebanon Range (~ 3000 m) 20 – 30 km inland. Moving eastward, the Mount Lebanon Range drops dramatically into the flat, agricultural center of the Bekaa Valley (~ 1000 m) before rising to the sparsely vegetated Anti-Lebanon Range (~2000 m) which forms the eastern border with Syria. Numerous E-W valleys deeply incise the western Mount Lebanon Range front, exposing alternating bands of Jurassic to Cretaceous-age limestone and sandstone. Four geologic units dominate the Lebanese landscape. Jurassic Kesaroune limestone forms a thick (up to 2.5 km) platform at the base of Lebanon's stratigraphic sequence and is abundantly exposed in the incised valleys between Beirut and Tripoli. Heavy fracturing in the Kesaroune limestone produces frequent rock falls (Abdallah and Faour, 2017). Uplift led to the fluvial-deltaic deposition of the early Cretaceous Chouf, a distinctive loosely-cemented sandstone prone to slumps and flows (Khawlie and Hassanain, 1984; Walley, 1998). Sea-level rise in the late Cretaceous renewed the deposition of carbonates including Mdairej limestone, recognizable as a single gray, shear-sided cliff which is a common source of rock falls (Khawlie and Hassanain, 1984). Massive (300 – 500 m) bluffs of late Cretaceous Sannine limestone cap

the high elevations in Lebanon and routinely produce debris flows and falls (Abdallah and Faour, 2017). Geotechnical strength parameters were assigned to mapped geologic units (Dubetret, 1945) after Grant et al. (2016), see **Appendix 5.1**, **Table A5.1.1**.

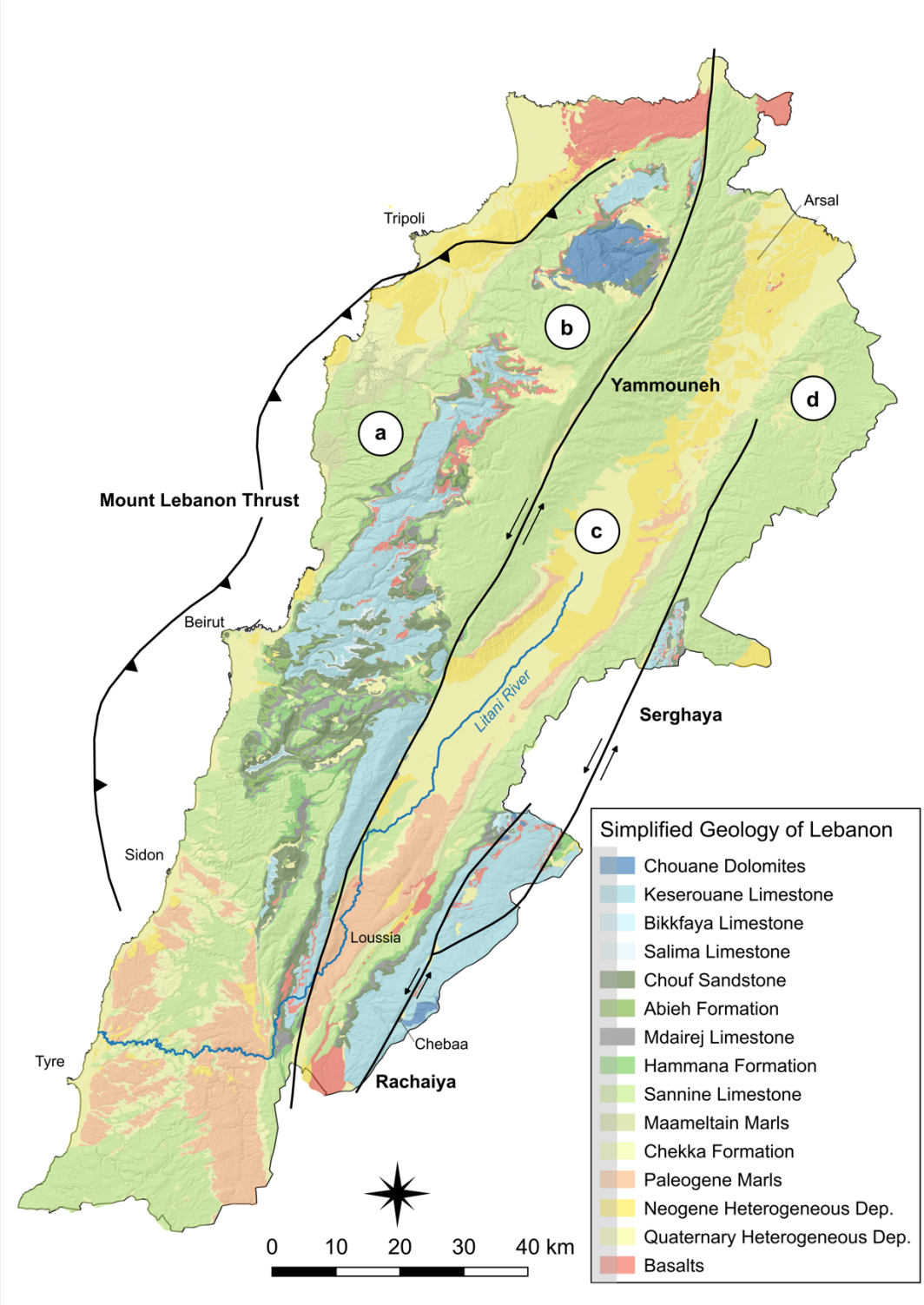

Figure 5.4. Major faults, regions, and geologic units referenced in this work. Topographic regions: (*a*) coastal band, (*b*) Mount Lebanon Range, (*c*) Bekaa Valley, and (*d*) Anti-Lebanon Range. Modified after Grant et al. (2016).

5.5.2 Tectonics

Lebanon's topography has been shaped by four major faults. The Mount Lebanon Range is bounded on the east by the left-lateral Yammouneh Fault, an NNE – SSW restraining bend of the Dead Sea Transform. Slip rates along the Yammouneh are 5.1 ± 1.3 mm/yr, and it is estimated to produce M > 7 earthquakes with a return period of 1127 ± 135 years (Daëron et al., 2004, 2007). The upland valley of the Bekaa is bounded by the Serghaya fault to the east and the Rachaya fault to the south. The Serghaya is estimated to be slipping at 1.4 ± 0.2 mm/yr and to produce large earthquakes with a return period of 1300 years (Gomez et al., 2003). The recently discovered Mount Lebanon Thrust fault (MLT) forms an offshore arc, from Tripoli in the north to Sidon in the south. Slip along the MLT is estimated to be 1 – 2 mm/yr with a return period of M ~7.5 earthquakes of 1500 – 1750 years (Daëron et al., 2005; Elias et al., 2007).

5.5.3 Climate

Lebanon has a characteristic Mediterranean climate, with cool, wet winters and hot, dry summers, moderated by elevation and distance from the coast. The coastal band, including the cities of Tyre, Beirut, and Tripoli, receives moderate annual rainfall (700 – 1000 mm) increasing to the north (**Appendix 5.1**, **Figure A5.1.4**). The Mount Lebanon Range experiences a strong rainfall gradient from 900 mm in Byblos to over 1400 mm annually in Qartaba. Springtime convective storms can bring rainfall intensities of 100 mm per hour (Verner et al., 2013). Moving away from the Mediterranean, the climate becomes more arid, with the Bekaa Valley

and western Anti-Lebanon Range receiving an average annual precipitation of 600 mm in the south to less than 200 mm in the north.

5.5.4 Previous work in Lebanon

The National Physical Master Plan of Lebanon (DAR-IAURIF, 2005) identifies landslides as an extensive and frequent hazard in Lebanon's rugged terrain, linked to $15 – 20 million (2018 USD) damages and numerous fatalities annually (Abdallah, 2007). Landslides are frequently triggered by severe winter storms, such as that of 1984, which caused 90 deaths and ~ $68 million in damages to infrastructure and agriculture across northern Lebanon (Khawlie, 1994; Abdallah, 2007). In March of 1992, a massive landslide near Zahle in the Bekaa Valley buried several houses, killing 20 people (Abadallah, 2010). The 551 AD Beirut-Tripoli earthquake triggered massive rotational slumps in the coastal region of Hamat, and recent, smaller earthquakes caused major failures near Hammana in 1924 and 1956 (Abdallah, 2007). Historical studies of landslides in Lebanon have been infrequent, localized, and primarily descriptive, starting with the geological map of Dubertret in 1945 (Abdallah, 2011). Since the Hyogo Framework for Action (UN, 2005), the GoL and international actors have made significant investments in landslide risk reduction initiatives throughout the country (GoL, 2015). Local landslide studies include the susceptibility to rock falls in the central Mount Lebanon district (Abdallah, 2010), an investigation of rock fall hazard outside of Kfar Nahbrakh (El Mohtar et al., 2016), and landslide hazard mapping in the Nahr Ibrahim watershed (Abdallah and Faour, 2017). The Lebanese National Council for Scientific Research (CNRS) released 1/50,000 (25 m effective resolution) scale maps of landslide hazard zones for the entire country based on

statistical methods (Abdallah, 2011; GoL, 2015). More recently, Grant et al. (2016) combined 10% in 50-year PSHA ground motion intensities (Huijer, 2010) and a suite of process-based slope stability models to predict the location, timing, and magnitude of coseismic landslides in Lebanon at high (15 m) resolution. To date, no work has been done to comprehensively assess the consequences (risk) of landslides to the human and built environment in Lebanon.

5.6 Methods

5.6.1 Quantitative risk analysis

Quantitative risk analysis (QRA) provides decision makers with an objective, reproducible, and transferable metric for making land use decisions. It allows for cost-benefit analyses, and the results can be easily transmitted between scientist, policy maker, and public in intuitive terms. Landslide risk is commonly expressed as the product of the probability of a phenomenon of a given magnitude in time and space with the consequences of the phenomenon:

$$R_{(Loss\ of\ Life)} = \sum_{1}^{n} \left(P_{(L)}\ x\ P_{(T:L)}\ x\ P_{(S:T)}\ x\ V_{(D:T)} \right) \quad \textbf{(5.1)}$$

where $R_{(Loss\ of\ Life)}$ is the annual probability that an individual will be killed (*risk*), $P_{(L)}$ is the probability in time and space of a landslide occurring (*hazard*), $P_{(T:L)}$ is the spatial probability of a landslide reaching the element at risk (*runout*), $P_{(S:T)}$ is the spatial-temporal probability of the element at risk being in the area affected by the landslide at the time of occurrence (*exposure*), and $V_{(D:T)}$ is the probability of injury or death given impact by a landslide (*vulnerability*) (Fell et

al., 2005; van Westen et al., 2006). The risk for each triggering case, mode of event, and magnitude are summed to produce the total annual probability of death. Although simple in form, application of the risk equation requires detailed input data and computational power, especially at high resolutions on large scales, making comprehensive regional or country-wide QRA difficult and rare (van Westen et al., 2006). In this work, we expand the multimodal landslide hazard model of Grant et al. (2016) and develop runout, exposure, and vulnerability analyses for our study area of Lebanon. A summary of our methodology is given below; for the full model description see **Appendix 5.1**.

5.6.2 Modes of failure

We focus on three fundamental modes of failure prevalent in Lebanon: 1) shallow, planar soil slides; 2) rock falls; and 3) rotational, coherent slumps in soil and rock (Hungr et al., 2014). These may be triggered by seismic shaking or precipitation. Statistical studies have found a correlation between slope and landslide mode (e.g. Keefer, 2013). We divide the terrain into slope-based zones susceptible to each failure mode based on previous work, existing landslide inventories in Lebanon, and our field observations (Abdallah and Faour, 2017; Grant et al., 2016). Slope ranges are 15 – 50°, 15 – 35°, and > 35° for shallow slides, rotational slumps, and rock falls, respectively. Slopes shallower than 15° were not considered prone to any mode of landsliding.

5.6.3 Seismic and precipitation triggers

Huijer (2010) modeled the major seismic sources in Lebanon, producing ground shaking intensities associated with 10% exceedance probability in 50, 100, and 500 years (**Appendix 5.1**, **Figure A5.1.4**). Annual average rainfall (Plassard, 1971) and recent maximum daily rainfall measurements from eight meteorological stations in Lebanon were used to estimate hydrologic landslide triggers (**Appendix 5.1**, **Section A5.1.1.4**). To account for both short-term and antecedent precipitation conditions, which control shallow and deep failure modes respectively, daily rainfall was linearly scaled by the average annual rainfall depths, creating a geographically continuous rainfall index for seven return periods (2, 3, 5, 10, 20, 50, and 100-year). From the rainfall index, we estimate pore pressure conditions, represented as percent of hillslope saturation, as the driver of precipitation-induced rock falls and coherent failures (**Appendix 5.1**, **Tables A5.1.2** and **A5.1.3**).

5.6.4 Model development

We adopt the pixel-based, multimodal coseismic landslide hazard method of Grant et al. (2016) and derive a parallel set of mode-specific models for precipitation-induced landslides (**Appendix 5.1**, **Section A5.1.1.2**). For coseismic failures, simple, physics-based models are used to calculate the factor of safety (FS) against shallow, disrupted slides; rotational, coherent slumps; and rock falls. These FS values are compared to peak ground accelerations through the simplified Newmark-sliding block method (Jibson, 2007) and converted to binary grids of failures zones based on threshold displacements (**Appendix 5.1**, **Section A5.1.1.2**). The

initiation of debris flows was assessed using the shallow landslide model SHALSTAB (Montgomery et al., 1994), which couples hydrologic and limit-equilibrium slope stability models to compute the critical daily rainfall to trigger a shallow soil failure. Rainfall-induced rock falls are modeled as Culmann wedge-like masses, including the effect of pore-pressure on the failure plane. Grant et al. (2016) developed a coherent failure model that combines larger hillslope conditions with individual grid-cell properties. The water pore pressure was added to the factor of safety equation, based on a saturation percentage of the maximum failure depth, and the model was expanded to three dimensions to account for edge effects.

5.6.5 Runout assessment

Under intense rainfall, debris flows can travel long distances in existing topographic channels. We extracted flowlines from a 15 m digital elevation model to calculate the runout path from each debris flow source. In the absence of empirical runout data in Lebanon, we limit each path to 750 meters, based on an inventory of relict debris flow tracks mapped from satellite imagery. Rock fall runout zones were calculated with a viewshed analysis from each source cell and limited by the reach angle of large rock falls observed in satellite imagery and during a field campaign in Lebanon in 2017 (**Appendix 5.1**, **Section A5.1.1.6**). The influence of coherent slumping failures was limited to the radius of the failing body, projected as a circular zone in a GIS environment (**Appendix 5.1**, **Section A5.1.1.5**).

5.6.6 Elements at risk

"Built-up" area maps use textural features from earth observation to identify the location, extent, and density of human settlement in an automated and consistent fashion across large regions (Ehrlich et al., 2010). We utilize 38 m binary grids of built-up area produced by the Global Human Settlement Layer from 2013 – 2014 Landsat Imagery (Pesaresi et al., 2015). We resampled built-up grids to 15 m and subtracted the Lebanese road network to produce separate grids of residential and road elements at risk (**Appendix 5.1**, **Figure A5.1.7**). To assess the evolving refugee population in Lebanon, we digitized UNHCR maps of the registered Syrian refugees by cadastre from 2013 – 2018 on three-month intervals. To support its work identifying vulnerable Lebanese, the UNHCR produced population projections of native Lebanese by cadastre in 2015. We adopt these values as the static Lebanese population from 2013 – 2018, acknowledging that this is an approximation in the absence of multi-temporal data. Since most cadastres are small (median ~2 km^2), containing a single urban cluster, we assume a constant population density within each cadastre, uniformly distributing the number of Lebanese and urban Syrian refugees among the built-up pixels, resulting in 15 m gridded urban population estimates. The UNHCR has performed country-wide sweeps every two months to identify the point location, population, and size of ITS in Lebanon. To approximate the areal extent of ITS, we buffer the settlement coordinates based on the number of tents (**Appendix 5.1**, **Section A5.1.1.7**).

5.6.7 Exposure and vulnerability

Human exposure within an ITS is calculated as the fraction of the area occupied by residents divided by the total area of the settlement. A resident density of 4.5 m^2 per person is adopted based on systematic UNHCR interviews (UNHCR, 2017a). The exposure of urban populations was estimated based on uniform occupancy within an average 3-story building and the expected zone of influence for each hazard mode. Vulnerability is a complex function of hazard type and magnitude, as well as the physical—and for humans, socio-economic—characteristics of the element at risk. For this reason, most assessments of vulnerability to landslides have been subjective (Lee and Jones, 2014). We adopt recommendations from the literature to estimate the physical vulnerability of urban (Lebanese and Syrian) populations and encamped refugees, distinguishing between hazard modes, as well as the source and runout zones of debris flows (Lee and Jones, 2014; **Appendix 5.1**, **Section A5.1.1.9**).

5.7 Results and discussion

5.7.1 Impacts of the Syrian Crisis

We estimate that landslides cause 37 deaths annually in Lebanon, based on the most current epoch of population data (**Table 5.1**). This is an increase in life-safety risk of 75% solely due to the massive population influx of Syrian refugees over the first seven years of the Syrian crisis. The breakdown of predicted landslide fatalities is biased toward Lebanese (58%) compared to 12% among the smaller urban Syrian refugee population. However, 30% of landslide casualties

in Lebanon are forecast to occur among encamped Syrian refugees even though they constitute only 5% of the total population. This is primarily a function of the encamped population's higher vulnerability. Encamped refugees showed no statistically meaningful settlement bias toward high-hazard cadastres, which, if found, would suggest socio-economic marginalization forcing them into less-desirable, hazard-prone land (Santi et al., 2011). Across the country, calculated exposures for encamped refugees were similar to those assigned for urban populations, with a median of 0.09 (encamped) compared to 0.067 and 0.333 (urban) for debris flow runout and source zones respectively, indicating that the inability to escape hazards vertically due to single-story dwellings is not a persistent contributor to greater risk. However, encamped refugees have a high physical vulnerability, their plastic and timber shelters offering little to no protection from landslide events. Although the quantitative vulnerability of refugees in ITS is subjective, literature agrees that informal settlers are qualitatively much more vulnerable to environmental hazards than those in formal residences (McCallin and Scherer, 2015; O'Hare and Rivas, 2005).

5.7.2 Spatial distribution of risk

Nearly all (93%) of the risk from landslides in Lebanon comes from debris flow runout. However, populations in Lebanon experience risk in disparate ways. Debris flows are a widespread source of risk to urban populations, especially in the highly populated, rugged Mount Lebanon district and the barren western flank of the Anti-Lebanon Range (**Figure 5.5**). Among urban populations, the majority of annual losses come from frequent and widespread low-intensity storms while the risk to encamped refugees is localized in 60 high-density settlements

scattered across only 11 cadastres. Other modes of failure result in annual risk orders of magnitude lower than that of debris flows, in part due to their limited spatial and temporal extent. Rock falls are limited to zones below exposures of cliff-forming units, and coherent failures occur infrequently, primarily in Mt. Lebanon's weak sandstone. Areas which have historically been affected by these localized modes of failure are less likely to be inhabited, whereas the vast extent of shallow failures and debris flows make human settlement in hazard zones inevitable; Lebanon simply does not have enough space. Coseismic landslides are an insignificant source of risk in Lebanon, primarily due to the long return periods of damaging earthquakes.

Table 5.1. Annual risk of loss of life due to landslides for Lebanese (2015), urban Syrian refugees (Jan. 2018), and encamped Syrian refugees (Dec. 2017). '<' indicates losses from 0.001 – 0.01, '<<' indicates losses less than 0.001 fatality per year. Population totals do not include Lebanon's ~ 500,000 Palestinian refugees.

Trigger	*Hazard*	*Population*		*Annualized Loss*
Precipitation-induced	Debris flows	Lebanese (4,017,000)	Runout	19.20
			Source	1.90
		Urban Syrian refugees (996,000)	Runout	3.82
			Source	0.40
		Encamped Syrian refugees (259,000)	Runout	11.25
			Source	na
	Rotational, coherent slumps	Lebanese		< 0.01
		Urban Syrian refugees		< 0.01
	Rock falls	Lebanese		0.17
		Urban Syrian refugees		0.21
Coseismic	Disrupted soil slides	Lebanese		< 0.01
		Urban Syrian refugees		<< 0.01
	Rock falls	Lebanese		< 0.01
		Urban Syrian refugees		< 0.01
		Encamped Syrian refugees		<< 0.01
Total				36.97

We highlight two locations of interest, due to the unique intersection of population groups, modes of failure, and the sociopolitical forces which have governed the refugee crisis in Lebanon.

The town of Arsal in northeastern Lebanon has been the epicenter of the country's political turmoil over the Syrian refugee crisis, as well as emblematic of the crisis to international media. During the summer of 2013, entire Syrian towns settled en-masse in Arsal, with 16,000 registered Syrian refugees mid-2013 and 40,000 one year later, manifest in the sprawling, white-sheeted ITS in which the majority of Syrians live. An additional 20,000 unregistered Syrians currently reside in Arsal (Al Ayoubi, 2018). Clashes with militants in 2014 made Arsal a "no-go" zone for NGOs, exacerbating the harsh living conditions of refugees. 36 out of Arsal's 124 currently active ITS are intersected by debris flow paths, some by more than one (**Figure 5.6a**). Arsal's intersection of high-density hazard and concentrated ITS make it the highest-risk cadastre among any population group, with six deaths among encamped refugees predicted annually.

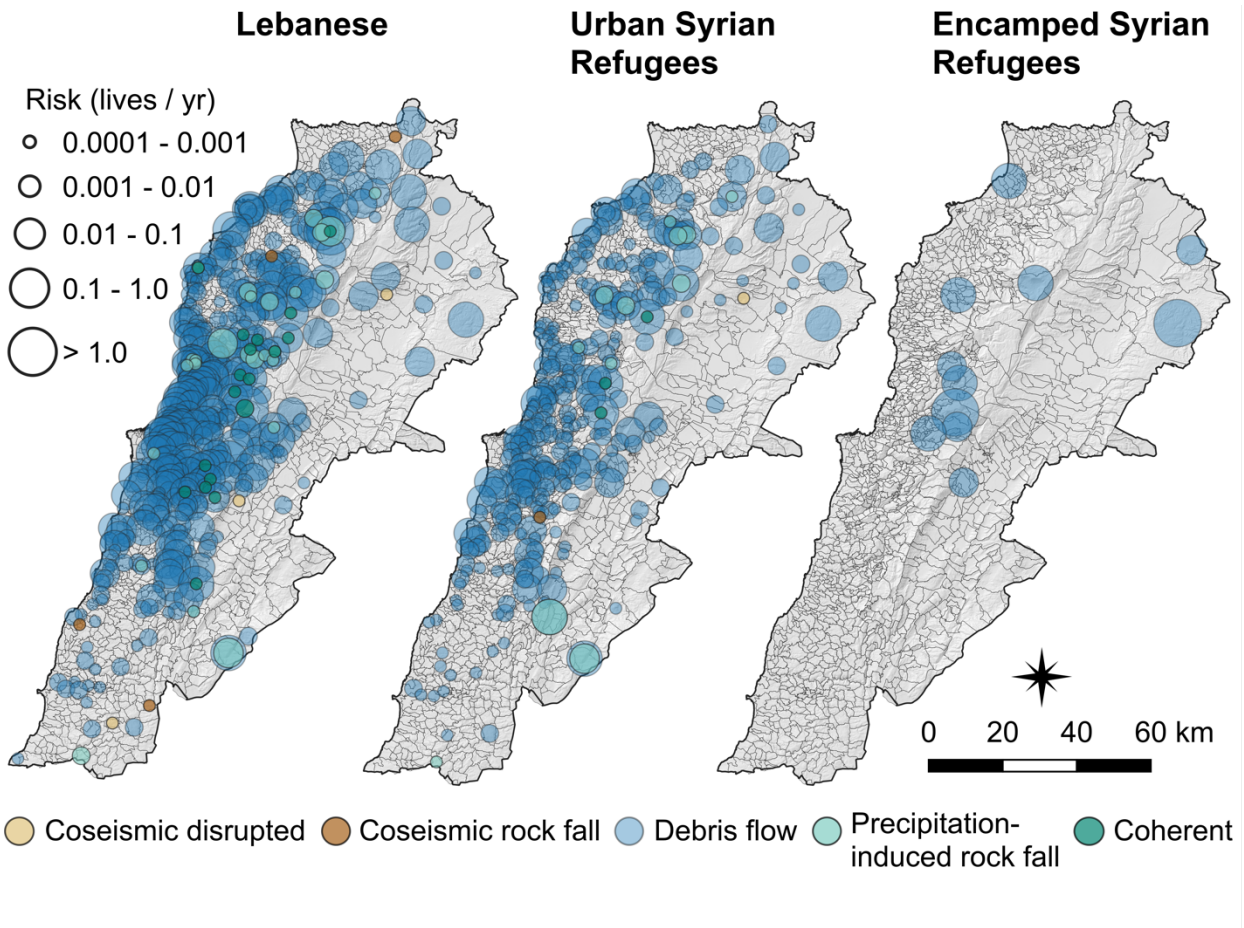

Figure 5.5. Spatial distribution of risk by cadastre and mode.

The town of Chebaa spans a rocky valley on Lebanon's southern border with the Golan Heights. Although host to only a tiny fraction of the country's registered Syrian refugees it has become a microcosm of the refugee crisis in Lebanon, with a surging refugee population – 1400 in August 2013 to over 3000 in January of 2018 – that has led to tension as limited resources are spread between poor Lebanese and poorer Syrians (UNHCR, 2018b). Chebaa has a disproportionately high percentage of the country's precipitation induced rock fall-risk at 30.7% and 13.6% for Lebanese and Urban Syrian refugees, respectively. Low cliffs on the SE side of the valley create a rock fall runout hazard zone which reaches midway through Chebaa (**Figure 5.6b**). In addition, debris flows from the barren bluffs to the NW and SE of the town cut through the

developments on Chebaa's main road connecting it to the Bekaa Valley. These contribute 1.4% and 3.8% of the country's debris flow risk to Lebanese and Urban Syrian refugees, translating to approximately one death every 7 and 3 years respectively.

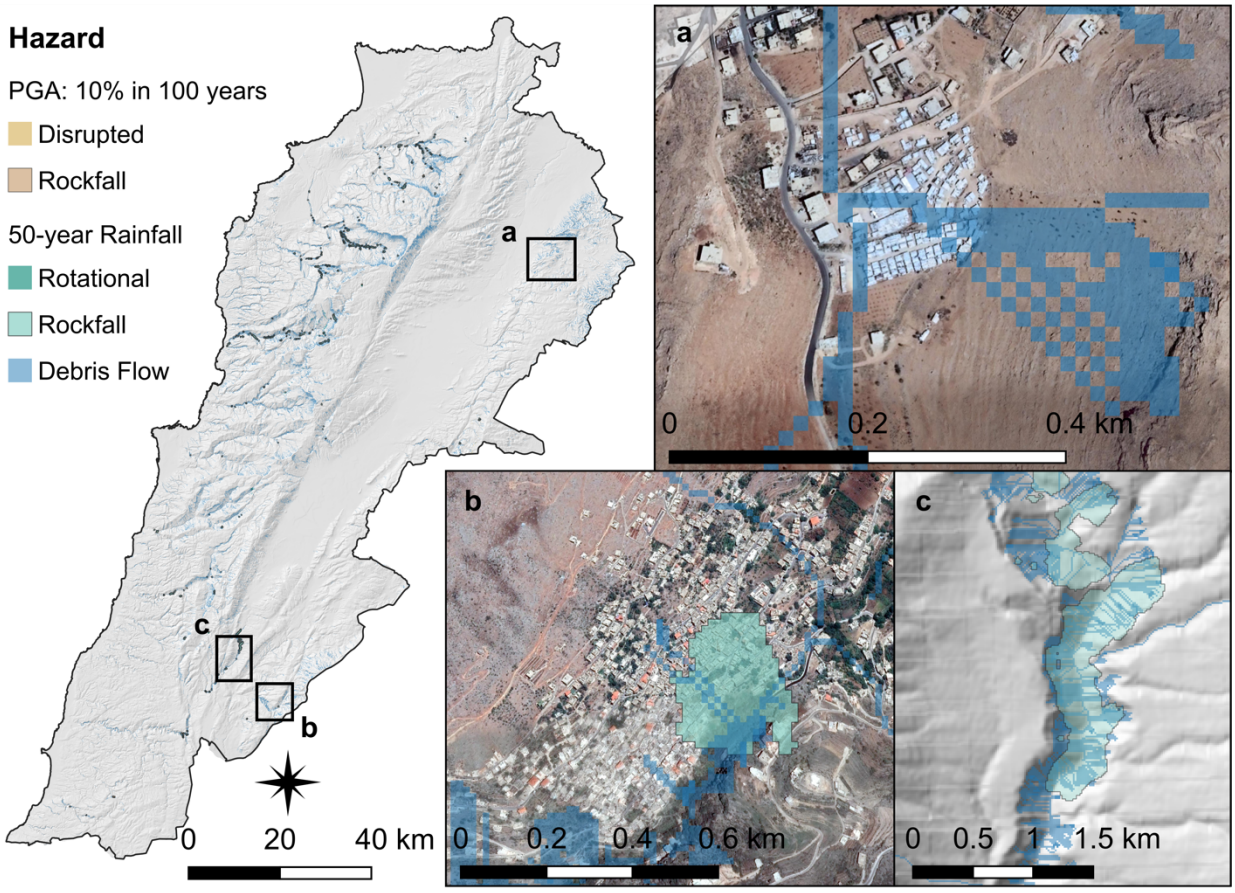

Figure 5.6. (*a*) An ITS outside of Arsal at risk from debris flow in all return period precipitation events (50-year shown). (*b*) Rock fall hazard to urban populations in Chebaa. (*c*) Precipitation-induced rock falls and debris flows from the high cliffs of the Litani River valley near Loussia. Base images from Google Earth™.

5.7.3 Societal risk profile

Societal risk to landslides is commonly expressed as the cumulative probability per year (F) that N or more lives will be lost to a hazard (Guzzetti, 2000). **Figure 5.7** shows the landslide risk F-N curves for native Lebanese, urban Syrian refugees, and encamped Syrian refugees, as well as those observed for other geomorphically-active regions of the world based on event inventories. The sharp bend in the F-N pairs for Lebanon highlights the diverging consequences of seismic and precipitation-triggered landslides. Coseismic landslides are predicted to cause fewer fatalities, in addition to occurring infrequently, whereas rainstorms are projected to have high consequences as well as high frequency. Encamped refugees experience much higher consequences during infrequent, severe precipitation events due to their limited but dense spatial extent. The predicted societal risk for all three groups has a steeper slope than the other regional observations, corresponding to more frequent, lower-consequence events. This discrepancy is in part due to recording bias favoring large events. Almost all of the inventories have medium-long recording intervals, from 30 – 175 years. Older, long-interval datasets are more likely to be missing less destructive events especially at the beginning of the recording period (Guzzetti, 2000). The exception is the inventory from Hong Kong from 1978 – 1998 (**Figure 5.7c**), which is comparably steep to our projections for Lebanon. The Geotechnical Engineering Office of Hong Kong was established in 1977 and has kept scrupulous records of landslide events in Hong Kong. Thus, the 1978 – 1998 dataset is considered comprehensive, and, in comparison, it indicates that the trend of predicted societal risk in Lebanon is not exceptional.

Numerous fatalities and injuries per year have been attributed to landslides in Lebanon (Abdallah, 2011), but quantitative data are lacking. We compiled a database of recorded landslide fatalities in Lebanon from 1975 – 2015, via an English and Arabic-language search of literature, news reports, disaster databases, and aid agency filings (**Appendix 5.1**, **Table A5.1.5**). We found 13 recorded events resulting in 146 fatalities conclusively caused by landslides (**Figure 5.7f**), an average of almost 4 deaths per year. However, this inventory is incomplete. Fatalities due specifically to landslides are often not differentiated from fatalities from other causes during complex multi-hazard events such as earthquakes and floods (Guzzetti et al., 2005). In Lebanon, this is especially true of floods, which take a significant annual toll on human lives and are accompanied by widespread landslides, yet the two are rarely disentangled (Abdallah, 2007). We only included events in which landslides were clearly described as the cause of death. Our catalogue shows a strong recording bias, with 82% of the low consequence (< 5 fatalities) events occurring in the last 20 years (1995 – 2015). No casualties were reported among Syrian refugees. In part this is due to the limited duration of the Syrian Refugee crisis in Lebanon; refugees have been present in the country too little time to appreciably measure the impact of landslides on refugees at medium and long intervals. The United Nations Office for Disaster Risk Reduction (UNISDR) estimates just over one precipitation-induced landslide fatality per year per million in Lebanon based on nation-scale statistical modeling of the International Disaster Database (EM-DAT; UNISDR, 2009). Although this estimate is in agreement with our Lebanon fatality database, the EM-DAT inventory is also considered incomplete and has been recently demonstrated to underestimate landslide fatalities by ~ 300 – 400 % (Froude and Petley, 2018; UNISDR, 2009)

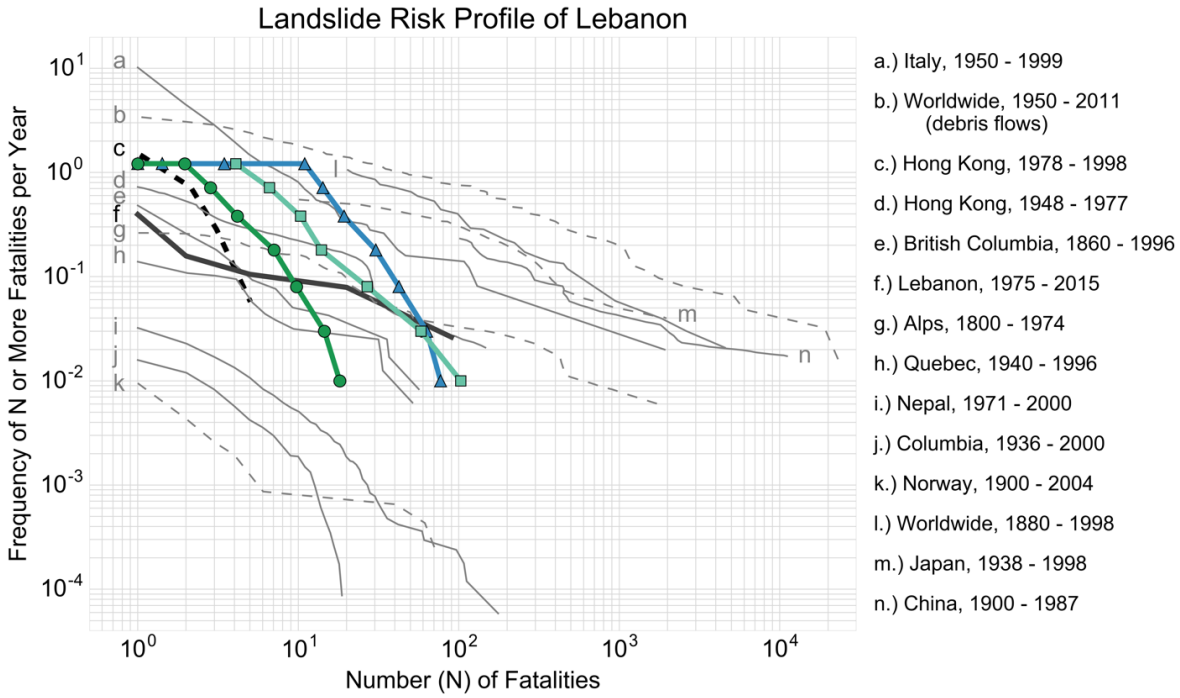

Figure 5.7. F-N curves of forecasted landslide risk to Lebanese (blue triangles), urban Syrian refugees (green circles) and encamped Syrian refugees (aqua squares). Historical data from Evans (1997), GEO (1998), Guzzetti (2000), Dowling and Santi (2014), and Düzgün and Lacasse (2005).

Incompleteness of recorded inventories excluded, we observe an order of magnitude difference in the upward direction when comparing our projected annual landslide fatalities and those recorded. We identify four primary reasons which, along with the methodological assumptions described above, contribute to the overprediction of risk.

1.) Our physically-based models trend toward conservativism. One- and two-dimensional factor of safety equations neglect stabilizing side forces. This is especially true for shallow, infinite-slope failure models, which have been demonstrated to be conservative in almost all cases (Griffiths et al., 2011).

2.) At 15 m resolution, our models cannot capture small-scale anthropogenic influences such as terracing and check dams, which impede the initiation and propagation of small landslides. The Mount Lebanon Range has been extensively terraced since ancient times. These terraces control water flow, shorten slope length, and promote vegetation, reducing erosion (Zurayk, 1994).

3.) We do not account for short term (sub-quarterly) variations in exposure, such as daily commuting from relative high-hazard peri-urban areas to the coastal cities. Furthermore, our methodology does not take into account the ability of humans to respond to impending or ongoing hazard. Warning and evacuation are effective landslide risk mitigation strategies (AGS, 2007c) and anecdotal evidence suggests that informal (non-governmental) risk avoidance in Lebanon has decreased the consequences of landslides in recent years.

4.) Due to limited quantitative population data, we treat "registered" and "encamped" as mutually exclusive categories among Syrian refugees, which may inflate the risk to urban refugees due to double counting. However, since urban refugees experience only 12% of the life-safety risk in Lebanon, the effect of double-counting on the total risk would be small.

5.7.4 Annual probability of death

An individual's annual probability of dying in a landslide may be expressed as the average number of deaths per year divided by the population within a given administrative unit (Evans, 1997). **Figure 5.8a-e** shows the multimodal individual and societal risk in Lebanon throughout the last five years of the Syrian crisis. Pursuant to their higher population, Lebanese experience the majority of the societal risk across all modes. The exception is precipitation-induced rock

falls, which during the peak of the refugee crisis in Lebanon contributed twice as much risk to urban Syrian refugees as Lebanese (**Figure 5.8b**). Additionally, the individual risk to rock falls is almost an order of magnitude higher among urban Syrian refugees. This is primarily due to a heavy refugee influx into the sparsely inhabited high-hazard cadastre, Loussia, in the southern Bekaa Valley. According to UNHCR data, almost 500 registered refugees had settled in the valley by August 2013. By June 2015, the population peaked at 862 refugees, dropping again to 556 by January 2018. In Loussia, the Litani River enters a narrow valley, 300 m deep and less than a kilometer across, with most of the inhabited land on a small plateau at its southern end and in the valley bottom. Strong (0.25 – 0.5g) ground shaking due to the Yammouneh fault ~3 km to the east triggers extensive rock falls throughout the valley. Despite its moderate 500 mm annual rainfall, the sparse vegetation on the valley margins promotes shallow failures, which overlap the valley floor in debris flows, in addition to widespread precipitation-induced rock falls (**Figure 5.6c**).

The trend of societal risk to urban Syrian refugees closely follows the registered refugee population, indicating that throughout the past five years there has been little preferential movement in or out of zones of high hazard. However, the trend of societal risk to encamped Syrian refugees is highly variable throughout time, dropping sharply in 2016 and then inconsistently increasing since then (**Figure 5.8a**). We interpret this as evidential of the highly transient nature of the encamped population. In between June 2015 and February 2016, the UNHCR reported many camps in Arsal, including some at risk from debris flows, as disappearing or shrinking, reflected in a decrease of over 1500 refugees living in at-risk settlements (**Figure 5.8f**). The cause of the shifting situation among Arsal's ITS is unclear,

although local instability from 2014 – 2017 offers a possible explanation. Fewer numbers of encamped refugees near Arsal in 2015 – 2016 may reflect the movement of rebel-allied Syrians during the peak of the militant presence, the desire of refugees to keep a low-profile under community scrutiny, or the limited access of NGOs (Al Ayoubi, 2018).

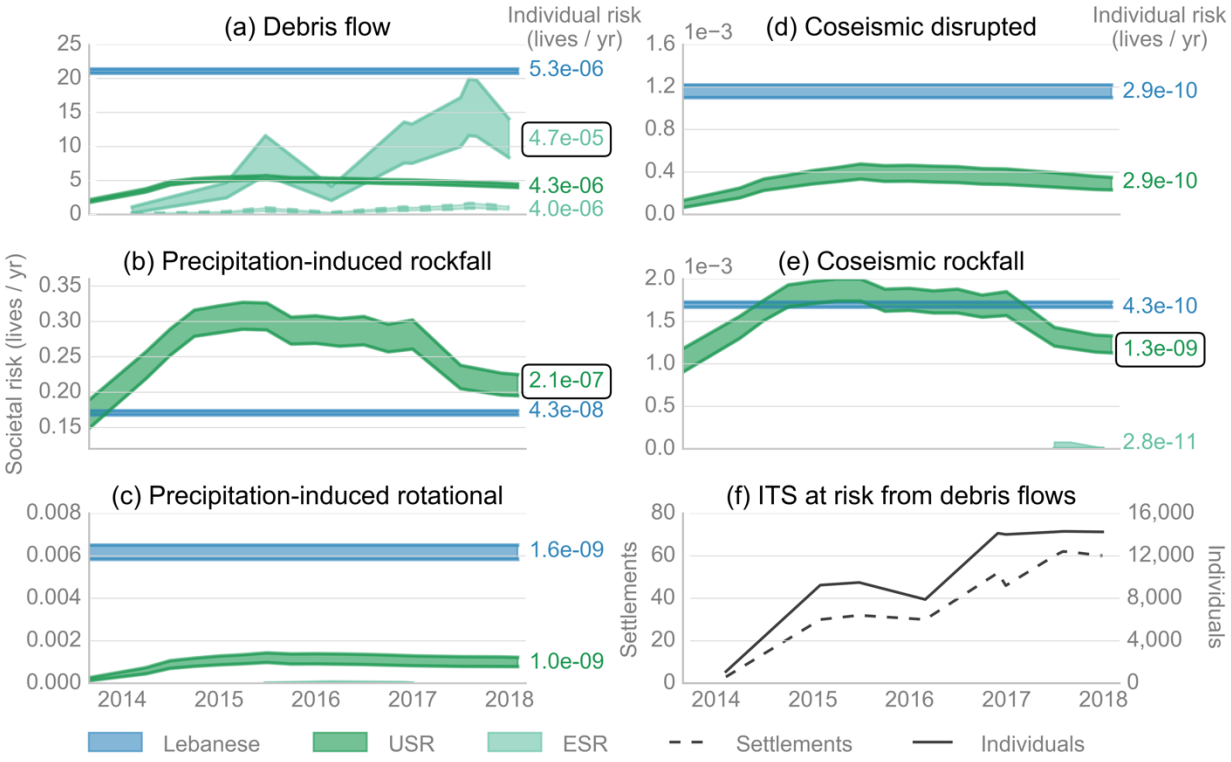

Figure 5.8. (*a*-*e*) Societal and individual risk from multimodal hazards during the Syrian Crisis from 2014 – 2018. The trend of the line shows societal risk and the width, individual risk. The dashed line in (*a*) corresponds to the risk to encamped Syrian refugees (ESR) if they had the same physical vulnerability as urban Syrian refugees (USR). (*f*) The number and population of informal tented settlements (ITS) intersected by debris flow zones over five years of the Syrian crisis.

5.8 Conclusions

We find that the ongoing Syrian crisis has had a dramatic spillover effect on societal life-safety risk from landslides in Lebanon. Since the start of the crisis in 2011, predicted landslide fatalities have risen from 21 to 37 deaths per year, an increase of over 75%. Although Lebanon's incomplete landslide fatality database suggests the actual societal risk in Lebanon is much lower, the risk profiles of other geomorphically-active countries demonstrate these results are not exceptional. Among both Lebanese and Syrian urban populations, risk is distributed widely across the country, primarily from frequent, precipitation-induced debris flows. The risk to encamped refugees is localized, mainly in the barren foothills of the Anti-Lebanon Range. Individual risk is 9 to 11 times greater among encamped refugees. This is not a function of marginalization of place, resulting in greater exposure to hazard, but a complex marginalization on economic, social, and policy levels which force refugees into sub-standard shelter.

The long-term trend of increasing individual risk to encamped Syrian refugees is concerning, as is the steady increase of informal tented settlements (ITS) in debris flow hazard zones. Although an explicit goal of international aid has been to find durable housing solutions for refugees dwelling in ITS, the number of camps and residents has been steadily growing since mid-2013 (UNHCR, 2017a). As Syrian families exhaust their savings and the humanitarian funding shifts away from Lebanon, more may be economically forced to seek shelter in ITS. In light of this work, we recommend emphasized aid for vulnerable residents of ITS in Lebanon, especially those in high-hazard debris flow zones.

In the last decade the number of forcibly displaced persons has increased from 6 to 9 out of every 1000 people, the majority of these residing in climate change hotspots, where they are at heightened risk of secondary displacement (UNHCR, 2015, 2017b). Since 1970, the likelihood of being displaced by geophysical and weather-related hazards has increased 60%, and climate change is expected to accentuate this trend (NRC, 2015). Increasing human exposure and vulnerability, in tandem with more frequent severe weather events, require data-informed policies for resettlement aid. Based on our case study of Syrian refugees in Lebanon, we conclude that, from an environmental hazard perspective, urban settlement appears preferable to encampment due to durable housing solutions; however, strict non-encampment policies without in-kind, informed resettlement aid can produce a high risk of secondary displacement.

References

Abdallah, C. (2007). Assessment of remote sensing and geographic information systems for the study of mass movements in Lebanon. (*doctoral dissertation*). Paris: University of Pierre and Marie Curie

Abdallah, C. (2010). Spatial distribution of block falls using volumetric GIS-decision-tree models. *International Journal of Applied Earth Observation and Geoinformation*, 12(5), 393-403. https://doi.org/10.1016/j.jag.2010.05.008

Abdallah, C. (2011). Assessment of erosion, mass movements, and flood risks in Lebanon. In: H. Kouyoumjian, M. Ham (*Eds*.), *Review and perspectives of environmental studies in Lebanon* (pp. 225-246). Beirut: National Council for Scientific Research

Abdallah, C., Faour, G. (2017). Landslide hazard mapping of Ibrahim river basin, Lebanon. *Natural Hazards*, 85, 237-266. https://doi.org/10.1007/s11069-016-2560-1

AGS. (2007a). Guideline for landslide susceptibility, hazard and risk zoning for land use planning. *Australian Geomechanics Journal*, 24(1), 13-36

AGS. (2007c). Practice note guidelines for landslide risk management 2007. *Australian Geomechanics Journal*, 24(1), 63-114

Al Ayoubi, B. (2018). Aarsal and its surrounding villages: A new dawn. Geneva: United Nations

Daëron, M., Benedetti, L., Tapponier, P., Sursock, A., Finkel, R. (2004). Constraints on the post ~25-ka slip rate of the Yammouneh fault (Lebanon) using in situ cosmogenic ^{36}Cl dating of offset limestone-clast fans. *Earth and Planetary Science Letters*, 227, 105-119. https://doi.org/10.1016/j.epsl.2004.07.014

Daëron, M., Klinger, Y., Tapponnier, P., Elias, A., Jacques, E., Sursock, A. (2005). Sources of the large A.D. 1202 and 1759 Near East earthquakes. *Geology*, 33(7), 529-532. https://doi.org/10.1130/G21352.1

Daëron, M., Klinger, Y., Tapponnier, P., Elias, A., Jacques, E., Sursock, A. (2007). 12,000-year-long record of 10 to 13 paleoearthquakes on the Yammouneh fault, Levant fault system, Lebanon. *Bulletin of the Seismological Society of America.*, 97(3), 749-771. http://dx.doi.org/10.1785/0120060106

DAR-IAURIF. (2005). National physical master plan of the Lebanese territory (Final Report). Beirut: Dar-al-Handasah and the Institut d' Amenagement et d'Urbanisme de la Region Ile-de-France

Dowling, C., Santi, P. (2014). Debris flows and their toll on human life: A global analysis of debris-flow fatalities from 1950-2011. *Natural Hazards*, 71, 203-227. https://doi.org/10.1007/s11069-013-0907-4

Dubertret, L. (1945). "Cartes geologiques a l'echelle de 1/50 000 (Hamidieh, Halba, Batroun, Tripoli, Sir El Dannieh, Jbail, Qartaba, Baalbeck, Beirut, Zahle, Rayak, Saida, Jezzine, Rachaya). Beirut: Republique Libanaise, Ministere des Travaux Publics

Düzgün, H., Lacasse, S. (2005). Vulnerability and acceptable risk in integrated risk assessment framework. In: O. Hungr, R. Fell, R. Couture, E. Eberhardt (*Eds*.) *Landslide Risk Management* (pp. 505-515). London: Taylor & Francis

Ehrlich, D., Zeug, G., Gallego, J., Gerhardinger, A., Caravaggi, I., Pesaresi, M. (2010). Quantifying the building stock from optical high-resolution satellite imagery for assessing disaster risk. *Geocarto International*, 25(4), 281-293. https://doi.org/10.1080/10106040903521829

El Mohtar, C., Abou-Jaoude, G., Abdallah, C., Harb, J. (2016). The Kfarnabrakh landslide of November 30th, 2015 (Geotechnical Extreme Events Reconnaissance-047). Arlington: National Science Foundation

Elias, A., Tapponnier, P., Singh, S., King, G., Briais, A., Daeron, M., Carton, H., Sursock, A., Jacques, E., Jomaa, R., Klinger, Y. (2007). Active thrusting offshore Mount Lebanon: Source of the tsunamigenic A.D. 551 Beirut-Tripoli earthquake. *Geology*, 35(8), 755-758. https://doi.org/10.1130/G23631A.1

Evans, S. (1997). Fatal landslides and landslide risk in Canada. In: D. Cruden, R. Fell, (*Eds*.) *Landslide Risk Assessment* (pp. 185-196). Rotterdam: Balkema

Felix, D., Monteiro, D., Feio, A. (2015). The role of pre-positioning of local temporary settlements for better crisis management. In: *The "State of DRR at the Local Level:" A 2015 Report on the Patterns of Disaster Risk Reduction Actions at Local Level*. Geneva: UNISDR

Fell, R., Corominas, J., Bonnard, C., Cascini, L., Lerio, E., Savage, W. (2008). Guidelines for landslide susceptibility, hazard and risk zoning for land use planning. *Engineering Geology*, 102, 85-98. https://doi.org/10.1016/j.enggeo.2008.03.022

Fell, R., Ho, K., Lacasse, S., Leroi, E. (2005). A framework for landslide risk assessment and management. In: O. Hungr, R. Fell, R. Couture, E. Eberhardt (*Eds*.) *Landslide Risk Management* (pp. 3-25). London: Taylor & Francis

Froude, M., Petley, D. (2018). Global fatal landslide occurrence from 2004 to 2016. *Nat. Hazards Earth Syst. Sci.*, 18, 2161-2181. https://doi.org/10.5194/nhess-18-2161-2018

Geotechnical Engineering Office (GEO). (1998). Landslides and boulder falls from natural terrain: Interim risk guidelines (GEO Report 75). Hong Kong: Geotechnical Engineering Office

GoL, UN. (2017). Lebanese crisis response plan 2017-2020. Beirut: Government of Lebanon and the United Nations

GoL. (2015). National progress report on the implementation of the Hyogo framework for action (2013-2015). Beirut: Government of Lebanon

Gomez, F., Meghraoui, M., Darkal, A., Hijazi, F., Mouty, M., Suleiman, Y., Sbeinati, R., Darawcheh, R., Al-Ghazzi, R., Barazangi, M. (2003). Holocene faulting and earthquake recurrence along the Serghaya branch of the Dead Sea fault system in Syria and Lebanon. *Geophysics*, 153, 658-674. https://doi.org/10.1046/j.1365-246X.2003.01933.x

Grant, A., Wartman, J., Abou-Jaoude, G. (2016). Multimodal method for coseismic landslide hazard assessment. *Engineering Geology*, 212, 146-160. https://doi.org/10.1016/j.enggeo.2016.08.005

Griffiths, D., Huang, J., deWolfe, G. (2011). Numerical and analytical observations on long and infinite slopes. *International Journal for Numerical and Analytical Methods in Geomechanics*, 35, 569-585. https://doi.org/10.1002/nag.909

Guzzetti, F. (2000). Landslide fatalities and the evaluation of landslide risk in Italy. *Engineering Geology*, 58, 89-107. https://doi.org/10.1016/S0013-7952(00)00047-8

Guzzetti, F., Stark, C., Salvati, P. (2005). Evaluation of flood and landslide risk to the population of Italy. *Environmental Management*, 36(1), 15-36. https://doi.org/10.1007/s00267-003-0257-1

Hewitt, K. (1997). *Regions of Risk: A Geographical Introduction to Disasters*. Essex: Longman

Hewitt, K. (2012). Environmental disasters in social context: Toward a preventative and precautionary approach. *Natural Hazards*, 66(1), 3-14. https://doi.org/10.1007/s11069-012-0205-6

Huijer, C. (2010). *Implications of the recent mapping of the offshore thrust fault system on the seismic hazard of Lebanon* (*masters thesis*). Beirut: American University of Beirut

Hungr, O., Leroueil, S., Picarelli, L. (2014). The Varnes classification of landslide types, an update. *Landslides*, 11, 167-194. https://doi.org/10.1007/s10346-013-0436-y

International Crisis Group (ICG). (2013). Too close for comfort: Syrians in Lebanon (Middle East Report No. 141). Brussels: International Crisis Group

Janmyr, M. (2016). Precarity in exile: The legal status of Syrian refugees in Lebanon. *Refugee Survey Quarterly*, 35, 58-78. https://doi.org/10.1093/rsq/hdw016

Janmyr, M. (2018). UNHCR and the Syrian refugee response: Negotiating status and registration in Lebanon. *International Journal of Human Rights*, 22(3), 393-419. https://doi.org/10.1080/13642987.2017.1371140

Janmyr, M., Mourad, L. (2018). Modes of ordering: Labelling, classification and categorization in Lebanon's refugee response. *Journal of Refugee Studies*, fex042. https://doi.org/10.1093/jrs/fex042

Jibson, R. (2007). Regression models for estimating coseismic landslide displacement. *Engineering Geology*, 91, 209-218. https://doi.org/10.1016/j.enggeo.2007.01.013

Keefer, D. (2013). Landslides generated by earthquakes: Immediate and long-term effects. In *Treatise on Geomorphology*, J. Shroder, L.A. Owen (*Eds*.), San Diego, CA: Academic Press, vol. 5, Tectonic Geomorphology, pp. 250-266. https://doi.org/10.1016/B978-0-12-374739-6.00091-9

Khawlie, M., Hassanain, H. (1984). Engineering geology of the Hammana landslides, Lebanon. *Quarterly Journal of Engineering Geology and Hydrogeology.*, 17, 137-148. https://doi.org/10.1144/GSL.QJEG.1984.017.02.05

Lee, M., Jones, D. (2014). *Landslide Risk Assessment*. London: Institution of Civil Engineers

LHIF. (2014). Background paper on unregistered Syrian refugees in Lebanon. Lebanon Humanitarian INGO Forum

McCallin, B., Scherer, I. (2015). Urban informal settlers displaced by disasters: Challenges to housing responses. Geneva: International Displacement Monitoring Centre

Montgomery, D., Dietrich, W. (1994). A physically based model for the topographic control on shallow landsliding. *Water Resources Research*, 30(4), 1153-1171. https://doi.org/10.1029/93WR02979

Morris, S., Neidecker-Gonzales, O., Carletto, C., Munguia, M., Medina, J., Wodon, Q. (2002). Hurricane Mitch and the livelihoods of the rural poor in Honduras. *World Development*, 30(1), 49-60. https://doi.org/10.1016/S0305-750X(01)00091-2

Mourad, L. (2017). 'Standoffish' policy-making: Inaction and change in the Lebanese response to the Syrian displacement crisis. *Middle East Law and Governance*, 9, 249-266. https://doi.org/10.1163/18763375-00903005

NRC. (2015). Global estimates 2015: People displaced by disasters. Geneva: Internal Displacement Monitoring Centre

O'Hare, G., Rivas, S. (2005). The landslide hazard and human vulnerability in La Paz City, Bolivia. *The Geographical Journal*, 171(3), 239-258. https://doi.org/10.1111/j.1475-4959.2005.00163.x

[dataset] Pesaresi, M., Ehrlich, D., Florczyk, A., Freire, S., Julea, A., Kemper, T., Soille, P., Syrris, V. (2015). GHS built-up grid, derived from Landsat, multitemporal (1975, 1990, 2000, 2014). European Commission, Joint Research Centre (JRC) http://data.europa.eu/89h/jrc-ghsl-ghs_built_ldsmt_globe_r2015b
Plassard, J. (1971). Pluviometric map of Lebanon at a scale of 1:200,000. Beirut: Government of Lebanon, Ministry of Public Works and Transport
Salloukh, B. (2017). The Syrian war: Spillover effects on Lebanon. *Middle East Policy*, 24(1), 62-78. https://doi.org/10.1111/mepo.12252
Santi, P., Hewitt, K., VanDine, D., Cruz, E. (2011). Debris-flow impact, vulnerability, and response. *Natural Hazards*, 56(1), 371-402. https://doi.org/10.1007/s11069-010-9576-8
Sanyal, R. (2017). A no-camp policy: Interrogating informal settlements in Lebanon. *Geoforum*, 84, 117-125. https://doi.org/10.1016/j.geoforum.2017.06.011
Sphere. (2011). Humanitarian charter and minimum standards in humanitarian response. Geneva: Sphere Association
Thorleifsson, C. (2016). The limits of hospitality: coping strategies among displaced Syrians in Lebanon. *Third World Quarterly*, 37(6), 1071-1082. https://doi.org/10.1080/01436597.2016.1138843
Turner, L. (2015). Explaining the (non-)encampment of Syrian refugees: Security, class and the labour market in Lebanon and Jordan. *Mediterranean Politics*, 20(3), 386-404. https://doi.org/10.1080/13629395.2015.1078125
UN. (2005). Hyogo framework for action 2005 – 2015: Building the resilience of nations and communities to disasters. Geneva: United Nations
UN. (2015). Sendai framework for disaster risk reduction 2015 - 2030. Geneva: United Nations
UNEP. (2018). A precarious environment for the Rohingya refugees. *News and Stories*. https://www.unenvironment.org/ (Sept. 07, 2018)
UNHCR. (2014). UNHCR policy on alternatives to camps. Geneva: UNHCR
UNHCR. (2015). UNHCR, the environment & climate change. Geneva: UNHCR
UNHCR. (2017a). Vulnerability assessment of Syrian refugees in Lebanon: VASYR 2017. Geneva: UNHCR
UNHCR. (2017b). Global trends: Forced displacement in 2017. Geneva: UNHCR
UNHCR. (2018a). Syria emergency. *Emergencies*. http://www.unhcr.org/en-us/ (June 21, 2018)
[dataset] UNHCR. (2018b). Syrian refugees registered by cadastral. *Documents*. https://data2.unhcr.org/en/situations/syria (Sept. 07, 2018)
UNHCR. (2018c). UNHCR, displacement and disaster risk reduction. Geneva: UNHCR
UNHCR. (2018d). Monsoon response effort in full swing as seasonal rains hit Bangladesh. *Briefing Notes*, UNHCR, http://www.unhcr.org/en-us/news/briefing/2018/5/5aec18114/ (June 22, 2018)
UNISDR. (2009). Global disaster risk: Patterns, trends and drivers, in *Global Assessment Report on Disaster Risk Reduction*. Geneva: UNISDR
van Westen, C., van Asch, T., Soeters, R. (2006). Landslide hazard and risk zonation—why is it still so difficult? *Bulletin of Engineering Geology and the Environment*, 65, 167-184. https://doi.org/10.1007/s10064-005-0023-0
Verdirame, G., Pobjoy, J. (2013). The end of refugee camps? (Univ. Cambridge Faculty of Law Research Paper No. 29/2013). In: *The Ashgate Research Companion to Migration Law, Theory and Policy*, S. Juss (*Ed*.) Available at SSRN: https://ssrn.com/abstract=2297741

Verner, D., Lee, D., Ashwill, M., Wilby, R. (2013). Increasing resilience to climate change in the agricultural sector of the Middle East: The cases of Jordan and Lebanon. Washington DC: The World Bank

Walley, C. (1998). Some outstanding issues in the geology of Lebanon and their importance in the tectonic evolution of the Levantine region. *Tectonophysics*, 298, 37-62. https://doi.org/10.1016/S0040-1951(98)00177-2

Wisner, B., Blaikie, P., Cannon, T., Davis, I. (2004). *At Risk: Natural Hazards, People's Vulnerability and Disasters*. London: Routledge

Wisner, B., Luce, H. (1993). Vulnerability: Scale, power and daily life. *GeoJournal*, 30(2), 127-140. https://doi.org/10.1007/BF00808129

Yassin, N., Osseiran, T., Rassi, R., Boustani, M. (2015). No place to stay? Reflections on the Syrian refugee shelter policy in Lebanon. Beirut: United Nations Human Settlements Programme and the American University of Beirut

Zurayk, R. (1994). Rehabilitating the ancient terraced lands of Lebanon. *Journal of Soil and Water Conservation*, 49(2), 106-112

Chapter 6 – Quantifying landslide risk in Seattle, Washington

6.1 Introduction

Landslides are a widespread and frequent problem in Seattle, chiseling away the city's steep hillsides "from a time to which the memory of man runneth not back" (R.H. Thomsen, Seattle city engineer, 1897). Recurrent precipitation- and earthquake-induced landslides have killed over a dozen individuals in Seattle since 1900 and caused hundreds of millions of dollars in damages to buildings and infrastructure. The City of Seattle, its scientific community, and its citizens have grappled with the region's unstable slopes through some of the most progressive land use regulation in the United States, numerous academic studies, and extensive landslide mitigation projects (Laprade and Tubbs, 2008). Nevertheless, losses continue to mount as ever-denser urban development expands into marginal, landslide-prone areas (Baum et al, 2005). Meanwhile, a changing climate threatens to bring more frequent and severe landslide-triggering storms to Washington's west coast (Rath et al., 2017; Mauger et al., 2015), and two regional faults—the offshore Cascadia subduction zone and the Seattle Fault—have produced devastating earthquakes in the past and are likely to do so again.

Rational landslide mitigation decisions require a knowledge of the consequences landslides will cause (Crozier and Glade, 2005). In this work I perform a probabilistic landslide risk analysis for the city of Seattle which provides quantitative, spatially explicit estimates of the consequences of landslides under a suite of probable precipitation and seismic landslide triggering scenarios. Risk is disaggregated to show the diverging consequences of precipitation-induced and coseismic landslides. The risk maps produced in this work provide significantly

more useable information than traditional susceptibility and hazard maps as a basis for targeted landslide mitigation to reduce preventable landslide losses in Seattle.

6.1.1 Landslides and landslide studies in Seattle, Washington

Since 1900, over 2080 landslides have been recorded in the City of Seattle (Laprade et al., 2000; City of Seattle, 2018; **Figure 6.1**). Forty-five percent of the recorded landslides are shallow, less than 3 m deep, while 13% are deep-seated landslides, most of which occur progressively along an arcuate failure surface. Four percent are categorized as "ground water blowout" failures, a catch-all term for flow-type landslides that initiate at the contact between sand and less permeable silts and clays. Two percent are considered "high bluff peel-offs" in which over-consolidated soil slides or slabs off of near-vertical bluff faces. The remainder are uncategorized. The Seattle landslide inventory is incomplete, as records kept by the City of Seattle focus on landslides that have impacted homes or infrastructure, and under-report landslides in Seattle's expansive greenspace and parks, many of which are on steep slopes and drainages (Schultz, 2005; Coe et al., 2000). For instance, in the winter of 1933 – 1934 landslides are under-reported in the city inventory by at least 120% (Evans, 1994) and in 1971 – 1974 by over 33% (Tubbs, 1975). Nevertheless, this inventory has formed the basis of most studies examining landslide susceptibility and hazard within the City (e.g. Coe et al., 2004; Schultz, 2005; Godt et al., 2004; Chleborad et al., 2006; Harp et al., 2006).

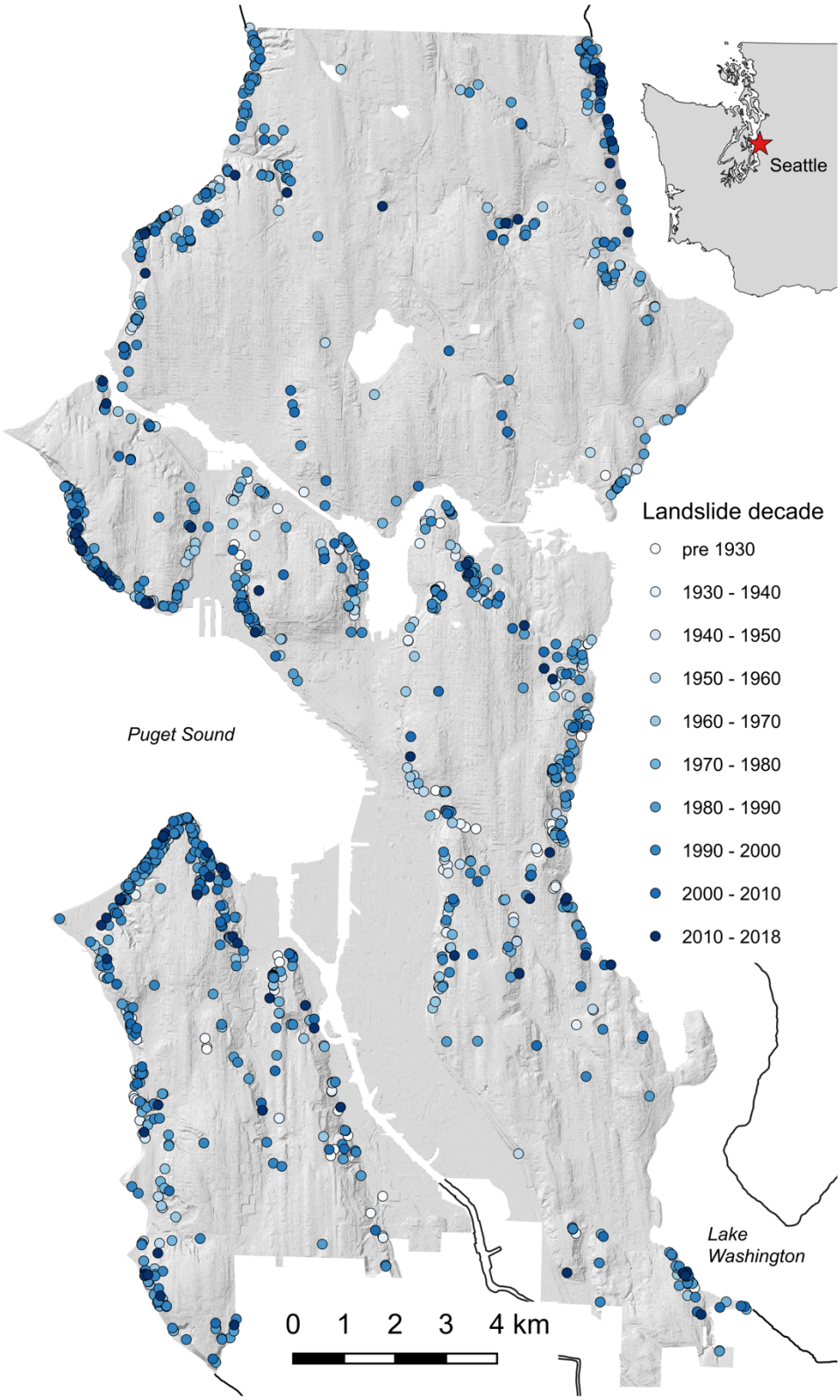

Figure 6.1. Mapped landslide locations in the City of Seattle landslide inventory (City of Seattle, 2018). All modes of landslides are shown, including those triggered by humans.

The earliest studies of landslides in Seattle focused on describing the conditions that lead to landsliding and identifying landslide susceptible areas (Laprade and Tubbs, 2008; **Table 6.1**). In the last two decades, considerable attention has been given to establishing the rainfall conditions that lead to shallow landslides. Coe et al. (2000, 2004) presented the most thorough treatment of landslide hazard throughout the entire City to date, including detailed maps of the recurrence interval of landslide density contours. However, their study utilizes the city landslide inventory and thus is biased toward prevalent, shallow, precipitation-induced landslides as well as being subject to the limitations of incomplete records and a relatively short recording period (Guzzetti, 2000). More recently, Allstadt et al. (2013) and Grant (2017) modeled the coseismic landslide hazard for two earthquake scenarios: a M7.0 Seattle Fault earthquake and an M9.0 Cascadia subduction zone earthquake. Grant (2017) also produced a preliminary map of probabilistic coseismic landslide hazard considering all three of Seattle's primary seismic hazard sources. Few landslide studies consider multiple failure types, such as rotational slumps and debris falls, despite the diverging consequences they have on the population and infrastructure of the region (Shipman, 2001).

To date, no study has quantitatively analyzed landslide risk in Seattle. In regard to a M7.0 Seattle Fault rupture scenario, Allstadt et al. (2013) estimated the number of buildings impacted by landslides using a 60 m buffer zone around modelled landslide sources, but they did not calculate the resulting damage. The City of Seattle utilizes the study of Laprade et al. (2000) and its derivatives to designate "landslide-prone" (susceptible) areas based on recorded locations and historically unstable terrain. These zones to not include potential runout (Seattle OEM, 2019). Designated landslide-prone zones cover approximately 13% of Seattle's land area and form the

basis of the City's landslide-related land use regulation under Washington's Growth Management Act (Miscolta-Cameron, 2016).

Table 6.1. A summary of the major landslide susceptibility and hazard studies including part or all of Seattle, ordered by their latest update. I adhere to the technical distinction between *susceptibility* as a spatial measure and *hazard* as a spatial and temporal measure of landslide occurrence. Some susceptibility studies provide additional information, such as the predicted landslide density, which is implicitly linked to frequency. I have labeled the product of these studies as "quantitative susceptibility" maps even when the authors refer to them as "hazard" maps.

Study	*Region*	*Modes*	*Method*	*Product*
Miller (1973)	West-central King Co.	all	reconnaissance, slope, geology	susceptibility map
Tubbs (1974, 1975)	Seattle	all	reconnaissance, slope, geology	descriptive summary susceptibility map
Shipman (2001)	Puget Sound	all	reconnaissance	descriptive summary
Wait (2001)	Seattle	deep	reconnaissance	descriptive summary
Montgomery et al. (2001)	Seattle	shallow	physical modelling	susceptibility map
Laprade et al. (2000)	Seattle	all	inventory, slope, geology	descriptive summary susceptibility map
Coe et al. (2000, 2004)	Seattle	all	inventory	hazard map
Harp et al. (2006)	Seattle	shallow	inventory, physical modeling	susceptibility map (quantitative)
Godt et al. (2004, 2006)	Seattle	shallow	inventory, rainfall data	precipitation intensity-duration threshold
Schultz (2005, 2007)	Seattle	all	inventory, LiDAR	susceptibility map (quantitative)
Brien and Reid (2007, 2008)	Alki Avenue	deep	physical modelling	susceptibility map
Chleborad (2000, 2003), Chleborad et al. (2006, 2008)	Seattle	shallow	inventory, rainfall data	cumulative and intensity-duration precipitation thresholds
Godt (2004), Godt et al. (2008a)	West Seattle	shallow	physical modelling	precipitation intensity-duration threshold map
Godt and McKenna (2008)	Seattle	shallow	physical modelling	precipitation intensity-duration threshold
Salciarini et al. (2008)	Alki Avenue	shallow	physical modelling	precipitation-induced landslide hazard map
Allstadt et al. (2013)	Seattle	shallow	physical modelling	coseismic hazard map for an M7.0 Seattle fault earthquake
Biasutti et al. (2016)	Puget Sound	general	inventory, rainfall data	precipitation intensity-duration threshold
Grant (2017)	Seattle and Mercer Island	shallow deep	physical modeling	probabilistic coseismic hazard map coseismic hazard map for an M9.0 Cascadia Subduction Zone earthquake

6.2 Natural environment of Seattle

6.2.1 Topography and geology

Seattle lies in the broad Puget lowlands between the Olympic mountain range to the west and the active Cascade volcanic arc to the east. The region's topography has been shaped by repeated advances of south-flowing Canadian ice during at least seven Pleistocene glaciations (Haugerud et al., 2017) The city of Seattle occupies a 217 km^2 hourglass-shaped isthmus bordered by the glacial troughs of the Puget sound to the west and the 35 km-long Lake Washington to the east. Topographically, Seattle is characterized by numerous north-south aligned ridges shaped by advancing ice. The Seattle Fault zone runs east – west underneath the southern end of Seattle, separating the Seattle basin to the north from the Seattle uplift to the south. A rupture on the Seattle Fault 1100 years ago raised Alki Point by about 7 m, while land north of the fault subsided by up to one meter (Troost and Booth, 2008).

Seattle has also been dramatically altered by humans. Lake Washington was hydraulically connected to the Puget sound via the Ship Canal in 1916. The linkage dropped the water level of Lake Washington by 2.7 m to its present height at 6.5 m above sea level, maintained by a series of locks in the Ballard neighborhood of Seattle (Williams, 2015). The ~5 km^2 of new land exposed by the shrinking shoreline of Lake Washington became prime residential real estate despite its precarious position underneath the steep bluffs of the former lake shore.

Seattle sits on a complex succession of glacial and non-glacial deposits. The depth to bedrock varies from 0 m at Alki Point to 550 m at the north and south ends of Seattle to ~ 1 km in Seattle basin north of the Seattle fault (Troost and Booth, 2008; Haugerud et al., 2017). Exposures of bedrock are rare, existing only south of the Seattle fault at Alki Point, in the Rainier Valley, and on the exposed promontory of Seward Park. Four widely documented glacial and non-glacial deposits dominate Seattle's stratigraphy: a thin (1 – 10 m) layer of dense glacial till ("Vashon Till," *Qvt*), a thick (~60 m) layer of sandy advance outwash deposits ("Esperence Sand," *Qva*), a thick (>30 m) layer of pre-glacial silty clay ("Lawton Clay," *Qvlc*), and an underlying, very dense layer of sand, silt, and gravel from the Olympia Interglaciation period ("Olympia Beds," *Qob*) (Troost and Booth, 2008; **Figure 6.2**).

Landslides in Seattle typically have been attributed to the contact between the advance outwash and Lawton clay where it is exposed along Seattle's steep coastal bluffs and inland ridges (Tubbs, 1974). Rainfall and runout infiltrate through the permeable, coarse-grained outwash and then is diverted laterally along the contact with the fine-grained material below. Episodic shallow debris flows and avalanches in saturated outwash sand mobilize material along the top of the Lawton clay unit, creating a benched topography blanketed in loose and highly mobile colluvium. These shallow failures may also undercut the more competent till cap which subsequently fails in block falls and avalanches (Shipman, 2001). Deep-seated rotational slumps often involve both the coarse- and fine-grained units (Gerstel et al., 1997).

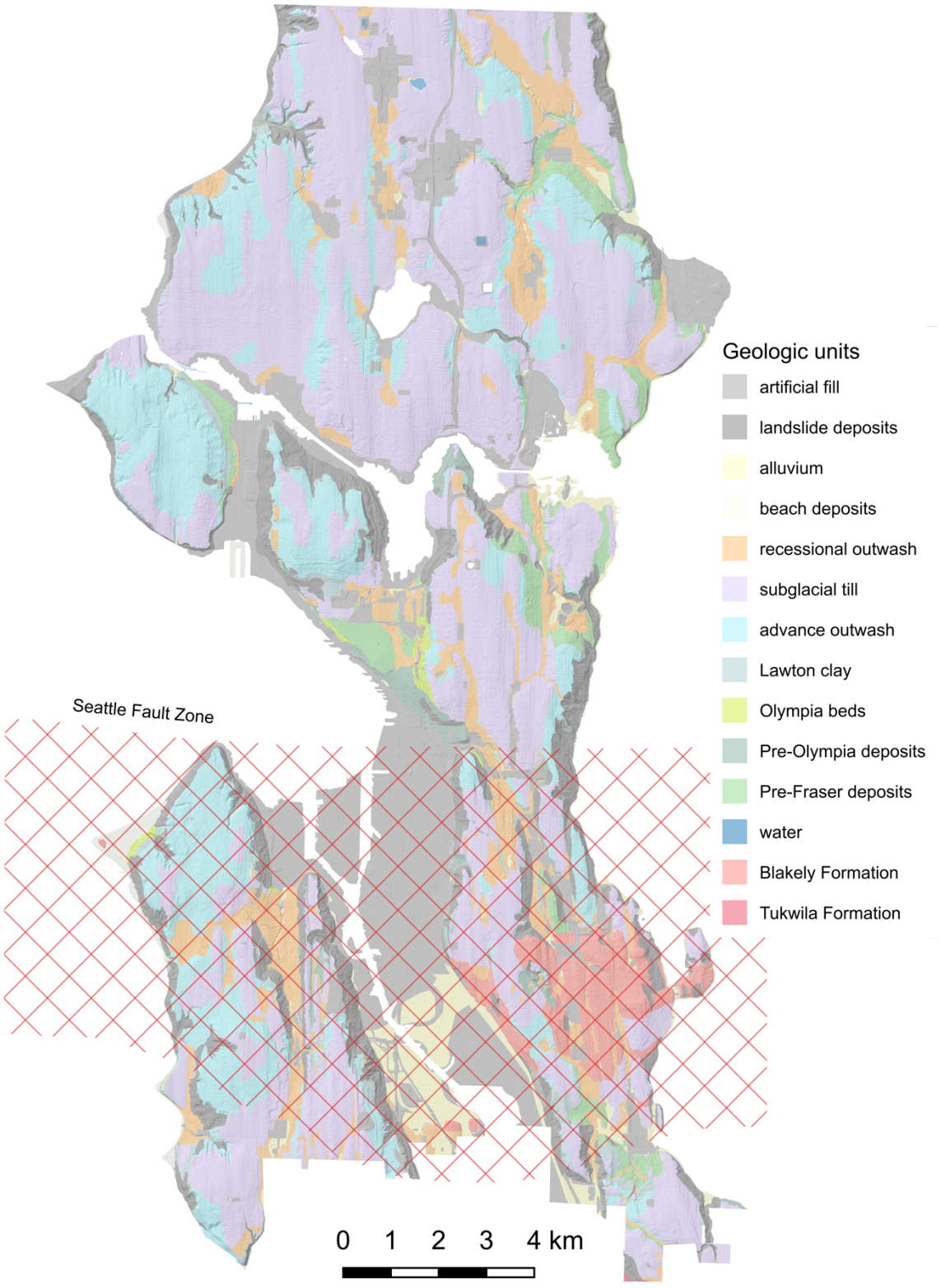

Figure 6.2. Geologic map of Seattle (simplified from Troost and Booth, 2008).

6.2.2 Seismicity

Seattle's location at the convergence of the Juan de Fuca and North American plates gives it three primary sources of seismic hazard: deep Benioff earthquakes within the subducting Juan de Fuca plate; shallow, crustal earthquakes within the North American plate, including on the Seattle Fault; and offshore, megathrust earthquakes in the Cascadia Subduction Zone.
Deep earthquakes are the most frequent in the Puget Sound, including the M7.1 1949 Olympia-Tacoma earthquake, the M6.7 1965 Seattle-Tacoma earthquake, and M6.8 2001 Nisqually earthquake (Chleborad and Schuster, 1990; Highland, 2003). The last major earthquake on the Seattle Fault was an M7.5 event around 900 years ago (Haugerud et al., 2017; Allstadt et al., 2013). Greater than M8.0 earthquakes on the Cascadia Subduction Zone have an estimated return period of 250 – 350 years (Grant, 2017), with the most recent large event occurring 26 January 1700 (Atwater et al., 2005).

6.2.3 Climate

Western Washington has a temperate maritime climate characterized by wet winters and relatively dry summers. Seattle receives approximately 950 mm of precipitation annually, with three-quarters of this occurring in the six month period between November – April (Neiman et al., 2011; Godt et al., 2006). Moisture-laden atmospheric rivers from the tropics and subtropics are responsible for most of Western Washington's extreme precipitation events, with one event in October 2003 dropping 128 mm of rain on Seattle in 24 hours (Neiman et al., 2011). Snow makes up only a small fraction of Seattle's precipitation, but rare heavy snowfalls followed by

warm, wet weather have triggered widespread shallow landsliding (Gerstel et al., 1997; Evans 1994).

6.3 Methods

A probabilistic landslide risk analysis of Seattle was conducted, including both precipitation and seismic triggering events, using the multimodal method outlined in **Chapter 2**. Some modifications to the method were made to account for local conditions, as described in the following sections. Digital elevation data was adopted from the 2016 King County LiDAR-derived DTM at 0.9 m (3 ft) resolution which was scaled down to 5 m resolution for stability and runout modeling and 10 m resolution for groundwater modeling.

6.3.1 Landslide modes

Seattle experiences five modes of landslides according to the updated Varnes classification: debris slides, debris avalanches, slumps, debris flows, and soil falls (Tubbs 1975; Hungr et al., 2014). Extensive study of landsliding in Seattle has led to these modes being re-categorized into a classification scheme unique to Seattle, including four broad types (**Table 6.2**). Due to the lack of large earthquakes in Seattle historical record, this classification scheme emphasizes the role of groundwater in landslide triggering (Laprade et al., 2000). "Shallow" landslides are considered to be less than 3 m (10 ft) in depth. Rock falls and avalanches are rare in Seattle limited to the exposures of Blakely and Tukwila sandstones in southern Seattle. However, due to massive glacial over-consolidation, the cohesive glaciolacustrine Lawton clay and older Olympia beds

stand near-vertically in Seattle's coastal bluffs and commonly fail in wedges and slabs similar to an argillaceous rock (Laprade and Tubbs, 2008). To capture this behavior, the definition of "rock fall" used in the multimodal method (**Chapter 2**, **Table 2.2**) was expanded to include debris falls where glacial deposits stand at slopes typically associated with rock exposures.

Table 6.2. Terminology and definitions of Seattle's landslide modes as well as the associated mode number in the multimodal framework (**Table 2.2**) and updated Varnes classification of Hungr et al, 2014. Definitions adopted from Laprade et al., 2000 and Chleborad et al, 2006.

Multimodal No.	*Seattle classification [Varnes classification]*	*Description*
(2)	Shallow colluvial [gravel/sand/debris slide]	A slide of saturated, loose, and heterogeneous soils on a steep slope. The term "skin slide" is sometimes applied to this slide type because a relatively thin depth of soil is normally involved.
(3)	Deep-seated [clay/silt rotational slide]	A block movement of soils where a mass of soil slides downhill on a failure surface that is often arc-shaped. As blocks of soil move downhill, a setdown of the ground surface occurs at the upper edge of the blocks, thus forming a slide scarp.
(2)	Groundwater blowout [debris flow]	Slope failure that occurs where a relatively impermeable deposit is overlain by a permeable deposit; high pore-water pressures that develop in perched water at the base of the permeable deposit result in a sand or debris "blowout" (flow).
(1)	High bluff peel-off [boulder/debris/silt fall]	A fall, slide, or topple that occurs on a near-vertical cliff face in glacial or other granular sediment.

6.3.2 Soil depth

Loose, heterogeneous colluvium, derived from weathering, creep, and prior landslides, mantles nearly all the hills in Seattle. Colluvium depth above the relatively unweathered glacial substrate ranges from centimeters to several meters and has a strong control on shallow landsliding, with most failures occurring at the contact between the two (Godt et al., 2008b). Where colluvium has been emplaced by repeated landsliding, it has been mapped as landslide deposits (*Qls*; see **Figure 6.2**); otherwise the underlying unit is mapped (Troost and Booth, 2008).

Multiple empirical relationships between topographic characteristics and colluvial depth have been proposed in Seattle (Schultz et al., 2001; Godt et al., 2008a; 2008b; Baum et al., 2010). Schultz et al. (2001) and Godt et al. (2008a) follow a rule-based methodology specific to Seattle, which requires terrain classification into four dominant landforms. Godt et al. (2008b) and Baum et al. (2010) adopt an exponential function based on topographic slope after empirical studies from New Zealand and Italy (DeRose et al., 1991; Salciarini et al., 2006). I adopt applied the relationship of Godt et al. (2008b) for its reproducibility, low parameterization, and consistency with observed depths of shallow landslides in Seattle:

$$h = 7.72e^{(-0.04\beta)} \quad \textbf{(6.1)}$$

where β is the topographic slope in degrees. **Equation 6.1** gives a range of colluvial thickness from a maximum of 7.72 m in flat locations and about 0.5 m on 68° slopes (**Figure 6.3**).

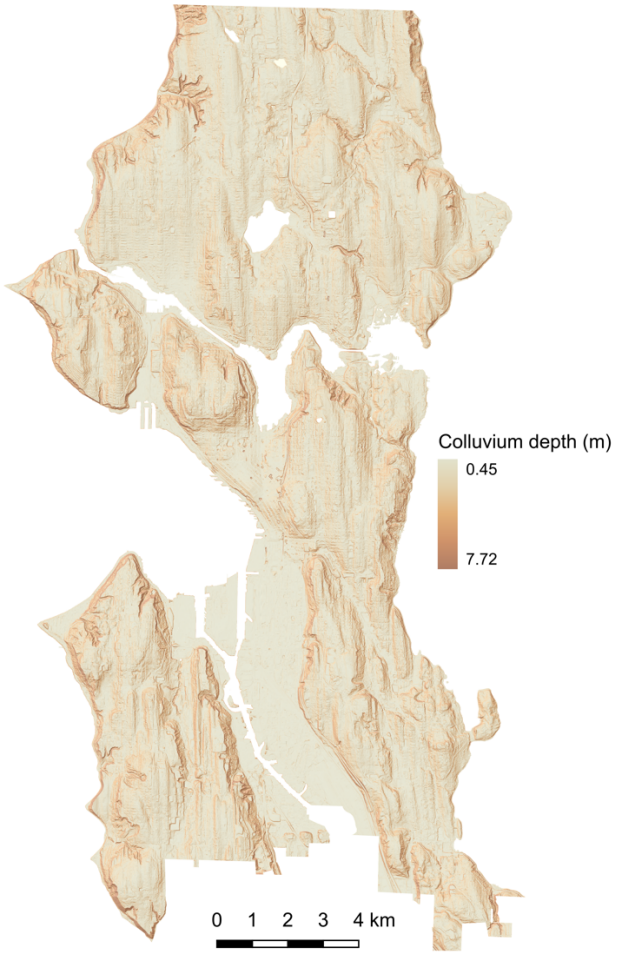

Figure 6.3. Modeled colluvium depth based on topographic slope.

6.3.3 Material parameters

Seattle's ubiquitous colluvial mantle necessitates defining two sets of material parameters within each mapped geologic unit (Harp et al., 2006): that of the colluvium in which shallow landslide forms and that of the underlying or exposed parent material which is involved in deep-seated rotational failures and rock/debris falls. Material parameters necessary for groundwater and stability modeling were adopted from previous studies of soils in Seattle, with the added condition that the mean material strength parameters must result in a static factor of safety

greater than one at initial groundwater conditions within the mode-specific susceptible zone of each mapped unit. This condition was applied by adopting initial values after Harp et al. (2006) and iteratively adjusting the friction angle and/or cohesion within the bounds provided by other studies (e.g. Savage et al., 2000; Debray and Savage, 2001; Baum et al., 2010; Brien and Reid, 2008; Godt et al., 2008a). Standard deviations of material strength parameters were assigned per unit based on coefficients of variation of 0.1 and 0.3 for friction angle and cohesion respectively (Jones et al., 2002; Grant, 2017; Wang, 2014; Wang and Rathje, 2015; Phoon and Kulhawy, 1999). Previous studies report hydraulic diffusivity to be 2 – 500 times saturated hydraulic conductivity, K_s, (The Viet et al., 2017; Liu and Wu, 2008; Baum et al., 2011). Based on values estimated for Seattle soils, we adopt hydraulic diffusivities of 20 x K_s (Godt et al., 2008a; Baum et al., 2010). The material parameters used in this study are given in **Tables 6.3** and **6.4**.

Table 6.3. Material hydrologic parameters modified from USDA (2019) and others. Unit codes are associated with **Figure 6.2**.

Unit	*Code*	K_{sat} *(m/s)*	±	θ_s	θ_r	α	*Reference*
Man-made fill	*Af*	2.21×10^{-5}	1.23×10^{-4}	0.375	0.053	3.92	Morgan and McFarland (1996)
Landslide deposits	*Ls*	4.27×10^{-5}	4.89×10^{-6}	0.400	0.065	0.29	Schultz et al. (2008), Godt (2004)
Alluvium	*Qal*	2.09×10^{-4}	9.88×10^{-4}	0.390	0.049	2.13	Nguyen (2013)
Beach deposits	*Qb*	2.09×10^{-4}	9.88×10^{-4}	0.375	0.053	3.13	Nguyen (2013)
Vashon recessional outwash	*Qvr*	4.38×10^{-4}	1.08×10^{-3}	0.390	0.049	2.13	Nguyen (2013)
Vashon subglacial till	*Qvt*	3.25×10^{-6}	2.68×10^{-5}	0.400	0.060	3.00	Morgan and Jones (1999)
Vashon advance outwash	*Qva*	7.25×10^{-5}	1.73×10^{-4}	0.410	0.070	3.50	Nguyen (2013)
Lawton clay member of the Vashon drift	*Qvlc*	3.48×10^{-9}	2.19×10^{-9}	0.410	0.060	3.00	Brien and Reid (2008), Vaccaro et al. (1997)
Pre-Fraser glaciation deposits	*Qpf*	5.89×10^{-7}	5.74×10^{-4}	0.384	0.063	0.74	Thomas et al. (1997)
Olympia beds	*Qob*	5.00×10^{-5}	5.74×10^{-4}	0.387	0.039	1.19	Godt et al. (2008a)
Pre-Olympia deposits	*Qpo*	5.89×10^{-7}	5.74×10^{-4}	0.384	0.063	0.74	Morgan and Jones (1999)
Blakely Formation	*Tb*	2.18×10^{-7}	9.73×10^{-7}	0.482	0.090	0.42	Welsch et al. (2014)
Tukwila Formation	*Tpt*	2.18×10^{-7}	9.73×10^{-7}	0.482	0.090	0.42	Welsch et al. (2014)

Table 6.4. Material strength parameters modified from Harp et al. (2006).

		parent material		*colluvium*	
Unit	*Code*	*φ (°)*	*c' (kPa)*	*φ (°)*	*c' (kPa)*
Man-made fill	*Af*	36	24	36	16
Landslide deposits	*Ls*	32	60	26	11
Alluvium	*Qal*	32	34	32	14
Beach deposits	*Qb*	34	20	34	14
Vashon recessional outwash	*Qvr*	32	22	32	12
Vashon subglacial till	*Qvt*	33	92	33	12
Vashon advance outwash	*Qva*	38	52	38	8
Lawton clay member of the Vashon drift	*Qvlc*	33	64	33	12
Pre-Fraser glaciation deposits	*Qpf*	34	46	34	19
Olympia beds	*Qob*	34	42	34	19
Pre-Olympia deposits	*Qpo*	34	44	34	19
Blakely Formation	*Tb*	40	29	40	29
Tukwila Formation	*Tpt*	40	48	40	48

6.3.4. Root cohesion

I use 3 m Planet Labs satellite imagery captured 02 June 2019 (Planet Team, 2020) to calculate the normalized difference vegetation index (NDVI). Using semi-automated classification, I define ranges of NDVI associated with un-vegetated surfaces, low vegetation, and dense tree cover. In moderately and densely vegetated areas (NDVI 0.35 – 0.63 and > 0.63,), I assign conservative values of root cohesion of 3 and 5 kPa respectively based on the shrubs and trees common in the Pacific northwest (**Figure 6.4**; Schmidt et al., 2001; Cislaghi et al., 2016).

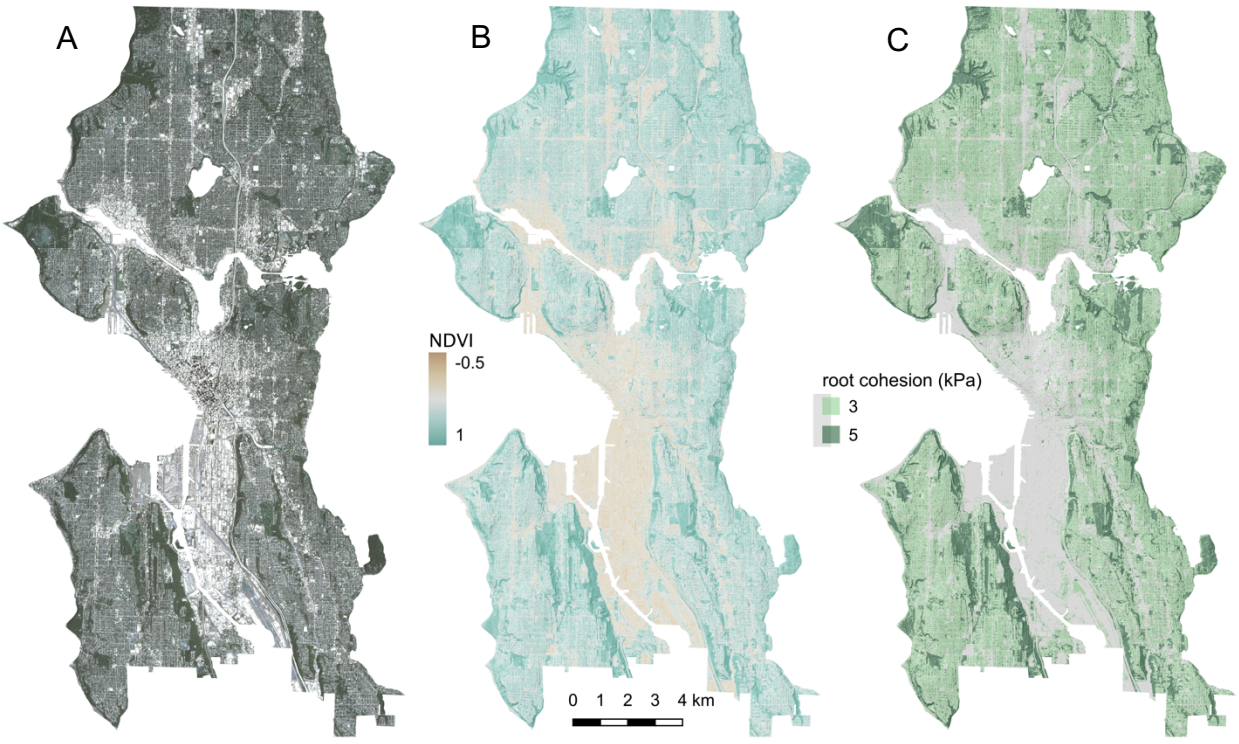

Figure 6.4. (*A*) Planet Labs 3 m satellite imagery captured 02 June 2019, (*B*) the normalized difference vegetation index, and (*C*) assigned root cohesion.

6.3.5 Water table depth

The initial position of the ground water table is one of the dominant factors in physically-based landslide hazard models (Baum et al., 2008; Reid et al., 2015), yet due to seasonal fluctuations, spatial heterogeneity, and sparse empirical data, it remains one of the least constrained model inputs. Previous landslides studies in Seattle have demonstrated the dramatic influence of differing ground water table assumptions. Allstadt et al. (2013) estimated a 517% increase in the number of shallow landslides triggered by a modeled M7.0 Seattle fault rupture scenario between totally saturated and dry conditions. Using summer and winter season hillslope saturation ranges of 0 – 20% and 40 – 60% respectively, Grant (2017) concluded that winter ground water conditions increased the potential areas of deep-seated landsliding by 515% in a scenario M9.0 Cascadia Subduction Zone earthquake scenario. In a detailed study of the bluffs at Alki point, Brien and Reid (2008) predicted up to 27.5% and 53.7% drops in factor of safety against moderately-sized rotational failures in typical and extreme rainy seasons, respectively.

Soil pore water pressure data collected from an instrumented landslide scar 18 km north of Seattle from July 2015 – August 2016 (Smith et al., 2017) was used to estimate the seasonal fluctuations in the ground water table (**Figure 6.5**). Saturation in the hillslope showed strong seasonality, with an elevated ground water table November – April. This is in line with previous estimates of Seattle's wet, winter season (Chleborad et al., 2006; Thorsen, 1987).

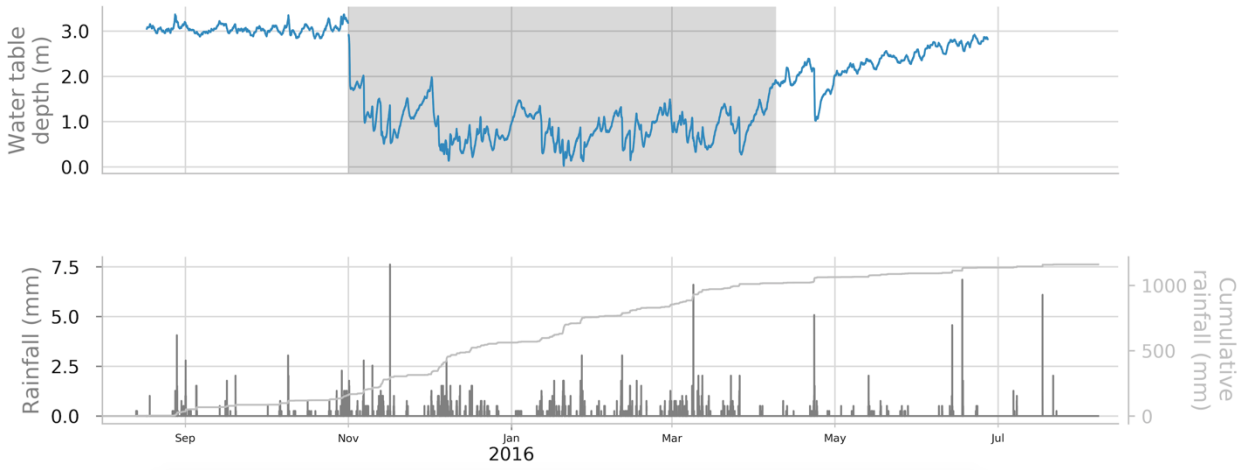

Figure 6.5. Fluctuations in the inferred ground water table based on pore water pressure data from an instrumented landslide scar north of Seattle. A series of small but steady rainfall accumulations at the end of October led to a rapid rise in the ground water table which remained elevated until early April (*in grey*).

The average wet- and dry-season depth of the ground water table within Seattle was estimated from boring logs within the City of Seattle extracted from the Washington Department of Natural Resources Subsurface Database (Jeschke et al., 2016). Six hundred and thirty well logs with water table data were separated by date into "winter" and "summer" seasons, November – April and May – October, respectively. After Peck and Payne (2003), I related the land surface elevation (LSE) to the water table elevation (WTE), with the added criteria of a zero intercept, representing a water table elevation equal to sea level at the shoreline:

$$WTE = a * LSE \quad \textbf{(6.1)}$$

Regression parameters are shown in **Table 6.5**. Water table depth was computed as water table elevation subtracted from surface elevation (**Figure 6.6**). The results predict seasonal water

table fluctuations from zero at sea level to 3.5 m at Seattle's highest elevation (158 m) in West Seattle.

Table 6.5. Regression parameters for Equation 6.1 under wet (winter) and dry (summer) conditions.

Season	*a*	R^2	*n*
Winter	0.9334	0.9671	328
Summer	0.9113	0.9873	302

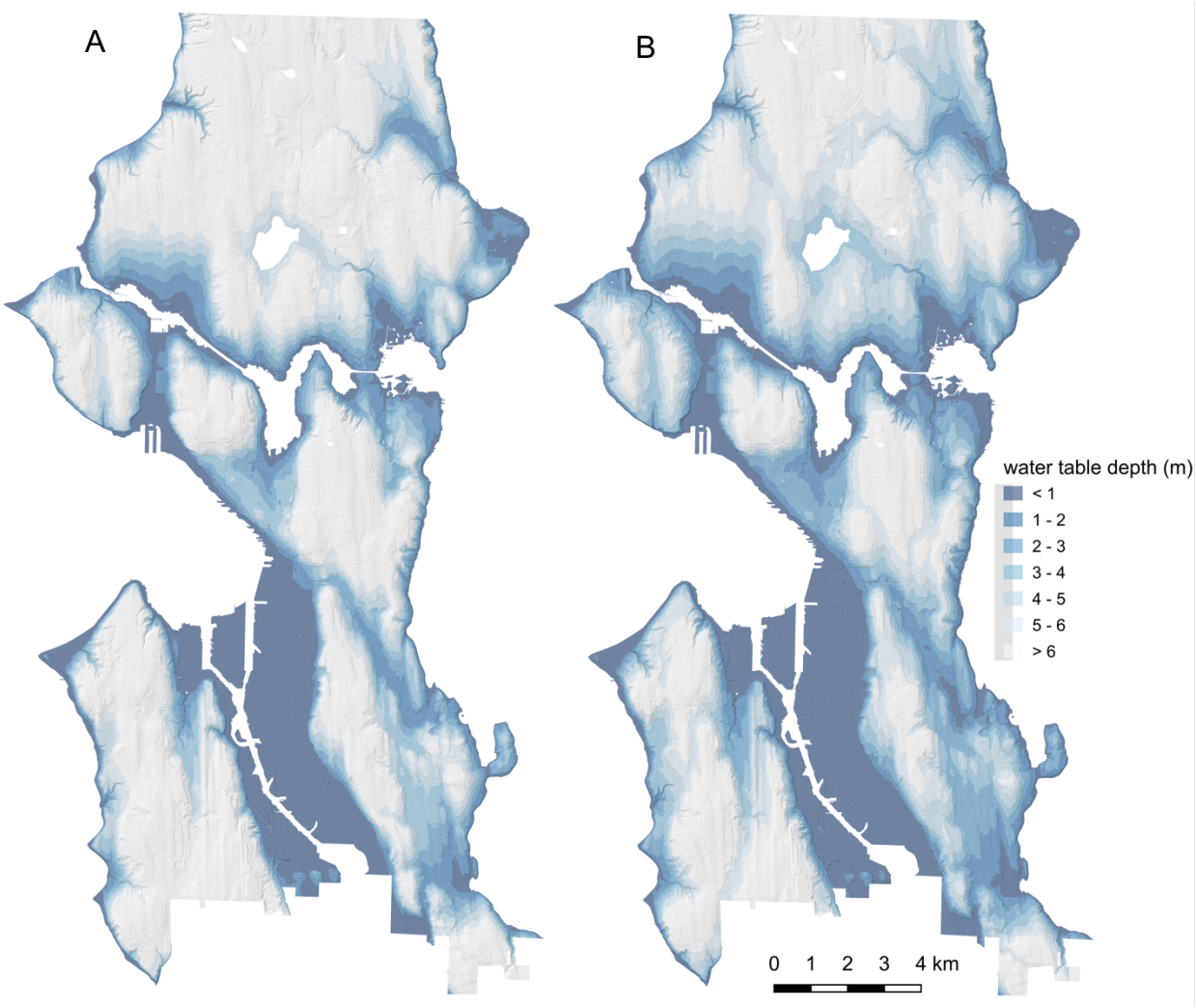

Figure 6.6. Assumed initial water table depth for (*A*) summer conditions and (*B*) winter conditions.

6.3.6 Local debris flow and avalanche runout relationship

During a field reconnaissance in Seattle 03 – 04 February 2020, I mapped seven precipitation included landslides which occurred 31 January – 01 February in addition to one landslide that I had mapped in January 2018 (18a; **Figure 6.7**). I estimated volumes from my measurements of the landslide deposits. All of these eight slides are classified as shallow, unconfined debris avalanches. When compared to unconfined flowslides globally (**Chapter 3**), these Seattle debris avalanches are significantly less mobile, with runouts being overestimated by 60 – 732% (**Table 6.6**). The overestimation is most pronounced for the small volume slides. The low mobility of these Seattle landslides may be partly attributed to the failure mechanism, as significant liquefaction did not occur in any of these events. With the exception of 20e, all of the landslides occurred in Seattle's glacially over-consolidated sand and clay units which are unlikely to undergo liquefaction due to their high density. Additionally 20a, 20c, and 20e were obstructed. 20a had a large log at its toe, behind which debris collected, and 20c and 20e ran into a shallow ditch on the edge of a bike trail. Vegetation may also play a significant role in runout length of low-volume debris avalanches. Events 20b, 20f, and 20g all occurred on slopes covered in mature Himalayan blackberry canes. Intertwined canes appear to have inhibited the runout of these landslides, creating a "balled up" web of canes around the deposit, with some canes tangled in live blackberries still rooted on the adjacent (unfailed) slope.

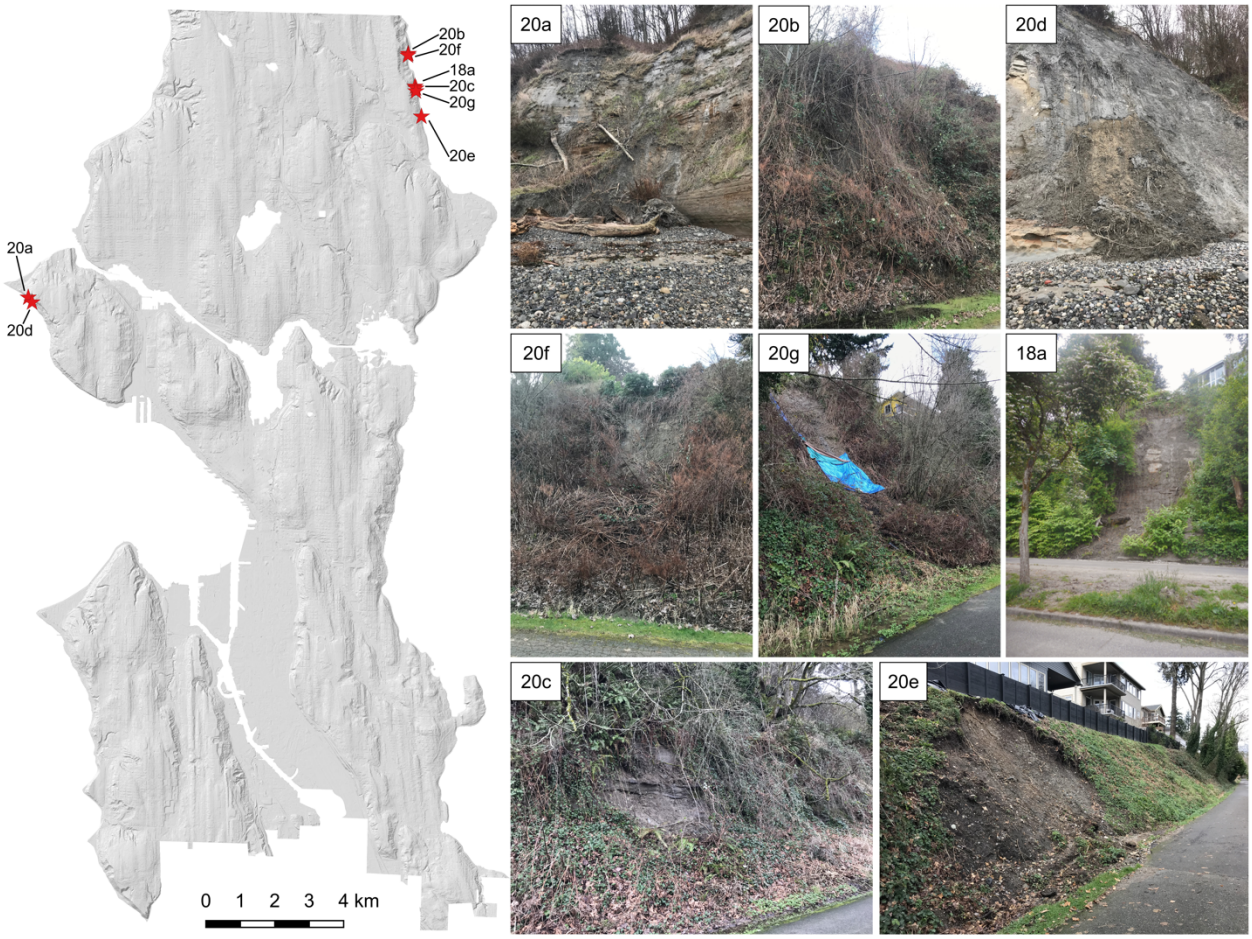

Figure 6.7. Locations of landslide mapped in January of 2018 and January – February 2020. Landslide 18a ran out into a garage behind the viewpoint of the camera. The tree in the foreground was buried in approximately 1.4 m (4.5 ft) of debris, evinced by mudlines left on the tree.

Table 6.6. Observed and predicted lengths of shallow debris avalanches mapped during the 2018 and 2020 winter seasons Predicted lengths are based on the global flowslide runout relationship from **Chapter 3**.

Location	*Approximate Volume (m^3)*	*Observed length (m)*	*Predicted length (m)* *(global flowslide relationship)*	*Difference*
20a	8.9	3	25	+ 732 %
20b	9.5	14	26	+ 85 %
20c	11.0	7	27	+ 290 %
20d	13.5	7	29	+ 317 %
20e	13.7	6	29	+ 360 %
20f	32.1	18	40	+ 120 %
20g	45.9	28	45	+ 60 %
18a	203.9	42	75	+ 79%

Baum et al. (2000) mapped landslides triggered during the extremely wet winters of 1996 and 1997 along a 40 km stretch of coastal railway between Seattle and the city of Everett to the north. Their inventory includes over 270 individual landslide polygons, most of which were shallow, rapid failures with minimal lateral confinement. Since Baum et al. (2000) did not record landslide volumes, I estimate them using an area-volume scaling relationship for soil landslides in Oregon and Washington:

$$V = 10^{-0.98} * A^{1.40} \quad (\mathbf{6.2})$$

where V is volume in m^3 and A is the area in m^2 (Larsen et al., 2010). I extracted the total runout length of from each landslide polygon as the maximum straight line measurement from headscarp to toe. The volume-length pairs of 250 shallow landslides were used to produce the ordinary least squares (OLS) regression runout relationship:

$$\log(L) = 0.2976 * \log V + 0.8120 \quad (\mathbf{6.3})$$

The standard deviation of the residuals is 0.1129, and the is $R^2 = 0.74$. Thirty-nine percent of the landslides had some degree of channelization. However, the OLS regression relationships between the channelized and un-channelized subsets were almost identical.

The runout relationship derived from the Seattle-specific landslide inventory of Baum et al. (2000) provides a better prediction of the mapped debris avalanches from **Table 6.6**, ranging

from an underprediction of 25% for event 18a to over prediction of 322% for event 20a (**Table 6.7**). Three of the four events with the greatest overprediction were noticeably obstructed. They were also three of the five smallest events, with volumes between 8.9 – 13.7 m^3, suggesting sensitivity to small-scale obstructions (e.g. vegetation, ditches, etc.). **Figure 6.8** shows both landslide datasets. I adopt **Equation 6.3** for modeling the runout of debris flows and debris avalanches in Seattle. Due to a lack of local, historical data, I use the general runout relationship for coseismic rock and soil landslides in **Chapter 2**, **Table 2.4**.

Table 6.7. Observed and predicted lengths of shallow debris avalanches mapped during the 2018 and winter seasons. Predicted lengths are based on the Seattle-specific runout relationship in **Equation 6.3**.

Location (year)	*Observed length (m)*	*Predicted length (m)* *(Seattle relationship)*	*Difference*
20a	3	13	+ 322 %
20b	14	13	- 6 %
20c	7	14	+ 96 %
20d	7	15	+ 107 %
20e	6	15	+ 128 %
20f	18	19	+ 5 %
20g	28	21	- 25 %
18a*	42	33	- 22%

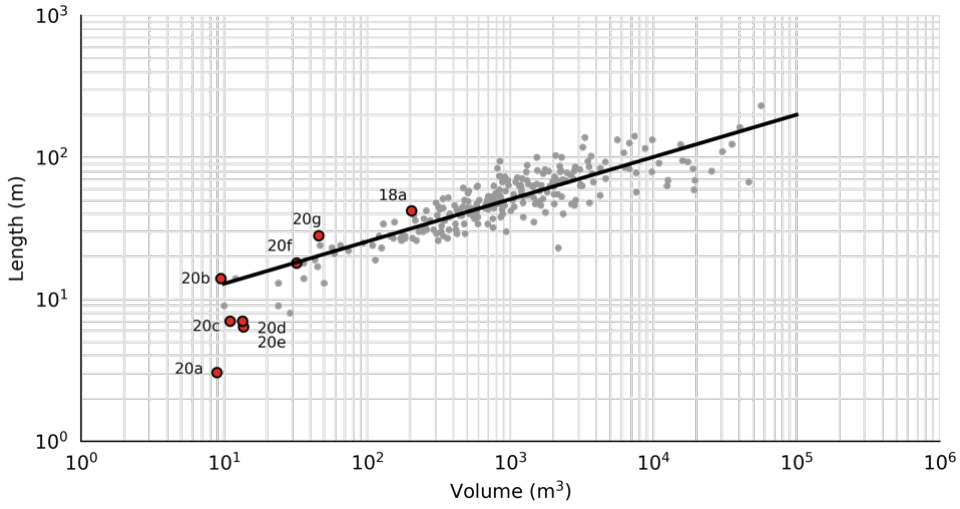

Figure 6.8. Runout relationship derived from the 1996 – 1997 landslides mapped by Baum et al. (2000; *grey*) compared to Seattle debris avalanches mapped as part of this work (*red*).

6.3.7 Elements at risk

I consider only the risk to structures and resident people in this work. Building outlines current to 2015 are available from the City of Seattle (**Figure 6.9 A**; Seattle Geodata, 2019). I removed non-occupied structural additions such as decks, patios, and garages from building profiles. Tax parcels were retrieved from the King County Assessor (King County Department of Assessments, 2020). This dataset contains information on the construction material, size, usage, number of bedrooms, and appraised value of buildings associated with each tax parcel. Population data was retrieved from the United States Census Bureau at the census tract level based on the 2017 five year American Community Survey (ACS) population estimates (U.S. Census Bureau, 2020). The ACS is a yearly long-form survey used by the U.S. Census Bureau to create sample-based population projections on intervening years between the comprehensive decennial censuses. Data is collected at the resolution of census tracts, two scales coarser than the block-level at which census data is collected. As such, the ACS provides lower-resolution and higher-uncertainty population data then the decennial census. However, in fast growing cities, such as Seattle, census data quickly becomes obsolete. Therefore, I chose the more accurate but less certain 2017 five year ACS population estimates which reflect the ~119,000 person population growth (19.5%) of Seattle since the 2010 census.

In order to assign both asset values and resident population on a building level I made two generalizing assumptions: 1.) the distribution of the resident population among tax parcels will be approximately the same as that of bedrooms and 2.) the distribution of both the resident population and the value among buildings on a given tax parcel will be approximately the same

as that of building footprint area. The odds of death of individuals on the ground floor of a landslide impacted building is approximately twelve times higher than those on upper floors (**Chapter 4**). For the Seattle risk analysis, I consider only the population on the ground floor to be at risk from landslides. An individual's exposure to landslides depends on his daily patterns of movement in and out of landslide hazard zones. Seattle's industry and business zones are concentrated in the generally low-relief Duwamish industrial district, downtown, Interbay, and I-5 corridor, while many of its residential zones occupy the steep and landslide-prone slopes abutting the Puget Sound, Lake Washington, and Ship Canal (**Figure 6.9 B**). I adopt a fixed exposure value of 0.65, representing the estimated proportion of time individuals will spend at home during the course of a year. This methodology implies that

1.) the population at risk is entirely indoors and located at their place of residence.
2.) only damage to major structures is accounted for. Damage to outbuildings (sheds, garages, decks), utilities, vehicles, landscaping, or the devaluation of the land itself is not included.

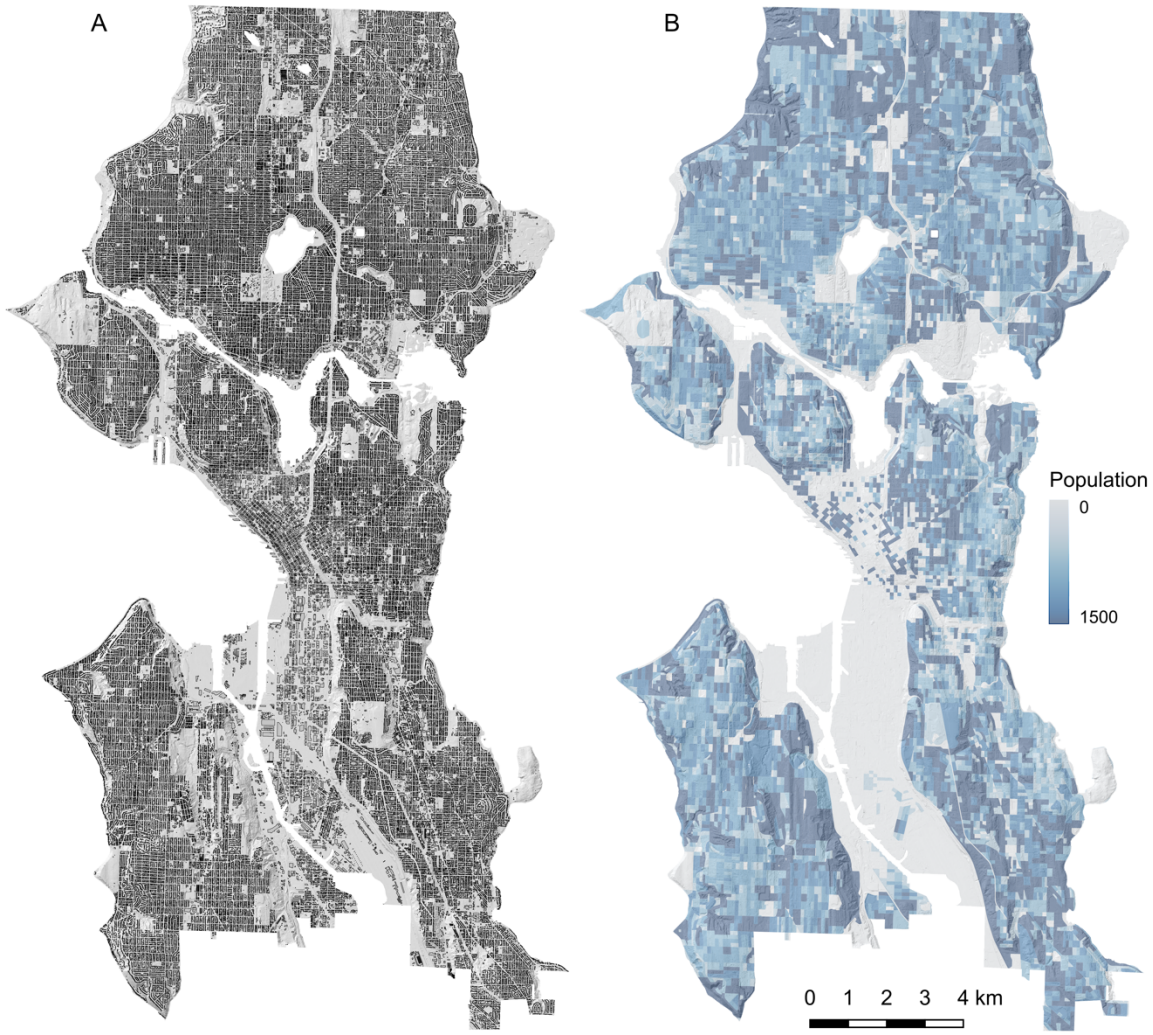

Figure 6.9. (*A*) 2015 Seattle building inventory and (*B*) 2017 American community survey population estimates distributed by building and reaggregated by census block for visualization.

6.3.8 Precipitation triggering

Precipitation—and the ensuing changes in the groundwater regime—is a significant trigger of landslides in Seattle, with 81% of landslides occurring during the wettest months of December – March, and 91% of all landslides occurring during the broader winter season, November – April. Tubbs (1974) concluded that short-term (1 – 3 day) rainfall was the driving factor in the timing of shallow landslides. Deep-seated slides are also triggered by precipitation, but they are more

sensitive to long-duration and antecedent rainfall. Deep-seated slides typically occur several days to several months after periods of moderate to extreme precipitation (Wait, 2001).

The critical duration of rainfall for shallow landsliding in Seattle is between 24 – 72 hours (Tubbs, 1974; Chleborad, 2000; Godt, 2004; Godt et al., 2006; Laprade et al., 2000). Shallow landslide stability modeling shows that the worst-case scenario (maximum landslides) occurs during rainfall durations of 72 hours (Salciarini et al., 2008). For precipitation-triggered landslide scenarios in Seattle, I use the 72 hour (3 day) rainfall intensities from the intensity duration frequency curves produced for Seattle Public Utilities (Rath et al., 2017; **Figure 6.10**). The seven return period intensities are given in **Table 6.8**).

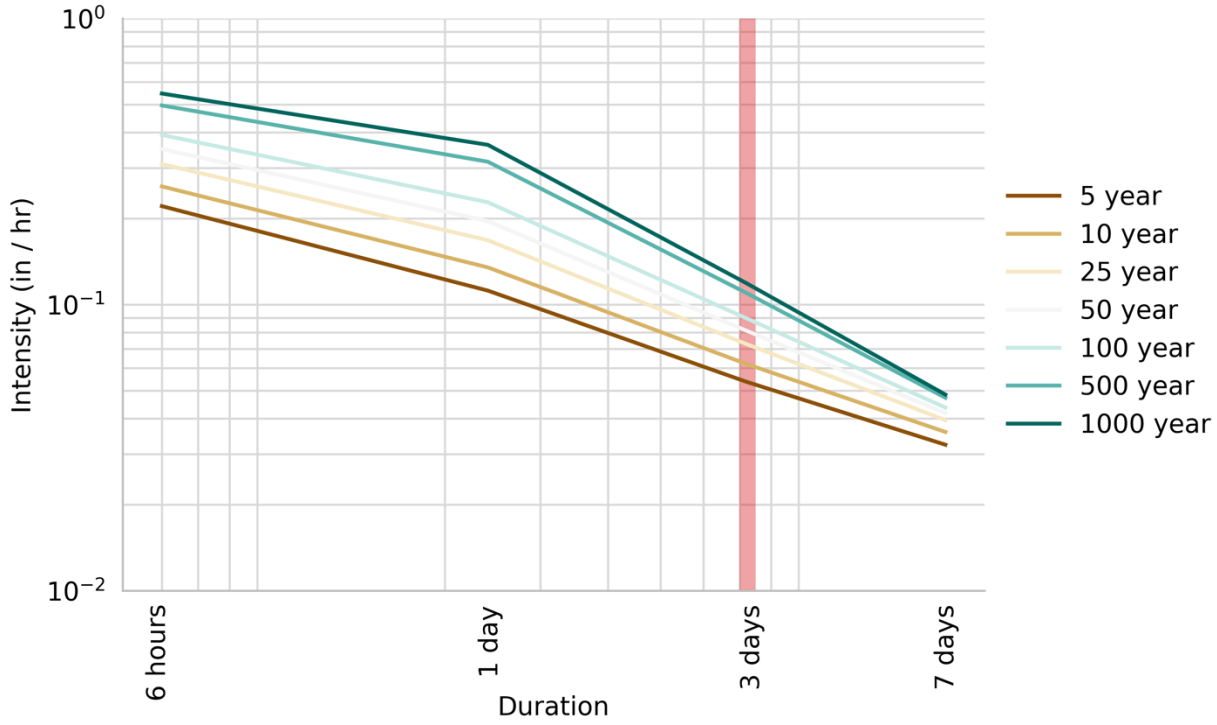

Figure 6.10. Precipitation intensity duration frequency curves for the Seattle region. I adopt the 3-day intensity values (*red*).

Table 6.8. Three day rainfall intensities and their associated frequency.

Return period (yrs.)	*5*	*10*	*25*	*50*	*100*	*500*	*1000*
Intensity (in/hr.)	0.0538	0.0621	0.0729	0.0812	0.0897	0.1100	0.1190

6.3.9 Seismic triggering

I extracted the peak horizontal ground accelerations from the 2018 update the to the National Seismic Hazard Map (NSHM) for the city of Seattle (USGS, 2018). The 2018 update incorporates the effects of basin amplification at select sites in the Western United States, including the Seattle region. In Seattle, the cumulative effect of these changes is an increase is total seismic hazard (Peterson et al, 2019).

Intensity-frequency pairs were extracted at 100 m spacing across the city of Seattle and the hazard curve for each location was developed via four-point interpolation (**Figure 6.11**; Frankel and Leyendecker, 2001.) The hazard curves were used to develop grids of ground-shaking intensity at set probabilities of exceedance ranging from 5 – 20% in 50 years. Five probabilities of exceedance were chosen, associated with return periods of 224, 308, 391, 475, and 975 years (**Figure 6.12**).

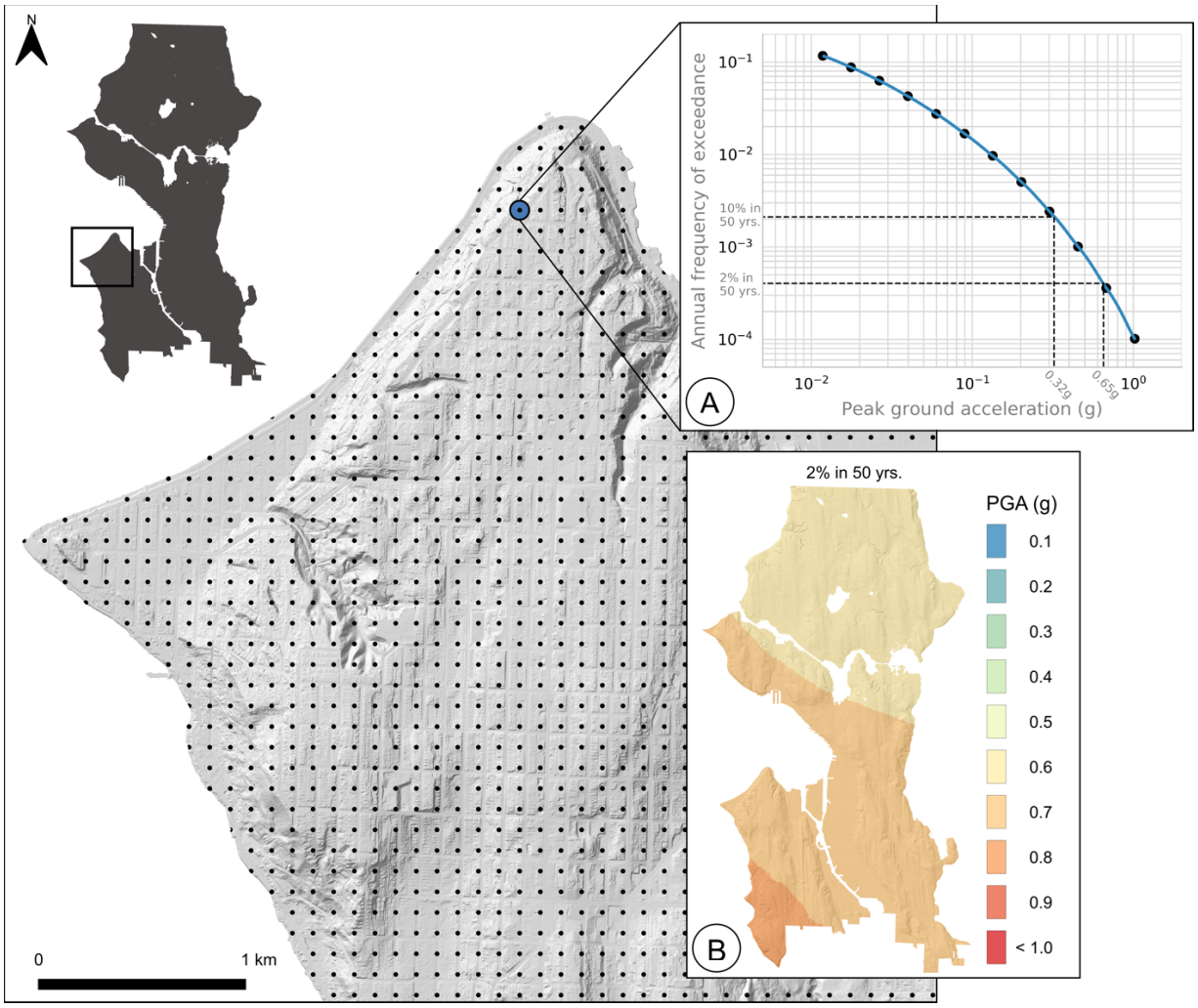

Figure 6.11. Seismic hazard curves were extracted from the 2018 update of the National Seismic Hazard Map at 100 m intervals across Seattle. (*A*) Example curve shown for a bluff above Alki Avenue (-122.38926, 47.59116). (*B*) The seismic hazard curves were used to produce 100 m grids of PGA associated with different probabilities of exceedance (*2% in 50 years shown*).

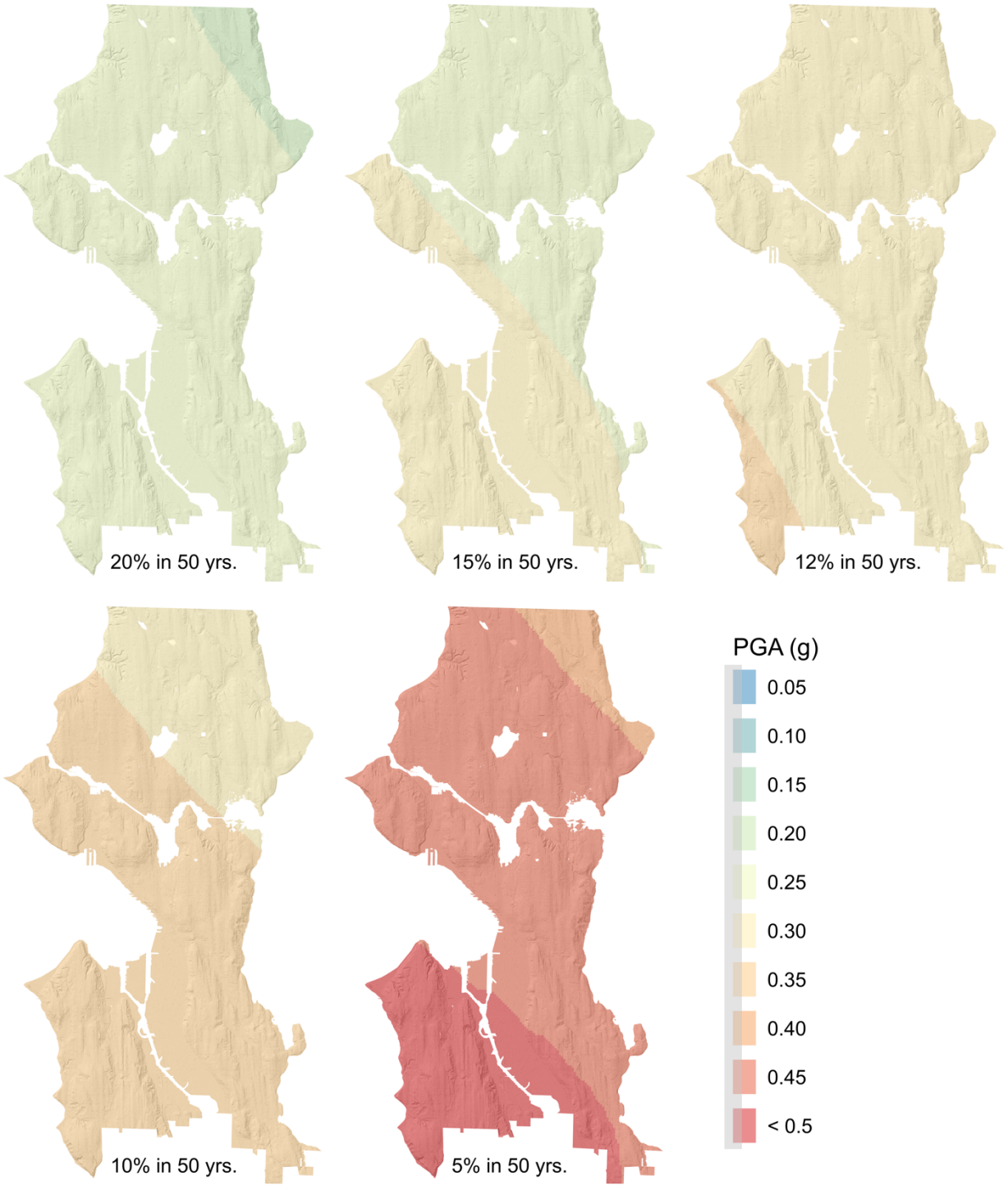

Figure 6.12. Peak horizonal ground accelerations for exceedance probabilities of 5 – 20% in 50 years.

6.3.10 Application of the multimodal method to Seattle

The probability of landslide initiation (source zones) and impact (runout zones) was computed for shallow soils slides, debris falls, and rotational slumps under each triggering scenario. Uncertainty in material parameters was modeled in a Monte Carlo process with 500 simulations for each precipitation scenario and 250 simulations for each seismic scenario, split between wet- and dry-season groundwater conditions.

6.4 Results

6.4.1 Probabilistic landslide hazard

The annual probability of landslide impact (all modes) is shown in **Figure 6.13.** Hazard is concentrated along Seattle's coastal bluffs and inland bodies of water, with the highest annual hazard near Carkeek and Golden Gardens Parks in northern Seattle, Discovery Park and the Queen Anne Greenbelt in Central Seattle, and Alki Point and the Arroyos natural area in southwest Seattle (**Figure 6.13 A**). Not incidentally, many of Seattle's parks and greenspaces have been preserved from development because of their unstable slopes (Williams, 2015).

Seattle's historical landslide inventory provides a first-order verification that the multimodal hazard model can accurately predict locations likely to experience landslides in future precipitation or earthquake events. Seventy-nine percent of the landslides recorded in Seattle's inventory fall within zones of nonzero hazard (**Figure 6.13 B**). Forty-one percent fall between

annual probabilities of 1 x 10^{-4} – 10^{-3}, and 29% fall between annual probabilities 1 x 10^{-5} – 10^{-4}. The significant minority (21%) of recorded landslides that fall outside of predicted hazard zones is likely due to two factors. First, the point locations of landslides in the City inventory are address-based and do not necessarily represent the actual location of the landslide. The address used for geolocating landslide points may be the address of the property where the landslide initiated, the address of the property affected by the landslide, or the address of the person(s) reporting the incident (Laprade et al., 2000). Points may be mislocated by up to about 50 m (Coe et al., 2000). Second, the majority (73%) of landslides in the City's inventory have had some degree of human influence on their initiation (Grant, 2017). Human-triggered landslides often occur in terrain that is otherwise not susceptible to landsliding.

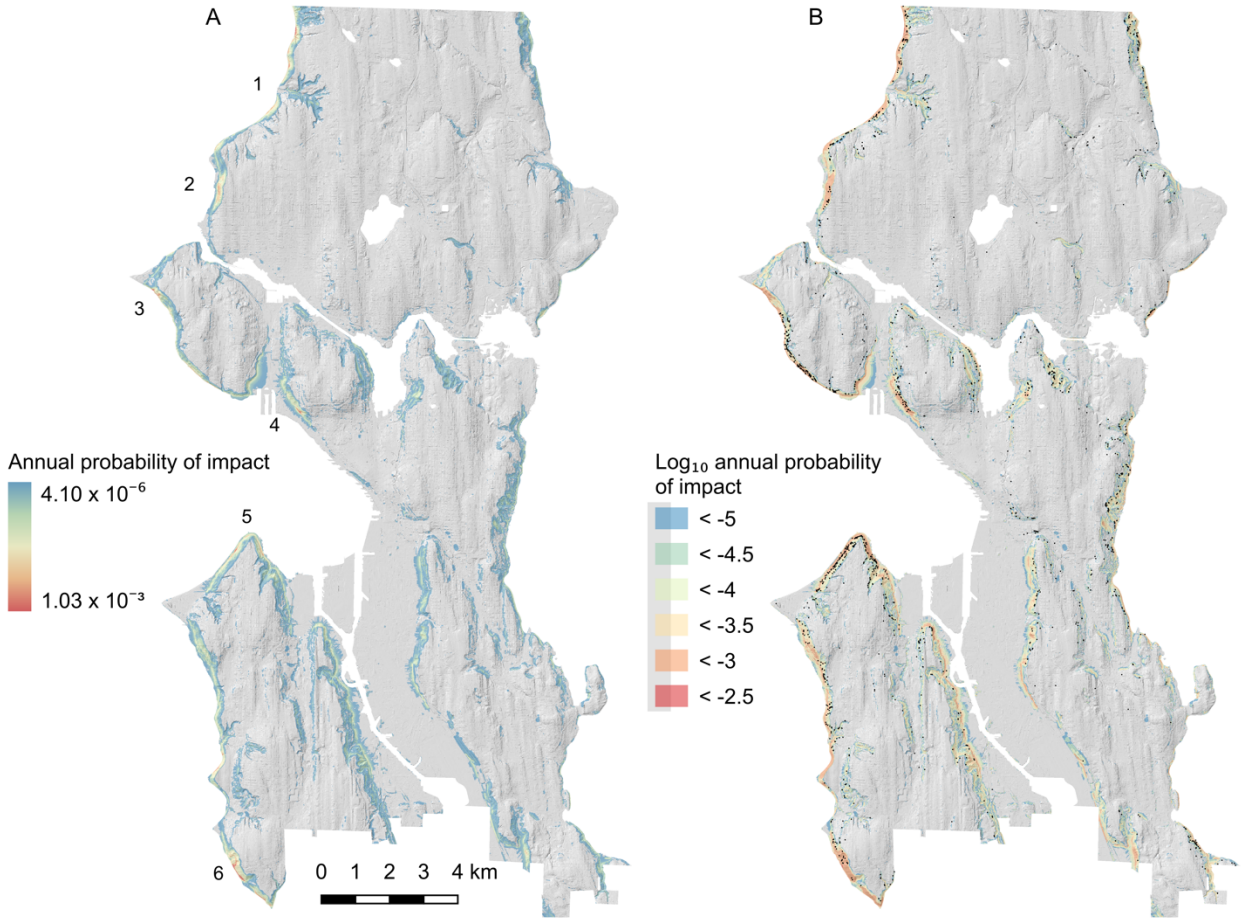

Figure 6.13. (*A*) annual probability of landslide impact from any mode linearly scaled to the minimum and maximum values. (*B*) the annual probability of impact binned on a log scale and overlain by the Seattle landslide inventory. Location in the text are (1) Carkeek Park, (2) Golden Gardens Park, (3) Discovery Park, (4) the Queen Anne greenbelt, (5) Alki Point, and (6) the Arroyos Natural Area.

6.4.2 Magnitude frequency relationships

Landslide event inventories can be summarized and compared through a magnitude-frequency (M-F) plots describing the relative occurrence of different-sized landslides. Previous studies suggest that landslide M-F distributions, like many natural phenomena, follow an inverse power law over part of the magnitude range (Tanyas et al., 2019; Malamud et al., 2004). M-F

distributions are characterized by three statistics: the exponent (slope) of the power law, β, the cutoff point at which the distribution diverges from power law behavior, , and the rollover point at which frequencies decrease for smaller landslides (**Figure 6.14**; Tanyas et al., 2018).

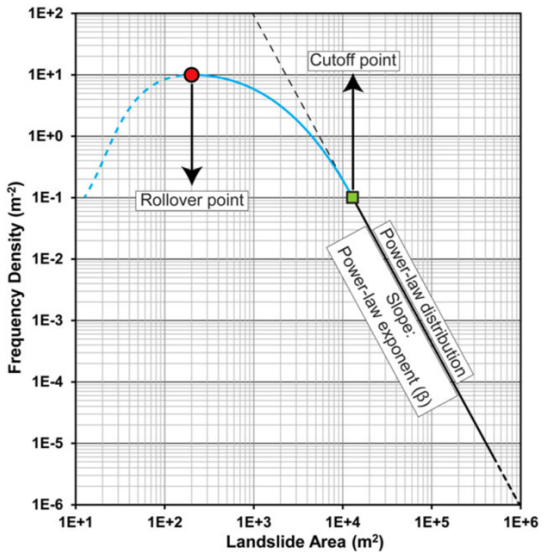

Figure 6.14. The main components of a landslide magnitude-frequency plot. Figure: Tanyas et al., (2018)

The exponent of the M-F power law for a realistic synthetic landslide inventory should mimic that of observed landslide inventories (Gallen et al., 2015). **Figures 6.15** and **6.16** show mean M-F statistics for the synthetic Seattle landslide inventories produced under each triggering scenario compared with those of observed historical and event-based landslide inventories. Only shallow landslide synthetic inventories are included for Seattle. Although less meaningful than source area or volume, I adopt total landslide area as the magnitude parameter following the convention of published M-F statistics for real landslide inventories.

The power law exponents for the precipitation-induced and coseismic synthetic landslide inventories show good agreement with observed landslide distributions. The precipitation

induced synthetic inventories show a prevalence of small landslides compared to observed inventories associated with a specific triggering event. This may be due to the topographic control, as most of Seattle's steep hillsides are of limited relief, promoting smaller landslides than the mountainous watersheds from which the other event inventories are derived. Simultaneously, I do not account for underwater landslide runout from Seattle's coastal bluffs, so the overall landslide area may be underestimated, especially or mobile, precipitation-induced debris flows and avalanches.

The synthetic coseismic landslide inventories for Seattle show a trend of greater landslide size with increasing trigger intensity, likely due to the aggregation of adjacent source cells. The synthetic inventory cutoff and rollover values are smaller by 1 – 2 orders of magnitude than those of observed inventories. This is a function of the base image resolution used to create real landslide inventories, as there is a threshold landslide size at which features can no longer be resolved visually. Approaching this threshold, an increasing number of landslides will be missed, leading to undercounting.

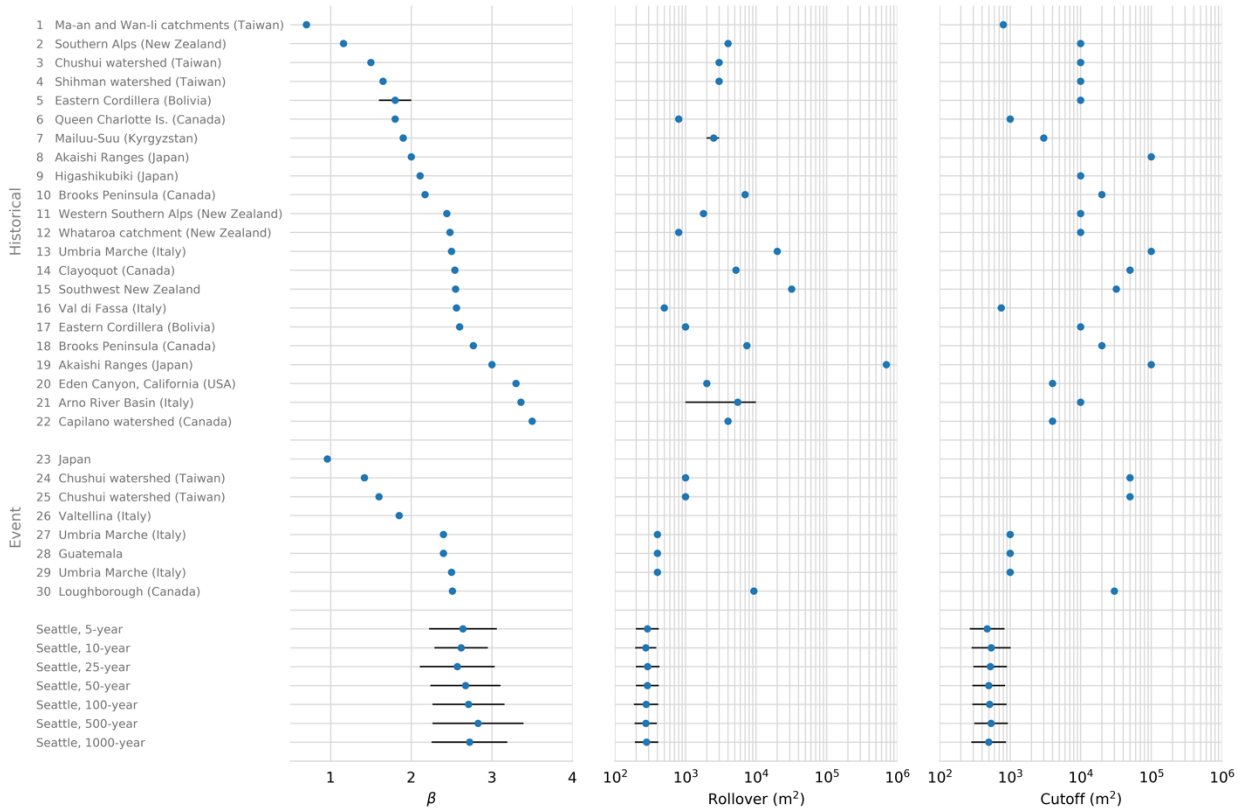

Figure 6.15. The magnitude-frequency power law exponent (β), rollover, and cutoff for precipitation-induced synthetic inventories in Seattle and observed historical (*No. 1 – 22*) and precipitation event (*No. 23 – 30*) landslide inventories. Observed inventory data from Van Den Eeckhaut et al. (2007) and Frattini and Crosta (2013).

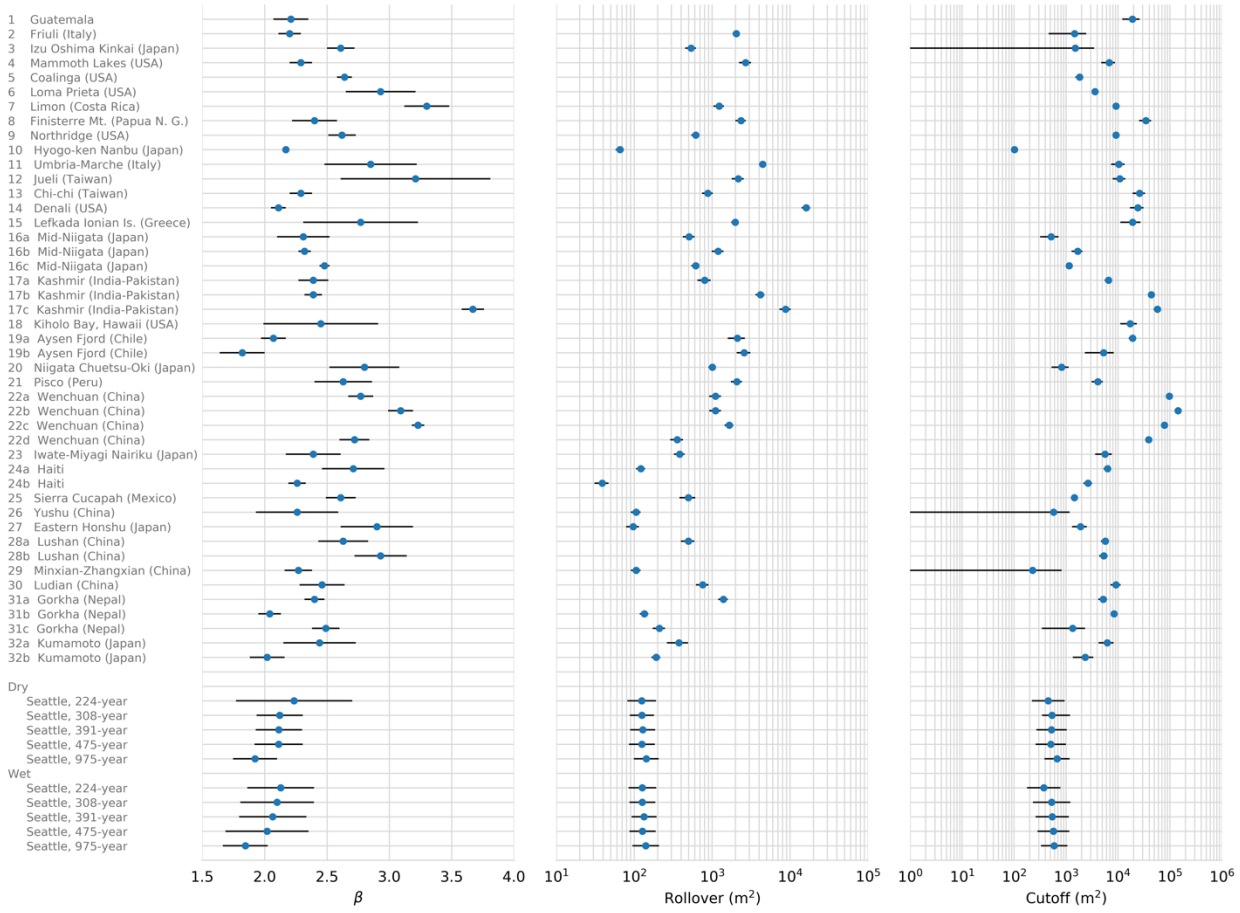

Figure 6.16. The magnitude frequency power law exponent (β), rollover, and cutoff for coseismic synthetic inventories in Seattle and observed coseismic landslide inventories. Observed inventory data from Tanyas et al. (2019).

6.4.3 The influence of seasonality and triggering on hazard severity

Both seasonality and triggering have a strong influence on the landslide hazard in Seattle. The mean area impacted by coseismic shallow landsliding increases 40% (975-year scenario) and 70% (475-year scenario) from dry- to wet-season conditions, with over 1000 additional landslides triggered in both cases (**Table 6.9**). At 5% in 50-year ground-shaking intensity, corresponding to peak ground acceleration of 0.4 – 0.5g throughout much of Seattle, almost

9000 landslides are triggered under wet-season conditions. However, in the most severe model run, associated with a ~1% probability under 5% in 50-year PGA, 17,000 landslides are triggered. By comparison, Allstadt et al. (2013) estimated that over 30,000 landslides would be triggered in a wet-season M7.0 Seattle Fault earthquake, with PGAs reaching 2g in localized areas on the hanging wall of the fault.

Fewer shallow landslides are triggered by precipitation, with 740 – 1040% more landslides in a 10% in 50 year (475-year) ground-shaking scenario than in the 500-year return period rainfall. Precipitation induced landslides are also smaller, averaging 443 m^2 per landslide compared to 497 m^2 and 623 m^2 under dry- and wet-season seismic triggering. Unlike coseismic landsliding, precipitation-induced landsliding saturates, with the total shallow landslide area reaching ~0.15 km^2 for long-return period rainfall.

Table 6.9. The relative severity of different return period triggering intensities and ground water conditions. The mean values for all model runs within a given return period are shown.

Trigger	*Ground water conditions*	*Return period (yr.)*	*Number of landslides*	*Source area (km^2)*	*Total area (km^2)*
Precipitation	Wet	5	226	0.014	0.107
		50	287	0.018	0.135
		500	344	0.020	0.153
		1000	328	0.020	0.145
Seismic	Dry	475	2889	0.300	1.437
		975	7542	0.929	4.534
	Wet	475	3921	0.504	2.442
		975	8801	1.308	6.278

Figures 6.17 and **6.18** highlight the shift in landslide hazard under wet and dry groundwater conditions and precipitation and seismic triggers above Alki Avenue in West Seattle. Under 500-year precipitation conditions, shallow landslides hazard is low (1 – 2%) but widespread across coastal bluffs and drainages. Under 10% in 50 year (475-year return period) ground

shaking intensities, the probability of impact increases to up to 70-80% under dry conditions, concentrated below a high-relief, mid-slope bench. Wet-season conditions produce a similar spatial pattern of hazard, but with ~10% higher probabilities of impact as the relatively saturated colluvium blanketing the bench are not capable of resisting moderate levels of shaking. The spatial pattern of hazard from rotational slumps is similar across the scenarios, with the exception of half a dozen high probability (70 – 80%) zones developing under seismic forcing. These areas of elevated hazard are located near historical deep-seated landslides, including four deep-seated landslides which damaged homes and roadways during the 2001 Nisqually earthquake (**Figure 6.19**).

The 500- and 1000-year precipitation scenarios are almost identical, indicating that hazard saturates to a point at which introducing more rainfall to the system does not trigger additional landslides. By comparison, the 5% in 50-year (975-year return period) seismic scenario increases both the spatial extent and the intensity of the hazard for all three modes when compared to more frequent events.

Figure 6.17. *(following page).* The probability of impact by the runout of shallow landslides (*A*, *C*, *F*) or debris falls (*E*, *H*) or probability of failure in a deep-seated, rotational slump (*B*, *D*, *G*) for Alki Point. 475 – 500-year return period triggering intensities are shown. No debris falls are triggered by precipitation.

Figure 6.18. *(page 266).* The probability of impact by the runout of shallow landslides (*A*, *C*, *F*) or debris falls (E, H) or probability of failure in a deep-seated, rotational slump (*B*, *D*, *G*) for Alki Point. 975 – 1000-year return period triggering intensities are shown.

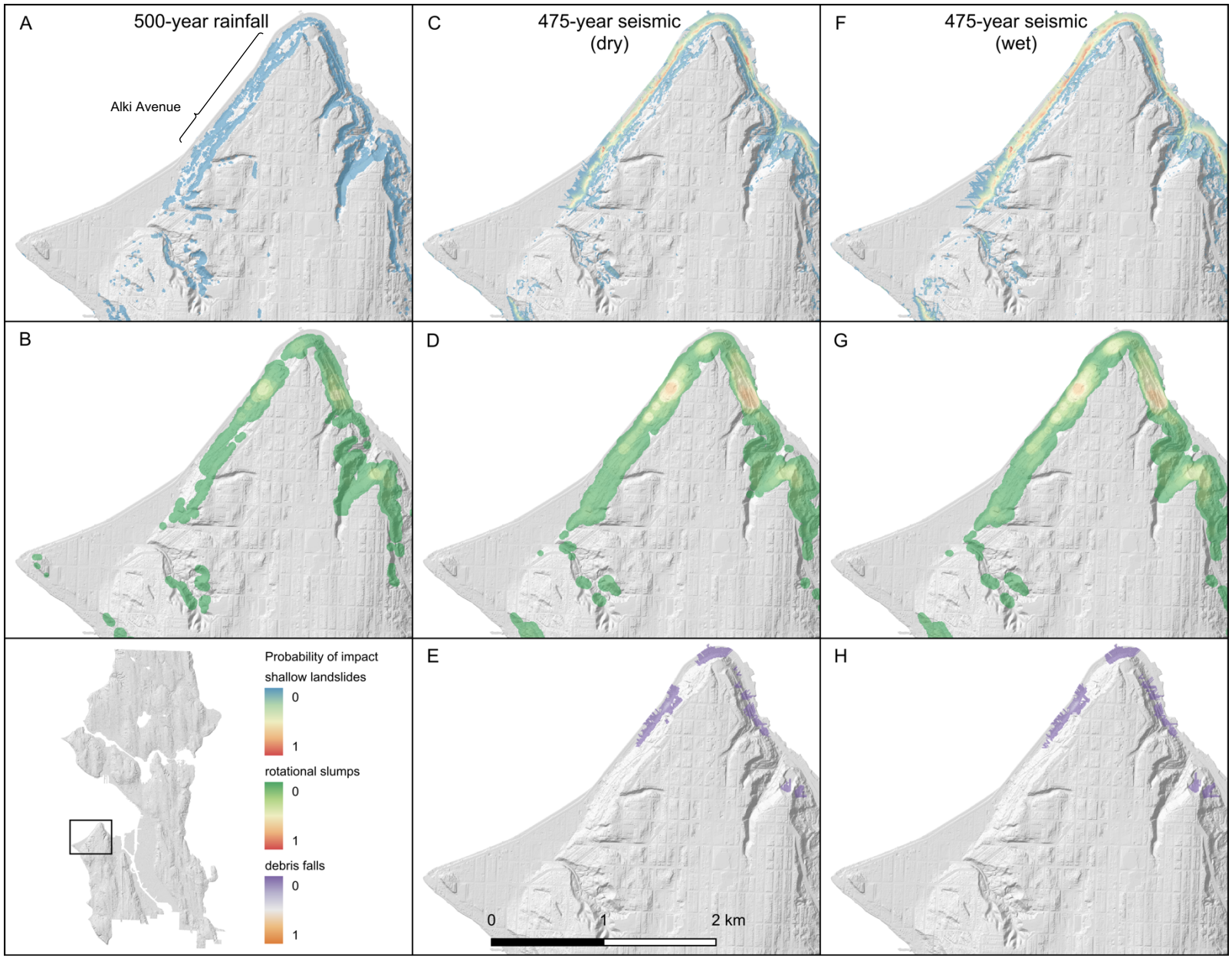
A
500-year rainfall
Alki Avenue
C
475-year seismic
(dry)
F
475-year seismic
(wet)
B
D
G
Probability of impact
shallow landslides
0
1
rotational slumps
0
1
debris falls
0
1
E
H
0
1
2 km

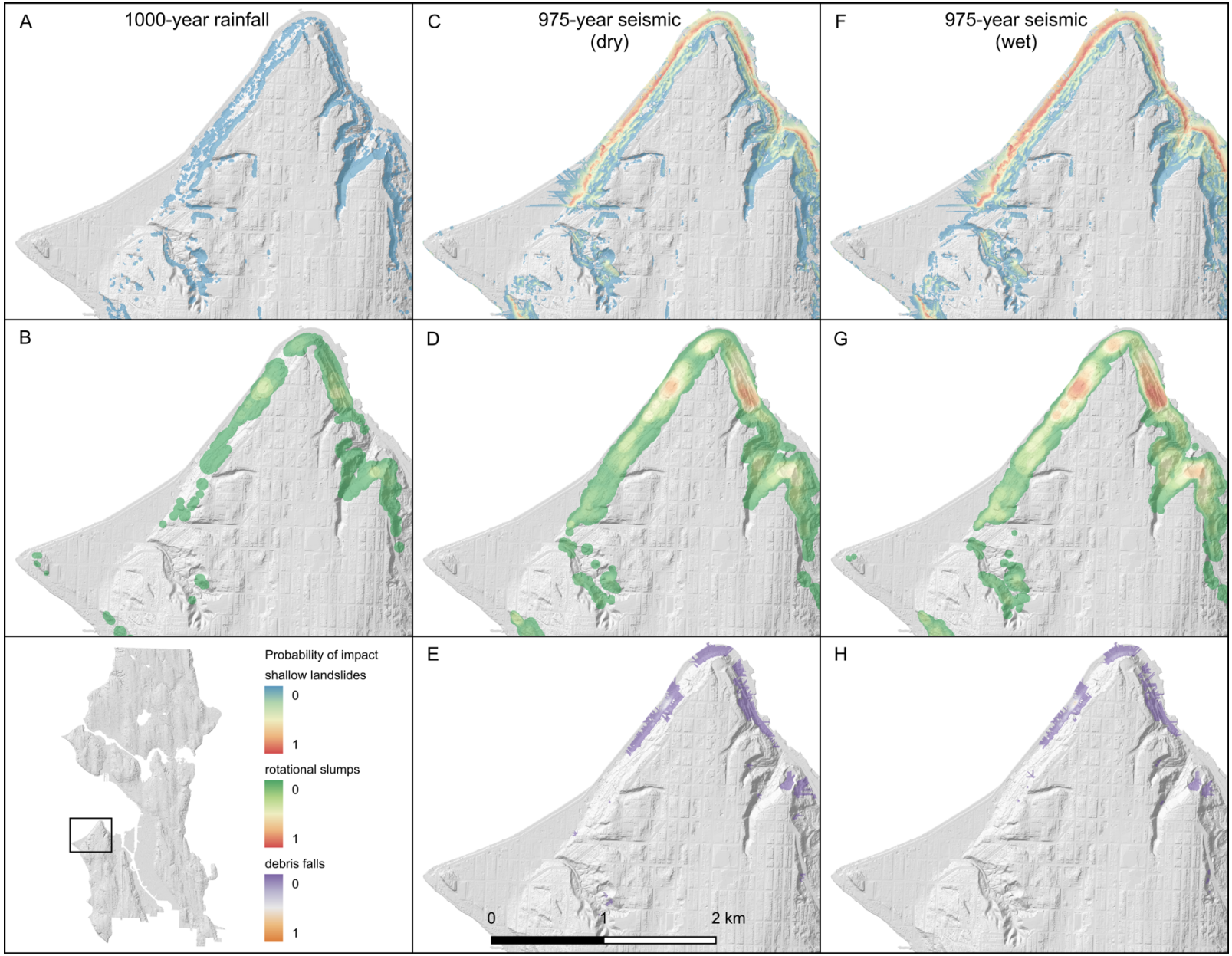
A
1000-year rainfall
C
975-year seismic
(dry)
F
975-year seismic
(wet)
B
D
G
Probability of impact
shallow landslides
0
1
rotational slumps
0
1
debris falls
0
1
E
H
0
1
2 km

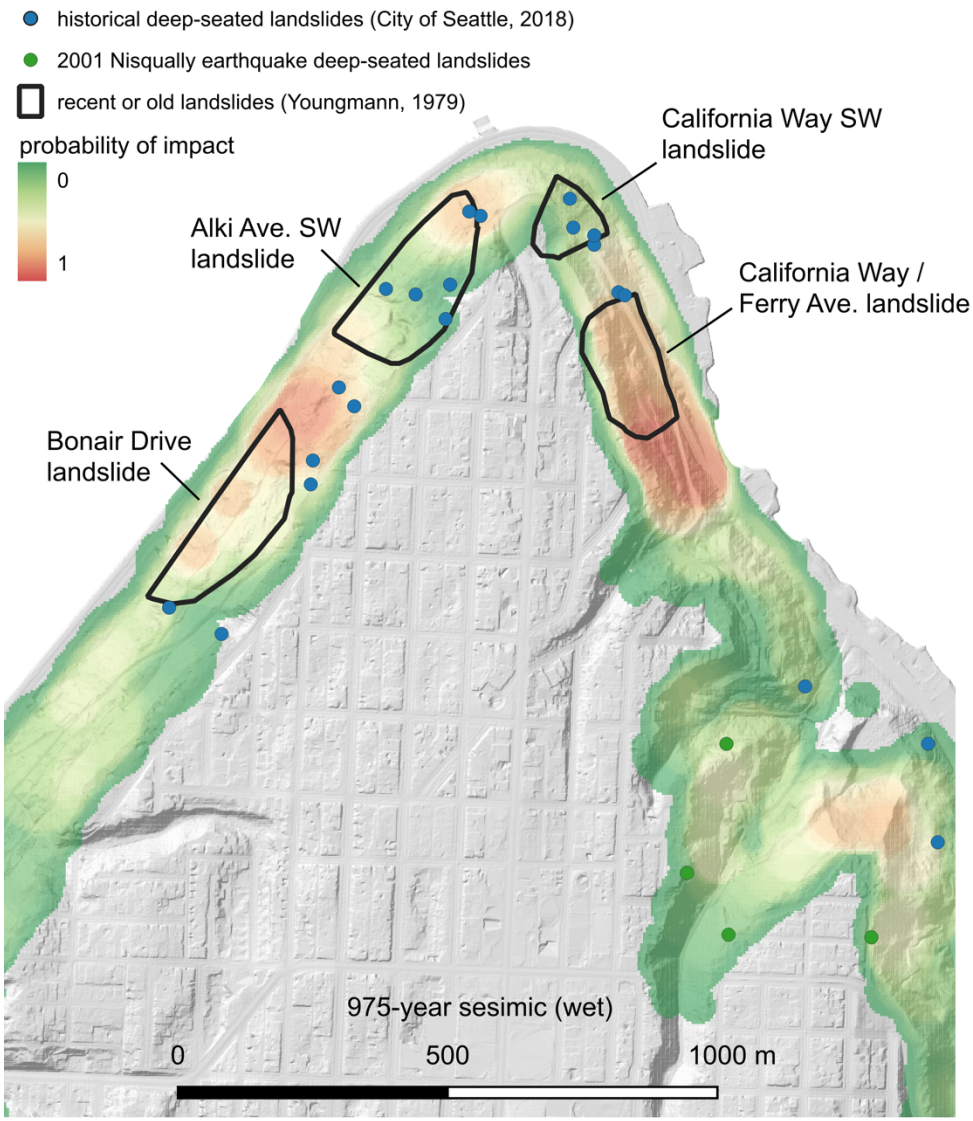

Figure 6.19. Hazard from deep-seated, rotational slumps around Alki Avenue in West Seattle under a wet-season, 975-year seismic triggering scenario. Historical landslide locations from Youngmann (1979) and the City of Seattle landslide inventory are shown, including four deep-seated landslides triggered by the 2001 Nisqually earthquake. Note that point locations are address-based rather than centered on the landslide body.

6.4.4 Probabilistic landslide risk

The total annual landslide risk in Seattle is substantial. Almost 38 landslide fatalities and $114 million in structural damage are predicted on an annual basis. Precipitation-induced landslides

contribute 77% and 84% of risk to humans and structures, respectively (**Table 6.10**). Shallow landslides dominate the risk profile of Seattle at 99% of human fatalities and 97 – 99% of structural damage across all modes. Rotational slumps contribute up to 1.7% of structural losses and debris falls contribute up to 1.0% under seismic triggering depending on the groundwater conditions. No precipitation-induced debris falls are predicted.

Table 6.10. Total annual risk to humans and structures in Seattle. Mean values are given.

Element at risk	*Trigger*	*Annualized risk (yr^{-1})*	*Percent*
Humans	precipitation	30.0	76.9
	seismic	8.7	23.1
	total	**37.7 lives**	
Structures	precipitation	96.2	84.2
	seismic	18.1	15.8
	total	**114.3 $M**	

The spatial distribution of landslide risk for humans and structures is shown in **Figure 6.20**, aggregated by census block for visualization. Structural risk is concentrated, with localized hotspots along Alki Avenue, Harbor Avenue, Westlake, and South Lake Union (see **Figure 6.20 A** for locations). With the exception of Alki Avenue, these locations have relatively low annual hazard, but a high annual risk, due their high-value business and residential complexes. Human risk is widespread, distributed across Seattle's many hillside residential areas along the Puget Sound, Lake Washington, and the topographic high of Queen Anne (**Figure 6.20 B**).

Elevated landslide risk occurs in many of the same landslide-prone locations highlighted in previous landslide susceptibility and hazards studies. These include in West Seattle along Alki Avenue, the western margin of the Duwamish waterway, coastal bluffs below Magnolia Avenue, the SW and NE slopes of Queen Anne, and near Arroyos Natural Area in South Seattle (Allstadt et al., 2013; Harp et al., 2006; Coe et al., 2000; Grant, 2017).

However examining landslide risk adds important information otherwise missed in susceptibility and hazard studies. While landslide hazard at Carkeek Park is relatively high, spurring projects to drain the hillslopes, (Harp et al., 2006; Allstadt et al., 2013; Laprade et al., 2000; Wait, 2001), the risk to humans and structures is relatively low (**Figure 6.20**). Other areas historically associated with elevated landslide hazard, such as the north end of Magnolia bluff, Ravenna, South Beacon Hill, and the inland drainages of West Seattle (Harp et al., 2006; Coe et al., 2004; Godt et al., 2008a), have very low risk due to low population density. Conversely, susceptibility and hazard maps cannot communicate the disproportionately high risk of areas such as SW Queen Anne and Westlake which is driven by their dense population and high building values.

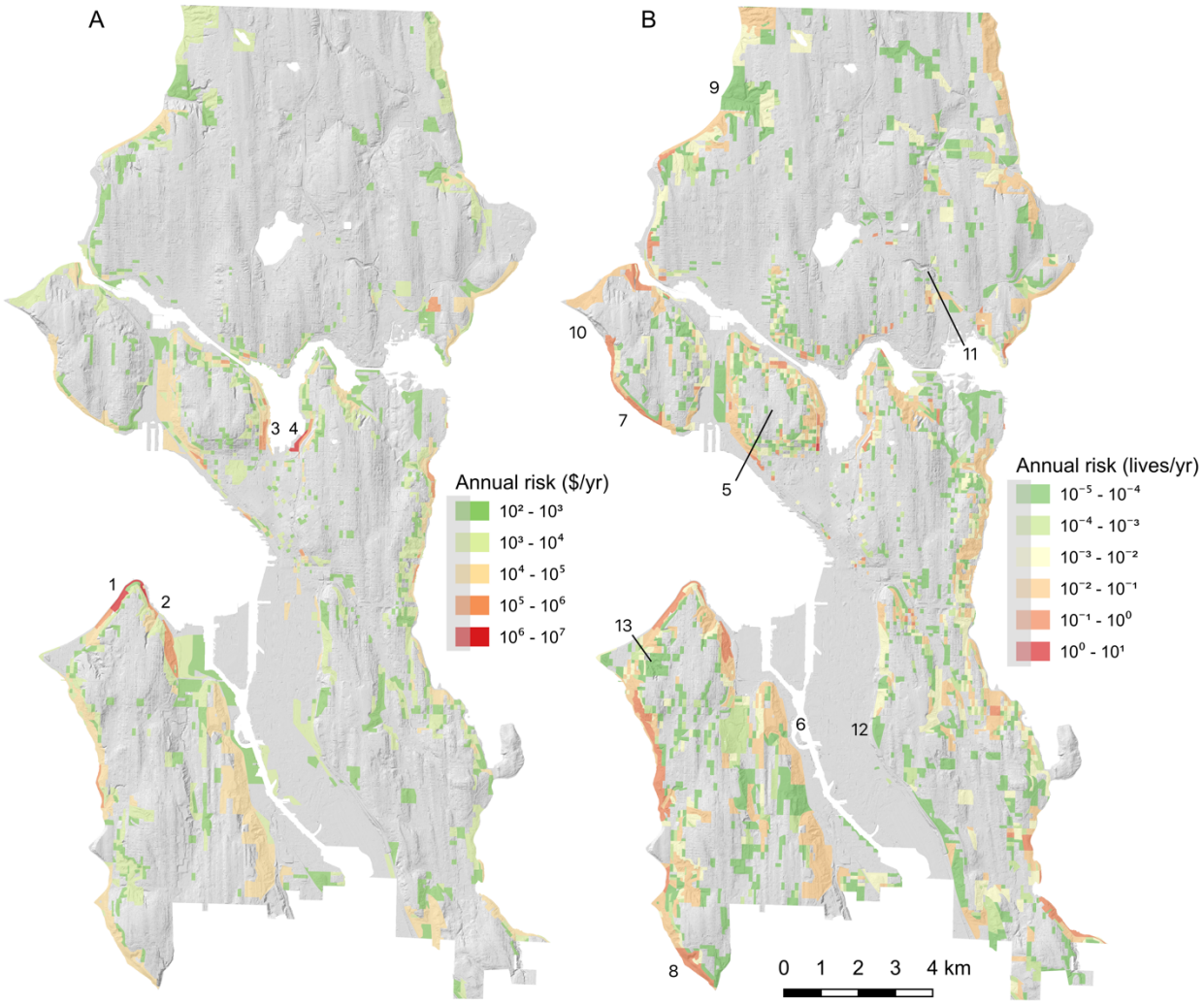

Figure 6.20. Annual risk aggregated by census block considering (*A*) structural damage and (*B*) human loss of life. Location in the text are *1*) Alki Avenue, *2*) Harbor Avenue, *3*) Westlake, *4*) South Lake Union, *5*) Queen Anne, *6*) the Duwamish waterway, *7*) Magnolia Avenue, *8*) Arroyos Natural Area, *9*) Carkeek Park, *10*) Magnolia bluff, *11*) Ravenna, *12*), S Beacon Hill, and *13*) West Seattle drainages.

Figure 6.21 shows a detail of the structural and human risk at two locations above Harbor Avenue and below Magnolia Avenue. At the southern end of Magnolia bluff, ongoing instability threatens homes both at the toe and crest of the bluff (**Figure 6:22 A1**). Recent failures have been primarily shallow colluvial slides originating mid-slope, including one which occurred days before the image **A2** was (**Figure 6.22**) taken from the deposit of a much larger

and older failure. To the south and east a series of homes lie on the deposit of an old slump and have been repeatedly damaged from shallow slides from the crest of the bluff. Above Harbor Avenue, a string of houses lie within the deep-seated California Way/Ferry Avenue landslide mapped by Youngmann (1979; **Figure 6.21 B**). The landslide was reactivated after heavy precipitation in early 1997 (Laprade et al., 2000). The home to the extreme NW in **Figure 6.21 B** crosses a tension crack at the head of the landslide (**Figure 6.22 B1**), and differential settlement has caused cracks to develop in the home's foundation. During a field reconnaissance 17 March 2020, we spoke to the owner of the home at arrow **B3** in **Figure 6.21**). He told us that the heavily cracked and patched pavement in front of his home had been settling since at least the summer of 2019 (**Figure 6.22 B2**), leaving a new 2 inch offset in the adjacent sidewalk. Cracks began developing in the masonry of his garage in the fall of 2019 (**Figure 6.22 B3**).

Especially when using risk maps on a building scale, such in **Figure 6.21**, it is important to note that there may be actual landslide risk even when the predicted risk is zero. The risk may be very small, beyond the precision of the tools used for calculation and visualization or it may not have been captured in the limited number of Monte Carlo runs used in this study. Predicted risk is also sensitive to the quality of the input data, especially where population or value information was incomplete for elements at risk. In addition, as illustrated in **Figure 6.21**, the multimodal method can produce the counterintuitive result of human risk in buildings where there is no structural risk and vice versa. This can occur because the structural and human vulnerability are assigned independently, and each have a probability of being zero in any given model run.

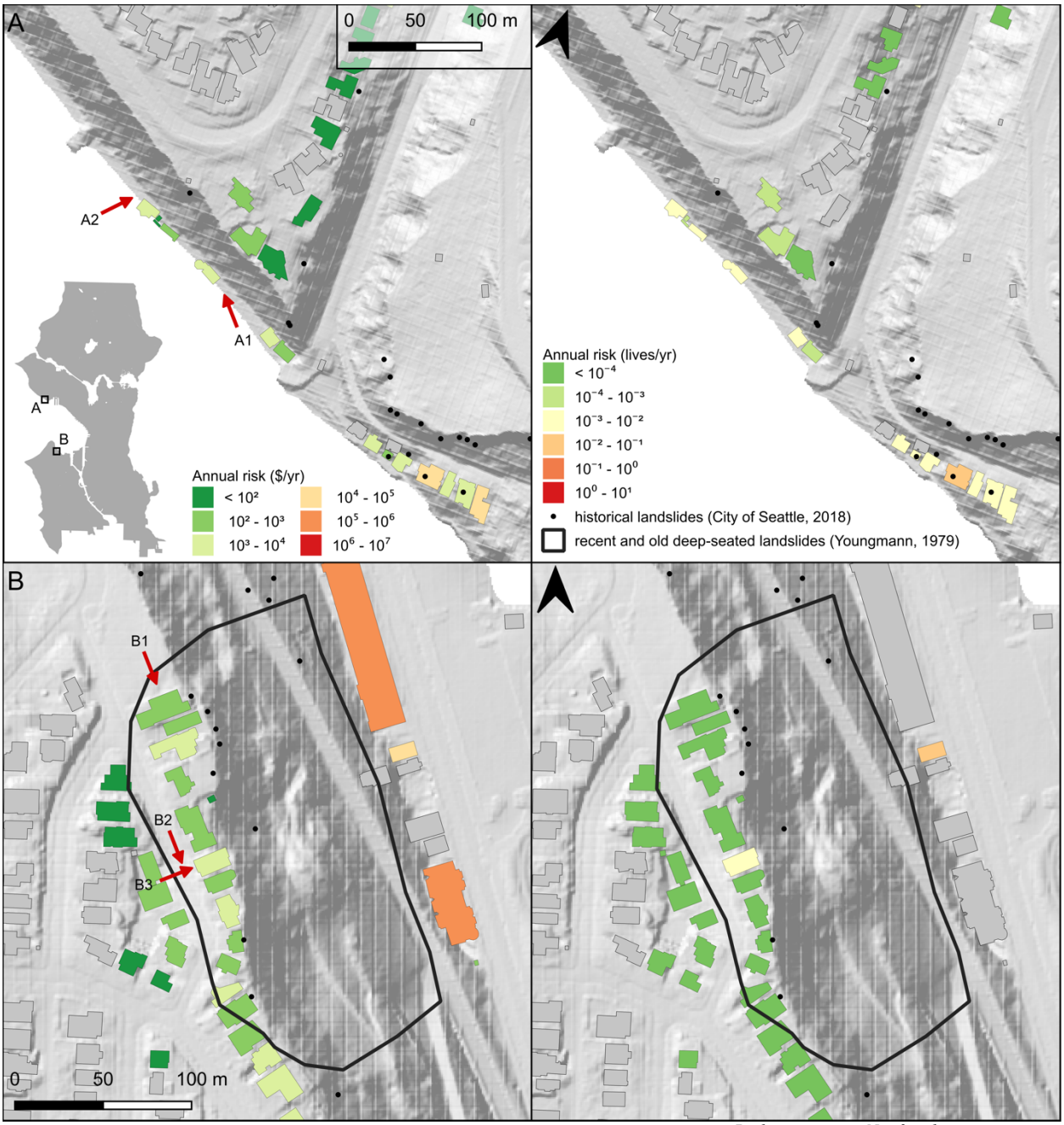

Preliminary map. Not for planning purposes.

Figure 6.21. Estimates of annual structural risk (*left*) and human risk (*right*) below Magnolia Avenue in Central Seattle (*A*) and above Harbor Avenue (*B*) in West Seattle. Red arrows correspond to camera positions for images in **Figure 6.22**. Historical landslides from Youngmann (1979) and City of Seattle (2018) are shown.

Figure 6.22. Images corresponding to the locations described in the text. Images: J. Wartman and W. Pollock.

Both human and monetary risk is distributed unequally across buildings. 70% of the total human risk is held in the top 5% of buildings with at least nominal risk (n = 915), while 92% of the structural risk is held in the top 5% of buildings (n = 1005, **Figure 6.23**). The ten highest-risk buildings for human and monetary risk contribute 14.7% and 40.5% of the total annual risk, respectively (**Table 6.11**). I anticipate that these highest-risk buildings, while over-represented in the total risk figures, are products of the simplifying assumptions made in the risk analysis process and complex factors not included here which are unique to performing landslide modeling in a heavily modified, urban terrain (see discussion in **Section 6.5.2**).

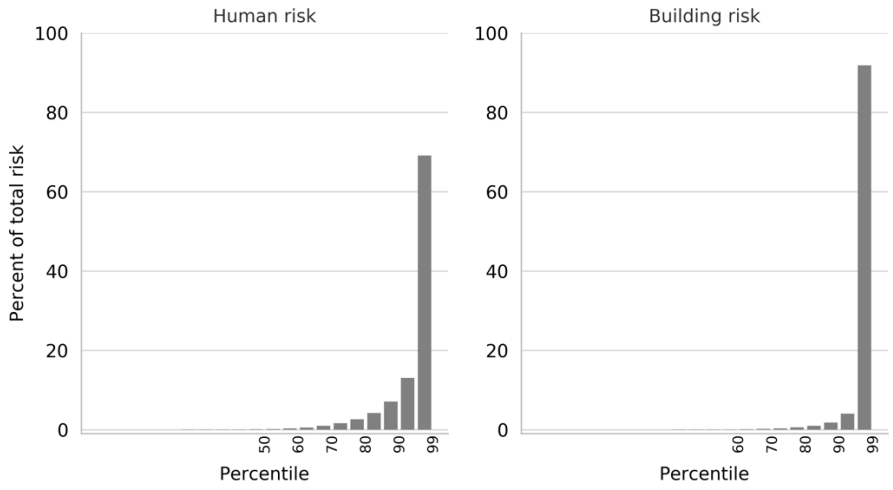

Figure 6.23. The percent distribution of risk for humans (left) and buildings (right).

Table 6.11. The annual risk contribution of the top 100, 10 and 1 building(s).

	human		*structural*	
Number of buildings	Annual risk (lives / yr.)	percent	Annual risk ($ M / yr.)	percent
100	14.10	37.4	79.8	69.8
10	5.55	14.7	46.3	40.5
1	1.52	4.0	11.1	9.7

6.4.5 Disaggregation of landslide hazard and risk

The multimodal method supports the disaggregation of the components of risk at every step in the risk calculation, including the intermediate steps of calculating hazard and exposure. Short return period, low-intensity precipitation dominates the annualized hazard, exposure, and risk (**Figure 6.24**). However, under comparable return period triggering scenarios, the annualized area impacted by coseismic landslides is up to 44 times higher than for precipitation-induced landslides. Interestingly, this only results in 2 – 3 times more structures and resident people falling within those hazard zones. While the low frequency of extreme precipitation events mutes their annual risk contribution, seismic triggering events show the opposite trend.

Figure 6.25 shows risk in absolute rather than annualized terms, highlighting the inverse proportionality between the consequences and frequency of seismic triggering events. The slight flattening of the seismic hazard curves at low return periods suggests a drop-off in the number of triggered landslides toward a baseline of terrain pixels which are marginally stable under static conditions. Including additional seismic triggering scenarios at the upper and lower ends of the temporal range (below 224-year return periods and above 975-year return periods) could provide insight into a lower PGA bound, below which no landslides are triggered, and the apparent linear scaling of hazard and risk under severe ground shaking intensities.

Precipitation-induced hazard and risk appear to saturate around the 100-year rainfall intensity (**Figure 6.26**). This trend may be a function of the saturated hydraulic conductivity of the surficial soil. When rainfall exceeds the infiltration capacity, excess water becomes surface runoff which is routed downslope until it infiltrates at a more permeable cell or reaches the margins of the terrain model. Thus few additional landslides are triggered in the simulated environment, just as excess rainfall may lead to flooding but no additional landslides in real storms. However, the trend is not consistent, especially in regard to exposure. Approximately 400 more buildings are exposed to landslide landslides in the 5-year return period scenario than in the 25-year scenario, indicating significantly different spatial distributions of landslides between scenarios. The fluctuations in the exposed number of people and buildings between scenarios suggest that there are too few model runs to fully capture the variability in input parameters. This is especially the case for saturated conductivity which can vary over multiple orders of magnitude.

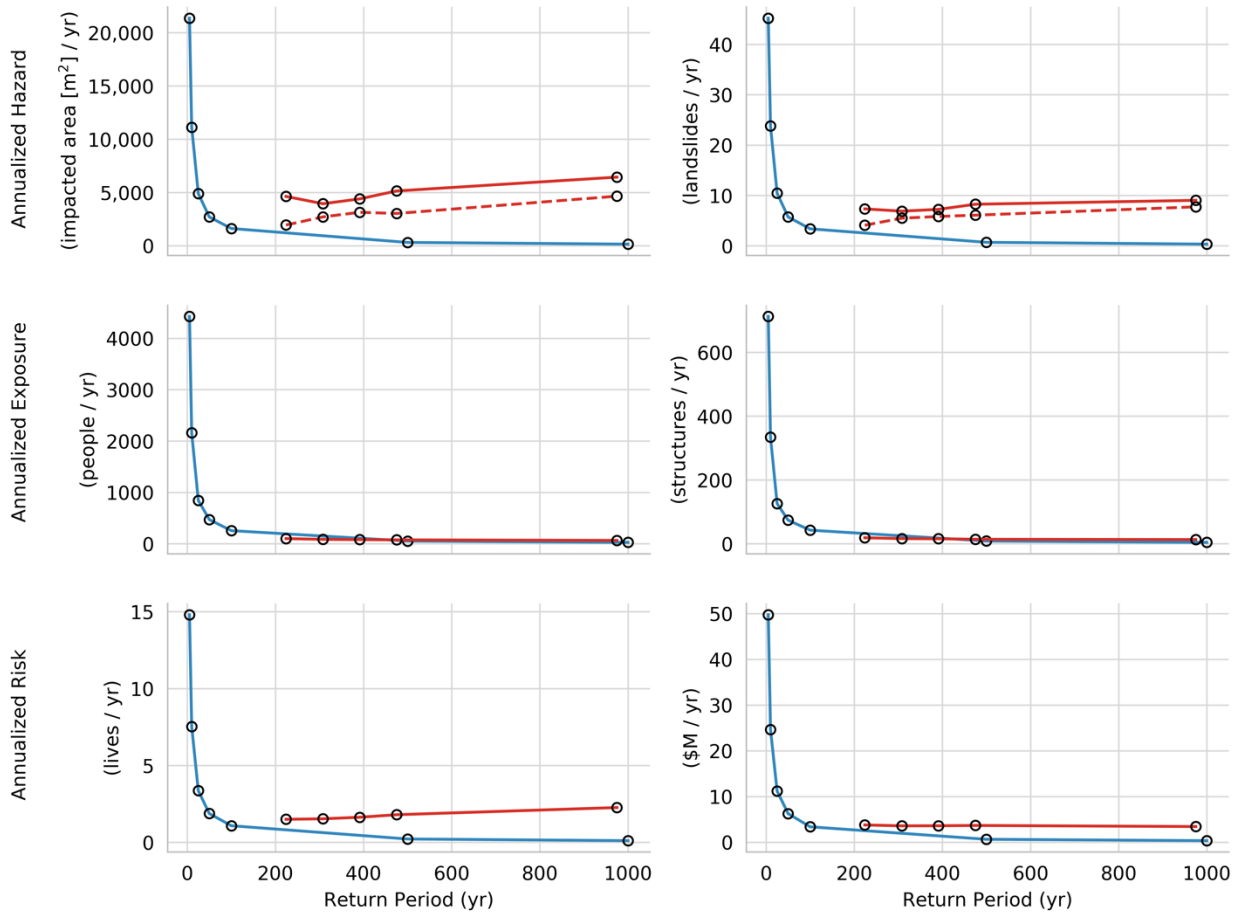

Figure 6.24. Annualized hazard, exposure, and risk curves for precipitation triggering (*blue*) and seismic triggering (*red*). *Top*: the annualized total hazard measured in area affected by landslides (*left*) and number of triggered landslides (*right*). Impacted area and number of landslides only consider the shallow mode. Dashed line indicates dry season conditions while wet-seasons conditions are shown with the solid line. Wet and dry groundwater conditions are combined in the other plots. *Middle*: the annualized exposure to any mode of landslide hazard of humans (*left*) and structures (*right*). *Bottom*: the annualized risk from landslides for humans (*left*) and structures (*right*).

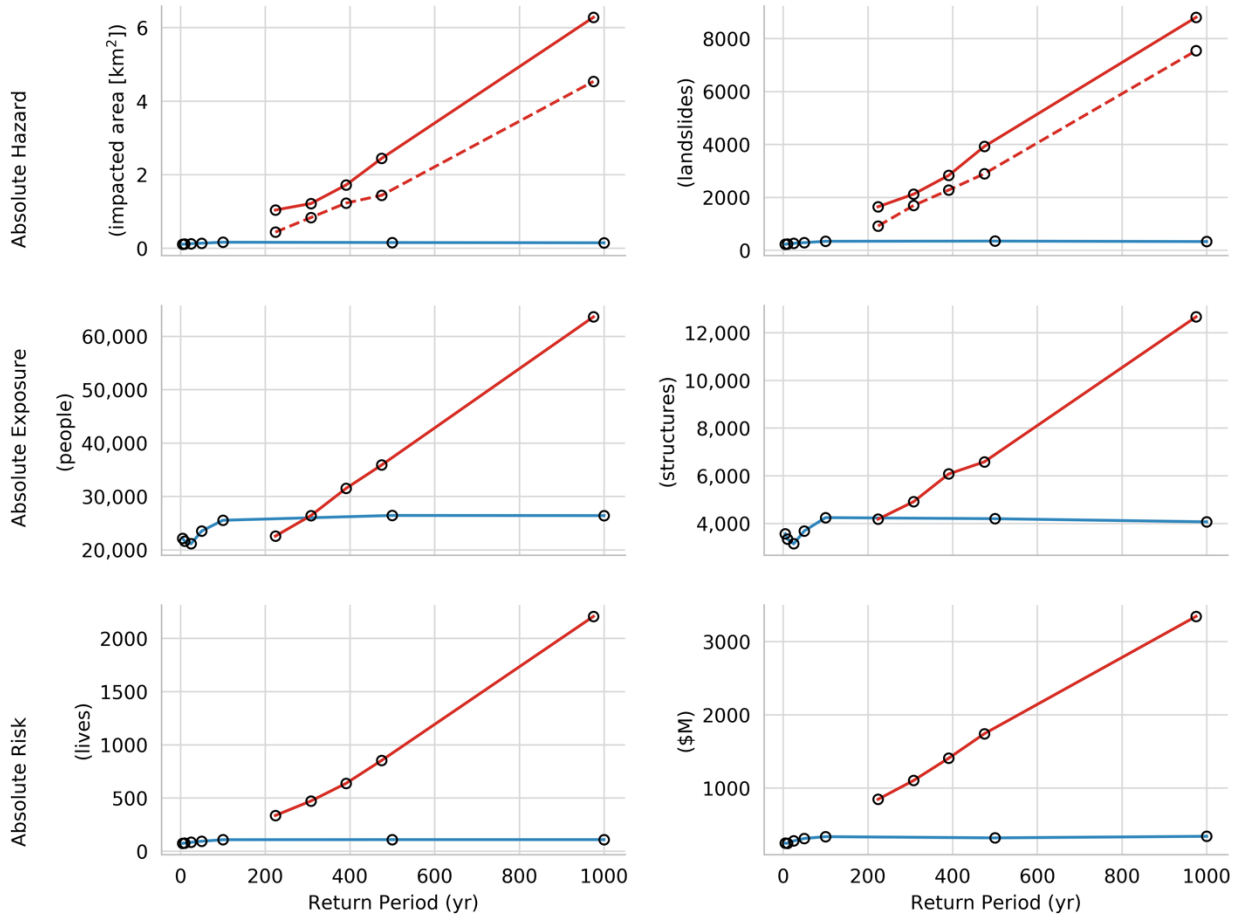

Figure 6.25. Absolute hazard, exposure, and risk curves for precipitation triggering (*blue*) and seismic triggering (*red*). *Top*: the annualized total hazard measured in area affected by landslides (*left*) and number of triggered landslides (*right*). Impacted area and number of landslides only consider the shallow mode. Dashed line indicates dry season conditions while wet-seasons conditions are shown with the solid line. Wet and dry groundwater conditions are combined in the other plots. *Middle*: the annualized exposure to any mode of landslide hazard of humans (*left*) and structures (*right*). *Bottom*: the annualized risk from landslides for humans (*left*) and structures (*right*).

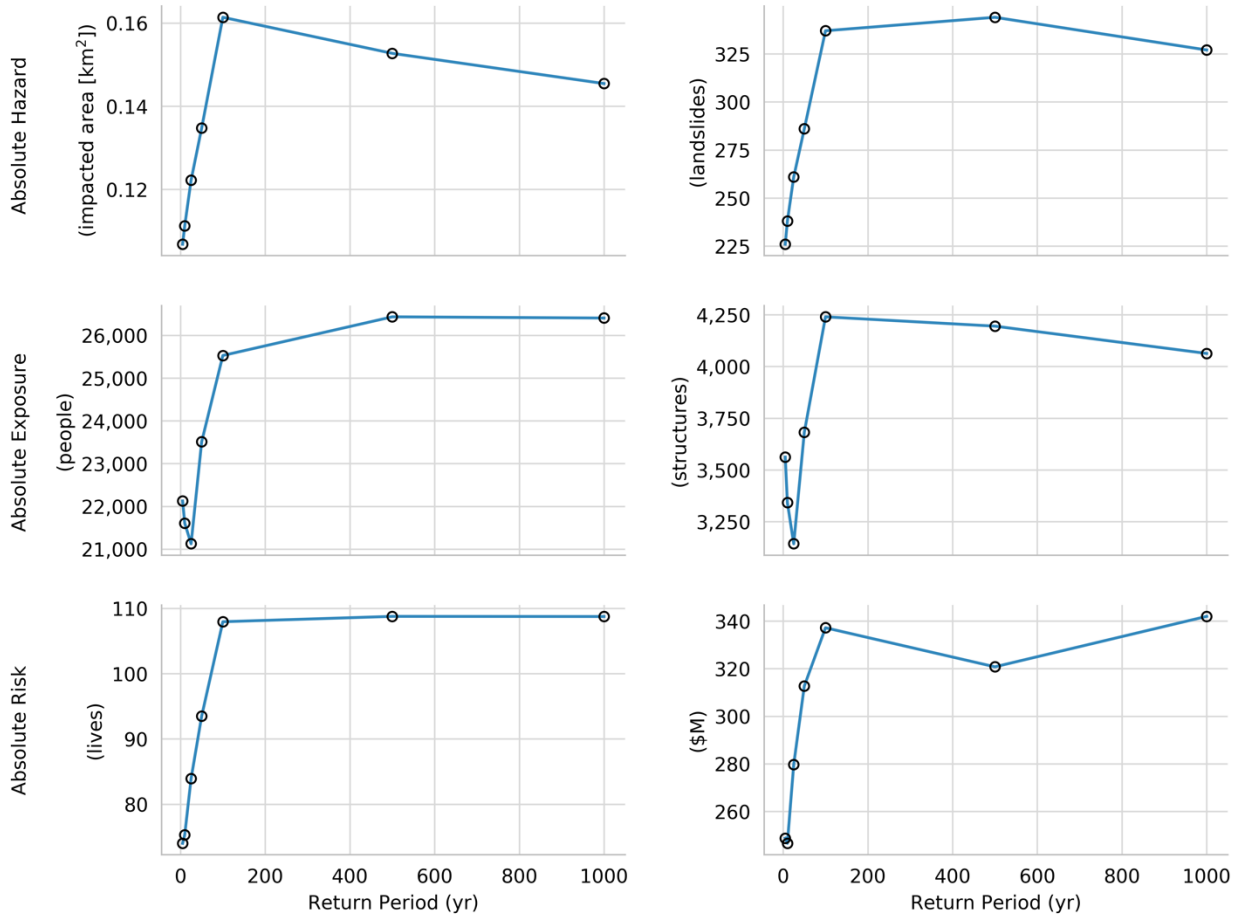

Figure 6.26. Absolute hazard, exposure, and risk curves for precipitation triggering only. The impacts of precipitation-induced landslides appears to saturate, although the trend is not consistent across hazard, exposure, and risk.

Spatial patterns of risk at the scale of individual buildings shows dramatic local variation, strongly controlled by position along the hillslope profile. **Figure 6.27** shows the annualized structural risk on a per-building basis for the Alki Point area of West Seattle. Most of the structural risk at building A at the toe of the slope (see **Figure 6.27**) comes from shallow landslides, split evenly between precipitation (34%) and seismic (35%) triggering (**Figure 6.28 A**). The other modes also contribute substantially to the structural risk, at 13% and 10% for slumps and debris falls, respectively. The dominance of shallow landslides in the structural and human risk of building A reflects its position in the runout zone of landslides initiating in the

high-relief topographic bench above it as well as the relatively high vulnerability of human and structures to shallow landslide debris. In contrast, at building B 100 m up the slope, 74% of structural risk comes from precipitation induced slumps undercutting the slope crest while only 2% comes from shallow landslides. However, due to the relatively low human vulnerability to slumps, 77% of the human risk at building B comes from shallow landslides triggered by intense but infrequent levels of seismic shaking (**Figure 6.28 B**).

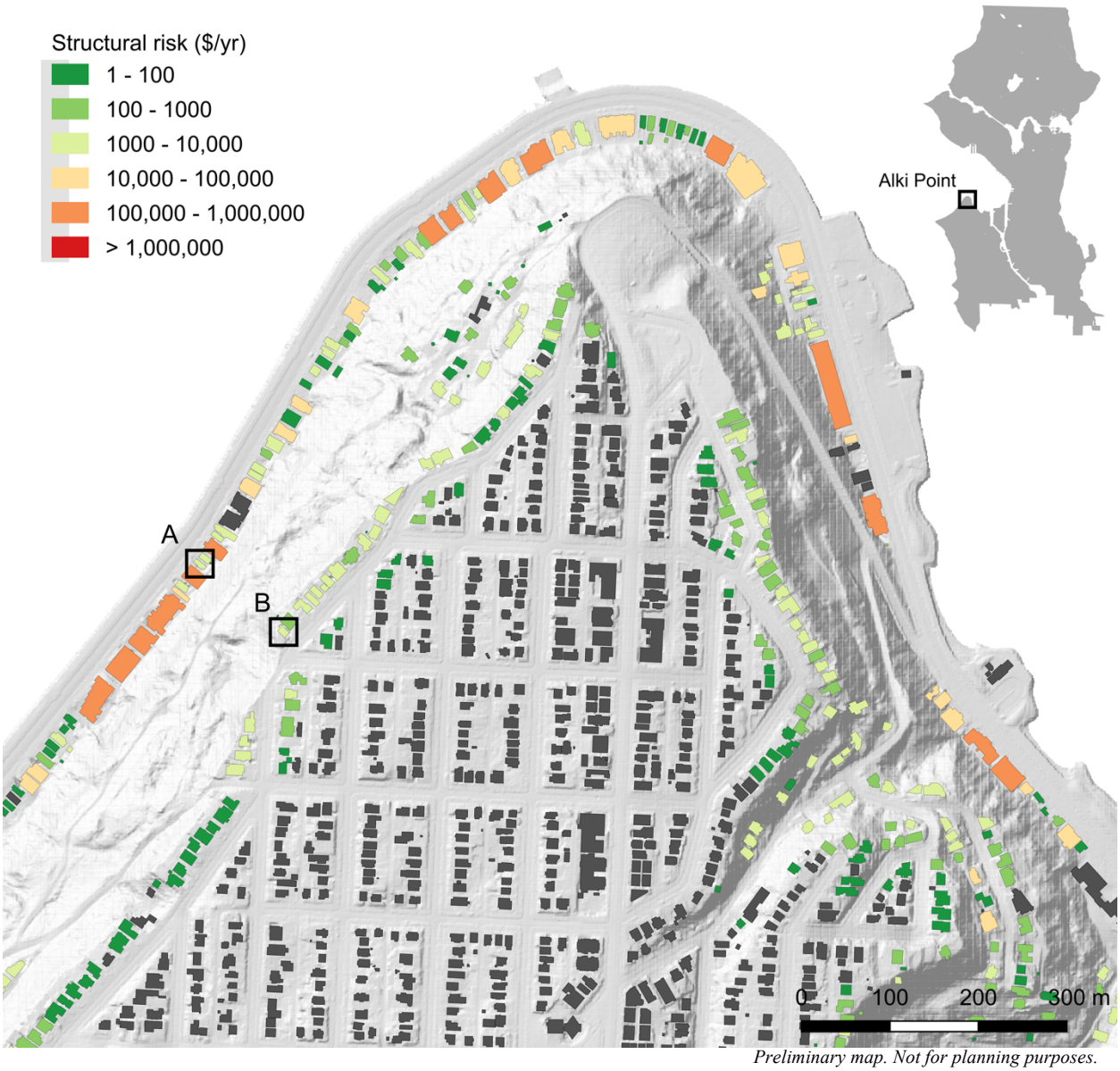

Figure 6.27. Annualized structural risk on a per building basis. The percent contributions of each landslide mode and triggering event can be disaggregated at each structure, as shown in **Figure 6.28** for the buildings highlighted at locations **A** and **B**.

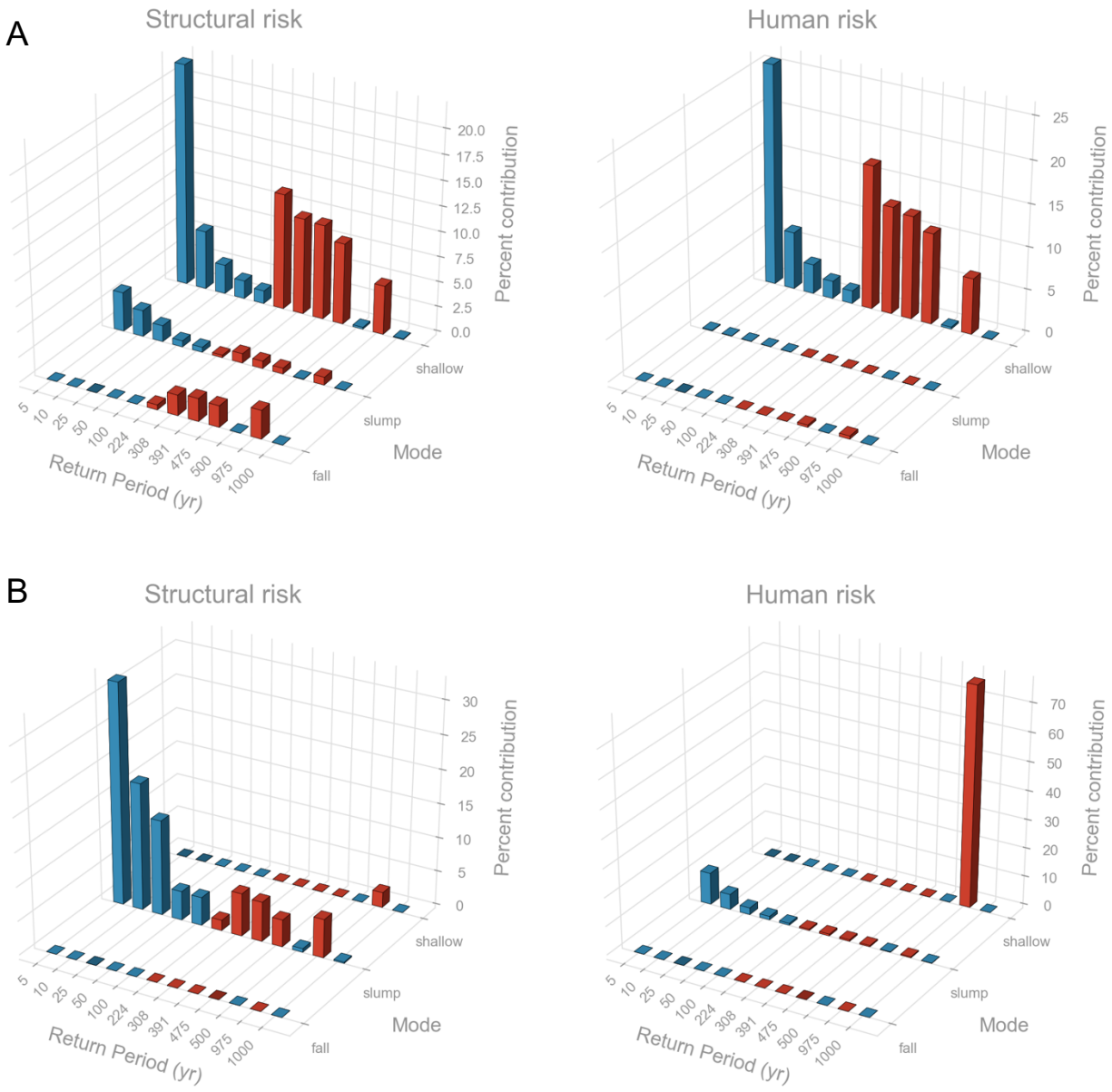

Figure 6.28. Annual risk disaggregation for buildings **A** and **B** in **Figure 6.27**. Return-period triggering events associated with precipitation (blue) and seismicity (red) are shown on the lower left axis while the landslide modes are shown on the lower right. Percent contributions are with respect to the total annual risk for each building.

6.5 Discussion

6.5.1 Implications for land use regulation

The City of Seattle has some of the most progressive landslide-related policies of any locality in the United States (Laprade and Tubbs, 2008). In 2006, Seattle codified the susceptibility maps produced by Laprade et al. (2000) and the USGS landslide susceptibility and hazard studies (Schultz, 2005; Harp et al., 2006) into the decision-making process (Miscolta-Cameron, 2016). However, development restrictions in landslide-prone areas within the city are based on areas of landslide susceptibility, and do not explicitly include considerations of the timing, runout, or consequences of landslides (Seattle OEM, 2019). The inclusion of landslide runout significantly expands the area potentially impacted by landslide hazards. **Table 6.12** compares the susceptibility map of Schultz (2005), the City's current landslide-prone areas (Seattle Geodata, 2018), and the zones of nonzero hazard produced in this work.

Table 6.12. The area, number of buildings, and number of people encompassed by the City of Seattle's designated landslide-prone areas, the susceptibility map of Schultz (2005) and the hazard zones modeled in this work.

Map	*Landslide area (km^2)*	*Exposed buildings*	*Exposed people*
City of Seattle	18.10	11,850	35,329
Schultz (2005)	33.07	23,634	73,191
landslide hazard zones *(this work)*	32.52	22,521	81,196

The susceptibility zones of Schultz (2005) and the hazard zones presented in this work are significantly larger than the potential landslide area defined by the City, covering 15% of Seattle's land area. We find that twice the number of buildings are exposed to landslide hazard than are designated as landslide prone by the City. Of these, over 7800 have an annual risk of

over $100 per year. Significantly, of the buildings that have substantive structural risk, 4200 fall *outside* of the City's landslide-prone areas. The most significant spatial differences between the City's landslide-prone areas and the modeled hazard zone come from shallow landslide runout in Interbay and along the Duwamish waterway, locally over-steepened terrain along the Ship Canal, and on the bluffs overlooking Lake Washington near Seward Park (**Figure 6.29**). These are locations in which different modes of failure, infrequent, intense triggering events, and post failure behavior is not represented in the landslide inventory which provides the basis for the City zoning. In practice, areas experiencing landslide risk outside the Seattle's landslide slope regulations represent an implicitly adopted threshold of acceptable risk.

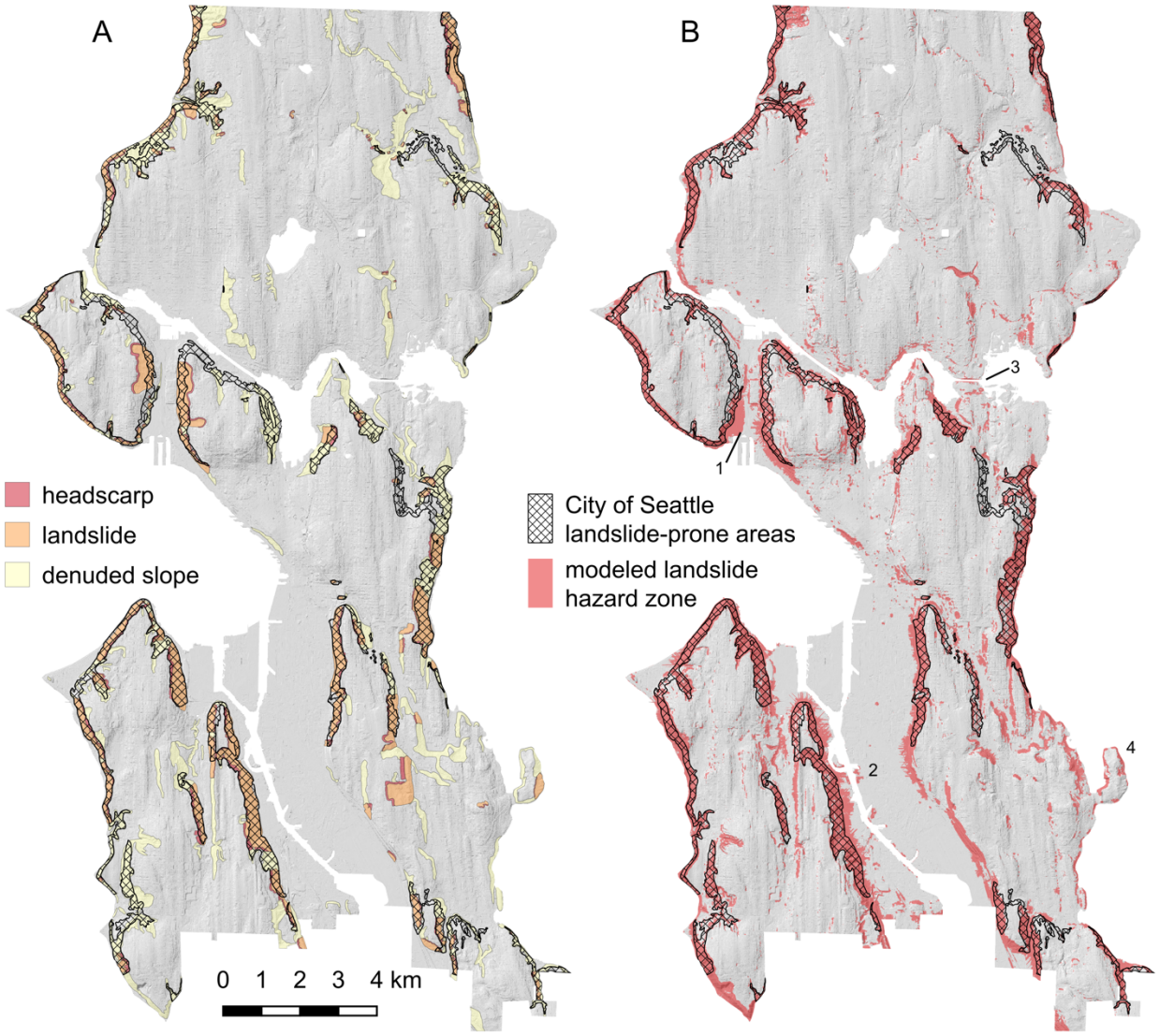

Figure 6.29. (*A*) Landslide susceptibility mapping of Schultz (2005) and (*B*) the area exposed to landslide hazard modeled in this work. Landslide prone-areas defined by the City of Seattle and used for regulating environmentally-critical areas development are overlain. Locations in the text are *1*) Interbay, *2*) the Duwamish waterway, *3*), the Ship Canal, and *4*) Seward Park.

Mapping risk provides additional information missed in susceptibility analyses. In **Tables 6.13** and **6.14** total annual risk is aggregated and ranked by neighborhood. While in landslide susceptibility maps, all landslide areas are treated equally, by mapping risk it is evident that some regions of Seattle are disproportionately affected by landslides. The Central Seattle

neighborhoods of Westlake, and East, North, and Lower Queen Anne hold 16% and 25% of the human and structural risk in Seattle, yet only 6.3% of the designated landslide-prone land (see **Figure 6.30** for locations). Meanwhile the Delridge neighborhoods of Riverview and Highland Park have 7.5% of the designated landslide-prone areas, but only 0.2% of annual risk for both humans and buildings.

Table 6.13: Ten highest-risk neighborhoods considering human loss of life. Neighborhood locations are given in **Figure 6.30**.

precipitation			*coseismic*			*total*		
Rank	*Neighborhood*	*Percent*	*Rank*	*Neighborhood*	*Percent*	*Rank*	*Neighborhood*	*Percent*
1	Westlake	6.96	1	South Lake Union	14.79	1	Westlake	5.97
2	Fremont	4.94	2	Alki	13.39	2	Alki	5.94
3	East Queen Anne	4.69	3	Westlake	8.87	3	Rainier Beach	4.75
4	North Beacon Hill	4.54	4	Lower Queen Anne	5.60	4	Fauntleroy	4.39
5	Rainier Beach	4.47	5	North Admiral	4.89	5	East Queen Anne	4.09
6	Fauntleroy	4.27	6	North Queen Anne	4.26	6	Seaview	4.03
7	Sunset Hill	4.19	7	Leschi	3.92	7	Fremont	3.90
8	Alki	3.72	8	Seaview	3.41	8	North Queen Anne	3.83
9	University District	3.41	9	Laurelhurst	3.13	9	North Beacon Hill	3.61
10	Lawton Park	3.28	10	East Queen Anne	2.98	10	Sunset Hill	3.36

Table 6.14. Ten highest-risk neighborhoods considering structural damage. Neighborhood locations are given in **Figure 6.30**.

precipitation			*coseismic*			*total*		
Rank	*Neighborhood*	*Percent*	*Rank*	*Neighborhood*	*Percent*	*Rank*	*Neighborhood*	*Percent*
1	Westlake	18.39	1	Alki	13.30	1	Westlake	16.89
2	Fremont	12.99	2	Seaview	8.20	2	Fremont	11.25
3	Laurelhurst	12.68	3	North Queen Anne	7.15	3	Laurelhurst	11.18
4	Belltown	8.18	4	Rainier Beach	5.66	4	Belltown	7.14
5	Wallingford	4.90	5	North Admiral	5.12	5	South Lake Union	5.65
6	Lower Queen Anne	4.17	6	Fauntleroy	4.82	6	Lower Queen Anne	4.39
7	South Lake Union	3.94	7	Leschi	4.66	7	Wallingford	4.21
8	Alki	2.32	8	Seward Park	3.20	8	Alki	4.06
9	East Queen Anne	1.91	9	Mount Baker	2.98	9	East Queen Anne	2.08
10	Central Business District	1.91	10	Gatewood	2.82	10	North Admiral	1.75

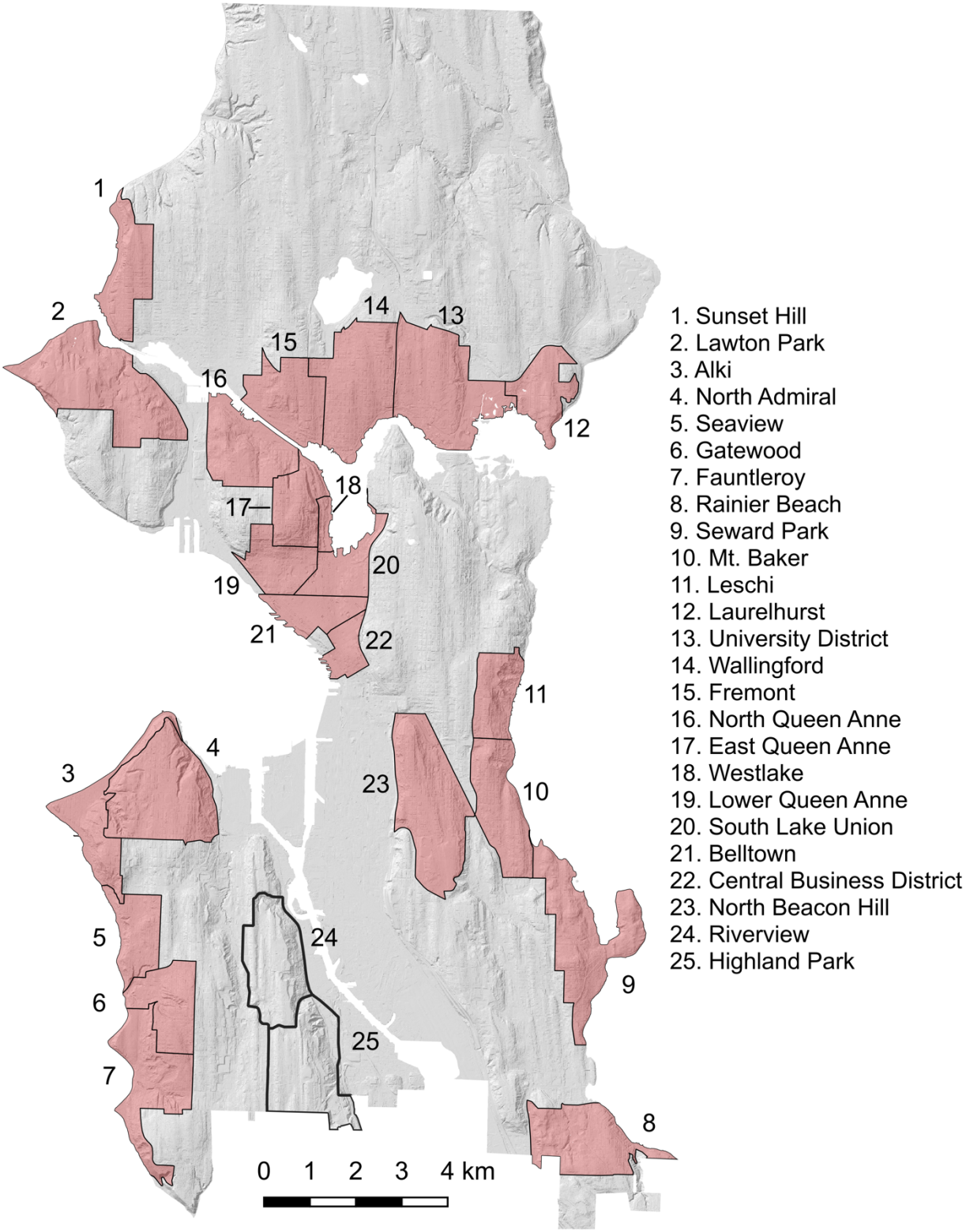

Figure 6.30. Highest-risk neighborhood locations from **Tables 6.13** and **6.14**.

6.5.2 Comparison with historical landslide damage

Historical records suggest that landslide damages in Seattle have been much lower than the values presented here. One reason for this is that Seattle has not experienced most of the triggering scenarios included in this work in the recent (recorded) past. Out of the nine most severe landslide winter seasons in Seattle in the last century, only one (1995/96) exceeded the three-day rainfall intensity associated with a 10-year return period. In the same time span, Seattle has experienced five notable earthquakes (1939, 1946, 1949, 1965, 2001), but with the exception of the 2001 Nisqually earthquake, these caused relatively minor landslide damage (Chleborad and Schuster, 1990; Highland, 2003). Peak ground accelerations in the Nisqually earthquake were around 0.1g throughout the city, smaller than any scenario considered in this work.

Nevertheless, comparison with historical landslide damage provides a useful first-order evaluation of the accuracy of predicted risk. Estimates of historical monetary landslide damage in Seattle are piecemeal and exist only for individual events. Note that all values are in 2020 dollars. The 28 February 2001 M6.8 Nisqually earthquake triggered ten deep-seated landslides in the City of Seattle. Landslide-related settlement affected at least 10 homes as well multiple roads and utilities, contributing to over $49 M in damages (Highland, 2003, City of Seattle, 2018). Landslides in the winter of 1972 caused $2.8 M of damage, associated with a 5-year return period three-day rainfall intensity (Tubbs, 1974). Extreme precipitation during the winter of 1996/97 triggered over 300 landslide in Seattle, causing $100 M in damages, $55 M of which was to City of Seattle facilities (Gerstel et al., 1997; Baum et al., 1998; Seattle OEM, 2019;

Shipman, 2001; Pageler, 1998). The maximum three-day rainfall intensity was associated with a 5-year return period event but occurred following a heavy snowfall which contributed to soil saturation and extensive flooding (NOAA, 2020). These estimates are minimum values, as catalogued damage is primarily to public infrastructure. Damage to private property is poorly reported.

As for human losses, no systematic record of landslide fatalities in Seattle exists. A non-exhaustive review of local and regional newspaper archives produced an inventory of 16 landslide fatalities within the present-day Seattle city limits (**Table 6.15**). This is a conservative estimate, as digitized newspaper records were only available from 1895-onward, and these are incomplete. Even within the time period for which records were available, I expect landslide fatalities to be under-reported, especially early in the reporting period, as has been found in other fatalities inventories (Guzzetti, 2000). Two of the fatalities occurred in explicitly man-made landslides triggered by hydraulic sluicing during the 1908 – 1911 Denny Regrade No. 1 (Williams, 2015). The last widely publicized landslide fatality in Seattle occurred in 1942 (Maier, 1997).

Table 6.15. Landslide fatalities in Seattle. [*]Not reported in local sources. [+]Triggered during the 1908 – 1911 Denny regrade.

Date	*Fatalities*	*Neighborhood*	*Source*
Feb. 1898	1	West Seattle	*Seattle Post Intelligencer* (1899a, b)
Oct. 1900	1[*]	*unknown*	*The Saint Paul Globe* (1900)
Nov. 1908	1[+]	Belltown	*Seattle Daily Times*[1] (1908)
Dec. 1909	1[+]	Belltown	*Seattle Daily Times* (1909)
Jan. 1913	1	West Seattle	*Daily Star-Mirror*[2] (1913)
Jan. 1914	1	West Seattle	*Seattle Post Intelligencer* (1914)
Feb. 1916	2	Magnolia	*Seattle Daily Times* (1916a, b)
Dec. 1921	3	West Seattle	*Seattle Star* (1921)
Dec. 1921	2	West Seattle	*Seattle Star* (1921)
Apr. 1922	2	Endolyne	*Seattle Post Intelligencer* (1922)
Dec. 1942	1	Capitol Hill	*Seattle Daily Times* (1942)
Total	*16*		[1] Now the *Seattle Times.* [2]Now the *Moscow-Pullman Daily News*.

At the annual fatalities rates of 1900 – 1940, Seattle would average between 0.5 – 0.8 landslide fatality per year at its 2017 population (**Table 6.16**). At the current rate, the expected annual fatalities drop to 0.12 due to the long time since anyone was killed by a landslide in Seattle. However, I note that not only is the inventory of landslide fatalities incomplete, the spatial boundary (city limits) is somewhat arbitrary. More recent landslide fatalities have occurred in Kirkland (1947; Seattle Daily Times, 1947) and Bainbridge Island (1997; Washington DNR, 2014).

Table 6.16. Estimate of the historical landslide fatality rate in Seattle. Landslides triggered by the Denny regrade projects are omitted. 1900 – 1940 population data from MacDonald (1970).

Year	*Population*	*Cumulative landslide fatalities since 1898*	*Reporting period (yrs.)*	*Population normalized annual fatality rate*	*Anticipated annual landslide fatalities in 2017*
1900	80,671	2	2	1.24×10^{-5}	9.04
1910	237,194	2	12	7.03×10^{-7}	0.51
1920	315,312	6	22	1.42×10^{-7}	0.63
1930	365,583	13	32	1.11×10^{-6}	0.81
1940	368,302	13	42	8.40×10^{-7}	0.61
2017	729,601	14	119	1.61×10^{-7}	0.12

The incompleteness of historical landslide loss data notwithstanding, the annual landslide risk estimates developed in this work overestimate recorded landslide losses by up to an order of magnitude. The following sections discuss the primary reasons for this overprediction of risk.

6.5.2.1 Direct landslide mitigation

Numerous damaging landslides in the winter of 1933 – 1934 caused angry homeowners to file $11.6 M (2020 USD) in lawsuits the City of Seattle for negligence. In 1935 the City began Works Progress Administration Slide Control Project No. 831, the first coordinated effort to deal with landslide problems in Seattle (Evans, 1994; Laprade and Tubbs, 2008). Since then, the City has undertaken numerous landslide mitigation projects to drain hillsides and install retaining and

catchment structures (Laprade et al., 2000). The success of these projects is evinced by Seattle's sharp decline in landslide fatalities in the 1930s even as development has expanded to marginal land and the City's population has increased. The multimodal model does not account for direct landslide mitigation, except incidentally insofar as it alters the underlying elevation data (e.g. regrading). As such, the results presented in this study represent the potential landslide risk in Seattle in the absence of human mitigation efforts.

6.5.2.2 Anthropogenic terrain modification

In few cities in the United States have humans more dramatically reshaped the natural environment than in Seattle, from flattening hills in the massive regrading projects of 1900 – 1930 to replumbing the City's lakes (Williams, 2015). Countless smaller human interventions also have a profound impact on the region's landslide hazards, both positive and negative. Impervious surfaces cover the city, removing surface water from some locations and concentrating it in others. taller and heavier urban architecture increases the load on marginally stable hillsides, while retaining walls and deep foundations buttress them. The overall effect of these anthropogenic modifications leads to an overestimate of risk (Coe et al., 2000), although local exceptions may occur. This is an unavoidable challenge of performing landslide risk analyses in the urban environment, and modeling these anthropogenic influences is a key area of future research.

6.5.2.3 Model simplification

The physically-based models of the multimodal method trend toward conservatism. One- and two-dimensional factor of safety equations neglect stabilizing side forces. This is especially true

for shallow, infinite-slope failure models, which have been demonstrated to be conservative in almost all cases (Griffiths et al., 2011). Applying idealized hillslope models to individual pixels will tend to overestimate the volume of material involved in individual failures, and thus the process intensity.

6.5.2.4 Human evasion

The ability of humans to notice and evade approaching landslides has a significant impact on vulnerability, as explored in **Chapter 4**. In my review of human fatality records, I noted numerous newspaper articles that told of Seattle residents surviving landslides due to quick evacuation after noting warning signs of an impending landslide or precautionary evacuation when landslides were likely (e.g. Maier, 1997). In the fatal landslides listed in **Table 6.16**, an average of 2 – 3 individuals escaped for every one who was killed. No analytical methods currently exist to model the ability of humans to evade landslide hazards.

6.5.2.5 Vulnerability curves that do not reflect "hardened" urban infrastructure

Building typology has a strong influence on vulnerability. Seattle's rapid urban development in recent years has led to large concrete condominiums and apartments replacing its timber-frame, single-family homes, especially in landslide-prone areas like Alki Avenue. Many of these buildings have reinforced rear walls for the purpose of preventing landslide damage (**Figure 6.31**; Shipman, 2001). Vulnerability curves for shallow landslides, such as those presented in **Chapter 2**, reflect primarily small, single-family residences which have lower resistance to landslides than multistory, dense urban architecture (Ciurean et al., 2017). Furthermore, very little landslide vulnerability data exists for reinforced concrete structures, and as a result, they are

often grouped with masonry buildings (Totschnig and Fuchs, 2013; Quan Luna et al., 2011; Totschnig et al., 2011) despite their greater resistance to landslide impact pressure (Kang and Kim, 2016).

Figure 6.31. An apartment building along Alki Avenue with a reinforced rear wall. A landslide overran the low concrete block wall in the center of the image and struck the building, leaving mud splash marks up to 8 ft high (above the kayaks). The undisturbed portion of the deposit is on the right side of the image.

6.5.2.6 Errors in the digital elevation model

Insufficient ground returns in LiDAR elevation data result in noisy, or "TIN-y" (triangular irregular network), surfaces which disrupt geomorphic analyses (Slaughter et al., 2017). This is especially prevalent around the margins of large buildings. **Figure 6.32** shows a large complex that has artificially high landslide risk because of "landslides" triggered on the low-resolution terrain at the margin of the structure.

Figure 6.32. *Left*: Building complex on low-relief and heavily modified terrain where landslides are unlikely (*red outline*). *Center*: irregularities in the DEM create oversteepened slopes on the building's margins. *Right*: these artificially oversteepened slopes create high-probability "landslides," such as the two at the lower edge of the building, which falsely elevate the landslide risk.

6.5.3 Additional sources of uncertainty

Although uncertainty in material parameters is explicitly modeled in the multimodal framework, other sources of uncertainty are more difficult to constrain. Modeled slope stability is strongly influenced by the height of the groundwater table (e.g. **Appendix 2.2**; Baum et al., 2008). Apart from wet- and dry-season conditions, I do not attempt to model very large (year, decade) or small (month, week) fluctuations in the initial groundwater table which depend on the observed antecedent rainfall. Also uncaptured in the multimodal method is the cascading effect of landslide hazards (Samia et al., 2017). Deep, rotational slumps frequently leave oversteepened headscarps which subsequently fail in shallow landslides. In Seattle, shallow debris flows and avalanches in permeable advanced outwash deposits undermine the more competent overlying glacial till leading to debris falls (Shipman, 2001).

I have also relied on broad assumptions regarding the human population in Seattle. The exposure values I use in this work rely on estimating the average amount of time individuals spend in and out of the home. This naturally varies person-to-person depending on age, employment status, and social role. Calculating exposure is further complicated by the fact that some residential areas are relatively safe from landslides, while some business and industrial areas are not. Individuals experiencing homelessness form a subpopulation that is challenging to include in population counts, and thus is incompletely represented in this work. In Seattle, over 3,500 individuals experiencing homelessness were unsheltered (e.g. not in an emergency shelter or transitional housing) during a point-in-time count in 2019 (All Home, 2019). Unsheltered individuals often live in temporary encampments found throughout Seattle's parks and green spaces, areas that also encompass some of the highest landslide hazard (**Figure 6.33**.)

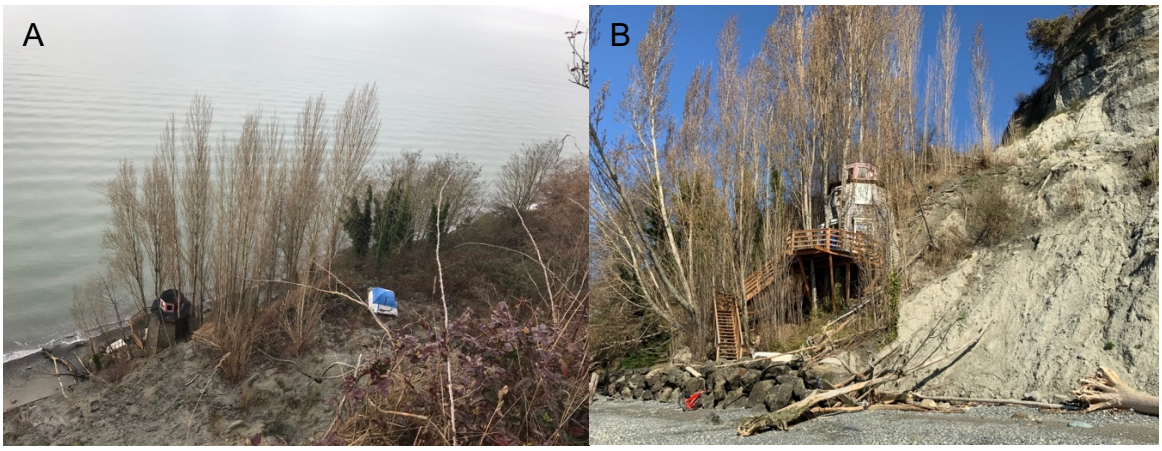

Figure 6.33. An actively occupied encampment (*A*) that is sitting on the deposit of a large debris fall that occurred in 2013 (*B*). Note the structure in both images for reference. Photos: J. Wartman and W. Pollock.

While the maps presented in this work are be useful for evaluating the *relative* risk of individual city blocks or buildings, I caution that the absolute risk values presented here have significant uncertainty (including spatial uncertainty) related to the factors discussed in above. These

include the necessary reduction of real-world conditions to (relatively) simple models and uncertainty in the initial conditions and data. As such, these maps are not intended to replace site-specific studies or the professional judgement of a geologist or geotechnical engineer.

6.6 Conclusions

The probabilistic hazard and risk maps developed in this work demonstrate that high-resolution, regional scale analyses are both realistic and achievable. Furthermore, these risk maps provide significantly more actionable information than the traditional landslide susceptibility maps which guide land use planning in Seattle. Significantly more buildings are at risk from landslides than are currently designated as in landslide-prone areas. Much of this difference is due to incorporating landslide runout into zoning considerations. While human and structural risk in Seattle is substantial, it is disproportionally held in a small number of localized zones, primarily around Queen Anne, South Lake Union, and the coastal bluffs of West Seattle. While risk in some of these areas is driven by elevated hazard, in others it is a function of high-property values and a dense urban population.

Landslide risk in Seattle comes primarily from frequent, low-intensity winter storms which trigger widespread shallow landslides. While the consequences of increasingly intense precipitation scenarios appear to saturate, the damages from seismic events do not. Strong ground shaking of ~0.4 – 0.5g in Seattle's dense urban environment would cause extensive landsliding. In such a case, over 10% of Seattle population could be exposed to landslides, with billions of dollars in structural damage.

Substantial challenges remain in performing landslide risk analysis in an urban environment generally and understanding the landslide risk in Seattle in particular. Developing methods to incorporate the extensive anthropogenic modifications common in heavily urbanized settings, including direct landslide mitigation efforts, is a crucial research task. Vulnerability curves specific to dense, "hardened" urban architecture need to be developed. Finally, neglecting the ability of individuals to respond in real-time to perceived threats significantly simplifies—and overstates—human risk to landslides. Within Seattle, an exhaustive review of City of Seattle files and newspaper archives could elucidate the actual human and infrastructural losses to landslides over the last 120 years. By collating these records with observed landslide triggering events, it would be possible to evaluate the effectiveness of the City's direct landslide mitigation projects and calibrate the hazard and risk maps developed in this work. These products facilitate the development of risk reduction strategies in Seattle to reduce preventable landslide losses in future events.

References

Allstadt, K, Vidale, J., Frankel, A. (2013). A scenario study of seismically induced landsliding in Seattle using broadband synthetic seismograms. *Bull. Seismological Soc. Am.*, 103, 2971-2992. https://doi.org/10.1785/0120130051

All Home. (2019). Seattle/King County point-in-time count of persons experiencing homelessness. *Count Us In Comprehensive Report Produced by ASR*. Seattle: All Home. Available at: http://allhomekc.org/king-county-point-in-time-pit-count/

Atwater, B., Satoko, M-R., Kenji, S., Yoshinobu, T., Kazue, U., Yamaguchi, D. (2005). *The Orphan Tsunami of 1700; Japanese Clues to a Parent Earthquake in North America*. Reston, VA: United States Geological Survey

Baum, R., Savage, W., Godt, J. (2008). TRIGRS—A Fortran program for transient rainfall infiltration and grid-based regional slope-stability analysis, version 2.0. *Open-File Report 2008-1159*. Reston, VA: United States Geological Survey

Baum, R., Chleborad, A., Schuster, R. (1998). Landslides triggered by the winter 1996-97 storms in the Puget lowland, Washington. *USGS Open-File Report 98-239*. Reston, VA: U.S. Geological Survey.

Baum, R., Coe, J., Godt, J., Harp, E., Reid, M., Savage, W., Schulz, W., Brien, D., Chleborad, A., McKenna, J., Michael, J. (2005). Regional landslide-hazard assessment for Seattle, Washington, USA. *Landslides*, 2, 266-279. https://doi.org/10.1007/s10346-005-0023-y

Baum, R., Godt, J., Coe, J. (2011). Assessing susceptibility and timing of shallow landslide and debris flow initiation in the Oregon Coast Range, USA. In: R. Genevois, D. Hamilton, A Prestininzi (*Eds*.) *Proceedings of the Fifth Int. Conf. on Debris Flow Hazards Mitigation—Mechanics, Prediction, and Assessment*. Padua, Italy: 7-11 June 2011.

Baum, R., Godt, J., Savage, W. (2010). Estimating the timing and location of shallow rainfall-induced landslides using a model for transient, unsaturated infiltration. *J. Geophys. Res*., 115. https://doi.org/10.1029/2009JF001321

Baum, R., Harp, E., Hultman, W. (2000). Map showing recent and historic landslide activity on coastal bluffs of Puget Sound between Shilshole Bay and Everett, Washington. *Miscellaneous Field Studies Map MF-2346*. U.S. Geological Survey.

Biasutti, M., Seager, R., Kirschbaum, D. (2016). Landslides in West Coast metropolitan areas: The role of extreme weather events. *Weather and Climate Extremes*, 14, 67-79. https://doi.org/10.1016/j.wace.2016.11.004

Brien, D., Reid, M. (2007). Modeling 3-D slope stability of coastal bluffs, using 3-D ground-water flow, southwestern Seattle, Washington. *Scientific Investigations Report 2007-5092*. Reston, VA: U.S. Geological Survey.

Brien, D., Reid, M. (2008). Assessing deep-seated landslide susceptibility using 3-D groundwater and slope-stability analyses, southwestern Seattle, Washington. In: R. Baum, J. Godt., L Highland, (*Eds*.) *Landslides and Engineering Geology of the Seattle, Washington Area*. Boulder: The Geological Society of America

Chleborad, A, Baum, R., Godt, J., Power, P. (2008). A prototype system for forecasting landslides in the Seattle, Washington, area. In: R. Baum, J. Godt., L. Highland, (*Eds*.) *Landslides and Engineering Geology of the Seattle, Washington Area*. Boulder: The Geological Society of America

Chleborad, A. (2000). Preliminary method for anticipating the occurrence of precipitation-induced landslides in Seattle, Washington. *USGS Open-File Report 00-469*. Reston, VA: U.S. Geological Survey

Chleborad, A. (2003). Preliminary evaluation of a precipitation threshold for anticipating the occurrence of landslides in the Seattle, Washington, area. *USGS Open-File Report 03-463*. Reston, VA: U.S. Geological Survey

Chleborad, A., Baum, R., Godt., J. (2006). Rainfall thresholds for forecasting landslides in the Seattle, Washington, area—Exceedance and probability. *USGS Open-File Report 2006-1064*. Reston, VA: U.S. Geological Survey

Chleborad, A., Schuster, R. (1990). Ground failure associated with the Puget Sound region earthquakes of April 13, 1949, and April 29, 1965. *USGS Open-File Report 90-687*. Reston, VA: U.S. Geological Survey

Cislaghi, A., Chiaradia, E., Bischetti, G. (2017). Including root reinforcement variability in a probabilistic 3D stability model. *Earth Surf. Process. Landforms*, 42, 1789-1806. https://doi.org/10.1002/esp.4127

City of Seattle. (2018). Historic landslide locations ECA. Available at http://data-seattlecitygis.opendata.arcgis.com/datasets/historic-landslide-locations-eca. Accessed May 2020.

Ciurean, R., Hussin, H., van Westen, C., Jaboyedoff, M., Nicolet, P., Chen, L., Frigerio, S., and Glade, T. (2017). Multi-scale debris flow vulnerability assessment and direct loss estimation of buildings in the Eastern Italian Alps. *Nat. Hazards*, 85, 929-957. https://doi.org/10.1007/s11069-016-2612-6

Coe, J., Michael, J., Crovelli, R., Savage, W. (2000). Preliminary map showing landslide densities, mean recurrence intervals, and exceedance probabilities as determined from historic records, Seattle, Washington. *USGS Open-File Report 00-303 online edition*. U.S. Geological Survey.

Coe, J., Michael, J., Crovelli, R., Savage, W. (2004). Probabilistic assessment of precipitation-triggered landslides using historical records of landslide occurrence, Seattle, Washington. *Environ. Eng. Geoscience.*, 10, 103-122. https://doi.org/10.2113/10.2.103

Crozier, M., Glade, T. (2005). Landslide hazard and risk: Issues, concepts and approach. In: T. Glade, M. Anderson, M. Crozier (*Eds*.) *Landslide Hazard and Risk*. West Sussex: John Wiley & Sons

Daily Star Mirror. (1913). "Landslide at Seattle kills one, hurts 3." The Daily Star-Mirror, 03 January 1913.

Debray, S., Savage, W. (2001). A preliminary finite-element analysis of a shallow landslide in the Alki area of Seattle, Washington. *USGS Open-File Report 01-0357*. Reston, VA: U.S. Geological Survey.

DeRose, R., Trustrum, N., Blaschke, P. (1991). Geomorphic change implied by regolith-slope relationships on steepland hillslopes, Taranaki, New Zealand. *Catena*, 18, 489-514. https://doi.org/10.1016/0341-8162(91)90051-X

Evans, S. (1994). Draining Seattle—WPA landslide stabilization projects, 1935-1941. *Washington Geology*, 22, 3-10.

Frankel, A., Leyendecker, E. (2001). Seismic hazard curves and uniform hazard response spectra for the United States. *A User Guide to Accompany Open-File Report 01-436*. Reston, VA: U.S. Geological Survey.

Frattini, P., Crosta, G. (2013). The role of material properties and landscape morphology on landslide size distributions. *Earth and Planetary Science Letters*, 361, 310-319. https://doi.org/10.1016/j.epsl.2012.10.029

Gallen, S., Clark, M., Godt, J. (2015). Coseismic landslides reveal near-surface rock strength in a high-relief, tectonically active setting. *Geology*, 43, 11-14. https://doi.org/10.1130/G36080.1

Gerstel, W., Brunengo, M., Lingley, W., Logan, R., Shipman, H., Walsh, T. (1997). Puget Sound bluffs: The where, why, and when of landslides following the Holiday 1996/97 storms. *Washington Geology*, 25, 17-31.

Godt, J. (2004). Observed and modeled rainfall conditions for shallow landsliding in the Seattle, Washington, area. (*doctoral dissertation*). University of Colorado.

Godt, J., Baum, R., Chleborad, A. (2006). Rainfall characteristics for shallow landsliding in Seattle, Washington, USA. *Earth Surf. Process. Landforms*, 31, 97-110. https://doi.org/10.1002/esp.1237

Godt, J., Baum, R., Savage, W., Salciarini, D., Schulz, W., Harp, W. (2008b). Transient deterministic shallow landslide modeling: Requirements for susceptibility and hazard assessments in a GIS framework. *Eng. Geol*., 102, 214-226. https://doi.org/10.1016/j.enggeo.2008.03.019

Godt, J., McKenna, J. (2008). Numerical modeling of rainfall thresholds for shallow landsliding in the Seattle, Washington, area. In: R. Baum, J. Godt., L Highland, (*Eds*.) *Landslides and Engineering Geology of the Seattle, Washington Area*. Boulder: The Geological Society of America

Godt, J., Schultz, W., Baum, R., Savage, W. (2008a). Modelling rainfall conditions for shallow landsliding in Seattle, Washington. In: R. Baum, J. Godt., L Highland, (*Eds*.) *Landslides and Engineering Geology of the Seattle, Washington Area*. Boulder: The Geological Society of America

Grant, A. (2017). Regional-scale coseismic landslide hazard modeling and consequence analysis. (*doctoral dissertation*). Seattle: University of Washington

Griffiths, D., Huang, J., deWolfe, G. (2011). Numerical and analytical observations on long and infinite slopes. *Int. J. Numerical and Analytical Methods in Geomechanics*, 35, 569-585. https://doi.org/10.1002/nag.909

Guzzetti, F. (2000). Landslide fatalities and the evaluation of landslide risk in Italy. *Eng. Geol.*, 58, 89-107. https://doi.org/10.1016/S0013-7952(00)00047-8

Harp, E., Chleborad, A., Schuster, R., Cannon, S., Reid, M., Wilson, R. (1997). Landslides and landslide hazards in Washington State due to February 5-9, 1006 storm. *U.S. Geological Survey Administrative Report*. Reston, VA: U.S. Geological Survey.

Harp, E., Michael, J., Laprade, W. (2006). Shallow-landslide hazard map of Seattle, Washington. *USGS Open-File Report 2006-1139*. Reston, VA: U.S. Geological Survey.

Harp, E., Michael, J., Laprade, W. (2008). Shallow landslide hazard map of Seattle, Washington. In: R. Baum, J. Godt., L Highland, (*Eds*.) *Landslides and Engineering Geology of the Seattle, Washington Area*. Boulder: The Geological Society of America

Haugerud, R., Troost, K., Laprade, W. (2017). Geology of Seattle: A field trip. In: R. Haugerud, H. Kelsey (*Eds*.) *From the Puget Lowland to East of the Cascade Range: Geologic Excursions in the Pacific Northwest*. Boulder: Geological Society of America

Highland, L. (2003). An account of preliminary landslide damage and losses resulting from the February 28, 2001, Nisqually, Washington, earthquake. *Open-File Report 03-211*. Reston, VA: U.S. Geological Survey.

Hungr, O., Leroueil, S., Picarelli, L. (2014). The Varnes classification of landslide types, an update. *Landslides*, 11, 167-194. https://doi.org/10.1007/s10346-013-0436-y

Jeschke, D., Eungard, D., Troost, K., Wisher, A. (2016). Subsurface database of Washington State—GIS data. *Washington Division of Geology and Earth Resources Digital Data Series 11, version 1.2*. Available at: http://www.dnr.wa.gov/publications/ger_portal_subsurface_database.zip

Jones, A., Kramer, S., Arduino, P. (2002). *Estimation of Uncertainty in Geotechnical Properties for Performance-based Earthquake Engineering*. PEER Report 2002/16. Berkeley, CA: Pacific Earthquake Engineering Research Center, University of California, Berkeley

Kang, H-s., Kim, Y-t. (2016). The physical vulnerability of different types of building structure to debris flow events. *Nat. Hazards*, 80, 1475-1493. https://doi.org/10.1007/s11069-015-2032-z

King County Department of Assessment. (2020). Assessments data download. Available at https://info.kingcounty.gov/assessor/DataDownload/default.aspx, accessed May 2020.

Laprade, W., Kirkland, T., Nashem, W., Robertson, C. (2000). Seattle landslide study. *Internal Report W-7992-01*. Shannon & Wilson Inc.

Laprade, W., Tubbs, D. (2008). Landslide mapping in Seattle, Washington. In: R. Baum, J. Godt., L Highland (*Eds*.) *Landslides and Engineering Geology of the Seattle, Washington Area*. Boulder: The Geological Society of America

Larsen, I., Montgomery, D., Korup, O. (2010). Landslide erosion controlled by hillslope material. *Nature Geosci*., 3, 247-251. https://doi.org/10.1038/ngeo776

Liu, C-N., Wu, C-C. (2008). Mapping susceptibility of rainfall-triggered shallow landslides using a probabilistic approach. *Environ. Geol*., 55, 907-915. https://doi.org/10.1007/s00254-007-1042-x

MacDonald, N. (1970). Population growth and change in Seattle and Vancouver, 1880-1960. *Pacific Historical Review*, 39, 297-321.

Maier, S. (1997). "In Seattle, lessons have been learned and lessons have been spurned." *The Seattle Post-Intelligencer*, 06 February 1997.

Malamud, B., Turcotte, D., Guzzetti, F., Reichenbach, P. (2004). Landslide inventories and their statistical properties. *Earth Surf. Process. Landforms*, 29, 687-711. https://doi.org/10.1002/esp.1064

Mauger, G., Casola, J., Morgan, H., Strauch, R., Jones, B., Curry, B., Busch Isaksen, T., Whitely Binder, L., Krosby, M., Snover, A. (2015). State of knowledge: Climate change in Puget Sound. *Report prepared for the Puget Sound Partnership and the National Oceanic and Atmospheric Administration*. Seattle: Climate Impacts Group, University of Washington. Available at: https://cig.uw.edu/resources/special-reports/ps-sok/

Miller, R. (1973). Map showing relative slope stability in part of west-central King County, Washington. *Folio of King County, Washington Map I-852 A*. U.S. Dept. of the Interior, United States Geological Survey.

Miscolta-Cameron, A. (2016). Science and strategy: How scientific and technical information are used in disputes over landslide regulations in Seattle, WA. (*masters thesis*). Bellingham, WA: Western Washington University

Montgomery, D., Greenberge, H., Laprade, W., Nashem, W. (2001). Sliding in Seattle: Test of a model of shallow landsliding potential in an urban environment. In: M. Wigmosta, S. Burges (*Eds*.) *Land Use and Watersheds: Human Influence on Hydrology and Geomorphology in Urban and Forest Areas*. https://doi.org/10.1029/WS002p0059

Morgan, D., Jones, J. (1996). Numerical model analysis of the effects of ground-water withdrawals on discharge to streams and springs in small basins typical of the Puget Sound Lowland, Washington. *USGS Open-File Report 95-470*. Reston, VA: U.S. Geological Survey.

Morgan, D., McFarland, W. (1996). Simulation analysis of the ground-water flow system in the Portland Basin, Oregon and Washington. *USGS Water-Supply Paper 2470-B*. Reston, VA: U.S. Geological Survey.

Neiman, P., Schick, L., Ralph, F., Hughes, M., Wick, G. (2011). Flooding in western Washington: The connection to atmospheric rivers. *J. Hydrometeor*., 12, 1337-1358. https://doi.org/10.1175/2011JHM1358.1

Nguyen, L. (2013). Evaluation of the relationship between saturated hydraulic conductivity and grain-size distribution of fluvio-glacial deposits, Puget lowland, Washington. (*masters thesis*). Seattle: University of Washington.

NOAA. (2020). "Climate data online." Available at: https://www.ncdc.noaa.gov/cdo-web/. Accessed: May 2020.

Pageler, M. (1998). Landslide policies for Seattle: Preliminary recommendations to the landslide ad hoc committee. *A Report to the Seattle City Council*. Seattle: Landslide Policy Group: City Budget Office, Seattle Public Utilities, and Department of Construction & Land Use.

Peterson, M., Shumway, A., Powers, P., Mueller, C., Moschetti, M., Frankel, A., Rezaeian, S., McNamara, D., Hoover, S., Luco, N., Boyd, O., Rukstales, K., Jaiswal, K., Thompson, E., Clayton, B., Field, E., Zeng, Y. (2019). The 2018 update of the US National Seismic Hazard Model: Overview of model and implications. *Earthquake Spectra*, 36, 5-41. https://doi.org/10.1177/8755293019878199

Phoon, K-K., Kulhawy, F. (1999). Characterization of geotechnical variability. *Can. Geotech. J.*, 36, 612-624. https://doi.org/10.1139/t99-038

Planet Team (2020). Planet Application Program Interface: In Space for Life on Earth. San Francisco, CA. https://www.planet.com/

Quan Luna, B., Blahut, J., van Westen, C., Sterlacchini, S., van Asch, T., Akbas, O. (2011). The application of numerical debris flow modelling for the generation of physical vulnerability curves. *Nat. Hazards Earth Syst. Sci.*, 11, 2047-2060. https://doi.org/10.5194/nhess-11-2047-2011

Rath, J., Roy, S., Butcher, J. (2017). Intensity duration frequency curves and trends for the City of Seattle: Technical memorandum. *Report for the Seattle Public Utilities CSO Reduction Program*. Tetra Tech.

Salciarini, D., Godt, J., Savage, W., Baum, R., Conversini, P. (2008). Modelling landslide recurrence in Seattle, Washington, USA. *Eng. Geol*., 102, 227-237. https://doi.org/10.1016/j.enggeo.2008.03.013

Salciarini, D., Godt, J., Savage, W., Conversini, P., Baum, R., Michael, J. (2006). Modeling regional initiation of rainfall-induced shallow landslides in the eastern Umbria Region of central Italy. *Landslides*, 3, 181-194. https://doi.org/10.1007/s10346-006-0037-0

Samia, J., Temme, A., Bregt, A., Wallinga, J., Guzzetti, F., Ardizzone, F., Rossi, M. (2017). Do landslides follow landslides? Insights in path dependency from a multi-temporal landslide inventory. *Landslides*, 14, 547-558. https://doi.org/10.1007/s10346-016-0739-x

Savage, W., Morrissey, M., Baum, R. (2000). Geotechnical properties for landslide-prone Seattle-area glacial deposits. *USGS Open-File Report 00-228*. Reston, VA: U.S. Geological Survey.

Schmidt, K., Roerring, J., Stock, J., Deitrich, W., Montgomery, D., Schaub, T. (2001). The variability of root cohesion as an influence on shallow landslide susceptibility in the Oregon Coast Range. *Can. Geotech. J.*, 38, 995-1024, https://doi.org/10.1139/t01-031

Schulz, W. (2005). Landslide susceptibility estimated from mapping using light detection and ranging (LIDAR) imagery and historical landslide records, Seattle, Washington. *USGS Open-File Report 2005-1405*. Reston, VA: U.S. Geological Survey.

Schulz, W. (2007). Landslide susceptibility revealed by LIDAR imagery and historical records, Seattle, Washington. *Eng. Geol*., 89, 67-87. https://doi.org/10.1016/j.enggeo.2006.09.019

Schulz, W., Lidke, D., Godt, J. (2008). Modeling the spatial distribution of landslide-prone colluvium and shallow groundwater on hillslopes of Seattle, WA. *Earth Surf. Process. Landforms*, 33, 123-141. https://doi.org/10.1002/esp.1535

Seattle Daily Times. (1908). "Denny Hill regrade claims another victim." The Seattle Daily Times, 21 December 1909.

Seattle Daily Times. (1908). "Man killed when land slides." The Seattle Daily Times, 27 November 1908.

Seattle Daily Times. (1916a). "Gurney funeral to be held tomorrow." The Seattle Daily Times, 10 February 1916.

Seattle Daily Times. (1916b). "Six West Seattle homes swept by avalanche." The Seattle Daily Times, 09 February 1916.

Seattle Daily Times. (1942). "Daughter tells of fatal slide." The Seattle Daily Times, 01 December 1942.

Seattle Daily Times. (1947). "Earth slide kills 2 children." The Seattle Daily Times, 03 February 1947.

Seattle Geodata. (2018). Potential Landslide Areas. Available at http://data-seattlecitygis.opendata.arcgis.com/datasets/potential-landslide-areas, Accessed: May 2020.

Seattle Geodata. (2019). Building Outlines 2015. Available at http://data-seattlecitygis.opendata.arcgis.com/datasets/building-outlines-2015, Accessed: May 2020

Seattle Office of Emergency Management (OEM). (2019). Seattle hazard identification and vulnerability analysis v7.0. City of Seattle. Available at: https://www.seattle.gov/emergency-management/hazards

Seattle Post-Intelligencer. (1899a). "Damages for a child's death." Seattle Post-Intelligencer, 18 January 1899.

Seattle Post-Intelligencer. (1899b). "County is absolved." Seattle Post-Intelligencer, 19 January 1899.

Seattle Post-Intelligencer. (1914). "Family swept in their home down a bluff." Seattle Post-Intelligencer, 07 January 1914.

Seattle Post-Intelligencer. (1922). "Two killed in landslide at Endolyne." The Seattle Post-Intelligencer, 14 April 1922.

Seattle Star. (1921). “Sluicing for bodies of 3, two more die.” The Seattle Star, 12 December 1921.
Shipman, H. (2001). Coastal landsliding on Puget Sound: A review of landslides occurring between 1996 and 1999. *Report #01-06-019*. Washington State Department of Ecology. Available at: https://fortress.wa.gov/ecy/publications/SummaryPages/0106019.html
Slaughter, S., Burns, W. Mickelson, K., Jacobacci, K., Biel, A., Contreras, T. (2017). Protocol for landslide inventory mapping from lidar data in Washington State. *Washington Geological Survey Bulletin 82*. Olympia: Washington Department of Natural Resources.
Smith, J., Baum, R., Mirus, B., Michel, A., Stark, B. (2017). Results of hydrologic monitoring on landslide-prone coastal bluffs near Mukilteo, Washington. *USGS Open-File Report 2017-1095*. Reston, VA: U.S. Geological Survey.
St. Paul Globe. (1900). “Red Wing Notes.” The St. Paul Globe, 30 October 1900.
Tanyas, H., Allstadt, K., van Westen, C. (2018). An updated method for estimating landslide-event magnitude. *Earth Surf. Process. Landforms*, 43, 1836-1847. https://doi.org/10.1002/esp.4359
Tanyas, H., van Westen, C., Allstadt, K., Jibson, R. (2019). Factors controlling landslide frequency-area distributions. *Earth Surf. Process. Landforms*, 44, 900-917. https://doi.org/10.1002/esp.4543
The Viet, T., Lee, G., Minh Thu, T., Uk An, H. (2017). Effect of digital elevation model resolution on shallow landslide modeling using TRIGRS. *Nat. Haz. Rev*., 18. https://doi.org/10.1061/(ASCE)NH.1527-6996.0000233
Thomas, B., Wilkinson, J., Embrey, S. (1997). The ground-water system and ground-water quality in Western Snohomish County, Washington. *USGS Water-Resources Investigations Report 96-4312*. Reston, VA: U.S. Geological Survey.
Thorsen, G. (1987). Soil bluffs + rain = slide hazards. *Washington Geologic Newsletter*, 15, 3-11.
Totschnig, R., Fuchs, S. (2013). Mountain torrents: Quantifying vulnerability and assessing uncertainties. *Eng. Geol.*, 155, 31-44. https://doi.org/10.1016/j.enggeo.2012.12.019
Totschnig, R., Sedlacek, W., and Fuchs, S. (2011). A quantitative vulnerability function for fluvial sediment transport. *Nat. Hazards*, 58, 681-703. https://doi.org/10.1007/s11069-010-9623-5
Troost, K., Booth, D. (2008). Geology of Seattle and the Seattle area, Washington. In: R. Baum, J. Godt., L Highland (*Eds*.) *Landslides and Engineering Geology of the Seattle, Washington Area*. Boulder: The Geological Society of America
Tubbs, D. (1974). Landslides in Seattle. *Information Circular No. 52*. Olympia: Washington Department of Natural Resources.
Tubbs, D. (1975). Causes, mechanisms and prediction of landsliding in Seattle. (*doctoral dissertation*). Seattle: University of Washington.
U.S. Census Bureau. (2020). Explore census data. Available at https://data.census.gov/cedsci/, Accessed: May 2020
USGS. (2018). NSHM: Conterminous U.S. 2018. Available at: https://github.com/usgs/nshm-cous-2018, Accessed: May 2020
Vaccaro, J., Woodward, D., Gannett, M., Jones, M., Collins, C., Caldwell, R., Hansen, A. (1997). Summary of the Puget-Willamette Lowland regional aquifer-system analysis, Washington, Oregon, and British Columbia. *USGS Open-File Report 96-353*. Reston, VA: U.S. Geological Survey.

Van Den Eeckhaut, M., Poesen, J., Govers, G., Verstraeten, G., Demoulin, A. (2007). Characteristics of the size distribution of recent and historical landslides in a populated hilly region. *Earth and Planetary Science Letters*, 256, 588-603. https://doi.org/10.1016/j.epsl.2007.01.040

Wait, T. (2001). Characteristics of deep-seated landslides in Seattle, Washington. (*masters thesis*). Golden, CO: Colorado School of Mines.

Wang, Y. (2014). Probabilistic assessments of the seismic stability of slopes: Improvements to site-specific and regional analyses. (*doctoral dissertation*). Austin, Texas: University of Texas at Austin.

Wang, Y., Rathje, E. (2015). Probabilistic seismic landslide hazard maps including epistemic uncertainty. *Eng. Geol*., 196, 313-324. https://doi.org/10.1016/j.enggeo.2015.08.001

Washington Department of Natural Resources (DNR). (2014). Significant deep-seated landslides in Washington State—1984 to 2014. Olympia: Washington Department of Natural Resources. Available at: https://www.dnr.wa.gov/publications/ger_list_large_landslides.pdf?yy063v

Welsch, W., Frans, L., Olsen, T. (2014). Hydrogeologic framework, groundwater movement, and water budget of the Kitsap Peninsula, west-central Washington. *USGS Scientific Investigations Report 2014-5106*. Reston, VA: U.S. Geological Survey.

Williams, D. (2015). *Too High & Too Steep: Reshaping Seattle's Topography*. Seattle: University of Washington Press

Youngmann, C. (*Ed*.) (1979). King County: Coastal zone atlas of Washington. Olympia: Washington Department of Ecology.

Chapter 7 – Conclusions

Regional scale landslide risk analysis is essential for pragmatic land use planning and regulation. This work presents a novel multimodal, multi-trigger framework for quantitative landslide risk analysis as presented in **Chapter 2**. New tools are developed to explore the interaction between landslides and the human-built environment (**Chapter 3** and **4**). The utility of risk products that can be fully disaggregated by trigger and landside mode is demonstrated in applications to a dynamic humanitarian crisis and a developed urban environment (**Chapters 5** and **6**).

In **Chapter 1**, I review the challenges of regional scale landslide risk analysis, including runout modelling and estimating the vulnerability of elements at risk. I identify five areas that need to be addressed in quantitative risk analysis frameworks to enhance the practicability and usefulness of landslide QRA, namely that methods should be 1) regional scale, 2) physically-based, 3) multimodal, 4) probabilistic, and 5) transparent (open-source).

In **Chapter 2**, I address these challenges by presenting a multimodal, multi-trigger framework for quantitative risk analysis. Physically-based models are developed for three common modes of precipitation-induced and coseismic landslides: shallow soil failures, rotational slumps, and rock falls. Post-failure runout characteristics are modeled using a rapid, empirical-statistical procedure, delineating hazard areas and intensity. Novel vulnerability curves are coupled with element-at-risk data to produce high-resolution, regional scale risk products that can be fully disaggregated by landslide mode and trigger.

Chapter 3 uses a database of over 550 flowslides to develop a practical, probabilistic tool for runout zoning. I find that the historical metric of fall height is a poor indicator of landslide

mobility and that flowslide runout behaves consistently across twelve orders of magnitude. I examine the special case of the North Fork of the Stillaguamish River valley in Washington State, concluding that the tragic 2014 Oso flowslide was not abnormally mobile and that significant human exposure to catastrophic flowslides continues in that area.

In **Chapter 4**, I address the lack of human vulnerability data available for quantitative risk analysis by presenting an empirical tool to estimate an individual's probability of death in a landslide, and I explore the human characteristics, behaviors, and settings that contribute to landslide mortality. I find that there exists a critical zone at intermediate inundation depths, in which human behavior, rather than landslide intensity, is the most significant factor in mortality. Individual action is key to reducing landslide risk, including simple strategies such as creating refuge spaces in a home, moving high-occupancy areas like bedrooms to higher floors, and becoming informed about potential local hazards.

The multimodal framework is applied to the country of Lebanon in **Chapter 5**, examining the impacts of the Syrian refugee crisis on landslide risk. Since the start of the crisis in 2011, I find that predicted landslide fatalities in Lebanon have risen 75%. Among both Lebanese and Syrian urban populations, risk is distributed widely across the country, primarily from frequent, precipitation-induced debris flows. Individual risk is 9 to 11 times greater among encamped Syrian refugees than among their urban neighbors due to a complex marginalization on economic, social, and policy levels which force refugees into sub-standard shelter. This work sheds light on camp-based refugee resettlement policy, suggesting that, from an environmental

hazard perspective, urban settlement appears preferable to encampment due to durable housing solutions.

Chapter 6 presents a probabilistic landslide risk analysis for the city of Seattle, Washington. Spatially explicit risk maps provide significantly more actionable information than the traditional landslide susceptibility maps which guide land use planning in Seattle. Significantly more buildings are at risk from landslides than are currently designated as in landslide-prone areas. I find that landslide risk in Seattle comes primarily from frequent, low-intensity winter storms which trigger widespread shallow landslides. The probabilistic hazard and risk maps developed in this work demonstrate that high-resolution, regional scale analyses are both realistic and achievable. However, substantial challenges remain in performing landslide risk analysis in an urban environment, such as incorporating the effects of anthropogenic modifications on slope stability and developing new vulnerability curves for dense, urban architecture.

Collectively, this work represents an advancement in the quantitative analysis of landslide risk, providing data and tools necessary for risk assessment and informed risk reduction strategies to reduce preventable landslide losses.

Note: The python code behind the multimodal framework for landslide risk analysis is currently being revised to make it more efficient and user-friendly. I hope to make the code and a user manual more widely available in the future.

APPENDICES

Appendix 2.1 – Evaluation and sensitivity analysis of the coseismic landslide models

Very few regions have detailed landslide inventories including both significant precipitation and seismic events. I am unaware of any locations which additionally have publicly-available loss data with which to verify the multimodal landslide risk analysis framework from start to finish with real data. Therefore I have adopted two locations based on the detail and availability of landslide-related data at which to evaluate different modules within the multimodal landslide risk analysis framework. A study are in the near Kaikoura, New Zealand, was selected to evaluate the accuracy and sensitivity of the coseismic landslide models, and two subareas in Western Multnomah County near Portland, Oregon, U.S., were selected to evaluate the accuracy and sensitivity of the precipitation-induced landslide models (see **Appendix 2.2**).

A2.1.1 Kaikoura, New Zealand

On 14 November 2016, the region surrounding Kaikoura, New Zealand, experienced a M7.8 earthquake which triggered over 10,000 landslides. The modes of landsliding were diverse, including shallow, soil slides; rock avalanches and rock falls; and massive, deep-seated rotational slumps (Massey et al., 2018). Extensive mapping of the landslides triggered by the November 2016 earthquake has been undertaken by the New Zealand Institute of Geological and Nuclear Sciences (GNS). The preliminary landslide inventory available at the time of this work included only the deposition area of each landslide (**Figure A2.1.1**).

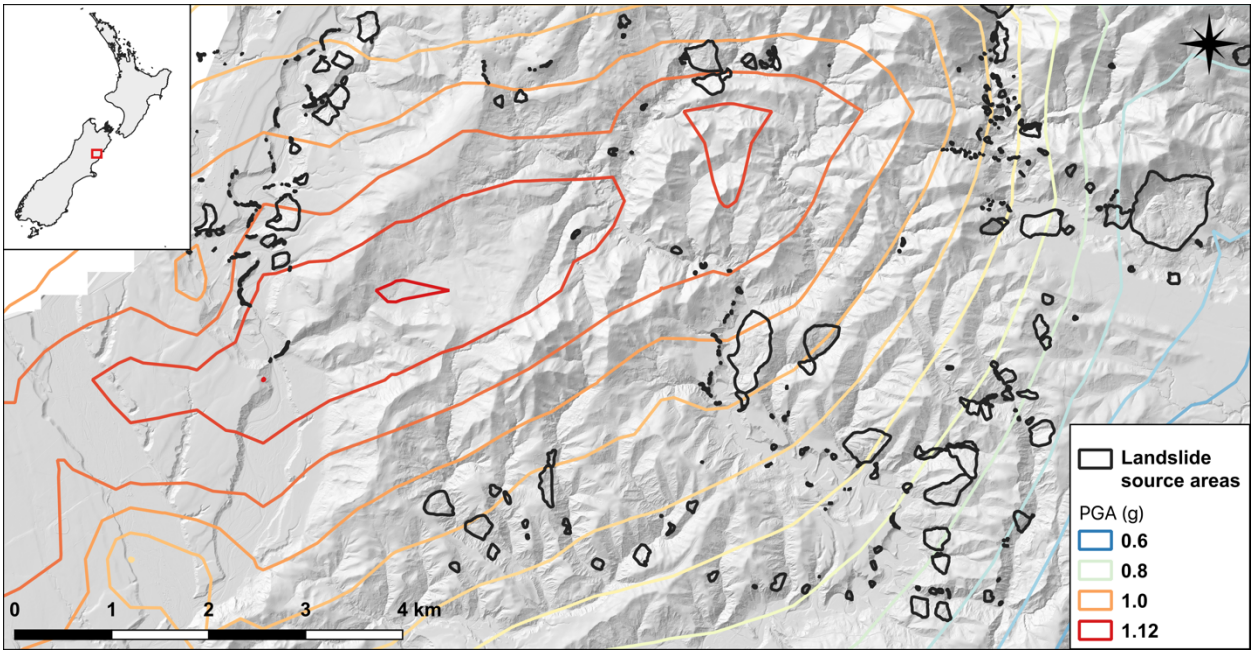

Figure A2.1.1. Kaikoura study area. Mapped coseismic landslide source zones from the 2016 Kaikoura earthquake are shown

A2.1.2 Updates to the landslide inventory

I updated the preliminary landslide inventory using a post-event 1 m digital elevation model and post-event 20 cm imagery provided by GNS Science (C. Massey, *personal communication*). The goal of the updates was to 1.) identify additional landslides not captured in the preliminary mapping, 2.) characterize the failure mode of each landslide, and 3.) delineate source and runout zones. **Figure A2.1.2** shows the updated landslide inventory, with the number of added landslide polygons of each mode of failure provided in **Table A2.1.1**. The modes are classified according to **Chapter 2, Table 2.1**.

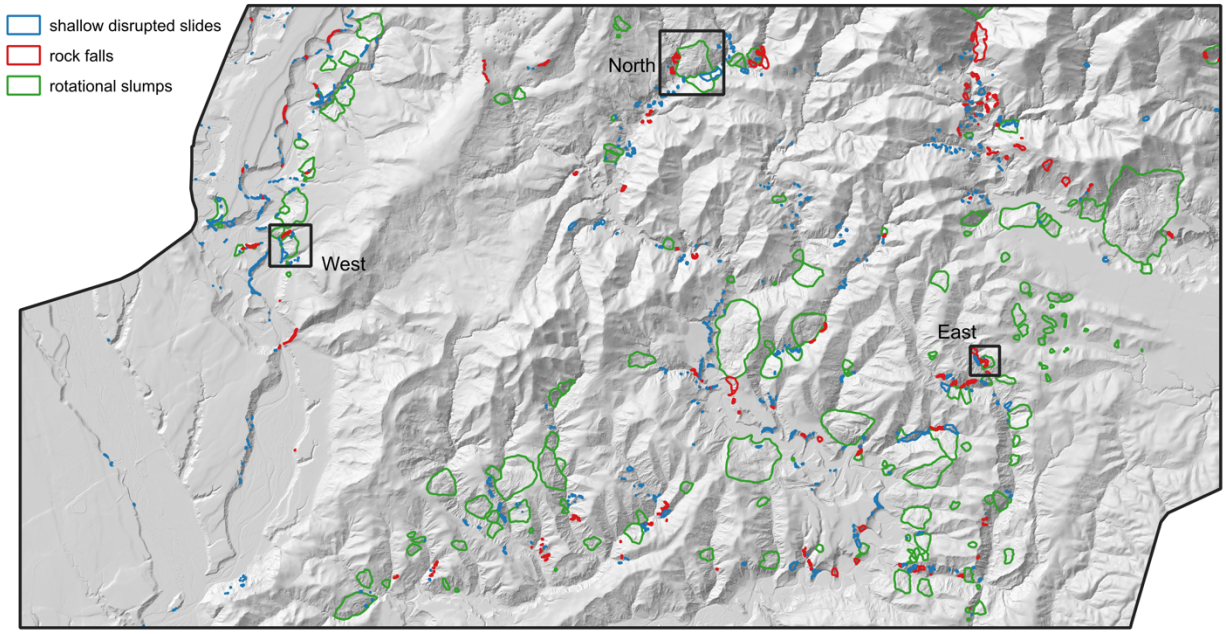

Figure A2.1.2. The updated landslide inventory. Landslide polygons are differentiated by mode and divided into source and runout zones. Boxes correspond to the subareas shown in **Figures A2.1.9 – A2.1.13** and **A2.1.18 – A2.1.21**.

Table A2.1.1. Number and mode of added landslide polygons.

Mode	*Original (GNS)*	*Updated*	*Percent change*
Shallow	91	169	86%
Rotational	280	576	106%
rock	133	197	48%
Total	504	942	87%

A2.1.3 Analysis with the multimodal method

I utilized geologic maps, pre-event terrain data, and soil parameters provided by GNS Science (C. Massey, *personal communication*) and PGA Shakemap (Wald et al., 2006) estimates from the 2016 Kaikoura earthquake to predict of the mode and extent of landslide source zones in the study area (e.g. **Figures A2.1.3 – A2.1.6**). Variability in material parameters was included in a Monte Carlo process with 100 runs, using the parameter distributions in **Table A2.1.2.** Scalar parameters the multimodal method were adjusted one at a time according to the testing schedule in **Table A2.1.3** in order to examine the sensitivity of the prediction accuracy to changes in the input parameters.

I quantitatively compared the output of the multimodal model with the mapped inventory using receiver-operating characteristic curves (ROC; Deleo, 1993; Fawcett, 2006). ROC curves are threshold-independent, which means that a threshold probability delineating "failing" and "non-failing" areas does not need to be assumed. The area under the curve (AUC) provides a global accuracy statistic accounting for the ability of the model to predict both failures and non-failures over the entire range of threshold values (Begueria, 2006; Corominas et al., 2014).

Landslide hazard maps usually involve a highly skewed dataset (e.g. the ratio between landslide and non-landslide terrain is very small). Precision-recall plots (PR) can be used to augment ROC plots for imbalanced datasets (Saito and Rehmsmeier, 2015; Davis and Goadrich, 2006). PR curves are sensitive to the degree of imbalance, so they cannot be compared between datasets (Boyd et al., 2012). I report the area under the PR curve for the full (imbalanced) hazard data and for a balanced dataset created by undersampling the non-landslide hazard cells (Boyd et al., 2012).

These metrics were used to evaluate the sensitivity of the coseismic models for each mode to changes in the assumed inputs and select an optimal set of values for use in **Chapter 6 (Figures A2.1.7** and **A2.1.8)**. None of the evaluation metrics listed above can be used to explicitly assess the spatial accuracy of predictive landslide hazard analysis. Therefore **Figures A2.1.9 – A2.1.13** highlight the qualitative spatial influence on landslide hazard for selected parameters at three subareas within the study site.

Figure A2.1.14 – A2.1.15 show the final ROC plots produce by the optimized set of user-input values for this dataset.

The accuracy of r.randomwalk was evaluated in a similar manner, using the testing schedule in **Table A2.1.4** and adopting the mapped source zones as starting cells. Runout relationship parameters *a* and *b* were derived from the coseismic landslide runout inventory described in **Section A2.3.2**.

Table A2.1.2. Geotechnical Parameters of Soil and Rock. Ranges given in sources were assumed to represent three standard deviations unless otherwise noted. * denotes where standard deviation is based on an assumed coefficient of variation of 0.1 for friction angle and 0.3 for cohesion (Jones et al., 2002). Friction angle is assumed to be normally distributed; cohesion is assumed to be lognormally distributed.

		Rock				Soil				Reference
		φ (°)		c' (kPa)		φ (°)		c' (kPa)		
Unit	Code	μ	σ	μ	σ	μ	σ	μ	σ	
Alluvial deposits (Holocene)	*Q1.alvgvl*	36	1.5	12	3.5	36	1.5	10	3.5	Burns et al. (2015)
Landslide deposits (Holocene)	*Q1.Indbrc, Q.Indbrc*	31	1.0	32	5.2	31	1.0	32	5.2	Burns et al. (2015)
Alluvial deposits (Pleistocene)	*Q2.alvgvl, Q2.fangvl, Q3.fangvl, Q4.alvgvl, Q4.fangvl, Q6.alvgvl, Q.alvgvl*	36	2.5	14	4.0	36	2.5	10	4.0	Burns et al. (2015)
Greta Formation	*Pl.zst*	32	3.2*	50	15*	24	2.4*	21	6.3*	Massey et al. (2016), Crozier et al. (1995), AECOM (2014)
Undifferentiated Motunau Group	*Mi.sst2*	40	4.0*	50	15*	34	3.4*	25	7.5*	Williams et al. (2010), Ridgley (2017)
Waima Formation	*Mi.zst*	32	3.2*	50	15*	24	2.4*	21	6.3*	Massey et al. (2010), Crozier et al. (1995), AECOM (2014)
Omihi Formation	*Ol.lst3*	40	4.0*	50	15*	20	2.0*	35	10.5*	--
Undifferentiated Cookson Volcanics Group	*Ol.bas2*	60	6.0*	200	60	32	2.0	24	7.8	Williams et al. (2010), Burns et al. (2015)
Amuri Limestone	*IKE.lst*	40	4.0*	50	15*	20	2.0*	35	10.5*	--
Undifferentiated Eyre Group	*IKPa.sst2*	40	4.0*	50	15*	34	3.4*	25	7.5*	Williams et al. (2010), Ridgley (2017)
Conway Formation	*IK.sst1*	40	4.0*	50	15*	34	3.4*	25	7.5*	Williams et al. (2010), Ridgley (2017)
Pahau Terrane	*eK.sst*	45	1.5	50	13.7	38	2.4	18	5.3	Muldrew et al. (2017), Massey (2016), McNamara et al. (2014)

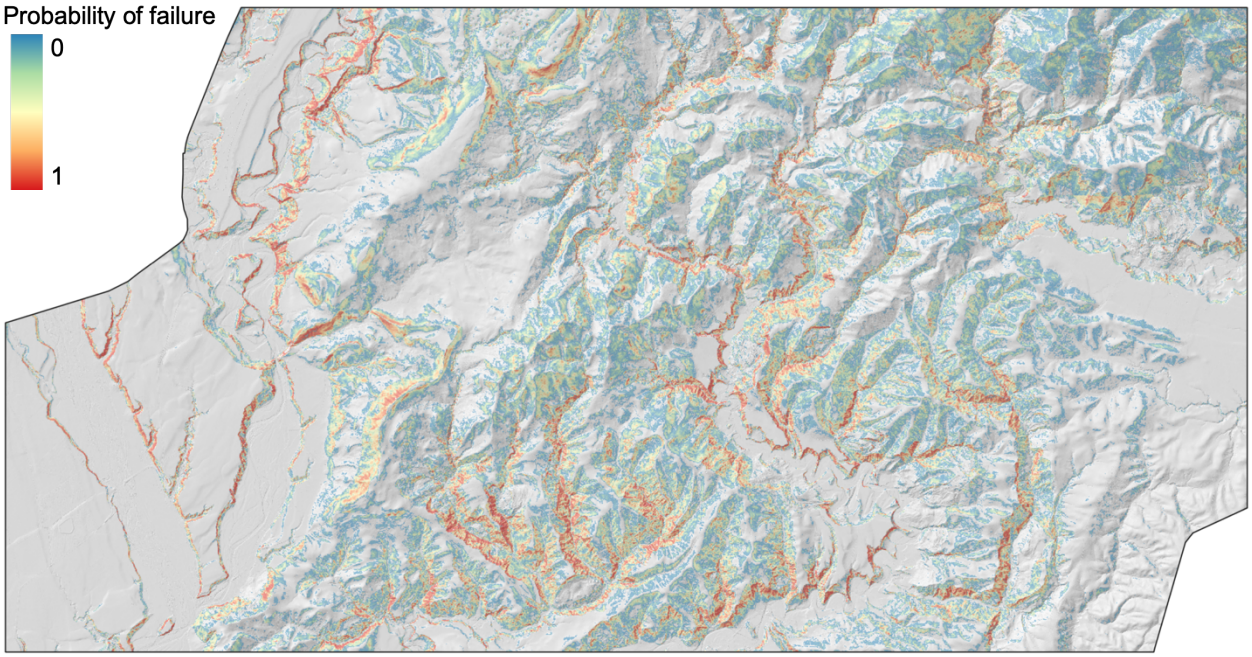

Figure A2.1.3. Example of landslide hazard for shallow, disrupted soil failures.

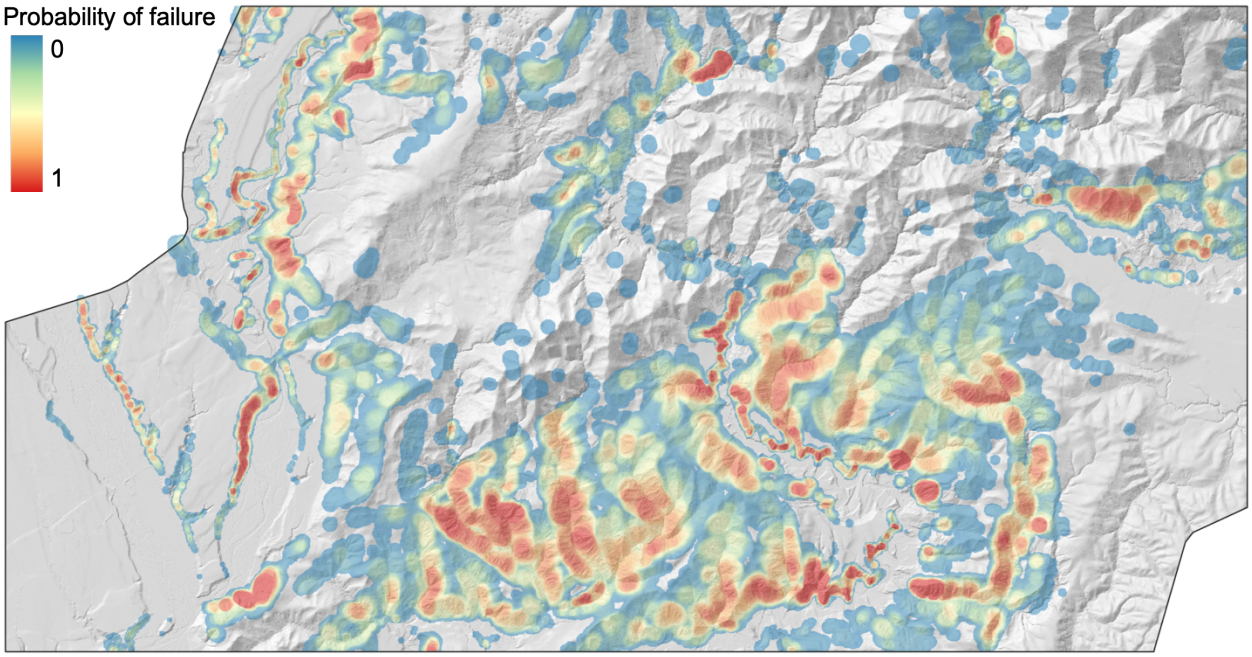

Figure A2.1.4. Example landslide hazard map for rotational slumps.

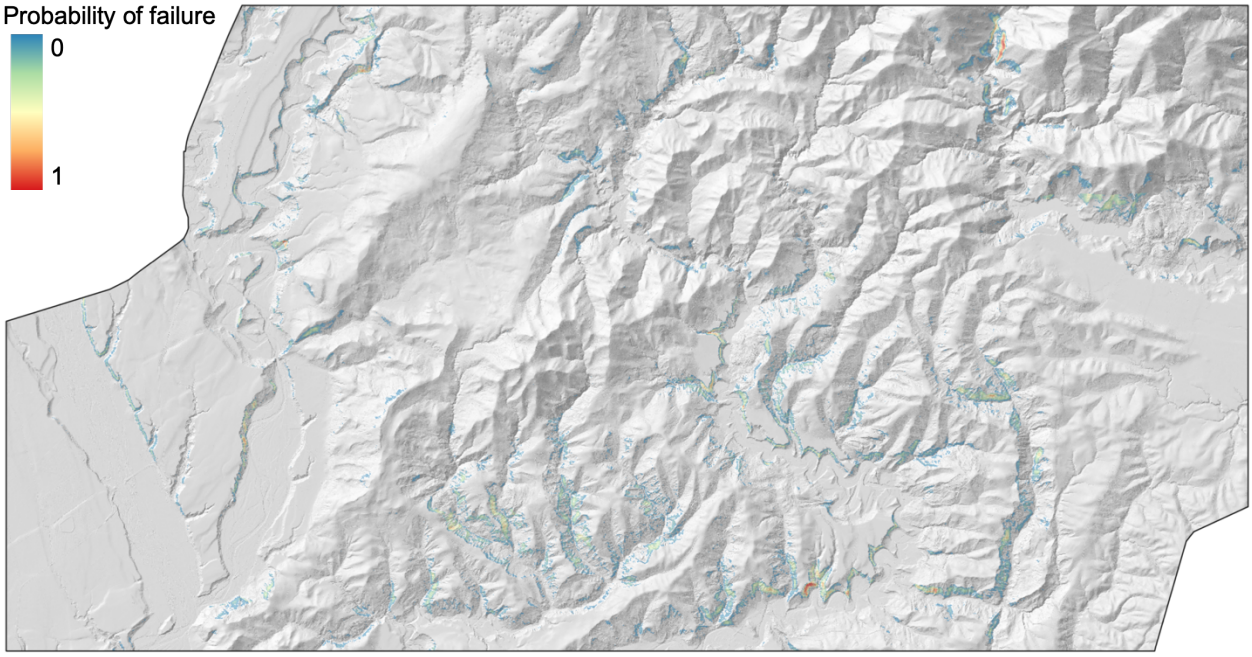

Figure A2.1.5. Example landslide hazard map for rock fall.

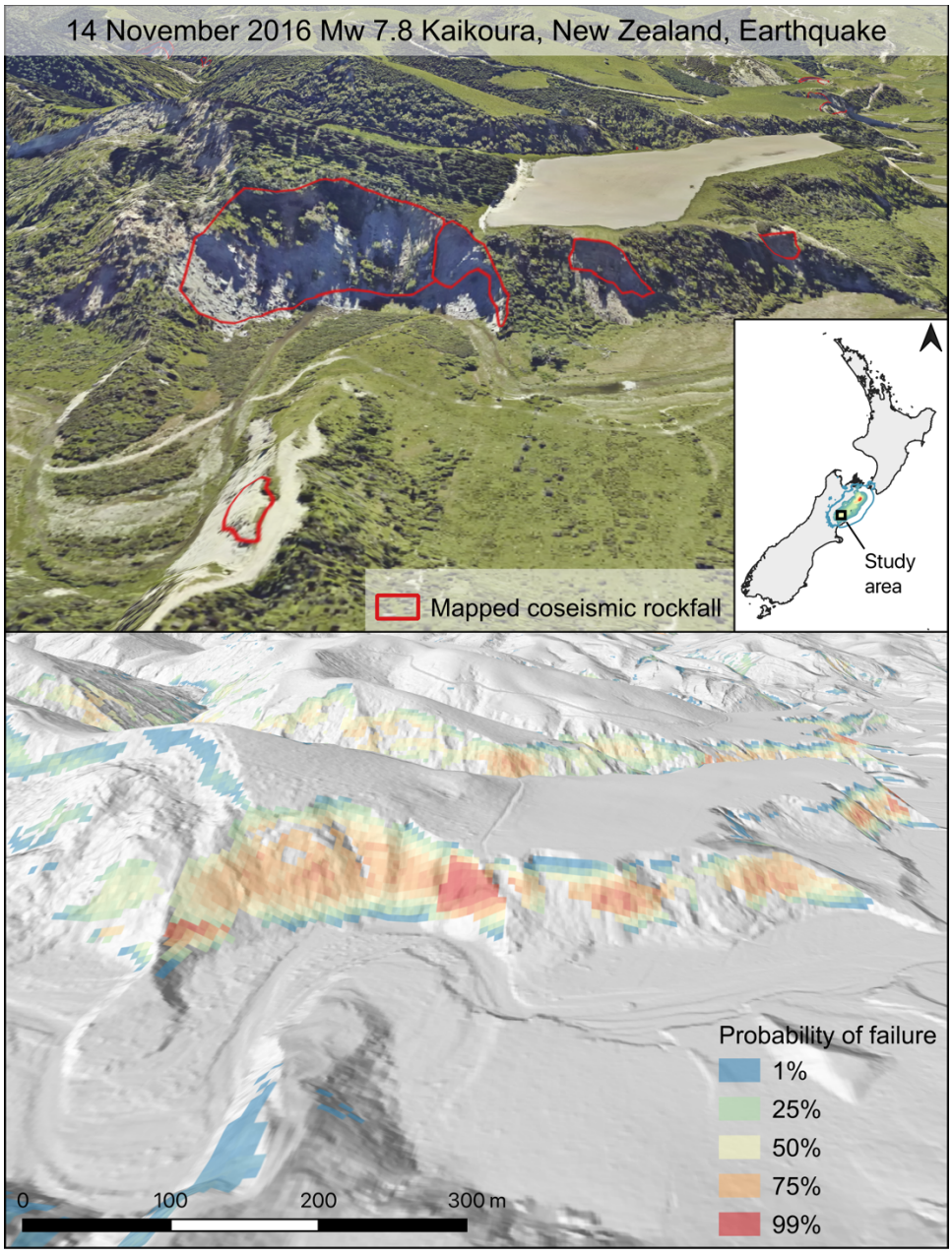

Figure A2.1.6. Areas of high probability of shallow landslide failure are closely aligned with observed landslides.

Table A2.1.3. Testing schedule for user-input variables in the multimodal method. Bold font indicates the baseline values.

parameter	*Values tested*								
Rotational compliance factor	0.2	0.3	0.4	**0.5**	0.6	0.7	0.8	0.9	1.0
Local relief window size (m)	50	100	150	**200**	250	300	350	400	450	500
Pixel size (m)	1	2	3	4	**5**	7.5	10	15
Coseismic displacement relationship	**Saygili and Rathje (2008) *scalar***			Saygili and Rathje (2008) *vector*			Jibson (2007) *scalar*		
Shallow landslide thickness (m)	0.5	1	1.5	**2**	2.5	3	3.5
root cohesion (kPa)	None (0,0,0)			Low (0, 3, 5)			**High (2, 5, 10)**		
Rock / soil dry unit weight (kN/m^3)	19/15		21/17	**23/19**		25/21		27/23	
Slump susceptibility range (deg.)	**10 - 35**			15 - 35			15 - 40		
Rock fall susceptibility range (deg.)	**35 - 90**		40 - 90		45 - 90		50 - 90		
Shallow susceptibility range (deg.)	15 - 40		15 - 45		**15 - 50**		15 - 55		
Rock fall / shallow / slump displacement failure criteria (cm)	2 / 2 / 10		**5 / 5 / 15**		10 / 10 / 50		15 / 15 / 100		
Rock wedge height as proportion of local relief	0.15		0.20	**0.25**		0.30		0.35	
Rock fall topographic amplification factor.	1		1.4	**1.5**		1.6		1.7	

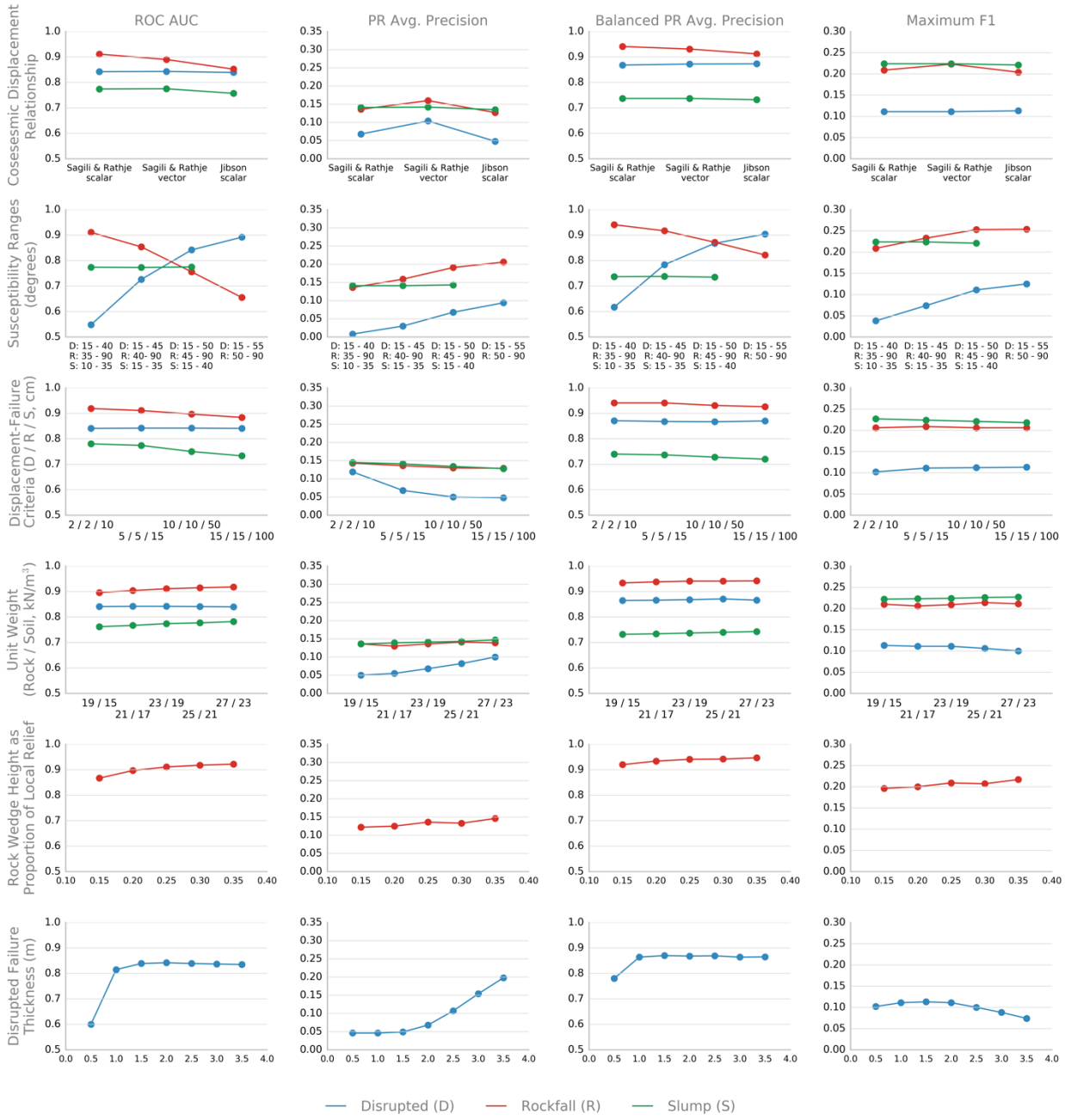

Figure A2.1.7. Sensitivity in the predictive accuracy for all three modes of the multimodal method (source zones, *part 1*).

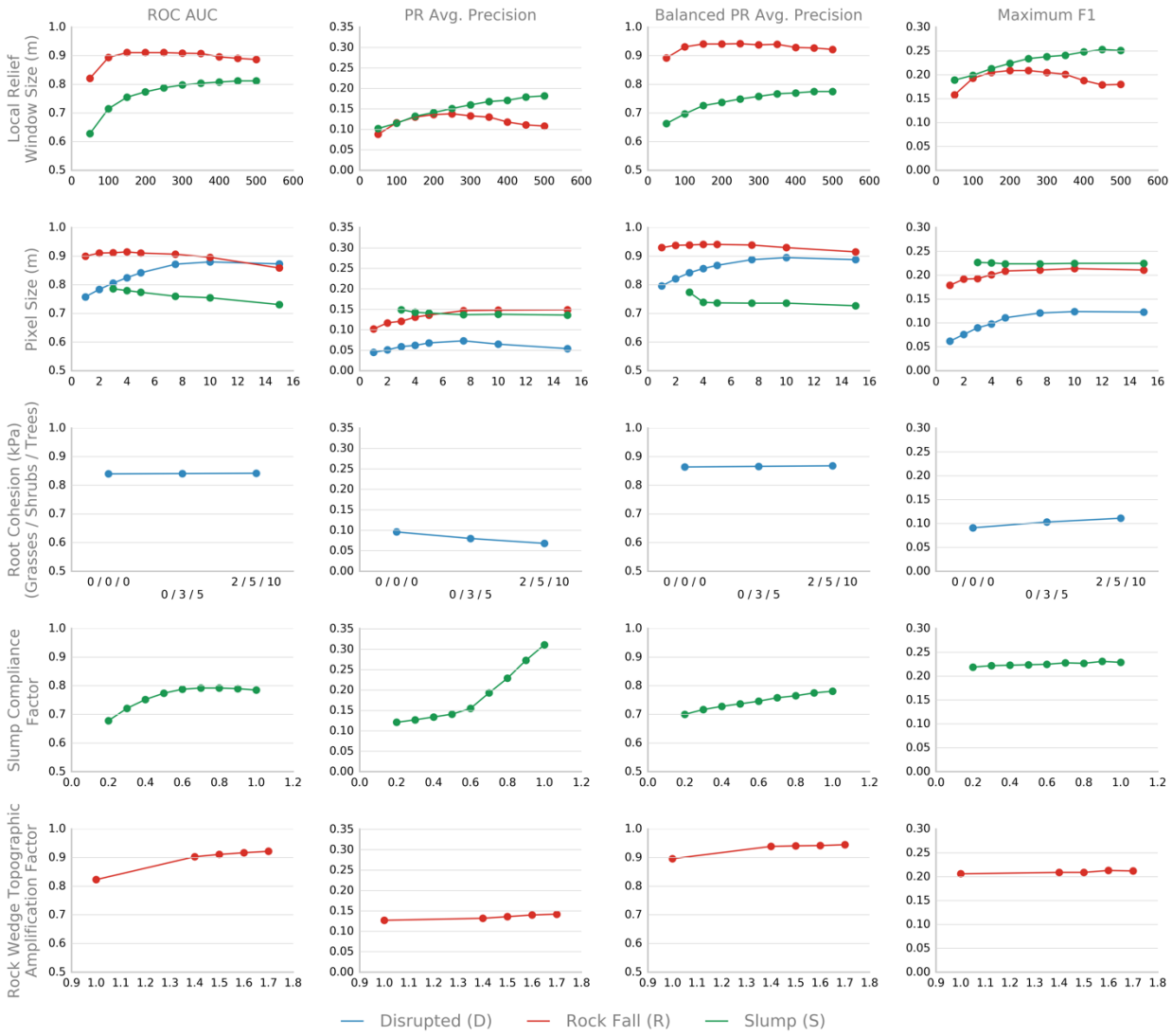

Figure A2.1.8. Sensitivity in the predictive accuracy for all three modes of the multimodal method (source zones, *part 2*).

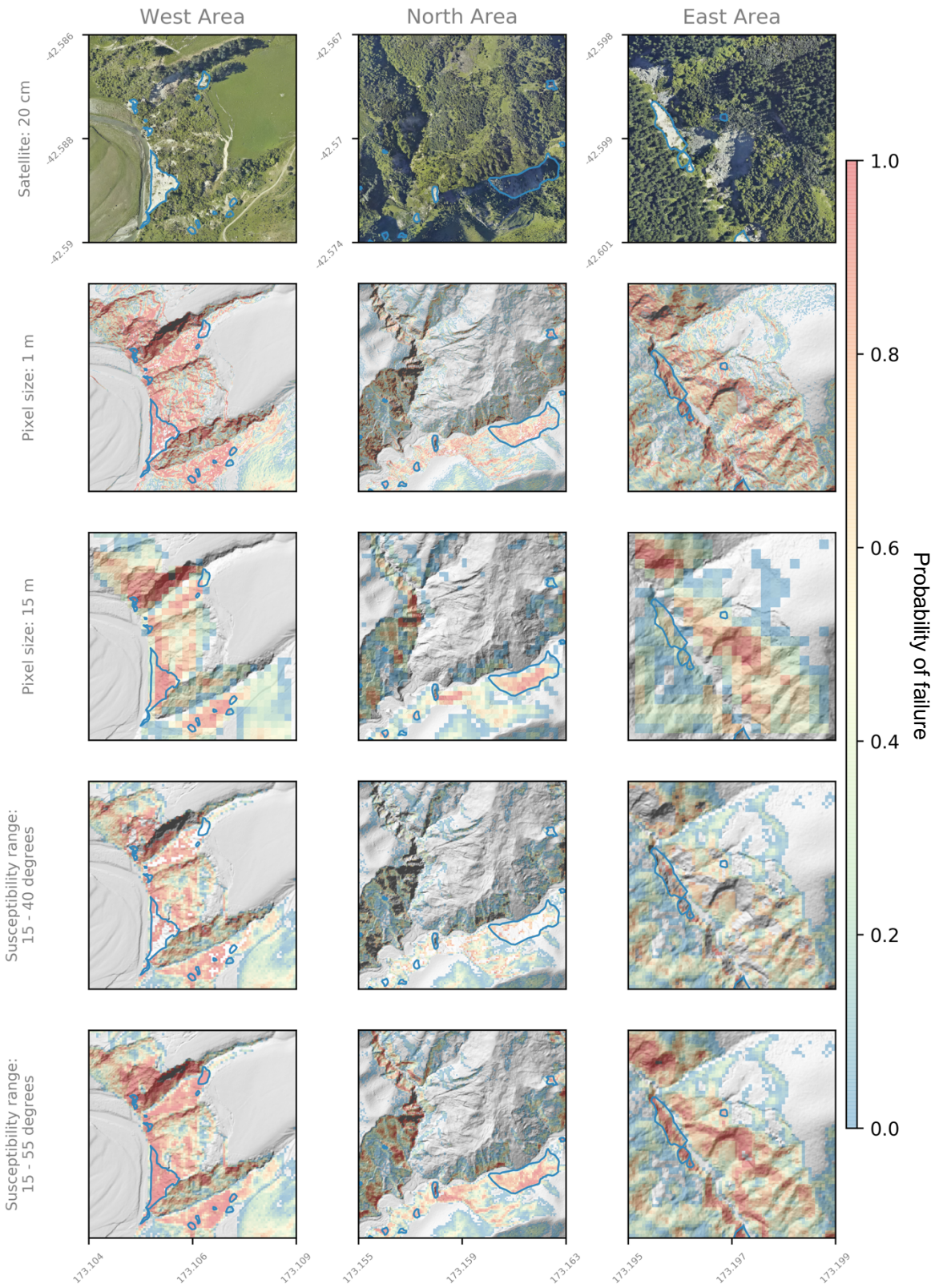

Figure A2.1.9. Spatial sensitivity to changes in user-input parameters for shallow landslides (source zones, *part 1*).

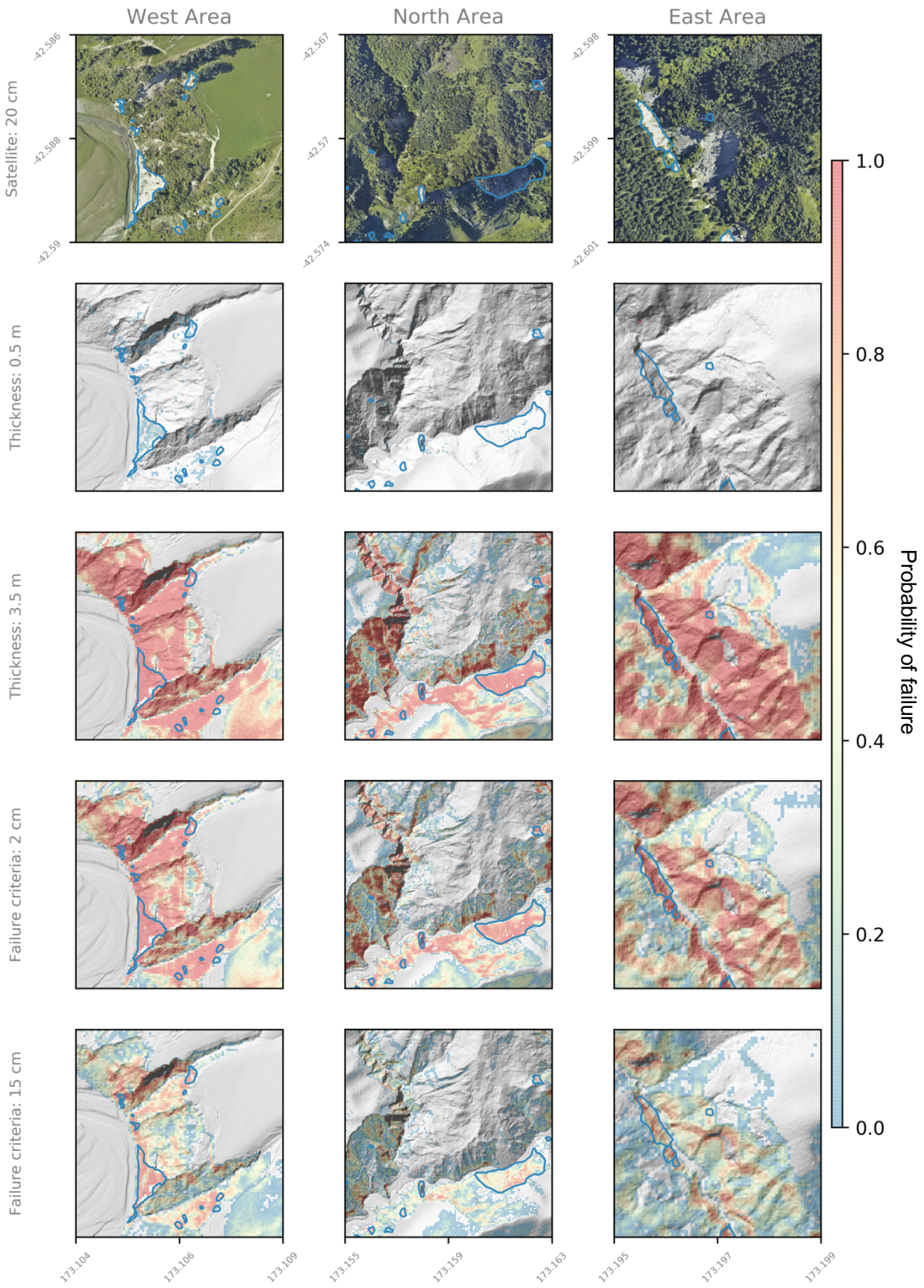

Figure A2.1.10. Spatial sensitivity to changes in user-input parameters for shallow landslides (source zones, *part 2*).

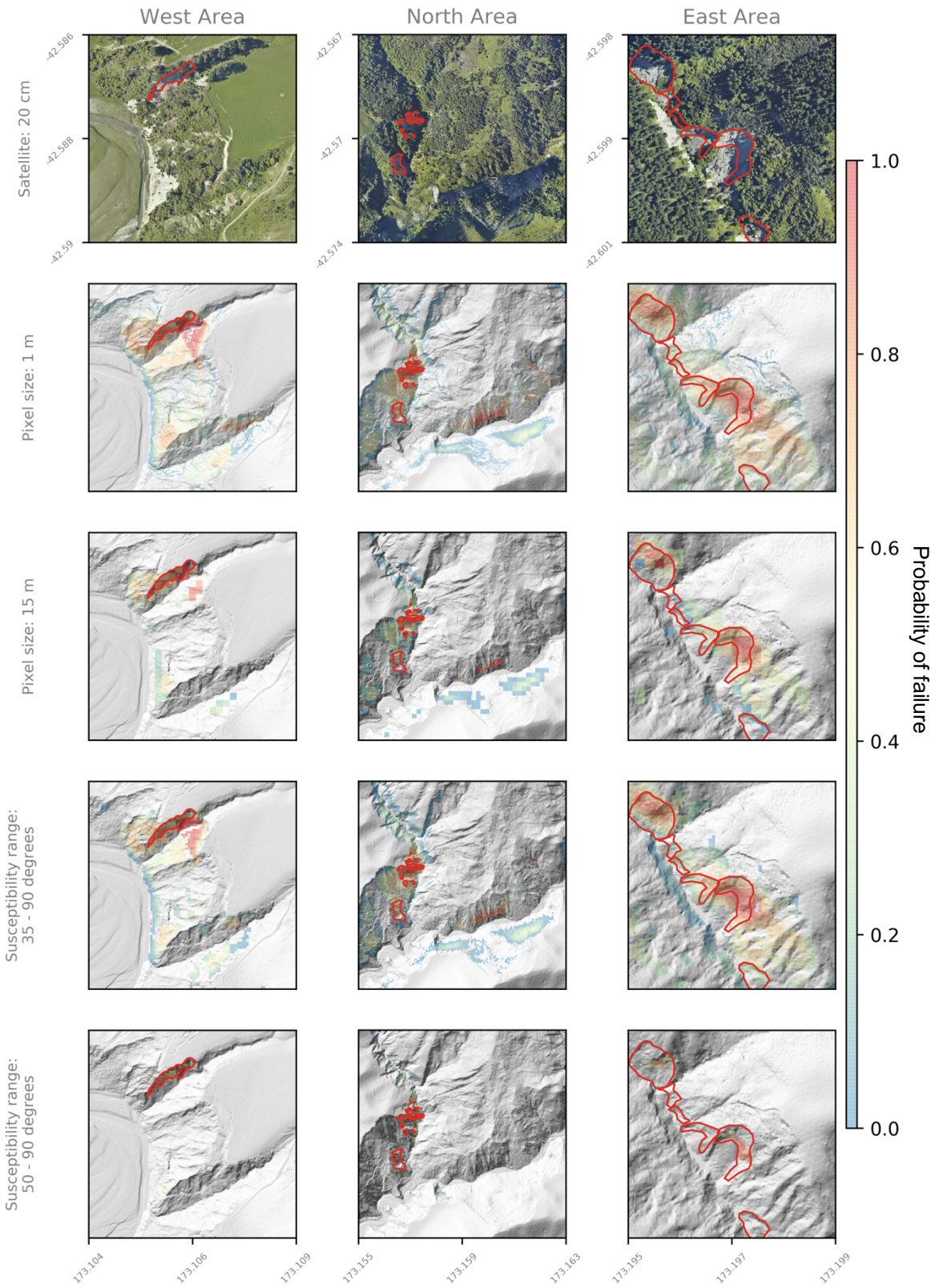

Figure A2.1.11. Spatial sensitivity to changes in user-input parameters for rock falls (source zones, *part 1*).

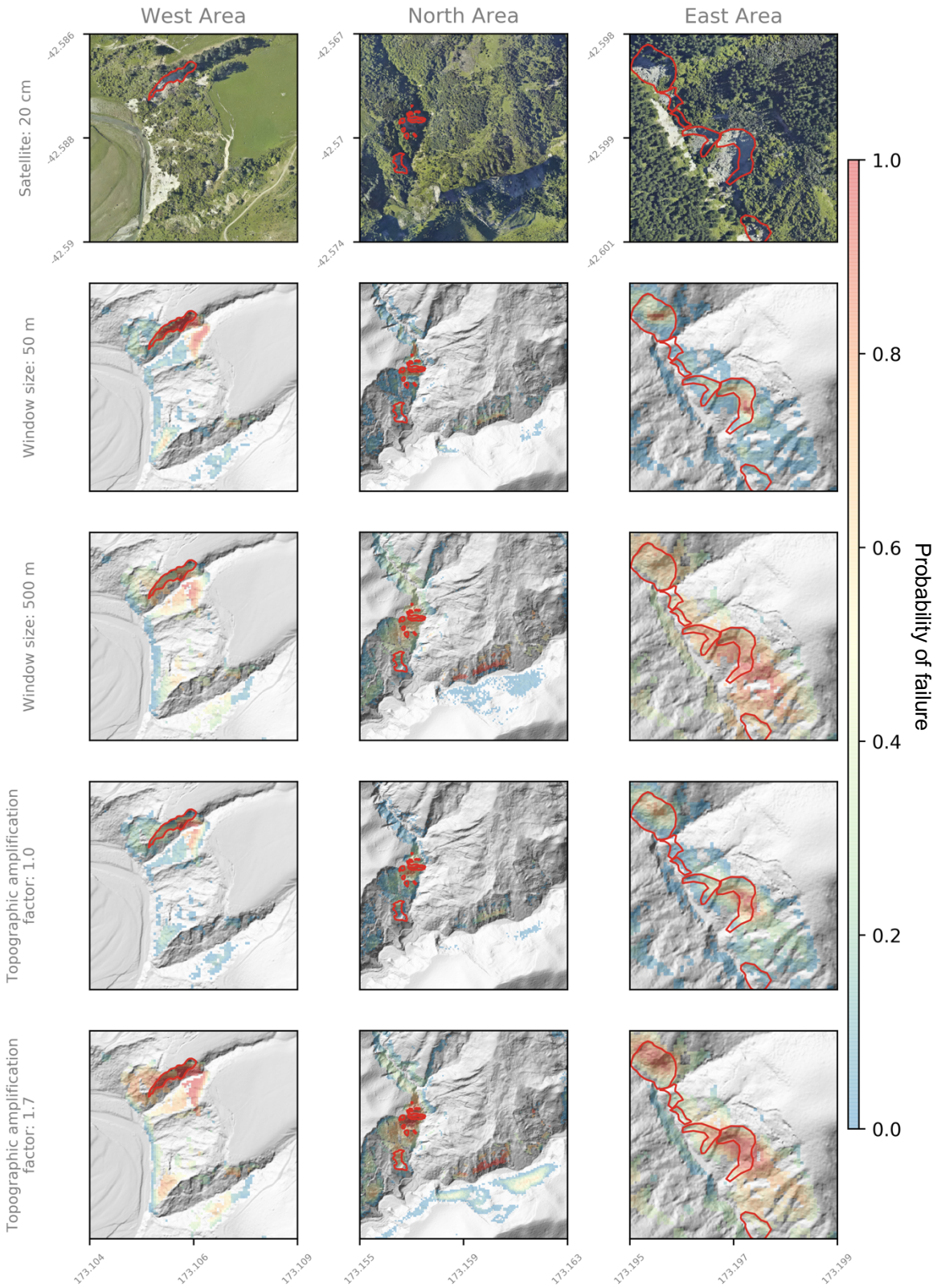

Figure A2.1.12. Spatial sensitivity to changes in user-input parameters for rock falls (source zones, *part 2*).

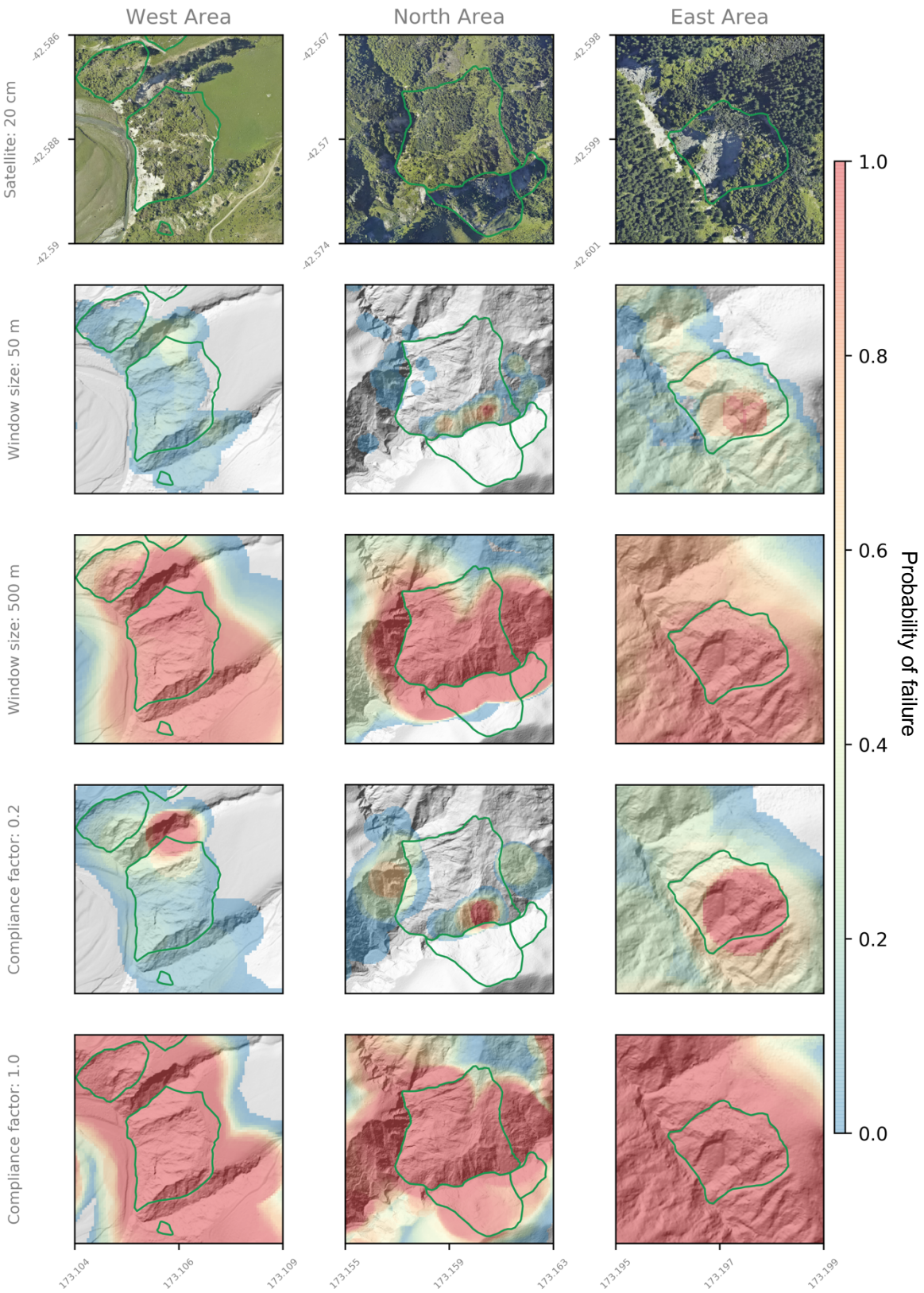

Figure A2.1.13. Spatial sensitivity to changes in user-input parameters for rotational slumps.

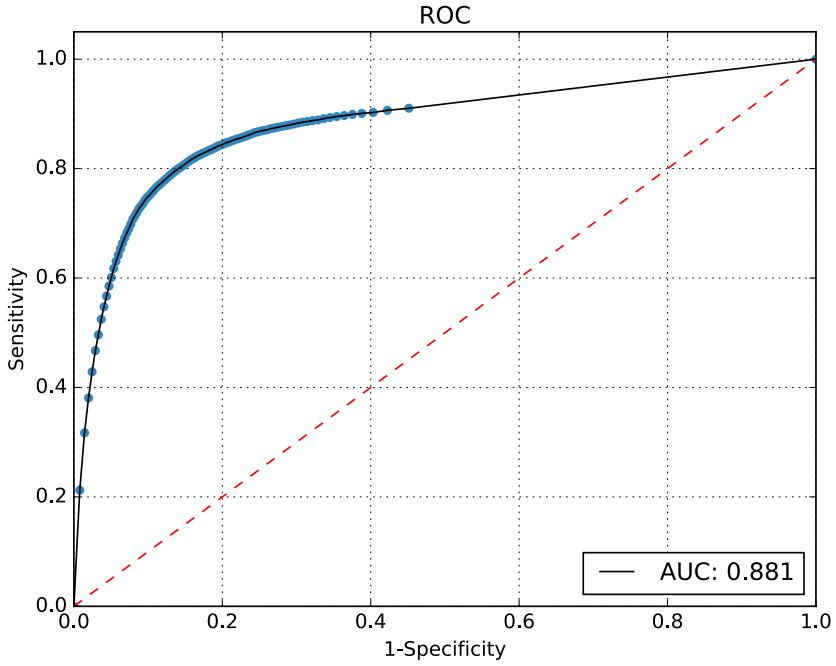

Figure A2.1.14. ROC curve for shallow failures using optimized parameters.

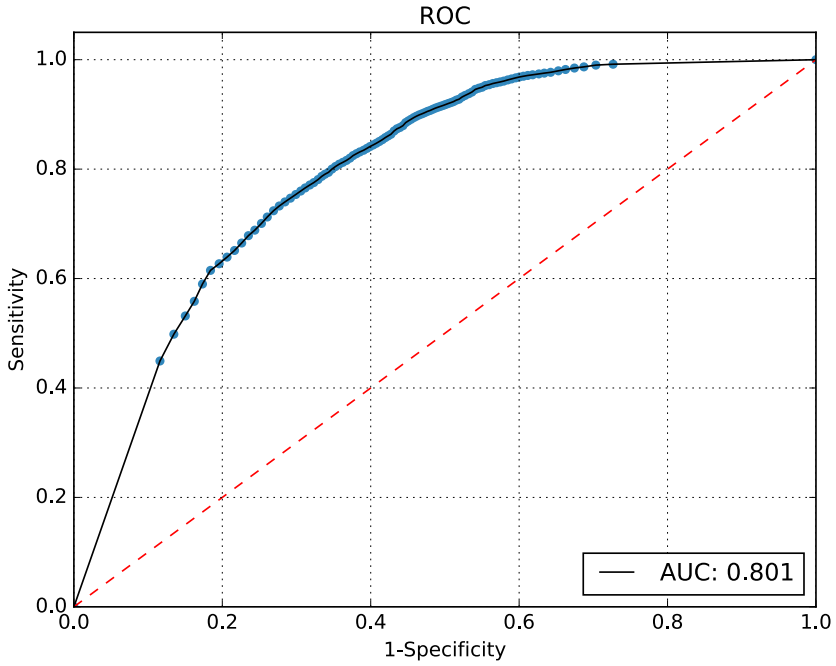

Figure A2.1.15. ROC curve for rotational failures using optimized parameters.

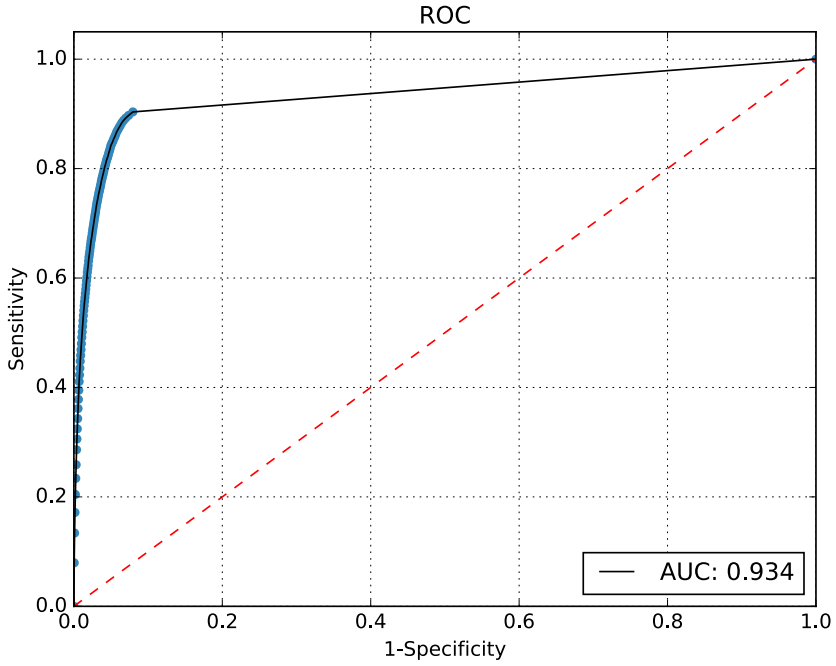

Figure A2.1.16. ROC curve for rock slope failures using optimized parameters.

Table A2.1.4. Testing schedule for user input variables in r.randomwalk. Bold font indicates the baseline values.

Parameter	*Values tested*									
Runout relationship	$L = a V^b$						$log_{10}(\tan(H/L)) = a log_{10}(V) + b$			
Control distance (m)	5	7.5	**10**	15	30	50				
Max runup height (m)	1	2	**5**	7.5	10					
Slope factor, f_β	1	2	3	4	**5**	6	7	8	9	10
Direction factor, f_d	1	**2**	3	4	5	6	7	8	9	10
Number of walks	**10**	50	100	500						
Segment length (m)	5	7.5	**10**	15	30	50				
Pixel size (m)	2	3	4	**5**	7.5	10	15			

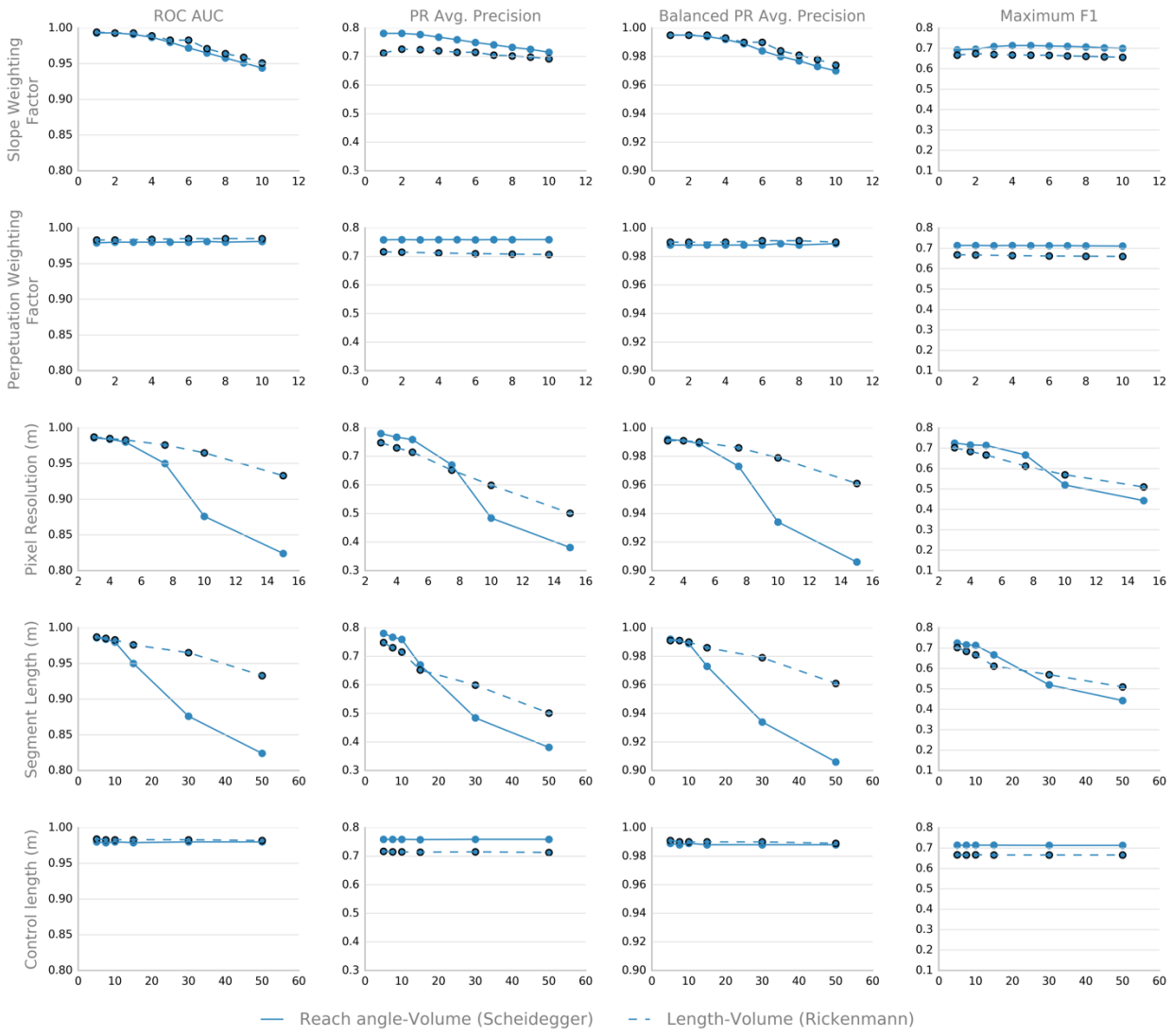

Figure A2.1.17. Sensitivity in the predictive accuracy of r.randomwalk for shallow slide and rock avalanche deposits (combined)

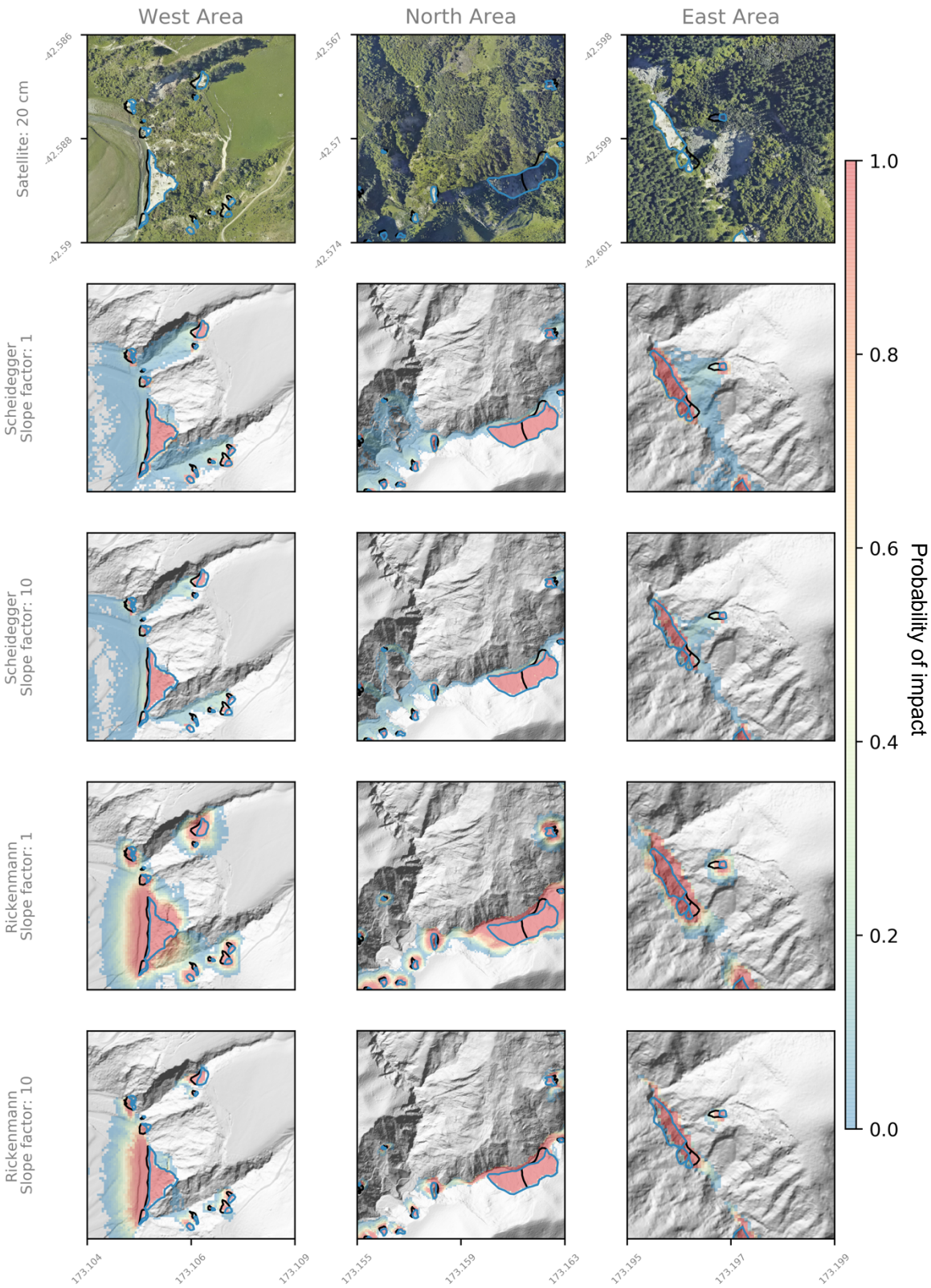

Figure A2.1.18. Spatial sensitivity to changes in user-input parameters for the runout of shallow slides and rock avalanches (*part 1*).

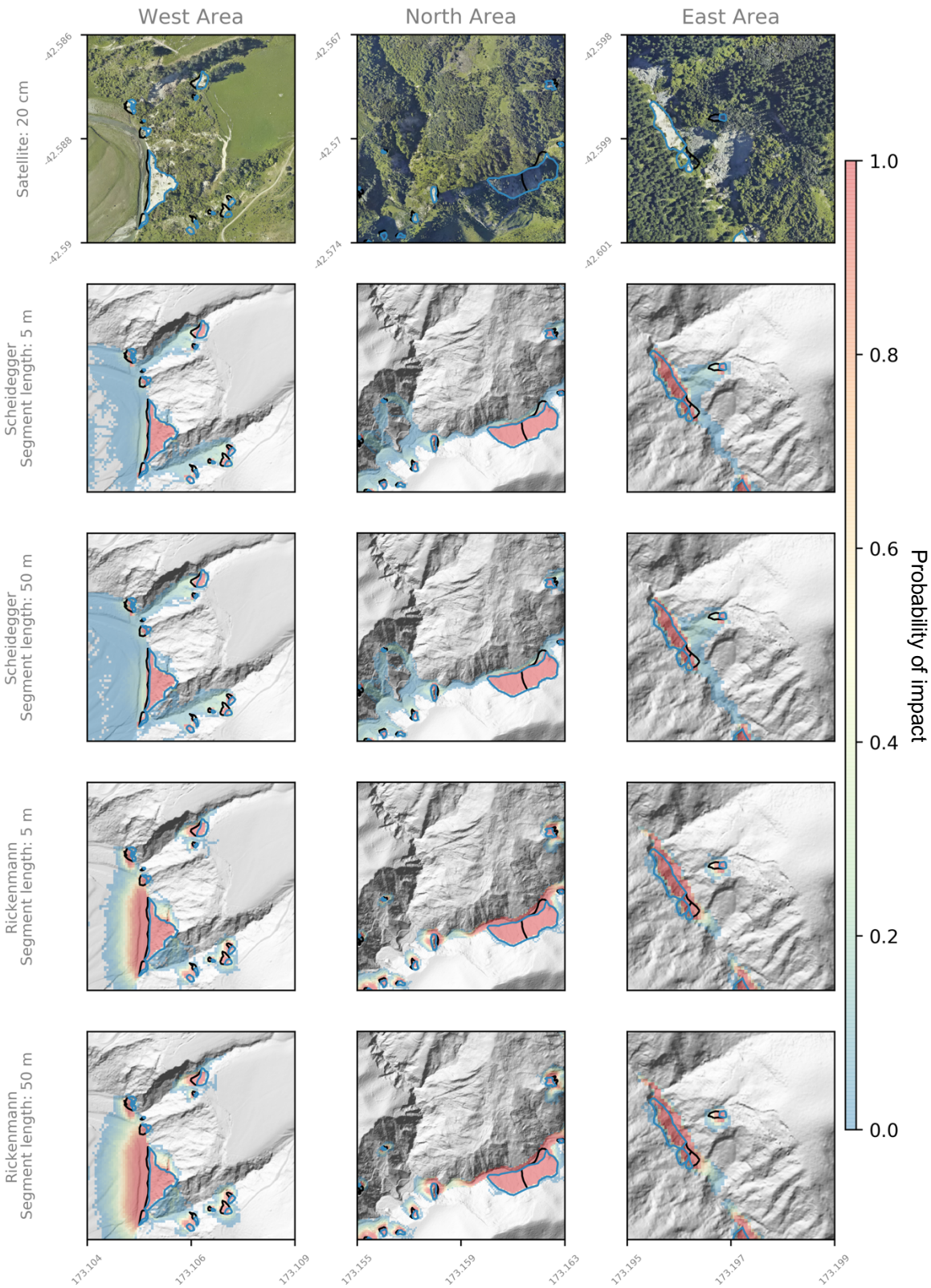

Figure A2.1.19. Spatial sensitivity to changes in user-input parameters for the runout of shallow slides and rock avalanches (*part 2*).

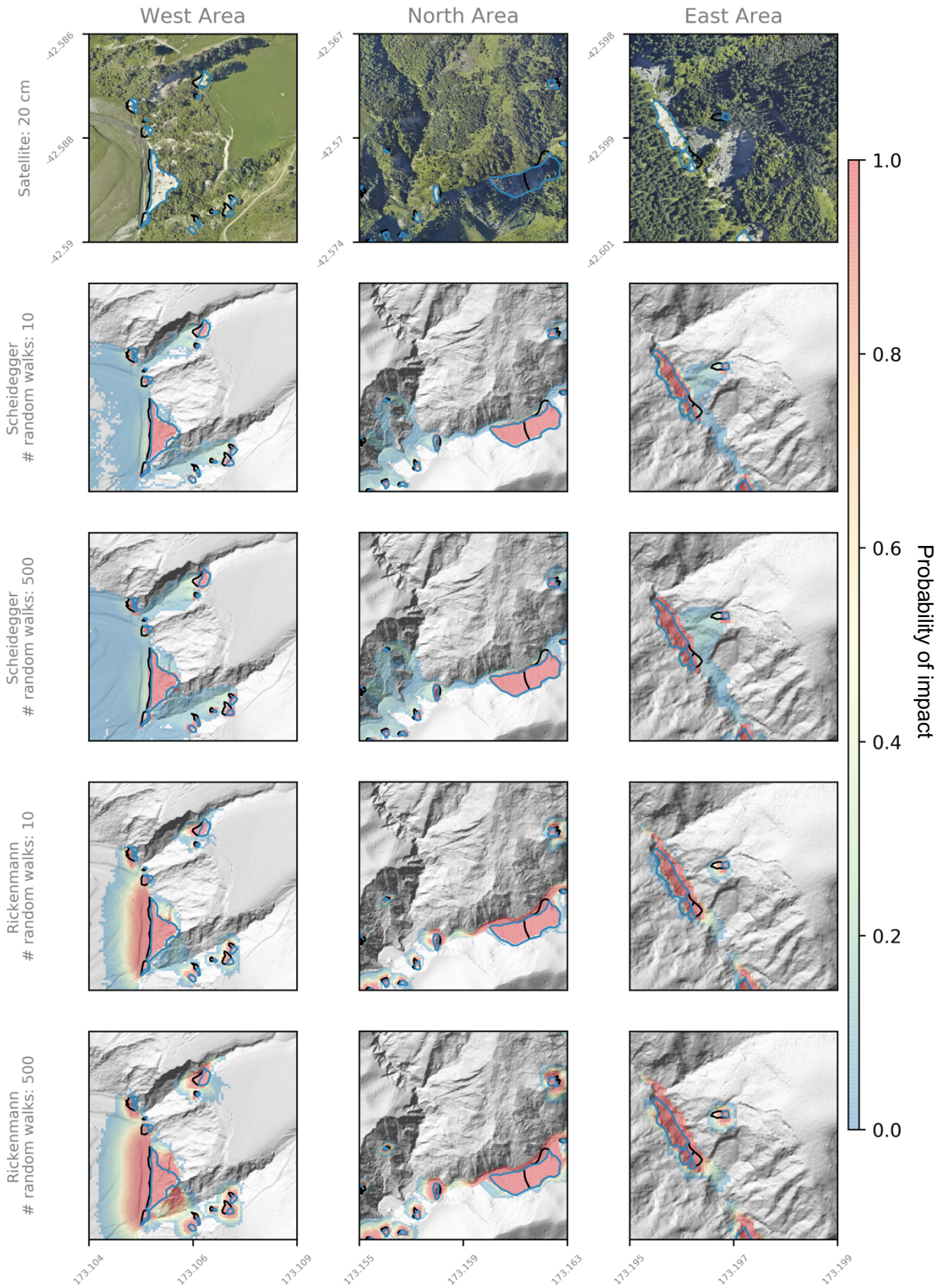

Figure A2.1.20. Spatial sensitivity to changes in user-input parameters for the runout of shallow slides and rock avalanches (*part 3*).

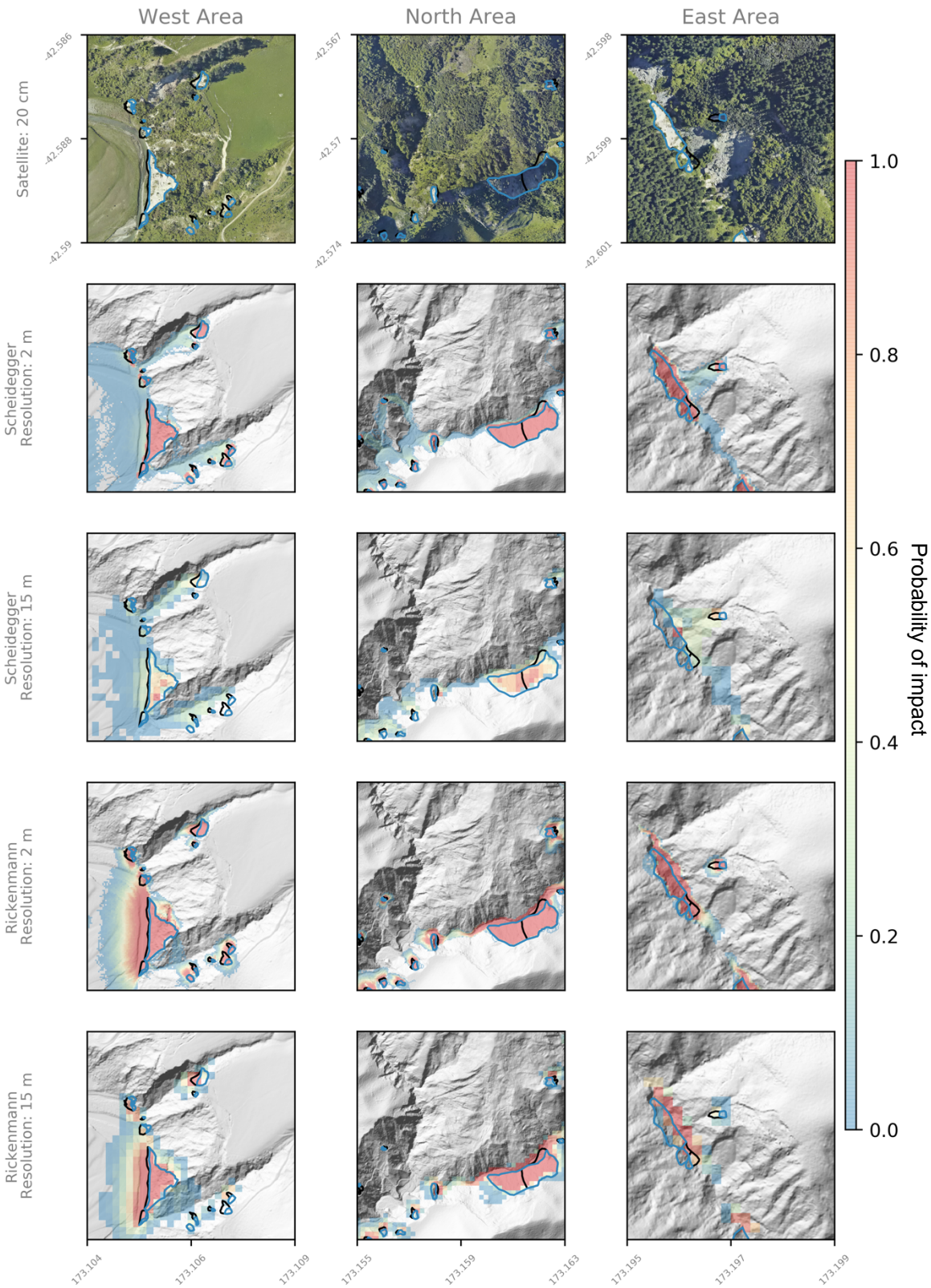

Figure A2.1.21. Spatial sensitivity to changes in user-input parameters for the runout of shallow slides and rock avalanches (*part 4*).

References

AECOM. (2014). Pendle Hill Station Upgrade: Geotechnical Investigation Report. AECOM.

Begueria, S. (2006). Validation and evaluation of predictive models in hazard assessment and risk management. *Nat. Hazards*, 37, 315-329.

Boyd, K., Costa, V., Davis, J., Page, C. (2012). Unachievable region in precision-recall space and its effect on empirical evaluation. In: *Proc. 29th Int. Conf. on Machine Learning*. Edinburgh.

Burns, W., Mickelson, K., Jones, C., Tilman, M., Coe, D. (2015). Surficial and bedrock engineering geology, landslide inventory and susceptibility, and surface hydrography of the Bull Run Watershed, Clackamas and Multnomah Counties, Oregon. OR Dept. of Geology and Mineral Industries.

Corominas, J., van Westen, C., Frattini, P., Cascini, L., Malet, J.-P., Fotopoulou, S., et al. (2014). Recommendations for the quantitative analysis of landslide risk. *Bull. Eng. Geol. Environ.*, 73, 209-263. https://doi.org/10.1007/s10064-013-0538-8

Crozier, M., Deimel, M, Simon, J. (1995). Investigation of earthquake triggering for deep-seated landslides, Taranaki, New Zealand. *Quat. Int.*, 25, 65-73

Davis, J., Goadrich, M. (2006). The relationship between precision-recall and ROC curves. In: *Proc. 23rd Int. Conf. on Machine Learning*. Pittsburgh, PA.

Deleo, J. (1993). Receiver operating characteristic laboratory (ROCLAB): Software for developing decision strategies that account for uncertainty. In: *Proc. 2nd Int. Symposium on Uncertainty Modelling and Analysis*. College Park: Computer Society Press.

Fawcett, T. (2006). An introduction to ROC analysis. *Pattern Recognition Letters*, 27, 861-874.

Jibson, R. (2007). Regression models for estimating coseismic landslide displacement. *Engineering Geology*, 91, 209-218. https://doi.org/10.1016/j.enggeo.2007.01.013

Jones, A., Kramer, S., Arduino, P. (2002). *Estimation of Uncertainty in Geotechnical Properties for Performance-based Earthquake Engineering*. PEER Report 2002/16. Berkeley, CA: Pacific Earthquake Engineering Research Center, University of California, Berkeley

Massey, C. (2010). The dynamics of reactivated landslides: Utiku and Taihape, North Island, New Zealand. (*doctoral dissertation)*. Durham: Durham University.

Massey, C., Abbot, E., McSaveney, M., Petley, D., Richards, L. (2016). Earthquake-induced displacement is insignificant in the reactivated Utiku landslide, New Zealand. In Aversa et al. (*Eds*.) *Landslides and Engineered Slopes: Experience, Theory, and Practice*. Rome: Associazoione Geotechnica Italiana

Massey, C., Petley, D., McSaveney, M., Archibald, G. (2016). Basal sliding and plastic deformation of a slow, reactivated landslide in New Zealand. *Eng. Geol*., 208, 11-28.

Massey, C., Townsend, D., Rathje, E., Allstadt, K., Lukovic, B., Kaneko, Y., Bradley, B., Wartman, J., Jibson, R., Petley, D., Horspool, N., Hamling, I., Carey, J., Cox, S., Davidson, J., Dellow, S., Godt, J., Holden, C., Jones, K., Kaiser, A., Little, M., Lyndsell, B., McColl, S., Morgenstern, R., Rengers, F., Rhoades, D., Rosser, B., Strong, D., Singeisen, C., Villeneuve, M. (2018). Landslides triggered by the 14 November 2016 M_w 7.8 Kaikoura earthquake, New Zealand. *Bull. Seismological Soc. Am*., 108, 1630-1648.

McNamara, D., Faulkner, D., McCarney, E. (2014). Rock properties of greywacke basement hosting geothermal reservoirs, New Zealand: Preliminary results. 39th Workshop on Geothermal Reservoir Engineering.

Muldrew, K., Robins, P., Hickman, R. (2017). Omaroro Lower Playing Field – Geotechnical Interpretive Report. BECA Lmt.
Ridgley, N. (2017). Westhaven Marina – Pile Berth Redevelopment Preliminary Geotechnical Assessment. BECA Lmt.
Saito, T., Rehmsmeier, M. (2015). The precision-recall plot is more informative than the ROC plot when evaluating binary classifiers on imbalanced datasets. *PLoS ONE*, 10.
Saygili, G., Rathje, E. (2008). Empirical predictive models for earthquake-induced sliding displacements of slopes. *Geotech. Geoenviron. Eng.*, 134(6), 790-803. https://doi.org/10.1061/(ASCE)1090-0241(2008)134:6(790)
Wald, D., Worden, B., Quitoriano, V., Pankow, K. (2006). ShakeMap manual. *Advanced National Seismic System Technical Manual, Users Guide, and Software Guide, draft version 1.0 6/19/06*. U.S. Geological Survey.
Williams, K., Sinclair, T. (2010). Western Ring Route – Waterview Connection: Geotechnical Interpretive Report. Tonkin & Taylor.

Appendix 2.2 – Evaluation and sensitivity analysis of the precipitation landslide models

A2.2.1 Sensitivity of the rotational slump model

The rotational slump model of **Equation 2.13** represents a significant improvement in the speed at which three-dimensional stability analyses can be performed across a region-scale terrain. Initial tests in the City of Seattle indicate that the rotational slump model runs 1 – 2 orders of magnitude faster than comparable commercial codes (Slide3, RocScience; Scoops3D, Reid et al., 2015) and provides similar results. However, in exchange for efficiency, the rotational slump model does not test multiple failure surfaces, but rather estimates a single critical surface.

As water table depth is driver of deep-seated slumping and simultaneously one of the least constrained physical parameters, I tested the sensitivity of rotational slump model to changes in the water table, as well as friction angle, cohesion, dry unit weight, local relief window, and pixel resolution in a small (~600 x 600 m) study area in the West Hills of Portland, Oregon, U.S. (**Figure A2.2.1 A**).

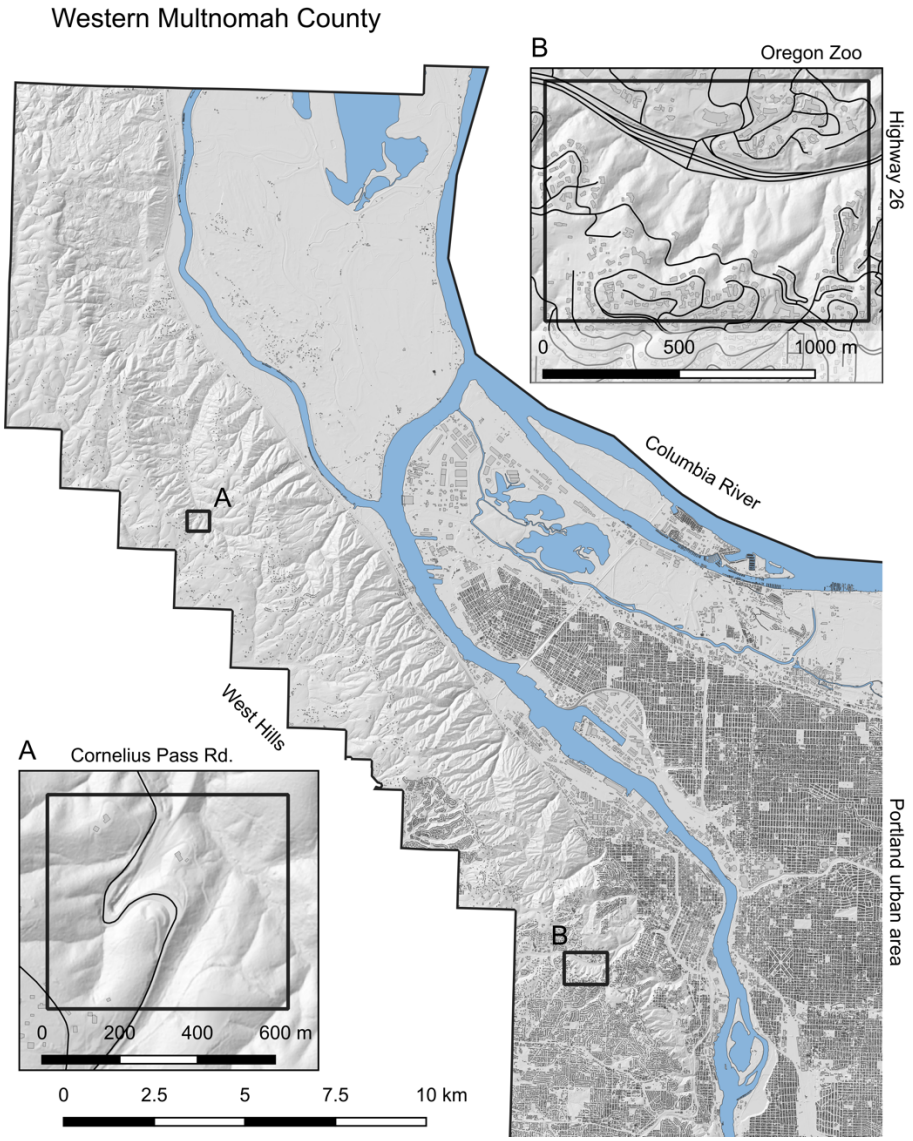

Figure A2.2.1. Subareas in Western Multnomah County, near Portland, Oregon, used to evaluate the precipitation-induced rotational slump and shallow landslide models. (*A*) "S" bend on Cornelius Pass Road and (*B*) study area on Highway 26, south of the Oregon Zoo.

Cornelius Pass Road has experienced repeated episodes of landsliding (Burns and Mickelson, 2009; Multnomah County, 2017; KGW8, 2017). I examined a 620 x 550 m area encompassing the "S" curve of northwest Cornelius Pass Road near milepost 3. This area is the subject of an ongoing Multnomah county project to improve safety along Cornelius Pass Road (Multnomah County, 2019; Multnomah County, 2020). This area is of particular interest because it has suffered repeated instances of deep-seated landsliding. Two landslides occurred on eastern side of the "S" curve during a February 1996 storm (Colle and Mass, 2000). A large (152 m long, 30 m wide) ~ 30 m deep rotational earth slide occurred near the upper driveway of the residence at 12814 NW Cornelius Pass Road, and a smaller (30 m long, 3 m wide, 21 m deep), second earth flow occurred approximately 100 m to the northwest around the "S" bend (Burns et al., 1998).

During the planning phase of the 2019 Cornelius Pass Road improvement project, the design team discovered a historic (undated) landslide north of the lower driveway of the 12814 NW Cornelius Pass Road residence. The landslide is up to 21 m (70 ft) deep (Multnomah County, 2017). Additionally, the eastern curve of the "S" bend has shown long-term evidence of ongoing slope deformation. Google imagery dating back to July 2000 shows denuded hillslopes consistent with shallow landsliding and a growing network of slope parallel cracks in the road surface and shoulder suggesting deep-seated landsliding. Two shallow landslides appear to have occurred between 1990 – 2000 and 2002 – 2005 (**Figures A2.2.2** and **A2.2.3**). A network of ~ 50 m long sub-parallel arcuate cracks developed between 2002 – 2005 in the wide paved pullout adjacent to the upper driveway (**Figure A2.2.3**). Based on historical Google imagery, since 2008, at least four sets of slope-parallel asphalt patches have been applied to the road surface adjacent to these cracks and to the south above the shallow landslide scars suggesting slow, ongoing deep-seated deformation of the slope below the curve (**Figure A2.2.4** and **A2.2.5**).

I compared the results of the three-dimensional rotational slump model described in **Section 2.5.4** to that of Scoops3D (Reid et al., 2015). Implicit in the multimodal approach is the assumption that a given mode of landsliding will occur only within a range of susceptible slope inclinations. In this test, I applied the rotational slump model to slopes of 10 – 45 degrees. However, in order to make a more direct comparison to Scoops3D, which does not enforce a similar constraint, I also ran the rotational slump model on a functionally unconstrained slope range of 1 – 90 degrees. I examined the global minimum factor of safety and the size of the associated failing mass across the ranges of input parameters given in **Table A2.2.1**. In order to exclude very small, shallow failures, I applied a volume restriction to Scoops3D of 10,000 – 1,000,000 m^3. Factors of safety were calculated in Scoops3D using both the Bishop's and Ordinary methods of slices.

Table A2.2.1. Ranges of parameter values testing using the rotational slump model and Scoops3D. Central values (held constant in the other runs) were: cohesion: 35 kPa, friction angle: 42 degrees, water table depth: 10 m, pixel resolution: 2 m, dry unit weight: 18 kN/m^3, and local relief window size: 150 m.

Parameter	*Range*
Cohesion (kPa)	0.1 – 62
Friction angle (degrees)	28 – 47
Water table depth (m)	2 – 20
Pixel resolution (m)	2 – 15
Dry unit weight (kN/m^3)	16 – 21
Local relief window size (m)	25 – 300

Results of the sensitivity analysis are shown in **Figures A2.2.6 – A2.2.8**. The rotational slump model and Scoops3D respond similarly to changes in cohesion, friction angle, and dry unit weight (**Table A2.2.2**). Scoops3D is slightly more sensitive than the rotational slump model to changes in the water table depth and produces marginally (0.08 – 0.18) more conservative estimates of the global minimum factor of safety when the water table is close to the ground surface. The rotational slump model is highly sensitive to the window size used to calculate local relief, as this is the driving parameter in pre-determining the critical slip surface.

Table A2.2.2. Minimum and maximum differences in the global minimum factor of safety between the rotational slump model and Scoops3D.

Parameter	*Minimum*	*Maximum*
Cohesion (kPa)	0.001	0.136
Friction angle (degrees)	0	0.101
Water table depth (m)	0.001	**0.180**
Pixel resolution (m)	0.001	**0.321**
Dry unit weight (kN/m^3)	0	0.071
Local relief window size (m)	0.001	**1.101**

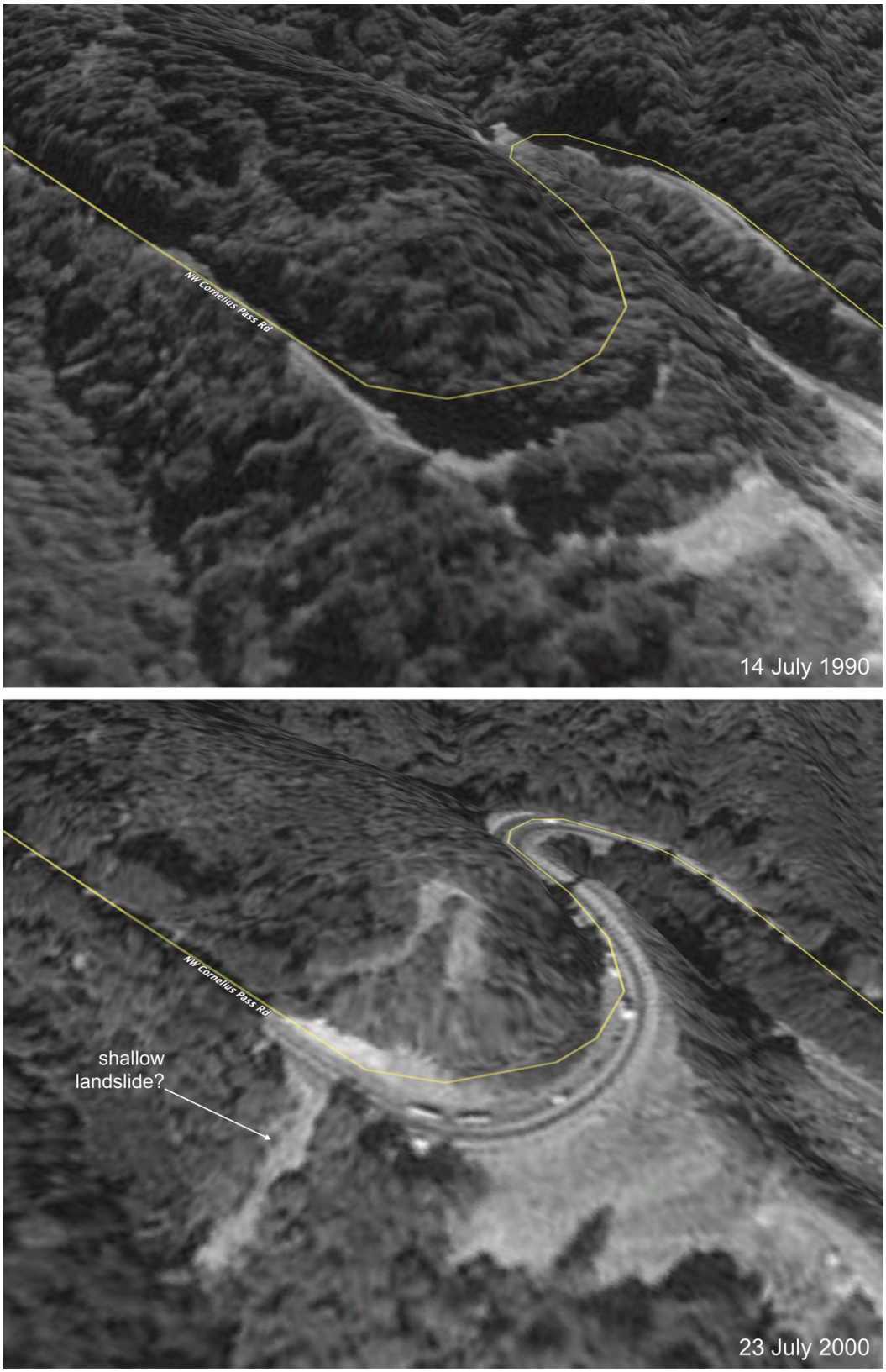

Figure A2.2.2. Shallow landslide between 1990 and 2000

Figure A2.2.3. Shallow landslide between 2002 and 2005. Cracks have begun to develop in the shoulder

Figure A2.2.4. Multiple set of slope parallel asphalt patches suggesting ongoing movement along a deep-seated failure plane

Figure A2.2.5. Well developed cracks in the shoulder and pullout above 12814 NW Cornelius Pass Rd. suggesting ongoing deep-seated slope deformation.

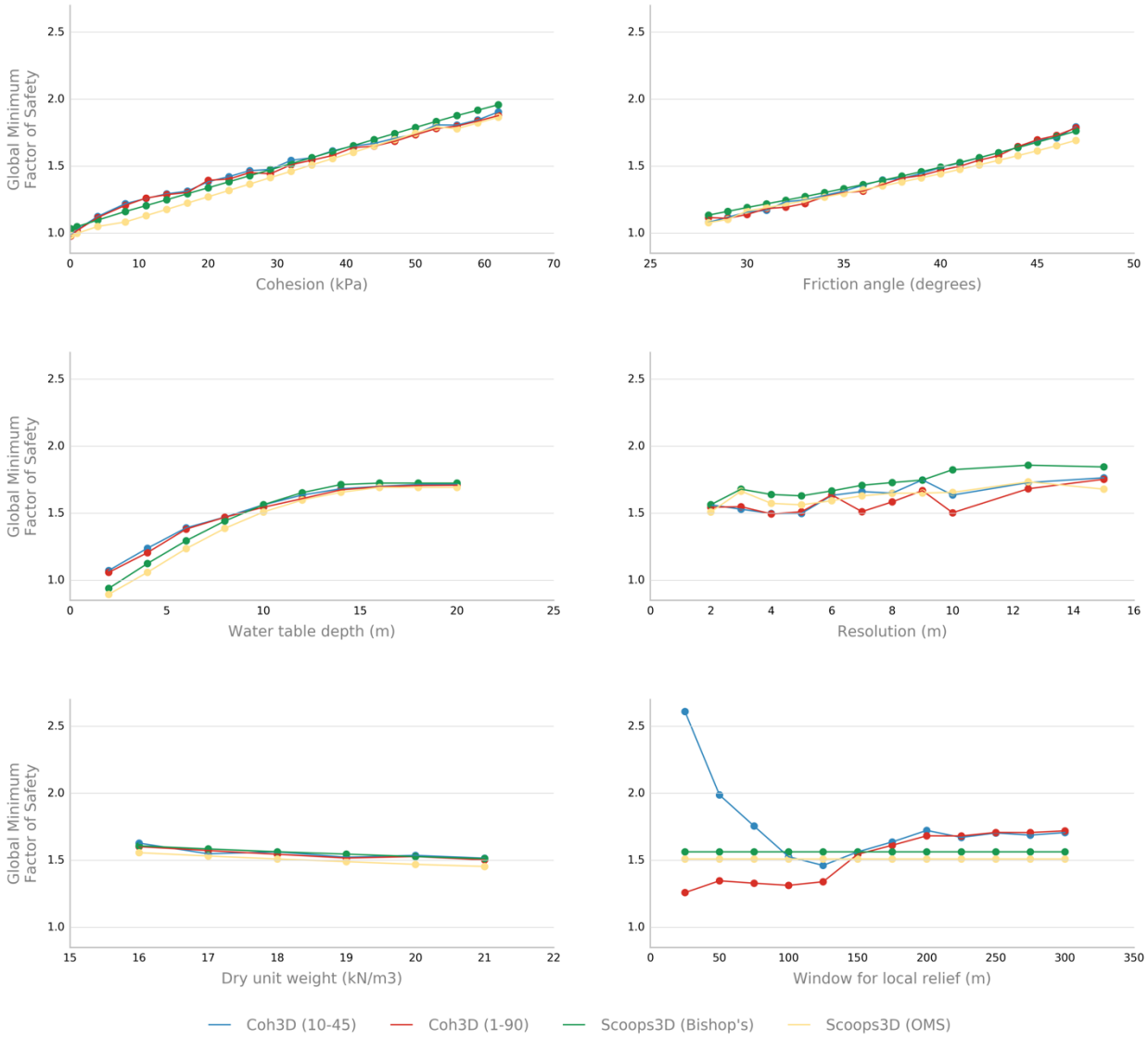

Figure A2.2.6. Sensitivity of the global minimum factor of safety to changes in input parameters. "Coh3D" refers to the rotational slump model described in **Section 2.5.4**.

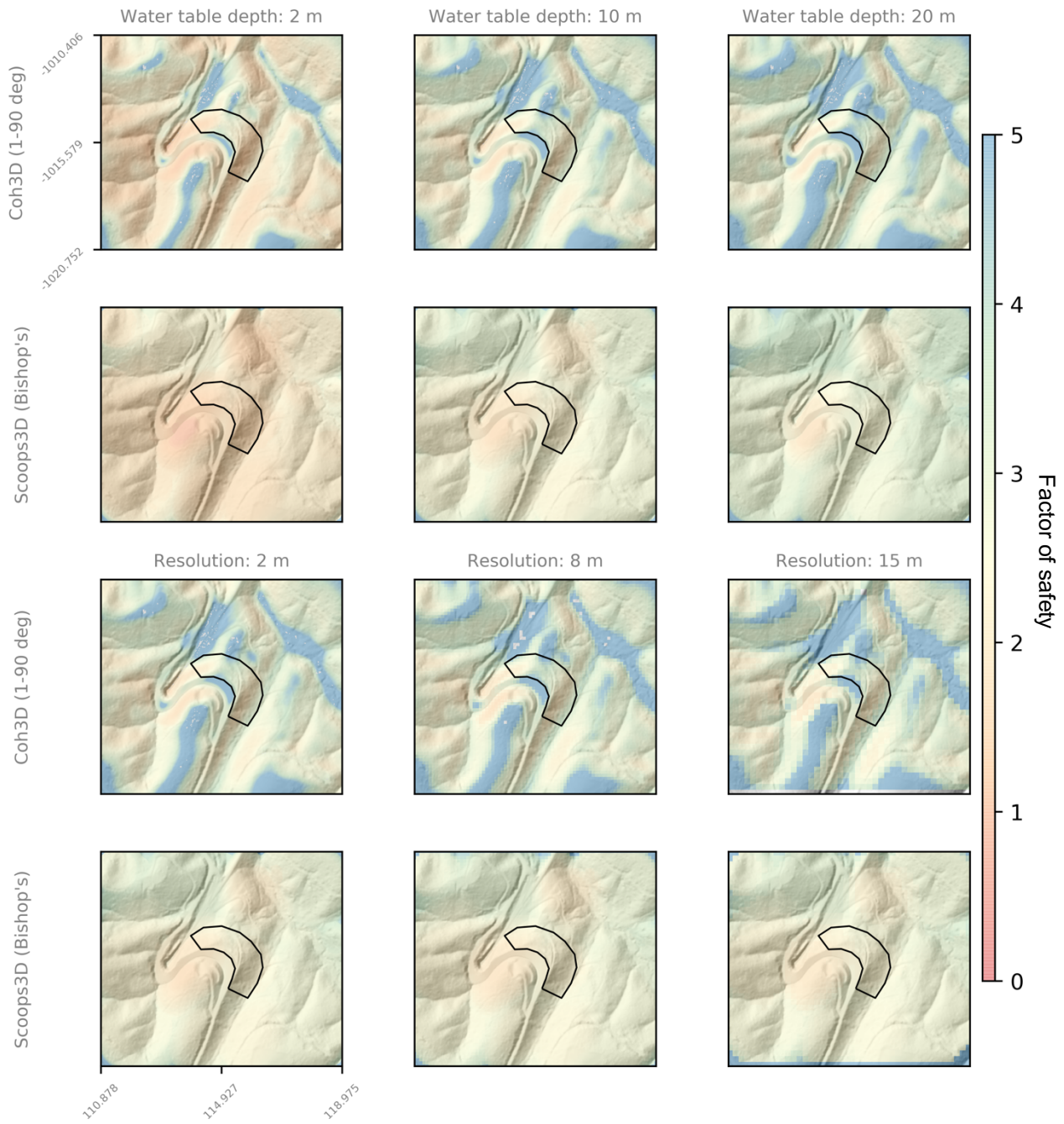

Figure A2.2.7. Spatial sensitivity of the factor of safety to changes in water table depth DEM resolution.

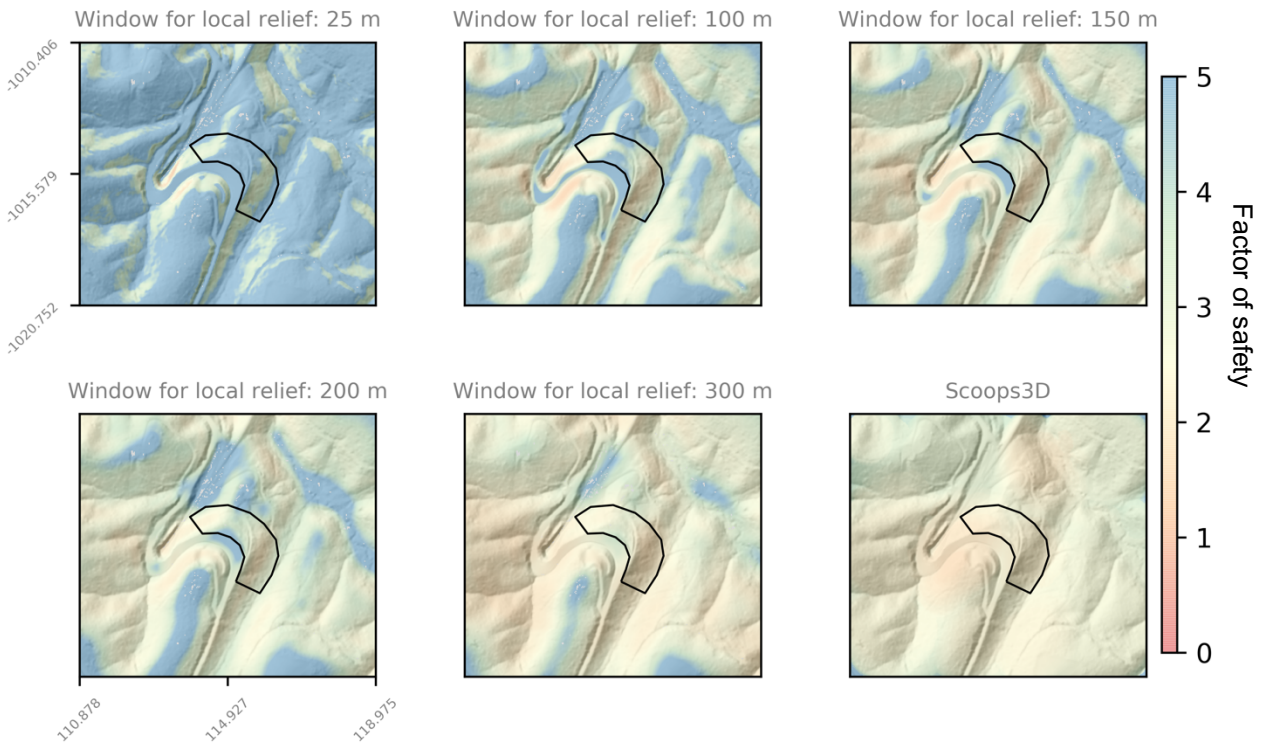

Figure A2.2.8. Spatial sensitivity of the factor of safety to changes in the moving window size for calculating local relief.

A2.2.2 – TRIGRS sensitivity analysis in the Portland West Hills, Oregon

A key limitation of the program TRIGRS (Baum et al., 2008) is the computational time to process large regions, which can approach the order of days for a single simulation at high-resolutions (Alvioli and Baum, 2016). Increases in parameters such as the number of time steps ("tx"), number of vertical increments ("nzs"), and number of grid cells (controlled by the resolution) directly increase computational time (Baum et al., 2008; Alvioli and Baum, 2016). In order to efficiently run TRIGRS within a Monte Carlo simulation, I tested the sensitivity of TRIGRS results in a ~ 1 km^2 subarea of Portland's West Hills (**Figure 2.2.1 B**) to changes in spatial and temporal discretization in order to optimize the input parameterization. I also tested the influence of changes to the initial water table depth, analysis duration after the initial input rainfall, soil thickness, saturated unit weight, initial infiltration rate, flow routing scheme, and shallow landslide susceptibility slope range. Thirteen shallow flows and slides were triggered by a record-setting four day rainfall event in February 1996, the locations of which are shown in **Figure A2.2.10** (Hofmeister, 2000). Only point locations are known for these events, so I also tested the influence of buffer size around each point on predictive accuracy of the shallow landslide module (**Figure 2.2.11**).

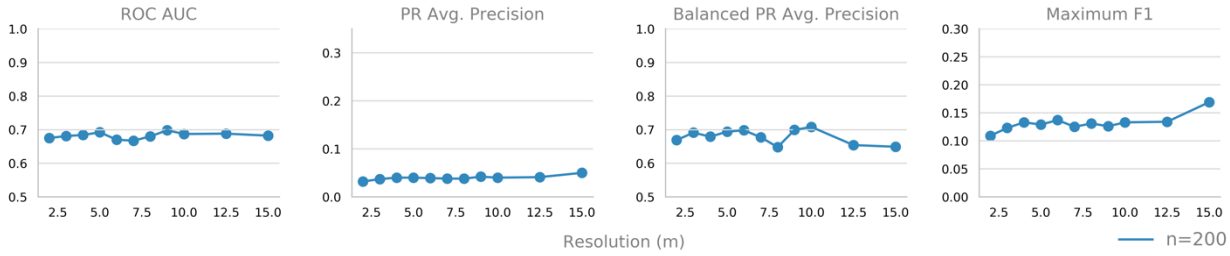

Figure A2.2.9. Sensitivity in the predictive accuracy for shallow landslides to changes in DEM resolution.

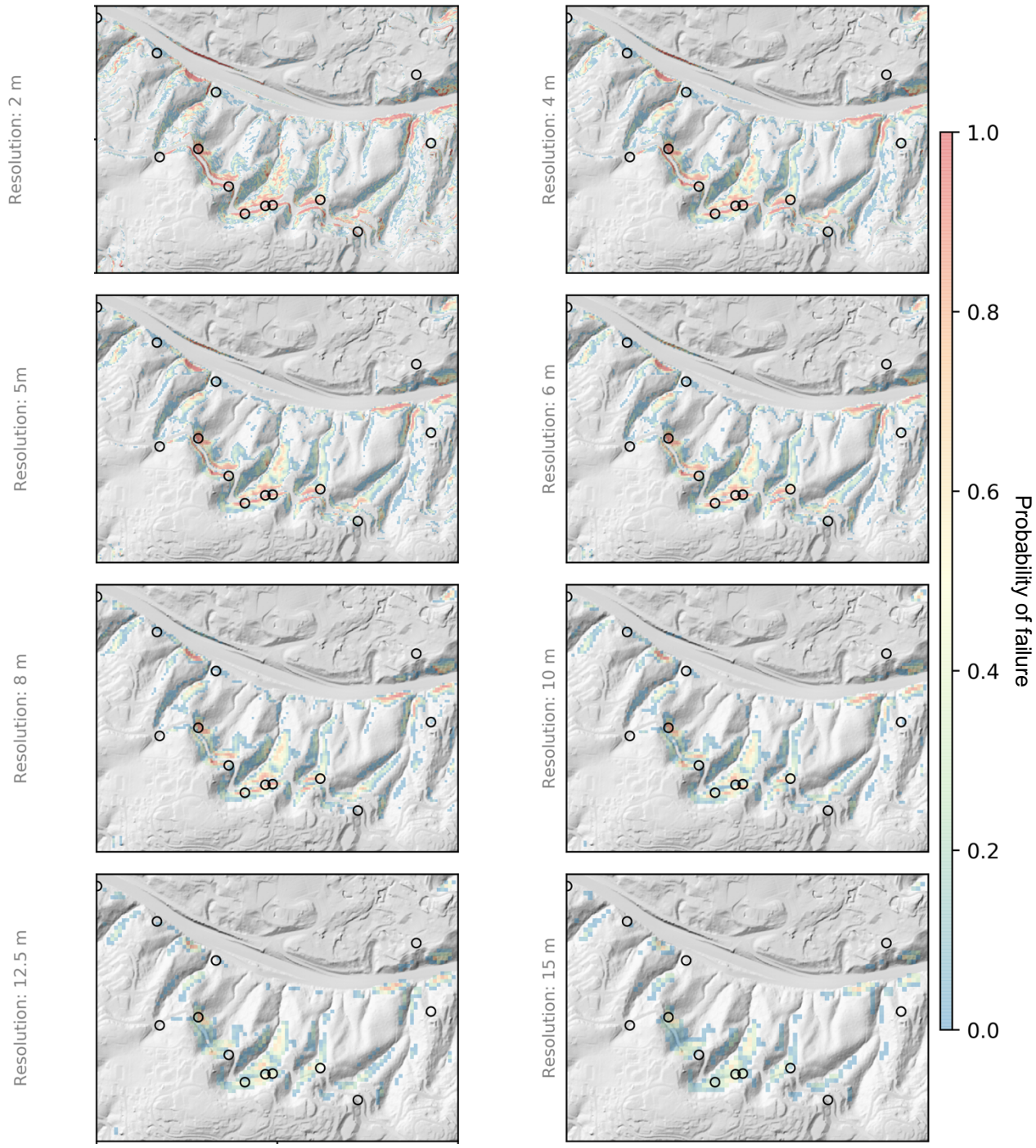

Figure A2.2.10. Spatial sensitivity of the probability of failure to changes in the DEM resolution. Black circles show the locations of shallow slides and flows triggered by the February 1996 rain storm.

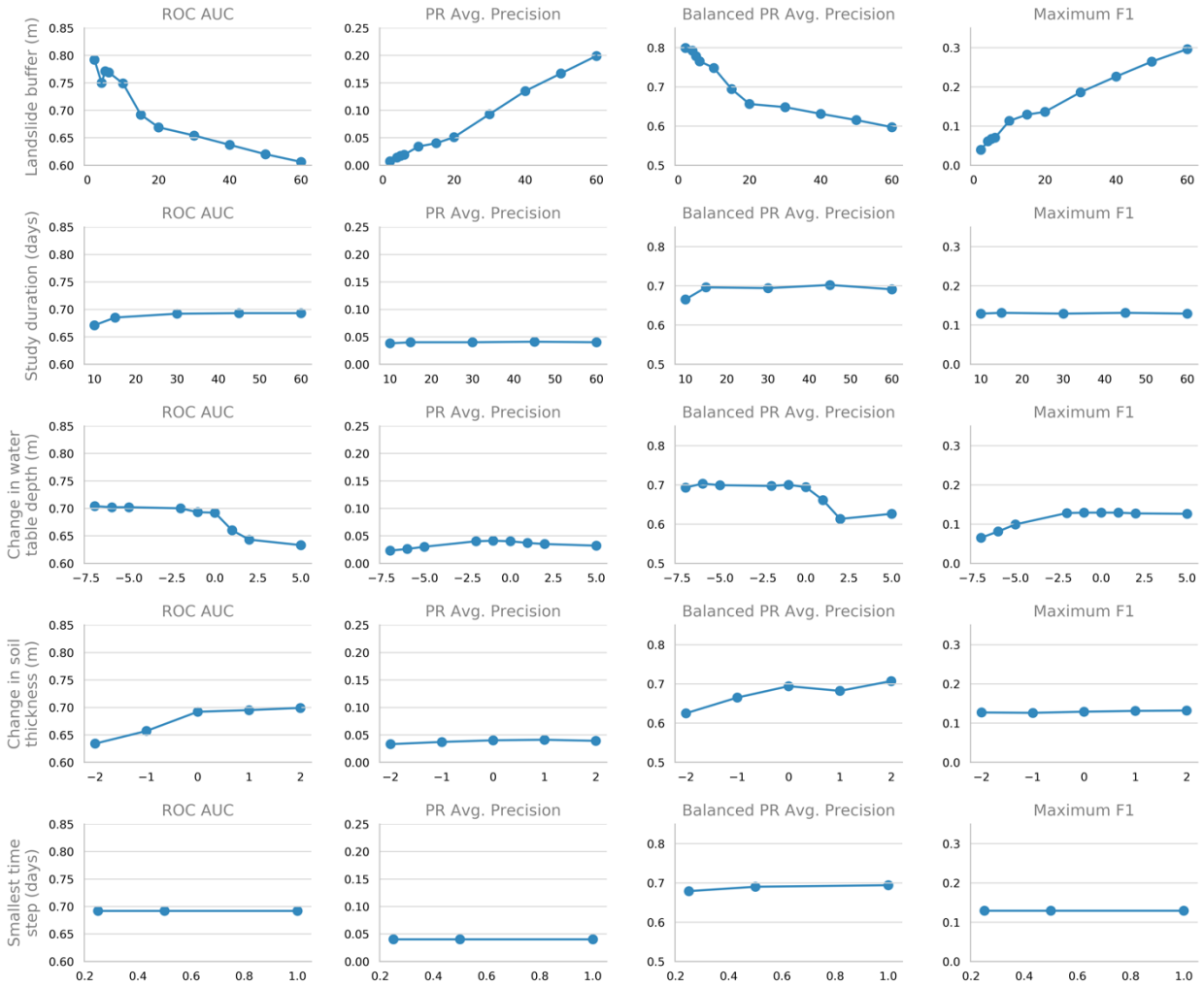

Figure A2.2.11. Sensitivity in the predictive accuracy for shallow landslides to changes in the input parameters (*part 1*).

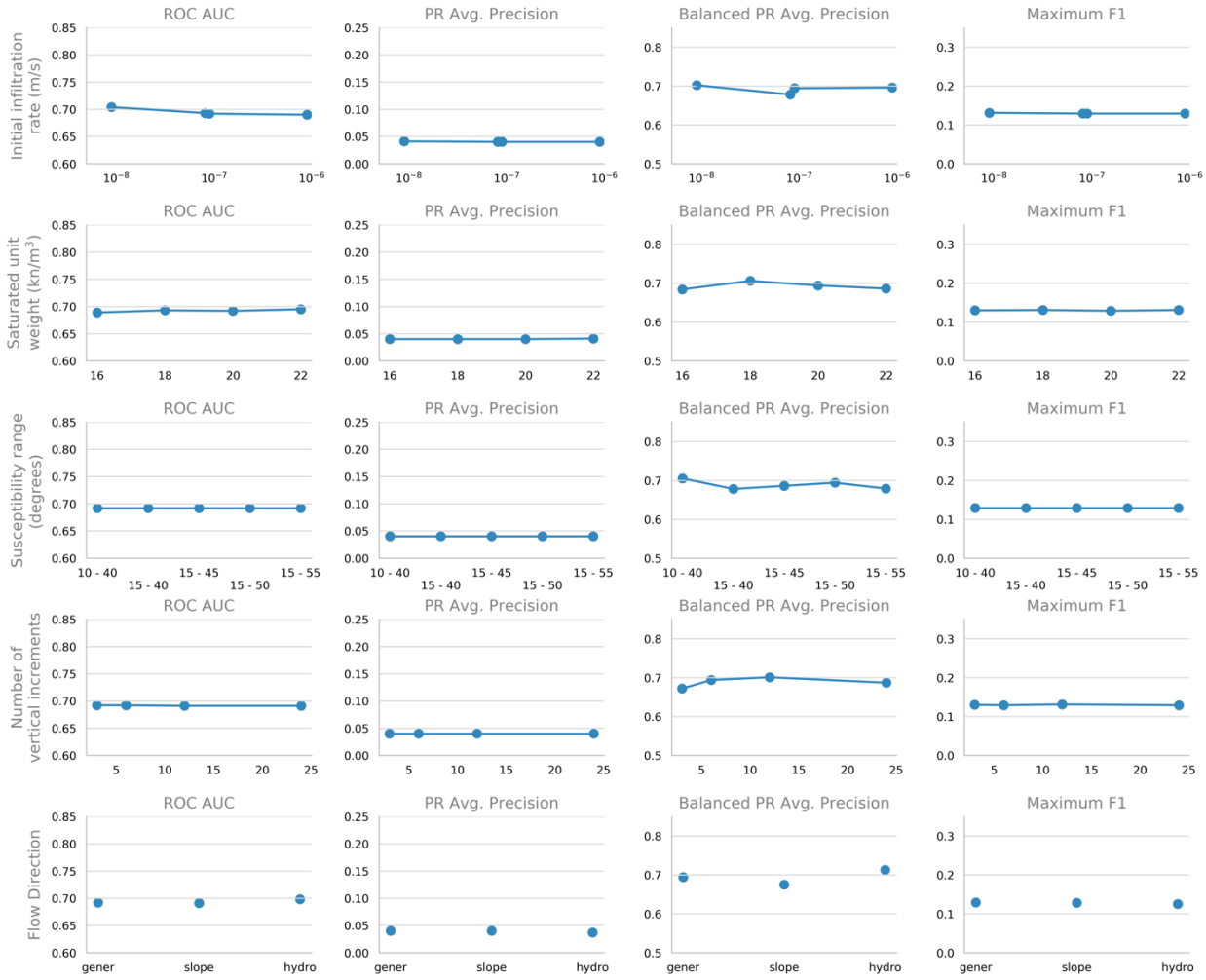

Figure A2.2.12. Sensitivity in the predictive accuracy for shallow landslides to changes in the input parameters (*part 2*). Flow directions options are general maximum pressure head ("gener"), slope parallel maximum pressure head ("slope"), and hydrostatic conditions ("hydro") as described in Baum et al. (2008).

References:

Alvioli, M., Baum, R. (2016). Parallelization of the TRIGRS model for rainfall-induced landslides using the message passing interface. *Environ. Modell. Software*, 81, 122-135.

Baum, R., Savage, W., Godt, J. (2008). TRIGRS—A Fortran program for transient rainfall infiltration and grid-based regional slope-stability analysis, version 2.0. *Open-File Report 2008-1159*. Reston, VA: United States Geological Survey

Burns, S., Burns, W., James, D., Hinkle, J. (1998). Landslides in the Portland, Oregon metropolitan area resulting from the storm of February 1996: Inventory map, database and evaluation. *A Report as Fulfillment of Metro Contract 905828*. Portland: Dept. of Geology, Portland State University.

Burns, W., Mickelson, K. (2009). Regional landslide susceptibility maps of the western half of the Linnton quadrangle, Washington and Multnomah counties, Oregon. *Technical Report to Washington County, Oregon*. Portland: Oregon Department of Geology and Mineral Industries.

Colle, B., Mass, C. (2000). The 5-9 February 1996 flooding event over the Pacific Northwest: Sensitivity studies and evaluation of the MM5 precipitation forecasts. *Mon. Wea. Rev*., 128, 593-617. https://doi.org/10.1175/1520-0493(2000)128<0593:TFFEOT>2.0.CO;2

Hofmeister, R. (2000). Slope failures in Oregon: GIS inventory for three 1996/97 storm events. *DOGAMI Special Paper 34*. Portland: Oregon Department of Geology and Mineral Industries.

KGW8 (2017). "Heavy rain causes landslides, closed roads in Portland." Available at: https://www.kgw.com/article/news/local/heavy-rain-causes-landslides-closed-roads-in-portland/283-401124128, (Accessed June 2020).

Multnomah County. (2017). Cornelius Pass Road safety improvements. Cornelius Pass Road Safety Improvements Project CAC Meeting 6 Presentation. Multnomah County, 05 January 2017.

Multnomah County. (2019). NW Cornelius Pass Road: Safety improvements project. Multnomah County Transportation Division, 28 January 2019.

Multnomah County. (2020). "Cornelius Pass project background." Available at: https://multco.us/roads/cornelius-pass-project-background, (Accessed June 2020).

Reid, M., Christian, S., Brien, D., Henderson, S. (2015). Scoops3D—Software to analyze three-dimensional slope stability throughout a digital landscape. Techniques and Methods 14-A1; Section A, Modeling Methods; *Book 14, Landslide and Debris-Flow Assessment*. Reston, VA: United States Geological Survey

Appendix 2.3 – Runout relationship data

A2.3.1 Debris flow database

ID	*Name*	*Location*	*L (m)*	*Volume (m3)*	*Reference*
DF001	Corbara	Corbara, Italy	135	750	Budetta & di Riso (2004)
DF002	Ospedaletto	Ospedaletto, Italy	450	10000	Budetta & di Riso (2004)
DF003	Pozzano	C. mara Stabia, Italy	750	40000	Budetta & di Riso (2004)
DF004	V. Montagnelle	Sarno, Italy	1050	30000	Budetta & di Riso (2004)
DF005	Avella	Avella, Italy	1200	20000	Budetta & di Riso (2004)
DF006	V. Chivano	Sarno, Italy	1400	38000	Budetta & di Riso (2004)
DF007	V. Mare	Sarno, Italy	1700	9000	Budetta & di Riso (2004)
DF008	V. S. Francesco	Quindici, Italy	2500	122000	Budetta & di Riso (2004)
DF009	V. Connola	Quindici, Italy	2800	264000	Budetta & di Riso (2004)
DF010	V. Trave-Chirico	Sarno, Italy	2920	506000	Budetta & di Riso (2004)
DF011	V. Foresta	Bracigliano, Italy	3000	85500	Budetta & di Riso (2004)
DF012	V. Tuoro	Sarno, Italy	3160	61100	Budetta & di Riso (2004)
DF013	V. S. Lucia	Sarno, Italy	3540	134500	Budetta & di Riso (2004)
DF014	499	Portland, Oregon, USA	5	47	Burns et al. (1998)
DF015	423	Portland, Oregon, USA	14	134	Burns et al. (1998)
DF016	480	Portland, Oregon, USA	15	18	Burns et al. (1998)
DF017	481	Portland, Oregon, USA	15	20	Burns et al. (1998)
DF018	646	Portland, Oregon, USA	15	708	Burns et al. (1998)
DF019	477	Portland, Oregon, USA	20	80	Burns et al. (1998)
DF020	458	Portland, Oregon, USA	20	198	Burns et al. (1998)
DF021	451	Portland, Oregon, USA	20	40	Burns et al. (1998)
DF022	452	Portland, Oregon, USA	20	22	Burns et al. (1998)
DF023	358	Portland, Oregon, USA	21	1388	Burns et al. (1998)
DF024	536	Portland, Oregon, USA	21	1982	Burns et al. (1998)
DF025	492	Portland, Oregon, USA	25	1130	Burns et al. (1998)
DF026	503	Portland, Oregon, USA	37	622	Burns et al. (1998)
DF027	485	Portland, Oregon, USA	40	40	Burns et al. (1998)
DF028	493	Portland, Oregon, USA	45	2226	Burns et al. (1998)
DF029	159	Portland, Oregon, USA	61	1190	Burns et al. (1998)
DF030	160	Portland, Oregon, USA	76	1416	Burns et al. (1998)
DF031	Newton Canyon	Malibu, California, USA	1006	5352	Campbell (1975)
DF032	Site 7	Italian, French, and Swiss Alps	1330	30000	Chiarle et al. (2007)
DF033	Site 12	Italian, French, and Swiss Alps	1650	200000	Chiarle et al. (2007)
DF034	Site 15	Italian, French, and Swiss Alps	2400	30000	Chiarle et al. (2007)
DF035	Site 8	Italian, French, and Swiss Alps	3000	150000	Chiarle et al. (2007)
DF036	Site 9	Italian, French, and Swiss Alps	3000	10000	Chiarle et al. (2007)
DF037	Site 4	Italian, French, and Swiss Alps	3400	100000	Chiarle et al. (2007)
DF038	Site 2	Italian, French, and Swiss Alps	4010	300000	Chiarle et al. (2007)
DF039	Site 10	Italian, French, and Swiss Alps	5000	1000000	Chiarle et al. (2007)
DF040	Site 16	Italian, French, and Swiss Alps	5050	32500	Chiarle et al. (2007)
DF041	Site 1	Italian, French, and Swiss Alps	5660	800000	Chiarle et al. (2007)
DF042	d094	E Pyrenees, Spain	41	60	Corominas (1996)
DF043	d092	E Pyrenees, Spain	82	1585	Corominas (1996)
DF044	d091	E Pyrenees, Spain	83	302	Corominas (1996)
DF045	d086	E Pyrenees, Spain	83	148	Corominas (1996)
DF046	d016	E Pyrenees, Spain	116	1230	Corominas (1996)
DF047	d025	E Pyrenees, Spain	120	1514	Corominas (1996)
DF048	d024	E Pyrenees, Spain	122	372	Corominas (1996)
DF049	d098	E Pyrenees, Spain	123	1202	Corominas (1996)
DF050	d073	E Pyrenees, Spain	176	3162	Corominas (1996)
DF051	d063	E Pyrenees, Spain	562	10965	Corominas (1996)
DF052	d033	E Pyrenees, Spain	625	9333	Corominas (1996)

DF053	Port Moody	British Columbia, Canada	940	5012	Corominas (1996)
DF054	Inverness	California, USA	1300	302	Corominas (1996)
DF055	Devastation	British Columbia, Canada	6500	28183829	Corominas (1996)
DF056	Rubble Creek	British Columbia, Canada	6900	25118864	Corominas (1996)
DF057	Nevado Ruiz	Columbia	87000	40738028	Corominas (1996)
DF058	Nissuntjarro	Sweden	820	10000	Corominas (1996)
DF059	Ontake	Japan	10900	36307805	Corominas (1996)
DF060	5	Fiames, Italy	254	5200	D'Agostino et al. (2009)
DF061	6	Fiames, Italy	375	2100	D'Agostino et al. (2009)
DF062	1	Fiames, Italy	472	15000	D'Agostino et al. (2009)
DF063	4	Fiames, Italy	481	11000	D'Agostino et al. (2009)
DF064	2	Fiames, Italy	634	10600	D'Agostino et al. (2009)
DF065	3	Fiames, Italy	800	46800	D'Agostino et al. (2009)
DF066	336	Nepal	210	21400	Dahlquist & West (2019)
DF067	23	Nepal	270	91700	Dahlquist & West (2019)
DF068	319	Nepal	300	297900	Dahlquist & West (2019)
DF069	335	Nepal	320	1500	Dahlquist & West (2019)
DF070	240	Nepal	340	24700	Dahlquist & West (2019)
DF071	302	Nepal	350	5800	Dahlquist & West (2019)
DF072	79	Nepal	350	13600	Dahlquist & West (2019)
DF073	47	Nepal	370	1200	Dahlquist & West (2019)
DF074	72	Nepal	370	24900	Dahlquist & West (2019)
DF075	268	Nepal	380	7100	Dahlquist & West (2019)
DF076	288	Nepal	400	161400	Dahlquist & West (2019)
DF077	330	Nepal	420	700	Dahlquist & West (2019)
DF078	69	Nepal	420	10000	Dahlquist & West (2019)
DF079	247	Nepal	430	4300	Dahlquist & West (2019)
DF080	76	Nepal	440	2800	Dahlquist & West (2019)
DF081	119	Nepal	450	6500	Dahlquist & West (2019)
DF082	121	Nepal	450	18200	Dahlquist & West (2019)
DF083	290	Nepal	470	25400	Dahlquist & West (2019)
DF084	326	Nepal	470	26700	Dahlquist & West (2019)
DF085	246	Nepal	480	60900	Dahlquist & West (2019)
DF086	38	Nepal	500	3900	Dahlquist & West (2019)
DF087	311	Nepal	500	1300	Dahlquist & West (2019)
DF088	80	Nepal	500	700	Dahlquist & West (2019)
DF089	275	Nepal	520	4200	Dahlquist & West (2019)
DF090	261	Nepal	550	57400	Dahlquist & West (2019)
DF091	248	Nepal	550	5400	Dahlquist & West (2019)
DF092	135	Nepal	590	3800	Dahlquist & West (2019)
DF093	264	Nepal	590	1000	Dahlquist & West (2019)
DF094	325	Nepal	590	4000	Dahlquist & West (2019)
DF095	293	Nepal	600	3100	Dahlquist & West (2019)
DF096	306	Nepal	610	900	Dahlquist & West (2019)
DF097	286	Nepal	610	1700	Dahlquist & West (2019)
DF098	291	Nepal	630	10500	Dahlquist & West (2019)
DF099	71	Nepal	640	104100	Dahlquist & West (2019)
DF100	294	Nepal	660	7900	Dahlquist & West (2019)
DF101	70	Nepal	660	44500	Dahlquist & West (2019)
DF102	110	Nepal	670	25900	Dahlquist & West (2019)
DF103	278	Nepal	680	13700	Dahlquist & West (2019)
DF104	12	Nepal	680	5100	Dahlquist & West (2019)
DF105	107	Nepal	690	8700	Dahlquist & West (2019)
DF106	297	Nepal	700	14200	Dahlquist & West (2019)
DF107	95	Nepal	700	3300	Dahlquist & West (2019)
DF108	5	Nepal	730	13800	Dahlquist & West (2019)
DF109	270	Nepal	760	12000	Dahlquist & West (2019)
DF110	304	Nepal	760	3000	Dahlquist & West (2019)

DF111	263	Nepal	780	5200	Dahlquist & West (2019)
DF112	287	Nepal	790	392500	Dahlquist & West (2019)
DF113	227	Nepal	800	9400	Dahlquist & West (2019)
DF114	327	Nepal	800	3200	Dahlquist & West (2019)
DF115	233	Nepal	800	458800	Dahlquist & West (2019)
DF116	17	Nepal	840	2500	Dahlquist & West (2019)
DF117	83	Nepal	850	500	Dahlquist & West (2019)
DF118	349	Nepal	850	22400	Dahlquist & West (2019)
DF119	269	Nepal	860	11900	Dahlquist & West (2019)
DF120	308	Nepal	870	33000	Dahlquist & West (2019)
DF121	272	Nepal	880	1100	Dahlquist & West (2019)
DF122	40	Nepal	880	19800	Dahlquist & West (2019)
DF123	245	Nepal	900	800	Dahlquist & West (2019)
DF124	118	Nepal	900	3100	Dahlquist & West (2019)
DF125	39	Nepal	910	800	Dahlquist & West (2019)
DF126	183	Nepal	920	19400	Dahlquist & West (2019)
DF127	249	Nepal	920	1600	Dahlquist & West (2019)
DF128	139	Nepal	920	10400	Dahlquist & West (2019)
DF129	323	Nepal	930	800	Dahlquist & West (2019)
DF130	320	Nepal	940	1400	Dahlquist & West (2019)
DF131	250	Nepal	970	1300	Dahlquist & West (2019)
DF132	60	Nepal	990	15100	Dahlquist & West (2019)
DF133	142	Nepal	1000	13900	Dahlquist & West (2019)
DF134	141	Nepal	1010	19200	Dahlquist & West (2019)
DF135	332	Nepal	1060	20100	Dahlquist & West (2019)
DF136	296	Nepal	1060	141600	Dahlquist & West (2019)
DF137	113	Nepal	1060	1700	Dahlquist & West (2019)
DF138	348	Nepal	1060	43600	Dahlquist & West (2019)
DF139	347	Nepal	1060	16900	Dahlquist & West (2019)
DF140	57	Nepal	1060	16900	Dahlquist & West (2019)
DF141	116	Nepal	1080	800	Dahlquist & West (2019)
DF142	309	Nepal	1090	21100	Dahlquist & West (2019)
DF143	266	Nepal	1190	4500	Dahlquist & West (2019)
DF144	324	Nepal	1190	6200	Dahlquist & West (2019)
DF145	239	Nepal	1210	12000	Dahlquist & West (2019)
DF146	328	Nepal	1210	400	Dahlquist & West (2019)
DF147	322	Nepal	1230	3000	Dahlquist & West (2019)
DF148	109	Nepal	1240	7200	Dahlquist & West (2019)
DF149	68	Nepal	1250	50600	Dahlquist & West (2019)
DF150	350	Nepal	1270	4400	Dahlquist & West (2019)
DF151	75	Nepal	1280	15600	Dahlquist & West (2019)
DF152	87	Nepal	1300	131400	Dahlquist & West (2019)
DF153	41	Nepal	1320	9600	Dahlquist & West (2019)
DF154	108	Nepal	1350	42700	Dahlquist & West (2019)
DF155	63	Nepal	1370	2400	Dahlquist & West (2019)
DF156	85	Nepal	1380	3300	Dahlquist & West (2019)
DF157	229	Nepal	1430	17700	Dahlquist & West (2019)
DF158	117	Nepal	1440	1400	Dahlquist & West (2019)
DF159	292	Nepal	1500	6500	Dahlquist & West (2019)
DF160	106	Nepal	1520	3000	Dahlquist & West (2019)
DF161	276	Nepal	1560	9100	Dahlquist & West (2019)
DF162	98	Nepal	1630	18500	Dahlquist & West (2019)
DF163	271	Nepal	1670	21400	Dahlquist & West (2019)
DF164	225	Nepal	1720	91600	Dahlquist & West (2019)
DF165	96	Nepal	1750	33200	Dahlquist & West (2019)
DF166	313	Nepal	1760	8500	Dahlquist & West (2019)
DF167	86	Nepal	1780	4300	Dahlquist & West (2019)
DF168	282	Nepal	1830	7200	Dahlquist & West (2019)

DF169	127	Nepal	1880	1600	Dahlquist & West (2019)
DF170	48	Nepal	2000	3900	Dahlquist & West (2019)
DF171	131	Nepal	2100	16800	Dahlquist & West (2019)
DF172	46	Nepal	2140	2700	Dahlquist & West (2019)
DF173	81	Nepal	2150	7100	Dahlquist & West (2019)
DF174	255	Nepal	2210	3600	Dahlquist & West (2019)
DF175	285	Nepal	2230	17200	Dahlquist & West (2019)
DF176	224	Nepal	2380	13500	Dahlquist & West (2019)
DF177	265	Nepal	2510	2400	Dahlquist & West (2019)
DF178	226	Nepal	2600	31000	Dahlquist & West (2019)
DF179	283	Nepal	2690	2400	Dahlquist & West (2019)
DF180	97	Nepal	2800	156100	Dahlquist & West (2019)
DF181	329	Nepal	3000	579600	Dahlquist & West (2019)
DF182	244	Nepal	3210	9300	Dahlquist & West (2019)
DF183	310	Nepal	3230	5000	Dahlquist & West (2019)
DF184	184	Nepal	3270	6700	Dahlquist & West (2019)
DF185	132	Nepal	3300	35000	Dahlquist & West (2019)
DF186	203	Nepal	3600	10400	Dahlquist & West (2019)
DF187	172	Nepal	3930	74700	Dahlquist & West (2019)
DF188	123	Nepal	4080	9400	Dahlquist & West (2019)
DF189	14	Nepal	5160	72200	Dahlquist & West (2019)
DF190	125	Nepal	5700	2600	Dahlquist & West (2019)
DF191	94	Nepal	6190	17800	Dahlquist & West (2019)
DF192	126	Nepal	9120	37500	Dahlquist & West (2019)
DF193	207	Nepal	9130	79900	Dahlquist & West (2019)
DF194	128	Nepal	10130	1500	Dahlquist & West (2019)
DF195	Khait, Tajikistan	Tajikistan	11000	400000000	Evans et al. (2006)
DF196	Nomash	Vancouver Is, British Columbia, Canada	2270	650000	Evans et al. (2006), McDougall & Hungr (2005)
DF197	Harold Price	British Columbia, Canada	4000	1600000	Geertsema et al. (2006)
DF198	Zymoetz	British Columbia, Canada	4300	1600000	Geertsema et al. (2006), McDougall et al. (2006)
DF199	Jiama / Gyama	China	1980	2000000	Guo et al. (2016)
DF200	Kolka-Karmadon	Russia	20000	115000000	Guo et al. (2016), Huggel et al. (2005)
DF201		West Nepal	309	5006	Hearn (2011)
DF202		West Nepal	315	5888	Hearn (2011)
DF203		West Nepal	364	1609	Hearn (2011)
DF204		West Nepal	376	8744	Hearn (2011)
DF205		West Nepal	382	5430	Hearn (2011)
DF206		West Nepal	406	5713	Hearn (2011)
DF207		West Nepal	412	4809	Hearn (2011)
DF208		West Nepal	497	23859	Hearn (2011)
DF209		West Nepal	587	179376	Hearn (2011)
DF210		West Nepal	593	135056	Hearn (2011)
DF211		West Nepal	941	44779	Hearn (2011)
DF212		West Nepal	952	742084	Hearn (2011)
DF213		West Nepal	1092	624845	Hearn (2011)
DF214		West Nepal	1189	1016666	Hearn (2011)
DF215		West Nepal	1196	470575	Hearn (2011)
DF216		West Nepal	1197	16763	Hearn (2011)
DF217		West Nepal	1288	48604	Hearn (2011)
DF218		West Nepal	1395	6242705	Hearn (2011)
DF219		West Nepal	1519	70762	Hearn (2011)
DF220		West Nepal	2000	104138	Hearn (2011)
DF221		West Nepal	2200	2157953	Hearn (2011)
DF222		West Nepal	2292	381410	Hearn (2011)
DF223		West Nepal	2486	2565617	Hearn (2011)
DF224		West Nepal	2602	413952	Hearn (2011)
DF225		West Nepal	3398	6468199	Hearn (2011)

DF226	Cerro Rabicano	Metropolitana, Chile	17000	15000000	Hungr & Evans (2004)
DF227	Nevados Huascaran	Peru	15600	53000000	Hungr & Evans (2004), Plafker & Ericksen (1978)
DF228	Outward Bound School	Hong Kong	63	900	Hunter & Fell (2001)
DF229	Sha Tin Heights Road Slide B	Hong Kong	105	170	Hunter & Fell (2001)
DF230	Ma On Shan Road	Hong Kong	107	3000	Hunter & Fell (2001)
DF231	Lantau Island C1	Hong Kong	215	1000	Hunter & Fell (2001)
DF232	Cefn Glas	South Wales, UK	310	45000	Hunter & Fell (2001)
DF233	Maerdy	South Wales, UK	440	70000	Hunter & Fell (2001)
DF234	Brownie (FCL)	British Columbia, Canada	580	50000	Hunter & Fell (2001)
DF235	Aberfan-Tip 4	South Wales, UK	600	170000	Hunter & Fell (2001)
DF236	East (GRH)	British Columbia, Canada	680	720000	Hunter & Fell (2001)
DF237	Abergorchi	South Wales, UK	740	100000	Hunter & Fell (2001)
DF238	East (GRH)	British Columbia, Canada	750	580000	Hunter & Fell (2001)
DF239	East (GRH)	British Columbia, Canada	780	480000	Hunter & Fell (2001)
DF240	Tsing Shan	Hong Kong	875	13000	Hunter & Fell (2001)
DF241	Brownie (FCL)	British Columbia, Canada	925	500000	Hunter & Fell (2001)
DF242	Brownie (FCL)	British Columbia, Canada	950	140000	Hunter & Fell (2001)
DF243	Pak Sha Wan	Hong Kong	80	150	Hunter & Fell (2001), Ayotte & Hungr (1998)
DF244	Pat Sing Leng 1	Hong Kong	100	300	Hunter & Fell (2001), Ayotte & Hungr (1998)
DF245	TC-5A/13, Tung Chung	Hong Kong	122	700	Hunter & Fell (2001), Ayotte & Hungr (1998)
DF246	JK 419, New Territories	Hong Kong	191	1000	Hunter & Fell (2001), Ayotte & Hungr (1998)
DF247	JK 529, New Territories	Hong Kong	227	400	Hunter & Fell (2001), Ayotte & Hungr (1998)
DF248	TC-5A/2, Tung Chung	Hong Kong	312	1500	Hunter & Fell (2001), Ayotte & Hungr (1998)
DF249	Pat Sing Leng 2	Hong Kong	600	50	Hunter & Fell (2001), Ayotte & Hungr (1998)
DF250	Sha Tau Kok	Hong Kong	1005	1500	Hunter & Fell (2001), Ayotte & Hungr (1998)
DF251	La Conchita	California, USA	350	200000	Jibson (2005)
DF252	OR4	New Zealand	239	3992	Kailey (2013)
DF253	C2	New Zealand	478	1091	Kailey (2013)
DF254	BH4	New Zealand	487	387	Kailey (2013)
DF255	OR3	New Zealand	522	5897	Kailey (2013)
DF256	BH2	New Zealand	536	638	Kailey (2013)
DF257	BH1	New Zealand	821	336	Kailey (2013)
DF258	OR1	New Zealand	823	10870	Kailey (2013)
DF259	C6	New Zealand	823	2350	Kailey (2013)
DF260	OR2	New Zealand	824	2170	Kailey (2013)
DF261	C14	New Zealand	836	570	Kailey (2013)
DF262	C11	New Zealand	838	445	Kailey (2013)
DF263	C1	New Zealand	841	757	Kailey (2013)
DF264	C12	New Zealand	907	2924	Kailey (2013)
DF265	C13	New Zealand	941	1328	Kailey (2013)
DF266	BH3	New Zealand	1039	2606	Kailey (2013)
DF267	C7	New Zealand	1054	883	Kailey (2013)
DF268	C3	New Zealand	1388	2999	Kailey (2013)
DF269		Japan	32	17000	Kimura et al. (2014)
DF270		Japan	53	68000	Kimura et al. (2014)
DF271		Japan	65	110000	Kimura et al. (2014)
DF272		Japan	65	22000	Kimura et al. (2014)
DF273		Japan	69	23000	Kimura et al. (2014)
DF274		Japan	70	17000	Kimura et al. (2014)
DF275		Japan	70	50000	Kimura et al. (2014)
DF276		Japan	75	320000	Kimura et al. (2014)
DF277		Japan	75	29000	Kimura et al. (2014)

DF278	Japan	81	58000	Kimura et al. (2014)
DF279	Japan	84	95000	Kimura et al. (2014)
DF280	Japan	114	300000	Kimura et al. (2014)
DF281	Japan	120	160000	Kimura et al. (2014)
DF282	Japan	125	170000	Kimura et al. (2014)
DF283	Japan	140	270000	Kimura et al. (2014)
DF284	Japan	140	45000	Kimura et al. (2014)
DF285	Japan	140	320000	Kimura et al. (2014)
DF286	Japan	145	140000	Kimura et al. (2014)
DF287	Japan	150	50000	Kimura et al. (2014)
DF288	Japan	155	230000	Kimura et al. (2014)
DF289	Japan	160	1500000	Kimura et al. (2014)
DF290	Japan	170	150000	Kimura et al. (2014)
DF291	Japan	190	970000	Kimura et al. (2014)
DF292	Japan	190	210000	Kimura et al. (2014)
DF293	Japan	200	1100000	Kimura et al. (2014)
DF294	Japan	200	640000	Kimura et al. (2014)
DF295	Japan	216	650000	Kimura et al. (2014)
DF296	Japan	225	740000	Kimura et al. (2014)
DF297	Japan	250	150000	Kimura et al. (2014)
DF298	Japan	258	560000	Kimura et al. (2014)
DF299	Japan	260	470000	Kimura et al. (2014)
DF300	Japan	260	270000	Kimura et al. (2014)
DF301	Japan	270	920000	Kimura et al. (2014)
DF302	Japan	275	1200000	Kimura et al. (2014)
DF303	Japan	285	560000	Kimura et al. (2014)
DF304	Japan	290	750000	Kimura et al. (2014)
DF305	Japan	300	1700000	Kimura et al. (2014)
DF306	Japan	320	760000	Kimura et al. (2014)
DF307	Japan	320	50000	Kimura et al. (2014)
DF308	Japan	321	29000	Kimura et al. (2014)
DF309	Japan	328	3600000	Kimura et al. (2014)
DF310	Japan	345	4300000	Kimura et al. (2014)
DF311	Japan	345	1100000	Kimura et al. (2014)
DF312	Japan	370	610000	Kimura et al. (2014)
DF313	Japan	390	280000	Kimura et al. (2014)
DF314	Japan	390	130000	Kimura et al. (2014)
DF315	Japan	400	710000	Kimura et al. (2014)
DF316	Japan	410	420000	Kimura et al. (2014)
DF317	Japan	420	3200000	Kimura et al. (2014)
DF318	Japan	440	240000	Kimura et al. (2014)
DF319	Japan	460	1400000	Kimura et al. (2014)
DF320	Japan	478	3000000	Kimura et al. (2014)
DF321	Japan	480	6700000	Kimura et al. (2014)
DF322	Japan	480	110000	Kimura et al. (2014)
DF323	Japan	530	6800000	Kimura et al. (2014)
DF324	Japan	600	9700000	Kimura et al. (2014)
DF325	Japan	680	750000	Kimura et al. (2014)
DF326	Japan	700	6000000	Kimura et al. (2014)
DF327	Japan	733	7000000	Kimura et al. (2014)
DF328	Japan	750	750000	Kimura et al. (2014)
DF329	Japan	830	1500000	Kimura et al. (2014)
DF330	Japan	845	710000	Kimura et al. (2014)
DF331	Japan	860	460000	Kimura et al. (2014)
DF332	Japan	870	3300000	Kimura et al. (2014)
DF333	Japan	925	1700000	Kimura et al. (2014)
DF334	Japan	1080	870000	Kimura et al. (2014)
DF335	Japan	1200	50000	Kimura et al. (2014)

DF336		Japan	1300	74000000	Kimura et al. (2014)
DF337		Japan	1660	200000000	Kimura et al. (2014)
DF338		Japan	2150	12000000	Kimura et al. (2014)
DF339		Japan	2240	97000000	Kimura et al. (2014)
DF340		Japan	2560	3500000	Kimura et al. (2014)
DF341		Japan	3600	260000000	Kimura et al. (2014)
DF342		Japan	6630	280000	Kimura et al. (2014)
DF343	Hoffman Creek	Oregon	30	35	Lancaster et al. (2003)
DF344	Hoffman Creek	Oregon	50	50	Lancaster et al. (2003)
DF345	Hoffman Creek	Oregon	60	110	Lancaster et al. (2003)
DF346	Hoffman Creek	Oregon	80	170	Lancaster et al. (2003)
DF347	Hoffman Creek	Oregon	100	370	Lancaster et al. (2003)
DF348	Hoffman Creek	Oregon	100	94	Lancaster et al. (2003)
DF349	Hoffman Creek	Oregon	110	480	Lancaster et al. (2003)
DF350	Hoffman Creek	Oregon	130	33	Lancaster et al. (2003)
DF351	Hoffman Creek	Oregon	150	495	Lancaster et al. (2003)
DF352	Hoffman Creek	Oregon	150	61	Lancaster et al. (2003)
DF353	Hoffman Creek	Oregon	170	290	Lancaster et al. (2003)
DF354	Hoffman Creek	Oregon	430	2500	Lancaster et al. (2003)
DF355	Soldier Canyon	Arizona	200	300	Magirl et al. (2010)
DF356	Esperero Canyon	Arizona	440	2000	Magirl et al. (2010)
DF357	Tributary 6	Santaquin City, Utah, USA	366	7646	McDonald & Giraud (2002)
DF358	Tributary 3	Santaquin City, Utah, USA	427	1682	McDonald & Giraud (2002)
DF359	Tributary 5	Santaquin City, Utah, USA	671	9939	McDonald & Giraud (2002)
DF360	Tributary 4	Santaquin City, Utah, USA	701	15291	McDonald & Giraud (2002)
DF361	Tributary 2	Santaquin City, Utah, USA	914	4205	McDonald & Giraud (2002)
DF362	An Teallach 2	Scotland	135	90	Milne (2008)
DF363	Glen Ogle 2	Scotland	610	3200	Milne (2008)
DF364	Glen Ogle 1	Scotland	800	8500	Milne (2008)
DF365	Mayflower Gulch	Climax, Colorado, USA	800	17000	Prochaska et al. (2008), Curry (1966)
DF366	Pilot Ridge	Stanislaus National Forest, California, USA	770	460	Prochaska et al. (2008)
DF367	Hummingbird Ck	Sicamous, British Columbia, Canada	5540	92000	Prochaska et al. (2008), Jakob et al. (2000)
DF368	Jughead	Lowman, Idaho, USA	1130	14600	Prochaska et al. (2008), Meyer et al. (2001)
DF369	Gulley #2	Port Alice, British Columbia, Canada	1420	4500	Prochaska et al. (2008), Nasmith & Mercer (1979)
DF370	Gulley #1	Port Alice, British Columbia, Canada	1560	22000	Prochaska et al. (2008), Nasmith & Mercer (1979)
DF371	Hishikari	Japan	103	7000	Sidle & Chigira (2004)
DF372	Minamata Fukagawa	Japan	340	370	Sidle & Chigira (2004)
DF373	Minamata Hogawachi	Japan	1700	26000	Sidle & Chigira (2004)
DF374	Brodska	Czech Republic	690	300000	Silhan (2019), Kirchner & Krejci (1998)
DF375	Ruapehu (Pukekahu)	New Zealand	56000	1560000000	Tost et al. (2014)
DF376	Ruapehu (Lower Whangaehu)	New Zealand	60000	2400000000	Tost et al. (2014)
DF377	Ruapehu (Mataroa)	New Zealand	64000	2900000000	Tost et al. (2014)
DF378	Ruapehu (Piriak-A)	New Zealand	72000	1350000000	Tost et al. (2014)
DF379	Ruapehu (Piriaka-B)	New Zealand	75000	1400000000	Tost et al. (2014)
DF380	Ruapehu (Oreore)	New Zealand	80000	3000000000	Tost et al. (2014)
DF381	West Salt Creek	Mesa County, Colorad, USA	4510	30000000	White et al. (2015)
DF382	Guanling	China	1300	985000	Xing et al. (2015)
DF383	Donghekou	China	2400	10000000	Yin et al. (2009)
DF384	Sanxicun, Dujiangyan, Sichuan	China	1200	1900000	Yin et al. (2017)
DF385	d1	Al-Hada Highway, Saudi Arabia	91	2268	Youssef et al. (2013)
DF386	d2	Al-Hada Highway, Saudi Arabia	103	1655	Youssef et al. (2013)
DF387	d3	Al-Hada Highway, Saudi Arabia	134	9072	Youssef et al. (2013)
DF388	d4	Al-Hada Highway, Saudi Arabia	156	6395	Youssef et al. (2013)
DF389	d5	Al-Hada Highway, Saudi Arabia	157	3108	Youssef et al. (2013)

DF390	d6	Al-Hada Highway, Saudi Arabia	211	6368	Youssef et al. (2013)
DF391	d8	Al-Hada Highway, Saudi Arabia	217	15901	Youssef et al. (2013)
DF392	d7	Al-Hada Highway, Saudi Arabia	222	31215	Youssef et al. (2013)
DF393	d14	Al-Hada Highway, Saudi Arabia	254	3382	Youssef et al. (2013)
DF394	d9	Al-Hada Highway, Saudi Arabia	286	10527	Youssef et al. (2013)
DF395	d10	Al-Hada Highway, Saudi Arabia	291	104844	Youssef et al. (2013)
DF396	d13	Al-Hada Highway, Saudi Arabia	303	3713	Youssef et al. (2013)
DF397	d11	Al-Hada Highway, Saudi Arabia	370	31914	Youssef et al. (2013)
DF398	d15	Al-Hada Highway, Saudi Arabia	548	28567	Youssef et al. (2013)
DF399	d12	Al-Hada Highway, Saudi Arabia	600	84914	Youssef et al. (2013)
DF400	Yu Tung Road	Hong Kong	600	3400	Zhao & Kowalski (2020)

A2.3.2 Runout data for coseismic soils slides and rock avalanches

In order to create an inventory of coseismic landslide runout, I developed an automated process to extract landslide fall height and runout length from mapped polygons. In a GIS framework, elevations are extracted from an underlying DEM at each vertex of a polygon. At each pair of maximum/minimum elevation points for a polygon, corresponding to the landslide scarp and toe, the elevation difference and horizontal straight line distance are calculated. These are an approximation of H_{max} and L_{max}, respectively, as described in **Section 2.7.2** (**Figure A2.3.2.1**).

I used this procedure to extract runout characteristics for 3999 soil and rock avalanches from the Gorhka, Ludian, and Kashmir earthquakes (Zhang et al., 2017; Xu et al., 2014; Basharat et al., 2016) and overlaid them on 30 m ALOS elevation data downloaded from the Japan Aerospace Exploration Agency (JAXA, available at: https://www.eorc.jaxa.jp/ALOS/en/aw3d30/index.htm). One thousand landslide polygons were selected randomly from each the original inventories (Schmitt et al., 2017). Note that one polygon was excluded upon examination for having an area finer than the elevation pixel size.

Landslide volumes are calculated based on the area-volume scaling relationship of Larsen et al. (2010) for Himalayan soil and bedrock landslides ($R^2 = 0.98$, n=428):

$$V = \alpha A^{\gamma} \quad \textbf{(A2.3.1)}$$

where $\log \alpha = -0.59$ and $\gamma = 1.36$.

A predictive coseismic landslide runout relationship (**Equation 2.20** and **Table 2.4**) was produced using the method described in **Chapters 2** and **3** using the runout length-volume pairs.

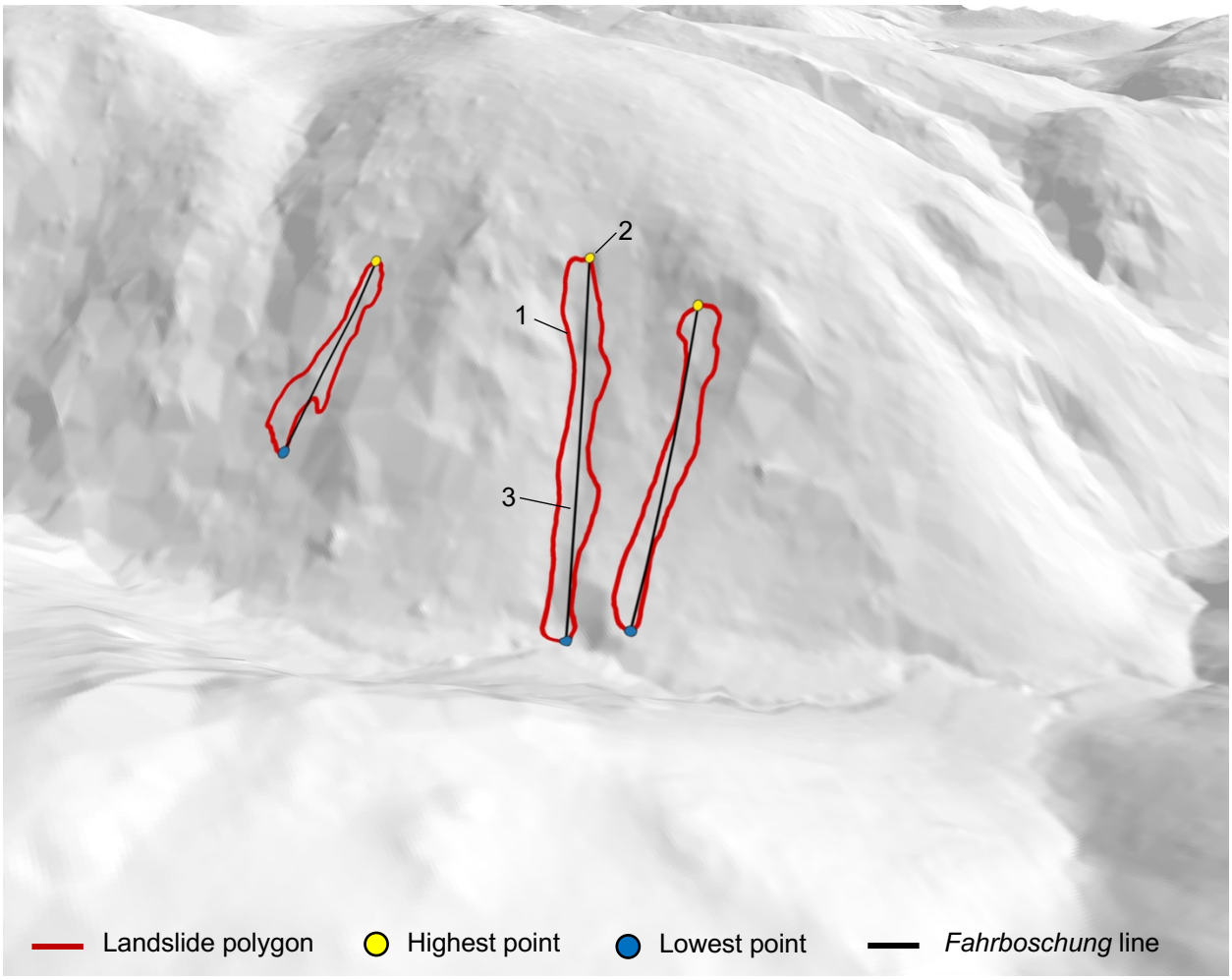

Figure A2.3.2.1. Example of extraction process for runout characteristics of coseismic landslides. (*1*) elevations are extracted at each vertex for a landslide polygon. (*2*) the maximum and minimum elevation points are identified. The elevation difference is H_{max}. (*3*) a straight line is drawn between the maximum and minimum points. The length the line projected on the horizontal plane is approximately L_{max}.

References

Ayotte, D., Evans, N., Hungr, O. (1998). Runout analysis of debris flows and debris avalanches in Hong Kong. *Report of the GEO*. Hong Kong: Geotechnical Engineering Office.

Basharat, M., Ali, A., Jadoon, I., Rohn, J. (2016). Using PCA in evaluating event-controlling attributes of landsliding in the 2005 Kashmir earthquake region, NW Himalayas, Pakistan. *Nat. Hazards*, 81, 1999-2017. https://doi.org/10.1007/s11069-016-2172-9

Budetta, P., de Riso, R. (2004). The mobility of some debris flows in pyroclastic deposits of the northwestern Campanian region (southern Italy). *Bull. Eng. Geol. Eng*., 63, 293-302.

Burns, S., Burns, W., James, D., Hinkle, J. (1998). Landslides in the Portland, Oregon metropolitan area resulting from the storm of February 1996: Inventory map, database and evaluation. *A Report as Fulfillment of Metro Contract 905828*. Portland: Dept. of Geology, Portland State University.

Campbell, R. (1975). Soil slips, debris flows, and rainstorms in the Santa Monica mountains and vicinity Southern California. *U.S. Geological Survey Professional Paper 851*. Washington: United States Government Printing Office.

Chiarle, M., Iannotti, S., Mortara, G., Deline, P. (2007). Recent debris flow occurrences associated with glaciers in the Alps. *Global and Planetary Change*, 56, 123-136.

Corominas, J. (1996). The angle of reach as a mobility index for small and large landslides. *Can. Geotech. J.*, 33, 260-271. https://doi.org/10.1139/t96-005

Curry, R. (1966). Observation of alpine mudflows in the Tenmile Range, central Colorado. *Geological Society of American Bulletin*, 77, 771-776.

D'Agostino, V., Cesca, M., Marchi, L. (2010). Field and laboratory investigations of runout distances of debris flows in the Dolomites (eastern Italian Alps). *Geomorphology*, 115, 294-304.

Dahlquist, M., West, A. (2019). Initiation and runout of post-seismic debris flows: Insights from the 2015 Gorkha earthquake. *Geophys. Research Letters*, 46, 9658-9668.

Evans, S., Mugnozza, G., Strom, A., Hermanns, R., Ischuk, A., Vinnichenko, S. (2006). Landslides from massive rock slope failure and associated phenomena. In: S. Evans et al. (*Eds*.) *Landslides from Massive Rock Slope Failure*. Netherlands: Springer.

Geertsema, M., Clague, J., Schwab, J., Evans, S. (2006). An overview of recent large catastrophic landslides in northern British Columbia, Canada. *Eng. Geol*., 83, 120-143.

Guo, C., Zhang, Y., Montgomery, D., Du, Y., Zhang, G., Wang, S. (2016). How unusual is the long-runout of the earthquake-triggered giant Luanshibao landslide, Tibetan Plateau, China? *Geomorphology*. 259, 145-54.

Hearn, G. (2011). *Slope Engineering for Mountain Roads*. London: Geological Society of London.

Huggel, C., Zgraggen-Oswald, S., Haeberli, W., Kaab, A., Polkvoj, A., Galushkin, I., Evans, S. (2005). The 2002 rock/ice avalanche at Kolka/Karmadon, Russion Caucasus: Assessment of extraordinary avalanche formation and mobility, and application of QuickBird satellite imagery. *Nat. Hazards Earth Syst. Sci*., 5, 173-187.

Hungr, O., Evans, S. (2004). Entrainment of debris in rock avalanches: An analysis of a long run-out mechanism. *GSA Bull*., 116, 1240-1252.

Hunter, G. and Fell, R. 2001. "Rapid" failure of soil slopes. *UNICIV Report R-400*. The University of New South Wales, School of Civil and Environmental Engineering, Sydney, Australia.

Jakob, M., Anderson, D., Fuller, T., Hungr, O., Ayotte, D. (2000). An unusually large debris flow at Hummingbird Creek, Mara Lake, British Columbia. *Can. Geotech. J.*, 37, 1109-1125.
Jibson, R. (2005). Landslide hazards at La Conchita, California. *Open-File Report 2005-1067*. Reston, VA: United States Geological Survey
Kailey, P. (2013). Debris flows in New Zealand alpine catchments. (*doctoral dissertation*). Christchurch: University of Canterbury.
Kimura, T., Hatada, K., Maruyama, K., Noro, T. (2014). A probabilistic approach to predicting landslide runout based on an inventory of snowmelt-induced landslide disasters in Japan. *Int. J. Erosion Control Eng*., 7, 9-18.
Kirchner, K., Krejci, O. (1998). Slope movements in the flysch Carpathians of eastern Moravia (Vsetin District), triggered by extreme rainfalls in 1997. *Moravian Geographical Reports*, 6, 43-52.
Lancaster, S., Hayes, S. (2003). Effects of wood on debris flow runout in small mountain watersheds. *Water Resources Research*, 39.
Larsen, I., Montgomery, D., Korup, O. (2010). Landslide erosion controlled by hillslope material. *Nature Geosci*., 3, 247-251. https://doi.org/10.1038/ngeo776
Magirl, C., Griffiths, P., Webb, R. (2010). Analyzing debris flows with the statistically calibrated empirical model LAHARZ in southeastern Arizona, USA. *Geomorphology*, 119, 111-124.
McDonald, G., Giraud, R. (2002). September 12, 2002, fire-related debris flows east of Santaquin and Spring Lake, Utah County, Utah. Salt Lake City: Utah Geological Survey.
McDougall, S., Boultbee, N., Hungr, O., Stead, D., Schwab, J. (2006). The Zymoetz River landslide, British Columbia, Canada: Description and dynamic analysis of a rock slide-debris flow. *Landslides*, 3, 195-204.
McDougall, S., Hungr, O. (2005). Dynamic modelling of entrainment in rapid landslides. *Can. Geotech. J.*, 42, 1437-1448.
Meyer, G., Wells, S. (1997). Fire-related sedimentation events on alluvial fans, Yellowstone National Park, U.S.A. J. Sedimentary Research, 67, 776-791. https://doi.org/10.1306/D426863A-2B26-11D7-8648000102C1865D
Milne, F. (2008). Topographic and material controls on the Scottish debris flow geohazard. (*doctoral dissertation*). Dundee: University of Dundee.
Nasmith, H., Mercer, A. (1979). Design of dykes to protect against debris flows at Port Alice, British Columbia. Can. Geotech. J., 16, 748-757. https://doi.org/10.1139/t79-082
Plafker, G., Ericksen, G. (1978). Nevados Huascaran rock avalanches, Peru. In: B. Voight (*Ed*.) *Rockslides and Avalanches, 1: Natural Phenomena*. Amsterdam: Elsevier.
Prochaska, A., Santi, P., Higgins, J., Cannon, S. (2008). Debris-flow runout predictions based on the average channel slope (ACS). *Eng. Geol*., 98, 29-40.
Schmitt, R.G., Tanyas, Hakan, Nowicki Jessee, M.A., Zhu, J., Biegel, K.M., Allstadt, K.E., Jibson, R.W., Thompson, E.M., van Westen, C.J., Sato, H.P., Wald, D.J., Godt, J.W., Gorum, Tolga, Xu, Chong, Rathje, E.M., Knudsen, K.L. (2017). An Open Repository of Earthquake-triggered Ground Failure Inventories. *U.S. Geological Survey data release collection*. https://doi.org/10.5066/F7H70DB4. Accessed June 2020.
Sidle, R., Chigira, M. (2004). Landslides and debris flows strike Kyushu, Japan. *EOS*, 85, 145-156.

Silhan, K. (2019). Tree ring evidence of slope movements preceding catastrophic landslides. Landslides, 17, 615-626. https://doi.org/10.1007/s10346-019-01300-w

Tost, M., Cronin, S., Procter, J. (2014). Transport and emplacement mechanisms of channelized long-runout debris avalanches, Ruapehu volcano, New Zealand. *Bull. Volcanol*., 76.

White, J., Morgan, M., Berry, K. (2015). The West Salt Creek landslide: A Catastrophic rockslide and rock/debris avalanche in Mesa County, Colorado. *Colorado Geological Survey Bulletin 55*. Golden, CO: Colorado Geological Survey.

Xing, A., Wang, G., Li, B., Jiang, Y., Feng, Z., Kamai, T. (2015). Long-runout mechanism and landsliding behavior of large catastrophic landslide triggered by heavy rainfall in Guanling, Guizhou, China. *Can. Geotech. J*., 52, 971-981.

Xu, C., Xu, X., Shen, L., Dou, S., Wu, S., Tian, Y., Li, X. (2014). Inventory of landslides triggered by the 2014 Ms 6.5 Ludian earthquake and its implications on several earthquake parameters. *Seismology and Geology*, 36, 1186-1203.

Yin, Y., Cheng, Y., Liang, J., Wang, W. (2016). Heavy-rainfall-induced catastrophic rockslide-debris flow at Sanxicun, Dujiangyan, after the Wenchuan Ms 8.0 earthquake. *Landslides*, 13, 9-23.

Yin, Y., Wang, F., Sun, P. (2009). Landslide hazards triggered by the 2008 Wenchuan earthquake, Sichuan, China. *Landslides*, 6, 139-151.

Youssef, A., Pradhan, B., Maerz, N. (2013). Debris flow impact assessment caused by 14 April 2012 rainfall along the Al-Hada Highway, Kingdom of Saudi Arabia using high-resolution satellite imagery. *Arab J. Geosci*., 7, 2591-2601. https://doi.org/10.1007/s12517-013-0935-0

Zhang, J-q., Liu, R-k., Deng, W., Khanal, N., Gurung, D., Murthy, M., Wahid, S. (2017). Characteristics of landslides in Koshi River basin, central Himalaya. J. Mountain Sci., 13, 1711-1722. https://doi.org/10.1007/s11629-016-4017-0

Zhao, H., Kowalski, J. (2020). Topographic uncertainty quantification for flow-like landslide models via stochastic simulations. *Nat. Hazards Earth Syst. Sci*., 20, 1441-1461. https://doi.org/10.5194/nhess-20-1441-2020

Appendix 2.4 – Comparison of the rock avalanche runout module with CONEFALL

Jaboyedoff and Labiouse (2011) describe a rock avalanche that occurred near Sion, Switzerland in August 1985. The total volume was 800,000 m^3, of which about 50 blocks reached the floor of the Rhone valley. Jaboyedoff and Labiouse (2011) used the program CONEFALL (Quanterra, 2003) to model the rock fall runout envelope and velocity. The runout envelope is defined by a cone projected from the rock fall source using the energy line method of Heim (1932). CONEFALL does not include the effects of fragmentation and overestimates the lateral extension of the runout envelope because the aperture of the cone exceeds the observed lateral dispersion of rock falls, generally ±20° (Jaboyedoff and Labiouse, 2011).

I compared the velocity and kinetic energy output of the runout module r.randomwalk implemented as described in **Section 2.7** to that of CONEFALL (**Figures A2.4.1** – **A2.4.3**). CONEFALL and r.randomwalk, run both with and without the fragmentation model described in **Section 2.8.2**, produce similarly shaped velocity profiles. However, velocities produced by r.randomwalk with the effects of fragmentation are of similar magnitude to those estimated by CONEFALL in the latter half of the runout profile, while r.randomwalk without the effects of fragmentation produces velocities 10 – 20 m/s greater despite the fact that CONEFALL does not account for fragmentation. This is likely a product of the geometric assumptions necessary to apply **Equation 2.29** in a GIS environment, including the conservative use of the *fahrboschung* line rather than the energy line, which overestimates velocity. Note that the runout envelope produced by r.randomwalk with fragmentation starts at a lower elevation due to the simplified procedure illustrated in **Figure 2.16** and produces much lower kinetic energies than CONEFALL due to the progressive reduction in individual block sizes (**Figure A2.4.3**). R.randomwalk also tends to produce a more realistic envelope, due to its control of sharp bends in the runout trajectory.

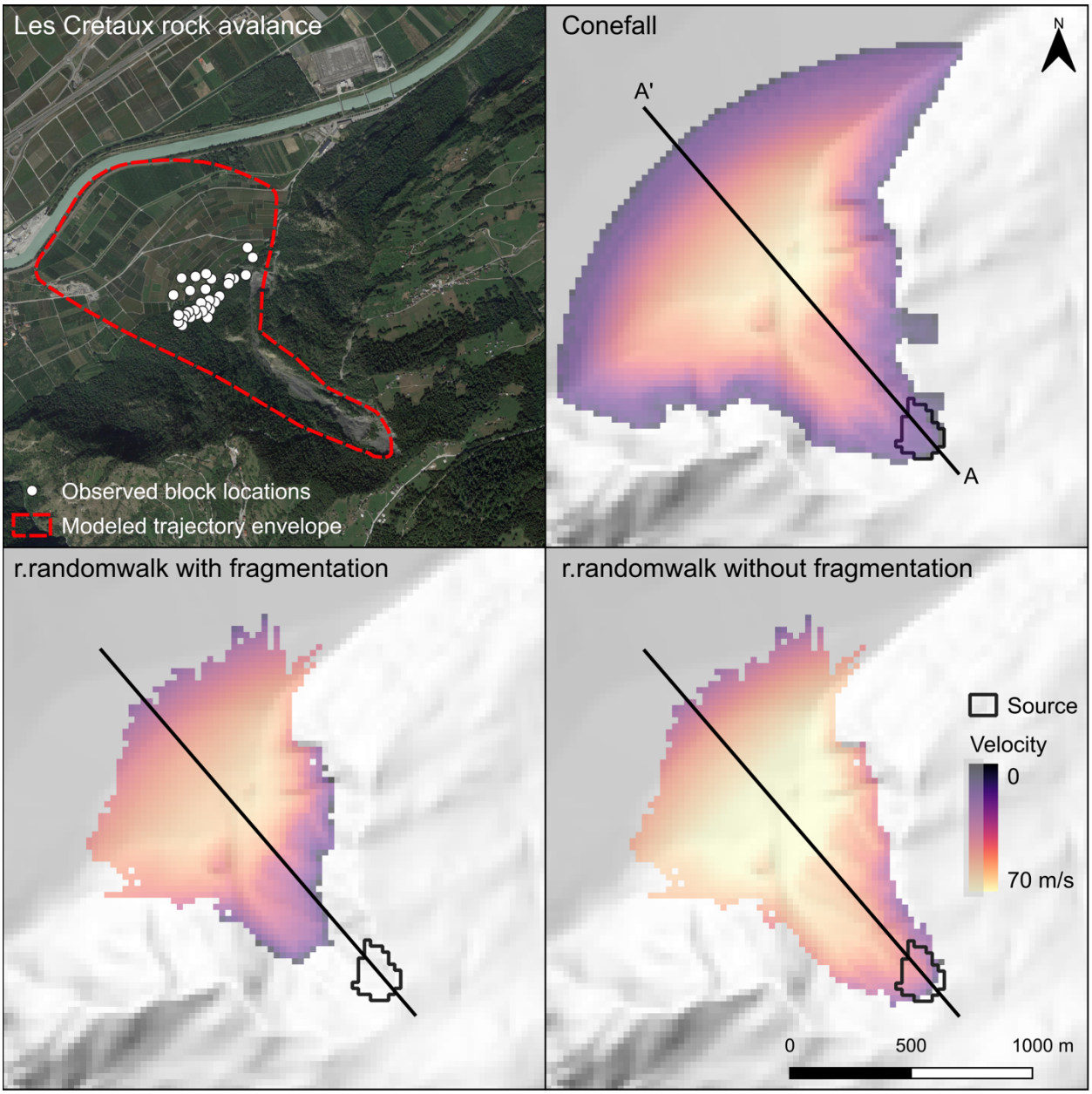

Figure A2.4.1. Observed block locations and the rock block trajectory envelope modeled using 20,000 simulated trajectories the 3D program EBOUL (Jaboyedoff et al, 2005; *top left*). Runout envelope and kinetic energy modelled using CONEFALL (*top right*), r.randomwalk with fragmentation (*bottom left*) and r.randomwalk without fragmentation (*bottom right*).

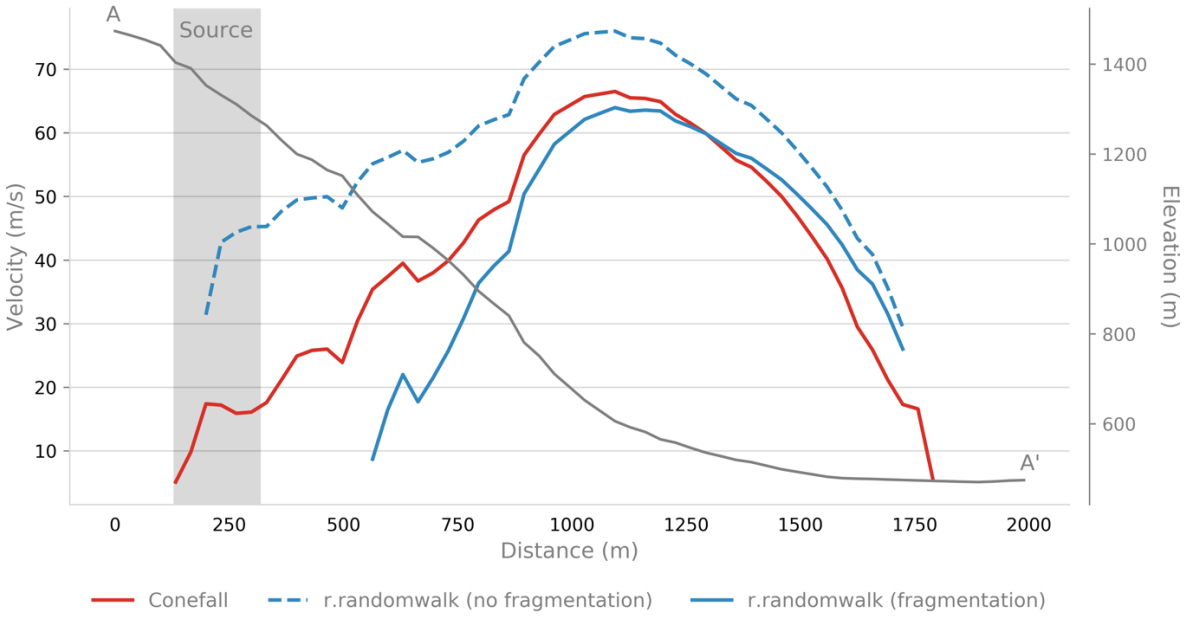

Figure A2.4.2. Block velocity along profile A – A' (see **Figure A2.4.1**) for CONEFALL, and r.randomwalk with and without fragmentation.

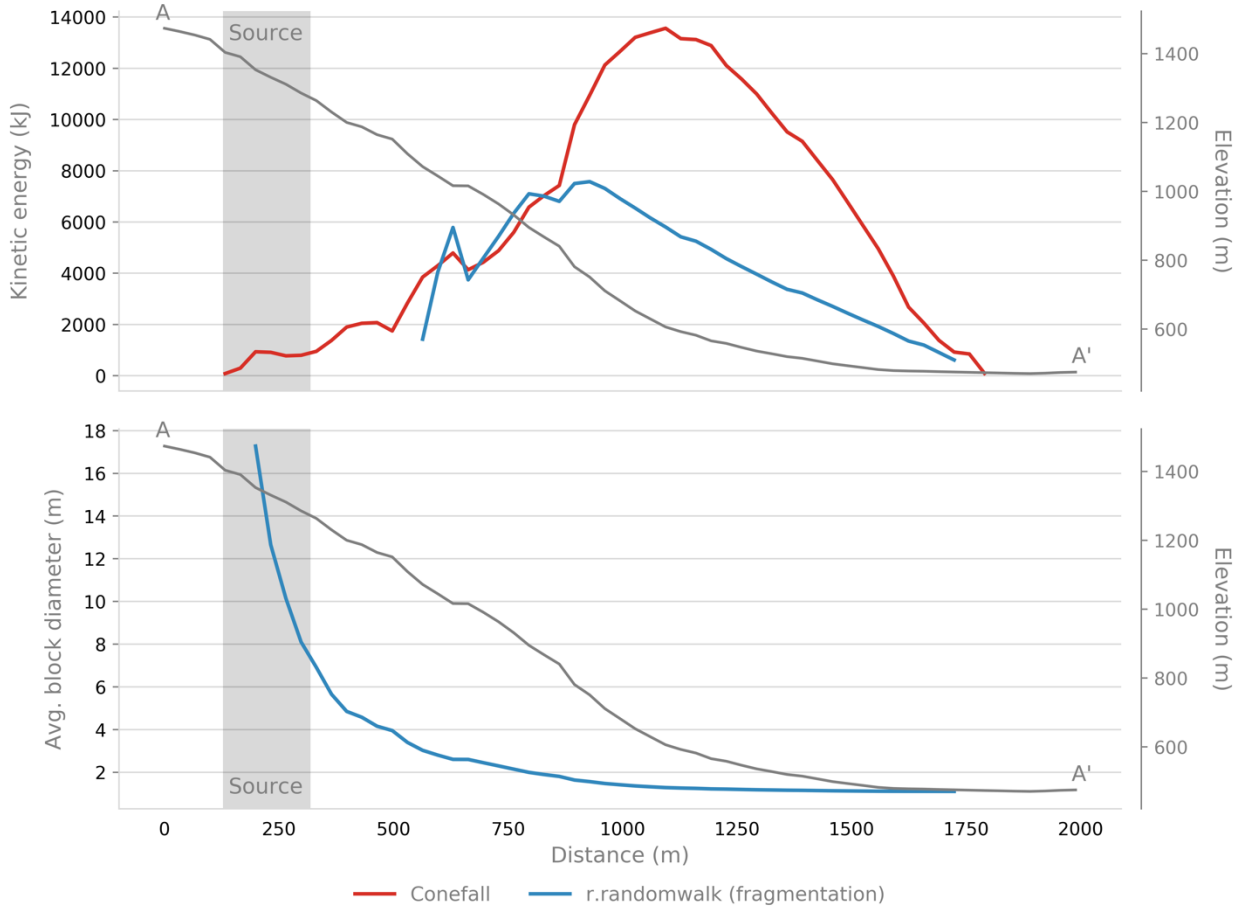

Figure A2.4.3. Block kinetic energy along profile A-A' (see **Figure A2.4.1**) calculated using CONEFALL and r.randomwalk with fragmentation (*top*). The fragmentation model also allows for the estimation of mean block size as the initial rock fall becomes a fragmented rock avalanche (*bottom*).

References

Heim, A. (1932). *Landslides and Human Lives (Bergsturz und Menschenleben)*. Trans. N. Skermer. BiTech Pub, Vancouver, B.C.

Jaboyedoff, M., Dudt, J., Labiouse, V. (2005). An attempt to refine rockfall hazard zoning based on the kinetic energy, frequency and fragmentation degree. *Nat. Hazards Earth Syst. Sci.*, 5, 621-632. https://doi.org/10.5194/nhess-5-621-2005

Jaboyedoff, M., Labiouse, V. (2011). Technical note: preliminary estimation of rockfall runout zones. *Nat. Hazards Earth Syst. Sci.*, 11, 819-828. https://doi.org/10.5194/nhess-11-819-2011

Quanterra. (2003). CONEFALL 1.0: User's Guide. *Open-report – SOFT – 01*. Lausanne: Quanterra.

Appendix 2.5 – Structural vulnerability data from the 2018 Montecito, CA, debris flows

A2.5.1 Introduction

Vulnerability is the means by which physical hazard can create disparate losses among different populations while impacting them, by all appearances, equally. In quantitative landslide risk assessment, the inclusion of vulnerability is limited to the physical damage (as a probability of death or a proportion of initial value lost) as correlated to a measurable intensity metric of the landslide hazard such as debris height, velocity, kinetic energy, or momentum (Lee and Jones, 2014).

A2.5.2 Quantifying structural vulnerability

The vulnerability of infrastructure is often evaluated economically, expressed through a damage ratio, D_r, between the cost to repair and the cost to replace the structure (Massey et al., 2019; Quan Luna et al., 2011; Papathoma-Koehle et al., 2015; Fuchs et al., 2007; Totschnig et al., 2013):

$$D_r = \frac{cost\ to\ repair}{cost\ to\ replace} \qquad \textbf{(A2.5.1)}$$

A damage ratio of one indicates complete destruction, although in practice it may indicate a building that is permanently rendered uninhabitable even if part of the structure still stands. Some structures may be repairable, but it is more cost effective to demolish and rebuild, creating a case in which the damage ratio is greater than one and does not directly reflect the physical damage to the structure (Massey et al., 2019). Although simple in form, no standardized method of calculating damage ratios exist (Lin et al., 2017). The exist cost to repair may not be known. It may be estimated from insurance claims or assessments, contractor bills with or without labor costs, assumptions of mean construction cost per square foot, or by summing individual costs of all replaced components with or without non-structural items such as appliances and furnishings (e.g. Kang and Kim, 2016; Lo et al., 2012). Similarly, the total or replacement cost may be assessed from pre-event market value, tax rolls, or assumed value per square foot of construction (e.g. Massey et al., 2019; Ciurean et al., 2017). The value of land inundated land should be considered separately, as should capital improvements not associated with the impacted structure, but this data is not always able to be disaggregated. The values used in the damage ratio equation may reflect the purpose of the study, such as to predict the physical damage strictly done to a structure or the total monetary loss experienced by a homeowner; however, in practice the values are almost always determined by data availability and vary between sites and studies.

Alternately, damage states are semi-qualitative levels of damage, such as *slight*, *moderate*, *extensive*, *complete*, each category corresponding to a percentage range of damage. Damage state schema used for landslides include HAZUS (FEMA, 2017; Kean et al., 2019a), RiskScape (King et al., 2009), GNS Science (Massey et al., 2019), Kang and Kim (2016), and Jakob et al. (2012). Although damage states are an easy and rapidly employable index of habitability or

damage severity, useful for emergency response and rebuilding, they are typically too general for quantitative risk assessment (Massey et al., 2019).

Vulnerability is a function of both the hazard and the element at risk. The ability of a building to resist damage depends on the landslide mechanism, volume, material, and characteristics of movement (Fell et al., 2008). A building that is reinforced against debris flows may be damaged by high-energy, localized rock fall. Highly fluid debris flows carrying smaller relative particles have been known to flow through and around buildings with minimal structural damage, while others propel boulders or trees catastrophically through homes or sweep them away completely (**Figures A2.5.1** and **A2.5.2**).

Figure A2.5.1. The 08 Feb. 1996 West Dodson, Oregon, debris flow carried away the furnishings of this home while leaving it on its foundations. Image: Iverson et al. (1997).

Figure A2.5.2. Home violently destroyed by the January 2018 Montecito, California, debris flow. Image: Kean et al. (2019b)

A building's resistance also depends on its maintenance condition, the quality and materials of its construction, its orientation, and the location of weak points such as windows and doors, collectively known as building typology (Kang and Kim, 2016; Massey et al., 2019). However, most studies reduce building typology to construction material, such as timber, masonry, or reinforced concrete (Massey et al., 2019; Du et al., 2013).

The intensity of a flow-type hazard is typically estimated by either the height or velocity of the flow. Without reliable eyewitness testimony or video evidence, flow velocity is difficult to assess post-event. The height of flow may be reliably estimated by mudlines on structures or nearby fixed objects, such as trees, fences, or utility fixtures (e.g. Kean et al., 2019a; Rheinberger et al., 2013). Alternatively, the height of accumulated debris may be used as a proxy for flow height; while it typically underestimates the flow height, it is more durable than mudlines, directly measurable in the field, and easily interpreted by non-experts, making debris height the most common intensity characteristic reported in media and many academic sources (Ciurean et al., 2017; Fuchs et al., 2007). The most commonly used rock fall intensity metric is kinetic energy.

A2.5.3 Existing data

Empirical vulnerability data is limited. Not only is it necessary to have qualitative data about the intensity (e.g. velocity, debris height, displacement, impact pressure) of the landslide event which is either highly perishable or unknown without real-time observation of the event, but vulnerability also requires detailed information about the material, maintenance state, orientation, and degree of damage of structures, information that is disparately collected and held by private citizens or insurance companies if at all. I have reviewed published landslide vulnerability literature and compiled a database of n = 437 previously published data points for

debris flow / debris avalanche vulnerability and n = 47 for rock fall. I considered only studies which report damage ratios. Data was compiled by digitizing the graphs presented in the studies unless tabulated data was provided. Significantly, only 19 (4%) of the debris flow data points are for timber structures. Eighteen of these come from a single study in New Zealand (Massey et al., 2019). The remaining 418 data points are for masonry or concrete structures, primarily in Italy, Austria, and Switzerland. The lack of information about landslides impacting timber structures is a significant source of uncertainty in performing risk analysis in much of North America, where timber is the principal material for residential construction.

Table A2.5.1. Primary sources of vulnerability data. [1]Data only from completely destroyed buildings. [2]From simulations. [3]Uses a "damage index" calculated as the percent of structural elements which fail.

Location	*Date*	*Landslide type*	*N*	*Primary building material*	*Reference*
Vipiteno/Sterzing, South Tyrol, Italy	Aug. 2012	debris flow	82	masonry, concrete	Papathoma-Kohle et al. (2015)
Various, South Korea	July – Aug. 2011	debris flow	11[1]	*various*	Kang and Kim (2016)
	various	debris flow	25[1]	*various*	Jakob et al. (2012)
St. Stephan, Wildersil, Sachseln, Rueun, Davos Glaris, Switzerland	July 1991, July 1987, July 1997, Nov. 2002, Aug. 1998	debris flow	103	masonry, concrete	Rheinberger et al. (2013
Fella river valley, Italy	Aug. 2003		39	masonry, concrete	Ciurean et al. (2017)
Valtellina valley, Lombardy, Italy	July 2008	debris flow	13[2]	masonry, concrete	Quan Luna et al. (2011)
Wellington, New Zealand	*na*	debris flow/avalanche	18	wood	Massey et al. (2019)
Martell Valley, S. Tyrol, Italy	Aug. 1987	debris flow	53	masonry, concrete	Eidsvig et al. (2014), Papathoma-Kohle et al. (2012)
Wartschenbach, Austria	Aug. 1995, Aug. 1997	debris flow	26	masonry, concrete	Totschnig and Fuchs (2013)
Various, Taiwan	Aug. 2009	debris flow	25	masonry, concrete	Fuchs et al. (2012)
Brienz, Switzerland	*na*	debris flow	8[1]	masonry, concrete	Massey et al. (2019)
Montecito, CA, U.S.	Jan. 2018	debris flow	98	wood	Kean et al. (2019a); *this study*
Oso, WA, U.S.	Mar. 2014	flowslide	50[1]	wood	*this study*
La Conchita, CA, U.S.		debris flow	2	wood	*this study*
Fiumelatte, Italy	Nov. 2004	rock fall	6	masonry, concrete	Agliardi et al. (2009)
model	*na*	rock fall	15[2,3]	concrete	Mavrouli and Corominas (2010)
Christchurch, New Zealand	Feb. 2011	rock fall	26	wood	Grant (2017)

In order to address this data gap, I used published descriptions of the flow and inundation dynamics of the recent Montecito, CA, debris flow disaster and public record building permits from Santa Barbara County, CA, to create a new dataset of 98 damage ratio-inundation height pairs, primary in timber-frame residential structures.

A.2.5.4. Structural vulnerability in the January 2018 Montecito, CA, debris flows

In the final weeks of 2017, the Thomas fire scorched almost 300,000 acres of Ventura and Santa Barbara Counties, CA, becoming one of the largest and costliest wildfires in state history.

Starting on 09 January, a cold front brought heavy precipitation to the recently burned section of the Santa Ynez Mountains above the city of Montecito. While overall precipitation totals were a moderate 2 – 5 inches, the storm produced periods of intense rain, up to 0.86 in. in fifteen minutes in Carpinteria, corresponding to a 100-year event (Oakley et al., 2018). The rainfall mobilized ~680,000 m^3 of debris flow sediment, which thundered out of steep catchments in the Santa Ynez and flowed 3 km across urbanized alluvial fans, carrying boulders up to 6m in diameter (Kean et al., 2019a). Twenty-three people were killed, 167 injured, and 408 homes were damaged or destroyed in the Montecito area.

Immediately after the event, inspectors from the California Department of Forestry and Fire Protection (CAL FIRE) performed an inventory of damaged structures in Montecito, including their location, damage state, structure type, and dimensions. Damage was assessed as a percentage of economic value lost in four levels: destroyed, 51% - 75% damaged, 10% - 25% damaged, and 1% - 9% damaged. USGS-led research team coupled this inventory with inundation characteristics of the five main debris flow paths in Montecito, including the depth of flow at the damaged structures and photographs at each location (Kean et al., 2019b). Kean et al. (2019a) paired the damage states estimated by CAL FIRE with HAZUS damage categories (slight: 0% - 5%; moderate: 5% - 25%, extensive 25% - 100%, and complete: 100%) to create empirical fragility curves correlating the inundation height with the expected damage state.

I coupled the geolocated inundation heights and damage assessment of Kean et al. (2019b) and CAL FIRE with public record building permits issued January 2018 – July 2019 by Santa Barbara County and tax lot data from the county assessor (available at: http://sbcassessor.com/assessor/search.aspx) to estimate the damage ratio of structures affected by the Montecito debris flows. To do this, I first associated each inundation height measurement with structures inventoried by CAL FIRE, including the associated tax parcel number. I then used the Santa Barbara County Department of Planning and Development Permit Status lookup (available at: https://www.countyofsb.org/plndev/permithistory.sbc) to see if building permits associated with the Montecito debris flow repairs had been filed for each of the affected parcels. I compared the total cost of repairs recorded on the building permits to the assessed "improvements" value (e.g. including structures, excluding value of land or mineral rights) of the parcel at the time of the permit issuing to estimate the damage state of the structure.

A modified Weibull damage function was fitted to the debris flow intensity-vulnerability data, of the form:

$$V = 1 - e^{-a * I^b} \qquad \textbf{(A2.5.2)}$$

where I is the debris flow intensity measured in flow depth [m] (Totschnig et al., 2011). **Table A2.5.2** gives the fitting parameters for the structural vulnerability curve derived from the Montecito damage data (**Figure A2.5.3**). In addition to the Montecito data, the vulnerability curves in **Table 2.5** and **Figures 2.18** and **2.19** include data from 52 homes impacted by landslides in Washington and California, most of which were completely destroyed (**Tables A2.5.4** and **A2.5.5**).

Table A2.5.2. Vulnerability curve metrics for timber-frame buildings impacted by the 2018 Montecito, CA, debris flows.

a	b	RMSE	pseudo R^2	n
0.9965	0.9607	0.3434	0.32	96

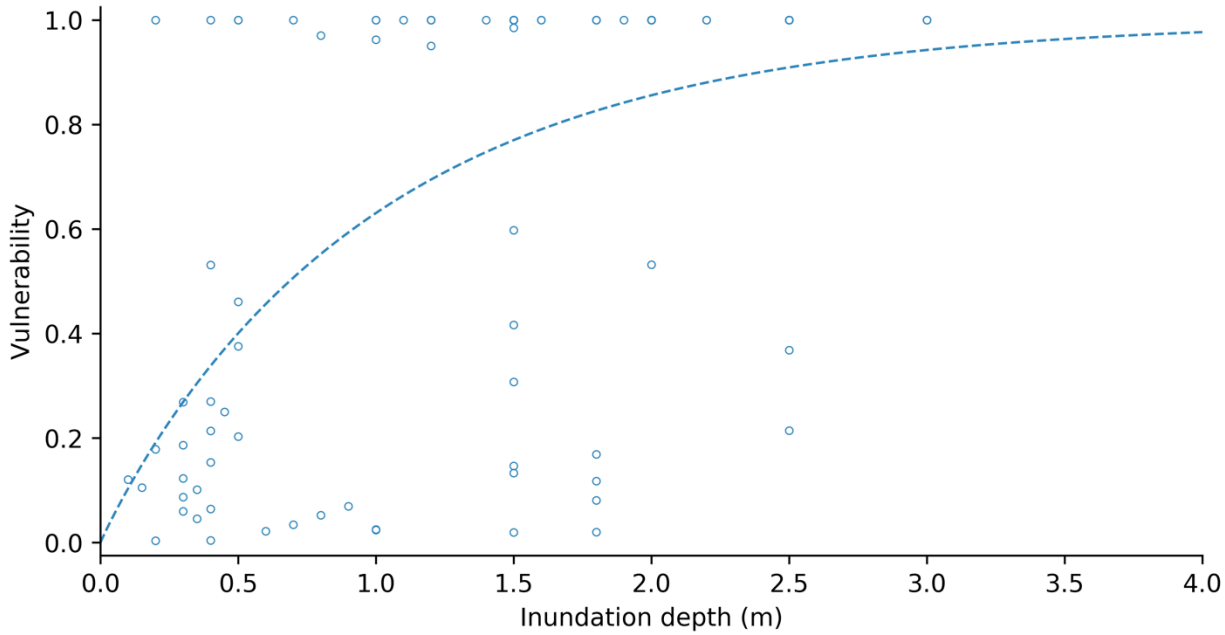

Figure A2.5.3. Vulnerability curve derived from timber-frame buildings impacted by the 2018 Montecito, CA, debris flows (n=96).

Table A2.5.3. Intensity-damage ratio pairs for 98 homes affected by the January 2018 Montecito, CA, debris flows. Flow heights are from Kean et al. (2019b). Damage ratios are calculated as part of this work.

ID	Flow height (m)	Damage Ratio	Material	ID	Flow height (m)	Damage Ratio	Material
1	0.60	0.20	brick	**50**	1.50	0.15	wood
2	2.00	1.00	brick	**51**	1.50	0.42	wood
3	0.10	0.12	wood	**52**	1.50	0.99	wood
4	0.15	0.11	wood	**53**	1.50	1.00	wood
5	0.20	0.18	wood	**54**	1.50	1.00	wood
6	0.20	0.00	wood	**55**	1.50	1.00	wood
7	0.20	1.00	wood	**56**	1.50	1.00	wood
8	0.30	0.09	wood	**57**	1.50	1.00	wood
9	0.30	0.27	wood	**58**	1.50	1.00	wood
10	0.30	0.06	wood	**59**	1.50	1.00	wood
11	0.30	0.19	wood	**60**	1.50	1.00	wood
12	0.30	0.12	wood	**61**	1.50	1.00	wood
13	0.35	0.10	wood	**62**	1.50	1.00	wood
14	0.35	0.05	wood	**63**	1.60	1.00	wood
15	0.40	0.53	wood	**64**	1.60	1.00	wood
16	0.40	0.06	wood	**65**	1.80	0.08	wood
17	0.40	0.00	wood	**66**	1.80	0.17	wood
18	0.40	0.21	wood	**67**	1.80	0.12	wood
19	0.40	0.27	wood	**68**	1.80	0.02	wood
20	0.40	0.15	wood	**69**	1.80	1.00	wood
21	0.40	1.00	wood	**70**	1.80	1.00	wood
22	0.45	0.25	wood	**71**	1.80	1.00	wood
23	0.50	0.20	wood	**72**	1.90	1.00	wood
24	0.50	0.46	wood	**73**	2.00	0.53	wood
25	0.50	0.38	wood	**74**	2.00	1.00	wood
26	0.50	1.00	wood	**75**	2.00	1.00	wood
27	0.50	1.00	wood	**76**	2.00	1.00	wood
28	0.60	0.02	wood	**77**	2.00	1.00	wood
29	0.70	0.03	wood	**78**	2.00	1.00	wood
30	0.70	1.00	wood	**79**	2.00	1.00	wood
31	0.80	0.97	wood	**80**	2.00	1.00	wood
32	0.80	0.05	wood	**81**	2.00	1.00	wood
33	0.90	0.07	wood	**82**	2.00	1.00	wood
34	1.00	0.03	wood	**83**	2.00	1.00	wood
35	1.00	0.96	wood	**84**	2.20	1.00	wood
36	1.00	0.02	wood	**85**	2.20	1.00	wood
37	1.00	1.00	wood	**86**	2.50	0.21	wood
38	1.00	1.00	wood	**87**	2.50	0.37	wood
39	1.10	1.00	wood	**88**	2.50	1.00	wood
40	1.20	0.95	wood	**89**	2.50	1.00	wood
41	1.20	1.00	wood	**90**	2.50	1.00	wood
42	1.20	1.00	wood	**91**	2.50	1.00	wood
43	1.20	1.00	wood	**92**	2.50	1.00	wood
44	1.20	1.00	wood	**93**	2.50	1.00	wood
45	1.40	1.00	wood	**94**	2.50	1.00	wood
46	1.50	0.02	wood	**95**	2.50	1.00	wood
47	1.50	0.13	wood	**96**	3.00	1.00	wood
48	1.50	0.31	wood	**97**	3.00	1.00	wood

49	1.50	0.60	wood	**98**	3.00	1.00	wood

Table A2.5.4. Damage states for 50 structures destroyed in the 2014 Oso, Washington, flowslide. Debris heights were calculated by differencing pre- and post-event LiDAR elevation data.

ID	Debris Height (m)	Damage State	Material	ID	Debris Height (m)	Damage State	Material
1	4.87	1	wood	**26**	8.03	1	wood
2	8.78	1	wood	**27**	1.37	1	wood
3	6.87	1	wood	**28**	8.64	1	wood
4	3.37	1	wood	**29**	1.75	1	wood
5	0.51	1	wood	**30**	5.52	1	wood
6	1.66	1	wood	**31**	6.12	1	wood
7	11.29	1	wood	**32**	7.58	1	wood
8	5.85	1	wood	**33**	3.69	1	wood
9	9.66	1	wood	**34**	3.78	1	wood
10	6.08	1	wood	**35**	0.98	1	wood
11	6.00	1	wood	**36**	0.46	1	wood
12	6.30	1	wood	**37**	8.06	1	wood
13	3.28	1	wood	**38**	4.16	1	wood
14	5.64	1	wood	**39**	9.78	1	wood
15	8.00	1	wood	**40**	2.09	1	wood
16	6.95	1	wood	**41**	2.46	1	wood
17	3.07	1	wood	**42**	8.07	1	wood
18	3.42	1	wood	**43**	5.69	1	wood
19	9.56	1	wood	**44**	4.00	1	wood
20	3.67	1	wood	**45**	2.12	1	wood
21	4.62	1	wood	**46**	1.82	1	wood
22	4.17	1	wood	**47**	1.53	1	wood
23	5.91	1	wood	**48**	4.83	1	wood
24	1.94	1	wood	**49**	3.71	1	wood
25	7.09	1	wood	**50**	1.27	1	wood

Table A2.5.5. Damage ratios for two structures impacted by landslides in La Conchita, California, in 1995 and 2005, respectively.

ID	Debris Height (m)	Damage State	Material
1	1.22	0.30	wood
2	9.10	1.00	wood

References:

Agliardi, F., Crosta, G., Frattini, P. (2009). Integrating rockfall risk assessment and countermeasure design by 3D modelling techniques. *Nat. Hazards Earth Syst. Sci.*, 9, 1059-1073. https://doi.org/10.5194/nhess-9-1059-2009

Ciurean, R., Hussin, H., van Westen, C., Jaboyedoff, M., Nicolet, P., Chen, L., Frigerio, S., and Glade, T. (2017). Multi-scale debris flow vulnerability assessment and direct loss estimation of buildings in the Eastern Italian Alps. *Nat. Hazards*, 85, 929-957. https://doi.org/10.1007/s11069-016-2612-6

Du, J., Yin, K., Nadim, F., Lacasse, S. (2013). Quantitative vulnerability estimation for individual landslides. Paris: Proceedings of the 18th International Conference on Soil Mechanics and Geotechnical Engineering.

Eidsvig, U., Papathoma-Kohle, M., Du, J., Glade, T., Vangelsten, B. (2014). Quantification of model uncertainty in debris flow vulnerability assessment. *Eng. Geol.*, 181, 15-26. https://doi.org/10.1016/j.enggeo.2014.08.006

Fell, R., Corominas, J., Bonnard, C., Cascini, L., Leroi, E., Savage, W. (2008). Guidelines for landslide susceptibility, hazard and risk zoning for land use planning. *Eng. Geol.*, 102, 85-98. https://doi.org/10.1016/j.enggeo.2008.03.022

FEMA. (2017). Hazus tsunami model technical guidance. Washington, D.C.: Federal Emergency Management Agency, 171 p. https://www.fema.gov/media-library/assets/documents/24609. (Accessed May 2020).

Fuchs, S., Heiss, K., and Hubl, J. (2007). Toward an empirical vulnerability function for use in debris flow risk assessment. *Nat. Hazards Earth Syst. Sci.*, 7, 495-506. https://doi.org/10.5194/nhess-7-495-2007

Fuchs, S., Tsao, T-C., Keiler, M. (2012). Quantitative vulnerability functions for use in mountain hazard risk management. Grenoble: Proceedings of the 12th Congress Interpraevent.

Grant, A. (2017). Regional-scale coseismic landslide hazard modelling and consequence analysis. *(doctoral dissertation)*. Seattle: University of Washington.

Iverson, R. (1997). The physics of debris flows. *Rev. Geophys.*, 35, 245-296. https://doi.org/10.1029/97RG00426

Jakob, M., Stein, D., Ulmi, M. (2012). Vulnerability of buildings to debris flow impact. *Nat. Hazards*, 60, 241-261. https://doi.org/10.1007/s11069-011-0007-2

Kang, H-s., Kim, Y-t. (2016). The physical vulnerability of different types of building structure to debris flow events. *Nat. Hazards*, 80, 1475-1493. https://doi.org/10.1007/s11069-015-2032-z

Kean, J., Staley, D., Lancaster, J., Rengers, F., Swanson, B., Coe, J., Hernandez, J., Sigman, A., Allstadt, K., Lindsay, D. (2019a). Inundation, flow dynamics, and damage in the 9 January 2018 Montecito debris-flow event, California, USA: Opportunities and challenges for post-wildfire risk assessment. *Geosphere*, 15. https://doi.org/10.1130/GES02048.1

Kean, J., Staley, D., Lancaster, J., Rengers, F., Swanson, B., Coe, J., Hernandez, J., Sigman, A., Allstadt, K., Lindsay, D. (2019b). Debris-flow inundation and damage data from the 9 January 2018 Montecito debris-flow event, *U.S. Geological Survey data release*, http://doi.org/10.5066/P9JQJU0E

King, A., Bell, R., Heron, D., Matcham, I., Schmidt, J., Cousins, W., Reese, S., Wilson, T., Johnston, D., Henderson, R., et al. (2009). RiskScape Project: 2004 – 2008. *GNS Science Consultancy Report 2009/247*. GNS Science.

Lee, M., Jones, D. (2014). *Landslide Risk Assessment, 2nd Ed*. London: Institution of Civil Engineers.

Lin, Q., Wang, Y., Liu, T., Zhu, Y., Sui, Q. (2017). The vulnerability of people to landslides: A case study on the relationship between casualties and volume of landslides in China. *Int. J. Environ. Res. Public Health*, 14, 212. https://doi.org/10.3390/ijerph14020212

Lo, W-C., Tsao, T-C., Hsu, C-H. (2012). Building vulnerability to debris flows in Taiwan: A preliminary study. *Nat. Hazards*, 64, 2107-2128. https://doi.org/10.1007/s11069-012-0124-6

Massey, C., Thomas, K-L., King, A., Singeisen, C., Taig, T., Horspool, N. (2019). SLIDE (Wellington): Vulnerability of dwellings to landslides (Project No. 16/SP740). *GNS Science report; 2018/17*. GNS Science.

Mavrouli, O., Corominas, J. (2010). Rockfall vulnerability assessment for reinforced concrete buildings. *Nat. Hazards Earth Syst. Sci.*, 10, 2055-2066. https://doi.org/10.5194/nhess-10-2055-2010

Oakley, N., Cannon, F., Munroe, R., Lancaster, J., Gomberg, D., Ralph, F. (2018). Brief communication: Meterological and climatological conditions associated with the 9 January 2018 post-fire debris flows in Montecito and Carpinteria, California, USA. *Nat. Hazards Earth Syst. Sci*., 18, 3037-3043. https://doi.org/10.5194/nhess-18-3037-2018.

Papathoma-Kohle, M., Keiler, M., Totschnig, R., Glade, T. (2012). Improvement of vulnerability curves using data from extreme events: Debris flow event in South Tyrol. *Nat. Hazards*, 64, 2083-2105. https://doi.org/10.1007/s11069-012-0105-9

Papathoma-Kohle, M., Zischg, A., Fuchs, S., Glade, T., Keiler, M. (2015). Loss estimation for landslides in mountain areas – An integrated toolbox for vulnerability assessment and damage documentation. *Environ. Modell. Software*, 63, 156-169. https://doi.org/10.1016/j.envsoft.2014.10.003

Quan Luna, B., Blahut, J., van Westen, C., Sterlacchini, S., van Asch, T., Akbas, O. (2011). The application of numerical debris flow modelling for the generation of physical vulnerability curves. *Nat. Hazards Earth Syst. Sci.*, 11, 2047-2060. https://doi.org/10.5194/nhess-11-2047-2011

Rheinberger, C., Romang, H., Brundl, M. (2013). Proportional loss functions for debris flow events. *Nat. Hazards Earth Syst. Sci*., 13, 2147-2156. https://doi.org/10.5194/nhess-13-2147-2013

Totschnig, R., Fuchs, S. (2013). Mountain torrents: Quantifying vulnerability and assessing uncertainties. *Eng. Geol.*, 155, 31-44. https://doi.org/10.1016/j.enggeo.2012.12.019

Totschnig, R., Sedlacek, W., and Fuchs, S. (2011). A quantitative vulnerability function for fluvial sediment transport. *Nat. Hazards*, 58, 681-703. https://doi.org/10.1007/s11069-010-9623-5

Appendix 3.1 – Global flowslide database

Identifier	*Common name*	*Location*	*L (m)*	*H/L*	*Volume (m^3)*	*Reference*
CC01		Folkestone Warren, Kent, UK	628	0.22	1150000	Bowman & Take (2015), Hutchinson (2002), Hutchinson (1988)
CC02		Abbot's Cliff, Kent, UK	471	0.28	260000	Bowman & Take (2015), Hutchinson (2002), Hutchinson (1988)
CC03		Abbot's Cliff, Kent, UK	442	0.32	280000	Bowman & Take (2015), Hutchinson (2002), Hutchinson (1988)
CC04		Shakespeare Cliff, Kent, UK	366	0.24	400000	Bowman & Take (2015), Hutchinson (2002), Hutchinson (1988)
CC05		St. Margaret's Bay, Kent, UK	394	0.19	182000	Bowman & Take (2015), Hutchinson (2002), Hutchinson (1988)
CC06		St. Margaret's Bay, Kent, UK	115	0.66	39000	Bowman & Take (2015), Hutchinson (2002), Hutchinson (1988)
CC07		Jasmund, Germany	227	0.28	126000	Bowman & Take (2015), Hutchinson (2002)
CC08		LaVal de la Mer , France	320	0.33	498000	Bowman & Take (2015), Hutchinson (2002)
CC09		St. Valery en Caux, France	125	0.54	125000	Bowman & Take (2015), Hutchinson (2002)
CC10		Beachy Head, UK	130	0.54	100000	Mortimore et al. (2004)
FD01	Sheffield Dam	California, USA	64	0.12	16000	Hunter & Fell (2001)
FD02	Lower San Fernando Dam	California, USA	177	0.18	400000	Hunter & Fell (2001)
FD03	Calaveras Dam	California, USA	440	0.13	600000	Hunter & Fell (2001)
FD04	Wachusett Dam	Massachusetts, USA	179	0.14	47000	Hunter & Fell (2001)
FD05	Fort Peck Dam	Montana, USA	880	0.07	8000000	Hunter & Fell (2001)
FD06	Nerlerk Berm Slide 1	Beaufort Sea, Canada	625	0.04	80000	Hunter & Fell (2001)
FD07	Nerlerk Berm Slide 2	Beaufort Sea, Canada	550	0.05	100000	Hunter & Fell (2001)
FD08	Nerlerk Berm Slide 4	Beaufort Sea, Canada	625	0.04	150000	Hunter & Fell (2001)
FD09	Willamette River Terminal 2	Oregon, USA	72	0.29	4000	Hunter & Fell (2001)
GF01	Attachie	British Columbia, Canada	1500	0.14	12400000	Fletcher et al. (2002)
GF02	Rowan	Stillaguamish River Valley, Washington, USA	1980	0.10	40598000	LaHusen et al. (2015)
GF03	Hazel	Stillaguamish River Valley, Washington, USA	550	0.26	1911000	Badger (2015), LaHusen et al. (2015)
GF04	Sharktooth	Shesley River, British Columbia, Canada	1200		3500000	Geertsema et al. (2006)
GF05	Inklin	Inklin River, British Columbia, Canada	700		2500000	Geertsema et al. (2006)
GF06	Halfway	Peace River Distric, British Columbia, Canada	1210	0.15	3600000	Van Esch (2012), Brobrowsky & Smith (1992)
GF07	CWR1	Cedar River Watershed, Washington, USA	729	0.15	1136000	*this study*
GF08	CWR2/Ced-6	Cedar River Watershed, Washington, USA	1146	0.15	1206000	Perkins et al. (2017)
GF09	CWR3/Ced-4	Cedar River Watershed, Washington, USA	743	0.20	447000	Perkins et al. (2017)
GF10	CWR4/Ced-3	Cedar River Watershed, Washington, USA	1032	0.18	896000	Perkins et al. (2017)
GF11	CWR5/Ced-2	Cedar River Watershed, Washington, USA	1123	0.16	985000	Perkins et al. (2017)
GF12	CWR6	Cedar River Watershed, Washington, USA	1202	0.16	2248000	*this study*
GF13	CWR7/Ced-7	Cedar River Watershed, Washington, USA	522	0.15	205000	Perkins et al. (2017)
GF14	CWR8/Ced-5	Cedar River Watershed, Washington, USA	467	0.30	63000	Perkins et al. (2017)

GF15	CWR9	Cedar River Watershed, Washington, USA	977	0.21	1036647	*this study*
GF16	CWR10	Cedar River Watershed, Washington, USA	417	0.28	184633	*this study*
GF17	CWR11	Cedar River Watershed, Washington, USA	492	0.38	371478	*this study*
GF18	CWR12	Cedar River Watershed, Washington, USA	795	0.26	566939	*this study*
GF19	CWR13	Cedar River Watershed, Washington, USA	489	0.27	502330	*this study*
GF20	CWR14	Cedar River Watershed, Washington, USA	464	0.51	244901	*this study*
GF21	CWR15	Cedar River Watershed, Washington, USA	450	0.56	238171	*this study*
GF22	CWR16	Cedar River Watershed, Washington, USA	564	0.22	212009	*this study*
GF23	SW1	Cedar River Watershed, Washington, USA	200	0.29	25923	*this study*
GF24	SW2	Cedar River Watershed, Washington, USA	267	0.23	64166	*this study*
GF25	MID1	Cedar River Watershed, Washington, USA	202	0.38	88938	*this study*
GF26	NW1	Cedar River Watershed, Washington, USA	87	0.36	11004	*this study*
GF27	BA6S	Stillaguamish River Valley, Washington, USA	1400	0.13	38228000	Badger (2015), LaHusen et al. (2015)
GF28	Houston Tommy	British Columbia, Canada	1200	0.11	15000000	Schwab et al. (2011), Geertsema & Cruden (2008)
L01	DC2	Heitai Terrace, Gansu, China	346	0.31	320300	Peng et al. (2018), Xu et al. (2017), Qi et al. (2018)
L02	DC3	Heitai Terrace, Gansu, China	293	0.35	773200	Peng et al. (2018), Xu et al. (2017), Qi et al. (2018)
L03	DC4	Heitai Terrace, Gansu, China	99	0.75	31100	Peng et al. (2018), Xu et al. (2017), Qi et al. (2018)
L04	JY1	Heitai Terrace, Gansu, China	226	0.58	286800	Peng et al. (2018), Xu et al. (2017), Qi et al. (2018)
L05	JY2	Heitai Terrace, Gansu, China	181	0.67	70500	Peng et al. (2018), Xu et al. (2017), Qi et al. (2018)
L06	JY3	Heitai Terrace, Gansu, China	218	0.61	81600	Peng et al. (2018), Xu et al. (2017), Qi et al. (2018)
L07	JY4	Heitai Terrace, Gansu, China	163	0.66	52600	Peng et al. (2018), Xu et al. (2017), Qi et al. (2018)
L08	JY5	Heitai Terrace, Gansu, China	201	0.46	73200	Peng et al. (2018), Xu et al. (2017), Qi et al. (2018)
L09	JJ1	Heitai Terrace, Gansu, China	353	0.34	343800	Peng et al. (2018), Xu et al. (2017), Qi et al. (2018)
L10	JJ2	Heitai Terrace, Gansu, China	426	0.28	889900	Peng et al. (2018), Xu et al. (2017), Qi et al. (2018)
L11	JJ3	Heitai Terrace, Gansu, China	515	0.24	928800	Peng et al. (2018), Xu et al. (2017), Qi et al. (2018)
L12	JJ4	Heitai Terrace, Gansu, China	610	0.20	3338100	Peng et al. (2018), Xu et al. (2017), Qi et al. (2018)
L13	JJ5	Heitai Terrace, Gansu, China	469	0.26	1526500	Peng et al. (2018), Xu et al. (2017), Qi et al. (2018)
L14	JJ6	Heitai Terrace, Gansu, China	326	0.33	332000	Peng et al. (2018), Xu et al. (2017), Qi et al. (2018)
L15	JJ7	Heitai Terrace, Gansu, China	323	0.31	105500	Peng et al. (2018), Xu et al. (2017), Qi et al. (2018)
L16	JJ8	Heitai Terrace, Gansu, China	391	0.26	528600	Peng et al. (2018), Xu et al. (2017), Qi et al. (2018)
L17	CJ3	Heitai Terrace, Gansu, China	284	0.37	556500	Peng et al. (2018), Xu et al. (2017), Qi et al. (2018)
L18	Ximiaodian	Jing River Basin, China	397	0.11	216000	Wang et al. (2018)
L19	Bailu Tableland	Xian, Shaanxi, China	150	0.54	95000	Zhuang & Peng (2014)
L20	Okuli	Dushanbe, Tajikistan	3500	0.02	30600000	Ishihara et al. (1990), Havenith (2015)
L21	Kainama	Alay, Kyrgyzstan	1250	0.26	700000	Havenith et al. (2015b), Danneels et al. (2008)
L22	Sale Mt.	Gansu, China	1600	0.20	30000000	Zhang et al. (2002)
M01	Gold Quarry	Nevada, USA	700	0.31	6500000	Whittall (2015)
M02	Sedlitz	Germany	2460	0.20	12000000	Wichter (2007)
MW01	Fforchman	South Wales, UK	290	0.34	40000	Hunter & Fell (2001)
MW02	Cilfynydd (Abercynon)	South Wales, UK	590	0.22	115000	Hunter & Fell (2001)
MW03	Nantewlaeth	South Wales, UK	170	0.24	20000	Hunter & Fell (2001)

MW04	Aberfan-Tip 7	South Wales, UK	690	0.26	150000	Hunter & Fell (2001)
MW05	Aberfan-Tip 7	South Wales, UK	390	0.27	10000	Hunter & Fell (2001)
MW06	Mynydd Comwig Fechan	South Wales, UK	320	0.31	40000	Hunter & Fell (2001)
MW07	Bedwelty	South Wales, UK	340	0.35	90000	Hunter & Fell (2001)
MW08	Rhondda Main	South Wales, UK	200	0.38	6000	Hunter & Fell (2001)
MW09	Penbre	South Wales, UK	300	0.38	50000	Hunter & Fell (2001)
MW10	Parc	South Wales, UK	213	0.41	10000	Hunter & Fell (2001)
MW11	Brownie (FCL)	British Columbia, Canada	910	0.49	225000	Hunter & Fell (2001)
MW12	13 Seam (FCL)	British Columbia, Canada	550	0.45	250000	Hunter & Fell (2001)
MW13	2-Spoil (FCL)	British Columbia, Canada	650	0.42	50000	Hunter & Fell (2001)
MW14	2-Spoil (FCL)	British Columbia, Canada	630	0.43	160000	Hunter & Fell (2001)
MW15	2-Spoil (FCL)	British Columbia, Canada	770	0.35	450000	Hunter & Fell (2001)
MW16	2-Spoil (FCL)	British Columbia, Canada	520	0.48	750000	Hunter & Fell (2001)
MW17	1690 MT (QCL)	British Columbia, Canada	1480	0.30	2200000	Hunter & Fell (2001)
MW18	South (FCL)	British Columbia, Canada	1270	0.39	3000000	Hunter & Fell (2001)
MW19	South (FCL)	British Columbia, Canada	1030	0.36	8000000	Hunter & Fell (2001)
MW20	Peak Downs	Hay Point, Australia	46	0.24	3500	Hunter & Fell (2001)
MW21	Saraji (2 South)	Hay Point, Australia	27	0.34	5000	Hunter & Fell (2001)
MW22	Saraji (1 South)	Hay Point, Australia	40	0.23	5600	Hunter & Fell (2001)
MW23	Goonyelta (1 North)	Hay Point, Australia	45	0.23	11300	Hunter & Fell (2001)
MW24	Saraji (1 South)	Hay Point, Australia	45	0.23	10900	Hunter & Fell (2001)
MW25	Saraji (1 South)	Hay Point, Australia	43	0.31	4500	Hunter & Fell (2001)
MW26	Peak Downs (Expt)	Hay Point, Australia	23	0.26	1250	Hunter & Fell (2001)
MW27	Peak Downs (Expt)	Hay Point, Australia	20	0.30	850	Hunter & Fell (2001)
MW28	Blackpool	UK	130	0.42	11000	Bishop (1973), Boyd (1992), McLemore et al. (2009)
MW29	Cholwich Town	UK	253	0.25	18000	Bishop (1973), Boyd (1992)
OS001	La Pintata	La Pintata, Mexico	612	0.21	125000	Alcantara-Ayala et al. (2017)
OS002		Vancouver Island, British Columbia, Canada	25	0.59	26	Brideau et al. (2019)
OS003		Vancouver Island, British Columbia, Canada	45	0.93	77	Brideau et al. (2019)
OS004		Vancouver Island, British Columbia, Canada	122	0.47	115	Brideau et al. (2019)
OS005		Vancouver Island, British Columbia, Canada	57	0.60	180	Brideau et al. (2019)
OS006		Vancouver Island, British Columbia, Canada	61	0.54	263	Brideau et al. (2019)
OS007		Vancouver Island, British Columbia, Canada	123	0.41	269	Brideau et al. (2019)
OS008		Vancouver Island, British Columbia, Canada	60	0.48	366	Brideau et al. (2019)
OS009		Vancouver Island, British Columbia, Canada	88	0.57	366	Brideau et al. (2019)
OS010		Vancouver Island, British Columbia, Canada	153	0.53	398	Brideau et al. (2019)
OS011		Vancouver Island, British Columbia, Canada	95	0.59	411	Brideau et al. (2019)
OS012		Vancouver Island, British Columbia, Canada	146	0.57	410	Brideau et al. (2019)
OS013		Vancouver Island, British Columbia, Canada	66	0.43	430	Brideau et al. (2019)
OS014		Vancouver Island, British Columbia, Canada	101	0.42	449	Brideau et al. (2019)
OS015		Vancouver Island, British Columbia, Canada	213	0.49	487	Brideau et al. (2019)

OS016		Vancouver Island, British Columbia, Canada	153	0.62	577	Brideau et al. (2019)
OS017		Vancouver Island, British Columbia, Canada	51	0.41	603	Brideau et al. (2019)
OS018		Vancouver Island, British Columbia, Canada	214	0.40	603	Brideau et al. (2019)
OS019		Vancouver Island, British Columbia, Canada	67	0.49	622	Brideau et al. (2019)
OS020		Vancouver Island, British Columbia, Canada	118	0.49	629	Brideau et al. (2019)
OS021		Vancouver Island, British Columbia, Canada	155	0.69	667	Brideau et al. (2019)
OS022		Vancouver Island, British Columbia, Canada	245	0.58	1033	Brideau et al. (2019)
OS023		Vancouver Island, British Columbia, Canada	400	0.64	1219	Brideau et al. (2019)
OS024		Vancouver Island, British Columbia, Canada	536	0.43	1244	Brideau et al. (2019)
OS025		Vancouver Island, British Columbia, Canada	447	0.43	1379	Brideau et al. (2019)
OS026		Vancouver Island, British Columbia, Canada	270	0.37	1539	Brideau et al. (2019)
OS027		Vancouver Island, British Columbia, Canada	644	0.43	1719	Brideau et al. (2019)
OS028		Vancouver Island, British Columbia, Canada	254	0.61	1835	Brideau et al. (2019)
OS029		Vancouver Island, British Columbia, Canada	328	0.50	2078	Brideau et al. (2019)
OS030		Vancouver Island, British Columbia, Canada	438	0.45	2207	Brideau et al. (2019)
OS031		Vancouver Island, British Columbia, Canada	491	0.41	2303	Brideau et al. (2019)
OS032		Vancouver Island, British Columbia, Canada	425	0.36	2335	Brideau et al. (2019)
OS033		Vancouver Island, British Columbia, Canada	146	0.58	2354	Brideau et al. (2019)
OS034		Vancouver Island, British Columbia, Canada	427	0.49	2502	Brideau et al. (2019)
OS035		Vancouver Island, British Columbia, Canada	411	0.43	2623	Brideau et al. (2019)
OS036		Vancouver Island, British Columbia, Canada	341	0.44	3053	Brideau et al. (2019)
OS037		Vancouver Island, British Columbia, Canada	539	0.44	4323	Brideau et al. (2019)
OS038		Vancouver Island, British Columbia, Canada	463	0.30	9192	Brideau et al. (2019)
OS039	Scrajo	Vico Equense, Italy	300	0.73	10000	Budetta & de Riso (2004)
OS040	M. Pendolo	Gragnano, Italy	375	0.55	7500	Budetta & de Riso (2004)
OS041	S. Pantaleone	Pagani, Italy	180	0.50	5000	Budetta & de Riso (2004)
OS042	S. Costanzo	Mitigliano, Italy	272	0.74	9000	Budetta & de Riso (2004)
OS043	Palma Campania	Palma C., Italy	400	0.46	8000	Budetta & de Riso (2004)
OS044	S. Pantaleone 2	Pagani, Italy	240	0.56	4500	Budetta & de Riso (2004)
OS045	M. Pendolo 2	Gragnano, Italy	210	0.60	4500	Budetta & de Riso (2004)
OS046	M. Pendolo 3	Pimonte, Italy	135	0.93	4300	Budetta & de Riso (2004)
OS047	S. Edigio M. Albino	S. Egidio, Italy	500	0.43	10000	Budetta & de Riso (2004)
OS048	V. Calabrici	Sarno, Italy	1800	0.33	274000	Budetta & de Riso (2004)
OS049	Monteforte Irpino	Monteforte Irpino, Italy	350	0.71	8000	Budetta & de Riso (2004)
OS050	Castello	Cervinara, Italy	2100	0.23	240000	Budetta & de Riso (2004)
OS051	Oldedalen	Norway	790	0.57	15000	Carey (2018)
OS052	Ringebu	Norway	175	0.39	350	Carey (2018)
OS053	d010	E. Pyrenees, Spain	223	0.36	398	Corominas (1996)
OS054	d007	E. Pyrenees, Spain	242	0.34	2188	Corominas (1996)
OS055	d022	E. Pyrenees, Spain	336	0.36	5888	Corominas (1996)
OS056	d028	E. Pyrenees, Spain	53	0.55	200	Corominas (1996)
OS057	d037	E. Pyrenees, Spain	236	0.58	977	Corominas (1996)

OS058	d039	E. Pyrenees, Spain	23	0.70	52	Corominas (1996)
OS059	d040	E. Pyrenees, Spain	34	0.71	219	Corominas (1996)
OS060	d041	E. Pyrenees, Spain	40	0.75	79	Corominas (1996)
OS061	d044	E. Pyrenees, Spain	74	0.50	933	Corominas (1996)
OS062	d050	E. Pyrenees, Spain	25	0.52	219	Corominas (1996)
OS063	d053	E. Pyrenees, Spain	33	0.45	407	Corominas (1996)
OS064	d054	E. Pyrenees, Spain	45	0.71	316	Corominas (1996)
OS065	d055	E. Pyrenees, Spain	35	0.46	200	Corominas (1996)
OS066	d057	E. Pyrenees, Spain	98	0.35	724	Corominas (1996)
OS067	d099	E. Pyrenees, Spain	147	0.38	1175	Corominas (1996)
OS068	Alba Road	Santa Cruz, California, USA	200		6800	Wieczorek et al. (1988)
OS069		Nepal	49		254	Hearn (2011)
OS070		Nepal	49		269	Hearn (2011)
OS071		Nepal	54		294	Hearn (2011)
OS072		Nepal	59		309	Hearn (2011)
OS073		Nepal	83		379	Hearn (2011)
OS074		Nepal	44		364	Hearn (2011)
OS075		Nepal	73		475	Hearn (2011)
OS076		Nepal	103		554	Hearn (2011)
OS077		Nepal	132		601	Hearn (2011)
OS078		Nepal	118		668	Hearn (2011)
OS079		Nepal	113		780	Hearn (2011)
OS080		Nepal	122		852	Hearn (2011)
OS081		Nepal	147		925	Hearn (2011)
OS082		Nepal	147		1199	Hearn (2011)
OS083		Nepal	171		1189	Hearn (2011)
OS084		Nepal	196		1399	Hearn (2011)
OS085		Nepal	211		1311	Hearn (2011)
OS086		Nepal	93		2099	Hearn (2011)
OS087		Nepal	548		16363	Hearn (2011)
OS088		Nepal	69		424	Hearn (2011)
OS089	Loch Quoich	Kinloch Hourn, Scotland	1000		4500	https://blogs.agu.org/landslideblog/page/2/ https://www.highland.gov.uk/news/article/11500/loch_quoich_landslip_update https://www.bbc.com/news/uk-scotland-highlands-islands-46193629
OS090		Hong Kong	65	0.49	210	Hunter & Fell (2001)
OS091		Hong Kong	33	0.46	250	Hunter & Fell (2001)
OS092		Hong Kong	72	0.47	14000	Hunter & Fell (2001)
OS093		Hong Kong	81	0.39	2000	Hunter & Fell (2001)
OS094		Hong Kong	14	0.72	200	Hunter & Fell (2001)
OS095		Hong Kong	83	0.35	150	Hunter & Fell (2001)
OS096		Hong Kong	12	1.07	70	Hunter & Fell (2001)
OS097		Hong Kong	28	0.56	1100	Hunter & Fell (2001)
OS098		Hong Kong	44	0.64	33	Hunter & Fell (2001)

OS099		Hong Kong	46	0.53	300	Hunter & Fell (2001)
OS100		Hong Kong	270	0.44	40000	Hunter & Fell (2001)
OS101		Hong Kong	49	0.59	250	Hunter & Fell (2001)
OS102		Hong Kong	24	0.52	1000	Hunter & Fell (2001)
OS103		Hong Kong	44	0.60	500	Hunter & Fell (2001)
OS104		Hong Kong	52	0.43	500	Hunter & Fell (2001)
OS105		Hong Kong	73	0.32	450	Hunter & Fell (2001)
OS106		Hong Kong	22	0.52	200	Hunter & Fell (2001)
OS107		Hong Kong	58	0.45	170	Hunter & Fell (2001)
OS108		Hong Kong	38	0.57	400	Hunter & Fell (2001)
OS109	Shum Wan	Hong Kong	219	0.32	26000	Hunter & Fell (2001)
OS110	Tao Fung Shan Cemetary A	Hong Kong	104	0.58	500	Hunter & Fell (2001)
OS111	Glorious Praise Christian Centre	Hong Kong	17	0.52	20	Hunter & Fell (2001)
OS112	Lido Beach	Hong Kong	83	0.39	750	Hunter & Fell (2001)
OS113		Hong Kong	55	0.63	225	Hunter & Fell (2001), Chan et al. (1996)
OS114	TC-6A/1, Tung Chung	Hong Kong	93	0.91	100	Hunter & Fell (2001), Ayotte & Hungr (1998)
OS115	TC-5A/10, Tung Chung	Hong Kong	73	0.68	300	Hunter & Fell (2001), Ayotte & Hungr (1998)
OS116	Lantau Island, Slide A6	Hong Kong	180	0.49	400	Hunter & Fell (2001), Ayotte & Hungr (1998)
OS117	JK 515, New Territories	Hong Kong	120	0.49	300	Hunter & Fell (2001), Ayotte & Hungr (1998)
OS118	JK 410, New Territories	Hong Kong	100	0.63	400	Hunter & Fell (2001), Ayotte & Hungr (1998)
OS119	Luk Keng	Hong Kong	150	0.38	170	Hunter & Fell (2001), Ayotte & Hungr (1998)
OS120	Fo Tan Station	Hong Kong	38	0.59	85	Hunter & Fell (2001), Ayotte & Hungr (1998)
OS121		Switzerland	16		17	Hurlimann et al. (2015)
OS122		Switzerland	20		14	Hurlimann et al. (2015)
OS123		Switzerland	23		14	Hurlimann et al. (2015)
OS124		Switzerland	27		14	Hurlimann et al. (2015)
OS125		Switzerland	34		14	Hurlimann et al. (2015)
OS126		Switzerland	74		16	Hurlimann et al. (2015)
OS127		Switzerland	43		18	Hurlimann et al. (2015)
OS128		Switzerland	45		19	Hurlimann et al. (2015)
OS129		Switzerland	42		22	Hurlimann et al. (2015)
OS130		Switzerland	46		23	Hurlimann et al. (2015)
OS131		Switzerland	63		125	Hurlimann et al. (2015)
OS132		Switzerland	68		134	Hurlimann et al. (2015)
OS133		Switzerland	53		153	Hurlimann et al. (2015)
OS134		Switzerland	32		144	Hurlimann et al. (2015)
OS135		Switzerland	24		260	Hurlimann et al. (2015)
OS136		Switzerland	39		385	Hurlimann et al. (2015)
OS137		Switzerland	50		350	Hurlimann et al. (2015)

OS138	Switzerland	55	396	Hurlimann et al. (2015)
OS139	Switzerland	68	400	Hurlimann et al. (2015)
OS140	Switzerland	76	369	Hurlimann et al. (2015)
OS141	Switzerland	43	24	Hurlimann et al. (2015)
OS142	Switzerland	110	802	Hurlimann et al. (2015)
OS143	Switzerland	93	756	Hurlimann et al. (2015)
OS144	Switzerland	129	958	Hurlimann et al. (2015)
OS145	Switzerland	204	917	Hurlimann et al. (2015)
OS146	Switzerland	167	653	Hurlimann et al. (2015)
OS147	Switzerland	60	675	Hurlimann et al. (2015)
OS148	Switzerland	45	198	Hurlimann et al. (2015)
OS149	Switzerland	51	210	Hurlimann et al. (2015)
OS150	Switzerland	75	160	Hurlimann et al. (2015)
OS151	Switzerland	75	255	Hurlimann et al. (2015)
OS152	Switzerland	33	25	Hurlimann et al. (2015)
OS153	Switzerland	94	256	Hurlimann et al. (2015)
OS154	Switzerland	80	112	Hurlimann et al. (2015)
OS155	Switzerland	81	106	Hurlimann et al. (2015)
OS156	Switzerland	168	2798	Hurlimann et al. (2015)
OS157	Switzerland	340	2255	Hurlimann et al. (2015)
OS158	Switzerland	462	937	Hurlimann et al. (2015)
OS159	Switzerland	435	559	Hurlimann et al. (2015)
OS160	Switzerland	24	27	Hurlimann et al. (2015)
OS161	Switzerland	22	29	Hurlimann et al. (2015)
OS162	Switzerland	16	26	Hurlimann et al. (2015)
OS163	Switzerland	24	32	Hurlimann et al. (2015)
OS164	Switzerland	20	38	Hurlimann et al. (2015)
OS165	Switzerland	26	39	Hurlimann et al. (2015)
OS166	Switzerland	27	42	Hurlimann et al. (2015)
OS167	Switzerland	31	40	Hurlimann et al. (2015)
OS168	Switzerland	45	30	Hurlimann et al. (2015)
OS169	Switzerland	44	32	Hurlimann et al. (2015)
OS170	Switzerland	52	33	Hurlimann et al. (2015)
OS171	Switzerland	57	31	Hurlimann et al. (2015)
OS172	Switzerland	68	33	Hurlimann et al. (2015)
OS173	Switzerland	56	47	Hurlimann et al. (2015)
OS174	Switzerland	62	47	Hurlimann et al. (2015)
OS175	Switzerland	60	50	Hurlimann et al. (2015)
OS176	Switzerland	66	57	Hurlimann et al. (2015)
OS177	Switzerland	74	62	Hurlimann et al. (2015)
OS178	Switzerland	101	54	Hurlimann et al. (2015)
OS179	Switzerland	93	90	Hurlimann et al. (2015)

OS180	Switzerland	119	105	Hurlimann et al. (2015)
OS181	Switzerland	100	112	Hurlimann et al. (2015)
OS182	Switzerland	146	108	Hurlimann et al. (2015)
OS183	Switzerland	141	100	Hurlimann et al. (2015)
OS184	Switzerland	145	90	Hurlimann et al. (2015)
OS185	Switzerland	150	63	Hurlimann et al. (2015)
OS186	Switzerland	186	42	Hurlimann et al. (2015)
OS187	Switzerland	194	132	Hurlimann et al. (2015)
OS188	Switzerland	175	194	Hurlimann et al. (2015)
OS189	Switzerland	145	179	Hurlimann et al. (2015)
OS190	Switzerland	121	170	Hurlimann et al. (2015)
OS191	Switzerland	99	165	Hurlimann et al. (2015)
OS192	Switzerland	108	191	Hurlimann et al. (2015)
OS193	Switzerland	87	210	Hurlimann et al. (2015)
OS194	Switzerland	181	150	Hurlimann et al. (2015)
OS195	Switzerland	219	159	Hurlimann et al. (2015)
OS196	Switzerland	141	279	Hurlimann et al. (2015)
OS197	Switzerland	118	318	Hurlimann et al. (2015)
OS198	Switzerland	107	346	Hurlimann et al. (2015)
OS199	Switzerland	98	330	Hurlimann et al. (2015)
OS200	Switzerland	120	379	Hurlimann et al. (2015)
OS201	Switzerland	113	392	Hurlimann et al. (2015)
OS202	Switzerland	146	377	Hurlimann et al. (2015)
OS203	Switzerland	178	342	Hurlimann et al. (2015)
OS204	Switzerland	35	30	Hurlimann et al. (2015)
OS205	Switzerland	40	40	Hurlimann et al. (2015)
OS206	Switzerland	43	45	Hurlimann et al. (2015)
OS207	Switzerland	45	44	Hurlimann et al. (2015)
OS208	Switzerland	48	45	Hurlimann et al. (2015)
OS209	Switzerland	42	48	Hurlimann et al. (2015)
OS210	Switzerland	41	50	Hurlimann et al. (2015)
OS211	Switzerland	34	56	Hurlimann et al. (2015)
OS212	Switzerland	32	60	Hurlimann et al. (2015)
OS213	Switzerland	27	62	Hurlimann et al. (2015)
OS214	Switzerland	25	65	Hurlimann et al. (2015)
OS215	Switzerland	30	70	Hurlimann et al. (2015)
OS216	Switzerland	31	50	Hurlimann et al. (2015)
OS217	Switzerland	24	48	Hurlimann et al. (2015)
OS218	Switzerland	17	50	Hurlimann et al. (2015)
OS219	Switzerland	20	60	Hurlimann et al. (2015)
OS220	Switzerland	20	62	Hurlimann et al. (2015)
OS221	Switzerland	22	80	Hurlimann et al. (2015)

OS222		Switzerland	44		56	Hurlimann et al. (2015)
OS223		Switzerland	48		64	Hurlimann et al. (2015)
OS224		Switzerland	49		70	Hurlimann et al. (2015)
OS225		Switzerland	46		70	Hurlimann et al. (2015)
OS226		Switzerland	45		80	Hurlimann et al. (2015)
OS227		Switzerland	44		88	Hurlimann et al. (2015)
OS228		Switzerland	51		86	Hurlimann et al. (2015)
OS229		Switzerland	52		80	Hurlimann et al. (2015)
OS230		Switzerland	56		80	Hurlimann et al. (2015)
OS231		Switzerland	61		77	Hurlimann et al. (2015)
OS232		Switzerland	61		72	Hurlimann et al. (2015)
OS233		Switzerland	64		84	Hurlimann et al. (2015)
OS234		Switzerland	66		89	Hurlimann et al. (2015)
OS235		Switzerland	59		97	Hurlimann et al. (2015)
OS236		Switzerland	47		97	Hurlimann et al. (2015)
OS237		Switzerland	41		100	Hurlimann et al. (2015)
OS238		Switzerland	37		100	Hurlimann et al. (2015)
OS239		Switzerland	35		96	Hurlimann et al. (2015)
OS240		Switzerland	28		113	Hurlimann et al. (2015)
OS241		Switzerland	32		120	Hurlimann et al. (2015)
OS242		Switzerland	32		125	Hurlimann et al. (2015)
OS243		Switzerland	38		117	Hurlimann et al. (2015)
OS244		Switzerland	46		128	Hurlimann et al. (2015)
OS245		Switzerland	51		125	Hurlimann et al. (2015)
OS246		Switzerland	59		120	Hurlimann et al. (2015)
OS247	Makiuchi	Nagano, Japan	250		200000	Japan Society of Landslides (1972)
OS248	Terao	Yui, Shizuoka, Japan	520		1200000	Japan Society of Landslides (1972)
OS249	Jizukiyama	Nagano, Japan	700		3500000	Japan Society of Landslides (1996)
OS250	Bishamon	Japan	250	0.32	1000000	Japan Society of Landslides (1996)
OS251	Shuicheng	Guizhou, China	1300	0.38	2000000	Li et al. (2019)
OS252	An teallach 1	Scotland	103		13	Milne (2008)
OS253	Glamaig 1	Scotland	158		181	Milne (2008)
OS254	Glamaig 2	Scotland	231		546	Milne (2008)
OS255	Lairig Ghru	Scotland	385		306	Milne (2008)
OS256	Drumochter	Scotland	435		604	Milne (2008)
OS257	Mill Glen	Scotland	73		20	Milne (2008)
OS258	Loch Eilt	Loch Eilt, Scotland	120	0.44	550	RAIB (2018)
OS259	Nocera Inferiore	Campania, Italy	580	0.49	27500	Revellino et al. (2013)
OS260		Tsing Shan, Hong Kong	3	0.62	2	Sun et al. (2003)
OS261		Tsing Shan, Hong Kong	5	0.63	2	Sun et al. (2003)
OS262		Tsing Shan, Hong Kong	10	0.55	3	Sun et al. (2003)
OS263		Tsing Shan, Hong Kong	7	0.57	4	Sun et al. (2003)

OS264	Tsing Shan, Hong Kong	3	0.56	4	Sun et al. (2003)
OS265	Tsing Shan, Hong Kong	7		5	Sun et al. (2003)
OS266	Tsing Shan, Hong Kong	9		5	Sun et al. (2003)
OS267	Tsing Shan, Hong Kong	12		5	Sun et al. (2003)
OS268	Tsing Shan, Hong Kong	8		6	Sun et al. (2003)
OS269	Tsing Shan, Hong Kong	19		6	Sun et al. (2003)
OS270	Tsing Shan, Hong Kong	7	0.56	7	Sun et al. (2003)
OS271	Tsing Shan, Hong Kong	9		8	Sun et al. (2003)
OS272	Tsing Shan, Hong Kong	7		8	Sun et al. (2003)
OS273	Tsing Shan, Hong Kong	6	0.59	9	Sun et al. (2003)
OS274	Tsing Shan, Hong Kong	11	0.50	12	Sun et al. (2003)
OS275	Tsing Shan, Hong Kong	17	0.61	12	Sun et al. (2003)
OS276	Tsing Shan, Hong Kong	19		14	Sun et al. (2003)
OS277	Tsing Shan, Hong Kong	7		14	Sun et al. (2003)
OS278	Tsing Shan, Hong Kong	12		18	Sun et al. (2003)
OS279	Tsing Shan, Hong Kong	15		18	Sun et al. (2003)
OS280	Tsing Shan, Hong Kong	28		18	Sun et al. (2003)
OS281	Tsing Shan, Hong Kong	9	0.56	22	Sun et al. (2003)
OS282	Tsing Shan, Hong Kong	13	0.66	24	Sun et al. (2003)
OS283	Tsing Shan, Hong Kong	12	0.52	25	Sun et al. (2003)
OS284	Tsing Shan, Hong Kong	10	0.57	27	Sun et al. (2003)
OS285	Tsing Shan, Hong Kong	4	0.58	30	Sun et al. (2003)
OS286	Tsing Shan, Hong Kong	24	0.48	32	Sun et al. (2003)
OS287	Tsing Shan, Hong Kong	9	0.57	35	Sun et al. (2003)
OS288	Tsing Shan, Hong Kong	48	0.62	39	Sun et al. (2003)
OS289	Tsing Shan, Hong Kong	27		40	Sun et al. (2003)
OS290	Tsing Shan, Hong Kong	37		40	Sun et al. (2003)
OS291	Tsing Shan, Hong Kong	39	0.50	42	Sun et al. (2003)
OS292	Tsing Shan, Hong Kong	17	0.41	43	Sun et al. (2003)
OS293	Tsing Shan, Hong Kong	15	0.50	44	Sun et al. (2003)
OS294	Tsing Shan, Hong Kong	30		47	Sun et al. (2003)
OS295	Tsing Shan, Hong Kong	23		47	Sun et al. (2003)
OS296	Tsing Shan, Hong Kong	12	0.47	54	Sun et al. (2003)
OS297	Tsing Shan, Hong Kong	20		58	Sun et al. (2003)
OS298	Tsing Shan, Hong Kong	16		59	Sun et al. (2003)
OS299	Tsing Shan, Hong Kong	47		62	Sun et al. (2003)
OS300	Tsing Shan, Hong Kong	51		62	Sun et al. (2003)
OS301	Tsing Shan, Hong Kong	31		63	Sun et al. (2003)
OS302	Tsing Shan, Hong Kong	71		63	Sun et al. (2003)
OS303	Tsing Shan, Hong Kong	60	0.45	65	Sun et al. (2003)
OS304	Tsing Shan, Hong Kong	55	0.47	68	Sun et al. (2003)
OS305	Tsing Shan, Hong Kong	27	0.52	70	Sun et al. (2003)

OS306		Tsing Shan, Hong Kong	13	0.57	70	Sun et al. (2003)
OS307		Tsing Shan, Hong Kong	44	0.58	76	Sun et al. (2003)
OS308		Tsing Shan, Hong Kong	25	0.48	80	Sun et al. (2003)
OS309		Tsing Shan, Hong Kong	21	0.49	81	Sun et al. (2003)
OS310		Tsing Shan, Hong Kong	44	0.52	90	Sun et al. (2003)
OS311		Tsing Shan, Hong Kong	63	0.50	95	Sun et al. (2003)
OS312		Tsing Shan, Hong Kong	26	0.44	99	Sun et al. (2003)
OS313		Tsing Shan, Hong Kong	53	0.46	125	Sun et al. (2003)
OS314		Lantau Is, Hong Kong	56	0.54	45	Sun et al. (2003), Wong et al. (1997)
OS315		Lantau Is, Hong Kong	26		50	Sun et al. (2003), Wong et al. (1997)
OS316		Lantau Is, Hong Kong	56		50	Sun et al. (2003), Wong et al. (1997)
OS317		Lantau Is, Hong Kong	50		70	Sun et al. (2003), Wong et al. (1997)
OS318		Lantau Is, Hong Kong	21		70	Sun et al. (2003), Wong et al. (1997)
OS319		Lantau Is, Hong Kong	98	0.60	100	Sun et al. (2003), Wong et al. (1997)
OS320		Lantau Is, Hong Kong	40		140	Sun et al. (2003), Wong et al. (1997)
OS321		Lantau Is, Hong Kong	103		140	Sun et al. (2003), Wong et al. (1997)
OS322		Lantau Is, Hong Kong	111	0.51	170	Sun et al. (2003), Wong et al. (1997)
OS323		Lantau Is, Hong Kong	64	0.56	320	Sun et al. (2003), Wong et al. (1997)
QC01	Hekseberg	Norway	700	0.06	175000	Hunter & Fell (2001), L'Heureux (2012)
QC02	Verdal	Norway	9100	0.01	55000000	Hunter & Fell (2001), L'Heureux (2012)
QC03	Selnes	Norway	450	0.06	140000	Hunter & Fell (2001), L'Heureux (2012)
QC04	Rissa	Norway	1100	0.03	5500000	Hunter & Fell (2001)
QC05	Skjalstadmerkan	Norway	2800	0.02	2000000	Hunter & Fell (2001)
QC06	Bergen	Norway	1500	0.02	120000	Hunter & Fell (2001)
QC07	Bekkelaget	Norway	160	0.10	100000	Hunter & Fell (2001)
QC08	Tulva	Sweden	850	0.02	400000	Hunter & Fell (2001)
QC09	Lakelse South	British Columbia, Canada	1100	0.03	11500000	Geertsema et al. (2017), Geertsema & Cruden (2008)
QC10	Saguenay River	Quebec, Canada	7200	0.02	206429812	LaSalle & Chagnon (1968)
RDA01	Lower Gros Ventre	Wyoming, USA	3400	0.17	35000000	Voight (1978), Legros (2002)
RDA02	Luanshibao	Tibetan Plateau, China	3830	0.21	79000000	Guo et al. (2016)
RDA03	Elm	Switzerland	2300	0.31	10000000	Legros (2002), Heim (1932), Hsu (1978)
RDA04	Blackhawk	California, USA	9600	0.13	280000000	Legros (2002), Johnson (1978), Voight & Pariseau (1978)
RDA05	Saidmarreh	Iran	18900	0.08	20000000000	Legros (2002), Harrison & Falcon (1937, 1938), Watson & Wright (1967)
RDA06	Pink Mt.	British Columbia, Canada	1950	0.21	1040000	Geertsema et al. (2006), Geertsema & Schwab (2006)
RDA07	Fagraskogarfjall	Iceland	1500	0.22	7000000	http://en.vedur.is/about-imo/news/displacements-in-fagraskogarfjall-for-some-time-before-the-landslide-fell https://blogs.agu.org/landslideblog/2018/07/26/fagraskogarfjall-landslide/ https://blogs.agu.org/landslideblog/2018/07/09/fagraskogarfjall-1/
RDA08	Guinsaugon	St. Bernard, Leyte, Philippines	3800	0.21	9200000	Evans et al. (2007), Makino et al. (2007), Voight et al. (2007)
RDA09	Chisca	British Columbia, CAN	1500	0.24	1000000	Geertsema et al. (2006), Egginton (2002)
RDA10	Sutherland	Sutherland River Valley, BC, CAN	1450	0.21	3000000	Blais-Stevens et al. (2007)
RDA11	Cheam	British Columbia, CAN	5700	0.28	170000000	Hewitt et al. (2008), Orwin et al. (2004)
RDA12	Frank	British Columbia, CAN	2700	0.33	30000000	Hewitt et al. (2008), Cruden & Hungr (1986), Hungr (2002)

RDA13	Cascade	New Zealand	4800	0.13	750000000	Barth (2013)
RDA14	Round Top North	New Zealand	4800	0.13	45000000	Dufresne et al. (2009), Wright (1998)
RDA15	Round Top South	New Zealand	1900	0.14	10000000	Dufresne et al. (2009), Wright (1998)
RDA16	Ghoro Choh I	Karakoram	7000	0.19	120000000	Hewitt (2002), Hewitt et al. (2008), Hewitt (1999)
RDA17	Baga Bogd	Mongolia	18500	0.01	50000000000	Philip & Ritz (1999)
RDA18	Marquartstein	Germany	3450	0.28	40000000	von Poschinger (1994)
RDA19	Tschingant	Austria	6200	0.23	225000000	Ostermann & Prager (2016), Abele (1994)
RDA20	Unzen	Japan	6500	0.13	340000000	Hayashi & Self (1992), Siebert (2002)
RDA21	Goldau	Switzerland	6000	0.20	35000000	Legros (2002), Erismann & Abele (2001), Heim (1932)
RDA22	Lavini di Marco	Italy	4750	0.21	200000000	Erismann & Abele (2001), Martin et al. (2014)
RDA23	Komansu	Kyrgyzstan	28000	0.11	8000000000	Robinson et al. (2015), Strom & Abdrakhmatov (2018)
RDA24	Waikaremoana	N. Is. New Zealand	7271	0.08	2500000000	Beetham et al. (2002)
RDA25	Tiniroto	N. Is. New Zealand	5786	0.06	1500000000	Beetham et al. (2002)
RDA26	Modalen	Modalen, Norway	730	0.42	100000	Evans et al. (2006), Kolderup (1955)
RDA27	Pusa	Pusa, Nayong, Guizhou, China	820	0.34	800000	Zhu et al. (2019), Fan et al. (2018), Xiao (2019)
RDA28	Pusa ZE	Pusa Nayong, Guizhou, China	100		8500	Fan et al. (2018)
RDA29	Platten	Obersee Valley, Switzerland	1600	0.39	11000000	Nagelisen et al. (2015), Aaron & McDougal (2019)
RDA30	Racehorse	Whatcom County, Washington, USA	3400	0.17	2500000000	Pringle et al. (1998)
RDA31	Van Zandt Complex, Lobe 3	Whatcom County, Washington, USA	1960	0.23	6500000	Malick (2018)
RDA32	Van Zandt Complex, Lobe 2	Whatcom County, Washington, USA	4000	0.14	51400000	Malick (2018)
RDA33	Marcus	Pheonix, Arizona, USA	1500	0.27	7250000	Douglass et al. (2005) http://azgs.arizona.edu/landslides-debris-flows/marcus-landslide
SA001	Grand Banks	*subaqueous*	110000	0.00	76000000000	Hampton et al. (1996)
SA002	Magdalena	*subaqueous*	24000	0.06	300000000	Hampton et al. (1996), Edgers & Karlsrud (1982)
SA003	Valdez	*subaqueous*	1280	0.13	75000000	Hampton et al. (1996), Edgers & Karlsrud (1982)
SA004	Orkdalsfjord	*subaqueous*	22500	0.02	25000000	Hampton et al. (1996), Edgers & Karlsrud (1982)
SA005	Sandnesjoen	*subaqueous*	1200	0.15	5000000	Hampton et al. (1996), Edgers & Karlsrud (1982)
SA006	Sokkelvik	*subaqueous*	2500	0.05	500000	Hampton et al. (1996)
SA007	Helsinki	*subaqueous*	400	0.03	6000	Hampton et al. (1996), Edgers & Karlsrud (1982)
SA008	Storegga	*subaqueous*	160000	0.01	800000000000	Hampton et al. (1996), Edgers & Karlsrud (1982)
SA009	Blake Escarpment	*subaqueous*	42000	0.09	600000000000	Hampton et al. (1996)
SA010	East Break East	*subaqueous*	70000	0.02	13000000000	Hampton et al. (1996)
SA011	East Break West	*subaqueous*	110000	0.01	160000000000	Hampton et al. (1996)
SA012	Kidnappers	*subaqueous*	11000	0.00	8000000000	Hampton et al. (1996)
SA013	Navarin Canyon	*subaqueous*	6000	0.03	5000000000	Hampton et al. (1996)
SA014	Seward	*subaqueous*	3000	0.07	2700000	Hampton et al. (1996)
SA015	Sur	*subaqueous*	70000	0.01	10000000000	Hampton et al. (1996)
SA016	Santa-Barbara	*subaqueous*	2300	0.05	20000000	Hampton et al. (1996)
SA017	Bassein	*subaqueous*	215000	0.01	800000000000	Edgers & Karlsrud (1982)
SA018	Spanish Sahara	*subaqueous*	700000	0.00	600000000000	Edgers & Karlsrud (1982)
SA019	Walvis Bay SW Africa	*subaqueous*	250000	0.01	90000000000	Edgers & Karlsrud (1982)

SA020	Ruatoria, Hikurangi Margin	*subaqueous*	110000		4106000000000	Collot et al. (2001)
SA021	Ice Bay/Malaspina	*subaqueous*	12000	0.01	32000000000	Edgers & Karlsrud (1982)
SA022	Copper River	*subaqueous*	8000	0.01	24000000000	Edgers & Karlsrud (1982)
SA023	Ranger	*subaqueous*	37000	0.02	20000000000	Edgers & Karlsrud (1982)
SA024	Mid Alb. Bank	*subaqueous*	5300	0.11	19000000000	Edgers & Karlsrud (1982)
SA025	Rockall	*subaqueous*	160000	0.00	300000000000	Hampton et al. (1996)
SA026	Wil. Canyon	*subaqueous*	60000	0.05	11000000000	Edgers & Karlsrud (1982)
SA027	Kayak trough	*subaqueous*	18000	0.01	5900000000	Edgers & Karlsrud (1982)
SA028	Paoanui	*subaqueous*	7000	0.03	1000000000	Edgers & Karlsrud (1982)
SA029	Mid. Atl. Cont. Slope	*subaqueous*	3500	0.09	4000000000	Edgers & Karlsrud (1982)
SA030	California	*subaqueous*	3500	0.04	250000000	Edgers & Karlsrud (1982)
SA031	Suva	*subaqueous*	110000	0.02	150000000	Edgers & Karlsrud (1982)
SA032	Kitimat	*subaqueous*	6000	0.03	200000000	Legros (2000), Prior (1984)
SA033	A1	*subaqueous*	370000	0.00	250000000000	Legros (2000)
SA034	A2	*subaqueous*	160000	0.01	22000000000	Legros (2000)
SA035	A3	*subaqueous*	140000	0.01	8500000000	Legros (2000)
SA036	A4A	*subaqueous*	130000	0.01	27000000000	Legros (2000)
SA037	A4B	*subaqueous*	400000	0.01	320000000000	Legros (2000)
SA038	Kae Lae	*subaqueous*	60000	0.08	40000000000	Legros (2000)
SA039	Molokai	*subaqueous*	130000	0.04	1100000000000	Legros (2000)
SA040	Oahu	*subaqueous*	180000	0.03	1800000000000	Legros (2000)
SA041	Roques de Garcia	*subaqueous*	130000	0.05	500000000000	Masson et al. (2001)
SA042	Traenadjupet	*subaqueous*	200000	0.00	760000000000	Elverhoi et al. (2002),
SA043	Bjornoyrenna	*subaqueous*	400000		1100000000000	Vorren et al. (1998), Laberg & Vorren (1993)
SA044	Finneidfjord	*subaqueous*	1000		1000000	L'Heureux (2012)
SA045	Pointe-du-Fort	*subaqueous*	1070	0.15	1950000	Locat et al. (2003)
SA046	Miller	*subaqueous*	50000	0.02	360000000000	Long et al. (2003)
SA047	Walker	*subaqueous*	1500		2000000	Long et al. (2003)
SA048	Afen	*subaqueous*	12000		400000000	Wilson et al. (2003), Long et al. (2003)
SA049	Brunei	*subaqueous*	120000		1200000000000	Gee et al. (2007)
SA050	Hinlopen	*subaqueous*	300000		1350000000000	Vanneste et al. (2006), Laberg et al. (2000)
SA051	Andoya	*subaqueous*	190000		900000000000	Vanneste et al. (2006), Leynaud et al. (2009)
SA052	Reloca	*subaqueous*	20500	0.11	24000000000	Volker et al. (2009)
SA053	Whittier Fjord	*subaqueous*	5000		20000000	Haeussler et al. (2014)
SA054	Santorini	*subaqueous*	21000	0.03	4400000000	Bell et al. (2013)
SA055	Mauritania Complex	*subaqueous*	320000		600000000000	Krastel et al. (2006)
SA056	Bagnara Calabra	*subaqueous*	600		16000	Avolio et al. (2009)
SA057	Sciara del Fuoco	*subaqueous*	30000	0.12	8500000000	Blahut et al. (2019)
SA058	East Gareloi	*subaqueous*	32000	0.11	600000000	Blahut et al. (2019)
SA059	Northwest Gareloi	*subaqueous*	42000	0.08	9000000000	Blahut et al. (2019)
SA060	Kanaga	*subaqueous*	58000	0.07	25000000000	Blahut et al. (2019)

SA061	Kiska	*subaqueous*	48000	0.04	59000000000	Blahut et al. (2019)
SA062	Sajaka I	*subaqueous*	27000	0.13	2900000000	Blahut et al. (2019)
SA063	Pico North A	*subaqueous*	28000	0.08	7000000000	Blahut et al. (2019)
SA064	Horgazales basin	*subaqueous*	65000	0.07	80000000000	Blahut et al. (2019)
SA065	Roque Nublo	*subaqueous*	55000	0.07	34000000000	Blahut et al. (2019)
SA066	El Golfo A	*subaqueous*	68000	0.07	84000000000	Blahut et al. (2019)
SA067	El Golfo B	*subaqueous*	73000	0.08	234000000000	Blahut et al. (2019)
SA068	El Julan	*subaqueous*	70000	0.07	130000000000	Blahut et al. (2019)
SA069	Las Playas II	*subaqueous*	60000	0.08	50000000000	Blahut et al. (2019)
SA070	Playa de la Veta	*subaqueous*	83000	0.08	650000000000	Blahut et al. (2019)
SA071	Guimar	*subaqueous*	90000	0.06	500000000000	Blahut et al. (2019)
SA072	Icod	*subaqueous*	122000	0.05	335000000000	Blahut et al. (2019)
SA073	Orotava	*subaqueous*	97000	0.06	1000000000000	Blahut et al. (2019)
SA074	Roques de Garcia	*subaqueous*	150000	0.04	120000000000	Blahut et al. (2019)
SA075	Fogo I	*subaqueous*	52000	0.11	145000000000	Blahut et al. (2019)
SA076	Nuuanu	*subaqueous*	270000	0.02	2500000000000	Blahut et al. (2019)
SA077	Martinique D1	*subaqueous*	90000	0.05	25000000000	Blahut et al. (2019)
SA078	Martinique D2	*subaqueous*	69000	0.06	13000000000	Blahut et al. (2019)
SA079	Martinique D3	*subaqueous*	13000	0.03	2000000000	Blahut et al. (2019)
SA080	Montserrat Deposit 1	*subaqueous*	16000	0.11	1800000000	Blahut et al. (2019)
SA081	Montserrat Deposit 3	*subaqueous*	14000	0.11	300000000	Blahut et al. (2019)
SA082	eF1	*subaqueous*	89000	0.07	50000000000	Blahut et al. (2019)
SA083	eF3	*subaqueous*	97000	0.03	5000000000	Blahut et al. (2019)
SA084	nN1	*subaqueous*	118000	0.05	100000000000	Blahut et al. (2019)
SA085	sF1	*subaqueous*	99000	0.06	50000000000	Blahut et al. (2019)
SA086	sF4	*subaqueous*	46000	0.10	50000000000	Blahut et al. (2019)
SA087	sN1	*subaqueous*	111000	0.06	100000000000	Blahut et al. (2019)
SA088	sN3	*subaqueous*	32000	0.03	5000000000	Blahut et al. (2019)
SA089	wN1a	*subaqueous*	85000	0.05	100000000000	Blahut et al. (2019)
SA090	wN5	*subaqueous*	38000	0.05	50000000000	Blahut et al. (2019)
SA091	wN8	*subaqueous*	18000	0.12	5000000000	Blahut et al. (2019)
SA092	Tahiti Nui N	*subaqueous*	85000	0.06	800000000000	Blahut et al. (2019)
SA093	Tahiti Nui S	*subaqueous*	82000	0.06	1150000000000	Blahut et al. (2019)
SA094	Mt Curry	*subaqueous*	60000	0.06	4000000000	Blahut et al. (2019)
SA095	Tristan da Cunha	*subaqueous*	53000	0.09	150000000000	Blahut et al. (2019)
SA096	Santa Cruz Basin 3	*subaqueous*	20000		2100000000	Brothers et al. (2019)
SA097	Santa Cruz Basin 6	*subaqueous*	9000		750000000	Brothers et al. (2019)
SA098	Santa Cruz Basin 8	*subaqueous*	20000		1800000000	Brothers et al. (2019)
SA099	Santa Cruz Basin 9	*subaqueous*	20000		2200000000	Brothers et al. (2019)
SA100	Santa Cruz Basin 10	*subaqueous*	11000		1400000000	Brothers et al. (2019)
SA101	Santa Cruz Basin 11	*subaqueous*	10000		1650000000	Brothers et al. (2019)
SA102	Valdes	*subaqueous*	6000		800000000	Volker et al. (2009), Anasetti et al. (2010)

TD01	Bafokeng, South Africa	South Africa	4900	0.01	3000000	Hunter & Fell (2001)
TD02	Saaiplass, Slide 2, South Africa	South Africa	160	0.08	120000	Hunter & Fell (2001)
TD03	Merriespruit, South Africa	South Africa	2330	0.03	600000	Hunter & Fell (2001)
TD04		Texas, USA	410	0.02	105000	Hunter & Fell (2001)
TD05	Saaiplass, Slide 1, South Africa	South Africa	255	0.05	60000	Hunter & Fell (2001)
WD01	Shenzhen	Guangdong, China	1100	0.10	2730000	Yin et al. (2016)
WD02	Bulbul Municipal Landfill	South Africa	460	0.07	160000	Blight (2008)
WD03	Leeuwigajah	Bandung, Java, Indonesia	1000	0.10	2700000	Lavigne et al. (2014), Blight (2008), Koelsch et al. (2005)
WD04	Rumpke	Rumpke, Cincinnati, Ohio, USA	575	0.21	1200000	Kenter et al. (1997), Eid et al. (2000), Stark et al. (2000)

References

Aaron, J., McDougall, S. (2019). Rock avalanche mobility: The role of path material. Eng. Geol., 257. https://doi.org/10.1016/j.enggeo.2019.05.003

Abele, G. (1994). Large rockslides: Their causes and movement on internal sliding planes. *Mountain Res. Development*, 14, 315-320.

Alcantara-Ayala, I., Garnica-Pena, R., Dominguez-Morales, L., Gonzalez-Huesca, A., Calderon-Vega, A. (2017). The La Pintada landslide, Guerrero, Mexico: Hints from the pre-classic to the disasters of modern times. *Landslides*, 14, 1195-1205.

Anasetti, A., Krastel, S., Weinrebe, W., Klaucke, I., Bialas, J. (2010). Detailed analysis of the Valdes slide: A landward facing slope failure off Chile. Abstract, EGU General Assembly 2010. Vienna, Austria. 2-7 May 2010.

Avolio, M., Lupiano, V., Mazzanti, P., Di Gregorio, S. (2009). A cellular automata model for flow-like landslides with numerical simulations of subaerial and subaqueous cases. In: V. Wohlgemuth, B. Page, K. Voight (*Eds*.) *Environmental Informatics and Industrial Environmental Protection: Concepts, Methods and Tools*. Aachen: Shaker Verlag.

Ayotte, D., Evans, N., Hungr, O. (1998). Runout analysis of debris flows and debris avalanches in Hong Kong. *Report of the GEO*. Hong Kong: Geotechnical Engineering Office.

Badger, T. (2015). SR 530 MP 35 to 41 geotechnical study. *Geotechnical Report*. Olympia: Washington State Department of Transportation.

Barth, N. (2013). The Cascade rock avalanche: Implications of a very large Alpine Fault-triggered failure, New Zealand. *Landslides*, 11, 327-341. https://doi.org/10.1007/s10346-013-0389-1

Beetham, R., McSaveney, M., Read, S. (2002). Four extremely large landslides in New Zealand. In: J. Rybar, J. Stemberk, P. Wagner (*Eds*.) *Landslides: Proceedings of the First European Conference on Landslides. Prague, Czech Republic, 24-26 June 2002*. Lisse: A.A. Balkema.

Bell, K., Carey, S., Nomikou, P., Sigurdsson, H., Sakellariou, D. (2013). Submarine evidence of a debris avalanche deposit on the eastern slope of Santorini volcano, Greece. *Tectonophysics*, 597-598, 147-160.

Bishop, A. (1973). The stability of tips and spoil heaps. *Q. J. Eng. Geol*., 6, 335-376.

Blahut, J., Balek, J., Klimes, J., Rowberry, M., Kusak, M., Kalina, J. (2019). A comprehensive global database of giant landslides on volcanic islands. *Landslides*, 16, 2045-2052. https://doi.org/10.1007/s10346-019-01275-8

Blais-Stevens, A., Geertsema, M., Schwab, J., van Asch, T., Egginton, V. (2007). The Sutherland River rock slide – debris avalanche, central British Columbia. 1st Int. Landslide Conf. Vail, CO.

Blight, G. (2008). Slope failures in municipal solid waste dumps and landfills: A review. *Waste Management Res*., 26, 448-463. https://doi.org/10.1177/0734242X07087975

Bobrowsky, P., Smith, C. (1991). Quaternary studies in the Peace River District, 1990: Statigraphy, mass movements and glaciation limits. *Geological Fieldwork 1991, Paper 1992-1*. British Columbia Geological Survey.

Bowman, E., Take, W. (2015). The runout of chalk cliff collapses in England and France—case studies and physical model experiments. *Landslides*, 12, 225-239.

Boyd, T. (1992). The use of the resistivity piezocone (RCPTU) for the geoenvironmental characterization of sulphide bearing tailings and native soils. (*masters thesis*). Vancouver: University of British Columbia.

Brideau, M-A., Stead, D., Millard, T., Ward, B. (2019). Field characterization and numerical modelling of debris avalanche runout on Vancouver Island, British Columbia, Canada. *Landslides*, 16, 875-891. https://doi.org/10.1007/s10346-019-01141-7

Brothers, D., Maier, K., Kluesner, J., Conrad, J., Chaytor, J. (2019). The Santa Cruz Basin submarine landslide complex, southern California: Repeated failure of uplifted basin sediment. *J. Sedimentary Res.*, 17, 117-134. https://doi.org/10.2110/sepmsp.110.05

Budetta, P., de Riso, R. (2004). The mobility of some debris flows in pyroclastic deposits of the northwestern Campanian region (southern Italy). *Bull. Eng. Geol. Eng*., 63, 293-302.

Carey, G. (2018). Back-analysis study of selected Norwegian debris flow and debris avalanche events: A comparison of DAN3D and GeoClaw runout models. (*masters thesis*). Oslo: University of Oslo.

Chan, Y., Pun, W., Wong, H., Li, A., Yeo, K. (1996). Investigation of some major slope failures between 1992 and 1995. *GEO Report No. 52*. Hong Kong: Geotechnical Engineering Office

Collot, J-Y. Lewis, K., Lamarche, G., Lallemand, S. (2001). The giant Ruatoria debris avalanche on the northern Hikurangi margin, New Zealand: Result of oblique seamount subduction. *J. Geophys. Res*., 106, 19271-19297.

Corominas, J. (1996). The angle of reach as a mobility index for small and large landslides. *Can. Geotech. J.*, 33, 260-271. https://doi.org/10.1139/t96-005

Cruden, D., Hungr, O. (1986). The debris of the Frank Slide and theories of rockslide-avalanche mobility. *Can. J. Earth Sci*., 23, 425-432. https://doi.org/10.1139/e86-044

Danneels, G., Bourdeau, C., Torgoev, I., Havenith, H-B. (2008). Geophysical investigation and dynamic modelling of unstable slopes: Case study of Kainama (Kyrgyzstan). *Geophys. J. Int.*, 175, 17-34.

Douglass, J., Dorn, R., Gootee, B. (2005). A large landslide on the urban fringe of metropolitan Phoenix, Arizona. *Geomorphology*, 65, 321-336.

Dufresne, A., Davies, T., McSaveney, M. (2010). Influence of runout-path material on emplacement of the Round Top rock avalanche, New Zealand. *Earth Surf. Process. Landforms*, 35, 190-201.

Edgers, L. and Karlsrud, K. (1982). Soil flows generated by submarine slides—case studies and consequences. In: J. Connor, C. Chryssostomidis (*Eds*.) *Proceedings of the 3rd International Conference on the Behavior of Offshore Structures, Massachusetts Institute of Technology, Cambridge, Mass*. New York: Hemisphere Publishing Corporation.

Egginton, V. (2005). Historical climate variability from the instrumental record in northern British Columbia and its influence on slope stability. (*masters thesis*). Burnaby, BC: Simon Fraser University.

Eid, H., Stark, T., Evans, W., Sherry, P. (2000). Municipal solid waste slope failure. I: Waste and foundation soil properties. *J. Geotech. Geoenviron. Eng*., 126, 397-407.

Elverhoi, A., De Blasio, F., Butt, F., Issler, D., Harbitz, C., Engvik, L., Solheim, A., Marr, J. (2002). Submarine mass-wasting on glacially-influenced continental slopes: processes and dynamics. In: J. Dowdeswell, C. O Cofaigh (*Eds*.) *Glacier-Influenced Sedimentation on High Latitude Continental Margins*. London: Geological Society of London.

Erismann, T., Abele, G. (2001). *Dynamics of Rockslides and Rockfalls*. Berlin: Springer.

Evans, S., Guthrie, R., Roberts, N., Bishop, N. (2007). The disastrous 17 Februrary 2006 rockslide-debris avalanche on Leyte Island, Philippines: A catastrophic landslide in tropical mountain terrain. *Nat. Hazards Earth Syst. Sci.*, 7, 89-101.

Evans, S., Mugnozza, G., Strom, A., Hermanns, R., Ischuk, A., Vinnichenko, S. (2006). Landslides from massive rock slope failure and associated phenomena. In: S. Evans et al. (*Eds*.) *Landslides from Massive Rock Slope Failure*. Netherlands: Springer.

Fan, X., Xu, Q., Scaringi, G., Zheng, G., Huang, R., Dai, L., Ju, Y. (2018). The "long" runout rock avalanche in Pusa, China, on August 28, 2017: A preliminary report. *Landslides*, 16, 139-154. https://doi.org/10.1007/s10346-018-1084-z

Fletcher, L., Hungr, O., Evans, S. (2002). Contrasting failure behavior of two large landslides in clay and silt. *Can. Geotech. J*., 39, 46-62.

Gee, M., Uy, H., Warren, J., Morley, C., Lambiase, J. (2007). The Brunei slide: A giant submarine landslide on the north west Borneo Margin revealed by 3D seismic data. *Marine Geol*., 246, 9-23.

Geertsema, M., Blais-Stevens, Kwoll, E., Menounos, B., Venditti, J., Grenier, A., Weibe, K. (2018). Sensitive clay landslide detection and characterization in and around Lakelse Lake, British Columbia, Canada. *Sedimentary Geol*., 364, 217-227.

Geertsema, M., Clague, J., Schwab, J., Evans, S. (2006a). An overview of recent large catastrophic landslides in northern British Columbia, Canada. *Eng. Geol*., 83, 120-143.

Geertsema, M., Cruden, D. (2008). Travels in the Canadian cordillera. In: J. Locat, D. Perret, D. Turmel, D. Demers, S. Leroueil (*Eds*.) *Proc. 4th Canadian Conf. on Geohazards: From Causes to Management*. Quebec.

Geertsema, M., Hungr, O., Schwab, J., Evans, S. (2006). A large rockslide-debris avalanche in cohesive soil at Pink Mountain, northeastern British Columbia, Canada. *Eng. Geol*., 83, 64-75.

Geertsema, M., Schwab, J. (2006). Challenges with terrain stability mapping in northern British Columbia. *Watershed Management Bull*., 10, 18-28.

Guo, C., Zhang, Y., Montgomery, D., Du, Y., Zhang, G., Wang, S. (2016). How unusual is the long-runout of the earthquake-triggered giant Luanshibao landslide, Tibetan Plateau, China? *Geomorphology*. 259, 145-54.

Haeussler, P., Parsons, T., Finlayson, D., Hart, P., Chaytor, J., Ryan, H., Lee, H., Labay, K., Peterson, A., Liberty, L. (2014). New imaging of submarine landslides form the 1964 earthquake near Whittier, Alaska, and a comparison to failures in other Alaskan fjords. In: S. Krastel et al. (*Eds*.) *Submarine Mass Movements and Their Consequences, Advances in Natural and Technological Hazards Research*, 37. Switzerland: Springer International Publishing.

Hampton, M., Lee, H., Locat, J. (1996). Submarine landslides. *Rev. of Geophy*., 34, 33-59. https://doi.org/10.1029/95RG03287

Harrison, J., Falcon, N. (1937). The Saidmarreh landslip, south-west Iran. *The Geographical Journal*, 89, 42-47.

Harrison, J., Falcon, N. (1938). An ancient landslip at Saidmarreh in southwestern Iran. *J. of Geol*., 46, 296-309.

Havenith, H., Torgoev, A., Scholgel, R., Braun, A., Torgoev, I., Ischuk, A. (2015). Tien Shan geohazards database: Landslide susceptibility analysis. *Geomorphology*, 249, 32-43.

Hayashi, J., Self, S. (1992). A comparison of pyroclastic flow and debris avalanche mobility. *J. Geophys. Res.*, 97, 9063-9071.

Hearn, G. (2011). *Slope Engineering for Mountain Roads*. London: Geological Society of London.
Heim, A. (1932). *Landslides and human lives (Bergsturz und menschenleben)*. Trans. N. Skermer. BiTech Pub, Vancouver, B.C.
Hewitt, K. (1999). Quaternary moraines vs catastrophic rock avalanches in the Karakoram Himalaya, northern Pakistan. *Quaternary Res*., 51, 220-237.
Hewitt, K. (2006). Styles of rock-avalanche depositional complexes conditioned by very rugged terrain, Karakoram Himalaya, Pakistan. *Rev. Eng. Geol*., 15, 345-377.
Hewitt, K., Clague, J., Orwin, J. (2008). Legacies of catastrophic rock slope failures in mountain landscapes. *Earth-Science Rev*., 87, 1-38.
Hsu, K. (1978). Albert Heim: Observations on landslides and relevance to modern interpretations. In: B. Voight (*Ed*.) *Rockslides and Avalanches, 1: Natural Phenomena: Developments in Geotechnical Engineering Vol 14A*. Amsterdam: Elsevier.
Hungr, O. (2002). Rock avalanche motion, process and modeling. In: S. Evans, S. Marino (*Eds*.) *Massive Rock Slope Failure: New Models for Hazard Assessment*. NATO Advanced Research Workshop Celano, Italy, 16–21 June 2002.
Hunter, G. and Fell, R. 2001. "Rapid" failure of soil slopes. *UNICIV Report R-400*. The University of New South Wales, School of Civil and Environmental Engineering, Sydney, Australia.
Hurlimann, M., McArdell, B., Rickli, C. (2015). Field and laboratory analysis of the runout characteristics of hillslope debris flows in Switzerland. *Geomorphology*, 232, 20-32.
Hutchinson, J. (1988). General report: Morphological and geotechnical parameters of landslides in relation to geology and hydrogeology. *Proc. 5th Int. Symposium on Landslides*. Lausanne, 10-15 July 1988.
Hutchinson, J. (2002). Chalk flows from the coastal cliffs of northwest Europe. *Rev. Eng. Geol., Volume XV*. In: S. Evans, J. DeGraff (*Eds*.) *Catastrophic Landslides: Effects, Occurrence, and Mechanisms*. Boulder, CO: Geological Society of America
Ishihara, K., Okusa, S., Oyagi, N., Ischuk, A. (1990). Liquefaction-induced flow slide in the collapsible loess deposit in Soviet Tajik. *Soils and Foundations*, 30, 73-89.
Japan Landslide Society. (1972). Landslides in Japan. The Japan Society of Landslide National Conference of Landslide Control.
Japan Landslide Society. (1996). Landslides in Japan: The fifth revision. The Japan Landslide Society National Conference of Landslide Control.
Johnson, B. (1978). Blackhawk landslide, California, U.S.A. In: B. Voight (*Ed*.) *Rockslides and Avalanches, 1: Natural Phenomena: Developments in Geotechnical Engineering Vol 14A*. Amsterdam: Elsevier.
Kenter, R., Schmucker, B., Miller, K. (1997). The day the earth didn't stand still: The Rumpke landslide. *Waste Age*, March 1997, 66-81.
Koelsch, F., Fricke, K., Mahler, C., Damanhuri, E. (2005). Stability of landfills – The Bandung dumpsite disaster. ANS e.V. HAWK, 66. Informationsgesprach.
Kolderup, N-H. (1955). Raset I Modalen: 14. August 1953. Norsk. Geol. Tidssk., 34, 211-217.
Krastel, S., Wynn, R., Hanebuth, T., Henrich, R., Holz, C., Meggers, H., Kuhlmann, H., Georgiopoulou, A., Schulz, H. (2006). Mapping of seabed morphology and shallow sediment structure of the Mauritania continental margin, northwest Africa: Some implications for geohazard potential. *Norwegian J. Geol*., 86, 163-176.

L'Heureux, J. (2012). A study of the retrogressive behavior and mobility of Norwegian quick clay landslides. *Proc. 11th Int. and 2nd North Am. Symposium on Landslides*. Banff, Canada.

Laberg, J., Vorren, T. (1993). A late Pleistocene submarine slide on the Bear Island Trough mouth fan. *Geo-Marine Lett*., 13, 227-234. https://doi.org/10.1007/BF01207752

Laberg, J., Vorren, T., Dowdeswell, J., Kenyon, N., Taylor, J. (2000). The Andoya Slide and the Andoya Canyon, north-eastern Norwegian-Greenland Sea. *Marine Geol*., 162, 259-275.

LaHusen, S., Duvall, A., Booth, A., Montgomery, D. (2015). Surface roughness dating of long-runout landslides near Oso, Washington (USA), reveals persistent postglacial hillslope instability. *Geology*, 44, 111-114.

LaSalle, P., Chagnon, J-Y. (1968). An ancient landslide along the Saguenay River, Quebec. *Can. J. Earth Sci.*, 5, 548-549.

Lavigne, F., Wassmer, P., Gomez, C., Davies, T., Hadmoko, D., Iskandarsyah, T., Gaillard, J., Fort, M., Texier, P., Heng, M., Pratomo, I. (2014). The 21 February 2005, catastrophic waste avalanche at Leuwigajah dumpsite, Bandung, Indonesia. *Geoenv. Disasters*, 1. https://doi.org/10.1186/s40677-014-0010-5

Legros, F. (2002). The mobility of long-runout landslides. *Eng. Geol*., 63, 301-31. https://doi.org/10.1016/S0013-7952(01)00090-4

Leynaud, D., Mienert, J., Vanneste, M. (2009). Submarine mass movements on glaciated and non-glaciated European continental margins: A review of triggering mechanisms and preconditions to failure. *Marine Petroleum Geol*., 26, 618-632.

Li, H-b., Xu, Y-r., Zhou, J-w., Wang, X-k., Yamagishi, H., Dou, J. (2020). Preliminary analyses of a catastrophic landslide occurred on July 23, 2019, in Guizhou Province, China. *Landslides*, 17, 719-724. https://doi.org/10.1007/s10346-019-01334-0

Locat, P., Leroueil, S., Locat, J., Duchesne, M. (2003). Characterization of a submarine flow-slide at Pointe-du-Fort, Saguenay Fjord, Quebec, Canada. In: J. Locat, J. Mienert, L. Boisvert (*Eds*.) *Submarine Mass Movements and Their Consequences. Advances in Natural and Technological Hazards Research*, 19. Springer.

Long, D., Stevenson, A., Wilson, C., Bulat, J. (2003). Slope failures in the Faroe-Shetland channel. In: J. Locat, J. Mienert (*Eds*.) *Submarine Mass Movements and their Consequences*. Netherlands: Kluwer Academic Publishing.

Makino, M., Mandanas, A., Catane, S. (2007). Gravity basement of the Guinsaugon landslide along the Philippine fault zone. *Earth Planets Space*, 59, 1067-1071.

Malick, G. (2018). Geologic development and ongoing activity of the Van Zandt landslide complex, northwest, WA, USA. (*masters thesis*). Bellingham, WA: Western Washington University.

Martin, S., Campedel, P., Ivy-Ochs, S., Vigano, A., Alfimov, V., Vockenhuber, C., Andreotti, E., Carugati, G., Pasqual, D., Rigo, M. (2014). Lavini di Marco (Trentino, Italy): ^{36}Cl exposure dating of a polyphase rock avalanche. *Quaternary Geochronology*, 19, 106-116.

Masson, D., Watts, A., Gee, M., Urgeles, R., Mitchell, N., Le Bas, T., Canals, M. (2002). Slope failures on the flanks of the western Canary Islands. *Earth-Science Rev*., 57, 1-35.

McLemore, V., Fakhimi, A., van Zyl, D., Ayakwah, G., Anim, K., Boakye, K., Ennin, F., Felli, P., Fredlund, D., Gutierrez, L., Nunoo, S., Tachie-Menson, S., Viterbo, V. (2009). Literature review of other rock piles: Characterization, weathering, and stability. *Questa Rock Pile Weathering Stability Project Open-file Report OF-517*. New Mexico Bureau of Geology and Mineral Resources.

Milne, F. (2008). Topographic and material controls on the Scottish debris flow geohazard. (*doctoral dissertation*). Dundee: University of Dundee.
Mortimore, R., Lawrence, J., Pope, D., Duperret, A., Genter, A. (2004). Coastal cliff geohazards in weak rock: The UK chalk cliffs of Sussex. In: R. Mortimore, A. Duperret (*Eds*.) *Coastal Cliff Instability*. London: Geological Society of London.
Nagelisen, J., Moore, J., Vockenhuber, C., Ivy-Ochs, S. (2015). Post-glacial rock avalanches in the Obersee Valley, Glarner Alps, Switzerland. *Geomorphology*, 238, 94-111.
Orwin, J., Clague, J., Gerath, R. (2004). The Cheam rock avalanche, Fraser Valley, British Columbia, Canada. *Landslides*, 1, 289-298.
Ostermann, M., Prager, C. (2016). Rock slope failures shaping the landscape in the Loisach-, Inn- and Otz Valley region (Tyrol, Austria). *Geo. Alp*., 13, 257-276.
Peng, D., Xu, Q., Liu, F., He, Y., Zhang, S., Qi, X., Zhao, K., Zhang, X. (2018). Distribution and failure modes of the landslides in Heitai terrace, China. *Eng. Geol*., 236, 97-110.
Peng, J., Zhuang, J., Wang, G., Dai, F., Zhang, F., Huang, W., Xu, Q. (2018). Liquefaction of loess landslides as a consequence of irrigation. *Quat. J. Eng. Geol. Hydrogeol*., 51. http://dx.doi.org/10.1144/qjegh2017-098
Perkins, J., Reid, M., Schmidt, K. (2017). Control of landslide volume and hazard by glacial stratigraphic architecture, northwest Washington State, USA. *Geology*, 45, 1139-1142.
Philip, H., Ritz. J-F. (1999). Gigantic paleolandslide associated with active faulting along the Bogd fault (Gobi-Altay, Mongolia). *Geology*, 27, 211-214.
Pringle, P., Schuster, R., Logan, R. (1998). New radiocarbon ages of major landslides in the Cascade Range, Washington. *Washington Geol*., 26, 31-39.
Qi, X., Xu, Q., Liu, F. (2018). Analysis of retrogressive loess flowslides in Heifangtai, China. *Eng. Geol*., 236, 119-128.
RAIB. (2018). Landslip and derailment at Loch Eilt, north-west Scotland: 22 January 2018. *Rail Accident Report 10/2018*. Derby: RAIB
Revellino, P., Guerriero, L., Grelle, G., Hungr, O., Fiorillo, F., Esposito, L., Guadagno, F. (2013). Initiation and propagation of the 2005 debris avalanche at Nocera Inferiore (southern Italy). *Ital. J. Geosci*., 132, 366-379.
Robinson, T., Davies, T., Reznichenko, N., De Pascale, G. (2015). The extremely long-runout Komansu rock avalanche in the Trans Alai range, Pamir Mountains, southern Kyrgyzstan. *Landslides*, 12, 523-535.
Schwab, J. (2011). Hillslope and fluvial processes along the proposed pipeline corridor, Burns Lake to Kitimat, West Central British Columbia. Bulkley Valley Centre for Natural Resources Research & Management.
Siebert, L. (2002). Landslides resulting from structural failure of volcanoes. *Rev. Eng. Geol*., 15, 209-235.
Stark, T., Eid, H., Evans, W., Sherry, P. (2000). Municipal solid waste slope failure: II: Stability analysis. *J. Geotech. Geoenviron. Eng*., 126, 408-419.
Strom, A., Abdrakhmatov, K. (2018). *Rockslides and rock avalanches of Central Asia: Distribution, morphology and internal structure*. New York: Elsevier.
Sun, H., Lam, T., Tsui, H. (2003). Design basis for standardized modules of landslide debris-resisting barriers. *GEO Report No. 174*. Hong Kong: Geotechnical Engineering Office.
Van Esch, K. (2012). Failure behavior of bedrock and overburden landslides of the Peace River Valley near Fort St. John, British Columbia. (*masters thesis*). Vancouver: University of British Columbia.

Vanneste, M., Mienert, J., Bunz, S. (2006). The Hinlopen slide: A giant, submarine slope failure on the northern Svalbard margin, Arctic Ocean. *Earth Planetary Sci. Lett*., 245, 373-388.
Voight, B. (1978). Lower Gros Ventre slide, Wyoming, U.S.A. In: B. Voight (*Ed*.) *Rockslides and Avalanches, 1: Natural Phenomena: Developments in Geotechnical Engineering Vol 14A*. Amsterdam: Elsevier.
Voight, B., Pariseau, W. (1978). Rockslides and avalanches: An introduction. In: B. Voight (*Ed*.) *Rockslides and Avalanches, 1: Natural Phenomena: Developments in Geotechnical Engineering Vol 14A*. Amsterdam: Elsevier.
Voight, S., Kemper, T., Riedlinger, T., Kiefl, R., Scholte, K., Mehl, H. (2007). Satellite image analysis for disaster and crisis-management support. *IEEE Transactions on Geoscience and Remote Sensing*, 45, 1520-1528.
Volker, D., Weinrebe, W., Behrmann, J., Klaeschen, D. (2009). Mass wasting at the base of the south central Chilean continental margin: The Reloca slide. *Adv. Geosci*., 7, 1-13.
von Poschinger, A. (1994). Some special aspects of the "impact" of a landslide on the valley floor. *Landslide News*, 8, 26-28.
Vorren, T., Laberg, J., Blaume, F., Dowdeswell, J., Kenyon, N., Mienert, J., Rumohr, J., Werner, F. (1998). The Norwegian-Greenland sea continental margins: Morphology and late quaternary sedimentary process and environment. *Quaternary Sci. Rev*., 17, 273-302.
Watson, R., Wright, H. (1969). The Saidmarreh landslide, Iran. *Geological Society of America Special Paper 123*. Boulder, CO: The Geological Society of America.
Whittall, J. (2015). Runout exceedance prediction for open pit slope failures. (*masters thesis*). Vancouver: University of British Columbia.
Wichter, L. (2007). Stabilization of old lignite pit dumps in Easter Germany. *Bull. Eng. Geol. Env*., 66, 45-51.
Wieczorek, G., Harp, E., Mark, R., Bhattacharyya, A. (1988). Debris flows and other landslides in San Mateo, Santa Cruz, Contra Costa, Alameda, Napa, Solano, Sonoma, Lake, and Yolo counties, and factors influencing debris-flow distribution. In: S. Ellen, G., Wieczorek (*Eds*.) *Landslides, Floods, and Marine Effects of the Storm of January 3-5, 1982, in the San Francisco Bay Region, California*. U.S. Geological Survey Professional Paper 1434. Washington: United States Government Printing Office.
Wilson, C., Long, D., Bulat, J. (2003). The Afen slide – A multistaged slope failure in the Faroe-Shetland channel. In: J. Locat, J. Mienert (*Eds*.) *Submarine Mass Movements and their Consequences.* Netherlands: Kluwer Academic Publishing
Wong, H., Lam, K., Ho, K. (1997). Diagnostic report on the November 1993 natural terrain landslides on Lantau Island. *GEO Report No. 69*. Hong Kong: Geotechnical Engineering Office.
Wright, C. (1998). The AD 930 long-runout Round Top debris avalanche, Westland, New Zealand. *New Zealand J. Geol. Geophys*., 41, 493-497.
Xiao, R. (2019). Difficulties in risk assessment of individual landslide – case study on rock avalanche at Nayong, Guizhou, China. *Geophys. Res. Abs*., 21. EGU General Assembly 2019.
Xu, Q., Li, H., He, Y., Liu, F., Peng, D. (2017). Comparison of data-driven models of loess landslide runout distance estimation. *Bull. Eng. Geol. Envion*., 78, 1281-1294. https://doi.org/10.1007/s10064-017-1176-3
Yin, Y., Li, B., Wang, W., Zhan, L., Xue, Q., Gao, Y., Zhang, N., Chen, H., Liu, T., Li, A. (2016). Mechanism of the December 2015 catastrophic landslide at the Shenzhen landfill

and controlling geotechnical risks of urbanization. *Engineering*, 2, 230-49. https://doi.org/10.1016/J.ENG.2016.02.005

Zhang, Z-Y., Chen, S-M., Tao, L-J. (2002). 1983 Sale Mountain landslide, Gansu Province, China. In: S. Evans, J. DeGraff (*Eds*.) *Catastrophic Landslides: Effects, Occurrence and Mechanisms*. Boulder, CO: Geological Society of America.

Zhu, Y., Xu, S., Zhuang, Y., Dai, X., Xing, A. (2019). Analysis of characteristics and runout behavior of the disastrous 28 August 2017 rock avalanche in Nayong, Guizhou, China. *Eng. Geol*., 259. https://doi.org/10.1016/j.enggeo.2019.105154

Zhuang, J-q., Peng, J-b. (2014). A coupled slope cutting—a prolonged rainfall-induced loess landslide: A 17 October 2011 case study. *Bull. Eng. Geol. Environ*., 73, 997-1011.

Appendix 4.1 – Landslide fatality database

Table A4.1.1. Landslide fatality database. Status of economic development determined on a per nation basis, corresponding to the United Nations threshold of economic development (United Nations, 2020). Abbreviation are given in **Table A4.1.2**, and their significance is described in the text of **Chapter 4**. *248 people were killed in a school building. This case is not included in the descriptive statistics or binary logistic regression in **Section 4.1** and following. This case is included in the non-linear regression equations described in **Table 4.2** and visualized in **Figures 4.1**, **4.2**, and **4.3**.

Victim ID	*Location*	*Developing?*	*Date*	*Time*	*Building ID*	*Gender*	*Age*	*Material*	*Distance*	*Floor*	*Debris height*	*Confidence*
*	Guinsaugon, S. Leyte, Philippines	Y	17-Feb-06	M	M4	na	na	H	H	na	30	M
2	La Conchita, California, USA	N	10-Jan-05	E	M1	F	YA	S	L	1	9.1	M
3	La Conchita, California, USA	N	10-Jan-05	E	M1	F	C	S	L	1	9.1	M
4	La Conchita, California, USA	N	10-Jan-05	E	M1	F	C	S	L	1	9.1	M
5	La Conchita, California, USA	N	10-Jan-05	E	M1	F	C	S	L	1	9.1	M
6	La Conchita, California, USA	N	10-Jan-05	E	M2	F	YA	S	L	1	1	M
7	La Conchita, California, USA	N	10-Jan-05	E	M2	F	na	S	L	1	1	M
8	La Conchita, California, USA	N	10-Jan-05	E	M19	F	A	S	L	na	9.1	M
9	Spring Bluff, Australia	N	10-Jan-11	E	M3	F	A	H	na	1	2.1	H
10	Spring Bluff, Australia	N	10-Jan-11	E	M3	M	A	H	na	1	2.1	H
11	Spring Bluff, Australia	N	10-Jan-11	E	M3	M	YA	H	na	1	2.1	H
12	Spring Bluff, Australia	N	10-Jan-11	E	M3	F	C	H	na	2	2.1	H
13	Tiwi, Albay, Philippines	Y	Jan-19	N	M5	M	C	na	L	1	1.4	L
14	Tiwi, Albay, Philippines	Y	Jan-19	N	M5	F	na	na	L	na	1.4	L
15	Tiwi, Albay, Philippines	Y	Jan-19	N	M5	F	na	na	L	na	1.4	L
16	Tiwi, Albay, Philippines	Y	Jan-19	N	M5	M	na	na	L	na	1.4	L
17	Salina, Colorado, USA	N	13-Sep-13	N	M6	F	A	S	L	1	1.4	H
18	Salina, Colorado, USA	N	13-Sep-13	N	M6	M	A	S	L	1	1.4	H
19	Salina, Colorado, USA	N	13-Sep-13	N	M6	M	A	S	L	1	1.4	H
20	Salina, Colorado, USA	N	13-Sep-13	N	M6	F	A	S	L	1	1.4	H
21	Salina, Colorado, USA	N	13-Sep-13	N	M6	M	C	S	L	2	1.4	H
22	Salina, Colorado, USA	N	13-Sep-13	N	M6	M	C	S	L	2	1.4	H
23	Salina, Colorado, USA	N	13-Sep-13	N	M6	F	na	S	L	1	1.4	H
24	Rangamati, Chittagong Hill Tracts, Bangladesh	Y	Jun-17	N	M7	F	YA	S	na	1	1.3	L
25	Rangamati, Chittagong Hill Tracts, Bangladesh	Y	Jun-17	N	M7	M	C	S	na	1	1.3	L
26	Rangamati, Chittagong Hill Tracts, Bangladesh	Y	Jun-17	N	M7	F	C	S	na	1	1.3	L
27	Rangamati, Chittagong Hill Tracts, Bangladesh	Y	Jun-17	N	M7	F	C	S	na	1	1.3	L
28	Cameron Highlands, Malaysia	Y	31-Dec-14	M	M8	M	C	S	na	1	1.2	L
29	Cameron Highlands, Malaysia	Y	31-Dec-14	M	M8	F	YA	S	na	1	1.2	L
30	Cameron Highlands, Malaysia	Y	31-Dec-14	M	M8	M	A	S	na	1	1.2	L
31	Elm, Switzerland	N	11 Sept 1881	E	M9	M	EA	S	na	1	1.5	M
32	Schenectady, New York, USA	N	28-Jan-18	N	M10	M	C	S	L	1	1.5	M
33	Schenectady, New York, USA	N	28-Jan-18	N	M10	M	YA	S	L	1	1.5	M
34	Schenectady, New York, USA	N	28-Jan-18	N	M10	M	C	S	L	1	1.5	M
35	Loma Mar, California, USA	N	3-Feb-98	N	M11	M	A	S	na	na	1.3	L
36	Loma Mar, California, USA	N	3-Feb-98	N	M11	F	na	S	na	na	1.3	L
37	Beijie Village, Zhougu, Gansu, China	Y	8-Aug-10	N	M12	F	C	na	na	na	1.6	L

38	Beijie Village, Zhougu, Gansu, China	Y	8-Aug-10	N	M12	M	na	na	na	na	1.6	L
39	Beijie Village, Zhougu, Gansu, China	Y	8-Aug-10	N	M12	F	na	na	na	na	1.6	L
40	Beijie Village, Zhougu, Gansu, China	Y	8-Aug-10	N	M12	M	na	na	na	na	1.6	L
41	Yueyuan Village, Zhougu, Gansu, China	Y	8-Aug-10	N	M13	M	A	na	na	1	1.3	L
42	Yueyuan Village, Zhougu, Gansu, China	Y	8-Aug-10	N	M13	M	C	na	na	1	1.3	L
43	Yueyuan Village, Zhougu, Gansu, China	Y	8-Aug-10	N	M13	na	na	na	na	na	1.3	L
44	Yueyuan Village, Zhougu, Gansu, China	Y	8-Aug-10	N	M13	na	na	na	na	na	1.3	L
45	Yueyuan Village, Zhougu, Gansu, China	Y	8-Aug-10	N	M13	na	na	na	na	na	1.3	L
46	Yueyuan Village, Zhougu, Gansu, China	Y	8-Aug-10	N	M13	na	na	na	na	na	1.3	L
47	Yueyuan Village, Zhougu, Gansu, China	Y	8-Aug-10	N	M13	na	na	na	na	na	1.3	L
48	Yueyuan Village, Zhougu, Gansu, China	Y	8-Aug-10	N	M13	na	na	na	na	na	1.3	L
49	Yueyuan Village, Zhougu, Gansu, China	Y	8-Aug-10	N	M13	na	na	na	na	na	1.3	L
50	Yueyuan Village, Zhougu, Gansu, China	Y	8-Aug-10	N	M13	na	na	na	na	na	1.3	L
51	Yueyuan Village, Zhougu, Gansu, China	Y	8-Aug-10	N	M13	na	na	na	na	na	1.3	L
52	Mt. Hagen, Western Highlands, Papua New Guinea	Y	31-Oct-16	N	M14	M	C	na	na	1	1.4	L
53	Mt. Hagen, Western Highlands, Papua New Guinea	Y	31-Oct-16	N	M14	M	na	na	na	1	1.4	L
54	Mt. Hagen, Western Highlands, Papua New Guinea	Y	31-Oct-16	N	M14	M	na	na	na	1	1.4	L
55	Old Topanga Canyon, Topanga, California, USA	N	25-Jan-69	N	M15	M	na	S	L	1	1.3	M
56	Silverado Canyon, California, USA	N	25-Feb-69	M	M16	M	C	S	L	1	1.5	M
57	Silverado Canyon, California, USA	N	25-Feb-69	M	M16	M	YA	S	L	1	1.5	M
58	Silverado Canyon, California, USA	N	25-Feb-69	M	M16	M	na	S	L	1	1.5	M
59	Silverado Canyon, California, USA	N	25-Feb-69	M	M16	M	C	S	L	1	1.5	M
60	Silverado Canyon, California, USA	N	25-Feb-69	M	M16	M	A	S	L	1	1.5	M
61	Silverado Canyon, California, USA	N	25-Feb-69	M	M16	F	YA	S	L	1	1.5	M
62	Silverado Canyon, California, USA	N	25-Feb-69	M	M16	M	YA	S	L	1	1.5	M
63	Silverado Canyon, California, USA	N	25-Feb-69	M	M16	F	YA	S	L	1	1.5	M
64	Silverado Canyon, California, USA	N	25-Feb-69	M	M16	F	na	S	L	1	1.5	M
65	Silverado Canyon, California, USA	N	25-Feb-69	M	M16	M	na	S	L	1	1.5	M
66	Silverado Canyon, California, USA	N	25-Feb-69	M	M16	M	C	S	L	1	1.5	M
67	Silverado Canyon, California, USA	N	25-Feb-69	M	M16	M	na	S	L	1	1.5	M
68	Silverado Canyon, California, USA	N	25-Feb-69	M	M16	M	na	S	L	1	1.5	M
69	Silverado Canyon, California, USA	N	25-Feb-69	M	M16	M	na	S	L	1	1.5	M
70	Silverado Canyon, California, USA	N	25-Feb-69	M	M16	M	na	S	L	1	1.5	M
71	Silverado Canyon, California, USA	N	25-Feb-69	M	M16	na	na	S	L	1	1.5	M
72	Silverado Canyon, California, USA	N	25-Feb-69	M	M16	na	na	S	L	1	1.5	M
73	Silverado Canyon, California, USA	N	25-Feb-69	M	M16	na	na	S	L	1	1.5	M
74	Silverado Canyon, California, USA	N	25-Feb-69	M	M16	na	na	S	L	1	1.5	M
75	Silverado Canyon, California, USA	N	25-Feb-69	M	M16	na	na	S	L	1	1.5	M
76	Silverado Canyon, California, USA	N	25-Feb-69	M	M16	na	na	S	L	1	1.5	M
77	Silverado Canyon, California, USA	N	25-Feb-69	M	M16	na	na	S	L	1	1.5	M
78	Silverado Canyon, California, USA	N	25-Feb-69	M	M16	na	na	S	L	1	1.5	M
79	Silverado Canyon, California, USA	N	25-Feb-69	M	M16	na	na	S	L	1	1.5	M
80	Silverado Canyon, California, USA	N	25-Feb-69	M	M16	na	na	S	L	1	1.5	M
81	Silverado Canyon, California, USA	N	25-Feb-69	M	M16	na	na	S	L	1	1.5	M
82	Silverado Canyon, California, USA	N	25-Feb-69	M	M16	na	na	S	L	1	1.5	M
83	Silverado Canyon, California, USA	N	25-Feb-69	M	M16	na	na	S	L	1	1.5	M
84	Silverado Canyon, California, USA	N	25-Feb-69	M	M16	na	na	S	L	1	1.5	M
85	Silverado Canyon, California, USA	N	25-Feb-69	M	M16	na	na	S	L	1	1.5	M
86	Silverado Canyon, California, USA	N	25-Feb-69	M	M16	na	na	S	L	1	1.5	M
87	Silverado Canyon, California, USA	N	25-Feb-69	M	M16	na	na	S	L	1	1.5	M
88	Silverado Canyon, California, USA	N	25-Feb-69	M	M16	na	na	S	L	1	1.5	M
89	Silverado Canyon, California, USA	N	25-Feb-69	M	M16	na	na	S	L	1	1.5	M
90	Silverado Canyon, California, USA	N	25-Feb-69	M	M16	na	na	S	L	1	1.5	M
91	Mercer Lake, Oregon, USA	N	18-Dec-15	N	M17	F	EA	S	L	1	1.2	M

92	Mercer Lake, Oregon, USA	N	18-Dec-15	N	M17	M	na	S	L	1	1.2	M
93	Summerland, Okanagan Valley, Canada	N	27-Sep-70	E	M18	M	na	na	L	na	4	L
94	Summerland, Okanagan Valley, Canada	N	27-Sep-70	E	M18	F	na	na	L	na	4	L
95	Ohope Beach, New Zealand	N	18-Jun-11	M	NZ1	M	C	S	L	1	3	H
96	Ohope Beach, New Zealand	N	18-Jun-11	M	NZ1	M	na	S	L	2	3	H
97	Dargaville, New Zealand	N	4-May-98	na	NZ2	F	na	na	na	na	3	H
98	Otuwhero Inlet, New Zealand	N	16-Jun-13	E	NZ3	F	EA	S	L	1	2	H
99	Montecito, California, USA	N	9-Jan-18	N	CA1	F	YA	S	E	1	2.3	H
100	Montecito, California, USA	N	9-Jan-18	N	CA1	M	C	S	E	1	2.3	H
101	Montecito, California, USA	N	9-Jan-18	N	CA1	F	YA	S	E	1	2.3	H
102	Montecito, California, USA	N	9-Jan-18	N	CA1	F	C	S	E	1	2.3	H
103	Montecito, California, USA	N	9-Jan-18	N	CA1	M	na	S	E	1	2.3	H
104	Montecito, California, USA	N	9-Jan-18	N	CA1	M	C	S	E	1	2.3	H
105	Montecito, California, USA	N	9-Jan-18	N	CA1	M	na	S	E	1	2.3	H
106	Montecito, California, USA	N	9-Jan-18	N	CA2	M	YA	S	E	1	3	H
107	Montecito, California, USA	N	9-Jan-18	N	CA2	M	C	S	E	1	3	H
108	Montecito, California, USA	N	9-Jan-18	N	CA2	M	EA	S	E	1	3	H
109	Montecito, California, USA	N	9-Jan-18	N	CA2	F	C	S	E	1	3	H
110	Montecito, California, USA	N	9-Jan-18	N	CA2	F	na	S	E	1	3	H
111	Montecito, California, USA	N	9-Jan-18	N	CA3	M	A	S	E	1	2.3	H
112	Montecito, California, USA	N	9-Jan-18	N	CA4	F	YA	S	E	1	2	H
113	Montecito, California, USA	N	9-Jan-18	N	CA4	F	C	S	E	1	2	H
114	Montecito, California, USA	N	9-Jan-18	N	CA4	F	C	S	E	1	2	H
115	Montecito, California, USA	N	9-Jan-18	N	CA4	F	na	S	E	1	2	H
116	Montecito, California, USA	N	9-Jan-18	N	CA5	M	EA	S	E	na	1.4	H
117	Montecito, California, USA	N	9-Jan-18	N	CA5	M	YA	S	E	na	1.4	H
118	Montecito, California, USA	N	9-Jan-18	N	CA6	M	E	S	E	na	1.5	H
119	Montecito, California, USA	N	9-Jan-18	N	CA6	F	EA	S	E	na	1.5	H
120	Montecito, California, USA	N	9-Jan-18	N	CA7	M	EA	S	E	1	1.5	H
121	Montecito, California, USA	N	9-Jan-18	N	CA7	M	na	S	E	1	1.5	H
122	Montecito, California, USA	N	9-Jan-18	N	CA8	M	C	S	E	na	2.5	H
123	Montecito, California, USA	N	9-Jan-18	N	CA8	F	C	S	E	na	2.5	H
124	Montecito, California, USA	N	9-Jan-18	N	CA8	F	A	S	E	1	2.5	H
125	Montecito, California, USA	N	9-Jan-18	N	CA9	M	A	S	E	1	2.2	H
126	Montecito, California, USA	N	9-Jan-18	N	CA9	F	YA	S	E	2	2.2	H
127	Montecito, California, USA	N	9-Jan-18	N	CA9	M	YA	S	E	2	2.2	H
128	Montecito, California, USA	N	9-Jan-18	N	CA10	F	EA	S	E	1	2.5	H
129	Montecito, California, USA	N	9-Jan-18	N	CA10	M	na	S	E	1	2.5	H
130	Montecito, California, USA	N	9-Jan-18	N	CA10	F	YA	S	E	1	2.5	H
131	Montecito, California, USA	N	9-Jan-18	N	CA25	M	YA	S	E	1	1.5	H
132	Montecito, California, USA	N	9-Jan-18	N	CA25	F	YA	S	E	1	1.5	H
133	Montecito, California, USA	N	9-Jan-18	N	CA11	F	EA	S	E	1	2.5	H
134	Montecito, California, USA	N	9-Jan-18	N	CA11	M	na	S	E	1	2.5	H
135	Montecito, California, USA	N	9-Jan-18	N	CA12	M	E	S	H	na	2.2	H
136	Montecito, California, USA	N	9-Jan-18	N	CA12	F	na	S	H	na	2.2	H
137	Montecito, California, USA	N	9-Jan-18	N	CA13	M	E	S	H	1	1.2	H
138	Montecito, California, USA	N	9-Jan-18	N	CA14	F	EA	S	E	1	1.8	H
139	Montecito, California, USA	N	9-Jan-18	N	CA15	M	na	S	E	1	0.3	H
140	Montecito, California, USA	N	9-Jan-18	N	CA15	F	na	S	E	1	0.3	H
141	Montecito, California, USA	N	9-Jan-18	N	CA15	na	na	S	E	1	0.3	H
142	Montecito, California, USA	N	9-Jan-18	N	CA15	na	na	S	E	1	0.3	H
143	Montecito, California, USA	N	9-Jan-18	N	CA16	F	na	H	H	1	0.8	H
144	Montecito, California, USA	N	9-Jan-18	N	CA16	F	na	H	H	1	0.8	H
145	Montecito, California, USA	N	9-Jan-18	N	CA16	F	na	H	H	1	0.8	H

146	Montecito, California, USA	N	9-Jan-18	N	CA16	na	na	H	H	1	0.8	H
147	Montecito, California, USA	N	9-Jan-18	N	CA17	M	na	S	E	1	0.2	H
148	Montecito, California, USA	N	9-Jan-18	N	CA17	F	na	S	E	1	0.2	H
149	Montecito, California, USA	N	9-Jan-18	N	CA17	M	C	S	E	1	0.2	H
150	Montecito, California, USA	N	9-Jan-18	N	CA18	M	A	S	E	2	0.4	H
151	Montecito, California, USA	N	9-Jan-18	N	CA18	F	na	S	E	2	0.4	H
152	Montecito, California, USA	N	9-Jan-18	N	CA18	M	YA	S	E	2	0.4	H
153	Montecito, California, USA	N	9-Jan-18	N	CA18	F	C	S	E	2	0.4	H
154	Montecito, California, USA	N	9-Jan-18	N	CA19	M	E	S	E	1	1.8	H
155	Montecito, California, USA	N	9-Jan-18	N	CA19	F	EA	S	E	1	1.8	H
156	Montecito, California, USA	N	9-Jan-18	N	CA19	F	na	S	E	2	1.8	H
157	Montecito, California, USA	N	9-Jan-18	N	CA20	M	E	S	E	1	1.4	H
158	Montecito, California, USA	N	9-Jan-18	N	CA20	F	EA	S	E	1	1.4	H
159	Montecito, California, USA	N	9-Jan-18	N	CA20	M	na	S	E	1	1.4	H
160	Montecito, California, USA	N	9-Jan-18	N	CA21	M	EA	S	E	1	1.8	H
161	Montecito, California, USA	N	9-Jan-18	N	CA22	M	YA	S	E	2	1.6	H
162	Montecito, California, USA	N	9-Jan-18	N	CA22	M	na	S	E	2	1.6	H
163	Montecito, California, USA	N	9-Jan-18	N	CA22	F	na	S	E	2	1.6	H
164	Montecito, California, USA	N	9-Jan-18	N	CA23	M	A	S	E	2	0.2	H
165	Montecito, California, USA	N	9-Jan-18	N	CA23	F	na	S	E	2	0.2	H
166	Montecito, California, USA	N	9-Jan-18	N	CA23	M	C	S	E	2	0.2	H
167	Montecito, California, USA	N	9-Jan-18	N	CA23	F	C	S	E	2	0.2	H
168	Montecito, California, USA	N	9-Jan-18	N	CA24	M	na	S	na	2	1.1	M
169	Montecito, California, USA	N	9-Jan-18	N	CA24	F	na	S	na	2	1.1	M
170	Montecito, California, USA	N	9-Jan-18	N	CA24	na	C	S	na	2	1.1	M
171	Montecito, California, USA	N	9-Jan-18	N	CA24	F	C	S	na	2	1.1	M
172	Montecito, California, USA	N	9-Jan-18	N	CA24	M	C	S	na	2	1.1	M
173	Oso, Washington, USA	N	22-Mar-14	M	WA2	F	YA	S	M	na	6.9	H
174	Oso, Washington, USA	N	22-Mar-14	M	WA2	M	EA	S	M	na	6.9	H
175	Oso, Washington, USA	N	22-Mar-14	M	WA2	M	A	S	M	na	6.9	H
176	Oso, Washington, USA	N	22-Mar-14	M	WA2	M	A	S	M	na	6.9	H
177	Oso, Washington, USA	N	22-Mar-14	M	WA6	M	A	S	M	1	4.8	H
178	Oso, Washington, USA	N	22-Mar-14	M	WA6	F	YA	S	M	1	4.8	H
179	Oso, Washington, USA	N	22-Mar-14	M	WA6	M	C	S	M	1	4.8	H
180	Oso, Washington, USA	N	22-Mar-14	M	WA6	M	C	S	M	1	4.8	H
181	Oso, Washington, USA	N	22-Mar-14	M	WA6	M	EA	S	M	1	4.8	H
182	Oso, Washington, USA	N	22-Mar-14	M	WA6	F	EA	S	M	1	4.8	H
183	Oso, Washington, USA	N	22-Mar-14	M	WA7	M	EA	S	M	na	8.1	H
184	Oso, Washington, USA	N	22-Mar-14	M	WA7	F	A	S	M	na	8.1	H
185	Oso, Washington, USA	N	22-Mar-14	M	WA8	M	EA	S	M	1	6.9	H
186	Oso, Washington, USA	N	22-Mar-14	M	WA1	M	A	S	M	1	6.1	H
187	Oso, Washington, USA	N	22-Mar-14	M	WA9	M	EA	S	M	na	7.1	H
188	Oso, Washington, USA	N	22-Mar-14	M	WA10	M	YA	S	M	na	11.3	H
189	Oso, Washington, USA	N	22-Mar-14	M	WA10	F	C	S	M	na	11.3	H
190	Oso, Washington, USA	N	22-Mar-14	M	WA10	M	EA	S	M	na	11.3	H
191	Oso, Washington, USA	N	22-Mar-14	M	WA10	F	EA	S	M	na	11.3	H
192	Oso, Washington, USA	N	22-Mar-14	M	WA11	M	A	S	M	1	8.8	H
193	Oso, Washington, USA	N	22-Mar-14	M	WA12	M	YA	S	M	1	9.6	H
194	Oso, Washington, USA	N	22-Mar-14	M	WA12	F	C	S	M	1	9.6	H
195	Oso, Washington, USA	N	22-Mar-14	M	WA12	F	C	S	M	1	9.6	H
196	Oso, Washington, USA	N	22-Mar-14	M	WA12	M	C	S	M	1	9.6	H
197	Oso, Washington, USA	N	22-Mar-14	M	WA12	M	C	S	M	2	9.6	H
198	Oso, Washington, USA	N	22-Mar-14	M	WA3	M	C	S	H	na	9.8	H
199	Oso, Washington, USA	N	22-Mar-14	M	WA13	M	A	S	H	na	5.5	H

200	Oso, Washington, USA	N	22-Mar-14	M	WA13	F	A	S	H	na	5.5	H
201	Oso, Washington, USA	N	22-Mar-14	M	WA14	M	EA	S	H	1	8.1	H
202	Oso, Washington, USA	N	22-Mar-14	M	WA15	F	A	S	H	1	8.6	H
203	Oso, Washington, USA	N	22-Mar-14	M	WA15	M	YA	S	H	1	8.6	H
204	Oso, Washington, USA	N	22-Mar-14	M	WA4	F	A	S	H	1	6.3	H
205	Oso, Washington, USA	N	22-Mar-14	M	WA4	F	C	S	H	1	6.3	H
206	Oso, Washington, USA	N	22-Mar-14	M	WA16	F	YA	S	H	1	4.2	H
207	Oso, Washington, USA	N	22-Mar-14	M	WA16	M	C	S	H	1	4.2	H
208	Oso, Washington, USA	N	22-Mar-14	M	WA17	F	A	S	H	1	5.9	H
209	Oso, Washington, USA	N	22-Mar-14	M	WA17	M	A	S	H	1	5.9	H
210	Oso, Washington, USA	N	22-Mar-14	M	WA19	F	E	S	H	1	6.1	H
212	Oso, Washington, USA	N	22-Mar-14	M	WA20	M	EA	S	H	2	3.4	H
213	Oso, Washington, USA	N	22-Mar-14	M	WA20	F	EA	S	H	2	3.4	H
214	Oso, Washington, USA	N	22-Mar-14	M	WA21	M	A	S	H	1	3.7	H
215	Oso, Washington, USA	N	22-Mar-14	M	WA21	F	EA	S	H	1	3.7	H
216	Oso, Washington, USA	N	22-Mar-14	M	WA21	M	A	S	H	1	3.7	H
217	Oso, Washington, USA	N	22-Mar-14	M	WA22	M	A	S	H	na	4.9	H
218	Oso, Washington, USA	N	22-Mar-14	M	WA22	F	A	S	H	na	4.9	H
219	Oso, Washington, USA	N	22-Mar-14	M	WA23	F	EA	S	H	na	3.7	H
220	Oso, Washington, USA	N	22-Mar-14	M	WA23	F	na	S	H	na	3.7	H
221	Oso, Washington, USA	N	22-Mar-14	M	WA5	F	EA	S	E	na	1.7	H
222	Oso, Washington, USA	N	22-Mar-14	M	WA5	M	E	S	E	na	1.7	H
223	Sham Tseng San Tsuen, Hong Kong	Y	23-Aug-99	M	HK1	M	na	H	L	1	2.9	H
224	Lai Chi Kok, Hong Kong	Y	16-Aug-82	M	HK2	F	na	na	L	1	3	M
225	Lai Chi Kok, Hong Kong	Y	16-Aug-82	M	HK2	na	C	na	L	1	3	M
226	Yau Kam Tau, Tsing Yi, Hong Kong	Y	17-Aug-82	N	HK3	na	na	na	L	1	0.8	M
227	Yau Kam Tau, Tsing Yi, Hong Kong	Y	17-Aug-82	N	HK3	na	na	na	L	1	0.8	M
228	Kau Wah Keng San Tsuen, Hong Kong	Y	16-Aug-82	M	HK4	na	C	H	L	1	2	M
229	Kau Wah Keng San Tsuen, Hong Kong	Y	16-Aug-82	M	HK4	na	C	H	L	1	2	M
230	Hong Kong	Y	2-Aug-79	M	HK5	na	na	na	L	1	3	M
231	Hong Kong	Y	2-Aug-79	M	HK5	na	na	na	L	1	3	M
232	Hong Kong	Y	9-Sep-83	M	HK6	na	na	na	L	na	4.5	M
233	Hong Kong	Y	9-Sep-83	M	HK6	na	na	na	L	na	4.5	M
234	Hong Kong	Y	29-May-82	na	HK7	na	na	na	L	1	2	M
235	Hong Kong	Y	29-May-82	na	HK7	na	na	na	L	1	2	M
236	Hong Kong	Y	29-May-82	na	HK7	na	na	na	L	1	2	M
237	Hong Kong	Y	3-Aug-79	na	HK8	na	na	na	L	1	1	M
238	Hong Kong	Y	3-Aug-79	na	HK8	na	na	na	L	1	1	M
239	Hong Kong	Y	29-May-82	N	HK9	na	na	na	L	1	1.5	M
240	Hong Kong	Y	29-May-82	N	HK9	na	na	na	L	1	1.5	M
241	Hong Kong	Y	29-May-82	N	HK10	na	C	H	L	1	5	M
242	Thredbo, New South Wales, Australia	N	30-Jul-97	N	AUS1	M	YA	H	L	1	2.5	L
243	Thredbo, New South Wales, Australia	N	30-Jul-97	N	AUS1	F	YA	H	L	1	2.5	L
244	Thredbo, New South Wales, Australia	N	30-Jul-97	N	AUS1	M	A	H	L	na	2.5	L
245	Thredbo, New South Wales, Australia	N	30-Jul-97	N	AUS1	F	A	H	L	na	2.5	L
246	Thredbo, New South Wales, Australia	N	30-Jul-97	N	AUS1	M	A	H	L	na	2.5	L
247	Thredbo, New South Wales, Australia	N	30-Jul-97	N	AUS1	F	YA	H	L	na	2.5	L
248	Thredbo, New South Wales, Australia	N	30-Jul-97	N	AUS1	M	YA	H	L	na	2.5	L
249	Thredbo, New South Wales, Australia	N	30-Jul-97	N	AUS1	F	YA	H	L	na	2.5	L
250	Thredbo, New South Wales, Australia	N	30-Jul-97	N	AUS1	M	A	H	L	na	2.5	L
251	Thredbo, New South Wales, Australia	N	30-Jul-97	N	AUS1	M	A	H	L	na	2.5	L
252	Thredbo, New South Wales, Australia	N	30-Jul-97	N	AUS1	M	YA	H	L	na	2.5	L
253	Thredbo, New South Wales, Australia	N	30-Jul-97	N	AUS1	M	YA	H	L	na	2.5	L
254	Thredbo, New South Wales, Australia	N	30-Jul-97	N	AUS1	F	YA	H	L	na	2.5	L

255	Thredbo, New South Wales, Australia	N	30-Jul-97	N	AUS1	F	YA	H	L	na	2.5	L
256	Thredbo, New South Wales, Australia	N	30-Jul-97	N	AUS1	F	A	H	L	na	2.5	L
257	Thredbo, New South Wales, Australia	N	30-Jul-97	N	AUS1	M	YA	H	L	na	2.5	L
258	Thredbo, New South Wales, Australia	N	30-Jul-97	N	AUS1	M	A	H	L	na	2.5	L
259	Thredbo, New South Wales, Australia	N	30-Jul-97	N	AUS1	M	YA	H	L	na	2.5	L
260	Thredbo, New South Wales, Australia	N	30-Jul-97	N	AUS2	M	A	S	L	na	2.5	L
261	Coledale, New South Wales, Australia	N	30-Apr-88	N	AUS3	F	na	S	L	1	1.6	L
262	Coledale, New South Wales, Australia	N	30-Apr-88	N	AUS3	M	C	S	L	1	1.6	L
263	Coledale, New South Wales, Australia	N	30-Apr-88	N	AUS3	M	C	S	L	1	1.6	L
264	Coledale, New South Wales, Australia	N	30-Apr-88	N	AUS3	F	C	S	L	1	1.6	L
265	Los Angeles, California, USA	N	10-Feb-78	N	CA27	M	na	H	H	1	3.7	M
266	Los Angeles, California, USA	N	10-Feb-78	N	CA27	F	na	H	H	1	3.7	M
267	Los Angeles, California, USA	N	10-Feb-78	N	CA27	M	C	H	H	1	3.7	M
268	Los Angeles, California, USA	N	10-Feb-78	N	CA27	F	C	H	H	1	3.7	M
269	Big Santa Anita Canyon, California, USA	N	Jan-69	N	CA28	M	na	S	na	1	0.9	M
270	Big Santa Anita Canyon, California, USA	N	Jan-69	N	CA28	F	na	S	na	1	0.9	M
271	Big Santa Anita Canyon, California, USA	N	Jan-69	N	CA28	na	na	S	na	1	0.9	M
272	Big Santa Anita Canyon, California, USA	N	Jan-69	N	CA28	na	na	S	na	1	0.9	M
273	Montecito, California, USA	N	9-Jan-18	N	CA26	M	na	H	E	3	1.8	H
274	Montecito, California, USA	N	9-Jan-18	N	CA26	na	na	H	E	3	1.8	H
275	Belvidere, New Jersey, USA	N	23-July-87	E	NJ1	F	EA	S	L	na	0.9	L
276	Belvidere, New Jersey, USA	N	23-July-87	E	NJ1	F	YA	S	L	na	0.9	L
277	Belvidere, New Jersey, USA	N	23-July-87	E	NJ1	M	na	S	L	1	0.9	L
278	Belvidere, New Jersey, USA	N	23-July-87	E	NJ1	F	na	S	L	na	0.9	L
279	Belvidere, New Jersey, USA	N	23-July-87	E	NJ1	F	na	S	L	na	0.9	L
280	Montecito, California, USA	N	9-Jan-18	N	CA29	M	na	S	E	1	0.3	H
281	Montecito, California, USA	N	9-Jan-18	N	CA29	F	na	S	E	1	0.3	H
282	Montecito, California, USA	N	9-Jan-18	N	CA29	M	na	S	E	1	0.3	H
283	Montecito, California, USA	N	9-Jan-18	N	CA29	M	na	S	E	1	0.3	H
284	Montecito, California, USA	N	9-Jan-18	N	CA29	F	na	S	E	1	0.3	H
285	La Crescenta, California	N	1-Jan-34	N	CA30	F	C	S	E	1	4.6	M
286	La Crescenta, California	N	1-Jan-34	N	CA30	M	C	S	E	1	4.6	M
287	La Crescenta, California	N	1-Jan-34	N	CA30	M	C	S	E	1	4.6	M
288	La Crescenta, California	N	1-Jan-34	N	CA30	M	na	S	E	1	4.6	M
289	La Crescenta, California	N	1-Jan-34	N	CA30	F	C	S	E	1	4.6	M
290	La Crescenta, California	N	1-Jan-34	N	CA30	F	na	S	E	1	4.6	M
291	La Crescenta, California	N	1-Jan-34	N	CA31	M	na	S	E	1	1.8	M
292	La Crescenta, California	N	1-Jan-34	N	CA31	F	na	S	E	1	1.8	M
293	La Crescenta, California	N	1-Jan-34	N	CA31	M	C	S	E	1	1.8	M
294	La Crescenta, California	N	1-Jan-34	N	CA31	M	na	S	E	1	1.8	M
295	La Crescenta, California	N	1-Jan-34	N	CA31	F	na	S	E	1	1.8	M
296	La Crescenta, California	N	1-Jan-34	N	CA31	F	E	S	E	1	1.8	M
297	La Crescenta, California	N	1-Jan-34	N	CA32	F	C	na	E	1	4.6	M
298	La Crescenta, California	N	1-Jan-34	N	CA32	M	C	na	E	1	4.6	M
299	La Crescenta, California	N	1-Jan-34	N	CA32	M	na	na	E	1	4.6	M
300	La Crescenta, California	N	1-Jan-34	N	CA32	F	C	na	E	1	4.6	M
301	La Crescenta, California	N	1-Jan-34	N	CA32	na	na	na	E	1	4.6	M
302	La Crescenta, California	N	1-Jan-34	N	CA32	na	na	na	E	1	4.6	M
303	La Crescenta, California	N	1-Jan-34	N	CA32	na	na	na	E	1	4.6	M
304	La Crescenta, California	N	1-Jan-34	N	CA32	na	na	na	E	1	4.6	M
305	La Crescenta, California	N	1-Jan-34	N	CA32	na	na	na	E	1	4.6	M
306	La Crescenta, California	N	1-Jan-34	N	CA32	na	na	na	E	1	4.6	M
307	La Crescenta, California	N	1-Jan-34	N	CA32	na	na	na	E	1	4.6	M
308	La Crescenta, California	N	1-Jan-34	N	CA32	na	na	na	E	1	4.6	M

309	La Crescenta, California	N	1-Jan-34	N	CA32	na	na	na	E	1	4.6	M
310	La Crescenta, California	N	1-Jan-34	N	CA32	F	na	na	E	1	4.6	M
311	La Crescenta, California	N	1-Jan-34	N	CA32	F	YA	na	E	1	4.6	M
312	La Crescenta, California	N	1-Jan-34	N	CA32	M	na	na	E	1	4.6	M
313	La Crescenta, California	N	1-Jan-34	N	CA32	M	na	na	E	1	4.6	M
314	La Crescenta, California	N	1-Jan-34	N	CA32	M	na	na	E	1	4.6	M
315	La Crescenta, California	N	1-Jan-34	N	CA33	na	na	H	E	1	3	M
316	La Crescenta, California	N	1-Jan-34	N	CA33	na	na	H	E	1	3	M
317	La Crescenta, California	N	1-Jan-34	N	CA33	na	na	H	E	1	3	M
318	La Crescenta, California	N	1-Jan-34	N	CA33	na	na	H	E	1	3	M
319	La Crescenta, California	N	1-Jan-34	N	CA33	na	na	H	E	1	3	M
320	La Crescenta, California	N	1-Jan-34	N	CA34	M	C	S	E	1	1	L
321	La Crescenta, California	N	1-Jan-34	N	CA34	M	C	S	E	1	1	L
322	La Crescenta, California	N	1-Jan-34	N	CA34	M	na	S	E	1	1	L
323	La Crescenta, California	N	1-Jan-34	N	CA34	F	na	S	E	1	1	L
324	La Crescenta, California	N	1-Jan-34	N	CA35	F	A	na	na	1	1.5	M
325	La Crescenta, California	N	1-Jan-34	N	CA36	M	na	na	E	1	0.9	L
326	La Crescenta, California	N	1-Jan-34	N	CA36	F	na	na	E	1	0.9	L
327	La Crescenta, California	N	1-Jan-34	N	CA36	M	C	na	E	1	0.9	L
328	La Crescenta, California	N	1-Jan-34	N	CA36	M	C	na	E	1	0.9	L
329	La Crescenta, California	N	1-Jan-34	N	CA36	F	C	na	E	1	0.9	L
330	La Crescenta, California	N	1-Jan-34	N	CA36	F	C	na	E	1	0.9	L
331	La Crescenta, California	N	1-Jan-34	N	CA36	M	C	na	E	1	0.9	L
332	Johnson's Landing, Canada	N	12-Jul-12	M	M20	M	EA	S	E	1	10	M
333	Johnson's Landing, Canada	N	12-Jul-12	M	M20	F	C	S	E	1	10	M
334	Johnson's Landing, Canada	N	12-Jul-12	M	M20	F	YA	S	E	1	10	M
335	Walhalla, Victoria, Australia	N	4-Aug-91	na	AUS4	M	na	na	L	na	1.8	M
336	Walhalla, Victoria, Australia	N	4-Aug-91	na	AUS4	M	na	na	L	na	1.8	M

Continuation of **Table A4.1.1**.

Victim ID	*Survived?*	*Aware?*	*Mitigative Action?*	*Escape/Rescue*	*Reference*
*	N	na	na	N	Lagmay et al. (2008)
2	N	na	na	N	http://www.nbcnews.com/id/6821292/ns/us_news/t/they-were-so-pure-good/#.XhfIS9ZKgvp https://www.firehouse.com/rescue/article/10513822/ventura-county-mudslide Jibson (2005) https://www.foxnews.com/story/four-killed-27-missing-in-california-mudslide
3	N	N	N	N	http://www.nbcnews.com/id/6821292/ns/us_news/t/they-were-so-pure-good/#.XhfIS9ZKgvp
4	N	N	N	N	https://www.firehouse.com/rescue/article/10513822/ventura-county-mudslide
5	N	N	N	N	Jibson (2005) https://www.latimes.com/local/california/la-me-la-conchita-20150104-story.html
6	N	na	na	N	https://losangeles.cbslocal.com/2015/01/10/la-conchita-residents-mark-10th-anniversary-of-deadly-landslide/ https://www.firehouse.com/rescue/article/10513822/ventura-county-mudslide Jibson (2005), Metivier-Hart (2017)
7	Y	Y	na	R	https://losangeles.cbslocal.com/2015/01/10/la-conchita-residents-mark-10th-anniversary-of-deadly-landslide/ https://www.firehouse.com/rescue/article/10513822/ventura-county-mudslide Jibson (2005) http://thenervousbreakdown.com/tnbnonfiction/2017/11/excerpt-from-sometimes-i-think-about-it-by-stephen-elliott/
8	Y	Y	Y	R	Metivier-Hart (2017)
9	N	Y	Y	N	Leiba (2013)
10	N	Y	Y	N	https://www.smh.com.au/environment/weather/if-we-dont-laugh-well-go-mental-murphys-creek-survivors-tell-of-the-horror-20110113-19p4i.html
11	Y	Y	Y	E	
12	Y	Y	Y	E	https://www.couriermail.com.au/news/queensland/parents-swept-away-by-murphys-creek-as-their-children-shelter/news-story/7bd2cebfd4ca98e4e9b7cbd6d2dc6774?sv=248927caef4b8055a6563467dda9c494 Barnes (2012)
13	Y	Y	N	R	https://www.rappler.com/nation/221085-tales-landslide-survivors-rescuers-tiwi-albay
14	N	N	N	N	
15	N	N	N	N	
16	N	N	N	N	
17	Y	N	N	R	https://www.rd.com/true-stories/survival/buried-mudslide/
18	Y	Y	Y	E	
19	Y	N	N	R	
20	Y	N	N	E	
21	Y	N	N	E	
22	Y	N	N	E	
23	Y	Y	Y	E	https://www.rd.com/true-stories/survival/buried-mudslide/ https://www.dailycamera.com/2013/09/21/eight-days-1000-year-rain-100-year-flood/
24	Y	N	N	R	https://www.thenewhumanitarian.org/analysis/2019/06/25/Bangladesh-landslides-climate-change-Indigenous
25	N	N	N	N	
26	N	N	N	N	
27	N	N	N	N	
28	N	Y	Y	N	https://www.theborneopost.com/2014/12/31/pregnant-woman-son-killed-husband-injured-in-camerons-landslide-2/
29	N	Y	Y	N	
30	Y	Y	Y	R	
31	Y	Y	N	R	Hsu (1975), Hsu (1978)
32	Y	Y	N	R	https://dailygazette.com/article/2018/04/30/report-details-cause-of-schenectady-landslide https://dailygazette.com/article/2018/04/24/landlside-victim-files-claim-against-schenectady-county https://www.news10.com/news/i-woke-up-and-everything-was-black-man-describes-moments-following-schenectady-mudslide/

33	Y	Y	N	E	https://dailygazette.com/article/2018/04/30/report-details-cause-of-schenectady-landslide https://dailygazette.com/article/2018/01/29/buildings-taken-down-following-mudslide https://www.news10.com/news/i-woke-up-and-everything-was-black-man-describes-moments-following-schenectady-mudslide/
34	Y	na	N	E	https://dailygazette.com/article/2018/04/30/report-details-cause-of-schenectady-landslide https://www.news10.com/news/i-woke-up-and-everything-was-black-man-describes-moments-following-schenectady-mudslide/
35	N	na	na	N	https://www.hmbreview.com/news/loma-mar-man-killed-in-slide-another-storm-expected-sooneric/article_5eb40311-3fc5-52fd-888a-a9fbc367b3c7.html
36	Y	na	na	E	
37	Y	Y	Y	R	http://www.china.org.cn/china/2010-08/14/content_20707729.htm
38	N	Y	na	N	
39	N	na	Y	N	
40	N	Y	Y	N	
41	Y	Y	N	R	https://www.chinadaily.com.cn/china/2010-08/09/content_11117379.htm
42	Y	Y	Y	R	http://www.china.org.cn/china/2010-08/09/content_20671813.htm
43	N	N	N	N	
44	N	N	N	N	
45	N	N	N	N	
46	N	N	N	N	
47	N	N	N	N	
48	N	N	N	N	
49	N	N	N	N	
50	N	N	N	N	
51	N	N	N	N	
52	N	N	N	N	https://www.thenational.com.pg/mt-hagen-landslide-buries-boys-alive/
53	N	N	N	N	
54	Y	Y	Y	R	
55	N	na	na	N	Campbell (1975)
56	Y	Y	Y	E	https://patch.com/california/orange-county/50th-anniversary-1969-fatal-mudslide-silverado-fire-hall
57	N	Y	Y	N	https://www.latimes.com/archives/la-xpm-1989-02-25-me-330-story.html
58	N	Y	Y	N	
59	N	Y	Y	N	
60	N	Y	Y	N	
61	N	Y	Y	N	
62	Y	Y	Y	R	
63	Y	Y	Y	R	
64	Y	Y	Y	R	
65	Y	Y	Y	E	
66	Y	Y	Y	E	
67	Y	Y	Y	E	
68	Y	Y	Y	E	
69	Y	Y	Y	R	
70	Y	Y	Y	R	
71	Y	Y	Y	E	
72	Y	Y	Y	R	
73	Y	Y	Y	R	
74	Y	Y	Y	R	
75	Y	Y	Y	R	
76	Y	Y	Y	R	
77	Y	Y	Y	R	
78	Y	Y	Y	R	
79	Y	Y	Y	R	

80	Y	Y	Y	R	
81	Y	Y	Y	R	
82	Y	Y	Y	R	
83	Y	Y	Y	R	
84	Y	Y	Y	R	
85	Y	Y	Y	R	
86	Y	Y	Y	R	
87	Y	Y	Y	R	
88	Y	Y	Y	R	
89	Y	Y	Y	R	
90	Y	Y	Y	R	
91	N	N	N	N	https://www.kgw.com/article/news/local/central-coast/woman-70-killed-in-landslide-near-florence/283-5692915 https://www.registerguard.com/article/20151219/NEWS/312199995
92	Y	N	N	E	
93	Y	na	na	N	EmergeX Planning (2006), Evans et al. (2002)
94	N	na	na	na	https://www.for.gov.bc.ca/hfd/library/documents/bib106111south2.pdf
95	N	N	N	N	Beetham (2011), Massey et al. (2019)
96	Y	N	N	E	
97	N	na	na	N	Massey et al. (2019) https://groups.google.com/forum/m/#!msg/soc.culture.new-zealand/L9ysBE8svS4/YL09QbBo0C0J
98	N	na	na	N	Massey et al. (2019), Page (2013)
99	N	na	na	N	https://www.sanluisobispo.com/news/local/article224213780.html https://apnews.com/54a7e52f43b74d218577df31e680241b/Mudslides-take-heavy-toll-on-immigrants-serving-posh-town
100	N	N	N	N	https://www.sanluisobispo.com/news/local/article224213780.html
101	N	N	N	N	https://apnews.com/54a7e52f43b74d218577df31e680241b/Mudslides-take-heavy-toll-on-immigrants-serving-posh-town
102	N	N	N	N	http://www.cadaverdog.net/oprah-thanks-rescue-teams-and-meets-search-dogs-hunting-for-missing-people-in-the-california-mudslides-that-have-left-19-dead-as-she-reveals-her-own-montecito-home-was-left/
103	Y	na	na	R	https://www.sanluisobispo.com/news/local/article224213780.html
104	Y	na	na	R	https://apnews.com/54a7e52f43b74d218577df31e680241b/Mudslides-take-heavy-toll-on-immigrants-serving-posh-town
105	Y	na	na	R	https://www.edhat.com/news/21st-victim-found-and-identified-in-montecito-mudslide
106	N	N	N	N	https://www.noozhawk.com/article/sutthithepa_taylor_family_rememberd_at_memorial_montecito_flooding_20180207 https://www.ksby.com/news/2018/12/20/family-of-montecito-mudslide-victims-files-wrongful-death-lawsuit https://www.noozhawk.com/article/richard_loring_taylor_traveled_the_world_as_professor_died_in_montecito_mud
107	N	N	N	N	https://www.noozhawk.com/article/sutthithepa_taylor_family_rememberd_at_memorial_montecito_flooding_20180208 https://www.noozhawk.com/article/richard_loring_taylor_traveled_the_world_as_professor_died_in_montecito_mud
108	N	N	N	N	https://www.noozhawk.com/article/sutthithepa_taylor_family_rememberd_at_memorial_montecito_flooding_20180209 https://www.ksby.com/news/2018/12/20/family-of-montecito-mudslide-victims-files-wrongful-death-lawsuit https://www.noozhawk.com/article/richard_loring_taylor_traveled_the_world_as_professor_died_in_montecito_mud
109	N	N	N	N	https://www.noozhawk.com/article/sutthithepa_taylor_family_rememberd_at_memorial_montecito_flooding_20180210
110	Y	na	na	R	https://www.noozhawk.com/article/richard_loring_taylor_traveled_the_world_as_professor_died_in_montecito_mud
111	N	N	N	N	https://www.ksbw.com/article/stories-of-how-mudslide-victims-died-survived-emerge/15167239
112	N	Y	N	N	https://www.ksbw.com/article/stories-of-how-mudslide-victims-died-survived-emerge/15167239
113	N	N	N	N	https://www.usatoday.com/story/news/local/2018/03/30/families-montecito-mudslide-victims-file-wrongful-death-suits-against-edison/471721002/ Panish Shea & Boyle (2018)
114	Y	N	N	R	https://www.ksbw.com/article/stories-of-how-mudslide-victims-died-survived-emerge/15167241 https://www.usatoday.com/story/news/local/2018/03/30/families-montecito-mudslide-victims-file-wrongful-death-suits-against-edison/471721002/ Panish Shea & Boyle (2018) https://www.latimes.com/local/california/la-me-montecito-mudslides-20180114-story.html

115	Y	Y	N	R	https://www.ksbw.com/article/stories-of-how-mudslide-victims-died-survived-emerge/15167242 https://www.usatoday.com/story/news/local/2018/03/30/families-montecito-mudslide-victims-file-wrongful-death-suits-against-edison/471721002/ Panish Shea & Boyle (2018)
116	N	Y	Y	N	https://www.latimes.com/local/california/la-me-montecito-mudslides-20180114-story.html
117	Y	Y	Y	na	https://www.ksbw.com/article/stories-of-how-mudslide-victims-died-survived-emerge/15167239 https://www.latimes.com/local/california/la-me-montecito-mudslides-20180114-story.html
118	N	na	na	N	https://www.latimes.com/local/california/la-me-montecito-mudslides-20180114-story.html
119	N	na	na	N	https://www.nbcnews.com/news/weather/search-victims-california-mudslides-widens-death-toll-grows-n836411
120	N	Y	Y	N	https://www.edhat.com/news/survivors-featured-in-montecito-debris-flow-documentary
121	Y	Y	Y	E	
122	N	Y	Y	N	https://www.latimes.com/local/california/la-me-montecito-mudslides-20180114-story.html https://headtopics.com/us/she-was-buried-in-a-mudslide-that-killed-her-father-and-brother-singing-has-been-her-salvation-5267693 https://www.cincinnati.com/story/news/2018/06/21/they-moved-mason-ca-then-disaster-hit-felt-like-being-inside-trash-compactor/717719002/
123	Y	Y	Y	R	https://www.latimes.com/local/california/la-me-montecito-mudslides-20180114-story.html https://headtopics.com/us/she-was-buried-in-a-mudslide-that-killed-her-father-and-brother-singing-has-been-her-salvation-5267694 https://www.latimes.com/local/california/la-me-montecito-mudslides-20180114-story.html https://www.cincinnati.com/story/news/2018/06/21/they-moved-mason-ca-then-disaster-hit-felt-like-being-inside-trash-compactor/717719002/
124	Y	Y	Y	R	https://www.latimes.com/local/california/la-me-montecito-mudslides-20180114-story.html https://headtopics.com/us/she-was-buried-in-a-mudslide-that-killed-her-father-and-brother-singing-has-been-her-salvation-5267695 https://www.cincinnati.com/story/news/2018/06/21/they-moved-mason-ca-then-disaster-hit-felt-like-being-inside-trash-compactor/717719002/
125	N	N	N	N	https://www.usatoday.com/story/news/nation-now/2018/01/13/all-people-who-died-california-mudslides/1031202001/
126	N	N	N	N	https://www.ksbw.com/article/stories-of-how-mudslide-victims-died-survived-emerge/15167239
127	Y	N	N	E	https://www.usatoday.com/story/news/nation-now/2018/01/13/all-people-who-died-california-mudslides/1031202001/ https://www.edhat.com/news/21st-victim-found-and-identified-in-montecito-mudslide
128	N	na	na	N	https://www.independent.com/2018/06/12/montecitos-history-violence/
129	Y	N	N	R	https://www.independent.com/2018/06/12/montecitos-history-violence/ https://www.washingtonpost.com/national/it-was-not-sufficient-california-officials-reevaluate-voluntary-evacuations-after-deadly-mudslides/2018/02/03/9a19410c-003d-11e8-9d31-d72cf78dbeee_story.html
130	Y	na	na	E	https://www.scpr.org/news/2018/01/17/79878/montecito-mudslides-one-story-of-luck-loss-and-nar/ https://www.rogerssheffield.com/news-and-commentary/206-special-client-bulletin-montecito-mudslide-disaster
131	Y	Y	Y	E	https://www.scpr.org/news/2018/01/17/79878/montecito-mudslides-one-story-of-luck-loss-and-nar/
132	Y	Y	Y	E	
133	N	Y	N	N	https://www.independent.com/2018/06/12/montecitos-history-violence/ https://www.cnn.com/2018/01/11/us/residents-describe-california-mudslide/index.html https://www.latimes.com/local/lanow/la-me-ln-mudslide-victims-20180111-htmlstory.html
134	Y	Y	N	R	https://www.cnn.com/2018/01/11/us/residents-describe-california-mudslide/index.html https://www.latimes.com/local/lanow/la-me-ln-mudslide-victims-20180111-htmlstory.html
135	N	na	na	N	https://www.nbclosangeles.com/news/roy-rohter-california-santa-barbara-montecito-storm-victims/38311/
136	Y	na	na	R	https://www.nbclosangeles.com/news/roy-rohter-california-santa-barbara-montecito-storm-victims/38311/ https://apnews.com/4e23b58468a44f6583244d819536f364/California-storm:-Cars-swept-away,-body-pinned-against-home

137	N	na	na	N	https://www.usatoday.com/story/news/nation-now/2018/01/13/all-people-who-died-california-mudslides/1031202001/ http://www.cadaverdog.net/oprah-thanks-rescue-teams-and-meets-search-dogs-hunting-for-missing-people-in-the-california-mudslides-that-have-left-19-dead-as-she-reveals-her-own-montecito-home-was-left/
138	Y	N	N	E	https://www.independent.com/2018/06/12/montecitos-history-violence/
139	Y	Y	Y	E	https://www.vcstar.com/story/news/2018/01/09/like-bomb-went-off/1019586001/
140	Y	Y	Y	E	
141	Y	Y	Y	E	
142	Y	Y	Y	E	
143	Y	Y	N	E	https://www.npr.org/2018/01/12/577713367/california-woman-shares-story-of-mudslide-survival
144	Y	Y	N	E	https://www.npr.org/2018/03/22/596179995/california-residents-bracing-for-more-mudslides
145	Y	Y	N	E	
146	Y	Y	N	E	
147	Y	Y	Y	E	https://www.cbc.ca/radio/asithappens/as-it-happens-wednesday-edition-1.4480907/canadian-who-survived-california-wildfires-forced-from-home-by-deadly-mudslides-1.4480917
148	Y	Y	Y	E	
149	Y	Y	Y	E	
150	Y	Y	Y	E	https://time.com/5099207/california-mudslides-man-saves-baby/
151	Y	Y	Y	E	https://www.cnn.com/2018/01/11/us/residents-describe-california-mudslide/index.html https://journal.crossfit.com/article/mudslide-achauer-2
152	Y	Y	Y	E	https://journal.crossfit.com/article/mudslide-achauer-2
153	Y	Y	Y	E	
154	Y	N	N	R	https://www.noozhawk.com/article/for_montecito_debris_flow_victims_rebuilding_can_be_a_painfully_long_proces
155	Y	N	N	R	
156	Y	N	N	E	https://www.santabarbarafamilylife.com/news/when-disaster-hit-recalling-a-familys-ordeal-through-the-montecito-mudslide/
157	Y	Y	Y	E	https://www.vcstar.com/story/news/2018/01/09/like-bomb-went-off/1019586001/
158	Y	Y	Y	E	
159	Y	Y	Y	E	
160	Y	Y	Y	E	https://www.edhat.com/news/survivors-featured-in-montecito-debris-flow-documentary https://www.washingtonpost.com/national/after-being-buried-by-mudslides-two-communities-chart-very-different-recoveries/2020/01/09/655f3b00-3327-11ea-9313-6cba89b1b9fb_story.html
161	Y	Y	Y	E	https://www.latimes.com/local/california/la-me-montecito-mudslides-20180114-story.html
162	Y	Y	Y	E	https://www.latimes.com/local/california/la-me-montecito-mudslides-20180114-story.html https://rogerssheffield.com/news-and-commentary
163	Y	Y	Y	E	https://www.latimes.com/local/california/la-me-montecito-mudslides-20180114-story.html https://ktla.com/2018/01/12/california-mudslides-search-for-a-miracle-enters-3rd-day/ https://www.scribd.com/article/369128028/When-Debris-Flowed-Montecito-Families-Had-Little-Chance-To-Flee
164	Y	Y	Y	E	https://www.scpr.org/news/2018/01/11/79721/another-victim-id-ed-in-montecito-mudslides/
165	Y	Y	Y	E	
166	Y	Y	Y	E	
167	Y	Y	Y	E	
168	Y	Y	Y	E	https://www.cnn.com/2018/01/10/us/family-rescued-california-mud-flooding/index.html
169	Y	Y	Y	E	https://www.sandiegouniontribune.com/news/public-safety/sd-me-mudslide-rescue-20180110-story.html
170	Y	Y	Y	E	https://www.npr.org/2018/04/07/599428526/bucket-brigade-volunteers-still-digging-california-homes-out-after-mudslides
171	Y	Y	Y	E	
172	Y	Y	Y	E	
173	N	na	na	N	https://www.tri-cityherald.com/latest-news/article32219559.html
174	N	na	na	N	https://www.tri-cityherald.com/latest-news/article32219559.html
175	N	na	na	N	https://graphics.latimes.com/towergraphic-washington-landslide-victims/
176	N	na	na	N	https://www.tri-cityherald.com/latest-news/article32219559.html
177	N	na	na	N	https://graphics.latimes.com/towergraphic-washington-landslide-victims/
178	N	na	na	N	

179	N	na	na	N	
180	N	na	na	N	
181	N	na	na	N	
182	N	na	na	N	
183	N	na	na	N	https://graphics.latimes.com/towergraphic-washington-landslide-victims/ Snohomish County MEO (2014)
184	N	na	na	N	https://graphics.latimes.com/towergraphic-washington-landslide-victims/ Snohomish County MEO (2014)
185	N	na	na	N	https://graphics.latimes.com/towergraphic-washington-landslide-victims/
186	N	na	na	N	
187	N	na	na	N	
188	N	na	na	N	https://graphics.latimes.com/towergraphic-washington-landslide-victims/ https://www.heraldnet.com/news/son-lost-to-slide-will-always-be-remembered-with-love/
189	N	na	na	N	https://graphics.latimes.com/towergraphic-washington-landslide-victims/
190	N	na	na	N	
191	N	na	na	N	
192	N	na	na	N	
193	N	na	na	N	https://q13fox.com/2014/04/02/mom-seeks-out-two-heroes-who-rescued-son-from-mudslide/
194	N	na	na	N	
195	N	na	na	N	
196	N	na	na	N	
197	Y	na	na	R	https://q13fox.com/2014/04/02/mom-seeks-out-two-heroes-who-rescued-son-from-mudslide/ https://mynorthwest.com/22212/volunteer-pilot-recalls-rescuing-jacob-from-oso-mudslide/
198	N	na	na	N	https://graphics.latimes.com/towergraphic-washington-landslide-victims/
199	N	na	na	N	
200	N	na	na	N	
201	N	na	na	N	
202	N	na	na	N	
203	N	na	na	N	
204	N	na	na	N	
205	N	na	na	N	
206	Y	Y	N	R	https://time.com/57045/washington-mudslide-oso-survivor-skorjanc/ https://mynorthwest.com/22177/baby-dukes-mom-tells-story-of-surviving-oso-mudslide/
207	Y	na	N	R	https://www.seattlemet.com/articles/2014/11/3/first-responders-of-the-oso-mudslide-november-2014 https://mynorthwest.com/22177/baby-dukes-mom-tells-story-of-surviving-oso-mudslide/
208	N	Y	Y	N	https://www.wsj.com/articles/washington-state-landslide-leaves-deep-scars-on-survivors-1426874659 https://www.columbian.com/news/2014/sep/21/after-oso-recovery-more-than-medicine-stitches/
209	Y	Y	Y	R	https://www.wsj.com/articles/washington-state-landslide-leaves-deep-scars-on-survivors-1426874658 https://theplanetmagazine.net/recovering-oso-7f7d856e533f https://www.youtube.com/watch?v=z7Oij64yafA https://www.youtube.com/watch?v=mEwkruklKeM
210	N	N	N	N	https://graphics.latimes.com/towergraphic-washington-landslide-victims/ https://www.heraldnet.com/news/all-i-can-say-is-thank-you-oso-survivors-meet-their-rescuers/ https://www.heraldnet.com/news/love-and-humor-help-two-slide-survivors-bear-their-losses/
212	Y	Y	N	R	https://www.king5.com/article/news/local/oso-landslide/landslide-survivors-recall-shock-wave-of-debris/281-246946218
213	Y	Y	N	R	https://www.heraldnet.com/news/all-i-can-say-is-thank-you-oso-survivors-meet-their-rescuers/ https://www.kiro7.com/news/oso-couple-credit-lives-friend-and-two-cars/82103613/ https://www.heraldnet.com/news/love-and-humor-help-two-slide-survivors-bear-their-losses/
214	N	na	na	N	https://graphics.latimes.com/towergraphic-washington-landslide-victims/
215	N	na	na	N	
216	N	na	na	N	

217	N	na	na	N	
218	N	na	na	N	
219	Y	Y	N	E	https://www.cbsnews.com/news/oso-washington-mudslide-survivor-hillside-hit-us-like-a-wave/ https://www.king5.com/article/news/local/rescued-from-the-rubble-survivors-recall-oso-landslide/157427391 https://special.seattletimes.com/o/html/localnews/2023259205_mudslidenarrativexml.html
220	Y	Y	N	E	https://www.cbsnews.com/news/oso-washington-mudslide-survivor-hillside-hit-us-like-a-wave/
221	N	Y	N	N	https://graphics.latimes.com/towergraphic-washington-landslide-victims/ https://www.nydailynews.com/news/world/mudslide-survivor-escapes-mud-loses-wife-45-years-article-1.1736365
222	Y	Y	N	R	https://www.nytimes.com/2014/03/26/us/washington-mudslide-search-continues.html https://www.nydailynews.com/news/world/mudslide-survivor-escapes-mud-loses-wife-45-years-article-1.1736366
223	N	na	na	N	Fugro-Wilson (2005)
224	N	na	na	N	Hudson (1982), Finlay (1996)
225	N	na	na	N	
226	Y	na	na	na	
227	N	na	na	N	
228	N	na	na	N	
229	N	na	na	N	
230	N	na	na	N	Finlay (1996)
231	Y	na	na	na	
232	N	na	na	N	
233	N	na	na	N	
234	N	na	na	N	
235	N	na	na	N	
236	N	na	na	N	
237	N	na	na	N	
238	Y	na	na	na	
239	N	na	na	N	
240	N	na	na	N	
241	N	na	na	N	
242	Y	Y	N	R	http://monumentaustralia.org.au/themes/disaster/landslide/display/23475-thredbo-landslide Hand (2000), Diver (1999)
243	N	Y	N	N	Hand (2000), Diver (1999)
244	N	na	na	N	
245	N	na	na	N	
246	N	na	na	N	
247	N	na	na	N	
248	N	na	na	N	
249	N	na	na	N	
250	N	na	na	N	
251	N	na	na	N	
252	N	na	na	N	
253	N	na	na	N	
254	N	na	na	N	
255	N	na	na	N	
256	N	na	na	N	
257	N	na	na	N	
258	N	na	na	N	
259	N	na	na	N	
260	N	na	na	N	
261	N	na	na	N	Flentje (1998) https://www.illawarramercury.com.au/story/1524962/blog-what-really-triggered-coledale-landslide/

					Hickey (n.d.), Osuchowski & Roberts (2011)
262	N	na	na	N	Flentje (1998), Hickey (n.d.), Osuchowski & Roberts (2011)
263	Y	na	na	na	Flentje (1998)
264	Y	na	na	na	https://www.salvationarmy.org.au/documents/pipeline_11nov2010.pdf Hickey (n.d.), Osuchowski & Roberts (2011)
265	Y	Y	Y	E	McPhee (1989) https://www.newyorker.com/magazine/1988/09/26/los-angeles-against-the-mountains-i Cobery (2012)
266	Y	Y	Y	E	McPhee (1989), Cobery (2012)
267	Y	Y	Y	R	
268	Y	Y	Y	R	
269	Y	na	na	E	McPhee (1989)
270	Y	na	na	E	
271	Y	na	na	E	
272	Y	na	na	E	
273	Y	Y	Y	E	https://www.independent.com/multimedia/1-9-a-documentary/
274	Y	Y	Y	E	https://www.independent.com/2018/05/31/after-debris-flow-scientists-and-survivors-are-looking-montecitos-worst-hit-neighborhood/
275	N	N	N	N	https://www.newspapers.com/clip/5567455/manuka_chunk_landslide_1887_snyder_fox/
276	N	N	N	N	http://www.gendisasters.com/new-jersey/7969/belvidere-nj-landslide-causes-death-july-1887
277	Y	N	N	E	https://www.state.nj.us/njoem/programs/pdf/mitigation2014/2014-Section-5-7.pdf
278	Y	N	N	E	
279	Y	N	N	E	
280	Y	Y	N	E	https://www.latimes.com/la-me-southern-california-storm-live-updates-htmlstory.html
281	Y	Y	N	E	https://www.gofundme.com/f/moe-family-montecito-mudslide-fund
282	Y	Y	N	E	https://www.newsandguts.com/montecito-mudslides-leave-debris-destruction-traumatized-residents/
283	Y	Y	N	E	
284	Y	Y	N	E	
285	Y	Y	N	R	Cobery (2012)
286	Y	Y	N	na	
287	Y	Y	N	na	
288	Y	Y	N	na	
289	Y	Y	N	na	
290	N	Y	N	N	
291	Y	Y	Y	E	
292	Y	Y	Y	E	
293	Y	na	Y	E	
294	Y	na	Y	E	
295	Y	na	Y	E	
296	Y	na	Y	E	
297	Y	Y	N	E	Cobery (2012)
298	Y	Y	N	R	https://medium.com/to-die-in-la/the-1934-new-years-flood-d63fc356f77b
299	Y	Y	N	R	
300	N	Y	N	N	
301	N	na	na	N	
302	N	na	na	N	
303	N	na	na	N	
304	N	na	na	N	
305	N	na	na	N	
306	N	na	na	N	
307	N	na	na	N	

308	N	na	na	N	
309	N	na	na	N	
310	N	Y	N	N	
311	N	na	na	N	Cobery (2012) https://medium.com/to-die-in-la/the-1934-new-years-flood-d63fc356f77b https://cdnc.ucr.edu/?a=d&d=SBS19340103.1.1&e=-------en--20--1--txt-txIN--------1
312	Y	Y	Y	E	Cobery (2012)
313	Y	Y	Y	R	https://medium.com/to-die-in-la/the-1934-new-years-flood-d63fc356f77b
314	Y	Y	Y	E	
315	Y	Y	Y	E	Cobery (2012)
316	Y	Y	Y	E	
317	Y	Y	Y	E	
318	Y	Y	Y	E	
319	Y	Y	Y	E	
320	Y	Y	Y	E	
321	Y	Y	Y	E	
322	Y	Y	Y	E	
323	Y	Y	Y	E	
324	Y	na	na	R	
325	Y	na	na	na	
326	Y	na	na	na	
327	N	na	na	N	
328	N	na	na	N	
329	N	na	na	N	
330	Y	na	na	na	
331	Y	na	na	na	
332	N	na	na	N	https://www.cbc.ca/news/canada/british-columbia/johnsons-landing-slide-yields-2nd-body-1.1230234 https://nationalpost.com/news/canada/b-c-landslide-rescue-crews-have-found-the-location-of-a-buried-home-that-could-contain-a-family-of-three Nicol et al. (2013) https://nationalpost.com/news/canada/b-c-landslide-rescue-crews-held-up-by-rain
333	N	na	na	N	https://www.youtube.com/watch?v=j8AHWIfxG54 https://www.cbc.ca/news/canada/british-columbia/johnsons-landing-slide-yields-2nd-body-1.1230234 https://nationalpost.com/news/canada/b-c-landslide-rescue-crews-have-found-the-location-of-a-buried-home-that-could-contain-a-family-of-three
334	N	na	na	N	https://www.cbc.ca/news/canada/british-columbia/johnsons-landing-slide-yields-2nd-body-1.1230234 https://nationalpost.com/news/canada/b-c-landslide-rescue-crews-have-found-the-location-of-a-buried-home-that-could-contain-a-family-of-three Nicol et al. (2013) https://nationalpost.com/news/canada/b-c-landslide-rescue-crews-held-up-by-rain
335	N	na	na	N	Geoscience Australia (2018)
336	N	na	na	N	

Table A4.1.2. Abbreviations corresponding to the columns in **Table A4.1.1**.

Time	
M (morning)	4 am – 12 pm
E (evening)	12 pm – 8 pm
N (night)	8 pm – 4 am
Gender	
F	female
M	male
Age	
C (child)	0 – 19
YA (young adult)	20 – 39
A (adult)	40 – 59
EA (elderly adult)	60 – 79
E (elderly)	80 – 99
Material	
H	rigid
S	flexible
Distance (m)	
L	0 – 99
M	100 – 499
H	500 – 999
E	> 1000
Confidence	
L	low
M	medium
H	high
Escape/Rescue	
N	did not survive
E	escaped
R	rescued

References

Barnes, M., (2012). Inquest into the deaths caused by the south-east Queensland floods of January 2011. Brisbane: Office of the State Coroner.

Beetham, D. (2012). Ohope Beach landslide of 18 June 2011. *GNS Science Report 2011/46*. GNS Science.

Campbell, R. (1975). Soil slips, debris flows, and rainstorms in the Santa Monica Mountains and vicinity, Southern California. *U.S. Geological Survey Professional Paper 851*. Washington: United States Government Printing Office

Cobery, A., Lawler, M., Lawler, P. (2012). *The Great Crescenta Valley Flood*. Charleston, South Carolina: History Press.

Diver, S. (1999). *Survival*. Sydney: Pan Macmillan Australia.

EmergeX Planning (2006). Hazard, risk and vulnerability assessment: District of Summerland. Final Report February 2006.

Evans, S., Couture, R., Raymond, E. (2002). Catastrophic Landslides and Related Processes in the Southeastern Cordillera: Analysis of Impact on Lifelines and Communities. Geological Survey of Canada – Natural Resources Canada.

Finlay, P. (1996). The risk assessment of slopes. (*doctoral dissertation*). Sydney: University of New South Wales

Flentje, P. (1998). Computer based landslide hazard and risk assessment (Northern Illawarra Region of New South Wales, Australia). (*doctoral dissertation*). Wollongong, New South Wales: University of Wollongong.

Fugro-Wilson (2005). Report on the debris flow at Sham Tseng San Tsuen of 23 August 1999: Findings of the investigation. *GEO Report No. 169*. Hong Kong Geotechnical Engineering Office.

Geoscience Australia. (2018). Australian landslide database. Available at: http://pid.geoscience.gov.au/dataset/ga/74273

Hand, D. (2000). Report of the inquest into the deaths arising from the Thredbo landslide. New South Wales: State Coroner.

Hickey, M. (n.d.). Now you see it—Now you don't: Slips, floods and washaways. Available at: http://railknowledgebank.com/Presto/content/GetDoc.axd?ctID=MTk4MTRjNDUtNWQ0My00OTBmLTllYWUtZWFjM2U2OTE0ZDY3&rID=NDUyMg==&pID=Nzkx&attchmnt=True&uSesDM=False&rIdx=MzQ5MQ==&rCFU=

Hsu, K. (1975). Catastrophic debris streams (Sturzstroms) generated by rockfalls. *Geol. Soc. Am. Bull.*, 86, 129-140. https://doi.org/10.1130/0016-7606(1975)86<129:CDSSGB>2.0.CO;2

Hsu, K. (1978). Albert Heim: Observations on landslides and relevance to modern interpretations. In: B. Voight (*Ed.*) *Developments in Geotechnical Engineering 14A: Rockslides and Avalanches, 1: Natural Phenomena*. Amsterdam: Elsevier.

Hudson, R. (1982). Report on the rainstorm of August 1982. *GCO Report No. 7/82*. Hong Kong Geotechnical Engineering Office.

Jibson, R. (2005). Landslide hazards at La Conchita, California. *Open-File Report 2005-1067*. Reston, VA: United States Geological Survey

Lagmay, A., Tengonciang, A., Rodolfo, R., Soria, J., Baliatan, E., Paguican, E., Ong, J., Lapus, M., Fernandez, D., Quimba, Z., Uichanco, C. (2008). Science guides search and rescue after the 2006 Philippine landslide. *Disasters*, 32, 416-433. https://doi.org/10.1111/j.1467-7717.2008.01047.x

Leiba, M. (2013). Impact of landslides in Australia to December 2011. *Australian J. Emergency Management*. 28, 30-36.

Massey, C., Thomas, K-L., King, A., Singeisen, C., Taig, T., Horspool, N. (2019). SLIDE (Wellington): Vulnerability of dwellings to landslides (Project No. 16/SP740). *GNS Science report 2018/17*. GNS Science.

McPhee, J. (1989). *The Control of Nature*. New York: Farrar, Straus and Giroux

Metivier-Hart, D. (2017). *A Silent Stillness—Buried Alive: One Woman's Remarkable Story of Survival, Hope and Rescue; the Last Survivor of the La Conchita Landslide*. Xlibris.

Nicol, D., Jordan, P., Boyer, D., Yonin, D. (2013). Johnsons Landing landslide hazard and risk assessment. Regional District of Central Kootenay (RDCK).

Osuchowski, M., Roberts, J. (2011). Landslides costs in the Wollongong Region. *Record 2011/32*. Geoscience Australia.

Page, M. (2013). Landslides and debris flows caused by the 15-17 June 2013 rain storm in the Marahau-Motueka area, and the fatal landslide at Otuwhero Inlet. *GNS Science Report 2013/44*. GNS Science.

Panish Shea & Boyle (2018). Carie Baker-Corey v. Southern California Edison Company: Complaint for Damages. *Case No. BC699727*. Superior Court of the State of California County of Los Angeles, Central District.

Snohomish County Medical Examiner's Office (MEO). (2014). Media update as of April 1, 2014 at 4:30 PM. Snohomish County, Washington. Available at: https://snohomishcountywa.gov/Archive.aspx?AMID=98

United Nations. (2020). World economic situation and prospects. New York: United Nations. Available at: https://www.un.org/development/desa/dpad/publication/world-economic-situation-and-prospects-2020/

Appendix 5.1 – Supplemental information for the Lebanon case study

The contents of this appendix are published as:

Pollock, W., Grant, A., Wartman, J., Abou-Jaoude, G. (2019). Multimodal method for landslide risk analysis. *MethodsX*, 6, 827-836. https://doi.org/10.1016/j.mex.2019.04.012.

Abstract

Quantitative landslide risk analysis is a key step in creating appropriate land use policies. However, regional scale landslide hazard and risk studies are traditionally based on a single, infinite-slope style of failure, belying the differing consequences of a diverse range of failure modes. In this paper we expand an existing multimodal coseismic landslide hazard model to create a method for multimodal, multi-trigger quantitative landslide risk analysis and apply it to the country of Lebanon.

- Physics-based, mode-specific models for coseismic and precipitation-induced landslides capture the effects of multiple failure types and triggering scenarios.
- A new model for analyzing slope stability against rotational failures allows for efficient, regional scale assessments
- Open-source mapping of built-up area is used to identify elements at risk

Graphical abstract

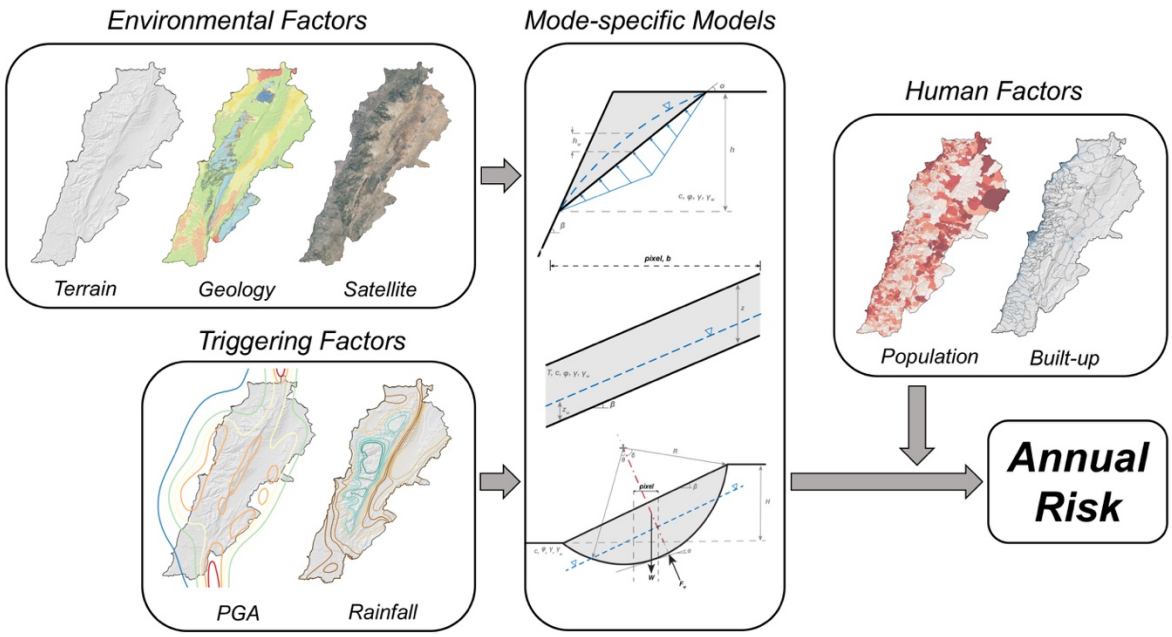

A5.1.1 Quantitative landslide risk model description

A5.1.1.1 Modes of failure

Traditional large-scale landslide hazard and risk analyses rely on the simplistic infinite slope method to capture all modes of mass wasting. However, unique modes of mass wasting cause unique consequences to the human environment. Slow moving landslides tend to impact static infrastructure, especially extensive transportation networks, while rapid, localized flows pose greater risk to human lives. General infinite slope assumptions miss nuanced consequences of unique modes of movement. Hungr et al. (2014) revise the traditional Varnes classification of landslide types to describe 32 unique modes of sliding. After Grant et al. (2016), we simplify this classification to three modes of movement—1) shallow, planar soil slides; 2) rock falls; and 3) rotational, coherent slumps in soil and rock. We further differentiate between triggering factors: seismic shaking which produces short-runout, disrupted failures and rainfall which can lead to confined, long runout debris flows. Statistical studies have found a correlation between slope and landslide mode (e.g. Keefer, 2013; Wartman et al., 2013). We divide the terrain into slope-based zones susceptible to each failure mode based on previous work and existing landslide inventories in Lebanon (Abdallah and Faour, 2017; Grant et al., 2016). Slopes from 15 – 50° are assumed to be prone to shallow, planar slides. Terrain prone to rotational slumps was expanded from 20 – 35° (Grant et al., 2016) to 15 – 35° based on observed slumps in Lebanon (e.g. Khawlie and Hassanain, 1984a). Rock falls were limited to slopes steeper than 35°. Slopes shallower than 15° were not considered likely to fail in any landslide mode (Marc et al., *under review*; Tanyas et al., 2017).

A5.1.1.2 Multimodal hazard model

We adopt the pixel-based, multimodal coseismic landslide hazard method of Grant et al. (2016) and present a parallel set of mode-specific models for rainfall-induced landslides. Simple, physics-based models are used to calculate the factor of safety (FS) against shallow, disrupted slides; rock fall; and rotational, coherent slumps. The model for coseismic rotational slumps was expanded to three dimensions (see formulation of precipitation-induced slump model below). We use the simplified Newmark-sliding block method (Jibson et al., 2000) to convert static FS values into the expected cumulative displacement of a landslide body caused by peak ground accelerations from a probabilistic seismic hazard analysis (PSHA). Failure was anticipated at coseismic displacements of 5 cm, 5 cm, and 15 cm for disrupted slides, rock fall, and coherent failures, respectively, after Grant et al. (2016).

The initiation of debris flows was assessed using the shallow landslide model SHALSTAB (Montgomery and Dietrich, 1998), which couples hydrologic and limit-equilibrium slope

stability models to compute the critical daily rainfall to trigger a shallow soil failure (**Figure A5.1.1)**:

$$Q_{cr} = \frac{T \sin\beta}{\left(\frac{a}{b}\right)}\left[\frac{c'}{\gamma_w z cos^2\beta tan\varphi} + \frac{\gamma}{\gamma_w}\left(1 - \frac{tan\,\beta}{tan\,\varphi}\right)\right] \qquad \textbf{(A5.1.1)}$$

where Q_{cr} is the critical rainfall [mm/d], T is the transmissivity of soil [m^2/d], a is the catchment area [m^2], b is the pixel width [m], β is the slope angle [rad], φ is the friction angle [rad], γ_w is the unit weight of water [kg/m^3], γ is the unit weight of soil [kg/m^3], z is the soil thickness [m], and c' is the effective cohesion including the contribution of vegetation [kN/m^2]. We assumed a failure plane thickness of z = 1 m, common to many shallow landslide studies (Ho et al. 2012; Montgomery and Dietrich, 1994; Montgomery et al., 2000). Adjacent failing cells were combined in a GIS environment to identify the spatial extent and volume of individual debris flow sources. These were classified by volume as low, medium, and high magnitude corresponding to failures of < 800 m^3, 800 – 2000 m^3, and > 2000 m^3, respectively, after Corominas (2003).

Rainfall-induced rock falls are modeled as simple Culman wedge-like masses (Duncan et al., 2014) including the effects of pore-pressure acting on the failure plane (**Figure A5.1.2**):

$$FS = \frac{2c \sin\beta}{\gamma h \sin(\beta-\alpha)\sin\alpha} + \frac{\tan\varphi}{\tan\alpha} - \frac{h_w\gamma_w \sin\beta \tan\varphi}{2h\gamma \sin(\beta-\alpha)\sin\alpha} \qquad \textbf{(A5.1.2)}$$

where FS is the factor of safety of the rock wedge, γ is the unit weight of rock [kN/m^3], h is the height of rock face [m], β is the slope angle [rad], φ is the friction angle [rad], γ_w is the unit weight of water [kN/m^3], h_w is the height of water [m], and c is the cohesion [kN/m^2], and α is the critical failure plane angle [rad] given by $\alpha = \left(\frac{\beta+\varphi}{2}\right)$.

To analyze the occurrence of rotational slumps, Grant et al. (2016) developed a uniform idealized failure surface that combines larger hillslope conditions with individual pixel properties such as cohesion and friction angle. However, the factor of safety equation was undefined for slopes < 20° and produced extreme failure geometries at the high and low extremes of the susceptible slope ranges. We modify the procedure of Grant et al. (2016) by adding a flexible failure depth parameter, p, to create realistic failure geometries at slopes of 15 - 35° in which rotational failures are commonly observed (Booth et al., 2013; Konsoer and Kite, 2014; Zezere et al., 2005; **Figure A5.1.3**). To account for wet conditions, the water pore pressure was added to the factor of safety equation, based on a slope-parallel ground water table at a percentage of the maximum failure depth. In addition, we project the radius of failure, R [m], perpendicular to the slope to create three-dimensional geometry:

$$FS = \frac{2\pi Rbc + (W\cos\alpha - F_w)\tan\varphi}{W\sin\alpha} \qquad \textbf{(A5.1.3)}$$

where c and φ are the cohesion [kPa] and friction angle [rad] of the soil mass, and α is the basal angle [rad] given by $\alpha = \sin^{-1}\frac{(4(\sin\delta)^3\sin\theta)}{3(2\delta-\sin 2\delta)}$. The weight of the sliding block, W, is

$$W = \frac{\pi\gamma b^2}{3}(3R - b) \qquad \textbf{(A5.1.4)}$$

and the resultant force of pore water pressure, F_w, is

$$F_w = \frac{1}{3}\pi\gamma_w q^2(3R - q) \qquad \textbf{(A5.1.5)}$$

Where b and q are defined as $b = R(1 - \cos\delta)$ and $q = R(1 - \cos\theta)$. The radius of failure is a function of local relief, $R = \frac{H}{4}\left(\frac{\cos\beta}{p(\sin\beta)^2} + \frac{p}{\cos\beta}\right)$ where H is local hillslope relief [m] and p is a depth factor empirically fixed at 1.0 to produce the minimum factor of safety in most cases for our study area. The internal angle, δ, is computed as $\delta = \sin^{-1}\frac{H}{2R\sin\beta}$ [rad] for slopes $15° \leq \beta \leq 35°$, and θ is determined by the level of saturation. The local hillslope relief was determined by a 23 m moving window, selected to capture the major topographical features of our study area.

A5.1.1.3 Strength parameters

Rock and soil parameters were based on mapped geologic units (Dubetret, 1945) and adjusted from those estimated by Grant et al. (2016) based on field observations of rainfall-induced slope failures (**Table A5.1.1**). Observed coherent failures occurred in a mixture of soil and rock. However, since the coherent rotational model assumes a homogeneous failing mass, single mid-range values of cohesion and friction angle were estimated. Values of friction angle in the debris flow triggering model were increased to 45, 50, and 55° to account for the cohesionless soil assumption in the SHALSTAB model, based on consultation with geotechnical practitioners in Lebanon (Montgomery and Dietrich, 1994). Soil transmissivity was coarsely estimated from the hydraulic conductivity in different geologic units (**Table A5.1.1**). The unit weights of soil and rock were assigned to be 20 kN/m^3 and 23 kN/m^3 respectively.

The presence and type of vegetation influences the location of shallow precipitation-induced landslides, primarily through its contribution to effective soil cohesion through a root network (Montgomery et al., 1998). Grant et al. (2016) observed a clear relationship between shallow coseismic landslide occurrence and the relative normalized difference in vegetation index (NDVI). Root cohesion was accounted for in the initiation of shallow failures based on the NDVI. In moderately and highly vegetated areas (NDVI 0.1 – 0.4 and > 0.4) we adopted

conservative values of 3 and 5 kPa respectively, based on the root cohesion contributed by shrubs and trees similar to that in our study area of Lebanon (Schmidt et al., 2001).

A5.1.1.4 Triggering events.

Huijer (2010) modeled the major seismic sources in Lebanon, producing contour maps of peak ground acceleration (PGA) with a 10% exceedance probability in 50, 100, and 500 years. We adopt model 2a which includes the four major faults as well as a Lebanon region areal source and is the most realistic the five models presented (Huijer, 2010; **Figure A5.1.4**).

Rainfall-induced buildup of groundwater pressure is the leading cause of damaging landslides worldwide (Petley, 2012). Rainfall time-scales significantly control the mode of slope failure. Debris flow and shallow landslide triggering has been observed on short times scales (minute - day) after intense rainfall (e.g. Chleborad et al., 2006; Peruccacci et al., 2017) whereas deep-seated, rotational slumps are controlled by antecedent rainfall and seasonality (Zezere et al., 2005). In turn, rainfall-induced shallow landslide triggering can be reasonably predicted using process- or empirically-based models using short term rainfall data (Guzzetti et al., 2007). However, hillslope response to antecedent rainfall involves extensive information about soil conditions at depth and complex, time-step infiltration models, making processed based prediction of rainfall-induced deep-seated landslides non-trivial at any scale.

Due to its 15-year civil war (1975 – 1990), Lebanon lacks long-term pluviometric data (Abdallah et al., 2005). In order to incorporate the geomorphic response to short- and long-term rainfall during major-return period storms while maintaining computational practicality, we combine continuous annual and localized daily rainfall measurements from Lebanon and from this estimate percent saturation of hillslopes. A map of annual average rainfall (Plassard, 1971, **Figure A5.1.4**) and point data of maximum daily rainfall from eight weather stations within Lebanon were used estimate the hydrologic inputs for each mode of failure. The weather station data was overlaid on the pluviometric zones and was linearly scaled by the average annual rainfall depths, creating a geographically continuous map of scaled "daily" rainfall for 2, 3, 5, 10, 20, 50, and 100-year return-period events (**Table A5.1.2**). As a first order estimation of the percent of hillslope saturation, we adopt a maximum 70% saturation and then linearly scaled saturation levels by the combined short- and long-term precipitation for each return period and pluviometric zone (**Table A5.1.3**).

A5.1.1.5 Runout

Landslide runout, rather than the initial failure, is the primary source of landslide-related casualties, making the analysis of post-failure motion a key step in landslide risk analyses (McDougall, 2017). We adopt a runout analysis method which combines published empirical

relationships, informal inventories in Lebanon, and the experience of Lebanese practitioners appropriate for the large scale and scarce site-specific data of our study area. Under intense rainfall, debris flows can travel long distances in existing topographic channels. We extract flowlines from a 15 m digital elevation model to calculate the runout path from each debris flow source. In the absence of empirical volume – runout data in Lebanon, we limit each path to 750 m, based on an inventory of 69 relict debris flow tracks observed in Google Earth. For each track, we made basic measurements of elevation, source zone slope, runout height and length in a GIS environment. Elevation and slope were poor predictors of runout length (R^2 of 0.48 and 0.02, respectively); thus, we chose a conservative threshold of 750 m, capturing 80% of the mapped debris flows. While this is likely to overestimate the runout of an isolated debris flow, the densely channeled terrain of the Mount Lebanon and Anti-Lebanon Ranges directs high and low elevation debris flow sources into the same flow path, extending the effective runout zone. Where overlapping, the runout path grids for lower magnitude debris flows were subtracted from the higher magnitudes, since the greatest damage will be done by the highest magnitude debris flow which crosses each pixel. If a pixel is both a debris flow source zone and in the runout path of an upslope debris flow, only the runout was considered in the risk equation for that pixel as the more damaging of the two hazard processes. Coseismic and precipitation-induced rock fall runout zones were calculated using a viewshed analysis from each initiation point. The horizontal extent of the rock fall zone was limited by the maximum and minimum aspect of the source cliff face plus 17 degrees based on observed lateral dispersion angles (Asteriou and Tsiambaos, 2016; Crosta and Agliardi, 2004; Lan et al., 2010). We limit runout based on the "angle of reach" (Corominas, 1996) of rock fall observed in Google Earth and during our field campaign in Lebanon, up to a maximum horizontal displacement of 265 m. The reach angles for small (less than 1000 m^3) and large (greater than 1000 m^3) rock fall were 42° and 34°, respectively, comparable to global observations (Corominas, 2003; Jaboyedoff and Labiouse, 2011). The influence of coherent slumping failures was limited to the radius of the failing body, projected as a circular zone in a GIS environment.

A5.1.1.6 Multimodal hazard output

A landslide hazard map was produced for each mode and triggering scenario (**Figure A5.1.5**). Our analysis found high debris flow hazard along the steeply-incised river valleys of the Mount Lebanon Range as well as in the northern Anti-Lebanon range where there is little vegetation to inhibit erosion. Coseismic disrupted slides were limited to isolated, sparsely-vegetated zones in the upper reaches of Mount Lebanon's river valleys and near Hamat. Coseismic and rainfall-induced rock fall shared similar extents, primarily limited to the exposed cliff bands in the Sannine and Keserouane formations of Western Lebanon. Extensive coseismic rock fall is also predicted in the steep valleys of the southern Litani River near the Yammouneh fault. Coherent failures are infrequent and concentrated in Mount Lebanon's weak sandstone. We undertook two field campaigns 2015 – 2017 to qualitatively assess the results of the multimodal hazard

model. These included both a broad reconnaissance across the region as well as detailed assessments at 59 sites. In general, the model correctly identified terrain susceptible to different modes of failure (**Figure A5.1.6**). However, few of the landslide deposits observed in the field were associated with a triggering event, so we could not assess the frequency component of the multimodal hazard model.

A5.1.1.7 Elements at risk

Although conceptually simple, mapping elements at risk on a country-scale presents a practical challenge in the amount and detail of information which must be collected in the ever-developing human-built environment. Due to the high resource demands of collecting this data on a regional scale, open, accurate, and high-resolution population and infrastructure data is scarce (Pesaresi et al., 2016). Recent advances in remote sensing have expanded the range of high resolution, satellite-derived data (e.g. landcover) with immediate benefit to the fields of urban planning, humanitarian aid, global development, etc. (Burke and Lobell, 2017; Corbane et al., 2016; Pesaresi et al., 2013). Human presence for risk analyses is evaluated through imagery-based mapping of human infrastructure, typically building stock, inventories of building location and footprint, or built-up presence, a binary map of made-made surfaces identified by textural features rather than spectral signature (Ehrlich and Tenerelli, 2013; Pesaresi, 2000). In disaster risk management, building stock data has the advantage of identifying individual structures at risk and associating them with unique attributes such as material, height, physical vulnerability, or number of residents. However, developing such inventories is costly and time-consuming, infeasible at greater than city scale (Ehrlich et al., 2010). Although built-up area does not allow for delineation of individual elements at risk, it does provide the location, extent, and density of human settlement in an automated, and consistent fashion, which makes it practical tool for risk analyses when large areas or rapid assessments are needed, such as in crisis management or tracking transient displaced peoples (Ehrlich et al., 2010; Pesaresi et al., 2013). We utilize binary grids produced by the Global Human Settlement Layer which assess the build-up presence (1 = yes, 0 = no) at 38m pixel resolution using Landsat Imagery collected from 2013-2014 (Pesaresi et al., 2015; **Figure A5.1.7**). Rather than identifying individual buildings at risk, we adopt the built-up grid as areas throughout which human activity is distributed. As only one epoch of built up area is available during the span of the Syrian crisis, we are unable to assess the impacts of the refugee influx on infrastructure expansion in Lebanon. We resampled built-up grids to 15 m and subtracted the Lebanese road network gridded from Open Street Map data (© Open Street Map, accessed 25 July 2017) to produce separate grids of residential area and road network. In this work, we do not differentiate between commercial and residential area.

The UNHCR has documented the Syrian refugee population in Lebanon since the outset of the Syrian crisis in 2011. In support of their aid distribution activities, the UNHCR published a map series showing the registered Syrian refugee population by cadastre on a bimonthly basis from

2013 – 2016 with infrequent updates 2017 - 2018. We digitized this map series on three-month intervals to assess the evolving refugee population in Lebanon from 2013 – 2018. On the UNHCR maps, population is given both as discrete numerical values and on a binned color scale. Where numerical values are absent for individual cadastres, the minimum population indicated by the background color was used, resulting in an underestimation of the national registered Syrian refugee population of about 5%. This unaccounted-for minority of registered Syrian refugees adds to the approximately 500,000 unregistered Syrian refugee population for which there is no spatial distribution data, representing a significant, unavoidable source of non-conservativism in our risk analysis, especially since the forces which dissuade refugees from registering with the UNHCR also promote marginalization and consequently higher vulnerability (Janmyr and Mourad, 2018; Thorleifsson, 2016).

In the absence of a national census since 1932, the United Nations Statistics Division's Population Prospects has been the most accurate source of population data in Lebanon. Prior to the outbreak of the Syrian crisis, Lebanon's population was predicted to increase by ~150,000 from 2013 – 2018 (UN, 2011). To support their work identifying vulnerable Lebanese, the UNHCR used the UN population projections to estimate the distribution of the native Lebanese population by cadastre in 2015. We adopt these values as the static, native Lebanese population from 2013 - 2018, acknowledging that this is an approximation. Since most cadastres are small (~6 km^2), containing a single urban cluster, we assume a constant population density within each cadastre, uniformly distributing the number of Lebanese and Urban Syrian refugees among the built-up pixels, resulting in 15 m gridded populations.

Built-up area maps of Lebanon have not been produced at sufficient temporal resolution to track the transience of informal tented settlements (ITS) in Lebanon or spatial resolution to resolve small settlements. However, the UNHCR and its partners have performed periodic, country-wide inventories to identify the coordinate location, number of tents, and population of ITS in Lebanon since 2013 in order to provide targeted humanitarian aid. We have access to ten ITS inventories from February 2014 – December 2017. To convert point coordinates to areal settlement extents, we apply a buffer of 10 m to every settlement of ten or fewer tents, increasing the buffer by 1 m for every tent in a settlement beyond ten. This guarantees that every settlement will be represented by at least one 15 m pixel and most or all of the settlement will be enclosed within the buffered zone. ITS zones were then rasterized at 15 m resolution (**Figure A5.1.7b**). The density and layout of informal settlements varies widely across Lebanon, influencing the accuracy of our ITS buffering method. Dense, elongate camps are more likely to be surrounded by a wide buffer of unoccupied area zoned as encamped, while sparse, blocky camps are more likely to have internal areas not occupied by tents but still within an ITS zone. To minimize inflation of risk by over-zoning encamped areas, we calculate human exposure on a per-camp basis. Since unoccupied areas within and around camps are included, the byproduct is an

implicit assumption that encamped refugees spend significant time outdoors in the vicinity of the ITS.

A5.1.1.8 Exposure

The human exposure within a buffered settlement is the area occupied by individuals divided by the total area of the settlement. Limited data is available on the shelter density of refugees in Lebanon, but the UNHCR estimates that 53% of households in ITS are overcrowded at less than 4.5 m^2 per person based on systematic interviews (UNHCR, 2017). Thus, the exposure within an ITS is:

$$E_{(ITS)} = \frac{4.5P}{A_{(ITS)}} \qquad \textbf{(A5.1.6)}$$

where P, is the population of the settlement and $A_{(ITS)}$ is the area of the buffered settlement [m]. The exposure of urban populations was estimated based on average building size and the expected zone of influence for each hazard mode (**Table A5.1.4**). We assumed an average building height of 3 floors based on a review of 164 for-sale residences across Lebanon as of 20 Dec. 2017 (Remax, 2017). Source zones of shallow failures were assumed to affect the entire bottom floor of a building through undercutting and scour. As channelized failures, debris flows were assumed to affect only 20% of the lowest floor of a building. Due to their size and depth, coherent failures affect the entire building. Fragmentation and spread of rock fall debris were not accounted for in the runout zonation; therefore we assume that only 10% the built-up pixels in a runout zone will actually be impacted by significant debris, and that, due to bouncing, debris will affect 20% of the lowest two floors of a building. Human occupants are assumed to spend equal time in all parts of a home, resulting in exposure values less than one.

A5.1.1.9 Vulnerability

At a minimum, vulnerability is a function of the type of hazard, its magnitude, and physical characteristics of the element at risk. For buildings this may include construction material, orientation, number of windows, height, etc. For humans, vulnerability includes a host of predisposing factors to physical injury, such age, health, gender, and mobility, as well as less intuitive intangibles: economic station, language, food security, educational level, etc. For this reason, virtually all assessments of human vulnerability to landslides have been subjective, based on expert judgement and a limited set of fatal landslide inventories (Lee and Jones, 2014). Data on landslide fatalities in Lebanon is scarce and does not include qualitative information on landslide magnitude, preventing the estimation of region-specific human vulnerability values (Table S5). Therefore, we follow existing literature to estimate the physical vulnerability of the urban (Lebanese and Syrian) and encamped populations in Lebanon (**Table A5.1.4**). Vulnerability of urban Lebanese and Syrians was assessed as that of indoor populations based on

fatal landslide incidents in Hong Kong and Australia (Lee and Jones, 2014; Michael-Leiba et al., 2004). Due to the temporary materials and irregular construction of ITS, encamped residents are assessed vulnerability values consistent with an outdoor population, although we note that the quality and protection of ITSs varies widely (Sanyal, 2017). Vulnerability to debris flow runout was assessed at an order of magnitude higher than that of hillslope source zones, due to greater channelization and velocity, after Michael-Leiba et al. (2004). Coherent failures generally develop slowly allowing residents to evacuate; thus, a nominal human vulnerability of 0.0001 was adopted.

A5.1.2 Data tables and figures

Table A5.1.1. Geologic units and geotechnical parameters used in this study. Geologic mapping after Dubetret (1945).

Age	Formation	Geologic Unit	Rock-slope failures		Coherent rotational slumps		Disrupted soil slides	
			Cohesion	Phi	Cohesion	Phi	Cohesion	Phi
Quaternary	Quaternary	*qd, qm*	20	20	20	20	20	20
	Heterogeneous	*ql, qs, qta, qaoi*	20	30	20	30	20	30
	Deposits	*q, qcg, ql1*	20	25	20	25	20	25
		qar	20	18	20	18	20	18
		a, ad	15	33	15	33	15	33
		Alluvium	15	33	15	33	15	33
		gravel slopes	15	33	15	33	15	33
		Alluvial fans	15	33	15	33	15	33
		Silt and mud	15	33	15	33	15	33
		Rocky	25	33	25	33	25	33
		Fill	15	33	15	33	15	33
		Scree	25	33	25	33	25	33
	Quaternary Basalt	*qb*	20	20	20	20	26	24
Neogene	Misc. Miocene units	*m*	48	21	48	21	32	25
		m2, m2a, m2b	55	25	55	25	35	22
		mcg, ml, ml1	48	21	48	21	14	26
	Misc. Pliocene Units	*p*	57	25	57	25	67	22
		p1	62	32	62	32	57	26
	Misc. Neogene Units	*n2, n*	58	30	58	30	62	25
		ncg	62	32	62	32	57	26
	Neogene Basalt	*bp, bp1-2, bp3*	62	27	62	27	27	30
		bn	52	24	52	24	26	24
Paleogene	Numilitic Eocene Formation	*e2, e2a*	42	18	44	21	18	21
		e2b	44	20	44	21	24	20
Cretaceous	Chouf Sandstone	*c1, c1-2, c1-2a, c2*	48	21	33	21	18	21
	Abieh Formation	*c2a*	45	20	45	20	47	20
	Mdairej Formation	*c2b*	68	33	77	34	35	25
	Hammana Formation	*c3, c3b, c3-4*	48	21	48	21	17	21
	Sannine Formation	*c4, c4-5*	59	24	45	22	34	18
	Maameltain Formation	*c5*	59	24	59	24	35	25
	Chekka Formation	*c6*	48	21	33	20	18	21
	Cretaceous Basalt	*bc, bc1, bc2a, bc2b, Bc*	56	27	56	27	13	24

Jurassic	Chouane Formation	*j1-3, j2, j3, j*	61	26	61	26	53	28
	Keserouane Formation	*j4, j6*	61	26	61	26	35	20
	Bikkfaya Formation	*j6a*	84	38	84	38	113	34
	Salima Formation	*j7*	45	21	45	21	35	20
	Jurassic Basalt	*bj, bj6, bj5*	52	24	18	24	13	24

Table A5.1.2. Scaled daily rainfall in each pluviometric zone.

Mean Annual Rainfall (mm/yr)	Return Period (yr) 2	3	5	10	20	50	100
	Scaled Daily Rainfall (mm/day)						
100	60	69	78	89	98	108	114
200	60	69	79	92	104	120	133
300	59	69	80	94	110	132	152
400	58	68	80	97	116	145	171
500	57	68	81	100	122	157	190
600	56	67	82	103	128	169	209
700	55	67	82	106	134	182	228
800	54	67	83	109	140	194	247
900	53	66	83	111	147	206	266
1000	52	66	84	114	153	219	285
1100	51	65	85	117	159	231	304
1200	50	65	85	120	165	243	323
1300	49	65	86	123	171	256	342
1400	48	64	87	126	177	268	361

Table A5.1.3. Hillslope saturation in each pluviometric zone.

Mean Annual Rainfall (mm/yr)	Return Period (yr) 2	3	5	10	20	50	100
	Saturation (%)						
100	12	13	15	17	19	21	22
200	12	13	15	18	20	23	26
300	11	13	15	18	21	26	29
400	11	13	16	19	22	28	33
500	11	13	16	19	24	30	37
600	11	13	16	20	25	33	41
700	11	13	16	21	26	35	44
800	10	13	16	21	27	38	48
900	10	13	16	22	28	40	52
1000	10	13	16	22	30	42	55
1100	10	13	16	23	31	45	59
1200	10	13	17	23	32	47	63
1300	9	13	17	24	33	50	66
1400	9	12	17	24	34	52	70

Table A5.1.4. Exposure and vulnerability estimates based on average building size and literature.

Hazard	**Magnitude**	**Zone**	**Exposure** (urban)	**Vulnerability** (urban)	**Vulnerability** (encamped)
Debris Flow/	High	Runout	0.067	0.050	1.00
Disrupted		Source	0.333	0.005	0.10
	Medium	Runout	0.067	0.025	0.30
		Source	0.333	0.0025	0.03
	Low	Runout	0.067	0.010	0.10
		Source	0.333	0.001	0.01
Coherent			1.000	0.0001	0.0001
Rock fall			0.013	0.050	0.50

Table A5.1.5. Inventory of fatal and significant non-fatal landslides in Lebanon.

Fatal Landslide Events in Lebanon 1975 – 2015					
Date	Event	Location	Deaths	Description	Source
Feb. 1975	landslide	Faraiya, Mount Lebanon	5	Damaged electric and communication network; $5M in losses	Abdallah (2007)
12 Mar. 1983	avalanche	Bcharre, North	1	Destroyed orchard	www.desinventar.net
Dec. 1983	landslide	Bekaa	20		www.emdat.be
1984	landslides / avalanches	North, Mount Lebanon, Baalbek-Hermel	90	Extensive damage to infrastructure; $68 M in losses	Abdallah (2007)
09 Feb. 1992	landslide	Beirut	1	Building collapsed, 2 injured	www.desinventar.net
18 Mar. 1992	landslide	Hazerta, Bekaa	20	Several houses buried	Abdallah (2010)
07 Feb. 1997	landslide	Mansourieh, Mount Lebanon	2	One house destroyed	www.desinventar.net
09 Oct. 2004	landslides	Ehden, North	2	6 injured	www.desinventar.net
07 Feb. 2005	avalanche / rock fall	Bcharre, North	1	Deceased was a Syrian worker; house destroyed	www.desinventar.net
05 Jan. 2013	landslide	Beirut	1	A child died when he and his mother were carried away by a bluff collapse	english.al-akhbar.com/node/14602
18 Sept. 2013	landslide	Karak, Bekaa	1	Deceased was a Syrian worker; 4 injured; landslide in a construction site	www.nna-leb.gov.lb/en/show-news/14119/Landslide-kills-one-Syrian-injures-four-in-Zahle
13 Mar. 2014	rock fall	Roumieh, Mount Lebanon	1	3 injured; rock fall into a construction site	data.nasa.gov/Earth-Science/Global-Landslide-Catalog/h9d8-neg4/data
27 Mar. 2014	landslide	Kfar Tebnit, Nabatiyeh	1	Deceased was a Syrian worker; 6 injured	www.lbcgroup.tv/news/d/lebanon-news/147134/one-killed-6-others-injured-in-kfartibnit-landslid/en
Other significant events					
09 July 551	rotational slumps	Chekka, Mount Lebanon		Triggered by M 7.5 Beirut-Tripoli earthquake	Abdallah (2007)
20 May 1202	rock falls	Mount Lebanon	200	Triggered by M 7.5 earthquake in the Bekaa Valley	Daeron et al. (2005)
18 Jan. 1767, 30 Nov. 2015	landslide / rock fall	Kfar Nabrakh, Mount Lebanon		1767: numerous deaths, major property damage 2015: 17 houses evacuated	El Mohtar et al. (2016)
1860-1983	many	Hammana, Mount Lebanon		Perennially unstable region; failures triggered by earthquakes in 1924 and 1956	Khawlie and Hassanain (1984b)
16 Feb. 2000	landslide	Biaqout, Mount Lebanon		Destroyed three apartment buildings; 300 people evacuated	www.dailystar.com.lb/News/Lebanon-News/2000/Feb-17/27252-landslide-causes-buildings-to-collapse-after-rain-soaks-foundations.ashx
25 Mar. 2000	landslide	Aayoun Orghosh, Mount Lebanon		Destroyed 10 houses and several ski resorts	Abdallah (2010)
26 Mar. 2003	landslide	Cheikh Taba, Akkar		Destroyed an apartment building; $300,000 in losses	www.desinventar.net

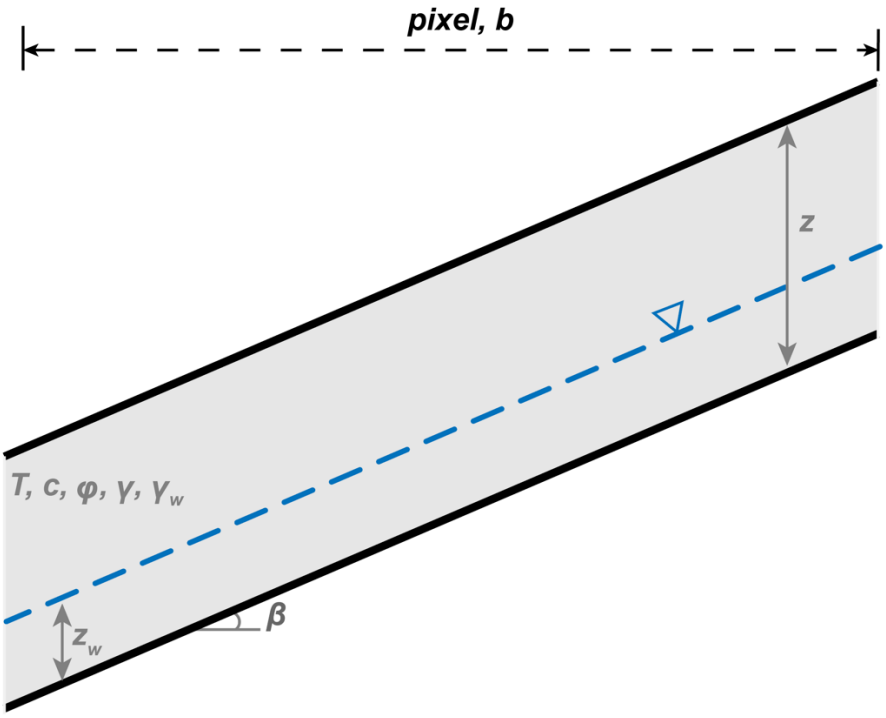

Figure A5.1.1. Geometry of debris flow initiation model.

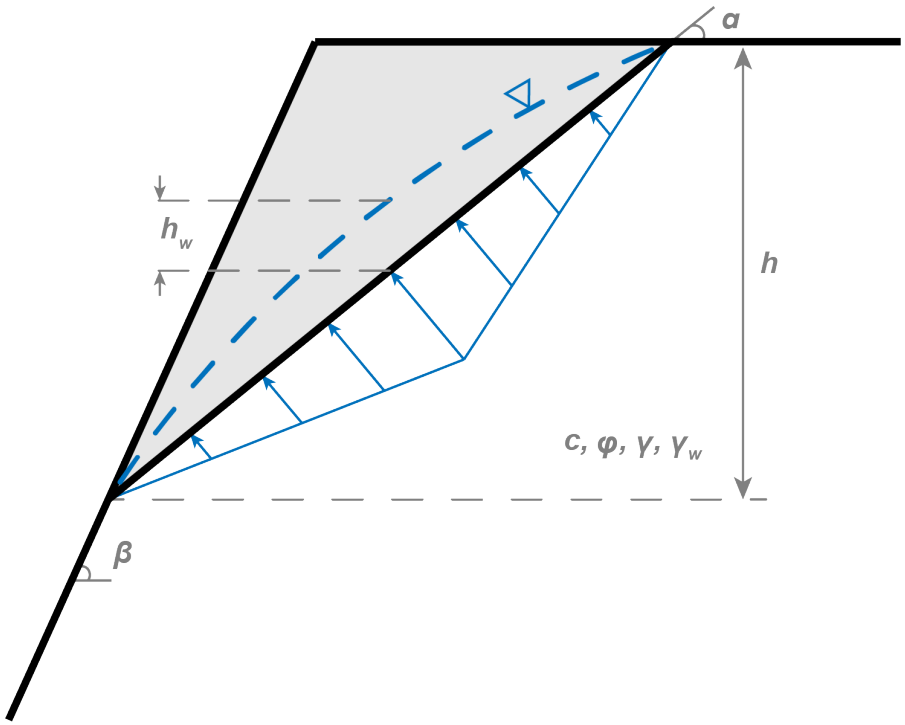

Figure A5.1.2. Geometry of precipitation-induced rock fall model.

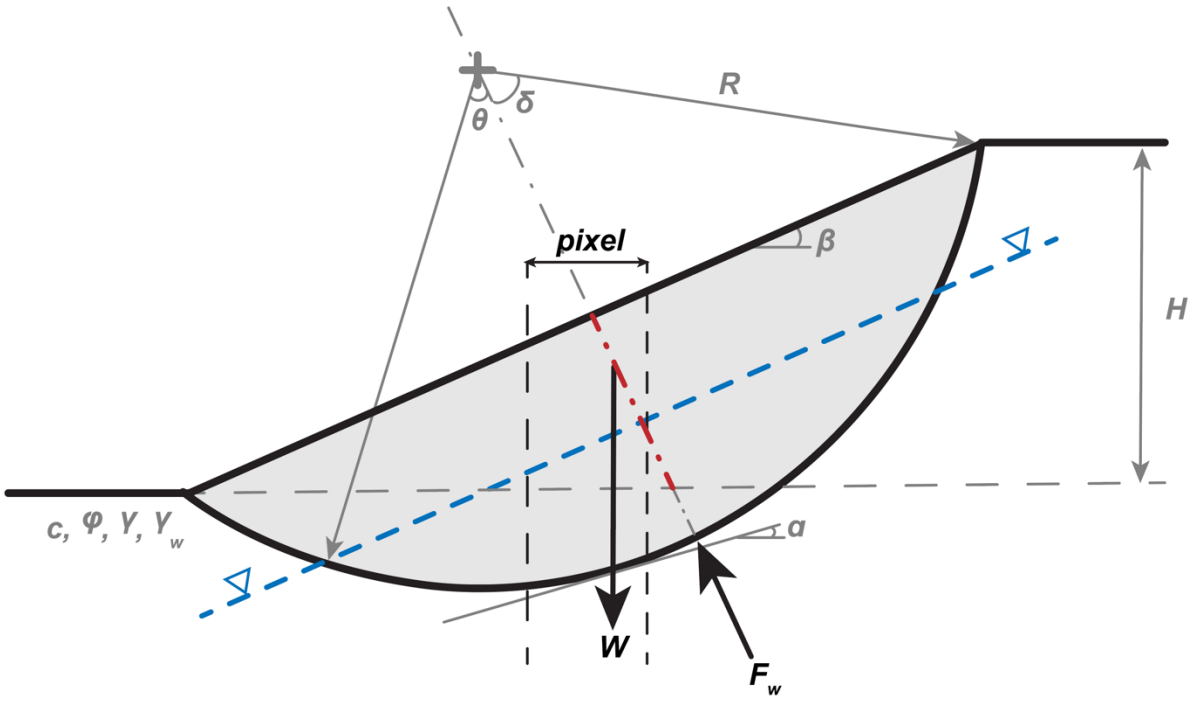

Figure A5.1.3. Geometry of rotational slump model. The depth of failure is determined as a percentage, *p*, of the perpendicular hillslope bisector segment in red. *p* may be greater than 100% (as shown).

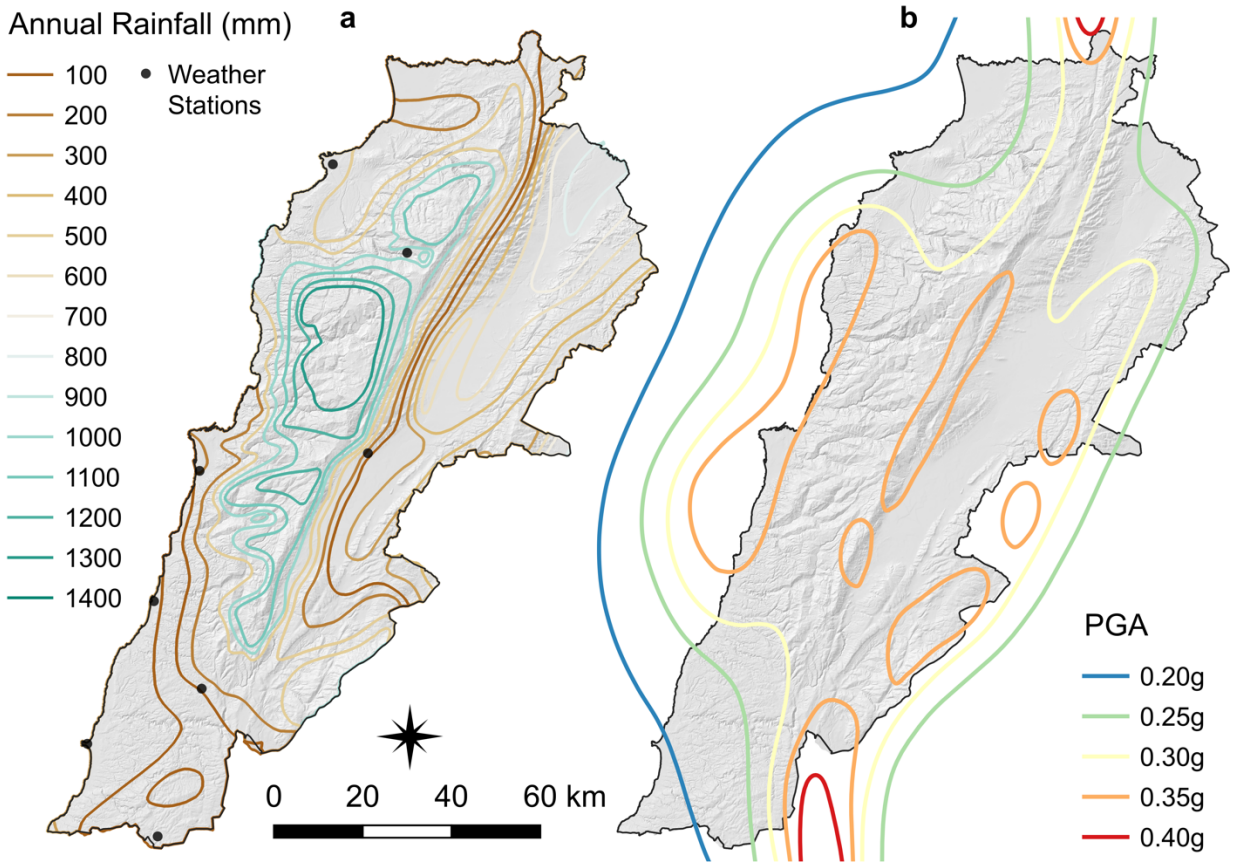

Figure A5.1.4. Multimodal landslide triggers. (*a*) Annual rainfall (Plassard, 1971) and (*b*) 949-year (10% in 100 years) return period PSHA ground shaking intensity contours (Huijer, 2010).

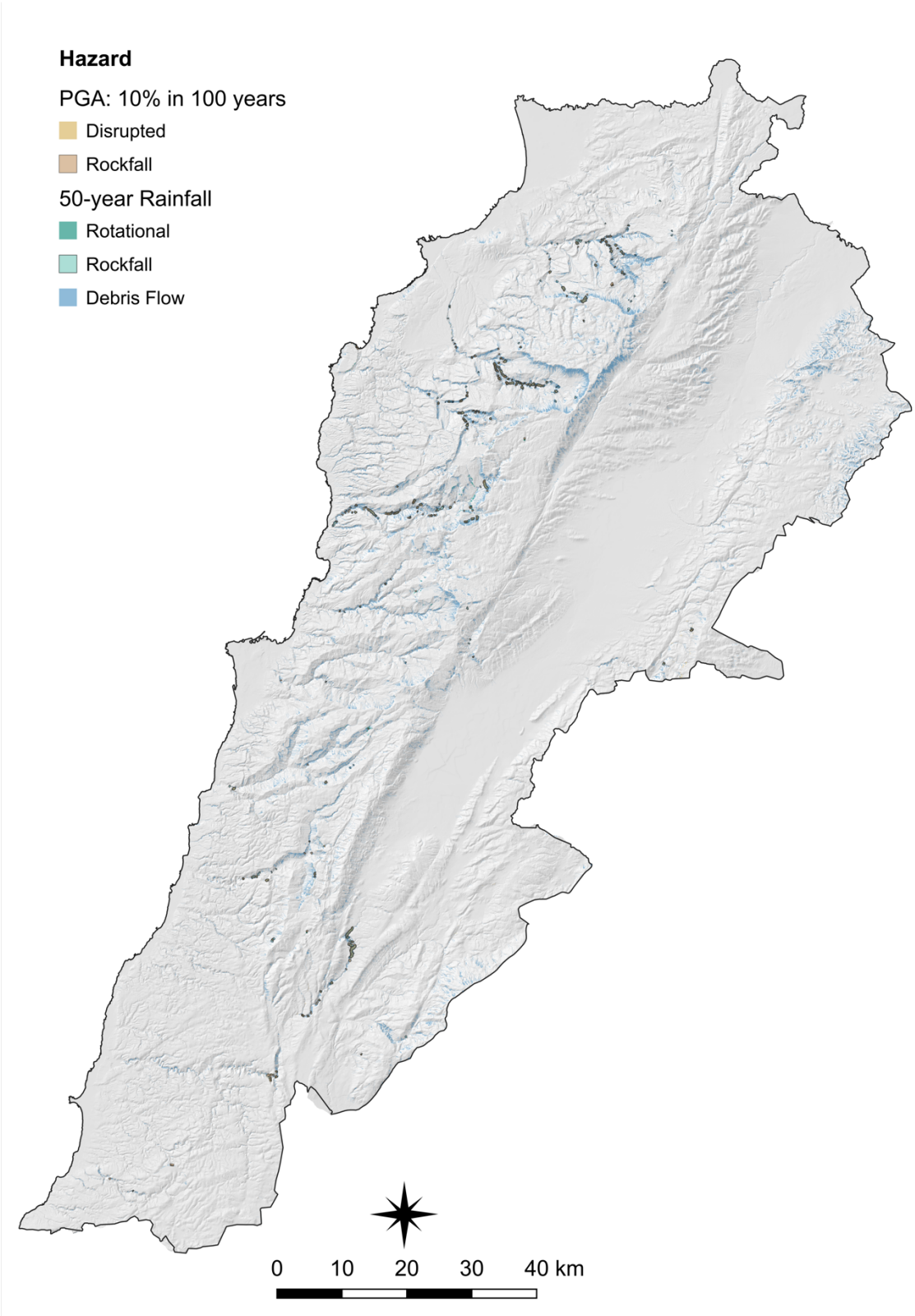

Figure A5.1.5: Multimodal landslide hazard output for 949-year (10% in 100 year) return period PSHA ground shaking intensities and for a 50-year rainfall.

Figure A5.1.6. Multimodal hazard model field observations. (*a*) Debris flow channels and a rock fall source zone above the towns of Aabra and Chouaneh, (*b*) A recent debris flow deposit in Hasroun, (*c*) A large rock fall above Ghabat. Rotational slumps were observed in the vicinity. Base images from Google Earth™.

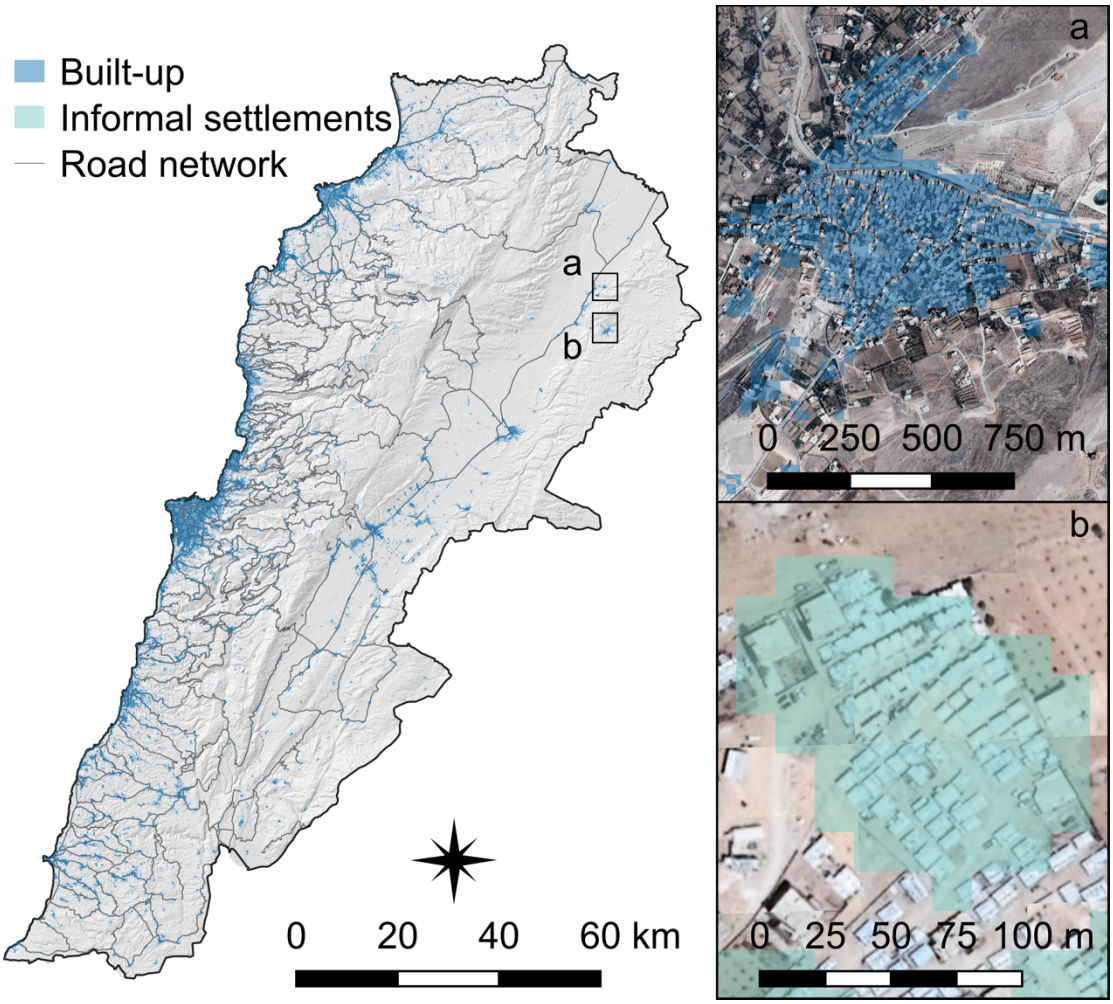

Figure A5.1.7. Elements at risk. (*a*) Built-up area in the city of Ras Baalbek. (*b*) Informal tented settlements on the outskirts of Arsal. Base images from Google Earth™.

References:

Abdallah, C. (2007). *Assessment of remote sensing and geographic information systems for the study of mass movements in Lebanon* (Doctoral dissertation). Paris: University of Pierre and Marie Curie

Abdallah, C. (2010). Spatial distribution of block falls using volumetric GIS-decision-tree models. *International Journal of Applied Earth Observation and Geoinformation*, 12(5), 393-403. https://doi.org/10.1016/j.jag.2010.05.008

Abdallah, C., Chorowicz, J., Bou Kheir, R., Khawlie, M. (2005). Detecting major terrain parameters relating to mass movement' occurrence using GIS, remote sensing and statistical correlations, case study Lebanon. *Remote Sens. Environ.*, 99, 448-461, https://doi.org/10.1016/j.rse.2005.09.014

Abdallah, C., Faour, G. (2017). Landslide hazard mapping of Ibrahim River Basin, Lebanon. *Nat. Hazards*, 85, 237-266, https://doi.org/10.1007/s11069-016-2560-1

Asteriou, P., Tsiambaos, G. (2016). Empirical model for predicting rockfall trajectory direction. *Rock Mech. Rock Eng.*, 49, 927-941, https://doi.org/10.1007/s00603-015-0798-7

Booth, A., Roering, J., Rempel, A. (2013). Topographic signatures and a general transport law for deep-seated landslides in a landscape evolution model. J. Geophys. Res. Earth Surf., 118, 603-624, https://doi.org/10.1002/jgrf.20051

Burke, M., Lobell, D. (2017). Satellite-based assessment of yield variation and its determinants in smallholder African systems. Proc. Natl. Acad. Sci. U.S.A., 114(9), 2189-2194, https://doi.org/10.1073/pnas.1616919114

Chleborad, A., Baum, R., Godt, J. (2006). Rainfall thresholds for forecasting landslides in the Seattle, Washington, area—exceedance and probability. USGS Open-File Report 2006-1064, USGS, Reston, VA

Corbane, C., Kemper, T., Freire, S., Louvrier, C., Pesaresi, M. (2016). Monitoring the Syrian humanitarian crisis with the JRC's global human settlement layer and night-time satellite data. EUR 27933, European Union, Luxembourg,

Coromias, J. (1996). The angle of reach as a mobility index for small and large landslides. *Can. Geotech. J.*, 33, 260-271, https://doi.org/10.1139/t96-005

Corominas, J., Copons, R., Vilaplana, J., Altimir, J., Amigo, J. (2003). Integrated landslide susceptibility analysis and hazard assessment in the principality of Andorra. *Nat. Hazards.*, 30, 421-435, https://doi.org/10.1023/B:NHAZ.0000007094.74878.d3

Crosta, G., Agliardi, F. (2004). Parametric evaluation of 3D dispersion of rockfall trajectories. *Nat. Hazards Earth Syst. Sci.*, 4, 583-598, https://doi.org/10.5194/nhess-4-583-2004

Daëron, M., Klinger, Y., Tapponnier, P., Elias, A., Jacques, E., Sursock, A. (2005). Sources of the large A.D. 1202 and 1759 Near East earthquakes. *Geology*, 33(7), 529-532. https://doi.org/10.1130/G21352.1

Dubertret, L. (1945). “Cartes geologiques a l’echelle de 1/50 000 (Hamidieh, Halba, Batroun, Tripoli, Sir El Dannieh, Jbail, Qartaba, Baalbeck, Beirut, Zahle, Rayak, Saida, Jezzine, Rachaya). Republique Libanaise, Ministere des Travaux Publics, Beirut

Duncan, J., Wright, S., Brandon, T. (2014). *Soil Strength and Slope Stability*. John Wiley & Sons, Hoboken

Ehrlich, D., Tenerelli, P. (2013). Optical satellite imagery for quantifying spatio-temporal dimension of physical exposure in disaster risk assessments. *Nat. Hazards*, 68, 1271-1289, https://doi.org/10.1007/s11069-012-0372-5

Ehrlich, D., Zeug, G., Gallego, J., Gerhardinger, A., Caravaggi, I., Pesaresi, M. (2010). Quantifying the building stock from optical high-resolution satellite imagery for assessing disaster risk. *Geocarto Int.*, 25(4), 281-293, https://doi.org/10.1080/10106040903521829

El Mohtar, C., Abou-Jaoude, G., Abdallah, C., Harb, J. (2016). The Kfarnabrakh landslide of November 30th, 2015 (Geotechnical Extreme Events Reconnaissance-047). Arlington: National Science Foundation

Grant, A., Wartman, J., Abou-Jaoude, G. (2016). Multimodal method for coseismic landslide hazard assessment. *Eng. Geol.*, 212, 146-160, https://doi.org/10.1016/j.enggeo.2016.08.005

Guzzetti, F., Peruccacci, S., Rossi, M., Stark, C. (2007). Rainfall thresholds for the initiation of landslides in central and southern Europe. *Meteorol. Atmos. Phys.*, 98, 239-267, https://doi.org/10.1007/s00703-007-0262-7

Ho, J., Lee, K., Chang, T., Wang, Z., Liao, Y. (2012). Influences of spatial distribution of soil thickness on shallow landslide prediction. *Eng. Geol.*, 124, 38-46, https://doi.org/10.1016/j.enggeo.2011.09.013

Huijer, C. (2010). Implications of the recent mapping of the offshore thrust fault system on the seismic hazard of Lebanon. M.S. thesis, American Univ. Beirut, Beirut

Hungr, O., Leroueil, S., Picarelli, L. (2014). The Varnes classification of landslide types, an update. *Landslides*., 11, 167-194, https://doi.org/10.1007/s10346-013-0436-y

Jaboyedoff, M., Labiouse, V. (2011). Technical note: preliminary estimation of rockfall runout zones. *Nat. Hazards Earth Syst. Sci.*, 11, 819-828, https://doi.org/10.5194/nhess-11-819-2011

Janmyr, M., Mourad, L. (2018). Modes of ordering: labelling, classification and categorization in Lebanon’s refugee response. *J. Refugee Studies*, fex042, https://doi.org/10.1093/jrs/fex042

Jibson, R., Harp, E., Michael, J. (2000). A method for producing digital probabilistic seismic landslide hazard maps. *Eng. Geol.*, 58, 271-289, https://doi.org/10.1016/S0013-7952(00)00039-9

Keefer, D. (2013). Landslides generated by earthquakes: immediate and long-term effects. In *Treatise on Geomorphology*, J. Shroder and L. Owen, (Eds.) Academic Press, San Diego, CA. vol 5, Tectonic Geomorphology, 250-266

Khawlie, M., Hassanain, H. (1984a). Engineering geology of the Hammana landslides, Lebanon. *Q. J. Eng. Geol.*, 17, 137-148, https://doi.org/10.1144/GSL.QJEG.1984.017.02.05

Khawlie, M., Hassanain, H. (1984b). Failure phenomena and environmental control of the relatively unstable Hammana area, Lebanon. *Eng. Geol.*, 20(3), 253-264, https://doi.org/10.1016/0013-7952(84)90005-X

Konsoer, K., Kite, J. (2014). Application of LiDAR and discriminant analysis to determine landscape characteristics for different types of slope failures in heavily vegetated, steep terrain: Horseshoe Run watershed, West Virginia. *Geomorphology*, 224, 192-202, https://doi.org/10.1016/j.geomorph.2014.06.030

Lan, H., Martin, C., Zhou, C., Lim, C. (2010). Rockfall hazard analysis using LiDAR and spatial modeling. *Geomorphology*, 118, 213-223, https://doi.org/10.1016/j.geomorph.2010.01.002

Lee, M., Jones, D. (2014). *Landslide Risk Assessment*. ICE, London

Marc, O., Stumpf, A., Malet, J., Gosset, M., Uchida, T., Chiang, S. (2018). Toward a global database of rainfall-induced landslide inventories: first insights from past and new events. *Earth Surf. Dyn. Discuss*. https://doi.org/10.5194/esurf-2018-20, *in review*

McDougall, S. (2016). 2014 Canadian geotechnical colloquium: landslide runout analysis—current practice and challenges. *Can. Geotech. J.*, 54, 605-620, https://doi.org/10.1139/cgj-2016-0104

Michael-Leiba, M., Baynes, F., Scott, G., Granger, K. (2004). Quantitative landslide risk assessment of Cairns, Australia. In *Landslide Hazard and Risk*, Glade, T., Anderson, M., and Crozier, M. (Eds.), John Wiley & Sons, Hoboken, pp 621-642

Montgomery, D., Dietrich, W. (1994). A physically based model for the topographic control on shallow landsliding. *Water Resour. Res.*, 30(4), 1153-1171, https://doi.org/10.1029/93WR02979

Montgomery, D., Schmidt, K., Greenberg, H., Dietrich, W. (2000). Forest clearing and regional landsliding. *Geology*, 28(4), 311-314, https://doi.org/10.1130/0091-7613(2000)28<311:FCARL>2.0.CO;2

Montgomery, D., Sullivan, K., Greenberg, H. (1998). Regional test of a model for shallow landsliding. *Hydrol. Processes*, 12, 943-955, https://doi.org/10.1002/(SICI)1099-1085(199805)12:6<943::AID-HYP664>3.0.CO;2-Z

Peruccacci, S., Bruneti, M., Gariano, S., Melillo, M., Rossi, M., Guzzetti, F. (2017). Rainfall thresholds for possible landslide occurrence in Italy. *Geomorphology*, 290, 39-57, https://doi.org/10.1016/j.geomorph.2017.03.031

Pesaresi, M. (2000). Texture analysis for urban pattern recognition using fine-resolution panchromatic satellite imagery. *Geog. Environ. Modelling*, 4(1), 43-63, https://doi.org/10.1080/136159300111360

Pesaresi, M., Ehrlich, D., Florczyk, A., Freire, S., Julea, A., Kemper, T., Soille, P., Syrris, V. (2015). GHS built-up grid, derived from Landsat, multitemporal (1975, 1990, 2000,

2014). European Commission, Joint Research Centre (JRC) [Dataset] PID: http://data.europa.eu/89h/jrc-ghsl-ghs_built_ldsmt_globe_r2015b

Pesaresi, M., Huadong, G., Blaes, X., Erlich, D., Ferri, S., Gueguen, L., Halkia, M., Kauffmann, M., Kemper, T., Lu, L., Marin-Herrera, M., Ouzounis, G., Scavazzon, M., Soille, P., Syrris, V., Zanchetta, L. (2013). A global human settlement layer from optical HR/VHR RS data: concept and first results. *IEEE J. Sel. Top. Appl. Earth Obs. Remote Sens.*, 6(5), 2102-2131, https://doi.org/10.1109/JSTARS.2013.2271445

Pesaresi, M., Melchiorri, M., Siragusa, A., Kemper, T. (2016). Atlas of the human planet 2016. EUR 28116, European Union, Luxembourg

Petley, D. (2012). Global patterns of loss of life from landslides. *Geology*, 40(10), 927-930, https://doi.org/10.1130/G33217.1

Plassard, J. (1971). Pluviometric map of Lebanon at a scale of 1:200,000. Govt. of Lebanon, Ministry of Public Works and Transport, Beirut

Remax. (2017). Homepage. http://www.remax.com.lb/, accessed 20 Dec. 2017

Sanyal, R. (2017). A no-camp policy: interrogating informal settlements in Lebanon. *Geoforum*, 84, 117-125, https://doi.org/10.1016/j.geoforum.2017.06.011

Schmidt, K., Roerring, J., Stock, J., Deitrich, W., Montgomery, D., Schaub, T. (2001). The variability of root cohesion as an influence on shallow landslide susceptibility in the Oregon Coast Range. *Can. Geotech. J.*, 38, 995-1024, https://doi.org/10.1139/t01-031

Tanyas, H., van Westen, C., Allstadt, K., Nowicki Jessee, M., Gorum, T., Jibson, R., Godt, J., Sato, H., Schmitt, R., Marc, O., and Hovius, N. (2017). Presentation and analysis of a worldwide database of earthquake-induced landslide inventories. *J. Geophys. Res. Earth Surf.*, 122, 1991-2015, https://doi.org/10.1002/2017JF004236

Thorleifsson, C. (2016). The limits of hospitality: coping strategies among displaced Syrians in Lebanon. *Third World Quarterly*, 37(6), 1071-1082, https://doi.org/10.1080/01436597.2016.1138843

UN. (2011). World population prospects: the 2010 revision. United Nations, Geneva

UNHCR. (2017). Vulnerability assessment of Syrian refugees in Lebanon: VASYR 2017. UNHCR, Geneva

Wartman, J., Dunham, L., Tiwari, B., Pradel, D. (2013). Landslides in eastern Honshu induced by the 2011 Tohoku earthquake. *Bull. Seismol. Soc. Am.*, 103(2B), 1503-1521, https://doi.org/10.1785/0120120128

Zezere, J., Trigo, R., Trigo, I. (2005). Shallow and deep landslides induced by rainfall in the Lisbon region (Portugal): assessment of relationships with the North Atlantic oscillation. *Nat. Hazards Earth Sys. Sci.*, 5, 331-344, https://doi.org/10.5194/nhess-5-331-2005